

**Cavitation Assisted and Enhanced Valveless Micropumping  
Integrated Optical Detection based Micro-Total Analysis  
System ( $\mu$ TAS): Design, Modeling, Fabrication and Testing**

ARVIND CHANDRASEKARAN

A Thesis

in

the Department

of

Mechanical and Industrial Engineering

Presented in partial fulfillment of the requirements for the  
Degree of Doctor of Philosophy (Mechanical Engineering) at  
Concordia University  
Montreal, Quebec, Canada

August 2011

**CONCORDIA UNIVERSITY**  
**SCHOOL OF GRADUATE STUDIES**

This is to certify that the thesis prepared

By: **Arvind Chandrasekaran**

Entitled: **Cavitation Assisted and Enhanced Valveless Micropumping Integrated Optical Detection based Micro-Total analysis System ( $\mu$ TAS): Design, Modeling, Fabrication and Testing**

and submitted in partial fulfillment of the requirements for the degree of

DOCTOR OF PHILOSOPHY (Mechanical Engineering)

complies with the regulations of the University and meets the accepted standards with respect to originality and quality.

Signed by the final examining committee:

\_\_\_\_\_ Chair  
Dr. A. Kishk

\_\_\_\_\_ External Examiner  
Dr. T. Thundat

\_\_\_\_\_ External to Program  
Dr. Z. Kabir

\_\_\_\_\_ Examiner  
Dr. R. Bhat

\_\_\_\_\_ Examiner  
Dr. R. Wuthrich

\_\_\_\_\_ Thesis Supervisor  
Dr. M. Packirisamy

Approved by \_\_\_\_\_  
Dr. W.-F. Xie, Graduate Program Director

August 8, 2011

\_\_\_\_\_  
Faculty of Engineering and Computer Science

# ***ABSTRACT***

## **Cavitation Assisted and Enhanced Valveless Micropumping Integrated Optical Detection based Micro-Total Analysis System ( $\mu$ TAS): Design, Modeling, Fabrication and Testing**

**Arvind Chandrasekaran, Ph.D.  
Concordia University, 2011**

This thesis presents the design, modeling, fabrication, and testing of an integrated Micro-Total Analysis System ( $\mu$ TAS) for carrying out high sensitive chemical and biomedical detections. The main components of this system are: Piezoelectric Actuated Valveless Micropump (PAVM) for fluid actuation, Microfluidic channels for the transportation of the fluid, and Optical detection platform that comprises of Absorption, Fluorescence and Evanescence based detection systems.

The PAVM works on the principle of flow rectification produced by a micronozzle/diffuser pair. In order to improve the efficiency of the valveless micropumping, a simple and microfabrication friendly geometrical tuning method is presented, which offers the user a broad range of dependent tunable geometric parameter to improve the performance the microdiffuser for valveless micropumps. The flow behavior and the variation of pressure coefficients of the microdiffuser/nozzle with geometric tuning have been studied for different flow conditions using Finite Element Modeling (FEM), and the experimental results show that the proposed method is highly suitable for enhancing the performance of valveless micropumps.

Many diffusers and nozzles of varying geometrical tuning parameters have been studied, fabricated and tested. Suitable operating zones for required flow behavior have been proposed through elaborate modeling and testing. The study also included the effect of frictional losses on the performance of the diffuser for valveless micropumping applications. It was interesting to note that straight tapered diffusers are not suitable for a wide range of operation of valveless micropumps.

The performance of the valveless micropump has been extensively studied through flow rate and pressure measurements under different actuation conditions, with water as the working fluid. The improvement in the micropump performance through geometric tuning of the diffuser has been verified. Experimental investigation of the effect of surface wettability on the performance of the micropump and bubble generation characteristics has also been carried out, and the results are presented.

This thesis identifies the important phenomenon of cavitation in micropumps, also explores in detail the different phases of cavitation along with its influence on the behavior of mechanically actuated valveless micropump. The development of cavitation in the micropumps is studied experimentally and through visualization of the fluid/bubble behavior inside the micropump chamber. The various stages of cavitation in micropumps have been identified and the variation of flow characteristics during each stage of cavitation is presented. The qualitative effect of cavitation on micropumps has been presented and different applications of cavitation in micropumping have also been



explored, including fluid mixing, fluid separation, chemical synthesis and cavitation assisted cleaning.

The feasibility of integration of optics and microfluidics have been studied, on both silicon and polymer platform, through external and internal hybrid integration techniques. For external hybrid integration, a recirculating microfluidic system has been developed that facilitates enhanced bio-interactions. Different bonding techniques were also developed for realizing hybrid integrated devices. Fiber optics based absorption and fluorescence detection techniques have been developed for the hybrid integrated systems and the results of the optical detections with the external and internal hybrid integrated systems have been presented.

A very novel Nano-Enhance Evanescence detection Technique (NEET) is proposed for the improvement of sensitivity of evanescence detection system. This technique includes the integration of nanoparticles on the surface of the evanescence detection system which facilitates the bio-optical interaction between the evanescent field of light and the chemical/biological substrates. Finite Difference Time Domain studies have been carried out in order to study the effect of nanofeatures on the evanescence behavior of the waveguide system and the implementation of NEET has been demonstrated on SU8-on-Silica waveguides using Multi-Walled Carbon NanoTubes (MWCNT). The results show that the proposed system is highly promising for developing high sensitive detection systems for the  $\mu$ TAS.

Upon the successful testing of the individual modules of the  $\mu$ TAS, the hybrid integrated  $\mu$ TAS is fabricated on Poly Dimethyl Siloxane (PDMS) platform. Waveguide based absorption, fluorescence and evanescence are implemented on SU8-on-PDMS. The integrated testing with the  $\mu$ TAS has been carried out successfully. Nano-enhanced evanescence testing with integrated micropumping has been demonstrated using Nanogold colloids, and integrated optical absorption has been used to study the Benedict's reaction for the determination of glucose in solutions, wherein cavitation assisted mixing has been used for facilitating the reaction between Benedict's solution and the glucose solution.

Thus, the proposed cavitation assisted micropumping integrated optical detection based  $\mu$ TAS, is highly suitable for many chemical and biological applications such as sensing, synthesis, mixing and particle separation.

## ***ACKNOWLEDGEMENTS***

At the outset, I sincerely thank Dr. Muthukumaran Packirisamy for his guidance, practical ideas and encouragement, which have been monumental and inspirational in the successful completion of this thesis. I would like to express my thanks to Dr. Rama Bhat for his course instructions, and also the thesis examination committee for their invaluable suggestions and inputs during the course of my thesis and oral examinations.

I sincerely thank the financial support offered by Concordia University, through different fellowships and bursaries, and I also thank the donors who sponsored the bursaries. I would also like to thank the Royal Bank of Canada and the Quebec Government for supporting me with educational loans and bursaries during the PhD program. I am very thankful to the Alberta Centre for Advanced MNT Products (ACAMP) for employing me as a Development Engineer. It has been a great experience to be a part of Canadian Institute of Photonics Innovation – Student board (CIPI-S) and I would like to thank their financial assistances and travel awards, which enabled me attend several conferences during the PhD.

My very sincere thanks to all the support staff at Concordia University: Leslie Hossein, Arlene Zimmerman, Sophie Merineau and Maureen Thuringer, from the MIE department; Joseph Hulet, Weimin Pu, William Wong, and other support staff from the ENCS help desk for their tremendous technical support to all computer related problems; Danius Juras, Henri Sczhwinski and Gilles Houard who have helped me a lot with the experimental setups. It has been a tremendous experience to work with Dylan Lu,

manager of ConSiM. His instructions and the hands-on tutoring of the clean room operation have been invaluable.

A special thanks to Florent Lefevre of UQAM for his suggestion to alter the PDMS fabrication process that subsequently formed the backbone of the thesis, and his selfless assistance during the microfabrication trials done at UQAM. I would also like to thank Eric Duchesne and Phillip Plamondon of Ecole Polytechnique, Montreal, for their assistance with Scanning Electron Microscopy (SEM).

It has been a pleasure to be a part of the Optical-Bio Microsystems laboratory, and I would like to appreciate the help of all my colleagues in the laboratory who have assisted me during the thesis. Many thanks to Shakhawat Hossein, Carlos Gustavo, Alfin Leo, Murali Pai, Gino Rinaldi, Karthik Balu, Selvaganesh Elangovan, Sankaran Janakiraman and Arvind Vyas for helping me at different stages of the thesis. I would like to acknowledge the help of Krithika Kasi, and all my other friends in Montreal who have made my stay a very memorable one.

Above all, I wish to express my heartfelt gratitude to my parents Mr. Chandrasekaran and Mrs. Neela Chandrasekaran, and Aparna-Arun-Ashvath, for encouraging me, supporting me and motivating me right through the ups and downs of my PhD and my life.

*Dedicated to my parents ...*

# ***TABLE OF CONTENTS***

(i)	List of Figures	xv
(ii)	List of Tables	xxvi
(iii)	Nomenclature	xxviii
(iv)	List of symbols	xxxiii

## **CHAPTER 1 - INTRODUCTION**

1.1	Introduction to Micro-Total Analysis Systems ( $\mu$ TAS)	1
1.2	History of $\mu$ TAS	5
1.3	Components of a $\mu$ TAS	19
1.3.1	Optical detection systems and integration with $\mu$ TAS	22
1.3.2	Introduction to Microfluidics	29
1.3.3	Micropump based fluid actuating systems in $\mu$ TAS	36
1.3.3.1	Fluid actuation techniques for mechanical displacement micropumps	38
1.3.3.2	Fluid actuation for electro/magneto hydrodynamic micropumps	42
1.4	Rationale and scope of the thesis	44
1.4.1	Subsystem and functionality identification for the proposed $\mu$ TAS	45
1.4.1.1	Micropumps for integration with $\mu$ TAS	45
1.4.1.2	Integrated microfluidic system and material platform	48
1.4.1.3	Optical detection system for $\mu$ TAS	50
1.4.2	Objectives of the thesis	52
1.5	Layout of the thesis	53

## **CHAPTER 2 – GEOMETRY TUNING OF MICRODIFFUSERS FOR VALVELESS MICROPUMP APPLICATIONS**

2.1	Introduction to microdiffusers	58
2.2	Geometric tuning of microdiffuser/nozzle for valveless micropumps	60
2.2.1	Introduction	61
2.2.2	Geometry tuning of microdiffuser	65
2.2.2.1	Geometry tuning method	69
2.2.3	Analysis of microdiffuser behavior with geometric tuning	71
2.2.3.1	Finite Element Modeling of the microdiffuser	72
2.2.3.2	Results of Finite Element Analysis	73
2.2.3.2.1	Variation of diffuser/nozzle coefficients with geometric tuning	74
2.2.3.2.2	Influence of geometry tuning on diffuser efficiency	78
2.2.3.3	Observations from FEM	85
2.2.4	Experimental verification	88
2.2.4.1	Fabrication of microdiffuser devices	89
2.2.4.2	Experimental setup	91
2.2.4.3	Results	92
2.2.5	Conclusion	97
2.3	Influence of Reynolds number on diffuser performance with geometric tuning	99
2.3.1	Finite Element Modeling	102
2.3.2	Summary of FEM results	120
2.4	Experimental verification	131
2.4.1	Fabrication of diffuser channels	132

2.4.2	Experimental setup	138
2.4.3	Results	139
2.5	Influence of friction on pressure loss of microdiffuser	150
2.5.1	Experimental results of variation of diffuser coefficients with friction	151
2.5.2	Discussion	157
2.6	Summary	159

### **CHAPTER 3 – DESIGN, FABRICATION AND TESTING OF PIEZOELECTRIC ACTUATED VALVELESS MICROPUMP**

3.1	Introduction	161
3.2	Understanding the behavior of valveless micropumps	164
3.3	Design and fabrication of valveless micropump	167
3.3.1	Design of the micropump	171
3.3.2	Micropump fabrication and assembly	173
3.4	Testing of micropump performance	177
3.4.1	Experimental setup	177
3.4.1.1	High voltage amplifier system	178
3.4.1.2	Flow measurement and dynamic characterization setup	180
3.5	Experimental results	182
3.5.1	Dynamic behavior of the micropump	183
3.5.2	Measurement of micropump flow rate	185
3.5.3	Measurement of micropump chamber pressure	189
3.5.4	Effect of diffuser geometry on micropump flow rate	195
3.5	Effect of surface affinity on micropump flow	197



3.6	Conclusion	204
-----	------------	-----

## **CHAPTER 4- STUDY OF CAVITATION BEHAVIOR IN VALVELESS MICROPUMPS**

4.1	Introduction	206
4.2	Cavitation theory for micropumps	208
4.3	Experimental investigation of cavitation behavior in micropumps	217
4.4	Experimental results	221
4.4.1	Cavitation inception	221
4.4.2	Growth of cavitation bubbles	228
4.4.2.1	Pressure measurement under cavitation growth	230
4.4.2.2	Cavitation growth induced flow	232
4.4.2.3	Comparison of pressure and flow measurements	236
4.4.3	Cavitation collapse	237
4.4.4	Supercavitation	240
4.5	Summary of cavitation phenomenon in micropumps	246
4.6	Effects of cavitation in micropump	247
4.7	Applications of cavitation	251
4.7.1	Improving micropump performance using cavitation	251
4.7.1.1	High Reynolds number flow	251
4.7.1.2	Enhanced priming of micropump	252
4.7.2	Cavitation assisted mixing of liquids	254
4.7.3	Cavitation assisted fluid separation	261
4.7.3.1	Blood fractionation	263
4.7.4	Cavitation assisted cell lysing	269

4.7.5	Cavitation induced chemical cleaning	270
4.8	Conclusion	271

## **CHAPTER 5 – DEVELOPMENT OF EXTERNAL HYBRID INTEGRATED OPTICAL DETECTION SYSTEM FOR $\mu$ TAS**

5.1	Introduction	273
5.2	Classification of Opto-microfluidic integration	274
5.3	Development of external hybrid integrated System	276
5.3.1	Design of recirculating microfluidic system for external hybrid integration	278
5.3.2	Fabrication of microfluidic chips	286
5.4	Demonstration of optical absorption using external hybrid integration	288
5.4.1	Experimental setup	291
5.4.2	Results of absorption detection	293
5.5	Demonstration of external hybrid integrated fluorescence detection	298
5.5.1	Experimental results	300
5.5.1.1	Recirculating development under Continuous flow	301
5.5.1.2	Diffusion of recirculating fluid under stopped flow	302
5.5.1.3	Continuous flow fluorescence detection in non-recirculating flow zone	304
5.5.2	Discussion	305
5.6	Conclusion	307

**CHAPTER 6 – IMPROVING SENSITIVITY OF HYBRID  
INTEGRATED SYSTEMS AND INTERNAL HYBRID  
INTERGRATED  $\mu$ TAS**

6.1	Introduction	310
6.2	Enhanced fluorescence based bio-detection through selective integration of reflectors in microfluidic Lab-on-a-Chip	312
6.2.1	Design, Fabrication and Bonding of microfluidic chip	314
6.2.2.	Test setup and experiment	319
6.2.3.	Experimental results	320
6.3	Integrated Microfluidic Biophotonic chip for Laser Induced Fluorescence Detection	324
6.3.1	Introduction	325
6.3.2.	Modeling and design	327
6.3.3.	Opto-Microfluidic chip synthesis	334
6.3.3.1	Fabrication	335
6.3.3.2	Integration and packaging	337
6.3.4.	Spectrometer-on-Chip testing	340
6.3.5	Biophotonic testing	341
6.4	Conclusion	348

**CHAPTER 7 - MODELING, FABRICATION AND TESTING OF  
NANO-INTEGRATED EVANESCENCE WAVEGUIDE  
DETECTION SYSTEM**

7.1	Introduction	352
7.2	Modeling of nano-integrated evanescence system	357

7.2.1	Implementation of NEET with nanopillars	360
7.2.2	Implementation of NEET with nanocavities and nanospheres	364
7.2.3	Discussion	368
7.3	Experimental investigation of evanescence with nano-integrated waveguide system	369
7.3.1	Fabrication of SU8 Waveguides	370
7.3.2	Nano-integration with SU8 waveguides	372
7.3.3	Experimental Results	373
7.4	Conclusion	377

## **CHAPTER 8 – FABRICATION AND ASSEMBLY OF HYBRID INTEGRATED $\mu$ TAS**

8.1	Introduction	379
8.2	Design of the integrated $\mu$ TAS	381
8.3	Fabrication of integrated optical microfluidic chip	386
8.3.1	Fiber integration	392
8.3.2	Micropump integration	394
8.4	Fabrication of nano-integrated evanescent waveguide system	396
8.5	Assembly	400

## **CHAPTER 9-TESTING OF INTEGRATED $\mu$ TAS**

9.1	Introduction	402
9.2	Integrated nano-enhanced evanescence measurements	404

9.2.1	Synthesis of gold nanoparticles	405
9.2.2	Experiment	406
9.2.3	Calculation of evanescence coefficient	410
9.3	Integrated optical absorption detection using cavitation assisted mixing in microreactor based $\mu$ TAS	412
9.3.1	Implementation of chemical synthesis with cavitation induced mixing	413
9.3.2	Preparation of chemicals for Benedict's test	414
9.3.3	Experimental setup	416
9.3.4	Results	418
9.4	Conclusion	429

## **CHAPTER 10- CONCLUSION**

10.1	Summary	431
10.2	Novelties of the present work	435
10.3	Scope for further research and development	435
10.4	Contributions of the present work	439
10.4.1	Journal papers	439
10.4.2	Conferences and presentations	441

	<b>REFERENCES</b>	444
--	-------------------	-----

## ***LIST OF FIGURES***

Figure 1.1	Generalized flow chart for a $\mu$ TAS	3
Figure 1.2	Major applications of $\mu$ TAS.	4
Figure 1.3	Fully integrated $\mu$ TAS fabricated by Burns et al.	7
Figure 1.4	Assembled biochip with sPROM microfluidic control system	12
Figure 1.5	Lab-on-a-chip developed by Balslev et al. with integrated waveguides, microfluidic channels, dye lasers and photodetectors	14
Figure 1.6	Scanning Electron Micrograph (SEM) of a $\mu$ TAS fabricated on SOI platform with integrated micropumps, microfluidic channels, metal electrodes, Mach-Zehnder interferometers, straight and tapered waveguides and photonic crystal structures	15
Figure 1.7	Different components used in a $\mu$ TAS.	22
Figure 1.8	Schematic of the wavelength interrogated optical sensor (WIOS) technology based on grating waveguide resonant coupling	25
Figure 1.9	Microfluidic chip on PDMS (b),(c) Nano-Bragg grating on SOI microfluidic channel (d) Schematic of the proposed integrated device.	28
Figure 1.10	Polymer microfabrication technologies (a) Casting (b) Hot embossing and (c) Injection molding, adapted from	35
Figure 1.11	Schematic and (b) Fabricated piezo actuated peristaltic micropump by Jang et al.	39
Figure 1.12	Typical range of (a) flow rate per unit outlet area and (b) backpressure for different mechanical micropumps	41
Figure 2.1	Schematic of the microdiffuser/nozzle used in micropump	66
Figure 2.2	Structural tuning of diffuser elements with concave and convex geometry tuning.	70
Figure 2.3	Plot of the streamlines for 90 diffuser with (a) No geometric tuning (b) Concave ( $\beta_{cv}$ ) = 3 and (c) Convex ( $\beta_{cx}$ ) = 0.1	75

Figure 2.4	Plot of variation of $\xi_n$ and $\xi_d$ with $\beta_{cv}$ for different diffuser angles	76
Figure 2.5	Plot of variation of $\xi_n$ and $\xi_d$ with $\beta_{cx}$ for different diffuser angles	77
Figure 2.6	Plot of variation of $\eta_{nd}$ for (a) Convex tuning, $\beta_{cx}$ (b) Concave tuning, $\beta_{cv}$ for different diffuser angles at $Re = 100$	79
Figure 2.7	Plot of the variation normalized nozzle and diffuser pressure with respect to the normalized diffusion length for convex diffusers	81
Figure 2.8	Plot of the variation normalized nozzle and diffuser coefficients with respect to the normalized diffusion length for concave diffusers	81
Figure 2.9	Comparison of effective diffuser lengths for straight walled diffusers and concave and convex diffusers.	83
Figure 2.10	(a) SEM image of the Silicon mould for a concave PDMS microdiffuser with $\beta = 1.5$ (b) Fabricated PDMS microdiffuser chip as seen under the microscope.	91
Figure 2.11	Schematic of the diffuser experimental setup	91
Figure 2.12	Comparison of the experimental and simulated pressure coefficients, and the diffuser efficiencies for convex diffusers with maximum efficiency at $Re_d = 100$ for different diffuser angles.	94
Figure 2.13	Comparison of the experimental and simulated pressure coefficients, and the diffuser efficiencies for concave diffusers with maximum efficiency at $Re_d = 100$ for wide angled diffusers	95
Figure 2.14	Comparison of best diffuser efficiencies obtained with convex and concave tuning for wide angled diffusers	97
Figure 2.15	Variation of pressure coefficients (a) $\xi_d$ and (b) $\xi_n$ with the diffuser Reynolds number ( $Re_d$ ) for diffusers with convex tuning ( $\beta_{cx}$ ) for different diffuser angles	104
Figure 2.16	Variation of pressure coefficients $\xi_d$ and $\xi_n$ with the diffuser Reynolds number ( $Re_d$ ) for diffusers with Concave tuning ( $\beta_{cv}$ ) for different diffuser angles	109

Figure 2.17	Variation of Diffuser efficiencies with Convex geometric tuning and Reynolds numbers for different diffuser angles	115
Figure 2.18	Variation of diffuser efficiencies with Concave geometric tuning and Reynolds numbers for different diffuser angles	117
Figure 2.19	Variation of the diffuser efficiencies with Reynolds numbers for convex tuned diffusers of different diffuser angles	121
Figure 2.20	Variation of the diffuser efficiencies with Reynolds numbers for concave tuned diffusers of different diffuser angles	124
Figure 2.21	Plot of the variation of the best efficiency zones with (a) convex and (b) concave geometric tuning for each diffuser angle	127
Figure 2.22	Comparison of the variation of diffuser efficiencies for (a) Convex tuning (b) Straight diffuser (c) Concave tuning	128
Figure 2.23	Layout of the photomask used for SU8 lithography of microdiffusers, obtained from Fineline Imaging	134
Figure 2.24	Fabricated diffuser chip with ports after bonding of the device layer with PDMS-on-glass substrate	137
Figure 2.25	Experimental setup for measuring the pressure across diffuser microchannels.	139
Figure 2.26	Variation of pressure at the inlet and outlet of the microdiffuser for Reynolds number 100 and schematic of the pressure variation inside the microdiffuser channels	140
Figure 2.27	Variation of pressure drop coefficients $\xi_d$ and $\xi_n$ with the throat velocity of the diffuser ( $v_{din}$ ) for best diffuser efficiencies	142
Figure 2.28	Plot of variation of the predicted and the experimental diffuser efficiency for different diffuser angles	147
Figure 2.29	Variation of pressure loss coefficients $\kappa_d$ and $\kappa_n$ with the throat velocity of the diffuser ( $v_{din}$ ) for best diffuser efficiencies	152
Figure 2.30	SEM of the SU8 mould, the thickness obtained from the lithography is 19.6 $\mu\text{m}$	158
Figure 3.1	Schematic of the valveless micropump	165
Figure 3.2	Schematic of the flow rectification due to the diffuser/nozzle configuration in a valveless micropump	166



Figure 3.3	Setup of the PVDF integrated micropump fabricated on silicon and Plot of the spectral response of the deflection of the PVDF membrane obtained at various excitation voltages using LDV	169
Figure 3.4	Layout of the diffuser/nozzle and the micropump chamber	173
Figure 3.5	Fully packaged micropump assembly	176
Figure 3.6	Schematic of the experimental setup for characterization of the valveless micropumps	178
Figure 3.7	Circuit diagram of the high voltage amplifier circuit for the actuation system	180
Figure 3.8	Experimental setup for flow measurement at the micropump outlet (b) Tracking the movement of the liquid meniscus inside the microfluidic tube against a calibrated reading	181
Figure 3.9	Experimental setup for dynamic characterization of the micropump	182
Figure 3.10	Plot of the spectral response of surface velocity for the piezo-actuated micropump	183
Figure 3.11	Plot of the variation of the pump deflection with applied voltage	185
Figure 3.12	Plot of variation of flow rate with pump operating frequency	186
Figure 3.13	Plot of variation of flow rate with applied voltage	187
Figure 3.14	Schematic of the micropump inlet and outlet pressure heads	188
Figure 3.15	Variation of the pump flow rate with pressure head due to water column at the micropump inlet, at different operating frequencies.	189
Figure 3.16	Schematic of the micropump pressure measurement setup and Experimental setup for the micropump chamber pressure measurement	190
Figure 3.17	Plot of variation of micropump chamber pressure for different actuation frequencies	192
Figure 3.18	Variation of pressure rise and flow rate with pump operating frequency	194
Figure 3.19	Plot of the flow rate as a function of driving frequency for micropump with different diffuser configurations	195

Figure 3.20	Demonstration of contact angle of water droplet on PDMS with Hydrophobic PDMS and Hydrophilic PDMS	199
Figure 3.21	Plot of variation of the net flow with the pump frequency for hydrophilic and hydrophobic micropumps	200
Figure 3.22	Images of the micropump chamber at different stages of pumping indicated in Figure 3.21, for hydrophilic and hydrophobic micropumps	201
Figure 3.23	Plot of variation of the bubble fraction with micropump operating frequency for hydrophilic and hydrophobic micropumps	202
Figure 4.1	Schematic of the energy level diagram in a valveless micropump	209
Figure 4.2	Variation of average diaphragm deflection with applied voltage for micropumps used in cavitation experiments with water	219
Figure 4.3	Experimental setup for study of cavitation	220
Figure 4.4	Experimentally obtained values for the critical cavitation frequencies for different micropump deflections for $H_s = 0$	225
Figure 4.5	Variation of critical cavitation frequency with inlet suction head for constant micropump diaphragm deflection of $3.75 \mu\text{m}$ .	226
Figure 4.6	Variation of cavitation parameter with inlet suction head for constant micropump diaphragm deflection	227
Figure 4.7	Schematic of the cavitation bubble growth inside the micropump chamber	229
Figure 4.8	Schematic of the pressure measurement due to bubble growth using stagnant microfluidic channel	231
Figure 4.9	Plot of the variation of the bubble pressure ratio with time for different frequencies	232
Figure 4.10	Measured variation of flow rate of the pump with operating frequency	233
Figure 4.11	Plot of variation of the shape number for the micropump with time at different pumping frequencies	235
Figure 4.12	Plot of variation of bubble growth time with cavitation frequency as identified by flow measurement, pressure	237

	measurement and flow visualization	
Figure 4.13	Plot of the time taken for cavitation collapse with frequency for different pump deflections	240
Figure 4.14	Variation of cavitation induced pressure with frequency	241
Figure 4.15	Images of different stages of cavitation in micropump leading to supercavitation, and the subsequent filling of the fluid inside the micropump chamber after stopping the micropump	243
Figure 4.16	Plot of the variation of supercavitation frequency with inlet pressure head based on reverse flow calculation	244
Figure 4.17	Expansion of the cavitation bubbles into the outlet channel and Formation of the vapor bubbles at the outlet port of the micropump after supercavitation	245
Figure 4.18	The outlet tube of the micropump (a) before supercavitation and (b) after supercavitation.	246
Figure 4.19	Sparks due to electrical overload on the actuator caused by growth and collapse of cavitation bubbles	248
Figure 4.20	Crack observed in micropump diaphragm caused by repeated collapse of cavitation bubble	249
Figure 4.21	Micropits created by the collapse of cavitation bubbles on the diaphragm and Crater crated by a cavitation bubble collapse	250
Figure 4.22	Priming of micropump chamber (a) before and (b) after supercavitation	253
Figure 4.23	Flow of ethanol and water inside the micropump chamber without mixing	256
Figure 4.24	Before the start of mixing due to micropumping/cavitation	257
Figure 4.25	Progress of cavitation induced mixing in the micropump chamber at different stages	258
Figure 4.26	Laminar flow with subsequent input of fluids after cavitation induced mixing	260
Figure 4.27	Different stages of cavitation assisted separation of water and oil	262
Figure 4.28	Image of micropump chamber after separation of oil and water	263

Figure 4.29	Input of blood sample into the micropump	264
Figure 4.30	Different stages of supercavitation assisted separation of blood plasma from blood cells	265
Figure 4.31	Separation of blood plasma from blood cells	266
Figure 4.32	SEM image of the Red Blood Cells and the White Blood Cells separated inside the micropump chamber	268
Figure 4.33	Images of the micropump chamber before and after cavitation assisted cleaning with milk	271
Figure 5.1	Schematic of the external hybrid integrated fluorescence detection setup	276
Figure 5.2	Design parameters for recirculating microfluidic chamber.	279
Figure 5.3	Predicted flow behavior within in the recirculating microfluidic chamber (b) x-velocity profile of the fluid flow across sections A-A and B-B in the R-Zone.	281
Figure 5.4	The development of recirculation with Reynolds number.	283
Figure 5.5	Variation of re-circulation center with Reynolds number	284
Figure 5.6	Unpackaged microfluidic chip fabricated by Protolyne process technology	287
Figure 5.7	Flow visualization carried out with fluorescent particles using epifluorescence microscope at $Re=0.7$ and Flow behavior at $Re = 0.7$ predicted through FEM.	288
Figure 5.8	Molecular structure of (a) HRP and (b) HRP- $H_2O_2$ after reaction	290
Figure 5.9	Experimental setup for measuring the recirculation flow aided optical absorption	292
Figure 5.10	Spectral absorption characteristics due to HRP and $H_2O_2$ in the microfluidic channel at 470 nm.	294
Figure 5.11	Spectral absorption characteristics due to HRP, $H_2O_2$ and their reaction in the microfluidic channel at different times.	296
Figure 5.12	Absorbance measurement during HRP- $H_2O_2$ reaction	297
Figure 5.13	(a) Schematic and (b) Experimental setup of the optical microfluidic testing setup	299

Figure 5.14	Continuous flow fluorescence detection in the re-circulation chamber for AF647 tagged AB	302
Figure 5.15	Results of the stopped flow fluorescence detection experiment	304
Figure 5.16	Fluorescence observed in the flow zone of the RC in a continuous flow system	305
Figure 6.1	Schematic representation of fluorescence amplification through partial gold sputtering on the microfluidic channel	313
Figure 6.2	Design of the microfluidic channel with simulated flow streamlines	314
Figure 6.3	Reflection curve for gold at different wavelengths	317
Figure 6.4	Fully gold-coated microfluidic chip and selectively gold integrated silicon chip after post-processing	317
Figure 6.5	Fully packaged SiPy and SGP microfluidic chips	318
Figure 6.6	External Hybrid integrated Fluorescence detection setup	319
Figure 6.7	Fluorescence detected for different concentrations of AF 647 with and without gold integrated microfluidic channels	321
Figure 6.8	Plot of the compensation factor for the different concentrations of the fluorophores	323
Figure 6.9	Schematic illustration of the opto-microfluidic chip integrated with the Spectrometer-on-chip	330
Figure 6.10	Typical response from the different output channels of the Spectrometer-on-Chip	331
Figure 6.11	Results of the Finite Element Analysis of the flow behavior within (a) anisotropically etched chamber and (b) rhombus chamber.	333
Figure 6.12	Comparison of $V_{\min}$ in the detection zone of anisotropically etched chamber with rhombus chamber.	334
Figure 6.13	Schematic diagram showing the etch progress of microchamber. (a) Etch mask indicating the etch fronts at four convex corners (b) Detailed view of propagation of etch front at convex corner	336
Figure 6.14	SEM images of fabricated microfluidic chip and V-slots for fiber integration	337

Figure 6.15	Integration of fibers with the microfluidic channels	338
Figure 6.16	Fully packaged hybrid optical microfluidic chip	339
Figure 6.17	a) Excitation spectrum from laser source at the input fiber of the microfluidic channel (b) Response of the Spectrometer-on-Chip at 670 nm from channel 11 (c) Response of the Spectrometer-on-Chip at 635 nm from channel 15	341
Figure 6.18	Biodetection testing setup using the integrated device and Spectrometer-on-Chip	342
Figure 6.19	Results of pulsed flow tests with Alexafluor 647 tagged antisheep antibody	345
Figure 6.20	Results of dynamic tests with 10% of 2 mg/ml AF 647 tagged antisheep antibody	346
Figure 6.21	Variation of the fluorescence loss for different coupling distance between the fibers	347
Figure 6.22	Fibers positioned in the optical channel during the on-chip opto-microfluidic integration with (a) straight coupled and (b) orthogonal coupled fiber configurations	350
Figure 6.23	Trace of light seen for (a) direct fiber coupling (b) orthogonal fiber coupling	351
Figure 7.1	Schematic illustration of evanescence wave phenomenon and (b) Evanescent wave detection using integrated microfluidics	353
Figure 7.2	Schematic of the silicon waveguide with integrated nanopillars	360
Figure 7.3	Plot of the relative Nano-enhanced Evanescent loss on silicon waveguide with integrated nanopillars for different surrounding medium (air and water)	362
Figure 7.4	Plot of variation of relative evanescence with $d_{np}/a_{np}$ ratio of nanopillars integrated on silicon waveguide	363
Figure 7.5	Schematic of the SOI waveguide with nanocavities	365
Figure 7.6	Relative Nano-enhanced evanescence loss from silicon waveguide with integrated nanocavities for different surrounding medium (air and water)	365
Figure 7.7	Schematic depiction of a silicon waveguide core strip integrated with nanospheres and nanocavities	366

Figure 7.8	Results of FDTD analysis of evanescence loss from the side walls of the silicon waveguide with and without integrated nanospheres	367
Figure 7.9	Schematic of the SU8-on-Silica waveguide cross-section	371
Figure 7.10	Experimental setup for evanescence detection using SU8-on-Silica waveguide	373
Figure 7.11	Plot of evanescent loss with time for water suspended with and without MWCNT	374
Figure 7.12	SEM image of (a) CNT deposited on the waveguide after water evaporation (b) close up of the carbon nanotubes	375
Figure 7.13	Plot of evanescent loss with time for MWCNT deposited directly on the waveguide	376
Figure 8.1	Schematic of the proposed hybrid integrated $\mu$ TAS	382
Figure 8.2	(a) Design of the optical waveguide system for absorption and fluorescence detection (b) Cross sectional view of the hollow waveguide	383
Figure 8.3	(a) Schematic of the evanescence detection system (b) Cross-section view of the integrated microfluidic waveguide system	385
Figure 8.4	Absorbance characteristics of different film thickness of SU8 with visible wavelength	387
Figure 8.5	SEM image of the waveguide slot with the microfluidic channel for (a) Absorption detection system and (b) Fluorescence detection system	388
Figure 8.6	Filling of the channels with SU8 for waveguide core as seen under the microscope	389
Figure 8.7	SEM image of the SU8 waveguide and the microfluidic channel.	392
Figure 8.8	Assembly of the fibers placed on the positioners	393
Figure 8.9	Integrated optical-microfluidic setup with absorption-fluorescence detection system and valveless micropump	395
Figure 8.10	Integrated microfluidic Evanescence measurement system	399
Figure 8.11	Fully integrated $\mu$ TAS under testing	401

Figure 9.1	(a) Schematic of the integrated $\mu$ TAS test assembly and (b) Integrated $\mu$ TAS testing setup	403
Figure 9.2	Plot of variation of evanescence with micropumping	407
Figure 9.3	Plot of variation of evanescence with micropumping	408
Figure 9.4	Different stages of color changes with the concentration of the sugar solution with the Benedict's test.	416
Figure 9.5	Experimental setup for integrated optical absorption measurements	417
Figure 9.6	Variation of Optical absorption under steady state flow with sugar solution and Benedict's solution at 632 nm wavelength	420
Figure 9.7	Benedict's reagent and the sugar solution entering the micropump chamber	421
Figure 9.8	Different stages of variation induced mixing of Benedict's solution with sugar solution	422
Figure 9.9	Reaction mixture inside the micropump chamber after cavitation	424
Figure 9.10	Variation of Optical absorption of the Benedict's reagent-sugar solution mixture	426
Figure 9.11	Distinct layers at the output reservoir after Benedict's test	428



## ***LIST OF TABLES***

Table 1.1	Prominent works in the development of microfluidic systems with integrated optical sensing for Lab-on-a-Chip systems and Micro-Total Analysis System applications during the last two decades.	17
Table 2.1	Classification of the diffuser angles used for the Finite Element Analysis	71
Table 2.2	Summary of variation of $\xi_n$ and $\xi_d$ with geometric tuning	78
Table 3.1	Fabrication steps for PDMS-Glass Micropump	174
Table 3.2	Comparison of the predicted and the experimental I and II natural frequencies of the micropump	184
Table 4.1	The different geometric parameters for the valveless micropump used for cavitation experiments	218
Table 5.1	Experimental procedure for enzymatic absorption study at 470 nm	294
Table 5.2	Experimental procedure for enzymatic absorption study using broadband light source	295
Table 5.3	Sequential procedure of continuous flow fluorescence detection experiment using AF647 tagged Antisheep Antibody	301
Table 5.4	Sequential procedure of stopped flow fluorescence detection in the RC using AF647 tagged AB	303
Table 5.5	Sequential procedure of continuous flow fluorescence detection in the flow zone	304
Table 5.6	Comparison of the time taken for tagged antibody to exhibit maximum fluorescence in the recirculation flow zone and non-recirculating flow zone	306
Table 6.1	Sequential experimental procedure for fluorescence detection in SGP and SiPy	320
Table 6.2	Different channels of the Spectrometer-on-Chip and their functions	329
Table 6.3	Sequential procedure for pulsed flow fluorescence measurement experiments with respect to the results presented in Figure 6.19.	344

Table 7.1	Waveguide and nanopillars dimensions used for FDTD modeling	361
Table 7.2	Evanescent coefficient for the CNT enhanced evanescence tests carried out with SU8-on-silicon waveguide at 632 nm.	376
Table 8.1	Fabrication steps for the optical microfluidic chip with integrated micropump, absorption and fluorescence optical detection systems	390
Table 8.2	Fabrication steps for Nano-integrated evanescence detection system	396
Table 9.1	Different stages of fluid actuation for evanescence detection	408
Table 9.2	Evanescent coefficient for the different tests carried out on the CNT integrated SU8 waveguides with Gold colloidal solution	411
Table 9.3	Absorption coefficient for the test specimens and the reaction mixture.	428

## ***NOMENCLATURE***

$\mu$ TAS	MicroTotal Analysis Systems
AF647	AlexaFluor 647
AFM	Atomic Force Microscope
BioMEMS	Bio-Micro-Electro-Mechanical Systems
CFF	Continuous Flow Fluorescence Detection
CFR	Continuous Flow Recirculating System
CMC	Canadian Microelectronics Corporation
CMOS	Complementary Metal Oxide Semiconductor
CNT	Carbon Nanotubes
COC	Cyclic Olefin Copolymer
DAQ	Data Acquisition
DEP	Dielectrophoresis
DI	Deionized
DNA	Deoxyribo Nucleic Acid
DRIE	Deep Reactive Ion Etching
EDP	Ethylenediamine Pyrocatechol
ER	Etch rate
EtOH	Ethanol
F*	Laminar flow zone in recirculating microfluidic chamber
FDTD	Finite Difference Time Domain
FEA	Finite Element Analysis

FEM	Finite Element Modeling
FET	Field Effect Transistor
FHD	Flame Hydrolysis Deposition
FSI	Fluid-Structure Interaction
GaAs	Gallium Arsenide
GRIN	Graded Index Lens
H <sub>2</sub> O <sub>2</sub>	Hydrogen Peroxide
HCl	Hydrochloric Acid
HEK	Human Embryonic Kidney
HF	Hydrofluoric Acid
HNA	Hydrofluoric and Nitric Acid
HRP	Horse Radish Peroxidase
ICP	Inductively Coupled Plasma
InP	Indium Phosphide
IPA	Isopropyl Alcohol
KE	Kinetic Energy
KOH	Potassium Hydroxide
LDV	Laser Doppler Vibrometer
LIF	Laser Induced Fluorescence
LOC	Lab-on-a-Chip
MEMS	Micro -Electro-Mechanical Systems
MHD	Magneto Hydrodynamic
MicraGeM	Micralyne Generalized MEMS

MOEMS	Micro-Opto-Electro-Mechanical Systems
MST	Micro Systems Technology
MUMPS	Multi-User MEMS Process System
MWCNT	MultiWalled Carbon Nanotubes
MZI	Mach-Zehnder Interferometer
NEET	Nano-Enhanced Evanescence detection Technique
NPSH <sub>a</sub>	Net Positive Suction Head Available
NPSH <sub>c</sub>	Critical Net Positive Suction Head
NPSH <sub>r</sub>	Net Positive Suction Head Required
O <sup>*</sup>	Overlap zone in a recirculating microfluidic chamber
OADM	Optical Add/Drop Multiplexers
OLED	Organic Light Emitting Diode
OSA	Optical Spectrum Analyzer
PAVM	Piezoelectric-Actuated Valveless Micropump
PBS	Phosphate Buffer Solution
PC	PolyCarbonate
PCL	PolyCaproLactone
PCR	Polymerase Chain Reaction
PDMS	Poly Dimethyl Siloxane
PECVD	Plasma Enhanced Chemical Vapor Deposition
PEEK	Poly Ethyl Ether Ketone
PMMA	Poly Methyl Methacrylate
POCT	Point-of-Care Testing

PON	Point-of-Need
psi	Pounds per square inch
PVDF	PolyVinylidene Fluoride
PZT	Lead Titanate Zirconate
RBC	Red Blood Cells
RC	Recirculation Chamber
RI	Refractive Index
RIE	Reactive Ion Etching
RPM	Revolutions Per Minute
R-Zone	Recirculating microfluidic zone
SEM	Scanning Electron Microscopy
SERS	Surface Enhanced Raman Scattering
SFR	Stopped Flow Recirculating system
SGP	Silicon-Gold-Polycarbonate
Si	Silicon
SiO <sub>2</sub>	Silicon dioxide
SiPy	Silicon-Pyrex
SMA	Shape Memory Alloy
SNR	Signal-to-Noise Ratio
SOC	Spectrometer-on-Chip
SOI	Silicon-on-Insulator
SOS	Silica-on-Silicon
SPR	Surface Plasmon Resonance

SPROM	Smart Programmable Microfluidic System
SSE	Error Sum of Squares
TE	Transverse Electric
TM	Transverse Magnetic
TMAH	Tetra Methyl Ammonium Hydroxide
UER <sub>max</sub>	Maximum under etch rate
UV	Ultra Violet Light
VCSEL	Vertical Cavity Surface Emitting Laser
WBC	White Blood Cells
WGM	Whispering Gallery Mode
WIOS	Wavelength Interrogated Optical Sensing
XeF <sub>2</sub>	Xenon difluoride

## ***LIST OF SYMBOLS***

$\alpha_{ab}$	Absorption coefficient in $\text{cm}^{-1}$
$\alpha_{ev}$	Evanescence coefficient in $\text{cm}^{-1}$
$\alpha_{ke}$	Kinetic energy correction factor
$\alpha_m$	Angle made by the photomask with respect to the wafer flat.
$\alpha_p$	Dimensionless coefficient for characterizing the deflection shape of the micropump
$\beta$	Geometry tuning parameter of the diffuser
$\beta_{ab}$	Absorbance loss in dB/cm
$\beta_{cv}$	Concave geometrical tuning parameter of the diffuser
$\beta_{cx}$	Convex geometrical tuning parameter of the diffuser
$\beta_{ih}$	Optical coupling loss in internal hybrid integrated system
$\beta_{ev}$	Total evanescent light loss in dB
$\beta_{HRP}$	Evanescent light loss due to HRP , in dB/cm
$\chi_a$	Evanescent loss when nanopillars are clustered together on the waveguide
$\chi_{cnt}$	Evanescent loss due to the integration of the Carbon Nanotubes
$\chi_{ev}$	Relative Nano-enhanced evanescent loss
$\chi_f$	Amount of fluorescent signal coupled into the collector waveguide
$\chi_{f \max}$	Maximum fluorescent signal coupled into the collector waveguide
$\delta_f$	Offset distance between microfluidic channel surface and optical fiber core
$\delta_p$	Maximum deflection at the center of the micropump diaphragm



$\nabla$	Differential operator
$\epsilon_{em}$	Permittivity of the medium
$\phi$	Generalized Electric or Magnetic field
$\phi_{av}$	Mean value of the volume flux of the micropump
$\dot{\phi}_p$	Rate of micropump chamber volume variation
$\gamma$	Kinematic viscosity of the fluid
$\eta_{nd}$	Efficiency of the diffuser
$\kappa_d$	Pressure loss coefficient of the diffuser
$\kappa_{ff}$	Frictional pressure loss coefficient in the diffuser
$\kappa_n$	Pressure loss coefficient of the nozzle
$\lambda$	Wavelength of light
$\mu$	Dynamic viscosity of the fluid
$\mu_{em}$	Permeability of the medium
$\mu\text{L}$	microlitres
$\mu\text{m}$	micrometers
$\mu\text{s}$	microseconds
$\nu_c$	Frequency of the micropump at the inception of cavitation
$\nu_{sc}$	Supercavitation frequency
$\pi$	Irrational number 22/7
$\theta$	Angle made by the fast etch planes with {100} plane
$\theta_d$	Diffuser angle
$\rho$	Density of the fluid

$\mathfrak{R}_n$	Norm of the residual for curve fitting
$\sigma_c$	Cavitation number
$\sigma_p$	Cavitation bubble pressure ratio
$\sigma_{sh}$	Cavitation shape number
$\tau_{abi}$	Total time taken for which antibody is passed into recirculation zone
$\tau_{abmax}$	Time taken for the antibody to attain maximum fluorescence emission, measured from the time of particle entry of the particle into the Recirculation chamber
$\tau_c$	Time taken for cavitation induced flow/cavitation collapse
$\tau_g$	Time taken for the cavitation bubble growth before collapse
$\tau_p$	Time of micropump operation
$\tau_{ss}$	Time taken for pressure across the diffuser to reach steady state
$\varpi_f$	Ratio of the total time of the input of fluid to the time taken to attain maximum fluorescence, denoted by $\varpi_f = \tau_{abi}/\tau_{abmax}$
$\omega_p$	Frequency of pump oscillation
$\Omega_{fi}$	Rate of fluorescence increase in recirculation zone
$\Psi_x$	x-coordinate of the recirculating microfluidic chamber
$\Psi_y$	y-coordinate of the recirculating microfluidic chamber
$\xi_d$	Pressure drop coefficient of diffuser
$\xi_n$	Pressure drop coefficient of nozzle
$\xi_p$	Cavitation parameter
$a_{np}$	Pitch between nanopillars used for FDTD modeling
$A_{av}$	Average cross-section of the micropump chamber
$A_{din}$	Area of cross-section of the diffuser inlet

$A_m$	Area defined by the monitor in FDTD analysis
$A_{mf}$	Area of cross-section of the microfluidic channel on top of the waveguide
$A_\lambda$	Absorbance measured with light of wavelength $\lambda$
$b_w$	Width of rib waveguide used in FDTD modeling
$c$	Velocity of light in vacuum, $3 \times 10^8$ m/s
cm	Centimeters
$^\circ\text{C}$	Degree Celsius
$d$	Waveguide width
$dP_c$	Variation of micropump chamber pressure
Da	Daltons, $1 \text{ Da} = 1.660540 \times 10^{-24}$ kg
dB	Decibels
$D_h$	Hydraulic diameter or wetted perimeter
$D_{in}$	Inlet diffuser
$D_{out}$	Outlet diffuser
$d_{np}$	Diameter of nanopillars used for FDTD modeling
$dx$	Incremental distances between the grid points in the x-direction
$dy$	Incremental distances between the grid points in the y-direction
$D_\lambda$	Dark Intensity
$D_f$	Coupling distance between fibers
$e$	Constant of value 2.71828
$E$	Electric field of Electro-Magnetic wave
$E_{bf}$	Energy transfer between surrounding fluid and bubbles during cavitation

$E_{db}$	Energy transfer between micropump diaphragm and bubbles during cavitation
$E_{df}$	Energy transfer between micropump diaphragm and fluid during cavitation
EP	Evanescent power loss computed by BPM
f	Under-relaxation factor for FD computation
$f_f$	Fanning friction factor
$F(x)$	Coefficient of polynomials for curve fitting
$F_{SGP}$	Maximum fluorescence measured from the SGP channels
$F_{SiPy}$	Maximum fluorescence measured from the SiPy channels
$H$	Magnetic field of Electro-Magnetic wave
hr	Hour
$h_{np}$	Height of the nanopillars used for FDTD modeling
$h_w$	Height of rib waveguide used in FDTD modeling
$H_b$	Head loss in the micropump delivery side
$H_d$	Dynamic pressure head in suction line of the micropump
$H_s$	Inlet suction head of the micropump
$\Delta H_s$	Change in inlet suction head of the micropump
Hz	Hertz
I	Time varying intensity of the output light during evanescence
$I_0$	Reference intensity used for evanescence measurement
j	Coordinates of points along y-axis
$k$	Wavenumber
$k_0$	Wavenumber of free space

kDa	kilo Daltons
kg	kilograms
KHz	kilo Hertz
kPa	kilo Pascals
$L_d$	Length of the diffuser
$L_{ev}$	Evanescent field length
$L_{np}$	Distance between nanopillars arrays used for FDTD modeling
m	meters
max	Maximum value
min	Minutes
$N_{nc}$	Number of arrays of nanocavities on the waveguide
$N_{np}$	Number of arrays of nanopillars on the waveguide
nL	Nanolitres
nm	Nanometers
$\Delta p_{net}$	Total pressure drop across diffuser (experimental)
$\Delta p_{diff}$	Pressure difference across the diffuser at steady state
$\Delta p_{init}$	Initial pressure difference across the diffuser (experimental)
$\Delta p_{ff}$	Frictional pressure drop across the diffuser and the channels
$P_{atm}$	Atmospheric pressure
$P_b$	Pressure exerted by the cavitation bubbles
$P_c$	Chamber pressure of the micropump
$P_{in}$	Pressure due to inlet liquid column of the micropump

$P_v$	Vapor pressure of the liquid
$\dot{Q}$	Flow rate of the micropump
$\dot{Q}_{\max}$	Maximum flow rate of the micropump
$Q_p$	Volume of fluid discharged from micropump due to the expansion of cavitation bubbles
$R_c$	Radius of the oscillating micropump diaphragm
$Re$	Reynolds number
$Re_{av}$	Average Reynolds number
$Re_d$	Reynolds number at the neck of the diffuser
$R_{\text{rms}}$	Root-Mean-Square roughness value
$R_\lambda$	Intensity of light passing through the reference medium
$S_\lambda$	Intensity of light passing through the sample
$S_0$	Launch power in FDTD analysis
$S(t)$	Time dependent power flow through the monitor domain in FDTD analysis
$s_w$	Height of waveguide slab used in FDTD modeling
$t$	Used to denote time
$\bar{u}$	Average flow velocity at the inlet of recirculating microfluidic channel
$V_0$	Amplitude of volume variation of micropump chamber
$V_c$	Initial volume of the micropump chamber
$V_p$	Volume of micropump chamber at any given time
$V_{pp}$	Peak-peak voltage
$v(x)$	Fluid velocity at position $x$ of a microchannel
$w$	Width of rib of waveguide core in $\mu\text{m}$

$w_c$	Width of microfluidic channel
$W$	Watts
$W_o$	Width of the optical channel in an internal hybrid integrated system
$W_m$	Width of the microfluidic channel in an internal hybrid integrated system
$x$	x-direction in the 3D axis
$y$	y-direction in the 3D axis
$Y_d$	Microfluidic channel aspect ratio
$z$	z-direction in the 3D axis
$Z_c$	Fluorescence compensation factor given as $Z_c = \frac{\{F_{SGP} - F_{SiPy}\}}{Max.(F_{SGP} - F_{SiPy})}$

## **Introduction to Micro-Total Analysis Systems**

### **1.1 Introduction to Micro-Total Analysis Systems ( $\mu$ TAS)**

Point-of-Care Testing (POCT) and Point-of-Need (PON) solutions to chemical and biomedical diagnosis are the needs of the hour for early and rapid target detections, instigating the necessity to develop a suitable and cost effective biosensor capable of addressing the needs of these medical requirements. The success of Micro-Electro-Mechanical Systems (MEMS) or microsystems have opened up a lot of opportunities to carry out cutting edge research towards chemical and biological applications, which gave rise to the field of study commonly known as BioMEMS or Bio Micro-Electro-Mechanical Systems (Bashir 2004).

BioMEMS essentially accomplishes the miniaturization of conventional chemical and biosensors to the micro level thereby improving upon the performance of a macro analysis system. In addition, they carry with themselves several advantages, such as, low sample volume consumption, portability of the device, rapid analysis and more importantly providing feasibility for the realization of Point-of-Care analysis. This is an enabling technology for higher functionality and cost reduction for improved chemical and biomedical diagnostics that demand fast, easy-to-use, economically viable and highly sensitive methods for the detection of analytes in several in-situ applications. These microdevices are synthesized by novel methods inspired from micro/nano-scale



fabrication, and are used for pre-processing, manipulation, analysis and/or delivery of chemical and biological entities. Over the last two decades, powerful tools and processes have been developed for the fabrication and development of several microbiosensors. However, all biosensors require more than one micro-component in order to carry out complex bio-analyses, which therefore, have involved the integration of several micro-components for a particular application.

A Micro-Total Analysis System ( $\mu$ TAS) is an integrated microscale analysis system consisting of one or more BioMEMS units, which in essence, improves the performance of a macro analysis system by virtue of its reduced size. Herein, all functions and functional modules which are present on a macro scale analysis system are miniaturized onto a single chip of a  $\mu$ TAS by means of integrating different microstructures. Micro Total Analysis Systems have also been interchangeably referred to as Lab-on-a-chip (LOC) or Biochips. However, the basic difference between a LOC and a  $\mu$ TAS is that, whereas LOC consists of static non-moving components and is often hybrid integrated with external macro devices for some of its functionalities, a  $\mu$ TAS consists of dynamic components which enable the complete miniaturization of the analysis system thereby forming a stand-alone device, more often monolithic, without the necessity to integrate with external macro units. A general flow chart of a  $\mu$ TAS is as shown in Figure 1.1.

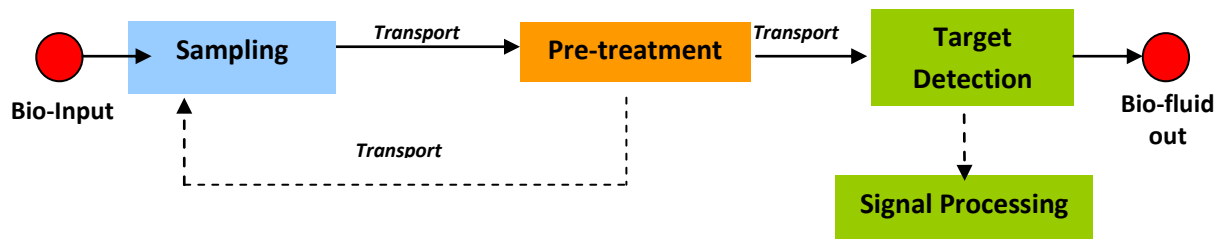


**Figure 1.1:** Generalized flow chart for a  $\mu$ TAS

Target identification is the key function of a  $\mu$ TAS. In biological applications,  $\mu$ TAS have been used to efficiently synthesize chemicals or biological molecules such as DNA, cancer cells etc., to perform an integrated chemical and biological operations on full scale ranging from cell introduction, molecular separation, manipulation and detection on a single miniaturized device (Fortina et al. 2002).  $\mu$ TAS have been used for a myriad of applications other than chemical and biological analysis as well. Figure 1.2 gives some of the prominent areas wherein  $\mu$ TAS is used. Environmental applications of a  $\mu$ TAS include the detection of toxins, security from bio-terrorism, detection of pollutants in soil and industrial wastes, disease testing for livestock, toxicology, remote minerals analysis, agriculture and soil monitoring, plant analysis, and also in the area of food safety. The various medical applications of the  $\mu$ TAS include Point-of-Care diagnosis for disease testing, targeted drug delivery, self assembly and sequencing of DNA, immunoassays, proteomics, among others.  $\mu$ TAS is also used in automotive and aeronautical applications, which call for humidity monitoring in aircraft cabins or passenger vehicles, and engine management systems which require monitoring of exhaust fumes.

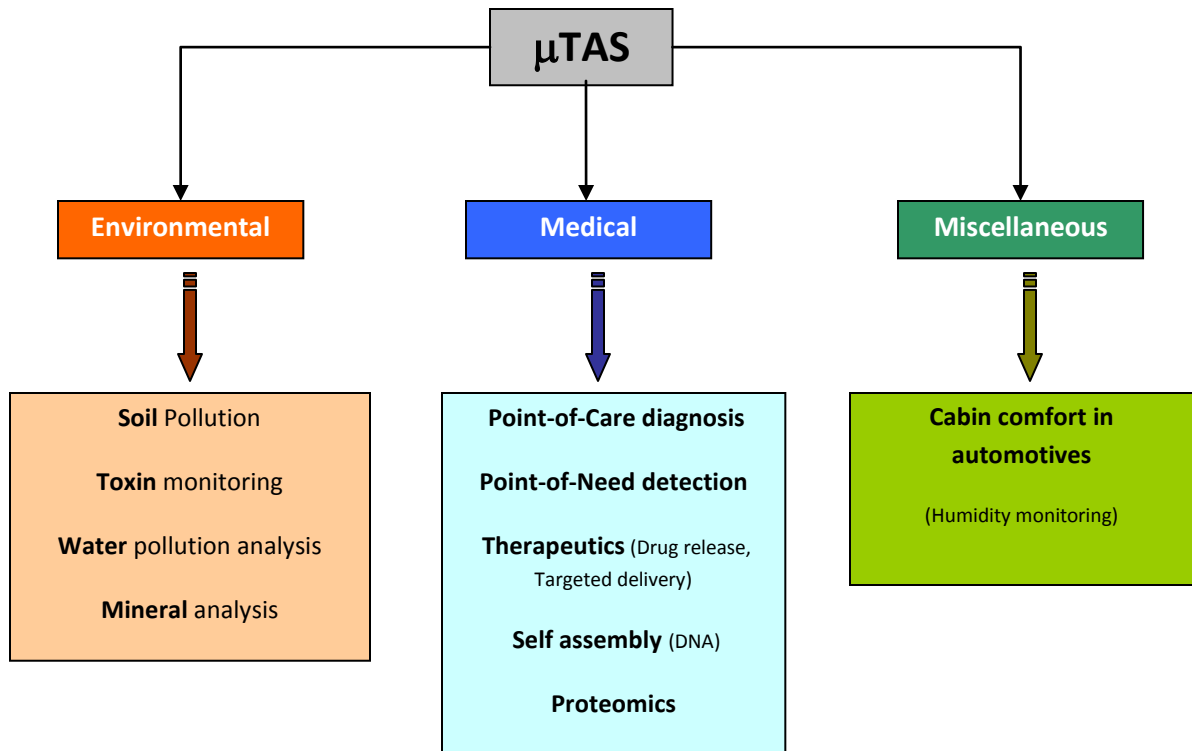


**Figure 1.2:** Major applications of  $\mu$ TAS.

Ever since the advent of  $\mu$ TAS, a lot of research has been carried out for the synthesis of  $\mu$ TAS for the above mentioned applications. At the same time, it is also a fact that the rate at which  $\mu$ TAS devices are being synthesized in quantity, outpaces the willingness of the market to accept them (Park, Kricka 2007). Thus, the advantages of a  $\mu$ TAS, even though form a strong economic driving factor, can only be valorized if the same degree of reliability can be obtained as in conventional analysis systems for any real-time application.

## 1.2. History of $\mu$ TAS

The earliest known work on a Micro Total Analysis System, outlining the feasibility of synthesizing a device and its potentials was carried out by Manz. et al. (1990) in 1990. Since then, Manz has contributed regularly to research and development of the  $\mu$ TAS (Reyes et al. 2002), (Auroux et al. 2002), (Vilkner et al. 2004), (Dittrich et al. 2006) and their fabrication methodologies, till date. The  $\mu$ TAS initially proposed by Verpoorte and Manz in 1991 (Verpoorte et al. 1991), which was the first ever fully synthesized  $\mu$ TAS device, was the optical detection system for cells using liquid chromatography as the method of separation. The system basically consisted of a flow cell fabricated out of anisotropic etching and bonding of oxidized silicon wafers. However, in this work, no experimental results have been provided by the authors. The paper mentioned merely about the fabrication and the feasibility of biodetection using the proposed method of optical absorption. By 1994, Verpoorte et al. had fabricated a 3D microfluidic flow system for analysis, which is believed to be the first fully synthesized miniaturized TAS device. Ion Sensitive Field Effect Transistors (ISFET) were used in this work for detection. The system consisted of two silicon micropumps connected with the ISFET through silicone rubber tubes. The device was used for pH detection and for phosphate measurement.

By 1996, Ramsey and Jacobson fabricated the integrated microdevice for DNA fragment analysis (Jacobson, Ramsey 1996). The samples, namely, the DNA and the enzyme were moved into the reaction chamber through electrophoresis. The particles were observed through Laser induced fluorescence and imaging was carried out with a CCD camera.

The fluorescence measurements were carried through a photomultiplier tube. However, the device was primarily a microfluidic chip in which optical detections were carried out. Optical components were externally integrated with the device.

The work on the first fully integrated multiphysics Micro Total Analysis System was published in 1998. Burns et al. (1998) fabricated an integrated nanoliter DNA analysis device, and the schematic of the device is shown in Figure 1.3. The device consisted of nanoliter liquid injector, sample mixing and positioning system, temperature controlled reaction chamber, electrophoretic particle separation system, and fluorescence detector. The device which was fabricated on silicon platform measured 47 mm in length, 5 mm in width and 1 mm in height. Samples are placed in the inlet ports, wherein the fluid was drawn into the mixing zone through capillary action. The diode photodetectors were implanted onto the silicon substrate. This monolithically integrated device is useful for DNA analysis for nanoliter volumes of fluids. Another advantage is the requirement of low voltages for all its operation, thereby making the device portable. The integration of a temperature sensor and a temperature controller is a novel idea for  $\mu$ TAS applications, though other groups have started working on the idea for other applications as well (Wu et al. 2000).

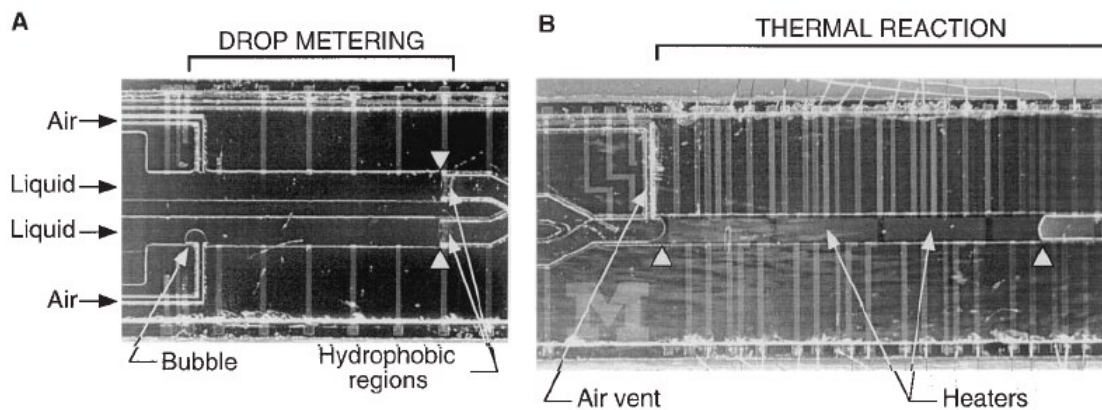
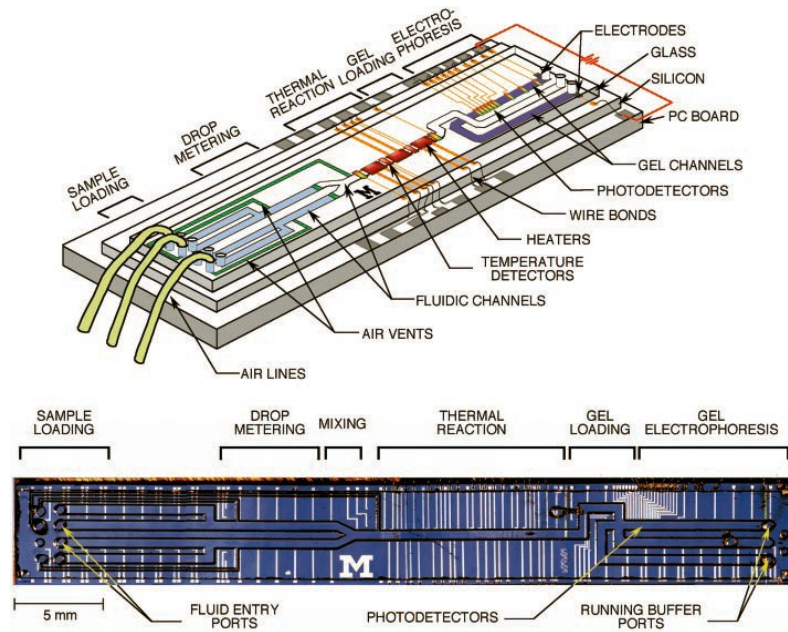


**Figure 1.3:** Fully integrated  $\mu$ TAS fabricated by Burns et al. (Burns et al. 1998). (A) and (B) show the micrographs of the drop metering system and the thermal reaction systems of the  $\mu$ TAS. The microfluidic channels were made of glass.

By the turn of 21st century, traditional silicon based materials were replaced with other materials for  $\mu$ TAS fabrication, such as Plastics, Poly-dimethylSiloxane (PDMS), Poly Methyl Metha-Acrylate (PMMA) etc. Bartholomeusz et al. adopted a bioluminescence detection method on PDMS microfluidic platform for potential application in Lab-on-a-chip devices (Bartholomeusz et al. 2000). Herein, the stoichiometric change in the

concentration of ATP (5.0 mM) during the reaction with Luciferin (1.25 mM)/ firefly Luciferase (1.84  $\mu$ M) was observed by measuring the change in the intensity of light produced during the reaction. PDMS microfluidic channels were fabricated by using SU8 as the mould. The channels were sealed using glass lid. Reaction chamber was fabricated using anisotropic micromachining. The bioluminescence was imaged using a CCD camera. The major limitation of this detection technique is that, it is applicable only to a few systems which could employ bioluminescence. The authors have however mentioned the feasibility of integrating the device with micro-needles for precise flow metering and also the technique of incorporation of silver micromirrors for enhanced CCD imaging and visualization.

Guenat et al. (2001) have described a  $\mu$ TAS based on the principle of using two electro-osmotically driven pumps. The analysis system consists of electromagnetic valves for the inlet of the fluids, reservoirs, for the fluid storage, and micromixer chamber to facilitate the interaction of two fluids. The device was fabricated in three layers on Pyrex substrate. A notable feature of this work is that the fluidic system has been designed carefully to enable continuous titrations of low volume buffer solutions with suitable characterization and calibration of the pump and the valve system using 10 mM borax solution. The maximum flow rate of 70 nL/s was achieved with 2 kV. The micromixers were also calibrated using Congo red indicator and 10 mM Nitric acid. Biological samples were however not used for testing with the device.

In the same year, Friis et al. (2001) had fabricated a Silica-on-Silicon (SOS) waveguide with integrated microfluidic channel. The device was used for flow cytometry. Polysilicon was used as a top sealing cover with anodic bonding for the microfluidic channels. Beam Propagation simulations have been carried out by the authors to study the optical behavior in the fabricated waveguides. While optical detection has been carried out in this work through both absorption and fluorescence detection (with 100 mM fluorescein), at 488 nm coupled into the Germanium doped waveguide through a single mode fiber, the principle of fluid actuation within the system has not been demonstrated therein.

Webster et al. (2001) fabricated a monolithic electrophoresis system for fluorescence based detection. The device was integrated with monolithically fabricated photodiodes which enable fluorescence sensing. Electrophoresis system is used for particle separation. The device has been tested for real-time fluorescence detection at 477nm using DNA labeled with YOYO dye (Molecular Probes) for different concentrations. However, the noise in the photocurrent was comparable to that of the signal and therefore, the use of a different excitation source has been suggested for better fluorescence detection. The device fabricated herein, proposes the method of monolithic fabrication and forms a platform for fabricating in-built light sources with suitable optical filters which would enable the realization of a fully integrated device for the application proposed herein.

In 2002, Cui et al. have demonstrated the hybrid integration of optical waveguides within the microfluidic channel for Dielectrophoresis (DEP) based fluorescence detection at



635/680 nm. Herein, SU8 microchannels integrated with metal electrodes for particle actuations have been fabricated. Input and output optical fibers were aligned on top of each other and glued within the channels to form a hybrid integrated setup. DEP was characterized using the principle of optical scattering. Light was coupled from external source and the detection system consisted of a photodiode with an interference filter fiber capable of detecting at 680 nm. The system under discussion herein presents an example of a typically hybrid integrated device.

Mogensen et al. (2003) have demonstrated the integration of SU8 waveguides with microfluidic channels. The optical characterization and the feasibility of biodetection using the proposed device was demonstrated through absorption measurements using bromothymol cells. The device was fabricated on borosilicate and Silica-on-silicon substrates. Three types of packaging were studied using borosilicate, UV gluing and adhesion bonding using a maninated film, and thirdly using PDMS as top cover. In this paper, the details of microfluidic actuations are not provided. Medero et al. (2003) have demonstrated an all electronic Lab-on-a-chip device with dielectrophoretic actuation of the particles to be sensed by measuring the impedance. The device was built on a PCB. The work also describes the characterization and the real-time testing of the device with bacteria, along with the computer assisted simulation results.

One of the important works of interest was carried out by Ruano et al. (2003) in the fabrication of integrated microfluidic waveguide based device for fluorescence based detection. In this work, the glass waveguide system, comprising of the longitudinally

tapering waveguides, beam splitters, S-bends and the Y-branch were fabricated using Flame Hydrolysis deposition (FHD) of doped Silica on oxidized Silicon, and the PDMS layer was bonded with the FHD glass with in reservoirs. Three layer PDMS microfluidic channel system was fabricated: one for the microfluidic channel, a seal cover and a final PDMS layer, for completely sealing the system. Fluid was injected into the system using a syringe pump and transmission losses for single mode propagation in the waveguide system was 0.4 dB /cm at 633 nm, measured with a silicon photodetector. Experimental characterization of the device was performed with 24  $\mu\text{M}$  Cy5 dye that yielded a SNR (signal to noise ratio) of  $\sim 9$ . However, the work was stopped at that stage with more to be reported about the real-time characterization of the device with fluorescent particles.

In the same year, Ahn et al. (2004) have fabricated a Lab-on-a-chip device for the detection of oxygen, lactate and glucose in blood. The work is novel for several reasons. Two types of fluidic systems have been described, namely the sPROM (Smart Programmable Microfluidic system) which consists of microvalves, and microdispenser, and secondly, the air-bursting detonators, wherein the fluid was pushed into the channels by pressurized gas stored in a chamber, which was released when the membrane of the chamber was deformed by a microheater, as shown in Figure 1.4. Another novelty of this work is that, the device was fabricated on a different material base, namely, Cyclic Olefin Copolymers (COC). Microfluidic channels were prepared by injection molding, details for which have been presented therein. Individual modules were tested and characterized for their performance. The method of electrolytic sensing has been employed in this work

to detect oxygen, glucose and lactate in blood. The overall device dimension is 1 in x 1 in x 0.25 in.

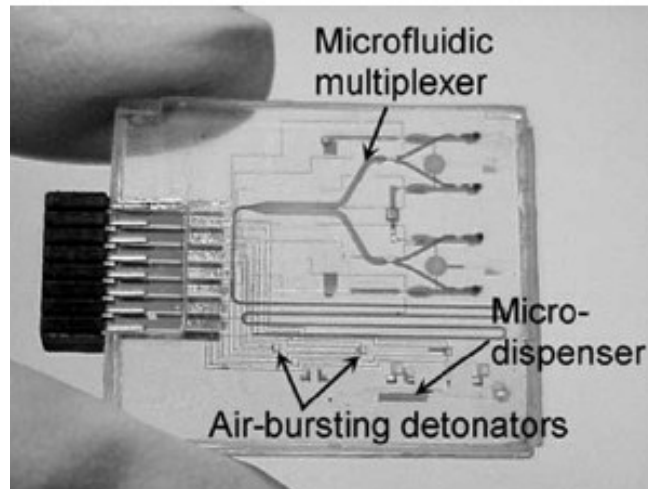


**Figure 1.4:** Assembled biochip with sPROM microfluidic control system (Ahn et al. 2004)

Minas et al. (2005) have demonstrated the fabrication of a Lab-on-a-chip device based on the principle of optical absorption. Herein, microfluidic channels were fabricated from SU8-on-glass. Optical filtering and detection systems have been fabricated separately and glued with the photodetector unit onto the microfluidic chip. The system was illuminated from the top and the optical filters ensured that only the appropriate wavelength range was sensed by the photodetectors. In this work, uric acid and protein samples were measured for their optical absorbance. However, the techniques of fluid actuation have not been detailed therein. The overall size of the device was  $2 \times 5.3 \text{ mm}^2$ .

While the trend of research has shifted from hybrid integration to monolithic and fully integrated systems, de la Fuente et al. (2005) in their work have developed an integrated

$\mu$ TAS with integrated photodiodes fabricated on silicon wafer. The main novelty of the present work is the coupling of SU8 polymeric waveguides with Silicon photodetectors, while there have been previous works carried out for coupling waveguides with Group III-V photodetectors. The input light to the waveguide is supplied from an external source through a fiber with connector coupled with the waveguide. The fabrication of the waveguiding system consisted of three layers with the top and the bottom cladding layers for the waveguide fabricated using SU8 with lower refractive index. Pyrex was used as the top cover for the microfluidic channels and bonded with the SU8 layer using Kapton thin film. In this work, however, the authors have merely characterized the optical components of the system. Though the present work serves as a paradigm and a platform for monolithic integration, it is important to carry out the microfluidic characterization with chemical and biological samples in order to utilize the presented device for real-time  $\mu$ TAS applications. The authors have also not demonstrated the feasibility of biodetection using biological molecules.

Balslev et al. (2004, 2006) fabricated a Lab-on-a-chip device which consisted of a dye laser, waveguides with integrated microfluidic channels, and photodiodes. The device is shown in Figure 1.5. The waveguide was fabricated in SU8 on Silicon substrate and the channels were etched on the SU8 using standard lithographic technique. The system also consisted of a diffusion mixer. Fluorescence was measured and detected by the photodiodes fabricated on the same chip. The research group has characterized the device for integration, by measuring the photodiode signal for different xylenol orange dye solutions. Optical characterization was carried out for the SU8 waveguides and the dye

laser. The method of fluid actuation has not been specified in this work. However, this device forms an example of a monolithically integrated device.

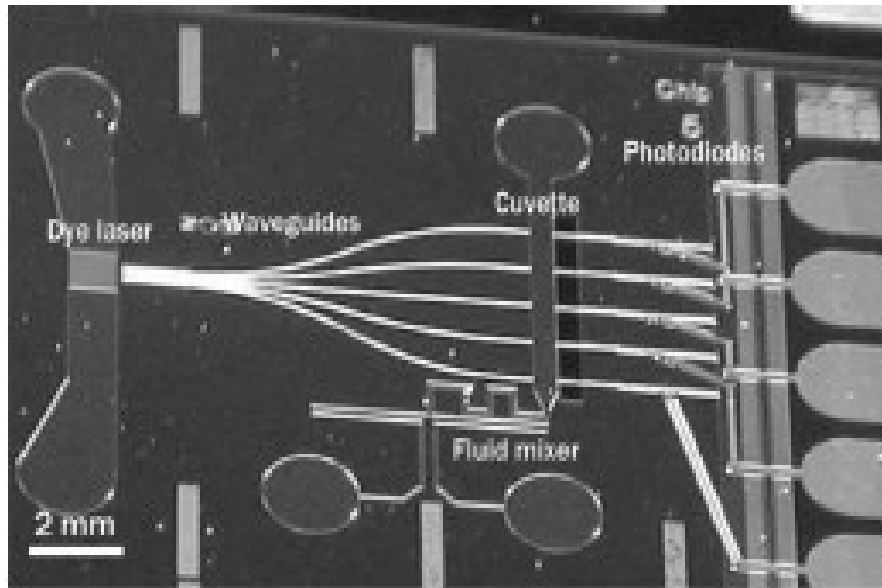


**Figure 1.5:** Lab-on-a-chip with integrated waveguides, microfluidic channels, dye lasers and photodetectors (Balslev et al. 2004)

Integrated waveguides with microfluidic channels for fluorescence based detection has been demonstrated by Mazurczyk et al. (2006). In this work, waveguides fabricated out of soda lime glass were used and microfluidic channels were fabricated through the waveguides by ion exchange machining. PDMS was used as the microfluidic channel sealant. Electro-osmosis and electrophoresis were used for actuation of the fluid through the microfluidic channels. The fluorescence study was carried out using Cy3 excited by Nd-Yag laser. In their subsequent publication (Vieillard et al. 2007), the research group has demonstrated the application of the microfluidic device and its characterization. The novelty of the presented work is the monolithic integration of the waveguide with the microfluidic channels. There have been other similar works demonstrated in which SU8

has been etched to form microfluidic channels. It is to be noted that SU8 offers good waveguiding due to very low surface roughness and also offers superior bioaffinity. Herein, the bioaffinity aspects of the microfluidic channel were developed and the real-time application of the proposed device for fluorescence detection was not demonstrated.

$\mu$ TAS configuration with a possibility of integrating micropump, microfluidic channels, integrated metal electrodes, Mach-Zehnder interferometers (MZI), Silicon-on-Insulator (SOI) lateral, tapered, and bent waveguides, and photonic crystal waveguide structures was fabricated through MicraGeM process technology (Micralyne Inc., Edmonton, Canada) and the SEM of the  $\mu$ TAS is as shown in Figure 1.6. In order to carry out the testing on the device, a wafer dicing method (Chandrasekaran and Packirisamy, 2007) was used to separate the different components of the  $\mu$ TAS.

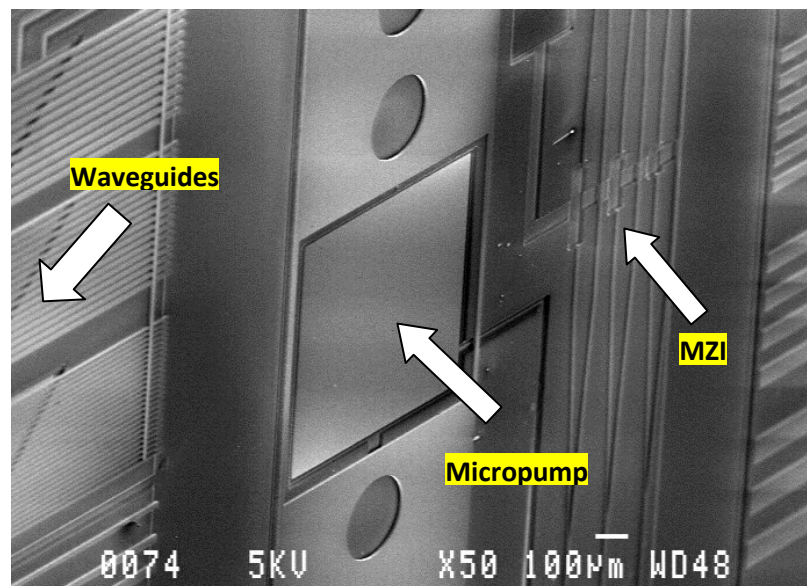


**Figure 1.6:** Scanning Electron Micrograph (SEM) of a  $\mu$ TAS fabricated on SOI platform with integrated micropumps, microfluidic channels, metal electrodes, Mach-Zehnder interferometers, straight and tapered waveguides and photonic crystal structures (Chandrasekaran, Packirisamy 2007).

Among the recent works on the synthesis of Lab-on-a-Chip systems, an integrated system for the sensing of antibiotics in milk was demonstrated by Suarez et al. (2009). The fluid within the system was actuated using an external syringe pump, and the wavelength interrogated optical sensing (WIOS) technique was implemented for biodetection. Sheridan et al. (2009) integrated PDMS based microfluidic channels with waveguides fabricated with acrylate polymer “True Mode” for carrying out optical absorption and fluorescence detection. The fluorescence detection was demonstrated using Fluorescein, and high sensitivity was reported. Carlborg et al. (2010) have fabricated a multilayer compact system-on-chip with ring resonator integrated with microfluidic system. The device was used for the sensing of methanol, ethanol and anti-Bovine Serum Albumin (anti-BSA). The integration of multilayer chip using double sided adhesive tapes and PDMS with plastic packaging material has also been discussed therein.

Apart from the works analyzed so far, several review papers have been published from different research groups on the  $\mu$ TAS. Many research groups have been working on the individual components of a  $\mu$ TAS and the feasibility of integration of the components with the device. Several methods have been proposed, for sensing and detection, sample transportation, sample treatment, surface modifications etc, for  $\mu$ TAS applications. There are also commercially available microfluidic devices that are used for Point-of-Care diagnosis, such as Abbott’s iSTAT (Steinfeldt et al. 2010), Epochal Point of Care (Laukts, I. and Maczuszenko, A., 2010) and Labnow’s Nanobiochip (Jokerst et al. 2010), among others.

The following table summarizes some of the prominent yearwise works in the development of Micro-Total Analysis Systems during the last two decades.

Reference	Year	Components of the integrated $\mu$ TAS	Material platform	Sensing	Actuation	Integration
Manz et al.	1991	Flow cell, optical coupling	Silicon channels with integrated fibers,	Absorption	Chromatography	Hybrid
Verpoorte et al.	1994	Microfluidic channels, Micropump, ISFET	Silicon, Glass,	Absorption	Piezoelectric actuated pumping	Hybrid
Ramsey et al.	1996	Reaction chamber, Separation column, Micromixers	Glass	Fluorescence detection	Electrophoresis	Hybrid
Burns et al.	1998	Sample injector, Mixer, Temperature controlled reaction chamber, Particle separator, Detection unit	Glass bonded with the substrate,	Fluorescence	Electrophoresis	Monolithic
Bartholomeausz	2000	Microfluidic channels, Reaction chamber,	PDMS channels, glass lid, SU8 mould for PDMS, Silicon	Bioluminescence	Capillary forces	Hybrid
Guenat	2001	Microvalves, EO micropump, Micro-reservoir, Micromixer	Pyrex, PMMA	Potentiometric	Electro-osmosis	Monolithic
Webster et al.	2001	Microfluidic channels, Reaction chamber, Photodiodes,	Oxidised Silicon, ParyleneC	Fluorescence	n/a	Hybrid
Friis et al.	2001	Microfluidic channels, waveguides	Glass, Silica-on-Silicon, Polysilicon	Absorption/Fluorescence	n/a	Hybrid
Cui et al.	2002	DEP, optical detection system,	SU8, silica fibers, glass cover	Fluorescence	DEP	Hybrid
Medoro et al.	2003	Integrated Electrodes on a PCB	PCB	Impedance	DEP	Monolithic
Ruano et al.	2003	Microfluidic channel, reaction chamber, waveguides	Silicon, PDMS, Glass waveguides	Fluorescence	Syringe injection	Hybrid
Mogensen et al.	2003	Microfluidic channels, Polymer waveguides,	SU8, Borosilicate, PDMS	Absorption	n/a	Hybrid
Leeds et al.	2004	Microfluidic channels, Integrated waveguides	SU8, PDMS	Fluorescence	Capillary	Hybrid



Ahn et al.	2004	Microfluidic channels, Micro-dispenser, Air detonators, Microheaters	Cyclic Olefin Copolymers	Amperometry	sPROM, Detonators	Monolithic
Minas et al.	2005	Microfluidics, Optical filtering, Photo detectors, read out systems	SU8 on glass, Silica photodiode,	Absorption	N/A	Hybrid
Delafuente et al.	2005	Microfluidic channels, Photodiodes, buried waveguides	SU8, Silicon, Pyrex, Kapton	N/A	N/A	Hybrid
Balslev et al.	2006	Microfluidics, Dye Laser, waveguide, photodiodes, Reaction chamber	SU8, PMMA lid, Doped Silicon,	Absorption	Capillary	Monolithic
Mazukczyk et al.	2006	Microfluidic channels, Integrated waveguides,	PDMS cover Soda lime Glass	Fluorescence	Electrophoresis	Hybrid
Viellard et al.	2007	Microfluidic channels, Integrated waveguides	Soda lime Glass, PDMS cover	Fluorescence	Electrophoresis	Hybrid
Yegnanarayanan et al.	2007	Microfluidic channels, Microdisk resonator, waveguide,	SOI waveguide, PDMS microfluidic channel	Resonance shift	Syringe injection	Monolithic
Luan et al.	2008	Microfluidic channel, Photodetector	InGaAs Photodetector, Glass channels, Silicon	Absorption, Fluorescence	Electrowetting	Hybrid
Jugessur et al.	2009	Bragg Grating, Microfluidic channel	PDMS microfluidic channel, SOI	Spectral shift	Syringe injection	Hybrid
Sheridan et al.	2009	Microfluidic channel, optical waveguides	PDMS, Acrylate "Truemode" waveguide	Fluorescence, Absorption	N/A	Hybrid
Suarez et al.	2009	Waveguide grating, microfluidic channel	Glass, PMMA	Evanesence	Syringe pump	Hybrid
Carlborg et al.	2010	Ring resonator, Slot waveguides	PDMS microfluidics, Silicon ring resonator	Refractive Index Shift	Syringe pumps	Hybrid

**Table 1.1:** Prominent works in the development of microfluidic systems with integrated optical sensing for Lab-on-a-Chip systems and Micro-Total Analysis System applications during the last decades.

### 1.3. Components of a $\mu$ TAS

There are several components which could be incorporated into a  $\mu$ TAS depending upon their application, but the prominent modules are those which enable the ease of biomolecule handling and transportation, suitable transduction, sensing and detection, with other integrated components. The main processes which take place in a  $\mu$ TAS are sample introduction, pretreatment of the sample, mixing, chemical and biological reactions, molecule separation and detection (Krawczyk 2003). Therefore, it is imperative to have a means of transporting the fluid into the sensing system, and it is herein that the role of microfluidics assumes significance. Target recognition for any analyte, chemical, biological or gas sample, is the key aspect for the success of a  $\mu$ TAS, which places a lot of importance on the development of a suitable sensing mechanism for the  $\mu$ TAS. Apparently, the limiting factor in scaling down the dimensions of a  $\mu$ TAS is set primarily by the analyte detector or the sensing system (Zourob et al. 2003), therefore, the detection system must be well integrated with its microfluidic counterpart. In summary, the most basic components of a  $\mu$ TAS include the microfluidic system, a fluid actuator and a suitable target detection system.

For chemical and biological sensing, detection issues arise when sensing systems are miniaturized. The reduced analyte volumes, which in turn reduce the quantity of fluid available for detection, therefore require an extremely efficient sensing system that is capable of sensing with nano and pico litres of available analytes. Thus, the two main factors that affect the choice of the detection method for microfluidic devices are sensitivity and scalability into smaller dimensions.

Mechanical resonant types (Chandrasekaran et al. 2011) were one of the earliest studies for MEMS based biodetections by virtue of the vibrational property changes in the structure upon the interactions of enzyme and antibody molecules. Electrochemical methods of detection reported in the literature (Schwarz, Hauser 2001) include potentiometric, conductimetric (measuring the ion conductivity), amperometry (based on the oxidation or reduction currents of analytes at a working electrode). EnFET's and Ion Sensitive Field Effect Transistors (ISFETs) are also incorporated into the sensing systems (Yuqing et al. 2003) and impedance sensing methods have also been explored for a  $\mu$ TAS. However, in all the above mentioned methods of biodetection, the most common feature observed is that, a number of sensitive physical parameters are involved which would result in the variation of the bio-detection with physical parameters. In electrochemical methods, the electrical characteristics of solutions are believed to play an important role in physiological functions that involve protein-protein and charged ligand interactions (Ayliffe et al. 1999). This leads to drawbacks such as dependence of the on geometry of the cells being studied, which needs to be overcome. Electrochemical detection techniques (e.g. conductivity, potentiometric sensing etc.) do not answer the issues with sensitivity and miniaturization for portable  $\mu$ TAS that are required to carry out high throughput sensitive biodetections. Optical detection methods provide solutions to the drawbacks of most of the other techniques. Hence there is an emerging interest to couple and integrate optical components into microfluidic devices.

Microfluidics is an important component of a  $\mu$ TAS because, it not only enables the transportation of specimens into the system but also enables the handling of smaller sample volumes conveniently. Some of the earliest  $\mu$ TAS developed were centered on the microfluidics module, by suitable integration subsequently with other complimentary modules. In some works, particle separators and microdialyzers have been used. Thermal conditioners have also been incorporated into a  $\mu$ TAS (Burns et al. 1998). Fluidic actuator system consists of methods of inducing the fluid movement within the microfluidic channel. Some of the common microfluidic actuation systems that have been used in  $\mu$ TAS are electrophoresis, electro-osmosis, dielectrophoresis and electrowetting. Microvalves have also been provided for controlling the fluid motion in and out of the system.

Thus, the successful synthesis of a  $\mu$ TAS depends on the effective integration of all the components of the device suitable for the various applications. Figure 1.7 provides a list of some of the components which can be integrated within a  $\mu$ TAS.

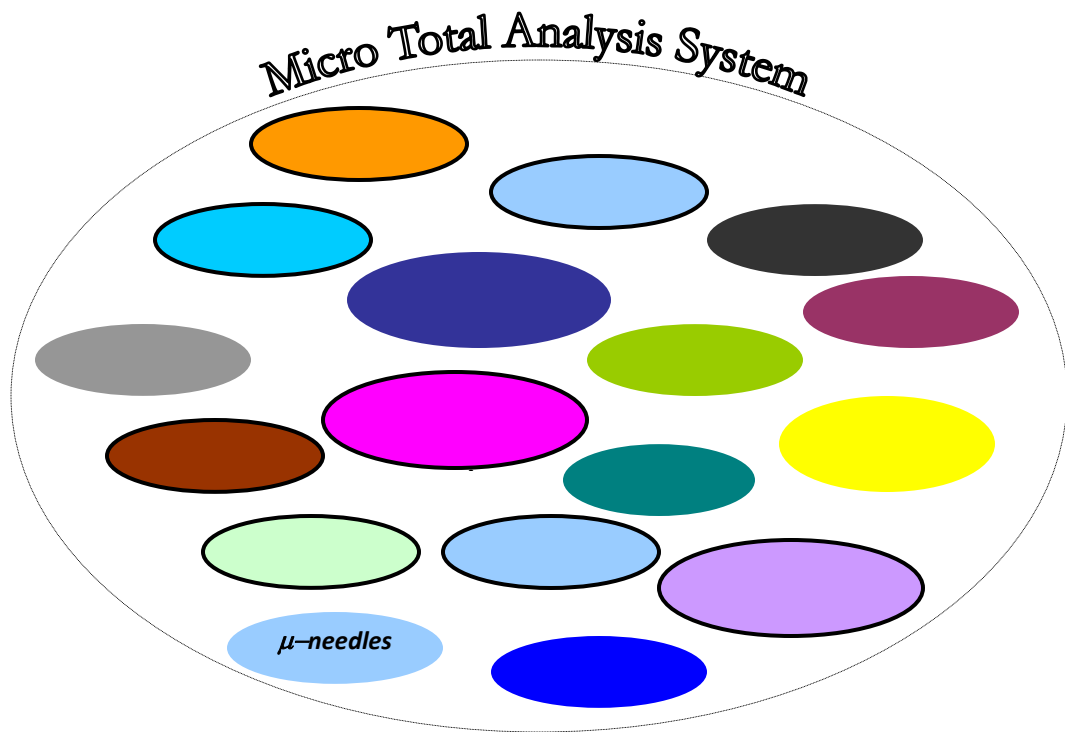


**Figure 1.7:** Different components that can be used in a μTAS.

### 1.3.1 Optical detection systems and integration with μTAS

Optical detection for biosensing consists of waveguide and non-waveguide based approaches.

Waveguide based optical devices offer a lot of advantages for biophotonic sensing compared to non-waveguide based devices due to the feasibility of miniaturization, and integration with μTAS. Among the waveguide based sensing techniques, optical absorbance (Ceriotti et al. 2003) is one of the earliest used biophotonic detection methods for a μTAS. But the method is not applicable to all bio-species, because not all biomolecule contain the chromophores that can exhibit optical absorption. Prominent

absorption of proteins is observed in the UV range and thus there would be a problem with integration of the UV sources within  $\mu$ TAS (Krawczyk 2003).

Fluorescence spectroscopy is another common and convenient method of detection compatible with several  $\mu$ TAS applications and fluid actuation systems. The main advantage of fluorescence detection is the possibility of carrying out simultaneous detection of multiple analytes through the detection of different fluorescent wavelengths. With the advancement in bioconjugation techniques and fluorescent markers, fluorescence detection has been very useful for the detection of smaller concentration of target molecule.

One of the main drawbacks of fluorescence detection is the necessity to tag the biomolecule with suitable fluorophore, which brings about the involvement of an additional processing step. Though fluorescent systems have also been used in commercially available Lab-on-a-chip devices (Jokerst et al. 2010), there is a surge in the requirement for simple detection systems which can be readily applied for Point-of-care testing. Therefore, it is important to identify suitable label free biodetection techniques for  $\mu$ TAS applications.

Among the different label free methods, Refractive Index (RI) measurements and Surface Plasmon Resonance (SPR) are some of the Evanescent wave methods, caused by the generation of the evanescent wave from the interface of the cladding and the core of the waveguide, have been commonly used for optical detections. Zourob et al. (2003) have

proposed a leaky waveguide system for  $\mu$ TAS applications. Utilizing the refractive index change measurements, Microring resonators (Yalin et al. 2006), (De Vos et al. 2006) have been developed by de Vos et al. consists of Silicon-On-Insulator (SOI) optical ring resonator with a radius of 5  $\mu$ m capable of detecting bulk refractive index changes of the order of  $10^{-4}$  through resonance shifts. Horvath et al. have demonstrated a reverse symmetry waveguide wherein the refractive index of the substrate is lesser than the refractive index of the aqueous covering medium (Horváth et al. 2002). The reverse symmetry waveguide (Skivesen et al. 2007) has been reported for real-time bacterial and cell detection. Skivensen et al. (2007) have reported on the Deep probe metal clad waveguide based biosensors. White et al. (2007) have proposed refractometric sensing based on ring resonators for Lab-on-a-chip applications wherein the Whispering Gallery Mode (WGM) spectral shift was used for the detection of ethanol solution with integrated microfluidic system. In other transducer configurations, the evanescent field sensors have been used as Mach-Zehnder Interferometers (Prieto et al. 2003), microdisks and directional couplers (Densmore et al. 2006b). Among the recently published articles on waveguide based detection for  $\mu$ TAS, Zourob has proposed an integrated deep probe waveguide system for bacterial detection (Zourob et al. 2007). Thereafter, Zourob has also worked on a dye clad leaky waveguide for other cell detection (Zourob et al. 2005). The feasibility of using evanescence detection on SOI platform using Infrared wavelength for integrated microfluidic  $\mu$ TAS has been demonstrated (Chandrasekaran and Packirisamy 2009). Surface-enhanced Raman scattering (SERS) has now enabled Raman spectroscopy to become a much more common detection method for microfluidic systems (Huh et al. 2009). This technique is now commonly used for biological

detections and biomolecular analysis including single molecule detections. The use of SERS for the detection of Dengue sequences was reported by Huh et al. (2009). In another work, Suarez et al. (2009) have demonstrated the method of wavelength interrogated optical sensing (WIOS) approach, based on using a collimated light beam from a vertical cavity surface emitting laser (VCSEL) as wavelength-tunable source for exciting waveguide modes in a dielectric waveguide by means of an input grating coupler. When the resonance condition is fulfilled, light is transmitted via an output grating coupler to a photodetector. The output signal of the photodetector represents the grating coupler resonance peak whose position indicates the surface mass density of analyte molecules adsorbed on the sensor chip's surface. The schematic is as shown in Figure 1.8.

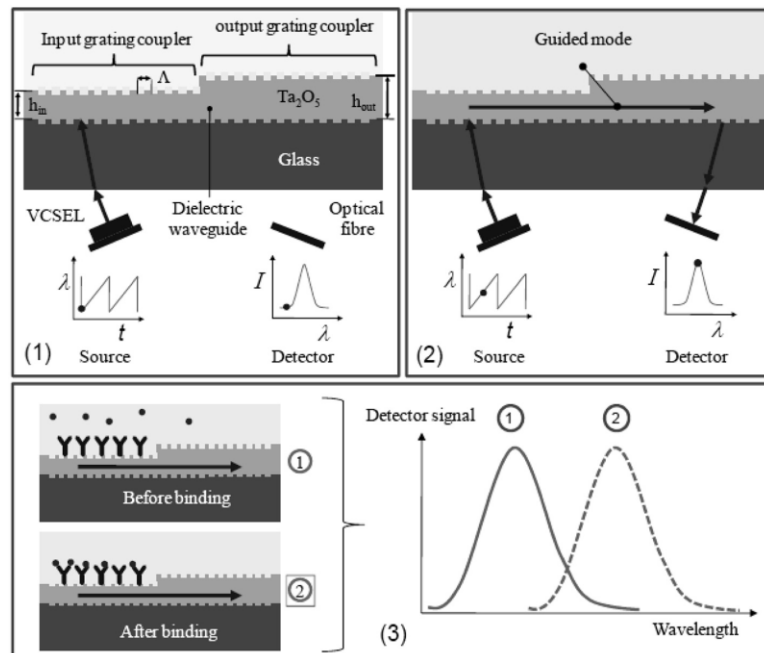


**Figure 1.8:** Schematic of the wavelength interrogated optical sensor (WIOS) technology based on grating waveguide resonant coupling (Suárez et al. 2009).



Although optical-detection devices can achieve the low detection limits, the optical detection has typically been implemented in most of the Labs-on-chips using externally hybrid integrated systems that do not offer the robustness, stability, or operator independence of fully integrated approaches. The greatest challenge in the synthesis of a  $\mu$ TAS is the development of integrated on-chip optical detection system. However, advanced fabrication technologies and packaging methods have now facilitated to a great extent, the monolithic fabrication of optical systems with microfluidic devices on several material platforms for  $\mu$ TAS synthesis.

The integration of SU8 waveguides with PDMS microchannels was studied in the work by Leeds et al. (2004). Herein, two types of devices have been proposed, namely, SU8 waveguides (50  $\mu$ m and 100  $\mu$ m core) and PDMS material used as a mold on a 2.5 x 7.5  $\text{cm}^2$  glass slide. The other type of device proposed is a hybrid device with SU8 waveguides and integrated PDMS microfluidic channels. The microfluidic channels were formed by selectively removing the non-waveguiding portion of the SU8. However, in order to reduce the optical loss due to the usage of two different materials, SU8 has been completely used for the fabrication of the integrated chip. The devices mentioned here have not been tested for real-time biological sensing applications.

Friis et al. (2001) had fabricated a Silica-on-Silicon waveguide with integrated microfluidic channel. The device was used for flow cytometry. Balslev (2004) has demonstrated the integration of waveguides and photodiodes with the microfluidic system for fluorescence detection. Cui et al. (2002) have demonstrated the hybrid

integration of optical waveguides within the microfluidic channel for dielectrophoresis based fluorescence detection at 635/680 nm. Herein, SU8 microchannels integrated with metal electrodes for particle actuations have been fabricated and input and output optical fibers were aligned, on top of each other and glued within the channels to form a hybrid integrated setup. Deposition of silica, with a variety of diffractive indices for low-loss planar waveguides purposes, to incorporate the microfluidic network in the same device, was presented by Ruano et al. (2003) who successfully tested it with a microtitration system. Minas et al. (2005) have demonstrated the fabrication of an optical detection based Lab-on-a-chip device wherein, microfluidic channels were fabricated from SU8 on glass. In this study, on-chip optical filtering and detection system were fabricated and the microfluidic chip was glued with the photodetector unit. Using a hybrid integrated setup, UV absorbance detection of tryptophan through PDMS channels was made possible using pre-aligned optical fibers to guide light to the channel and collect the transmitted light onto the detector (Ceriotti et al. 2003). The feasibility of integrating a Spectrometer-on-Chip with a hybrid integrated opto-microfluidic setup was demonstrated by Chandrasekaran et al. for fluorescence based biodetection (Chandrasekaran et al. 2007).

Integration of polymer based sub-micron grating optical elements using injection molding technique was one of the works done by Angelov and Coulter (2008). Among the more recent works, the feasibility of fabricating a Lab-on-a-chip device using SOI and PDMS platform has been demonstrated by Yegnanarayanan et al. (2007) wherein, micro disk resonators have been integrated with fluidic channels and the performance of the device has been tested using a shift in the absorbance wavelength for a refractive index change

in a test fluid used. The group is currently working on the integration of the device to an on-chip spectrometer (Momeni et al. 2006). The main advantage of the device is the feasibility of monolithic integration, with the dimensions of the sensing unit being of the order of nanometers. The integration of photonic nano-Bragg grating device with microfluidic channels have been demonstrated by Jugessur et al. (2009) wherein the wire Bragg grating structure was fabricated using electron beam lithography and reactive ion etching on SOI material and integrated with PDMS microfluidic chip using a reversible active sealing method, as shown in Figure 1.9. Most recently, Carlborg et al. (2010) have fabricated a multilayer compact system-on-chip with ring resonator integrated with microfluidics and demonstrated the detection of Bovine Serum Albumin (BSA).

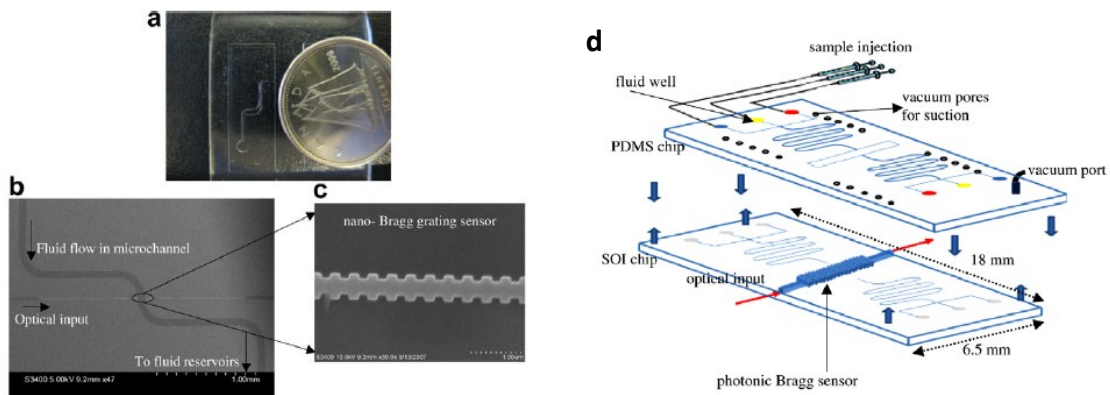


**Figure 1.9** (a) Microfluidic chip on PDMS (b),(c) Nano-Bragg grating on SOI microfluidic channel (d) Schematic of the proposed integrated device fabricated by Jugessur et al (2009).

Orthogonally integrated waveguides for laser induced fluorescence detection has been used by Fu et al. (2006) for the detection. The integration of Organic Light Emitting Diode (OLED) with PDMS based microfluidic channels were presented by Azam et al.

(2008). In another work, selective integration of gold micromirror reflectors with anisotropically etched silicon microfluidic channels to enhance fluorescence based biodetection was presented (Chandrasekaran, Packirisamy 2008). The feasibility of integrating polymer based sub-micron grating optical elements was demonstrated by Angelov and Coulter (2008) using injection molding technique. Photonic crystals fabricated in optical polymer (Norland Optical adhesive, NOA63) have been integrated with microfluidic channels for refractive index based measurements (Wu et al. 2008).

Thus, even though an abundance of optical sensor principles has been demonstrated, very few have successfully been integrated in complete labs-on-chips and  $\mu$ TAS. The success of a  $\mu$ TAS depends upon the suitability of integration of detection unit with the microfluidic module in a monolithic manner, with these optical detection units being fabricated on the same material platform as the other  $\mu$ TAS modules usually involving multiple lithographic processes or in an internally hybrid integrated manner on the same device.

### **1.3.2 Introduction to Microfluidics**

The main processes which take place in a  $\mu$ TAS are sample introduction, pretreatment of the sample, mixing, chemical and biological reactions, molecule separation, particle sensing, and the ejection of the sample out of the system (Krawczyk 2003). Therefore, it is imperative to have a suitable means of transporting the fluid in and out of the sensing system, and it is herein that the role of microfluidics assumes significance. A microfluidic

system in a  $\mu$ TAS, apart from enabling the handling of smaller sample volumes of reagents, also assists in transportation and ejection of the chemical and biological specimens and carrying out other functions such as fluid preprocessing, and mixing. Several microfluidics based  $\mu$ TAS have been synthesized for various applications such as chromatography, electrophoresis, pH monitoring, toxicology, forensic analysis, etc. Apart from fluid transport, the other main functionalities of microfluidic systems in Lab-on-a-Chip and  $\mu$ TAS include fluid metering, fluid mixing, separation, concentration amplification, reagent storage, etc. (Haeberle, Zengerle 2007).

Most of the microfluidic systems for  $\mu$ TAS and LOC have been developed for biological and chemical detections. Drug delivery (Chung et al. 2008) is an important application of microfluidics in LOC. Madou group (Lai et al. 2004) from the University of California, Irvine, used a series of capillary valves to perform ELISA on the centrifugal platform and demonstrated that centrifugally conducted assay has the same performance in terms of detection range as the conventional method. The main advantages of this system over the conventional method are less reagent consumption and shorter assay time. An integrated device with fluidic and thermal components such as heaters, temperature sensors, and addressable valves to control two nanoliter reactors in series, followed by an electrophoretic separation, was presented (Pal et al. 2005) for influenza and genetic analyses. Fully integrated PCR (Polymerase Chain Reaction) - capillary electrophoresis microsystem consisting of microfabricated heaters, temperature sensors, and PCR chambers directly connected to capillary electrophoretic separation channels for DNA analysis was demonstrated by Lagally et al. (2001). Other biological applications of

microfluidics include cell sorting (Krüger et al. 2002), particle separation (Huang et al. 2004), cytometry (Huh et al. 2005), passive immobilization, DNA analysis (Kim, Gale 2008), protein analysis, identifying gene expressions (Zhong et al. 2008), among several others. The commercial availability of microfluidic devices (Epigem Inc.) and Lab-on-a-Chip kits (Micronics Inc.) definitely boost the reliability and the confidence of these systems for molecular diagnosis and other practical biomedical applications, thereby motivating further research in this technology.

In the past, several material platforms have been explored for the fabrication of microfluidic systems. Materials such as silicon (Pattekar, Kothare 2004), (Ke et al. 2007) glass (Wilson, McCreedy 2000), quartz (Tadd et al. 2005) polymers and plastics, metals and a combination of the above, for e.g. silicon and quartz (Lu et al. 2001), silicon and plastic (Chandrasekaran et al. 2007), have all been used for microfluidic components. There are also works which have been carried out with the introduction of ceramic materials in microfluidics (Alm et al. 2008), (Groß et al. 2008), (Mitchell et al. 2006) as these ceramic materials combine high chemical stability with high thermal stability. Silica/Glass (Chandrasekaran, Packirisamy 2006), (Hessel et al. 2003), is a popular choice because of its chemical and biological inertness, its biocompatibility (Chandrasekaran et al. 2007), cost-effectiveness, ease of integration with Micro-opto-electro-mechanical systems (MOEMS) (Chandrasekaran, Packirisamy 2006) and also due to the fact that its fabrication technologies are fully developed. While silicon and glass dominated the early years, an increasing trend towards polymers as substrate materials in microfluidic devices is important to be observed.

A wide variety of polymers have been used to fabricate microchannels, such as Poly DimethylSiloxane (PDMS) (McDonald et al. 2000), Polycarbonate (Weston et al. 2001) PMMA (Polymethylmethacrylate) also known as Plexiglas, Perspex and Acrylic (de Mello 2002), Polyimide (Metz et al. 2004), Poly-xylene (parylene) (Webster et al. 1998b), Polyolefins (Lin, Burns 2005), Polycaprolactone (Armani, Liu 2000), Polysulfone (Schomburg et al. 1994), Polypropylene (Edwards et al. 2002) Isobornyl Acrylate (Kim, Beebe 2007) and photosensitive epoxy (Jackman et al. 2001). PolyethyletherKetone (PEEK) is also a commonly used polymer in microfluidics. It has been used for the manufacturing of connecting tubes (Günther et al. 2004). Polycarbonate is a popular material due to their temperature resistivity, transparency at visible range, rigidity and easier machinability, though they are chemically reactive to aromatic hydrocarbons which are used as microfluidic cleansing agents, like acetone, methanol and isopropanol (IPA). Other types of plastic substrates used are cellulose (acetate), Kapton® and Teflon® from DuPont, Appear™ 3000, Arylite™ A100. Cyclic Olefin Copolymers (COC) has been used by Ahn et al. (2004) for the fabrication of their disposable Lab-on-a-Chip system. An electrophoretic system for mutation detection on parylene-C based microchannels was demonstrated by Sukas et al. (2008). Borosilicon carbon nitride microstructures (Yang et al. 2001) have been fabricated and could also be used for microfluidic applications. The use of Topas as a material platform for Lab-on-a-Chip fabrication was demonstrated by Bilbenberg et al (Bilenberg et al. 2005). Channel surfaces with nano-structured patterns have been fabricated by injection molding technique (Pranov et al. 2006).

Several techniques have also been used for fabrication of polymer microfluidic devices. Hot embossing has been one of the techniques used for fabrication of microfluidic devices on polymers (Becker, Heim 2000). Photopolymerization of a prepolymer mixture of monomers and a photoinitiator through a mask was used by Beebe et al. (2000) to manufacture microfluidic systems. The review of Kim et al. (2008) details the different soft lithography works that have been carried out for microfluidic fabrication. Kenis et al. (2000) showed that lines could be patterned on PDMS, glass, and silicon by the transport of reactive species throughout a channel using laminar flow. The use of Benzophenone as a photoinitiator at wavelengths below 365 nm for PDMS microstructuring has been detailed by Bhagat et al. (2007b) which proves an alternate technique for fabrication of microfluidic channels on PDMS without master moulds or standard clean room lighting conditions. Also methyl methacrylate materials containing 2-2-azobisisobutyronitrile can be polymerized using the redox-initiation couple benzoyl peroxide and N,N dimethylaniline (Chen et al. 2007). A review of the fabrication of microfluidic devices for different applications has been carried out by McDonald et al. (2000).

Injection molding technique is used in the fabrication of several microfluidic devices on polymer material platforms. Experiments have been reported on using injection moulding to successfully replicate sub-micron test features (Monkkonen et al. 2002), (Liou, Chen 2006). Injection moulding is useful for the fabrication of several polymer microstructures, apart from those that have been commonly used for microfluidics applications. Research is still on going to study the feasibility of integrating those material platforms with classic silicon technology and polymer microfluidics. Among the



fabrication techniques for different polymer based materials, a direct writing method for the three-dimensional fabrication of Teflon was developed by Katoh and his group (Katoh et al. 2001). Teflon machining using ion beam etching has also been reported (Lee et al. 1998) and the fabrication of Borosilicon Carbonitride ceramic microstructures was described by Yang et al. (2001) for microchannels. Figure 1.10 shows the schematic of the three different polymer microfabrication technologies.

Microchannels on stretched Poly-ethylene terephthalate films using laser ablation were reported by Wagner and Hoffman (Wagner, Hoffmann 1999) Webster et al. (Webster et al. 1998a) fabricated parylene-C channels on polycarbonate substrates which were used for Capillary Electrophoresis, using vapor deposition. Fiorini et al (2007) suggest improvements for the fabrication of microfluidic channels using Thermoset Polyester. Van Kan et al. (2001) used Proton Beam Micromachining, a technique that focuses megaelectronvolt protons to produce 3D high-aspect-ratio microstructures on SU8 and PMMA, which were then electroplated to be used for micromolding and imprinting (Van Kan et al. 2001). Methods for the fabrication of embedded microchannels in positive and negative photoresists have been reported by Alderman et al. (Alderman et al. 2000), (Alderman et al. 2001). A porous microfluidic device useful for transporting the fluid in and out of the system has been fabricated by de Jong et al. (de Jong et al. 2007) using phase separation micromolding/microfabrication technique. Recently, integrated waveguides with microfluidic channels were fabricated on photopatternable acrylate polymer using lithography technique for fluorescence detections (Sheridan et al. 2009).

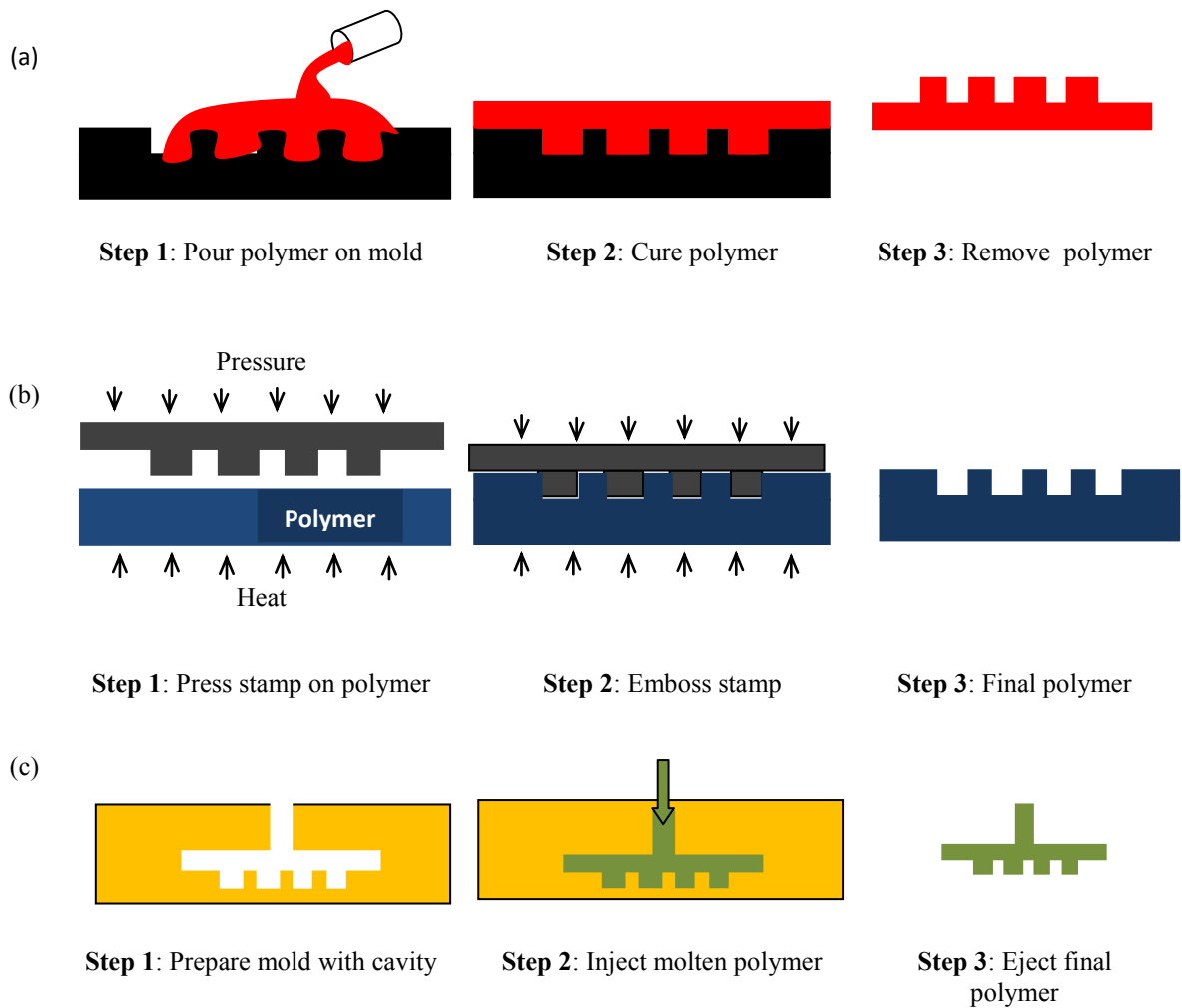


**Figure 1.10:** Polymer microfabrication technologies (a) Casting (b) Hot embossing and (c) Injection molding, adapted from (Bhushan 2006)

Among the different techniques for fabrication of moulds for polymers, conventional micromachining techniques have been used fabrication with minimum features as small as  $10\ \mu\text{m}$  (Becker, Gartner 2000). Microelectrodischarge machining has also been used for fabrication of three dimensional mould structures (Becker, Gartner 2000).

Several complimentary modules have been integrated with microfluidic systems for different  $\mu$ TAS applications. Fluid actuators are essential to cause the motion of the fluid within microfluidic systems. In most of the classical fluid actuating systems, a means of applying pressure difference across the channel is identified. This can be realized using micropumps with or without check-valves. Whereas digital microfluidic systems employ techniques such as electro-osmosis, electrophoresis, dielectrophoresis etc., mechanical fluid actuating systems such as micropumps are also commonly used for microfluidic actuation and manipulation. Integration of optical waveguides with microfluidic channels has been one of the primary and the most commonly employed optical integration methods for sensing applications, involving techniques such as absorption measurements, fluorescence studies, refractive index variation experiments etc. A review of different optical sensing systems that have been used with microfluidics systems was carried out by Kuswandi et al. (2007).

### **1.3.3. Micropump based fluid actuating systems in $\mu$ TAS**

Fluid actuation systems are necessary to be integrated with  $\mu$ TAS because they provide the feasibility of independently controlling the delivery and transportation of the biofluid through the system, thereby avoiding the necessity to hybrid integrate the microfluidic system with external macro actuation units such as the syringe pumps. As a part of the fluid actuation system, the micropump pose some important requirements, such as, ease of integration, biocompatibility with the fluid, actuation safety, small size, low power consumption, and flow rate controllability over a wide range of external conditions,

among others. To meet the above demands for biofluid actuation, several types of micropumps with different actuation mechanisms have been developed in recent years. Several comprehensive review papers have surveyed most of the developed microscale pumping technologies for  $\mu$ TAS applications (Amirouche et al. 2009), (Laser , Santiago 2004), thus throwing useful light on the different types of micropumps used with microfluidics and their applications.

Micropumps mainly fall under two categories, namely, displacement micropumps that use oscillatory or rotational pressure forces on the working fluid through a moving microstructure (vibrating diaphragm, peristaltic, rotary pumps), and continuous flow electro- or magneto-kinetic micropumps, wherein direct transformation of mechanical and non-mechanical energy to pumping power generates steady flows due to the continuous addition of energy (for e.g., electrohydrodynamic, magnetohydrodynamic). While traditional  $\mu$ TAS applications have extensively used mechanical micropumps, substantial progress has been made recently to develop electrohydrodynamic and magnetohydrodynamic micropumps on low-cost glass substrates and polymers, thereby making them an attractive option for disposable  $\mu$ TASs and labs-on-chips. The main advantages of mechanical micropumps over continuous flow actuator systems are robustness and independence to the nature of the transported fluid.

### ***1.3.3.1 Fluid actuation techniques for mechanical displacement micropumps***

Piezoelectric actuation was the first actuation principle used in micropumps. It is a very attractive concept, as it provides a comparatively high stroke volume, a high actuation force and a fast mechanical response. Moreover, commercial piezoelectric material, such as the PZT and Poly-vinylidene Fluoride (PVDF) is readily available (Piezo Systems Inc., <http://www.piezo.com>) for hybrid integration with the  $\mu$ TAS. The most common method of piezo-integration has been with the use of conductive epoxy to bond the PZT disk with the diaphragm surface. The comparatively high actuation voltage and the mounting procedure of the PZT disk can be regarded as disadvantages, however, a systematic optimisation of the mounting process can significantly improve reliability and yield of this type of actuator. Screen printing (Koch et al. 1998a) and mixing of piezo powder with diaphragm substrate (Koch et al. 1998b) have also been studied as a monolithic integration technique, though the resulting strokes are small in comparison to integrated PZT disks. Optimisation of the PZT-epoxy bimorph characteristics and actuator shape has also been carried out in order to achieve higher strokes at lower voltages for improving the performance of the piezo-actuated micropumps (Hsu et al. 2009), (Morris, Forster 2000), (Li, Chen 2003). Apart from the integration of piezo disks, modified poly(vinylidene fluoridetrifluoroethylene) [P(VDF-TrFE)] polymer and electrostrictive PVDF polymers have been studied for fabricating a unimorph actuating system for micropumping applications (Xia et al. 2006). Figure 1.11 shows a three chamber piezo actuated peristaltic micropump fabricated by Jang et al. (2007).

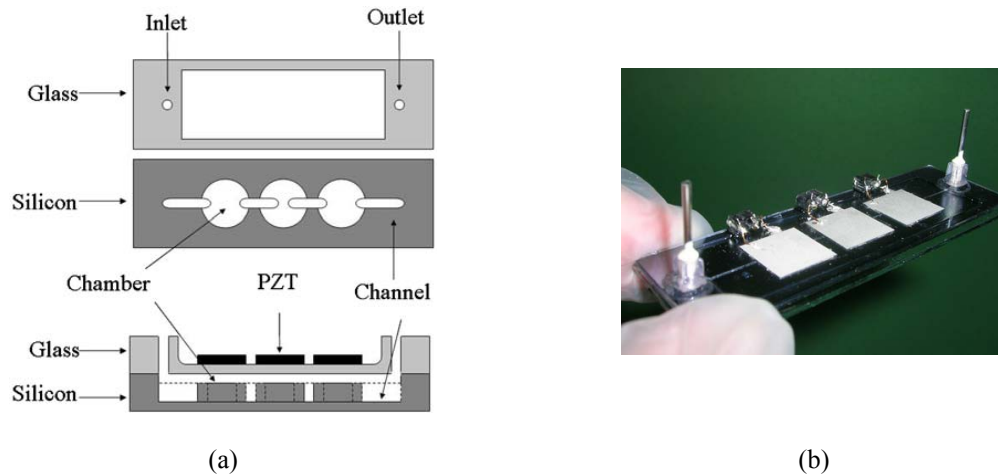


**Figure 1.11:** (a) Schematic and (b) Fabricated piezo actuated peristaltic micropump by Sheng Jang et al. (Jang et al. 2007)

The thermopneumatic actuator provides a low-voltage alternative to the piezoelectric actuation technique, and they can also be made very compact and capable to generate strokes up to several microns to achieve high pump rates (Wego, Pagel 2001). Integration into standard silicon processing is easily achievable (Acero et al. 1997). An important drawback of this actuation principle is a relatively long thermal time constant, especially during the cooling process. This limits the upper actuation frequency to approximately 50 Hz (Woias 2005). The typical electrical power consumption is in the range of several watts and at these power levels, which may lead to the heating of the transported fluid, which in certain cases will be detrimental for biological applications. Bimetallic actuator based micropumps, despite the requirement of only very low voltages are not suitable for high frequency actuations (Yang et al. 1996). For Shape Memory Alloy (SMA) materials, a reversible thermally induced two solid-phase transition from the martensitic phase (at low temperature) to the austenitic phase (at high temperature) exerts a large force and

thus, this phase transition can be utilized as a driving force on a membrane or a diaphragm of a micropump. High power to weight ratio, high damping capacity, good chemical resistance and biocompatibility make SMA materials promising in the field of MEMS applications (Fu et al. 2004). However, SMA based microactuation suffer from a few drawbacks. Apart from the limited availability of special alloys, such as AuCu, InTi, NiTi etc and thermally induced high power consumption, the deformation of SMA cannot be accurately controlled and predicted due to its sensitivity to temperature and SMA materials cannot cool sufficiently at high excitation frequencies (Amirouche et al. 2009).

Electrostatic actuation (Bourouina et al. 1997) offers operation frequencies up to several kHz, an extremely low power consumption and high fabrication compatibility to MEMS and  $\mu$ TAS. A major disadvantage results from the inherently small actuator stroke, which is usually limited to practical values around 5  $\mu$ m with corresponding actuation voltages around 200V (Woiias 2005). Degradation of the actuator performance cannot also be ruled out in long-term high voltage operation.

Apart from the above discussed methods, fluid actuations for mechanical micropumps have also been achieved by changing surface topography and surface charge (Stroock, Whitesides 2003) and thermocapillary actuation by the modification of the microchannel surface stress (Darhuber et al. 2003). Electromagnetic actuation has also been implemented on micropumps. For example, a permanent magnet cast in PDMS with flow rectification provided by ball valves was developed by Yamahata et al. (2005). Liquid pumping systems through microchannel wall vibration has also been reported in the

literature (Ogawa et al. 2009). Static capillary force has recently become a popular actuation mechanism for microfluidics (Vestad et al. 2004). Optical flow actuation techniques have also been reported for micropumps (Neale et al. 2005). Figure 1.12 gives the comparison of the typical flow rates achieved with different mechanical micropumps (Amirouche et al. 2009).

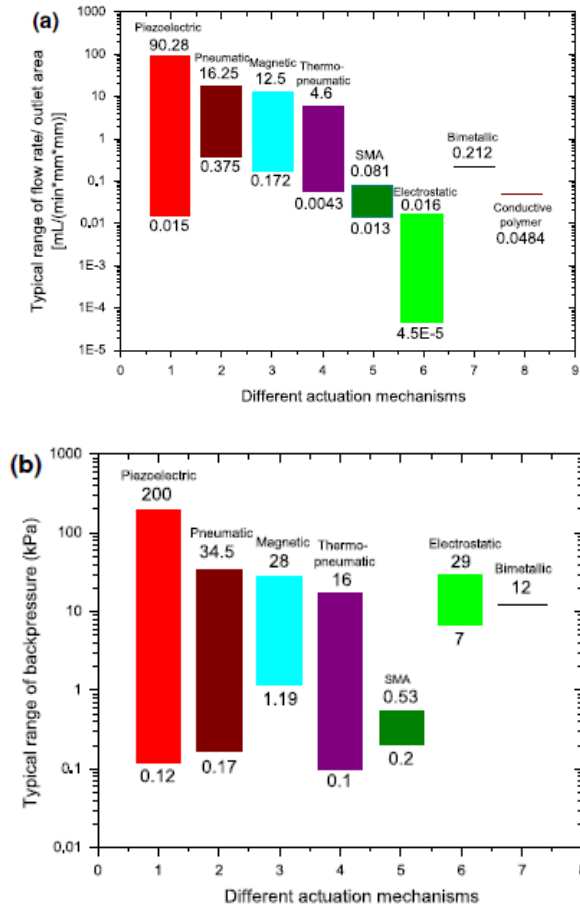


**Figure 1.12:** Typical range of (a) flow rate per unit outlet area and (b) backpressure for different mechanical micropumps (Amirouche et al. 2009)



### ***1.3.3.2 Fluid actuation for electro/magneto hydrodynamic micropumps***

Ionic species, charges or dipoles in liquid can gain electrokinetic energy from the applied electric field, and move along the electric field. When they move in the liquid, a dragging force is produced through friction of the particles with liquid surrounding them and induces a liquid flow (Luo et al. 2009). Significant micropump technologies using the electrokinetic force have been developed including dielectrophoresis, asymmetric electric field, electroosmosis and electrophoresis. Magneto-Hydrodynamic (MHD) pumps also belong to this category though an external magnetic field is required to produce the flow.

Electroosmosis (Chen, Santiago 2002) and Electrophoresis are part of the Electro-Hydrodynamic effect and co-exist in most microfluidic systems and the combined electrokinetic forces are more effective in transporting the liquids. With the application of nanoporous structures on the walls of the microfluidic channels and integration of nanoparticles in the channels, Electroosmotic pumps with differential pressure up to 20 atm have been developed (Bruus et al. 2004), which is suitable for high volumetric pumping. The voltage used for Electroosmotic micropumps is in the range of a few tens of volts and it increases up to 1.5 kV for those with high differential pressure.

An electrophoretic micropump works by either injecting ions or inducing the production of ions in a fluid and then using an electric field to drag those ions. Since the fluids used for biological or medical research and life sciences are mostly fluids containing various ions such as  $\text{Na}^+$ ,  $\text{K}^+$  and  $\text{Cl}^-$ , electrophoretic micropumps are very useful in microfluidics and lab-on-chips. EP micropumps require high electric field intensity,

typically in the range of tens to hundreds of volts. Developments in microfabrication technologies have enabled the fabrication of electrodes with a gap in the order of microns and even nanometers easily, in turn reducing the operating voltage substantially.

Dielectrophoresis (DEP) has become one of the most popular electrokinetics based micropump (Jones et al. 2001) as they can not only used as an effective fluid actuation method, but they also dispense and manipulate droplets on the wall-less surface with a speed up to 5 cm/s, more than one order of magnitude higher than the other micropumps (Ahmed, Jones 2007). DEP micropumps have also been utilized to separate particles and bio-species in the liquids (Demierre et al. 2008), (Hu et al. 2005). Electrowetting has been commonly used for fluid actuations in several Lab-on-a-Chip and  $\mu$ TAS applications. This technique basically involves the movement of droplets by energizing its surface through the application of potential to it (Zeng, Korsmeyer 2004), Additionally, microdroplets could also be split apart, merged together or dispensed from a fluid reservoir using the same microactuator structure (Pollack et al. 2002.)

MHD actuation (West et al. 2002) is realised when an electric current is applied across a channel in a fashion that is perpendicular to a magnetic field originating from beneath the channel. This orthogonal arrangement generates a Lorentz force that is perpendicular to both electric and magnetic fields, and acts to induce fluid circulation. MHD pumps require high current and high magnetic field to generate sufficient ion movement for pumping and they consume high power. Nevertheless, MHD micropumps have high pump power and are able to deal with liquids with volume up to several hundreds of

microliters. But the velocity is low, typically in the range of a few tens to hundreds of microns per second (Luo et al. 2009).

#### **1.4. Rationale and scope of the thesis**

Point-of-care testing and in-situ biomedical analysis have always demanded the synthesis of completely independent, cost effective, Lab-on-a-Chip systems and  $\mu$ TAS which can be used in real-time applications. It is evident from the scientific literature that although significant research has gone into the development of  $\mu$ TASs, only a very few have been implemented in the industry laboratories. The main reason is that Lab-on-a-Chip systems and  $\mu$ TAS devices still depend upon their hybrid integration with macro systems, and that essentially nullifies the concept of convenience and a portability of  $\mu$ TAS useful for biosensing and Point-of-care testing. However, when compared with the macro scale counterparts, these  $\mu$ TAS have lots of application possibilities and several advantages such as lower sample volume consumption, high throughput and environmental friendliness through less waste generation. This has motivated and thrown open the doors for further research and improvement of  $\mu$ TAS for enhanced chemical and bioanalysis, which could be used for everyday applications, thereby also opening up vistas for commercialization.

### **1.4.1 Subsystem and functionality identification for the proposed $\mu$ TAS**

Though several functionalities can be integrated within the  $\mu$ TAS, it is essential to identify the main components that will be integrated, in order to perform an integrated biochemical analysis. Therefore, it is important to select the suitable subsystems required for the proposed  $\mu$ TAS.

#### ***1.4.1.1 Micropumps for integration with $\mu$ TAS***

Although it is possible to integrate external fluid controllers that aid in fluid transportation through the biosystem, suitable microfluid actuating unit integrated within the  $\mu$ TAS is very essential in order to realize the concept of an independent system-on-chip without external macro support that enables the portability and convenient handling of the device. Reliable microfluidic systems along with suitably integrated sensing and fluid actuating units thus form the key components in the success of a  $\mu$ TAS or LOC. Micropumps which have been integrated with  $\mu$ TAS are limited to only a particular range of the Reynolds number ( $Re$ ), the concentration and distribution of ionic charge. Therefore, it is important to develop a suitable micropumping system that could be used for a wide range of flow conditions and that which is also immune to the nature of fluid.

Model complexity and complementarity nature of the working of the micropump with other modules of a  $\mu$ TAS render the selection of micropump actuating system a difficult as well as challenging task. Even though several fluid actuation techniques are available for integrated  $\mu$ TAS, it is important to choose the actuation system based on the

requirements such as ease of integration, flow rate, power requirements, operating pressure, biocompatibility, etc. The micropumping system of a  $\mu$ TAS must be able to handle fluids with a wide variety of properties, i.e. viscosity, density, ion strength, pH, temperature, and surfactants. Thus, the micropump's sensitivity to fluid properties is dependent on the principle used for fluid movement. (Andersson et al. 2001).

Most of the recent microchemical analysis systems are based on electroosmotic and electrohydrodynamic pumping. The underlying pump principles for these electrohydrodynamic actuation systems build on the specific fluid properties of the pumped medium, wherein the kinetic energy of ions present in the liquid is used to create the pump action. Excessive Joule heating and easy electrolysis due to direct contact of the electrodes and biofluid, which may limit their applications for real time biological analysis, though these problems have been overcome with the application of advanced dielectric coatings, AC voltage with higher frequency (Demierre et al. 2008) and miniaturized microelectrodes (Ahmed, Jones 2007). Electroosmotic pumps use the presence of immobilized surface charges, mobile charges in the sample and an externally applied electrical field. Thus, these properties make these pumps inherently dependent on the properties (pH, ionic strength) of the pumped medium, making them unsuited for a large number of biochemical liquids and biological applications. DEP micropumps can also be used only in liquids with low conductivity in order to avoid Joule heating (Jones et al. 2001). Thus, although the electrokinetic pumps can transport liquid, handle manipulation of cells and particles, and are easily integrable with  $\mu$ TAS, these techniques may suffer from problems with sample dilution or electrophoretic damage to sensitive

cells (Fiedler et al. 1998), strong dependence on the polarity of the fluid, applied voltage, etc. Electrokinetic pumps are also not good for mixing liquids in the channels due to low Reynolds number flow conditions. Most electrokinetic pumps can only be used for continuous flow application which typically requires channels with walls to confine the liquid. This limits their applications for quantitative analysis. Therefore, mechanical micropumps with diaphragm displacement using suitable actuating systems, and capable of generating substantial pressure to drive the fluid, is highly relevant for the present  $\mu$ TAS application. However, as with other dynamic microfluidic systems, mechanical micropumps are also prone to cavitation (Mishra, Peles 2005a), (Mishra, Peles 2005b), (Mishra, Peles 2006), (Singh, Peles 2009), (Krishnamurthy, Peles 2010). Therefore, it is necessary understand the behavior of cavitation in micropumps before integration with the  $\mu$ TAS.

In comparison to devices with different actuation principles for mechanical micropumps, piezoelectric micropumps can be designed to work at required frequency ranges, which translate to increased flow rates, despite compromising on high voltage requirements. This feature is in opposition to other actuation systems, for e.g., pneumatic or shape memory alloy actuation (Hernandez et al. 2010). Additionally, piezoelectric discs also possess the ability of being synthesized and shaped at very small scale which allows for easy integration in micro-devices. Also, valveless micropumping systems offer a lot of advantages over their valve based counterparts, in terms of reduction of mechanical fatigue based failure and overcoming the need for additional actuating system for the valves. By using the valveless micropump implemented with the help of a

micronozzle/diffuser pair, high frequencies, strong shear forces and high pump temperatures are avoided. In addition, there is no need for sample dilution to overcome the barrier posed by the valves, and thus the pump can handle fluids and biological specimens loaded with particles (Andersson et al. 2001).

Therefore, for the present work, a Piezoelectric-Actuated Valveless Micropump (PAVM) is proposed for integration with the  $\mu$ TAS.

#### ***1.4.1.2 Integrated microfluidic system and material platform***

At this point, it is clear that microfluidics is an absolute necessity for a  $\mu$ TAS, and it is imperative to design a non-stagnant microfluidic system for the transportation of fluids in a  $\mu$ TAS. An important consideration for the microfluidic system is the choice of material platform. The selection of microfluidic material platform depends on several factors which include thermal stability, ease of fabrication, biochemical inertness, re-usability, compatibility with fluid flow characterization techniques, and ease of integration with other complimentary modules of the  $\mu$ TAS. For biological applications, it is also important to ensure that the packaging technique/material of the microfluidic system is compatible with biological substrates, without any unwanted passive surface immobilization.

Though traditional microfluidic systems were developed on silicon and silica/glass, deformation based fluid actuation systems call for the integration of materials in such a way that the microfluidic base, which houses the channels, reaction chambers, etc., is soft

and not rigid. For this purpose, PDMS has proven to be a useful material because of their mechanical properties, flexibility and ease of using them as a packaging material.

There are several advantages of using PDMS for microfluidic systems (Fiorini, Chiu 2005) in a  $\mu$ TAS, such as cost effectiveness, unrestricted geometric feasibility, mechanical properties, and the control over surface properties through appropriate modification techniques depending upon the required application. The elastomeric nature of PDMS makes possible the easy integration of fluidic interconnects. Commercially available ferrules and connectors (Upchurch Scientific) attached with PDMS microfluidic systems have also enabled reusable and reconnectable microfluidic interconnects (Bhagat et al. 2007a).

Another advantage of using PDMS is the variety of fabrication techniques available. It is possible to take advantage of standard photolithography technique for microfluidic fabrication. For this, SU8 can be used for patterning silicon substrates which can be used as a mould for PDMS microchannels. Though soft lithography using rigid mould has been the most common technique for the fabrication of PDMS based microfluidic devices, other fabrication methods have also been explored. PDMS micromachining using Ti: Sapphire laser to create topographical layers was also demonstrated by Wolfe et al. (Wolfe et al. 2003) Replica molding method has also been implemented on PDMS which is simply the casting of the prepolymer against the master and generating the negative replica of the master (McDonald et al. 2000). For metal moulds, surfactants such as Tween 20 are coated on the surface before pouring the PDMS which would ensure that



there would not be any adhesion of the polymer with the surface of the mould. PDMS also offers the possibility of fabricating 3D aligned microstructures as demonstrated by Tien et al. (2002).

Employing oxygen plasma activation of PDMS surface, quick irreversible bonds with glass, silicon, and other polymer substrates are achieved while the surface is rendered hydrophilic (McDonald et al. 2000). PDMS substrates have a wide variety of characteristic material properties, such as mechanical strength, optical transparency, biocompatibility, chemical stability, excellent replication fidelity i.e capability of reproducing very small feature sizes of even a few nanometers (Attia et al. 2009). PDMS also offer good electrical insulation compared to silicon.

Therefore, for the present application, PDMS is chosen as the base material platform for the non-stagnant microfluidic system of the  $\mu$ TAS.

#### ***1.4.1.3. Optical detection system for $\mu$ TAS***

Biophotonic sensing techniques offer a lot of possibilities to carry out high throughput biomedical diagnosis. However, no single optical detection technique can be used commonly for performing widely varying and myriad biomedical applications. Therefore, it is important to integrate more than one optical detection system on a single platform to enable perform a variety of biodetection, depending upon the nature of biological specimen detected. Literature suggests that only a very few works have been carried out in that direction.

Waveguide based absorption and fluorescence detection systems with integrated microfluidics have been traditionally used in Lab-on-a-Chip and  $\mu$ TAS devices, and have also proven to be very useful for the simple detection of chemical and biological specimens. Among other label-free optical detection techniques, biosensing using evanescent wave techniques have been employed in the past for different biological specimens. However this technique has not been much investigated on  $\mu$ TAS (Densmore et al. 2006a). Evanescence measurement is very useful for performing high sensitive biodetections with very low sample volume. This method is non-destructive to the biological specimen, which enables the reusability of the sample for further analyses. Integrated microfluidic evanescent wave biosensing on a  $\mu$ TAS platform is an area which has not yet been investigated. Considering the advantages realized from microfluidics and also evanescent wave detection, it would be interesting to study the performance of an integrated microfluidic evanescent wave detector for applications on a  $\mu$ TAS. Also, it is important to develop a suitable technique in order to improve the sensitivity of the evanescence detection system.

Development of efficient waveguide based integrated microfluidic optical detection systems is essential in order to study the bio-optical interaction brought about through absorption, fluorescence and evanescence detection techniques. A high Signal-to-Noise Ratio (SNR) can only be achieved if the optical losses in these systems are minimized. Losses in waveguides also occur due to waveguide imperfections, such as scattering losses caused by surface roughness, and material absorption losses. Integrated optical

microfluidic systems can also suffer losses at the interface of different materials (Roulet et al. 2002). Therefore, the only solution to minimize optical losses in integrated optical microfluidic systems is the integration of the micro-optical components with microfluidics on the same platform, thereby forming a robust optical detection platform for the  $\mu$ TAS. In order to achieve this, it is also important to choose the suitable waveguide core material which can be integrated with PDMS for the optical-microfluidic integration.

#### **1.4.2 Objectives of the thesis**

Thus, the present thesis is built upon the following objectives:

- (i) To design, fabricate and experimentally characterize an integrated optical detection based Micro-Total Analysis System.
- (ii) To design a non-stagnant microfluidic system compatible with the  $\mu$ TAS for biofluid delivery and handling.
- (iii) To design, fabricate and test a Piezo-Actuated Valveless Micropump (PAVM) for fluid actuation and integration with the  $\mu$ TAS.
- (iv) To design, fabricate and test a micronozzle/diffuser system for flow rectification in the PAVM, and to devise suitable methods for enhancing the performance of the microdiffuser system.
- (v) To study the phenomenon of cavitation in valveless micropump, and to explore the different chemical and biological applications of cavitation for  $\mu$ TAS.

- (vi) To design, fabricate and experimentally characterize an integrated optical detection platform for carrying out biophotonic detections through absorption, laser-induced fluorescence spectroscopy and label-free evanescence for the detection of active enzymes and other chemical and biological specimens.
- (vii) To develop a Nano-integrated Evanescence detection Technique (NEET) for improving the sensitivity of evanescence sensing.
- (viii) To identify suitable material base, and fabrication techniques for the integrated optical microfluidic system.
- (ix) To develop simple and robust bonding and packaging techniques, for the external and internal hybrid integration of microfluidic, micromechanical and microphotonic ensembles.
- (x) To carry out testing and characterization of the performance of integrated  $\mu$ TAS.
- (xi) To identify potential chemical and biological applications of the  $\mu$ TAS for carrying out real-time and Point-of-Care analyses.

## **1. 5. Layout of the thesis**

This thesis has been organized as follows:

Chapter 1 introduces the concept of  $\mu$ TAS along with the different components of a  $\mu$ TAS with their application. A review of components of the  $\mu$ TAS, microfluidic technologies and integrated optical sensing systems has been presented. The presented literature review forms the background for the development of the idea towards the

design, fabrication and testing of an integrated  $\mu$ TAS. The chapter also presents the rationale and the scope of the present thesis along with the layout and the contributions.

Chapters 2-4 describe the development of valveless micropump, from the nozzle/diffuser system for flow rectification, implementation of the valveless micropump using the diffuser/nozzle system with Piezo-actuation and the study of cavitation in micropumps.

Chapter 2 provides an introduction to the flow rectification through microdiffuser/nozzle for micropump applications. A simple microfabrication friendly geometry tuning method of the microdiffuser is presented, which can be used for enhancing the flow rectification in micropump. Finite Element Modeling (FEM) of the microdiffuser behavior are presented for different diffuser angles over a wide range of Reynolds numbers. This chapter also presents the design and fabrication techniques for the geometrically tuned microdiffuser, along with the experimental results used for calculation of pressure coefficients and diffuser efficiencies of microdiffuser elements of different angles and geometries. The experimental results are compared with the results obtained from the FEM. The effect of friction on the performance of the microdiffusers is also presented.

Chapter 3 presents the development of a Piezo-Actuated Valveless Micropump (PAVM) system on PDMS platform, for integration with the  $\mu$ TAS. The design, fabrication and assembly of the micropump is presented. A suitable experimental setup is designed for the testing of valveless micropumps. The micropump is characterized for its performance through pressure and flow measurements. The implementation of flow rectification in a

valveless micropump through geometry tuned microdiffuser has also been demonstrated. The effects of surface affinity on the bubble generation and pump performance are also studied.

Chapter 4 presents the detailed study of the cavitation behavior in valveless micropumps. The theory of cavitation in valveless micropumps is presented along with the results on the development of cavitation. Based on the results, the different stages of cavitation are identified. This chapter also explores the effect of cavitation on the performance of valveless micropumps, and also some biological applications of cavitation which can be implemented in integrated  $\mu$ TAS.

Chapters 5-7 present the optical integration and background of development of different optical detection techniques that could be implemented for  $\mu$ TAS. The work presented in these chapters aim to develop an expertise on integration, from simpler to more complex designs implemented in the  $\mu$ TAS.

Chapter 5 presents the feasibilities of “off-chip” hybrid integration of optical detection system and microfluidics for implementation in a  $\mu$ TAS. This chapter also discusses the development of a recirculating microfluidic system in order to improve the biointeraction between two fluids. The different types of hybrid integrated systems are discussed and the results of the experiments carried out with hybrid integrated devices have been presented for fluorescence detection.

Chapter 6 presents the different techniques developed in order to improve the sensitivity of the external hybrid integrated system. The method of partial reflector integration with the microfluidic channel surface is presented, which improves the sensitivity of fluorescence detection in external hybrid integrated system. Thereafter, this chapter presents the implementation of an internal hybrid integrated system using a Spectrometer-on-Chip with the integration of fiber optics based fluorescence detection system and microfluidics.

Chapter 7 presents the development and implementation of Nano-Enhanced Evanescence detection Technique (NEET). The effect of NEET on simple waveguide based evanescence detection systems was studied using the Finite Difference Time Domain (FDTD), for nanopillars, nanocavities and nanospheres and the experimental results of NEET based sensing on SU8 waveguides using Multi Walled Carbon Nanotubes (MWCNT) are also presented.

Chapters 8-9 discuss about the development and testing of fully integrated  $\mu$ TAS.

Chapter 8 presents the synthesis of a fully integrated  $\mu$ TAS, with micropump, micro-optical detection system and suitable microfluidic system. The design of the waveguide based integrated optical microfluidic system is presented. The fabrication on PDMS platform along with SU8 optical detection system is also discussed. This chapter also presents the method of integration of the optical fibers with the waveguides and the hybrid integration of the Piezo-actuated valveless micropumping system with the optical microfluidic system.

Chapter 9 presents the integrated testing with the hybrid integrated  $\mu$ TAS. The different testing methods for nano-integrated evanescence detection and optical absorption detection, both with integrated micropumping, are described. This chapter also describes the implementation of cavitation induced micromixing in valveless micropump, which has been exploited to carry out Benedict's test for the determination of glucose in sugar solution using optical absorption method. At the end of chapter 9, the potential of using the proposed integrated  $\mu$ TAS for real-time biochemical detections and applications is discussed.

Chapter 10 presents the conclusions of the present work. The work from the present thesis has been published in several popular and international journal papers, and also presented in national and international level conferences as presentations and posters, which are listed in Chapter 10.



# Geometric Tuning of Microdiffusers for Improved Flow Rectification in Valveless Micropumps

### 2.1. Introduction to microdiffusers

In most mechanical microfluidic systems, the flow is pressure driven, i.e. pressure difference between the inlet and the outlet drives the fluid. This pressure driven flow is brought about by means of external hybrid integration with macropumps (Peristaltic pumps, syringe pumps etc.) For a fully integrated  $\mu$ TAS, to enable the transportation of fluid through the system, it is essential to use microfluidic actuators or *micropumps* suitably integrated with the system. Among all the micropumps, mechanical micropumps based on oscillating diaphragm offers a lot of advantages for integration with the  $\mu$ TAS as discussed in Chapter 1. These mechanical micropumps operate with valves or through the valveless mechanism. In traditional mechanical micropumps, check valves have been used to ensure the unidirectional flow of the fluid for micropump actuated flows. High flow rates are achieved with check valve configuration for the micropumps. However, the complexity of coupling another suitable actuating mechanism for the valves poses a lot of challenges for integration and packaging in the micro regime. Also there is always the danger of mechanical failure of the valves, which then becomes impossible to replace. This forms the motivation of developing a valveless micropumping system, which have

clear advantages over their valve based counterparts for integration with  $\mu$ TAS, such as simplicity of design, reduction of an additional fabrication and packaging techniques, etc. For a valveless micropumping system, fluid flow through reciprocating displacement micropumps is rectified by leveraging suitable fluid dynamic effects in inlet and outlet channels with suitable geometries. The unidirectional flow in a valveless micropump is realized through a microdiffuser pair has been, which by operating in conjunction with the diaphragm displacement of the micropump, takes advantage of the differential pressure drops across the diffuser/nozzle elements during one operating cycle and thus translates the pulsating flow into a unidirectional stream. This concept was first introduced by Stemme and Stemme in 1993 (Stemme, Stemme 1993) and has been adapted by several researchers ever since.

In order to design microdiffusers for valveless micropump applications, it is very essential to clearly understand the principle of flow rectification by which the microdiffusers operate. It is also important that the behaviour of microdiffusers are well understood over a wide range of flow conditions. This chapter presents the study of the performance of microdiffusers for their flow rectification behavior for valveless micropump applications. Herein, a simple principle of geometric tuning is proposed through which flow rectification through microdiffusers are improved significantly. The following segments of this chapter give the detailed description of the diffuser working principle, modeling and Finite Element Analysis of the flow behaviour within a microdiffuser based on geometric tuning, flow parameter variations etc, followed by the experimental verification of the flow rectification effects of the microdiffusers.

## **2.2 Geometric tuning of microdiffuser/nozzle for valveless micropumps**

The principle of geometric tuning for microdiffusers is explained in this section, and this work has been published in the *Journal of Micromechanics and Microengineering* (Chandrasekaran and Packirisamy, 2011).

### **Abstract**

Valveless micropumps require the integration of microdiffusers/nozzles for flow rectification in microfluidic and nanofluidic systems. The flow directing capability of the micropump is determined by the efficiency of the diffuser. With the reduction in size of the micropump, conventional microdiffuser geometrical parameters are not suitable to obtain high flow efficiencies due to several fluidic effects such as channel friction, wall shear stress, vena contracta, etc., and therefore it is important to modify the diffuser geometry according to the requirements of the pressure coefficients in order to obtain improved flow rates. This paper presents a simple, microfabrication friendly geometrical tuning method which offers the user a broad range of single variable dependent tunable parameter to improve the performance the microdiffuser for valveless micropumps. Herein, for a given flow condition, the flow behavior and the variation of pressure coefficients of the microdiffuser/nozzle with geometric tuning, have been studied for different diffuser angles using Finite Element Modeling (FEM). The results show that the proposed method is highly suitable for tuning the geometry of microdiffusers for a wide range of operating conditions of valveless micropumps. The performances of the best

diffuser geometries for different diffuser angles have been experimentally verified, and the results obtained there from are used for the validation of the results of the FEM.

### **2.2.1. Introduction**

Fluid flow in a valveless micropumping system is realized with the integration of microdiffusers/nozzles, which are also known as dynamic micro valves (F.C.M. van de Pol 1989). The microdiffuser pair causes the flow rectification, i.e translation of the pulsating flow due to micropump actuation into a unidirectional stream. Ever since this concept was first introduced by Stemme and Stemme in 1993 (Stemme, Stemme 1993), these valveless diffuser configurations have replaced the traditional check valves banking on certain clear advantages over their valve based counterparts. The advantages of valveless configuration for micropump include simplicity of design, reduction of additional fabrication and packaging processes, elimination of fatigue induced failure of valve structures and thereby, the ease of integration with Lab-on-a-Chip (LOC) systems or Micro-Total Analysis Systems ( $\mu$ TAS).

Several types of microdiffusers have been used for the micropump application. Different diffuser profiles have also been used for valveless micropumps, such as conical (Stemme, Stemme 1993), pyramidal (Gerlach 1998), flat-walled (Olsson et al. 1995) etc. The choice of diffuser configuration is also dependent on the fabrication process. Since the valveless micropump configuration is geometry dependent, there is also a need to fabricate suitable cost effective diffuser designs. Flat walled diffusers, also called planar diffusers have

several advantages over other geometries, as they can be fabricated using standard micromachining techniques. In addition to precision milling of metals and etching of silicon, one can also apply thermoplastic molding and replication techniques for fabricating plastic based diffuser elements. Polymer diffuser elements have also been fabricated and tested for their flow behavior.

In order to design a microdiffuser, two aspects of its performance need to be investigated thoroughly, namely, the individual pressure coefficients in both nozzle and diffuser, and the overall efficiency of the diffuser. The main parameters to which the diffuser behaviour is sensitive are geometric parameters such as which includes the length, width, angle, inlet curvature, aspect ratio etc. and fluid properties such as density and viscosity, and the flow velocity (Ahmadian, Mehrabian 2006). For a microdiffuser integrated with the micropump, flow velocity is a function of the pump parameters. As fluid properties cannot be altered during operation, the possible parameter that can be modified in order to achieve better results is the diffuser geometry.

Several works have been carried out to study the behaviour of the microdiffuser based on its geometry. Apart from the classical diffuser geometries, literature suggests that different modified diffuser configurations have been proposed for applications with micropumps. Deshpande et al. (1998) analyzed the tesla type rectification element comparing with the diffuser valve and have concluded that tesla configuration can be used to achieve better flow rectification. Izzo et al. (2007) have proposed a valveless diffuser configuration for micropumps in which the diffuser channels were designed in accordance

to the vortex area formed along its fluid-dynamic pattern, and thus improving the micropump performance within the diffuser elements taking advantage of the recirculating flow. Asymmetric obstacles have also been used by Lee et al. (Lee et al. 2009) to create pressure drop in microfluidic channels thereby creating nozzle/diffuser effect for use in micropumps. Curved profile diffuser has been used to improve the diffuser efficiency by Chen et al. (Chen et al. 2008). Li et al (Li et al. 2007) have used fins on the sidewalls of the microdiffuser to improve the rectification efficiency in a micropump. More recently, the use of vanes to reduce the flow separation in diffusers has also been presented (Sun, Lin 2010). Among other studies carried out to understand the influence of geometry on microdiffuser behaviour, Yang et al (Yang et al. 2004) have reported that the influence of the diffuser length on pressure coefficients is small. Also, it has been reported that for similar inlet conditions, the best flat-walled diffuser is upto 80% shorter than the best conical design (Wang et al. 2009). Sun and Yang (2007) have studied analytically and through flow visualization that, for wide angled diffusers, flow separation plays an important role in increasing the pressure drop in diffuser direction. This shows that the flow behaviour inside the diffuser has a significant influence on the pressure drop across the diffuser. Wang et al. (Wang et al. 2009) have reported that the flow separation is useful to reduce the wall shear stress and thus reducing the pressure drop in the diverging direction. Additionally, flow rectifiers have also been studied for viscoelastic fluids (Sousa et al. 2010), (Nguyen et al. 2008), and multiphase flows (Liu et al. 2009) and the behaviors have been reported to be different from the behavior of the diffusers with Newtonian fluids.

In most of the studies, the effect of microdiffuser geometry have been studied in conjunction with the effect of flow Reynolds numbers, while studies focusing only on the geometric influence alone need more attention. Though several geometric modifications have been suggested, it is still unclear as to how the diffuser geometry influences the pressure coefficients and the overall efficiency. Both the above mentioned properties of the diffuser are complimentary to each other, and therefore it is important to understand the methods and mechanisms to improve further these diffuser characteristics in favour of the working mechanism of the micropump through microfabrication friendly geometric modifications alone. Most of the present data available in the literature are available for the diffuser coefficients and the losses for different geometries are for macro-scale elements. As the sizes of the valveless micropumps are reduced for real-time microfluidic and nanofluidic applications, the performance of the diffusers varies due to the inception of the pressure losses in the diffusers by channel friction, wall shear stress, vena contracta etc. In such cases, the conventional diffuser geometries are not suitable to obtain high diffuser efficiencies and therefore, it is essential to apply suitable geometry modifications in order to control the pressure coefficient and improve the diffuser efficiency. It is also important that the mechanism of microdiffuser geometry modification be understood so that the geometry modifications can be applied over a wide range of operating parameters for the micropump. This forms the motivation for a detailed analysis and recommendations on the influence of the geometry on the behaviour of diffusers in the microscale.

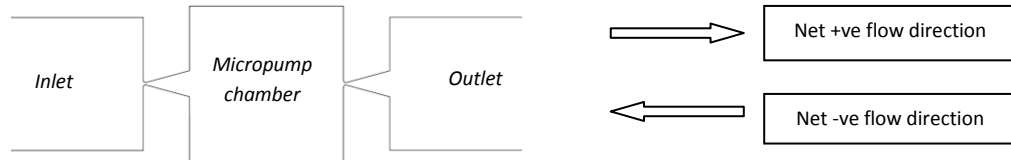
In this paper, a simple power law method to modify the sidewall geometry of a microdiffuser is presented which can be applied to tune the microdiffuser parameters, namely the pressure coefficients and also the diffuser efficiency. Herein, the behaviour of the microdiffuser based on its geometric tuning is studied and the mechanisms by which the geometry of the microdiffuser influences its behaviour are explored. This provides a lot of details for the design of microdiffuser to obtain improved flow efficiency for valveless micropump applications. The following sections of the paper include the description of the power law geometry tuning, analysis of the flow behaviour in geometry tuned microdiffusers through Finite Element Analysis (FEA), experimental verification of the microdiffuser performances and the conclusions.

### **2.2.2. Geometry tuning of microdiffuser**

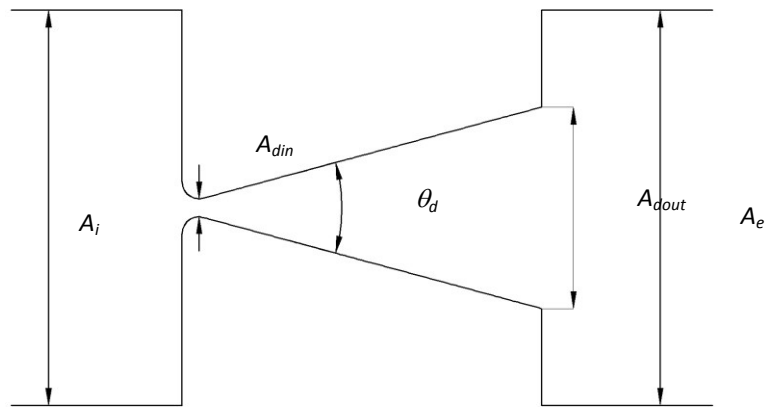
The schematic of a valveless micropump is shown in Figure 2.1(a). The micropump chamber is connected to the inlet and the outlet through symmetrically positioned microdiffusers. Flow direction in the valveless micropump is brought about by the differential pressure drop across the nozzle and the diffuser elements (Stemme, Stemme 1993). Since the net flow is from the inlet to the outlet, the flow in the diffuser direction is taken as positive and the flow in the nozzle direction is taken as negative. The schematic of the diffuser element is shown in Figure 2.1(b). Herein, the diffuser is connected between two channels of cross-sectional areas of  $A_i$  and  $A_e$ , respectively. The section of the least cross-sectional area of the diffuser is herein referred to as the *throat*. For the flow in the positive direction, the throat forms the inlet. Conversely, the flow in



the negative direction exits from the throat. The inlet and outlet cross-sectional areas of the diffuser are denoted by  $A_{din}$  and  $A_{dout}$ , respectively, with the respective widths  $w_{din}$  and  $w_{dout}$ . The angle of the diffuse is denoted by  $\theta_d$ , which is the angle between the sidewalls of the diffuser.



(a)



(b)

**Figure 2.1:** Schematic of the microdiffuser/nozzle used in micropump

The energy equation (per unit volume of fluid) between any two cross-sectional planes denoted by subscripts  $i$  and  $e$  can be expressed as

$$p_i + \frac{1}{2}c_i\rho\bar{V}_i^2 = p_e + \frac{1}{2}c_e\rho\bar{V}_e^2 + \Delta p_{i-e} \quad \dots 2.1$$

Here,  $p$  is the hydrostatic pressure across the cross-section,  $\bar{V}$  is the volume average flow velocity, and  $c$  is the kinetic energy correction factor which is given as

$$c = \frac{1}{A\bar{V}^3} \int_A u^3 dA \quad \dots 2.2$$

where  $u$  is the axial velocity of the fluid. As indicated in the Figure 1, the flow in the diffuser direction is taken as positive direction and the flow in the nozzle direction is taken as the negative direction. In the positive direction of fluid flow, pressure loss between the inlet and the outlet consists of three components, namely, the pressure loss in the inlet channel before the diffuser inlet, the pressure drop in the diffuser element and finally the pressure loss in the outlet channel after the diffuser. Thus,

$$\Delta p_{i-e} = \Delta p_{i-din} + \Delta p_{din-dout} + \Delta p_{dout-e} \quad \dots 2.3$$

The pressure loss in the inlet and the outlet channel is contributed by the friction factors, constrictions of fluid flows, bend losses etc. However for a straight inlet and outlet channel, the pressure loss arises only from the friction factor. The loss coefficient  $K_{ie}$  between the sections  $i$  and  $e$  is given by

$$K_{ie} = \frac{\Delta p_{i-e}}{\frac{1}{2} \rho v_{din}^2} \quad \dots 2.4$$

If the pressure coefficient of the diffuser,  $\xi_d$ , is defined based only on the pressure drop in the system, then, from Equations 1, 3 4

$$\xi_d = \frac{p_i - p_e}{\frac{1}{2} \rho v_{din}^2} + c_i \left( \frac{A_{din}}{A_i} \right)^2 - c_e \left( \frac{A_{din}}{A_e} \right)^2 \quad \dots 2.5$$

When  $A_i, A_e \gg A_{din}$ , the pressure coefficient of the diffuser is given by the expression

$$\xi_d = \frac{p_i - p_e}{\frac{1}{2} \rho v_{din}^2} \quad \dots 2.6$$

Similarly, for the nozzle flow, the pressure coefficient in the nozzle direction is given as

$$\xi_n = \frac{p_e - p_i}{\frac{1}{2} \rho v_{din}^2} \quad \dots 2.7$$

The flow rectification of the diffuser depends on the ratio of  $\xi_n$  over  $\xi_d$ . Thus, the diffuser efficiency  $\eta_{nd}$  is defined as the ratio of pressure coefficients in the nozzle and the diffuser flow directions.

$$\eta_{nd} = \frac{\xi_n}{\xi_d} \quad \dots 2.8$$

For a symmetric diffuser based micropump, i.e micropump with similar diffuser configuration at the inlet and the exit, the volumetric efficiency (Stemme, Stemme 1993) is given as

$$\eta_{pump} = V_p \left( \frac{\sqrt{\eta_{nd}} - 1}{\sqrt{\eta_{nd}} + 1} \right) \quad \dots 2.9$$

where  $V_p$  is a constant based on the micropump dynamic characteristics. Therefore, in order to improve the efficiency of the valveless micropump it is important to increase the efficiency of the diffuser to obtain higher flow rates.

### 2.2.2.1 Geometric tuning method

As seen from Equation 9, for a given valveless micropump configuration with fixed dynamic characteristics, the volumetric efficiency can be improved only with the increase in the efficiency of the diffuser. This is possible only by the variation of the geometry of the microdiffuser in such a way that the pressure coefficients are altered in such a way that the geometry helps in both the increase in the nozzle coefficient as well as the decrease in the diffuser pressure coefficient. Though several geometric modifications are feasible, it is important that the chosen method is compatible with standard microfabrication techniques for different material platforms. Above all, to avoid complexities, it is also important that the geometry tuning method is single parameter dependent, so that the diffuser behavior can be controlled with that tuning parameter, and variation of diffuser performance can be studied with reference to one parameter only.

The geometry tuning of the microdiffuser presented herein refers to non-classical tapering of the microdiffuser along the axis of fluid flow, which can be used to target specific performances both in the nozzle and diffuser flow directions. The profile of the geometry is modified as per the power law, wherein the modified width,  $w_d(L)$ , of the microdiffuser is derived from the width of the *throat*,  $w_{din}$ , and a geometry tuning function,  $\psi(x)$ , and may be expressed by

$$w_d(x) = w_{din} \psi(x) \quad \dots 2.10$$

Herein, two types of geometry tuning functions based on power law are studied, namely, the *concave* and the *convex* tuning. For *concave* diffusers, the tuning function is given by

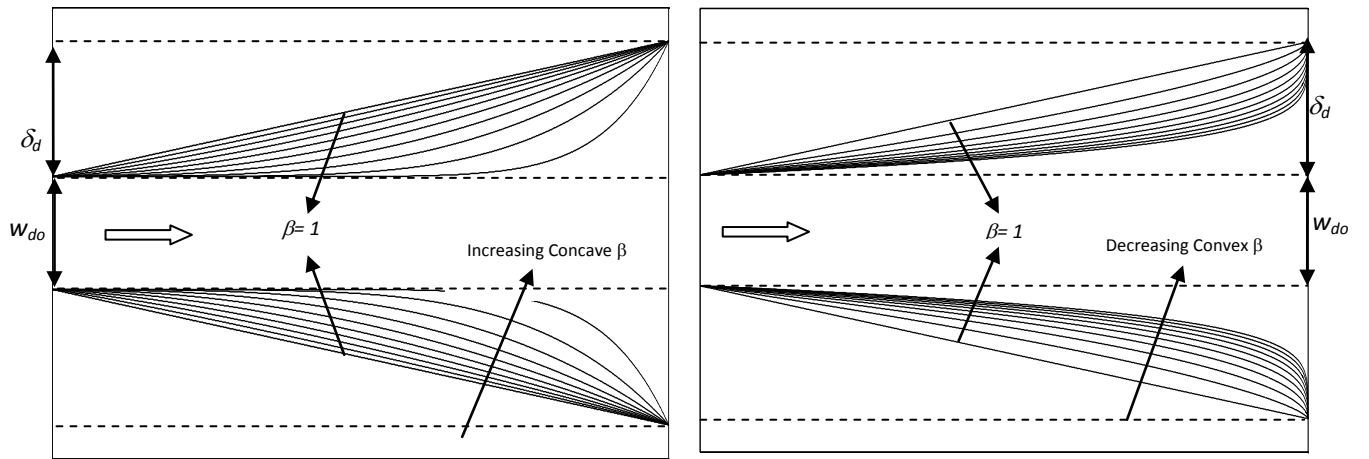
$$\psi_{cv}(x) = 1 + (\chi - 1)x^\beta \quad \dots 2.11$$

and for *convex* diffusers, the tuning function is given as,

$$\psi_{cx}(x) = 1 + (\chi - 1)(1 - x)^\beta \quad \dots 2.12$$

where  $\chi = (w_{din} + 2\delta_d)/w_{din}$ .

For a given diffuser with fixed length, inlet and outlet widths  $\delta_d$  remains constant. Thus, the tuning functions  $\psi_{cv}$  and  $\psi_{cx}$  determine whether the profile of the diffuser is concave or convex through the tuning parameter  $\beta$ , which may be varied from zero to infinity. For  $\beta = 1$ , for both concave and convex conditions, diffuser with straight sidewalls are obtained. Figure 2.2 shows the schematic of geometry tuning in microdiffusers for both concave and convex  $\beta$ s.



(a) Concave tuning

(b) Convex tuning

**Figure 2.2:** Structural tuning of diffuser elements with concave and convex geometry tuning.

### 2.2.3. Analysis of microdiffuser behavior with geometric tuning

In the present analysis, the performances of five different diffuser angles were analyzed by geometry tuning. The diffuser angle,  $\theta_d$ , refers to the included angle between the sidewalls and not the half angle, as shown in Figure 2.1. The classifications of the diffuser angles chosen for the present analyses are given in Table 2.1.

Diffuser angle	Classification
5°	Very small angled
15°	Small angled
30°	Intermediate angled
60°	Wide angled
90°	Very wide angled

**Table 2.1:** Classification of the diffuser angles used for the Finite Element Analysis

Herein, the geometry tuning of a diffuser represents tuning the diffuser geometry by either increasing the concave tuning parameter,  $\beta_{cv}$ , from 1 to 3 in steps of 0.5, or decreasing the convex tuning parameter  $\beta_{cx}$  from 1 to 0.2 in steps of 0.2. For wide angled diffusers, in order to further explore the effect of geometry tuning,  $\beta_{cx}$  of 0.1 and 0.05 were also analyzed.

Therefore, even though unrestricted geometric variations are possible for the design of the diffuser, the power law geometric tuning method offers the following advantages, namely, ease of implementation, single variable dependent geometric control, and ease of microfabrication.

### 2.2.3.1 Finite Element Modeling (FEM) of the microdiffuser

In order to study the flow behavior in the microdiffuser, 2-D Finite Element Analysis (FEA) was carried out by solving the incompressible Navier Stokes Equation given in Equations 12 and 13 as

$$\nabla \cdot \vec{u} = 0 \quad \dots 2.13$$

$$(\vec{u} \cdot \nabla) \vec{u} = \frac{-\nabla p}{\rho} + \gamma \nabla^2 \vec{u} \quad \dots 2.14$$

wherein,  $\vec{u}(x, y)$  is the velocity vector of the fluid,  $p$  is the pressure,  $\rho$  is the fluid density,

$\gamma$  is the kinematic viscosity and  $\nabla \equiv i \frac{\partial}{\partial x} + j \frac{\partial}{\partial y}$ . Boundary conditions for ideal liquid

flows are always assumed to be at no slip. The computation domain is similar to the diffuser model presented in Figure 1. The throat width of the diffuser used for the FEM is 100  $\mu\text{m}$  and the width at the nozzle entrance was calculated based upon the diffuser divergence angle. The length of the diffuser is 2000  $\mu\text{m}$ . In order to minimize the entrance loss of the diffuser (Olsson et al. 2000), a well-rounded entrance with fillet radius 100  $\mu\text{m}$  was provided at the entrance in the positive diffuser direction. Since the diffuser designs are non-classical, the geometry was imported from CAD modeling into the FE environment as a set of co-ordinates, and converted into a computation domain subsequently. The FEM was implemented using COMSOL v3.5.

Water was used as the operating fluid. The pressure-velocity coupling is solved using direct SPOOLES solver (COMSOL v3.5a). All the analyses have been done for flow Reynolds number 100. Herein the Reynolds number is defined with respect to the mean

velocity of the fluid at the neck of the diffuser. Based on the Reynolds number, the inlet boundary condition was set to velocity input accordingly. The outlet is set to zero gauge pressure. The boundary conditions for the inlet and the outlet are reversed when computing for the diffuser and the nozzle efficiencies respectively. No-slip boundary conditions are imposed on the walls of the diffuser. The flow is considered incompressible and laminar. The relative tolerance in the computation was set to 1%. Triangular mesh was used for the models. The number of mesh elements varied from 12000 – 18000 depending upon the angle of the diffuser. Initial investigation was carried out on the mesh size and the optimization of the mesh parameters were carried out with COMSOL. The mesh refinement and sensitivity was verified by computing the pressure coefficients for a few arbitrarily chosen models. The mesh size for the analysis is the result of that investigation. In order to validate the results, a few of the models from previously published data (Wang et al. 2009) were also modeled and the results were verified. The variation in prediction of diffuser coefficient due to the mesh is less than 2%. The mesh refinement and sensitivity was verified by computing the pressure coefficients for a few arbitrarily chosen models. Steady state non-linear analysis was carried out to calculate the pressure coefficients in nozzle and diffuser flow directions, for the diffuser models with geometric tuning.

### ***2.2.3.2 Results of Finite Element Analysis***

The pressure coefficients in both the nozzle and diffuser directions were calculated from equations 6 and 7 respectively. Since the model does not take into account the frictional pressure losses in the connecting channels, the pressure values for the diffuser at the inlet

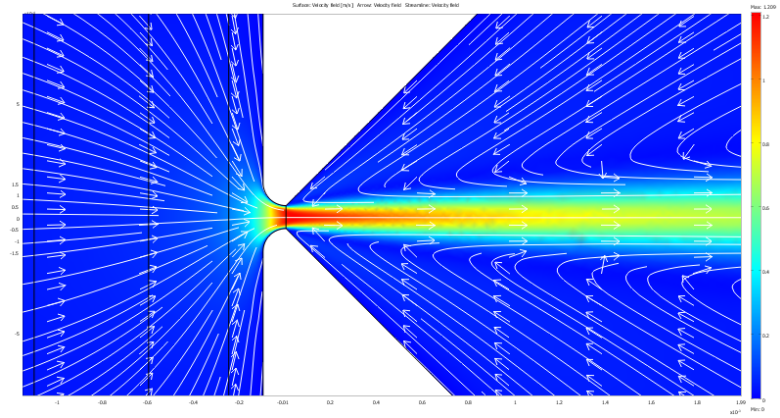


and exits were taken as the average pressure at the respective cross-sections of the channel. The mean velocity at the throat of the microdiffuser is taken as the ratio of the boundary integration of fluid velocity at the throat, over the width.

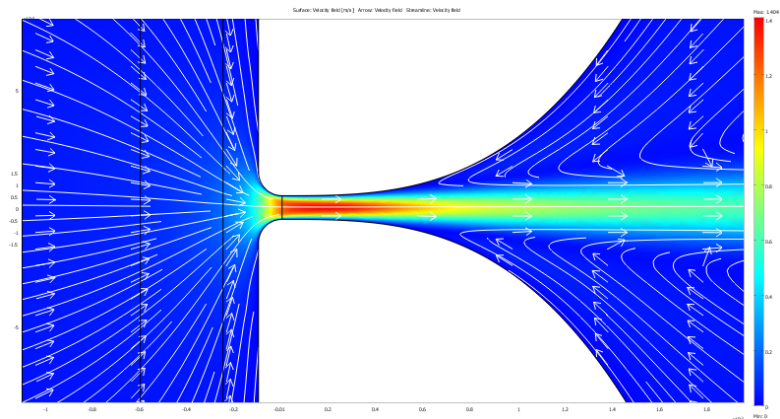
#### *2.2.3.2.1 Variation of diffuser/nozzle coefficients with geometric tuning*

A study of the streamlines of the flow in the microdiffuser shows that, in the positive flow direction, a flow separation is created between the main stream and the side walls of the diffuser. The flow separation increases with the increase in the angle of the diffuser, thereby creating recirculating zones in the positive direction. However no flow separation in the nozzle direction with the increase in diffuser angle. Through geometry tuning, it is possible to reduce the recirculating flow due to which the pressure coefficients are significantly influenced for both convex and concave tuning. This is shown in the streamline plot, Figure 2.3, for  $90^\circ$  diffuser with straight walls and compared with the diffuser configuration  $\beta_{cv} = 3$  and  $\beta_{cx} = 0.2$ .

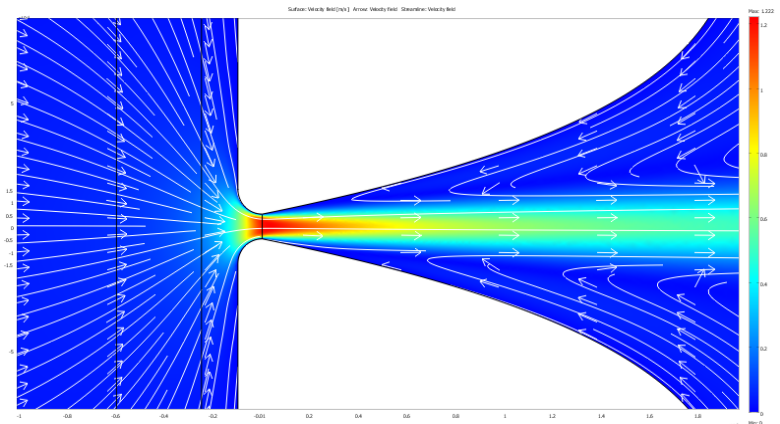
The results for the variation in pressure coefficients with geometric tuning for different diffuser angles are presented in Figures 2.4 and 2.5 for concave and convex diffusers respectively, together with the schematic of the variation of diffuser geometries. For both convex and concave diffusers, the pressure coefficient in the nozzle direction is always greater than the diffuser direction. For flows without recirculation, the variations of nozzle and diffuser coefficients also follow the power law according to the geometric tuning, and any deviation in the trend of variation of pressure coefficients indicates the onset of flow separation.



(a) Straight wall



(b) Concave tuning



(c) Convex tuning

**Figure 2.3:** Plot of the streamlines for 90 diffuser with (a) No geometric tuning (b) Concave ( $\beta_{cv}$ ) = 3 and (c) Convex ( $\beta_{cx}$ ) = 0.1

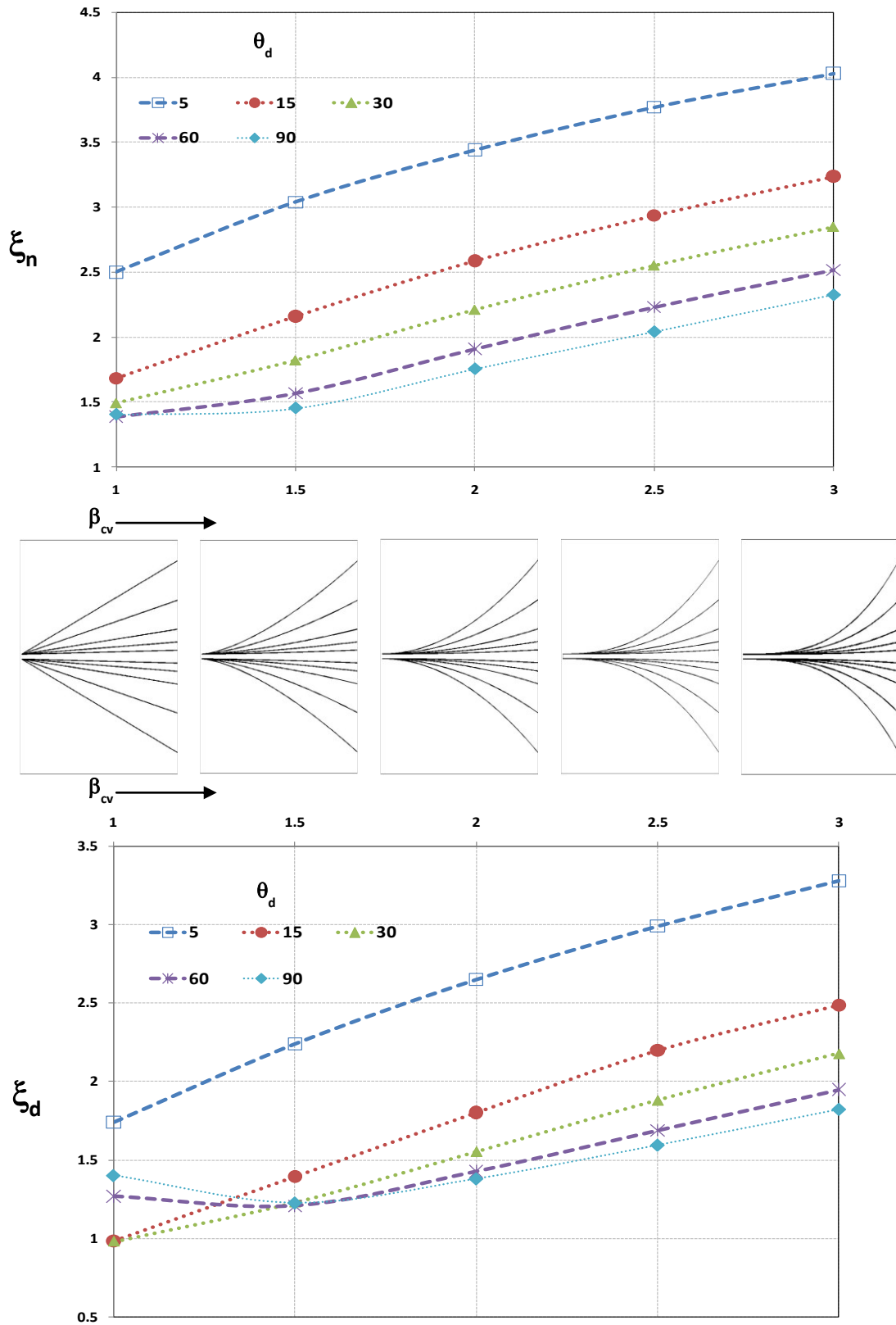


Figure 2.4: Plot of variation of  $\xi_n$  and  $\xi_d$  with  $\beta_{cv}$  for different diffuser angles

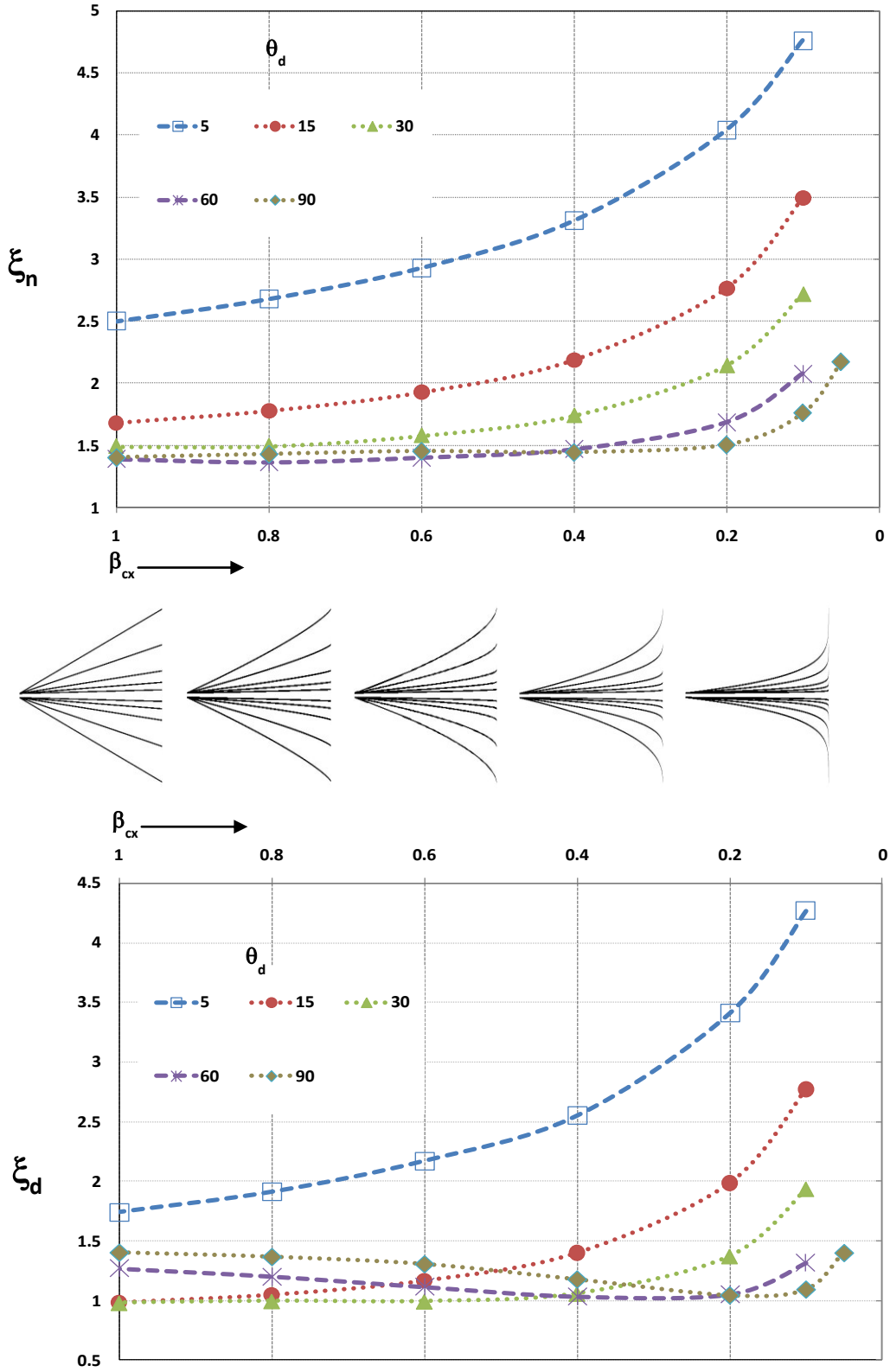


Figure 2.5: Plot of variation of  $\xi_n$  and  $\xi_d$  with  $\beta_{cx}$  for different diffuser angles

For smaller diffuser angles, the pressure coefficients in both the nozzle and diffuser direction increase with geometry tuning (i.e decrease in convex beta,  $\beta_{cx}$ , and increase in concave beta,  $\beta_{cv}$ ). As the angle of the diffuser is increased, for concave diffusers, the nozzle and the diffuser pressure drops increase with the increase in beta and a slight decrease in pressure coefficient is observed for higher diffuser angles, as a result of reduction in the flow separation from the walls. When convex geometry tuning is applied for wide angled diffusers, whereas the pressure coefficient in the nozzle direction always increases, a significant decrease is observed for the diffuser coefficient initially until the flow separation is removed in the positive flow direction and then increases. Therefore, convex diffusers help reduce flow separation better than concave diffusers. The results are summarized in Table 2.2.

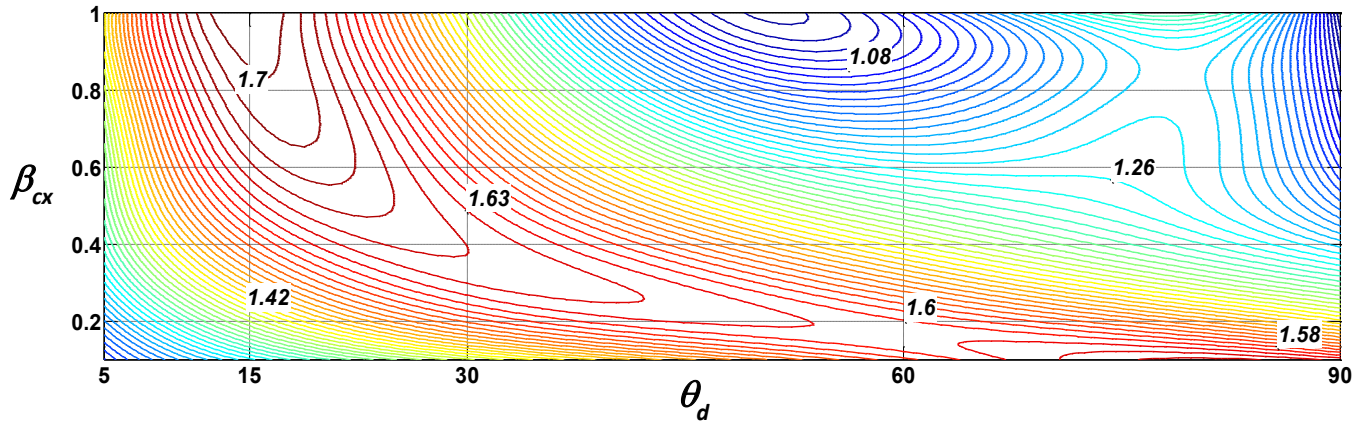
Coefficient	Diffuser Angle ( $\theta_d$ )	Effect of decreasing $\beta_{cx}$	Effect of increasing $\beta_{cv}$
$\xi_n$	5°, 15°	Always increases	Always increases
	30°, 60°, 90°	Always increases	Always increases
$\xi_d$	5°, 15°, 30°	Always increases	Always increases
	60°, 90°	Significant decrease with offset of flow separation; subsequent increase	Slight decrease due to offset of flow separation ; subsequent increase

**Table 2.2:** Summary of variation of  $\xi_n$  and  $\xi_d$  with geometric tuning

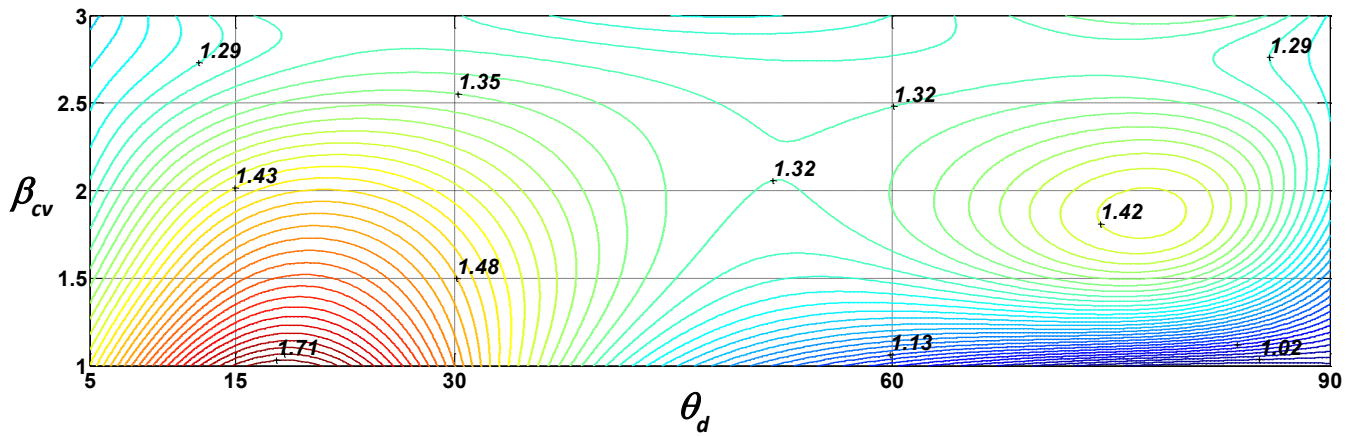
#### 2.2.3.2.2 Influence of geometry tuning on diffuser efficiency

The plot of the variation of efficiency of the diffuser with geometry tuning for different diffuser angles at  $Re = 100$  is presented in Figure 2.6. Since the simulations were carried out separately for concave and convex conditions in nozzle and diffuser directions, the relative error in efficiency was computed from the variation in the efficiency values for

straight walled diffuser. From Figures 2.6(a) and 2.6(b), it can be seen that for  $\beta = 1$ , the diffuser efficiencies are the same for all angles. This shows that the simulation is repeatable and the error in the modeling is very negligible.



(a)



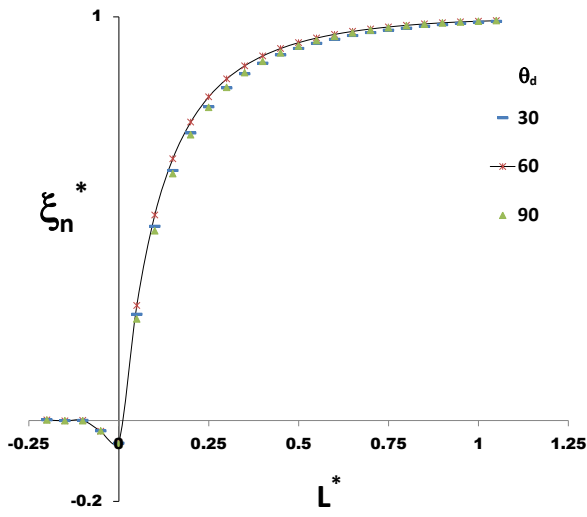
(b)

**Figure 2.6:** Plot of variation of  $\eta_{nd}$  for (a) Convex tuning,  $\beta_{cx}$  (b) Concave tuning,  $\beta_{cv}$  for different diffuser angles at  $Re = 100$

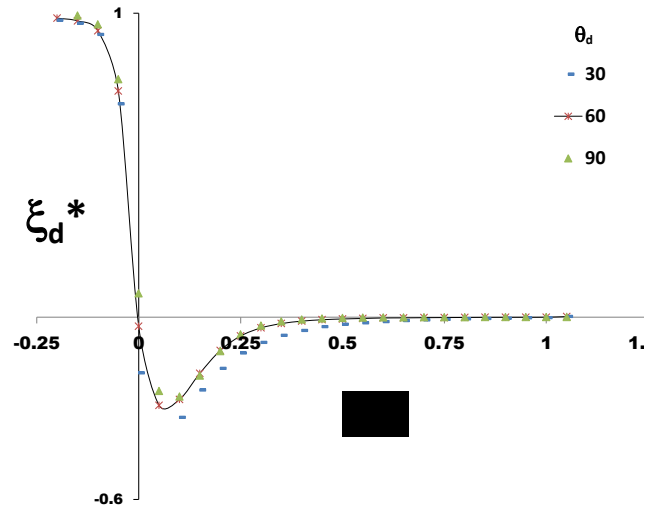
From among the different tuning parameters chosen for the present analysis, for lower diffuser angles, the maximum diffuser efficiency is obtained only for  $\beta = 1$ , i.e with the straight walled diffusers. For smaller diffuser angles, both convex and concave tuning decreases the overall efficiency of the diffuser upto 25 – 45%. As the angle of the diffuser

is increased, straight walled diffusers show a poor efficiency and the geometric tuning helps to improve the efficiency of the diffusers by upto 40%. For convex tuning, the efficiency of the diffuser continues to increase with decrease in the convex tuning parameter till it reaches a maximum, and any further decrease in the tuning parameter causes a drop in the diffuser efficiency. For concave tuning, the efficiency of wider angle diffuser initially increase with concave tuning, and decreases slightly for very wide angle diffuser. In comparison to the concave tuning, the better diffuser efficiency is achieved with convex tuning for wide angled diffusers. This can be attributed to the decreased diffuser coefficients with convex tuning for wide angled diffusers. Therefore, for larger diffuser angles higher diffuser efficiencies can be obtained only through geometric tuning of the diffuser element.

Extending the results obtained so far, the pressure distribution within the diffuser for concave and convex tuning parameters that yield the best efficiencies was studied. Axial pressure variations at different sections on a diffuser element was plotted with respect to the diffuser length to identify the region of the diffuser that causes the maximum pressure drop for a given  $\beta$ . The pressure drop at each segment was normalized with respect to the inlet pressure. This normalized pressure coefficient is denoted by  $\xi_n^*$  and  $\xi_d^*$ , where the subscripts  $n$  and  $d$  denote nozzle and diffuser directions of pressure drops respectively. The values of  $\xi_n^*$  and  $\xi_d^*$  were plotted against the normalized diffuser length  $L^*$ , which is the ratio of the distance from the throat of the diffuser on the axis along which the pressure drop is measured, to the overall diffuser length. The plot of  $\xi_n^*$  and  $\xi_d^*$  against  $L^*$ , for concave and convex tuning is as shown in Figures 2.7 and 2.8.

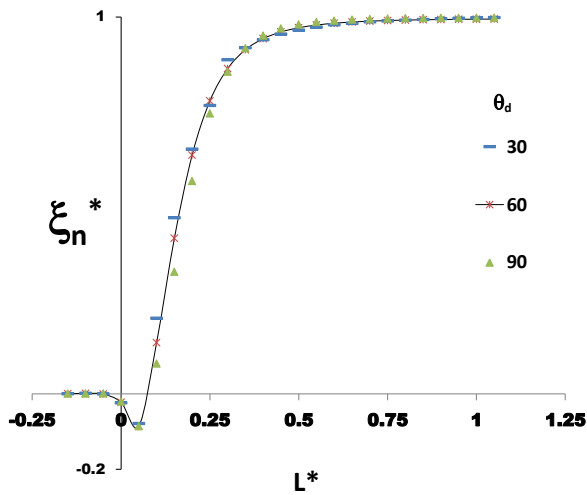


(a)

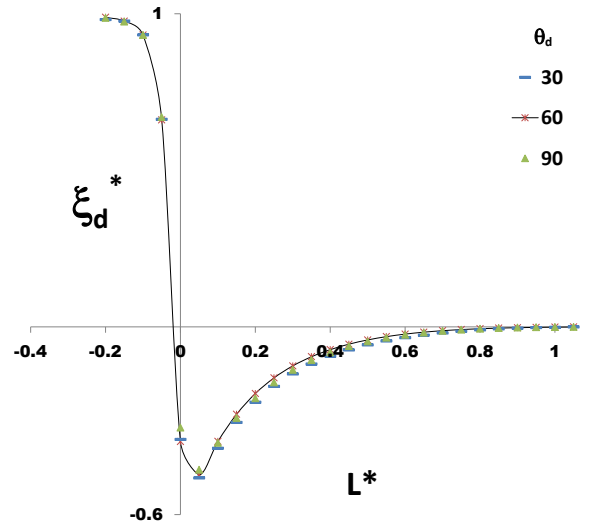


(b)

**Figure 2.7:** Plot of the variation normalized nozzle and diffuser pressure coefficients with respect to the normalized diffusion length for convex diffusers



(a)



(b)

**Figure 2.8:** Plot of the variation normalized nozzle and diffuser pressure coefficients with respect to the normalized diffusion length for concave diffusers



For both the concave and convex tuning for different diffuser angles, the pressure drop signatures are unique so as to achieve the best diffuser efficiency. A slight deviation in case of concave tuning suggests that the exact tuning parameter to achieve the best diffuser efficiency is close to, and not exactly, the chosen value. From the above graphs it is very clear that, for all the diffuser angles, the mechanism by which geometry tuning renders the best diffuser efficiency is the same, as seen from the identical and unique pressure drop signatures. In order to further understand how the geometry tuning improves the efficiency of wide- angled diffuser, the axial pressure distribution of the flow in both nozzle and diffuser directions was studied and compared for straight walled diffuser and also the concave and convex diffuser. From another perspective, this study was carried out to identify the regions within the diffuser which are significantly influenced by the geometric tuning. The comparison of the pressure distribution signatures for concave convex and straight-walled diffusers is as shown in Figure 2.9.

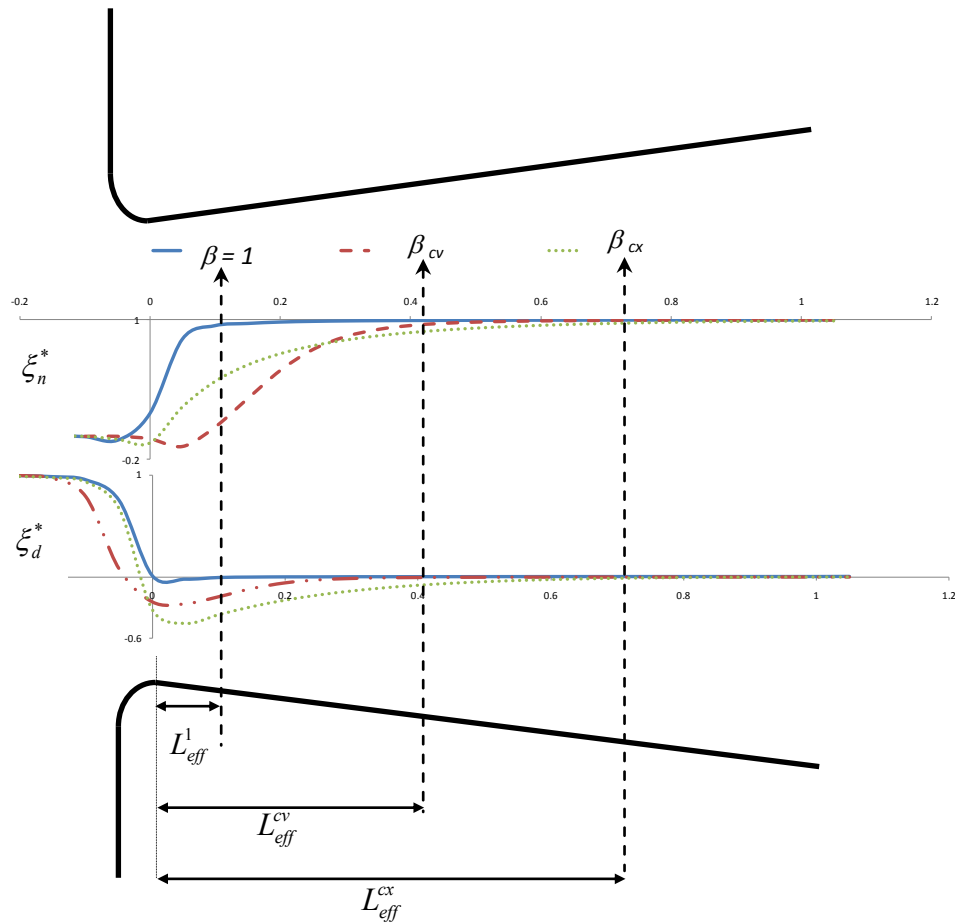


**Figure 2.9:** Comparison of effective diffuser lengths for straight walled diffusers and concave and convex diffusers.

For a given diffuser geometry, the onset of pressure drop (in the nozzle direction) and the completion of pressure drop (in the diffuser direction) occurs at the same distance from the throat of the diffuser, which is referred to as the effective diffuser length,  $L_{eff}$  (as shown in Figure 9 with  $L_{eff}^1$ ,  $L_{eff}^{cv}$  and  $L_{eff}^{cx}$  representing the effective diffuser lengths for straight, concave and convex betas respectively). In other words, the effective diffuser length is the length of the diffuser measured from the throat over which the net pressure drop occurs in both the nozzle and the diffuser directions. It can be clearly seen that the

efficiency of the diffuser is clearly the function of the effective diffuser length. As the diffuser angle increases, the efficiency of the diffuser is increased only through concave and convex tuning. However, it is also clear that the efficiency of the best convex tuning is better than the best concave tuning. This is clearly proved with the help of effective diffuser length. For the best convex diffusers, the effective diffuser length is greater than that of the best concave diffuser, which is in turn better than straight walled diffusers in case of wide angled diffusers. Thus, the diffuser efficiency can now be expressed in terms of the effective diffuser length, which therefore replaces the necessity to study the pressure coefficients in nozzle and diffuser directions individually.

Geometry tuning improves the efficiency of the diffuser by increasing the effective diffuser length across which the pressure drop takes place in the diffuser and the nozzle direction. Through convex and concave tuning of the microdiffuser geometry, the length over which the pressure drop occurs is widened. The region of the diffuser beyond the effective diffuser length does not contribute to the pressure drop. Therefore, as reported by Yang et al (2004), the length of the diffuser does not have any significant influence on the performance of the diffuser if and only if it is greater than the effective diffuser length. For straight walled diffusers, the effective diffuser length is very small and hence, the effect of diffuser length on diffuser performance is minimum. However one must ensure that the diffuser length is greater than  $L_{eff}$  when applying the geometric tuning technique in order to improve the efficiency of the diffuser.

### **2.2.3.3 Observations from FEM**

From the Finite Element Analysis, the following inferences are made with regard to the effect of geometry tuning on the performance of the microdiffuser.

1. For all diffuser configurations, the nozzle coefficient is always higher than the diffuser coefficient. This phenomenon has also been reported by Yang et al. (Yang et al. 2004).
2. For diffusers with  $\beta = 1$ ,  $\xi_n$  decreases with increase in  $\theta_d$ , as also reported by Olsson et al (1996), Jiang et al (1998) , Sun and Yang (2007) and Wang et al.( 2009). According to Singhal et al. (2004), for both planar and conical diffusers,  $\xi_d$  decreases with an increase in diffuser angle  $< 20$ , and then increases with an increase in diffuser angles  $> 20$ . Similar trend is observed in the present study also.
3. The critical diffuser angle for the inception of flow separation in the diffuser direction is  $20^\circ$  (Wang et al. 2009) and  $30^\circ$  (Sun, Yang 2007). In the present FEM, the flow separation has been identified from the increase in pressure coefficient in the diffuser direction and that happens at  $\theta_d = 30^\circ$ , and the diffuser coefficient increases with the onset of flow separation in microdiffusers with increase in diffuser angle. Through the method of geometric tuning presented herein, it is possible to modify the diffuser geometry in such a way so as to reduce the flow separation and thereby reduce the pressure coefficient in the diffuser direction.

4. For small and intermediate angle diffusers, structural tuning of microdiffuser geometry with concave and convex tuning helps improve tremendously both  $\xi_n$  and  $\xi_d$ . For higher diffuser angles, convex tuning helps in reducing the pressure drop in the diffuser direction, while increasing the pressure drop in the nozzle direction.

5. For straight walled diffusers, the overall diffuser efficiency increases from  $5^\circ$  to  $15^\circ$ , and then decreases with increase in diffuser angle. This phenomenon has also been reported before (Wang et al. 2009), and the results of the present FEM are in concurrence.

6. For wide angled diffusers, convex tuning improves diffuser efficiencies tremendously. Though concave tuning improves the diffuser efficiency in comparison with straight walled diffusers, the efficiency values are higher with concave tuning than convex tuning.

7. The pressure distribution signatures for the improvement of diffuser efficiencies through concave and convex tuning are unique. For the flow in both converging and diverging wall directions, the maximum pressure drop occurs only in the vicinity of the diffuser throat. The efficiency of the diffuser can be improved by increasing the effective diffuser length  $L_{eff}$ . Yang et al (Yang et al. 2004) have reported that the influence of the diffuser length on pressure coefficients is small. However, the influence of diffuser length is small only if it is greater than the effective diffuser length.

8. The pressure distribution study also explains that, the improvement in efficiency of the diffuser is achieved when the pressure drop is lower in the diverging wall direction and

the onset of pressure drop starts early in the converging wall direction, which should be taken into consideration when designing a diffuser for micropump application.

Thus, in order to improve the efficiency of the diffuser for valveless micropumping, through the power law geometric tuning, it is now possible to decrease the diffuser coefficient while simultaneously increasing the nozzle pressure coefficient. For a microdiffuser/nozzle of a constant inlet width, opening angle, and the diffuser length, the geometric tuning method presented herein gives a wide range of pressure coefficient values and the choice of the microdiffuser configuration can be made in accordance to the pressure coefficient values required for any particular micropump applications. Convex tuning increases the efficiency of the diffusers more than concave tuning. This was verified for all diffuser angles. Even for lower diffuser angles, it was verified that increasing convex beta beyond 1 improved the efficiency significantly. However, the results for improving diffuser efficiencies for smaller diffuser angles are not explored further because with decrease in diffuser angles, the efficiencies are highly sensitive to variations in betas and also, small angled diffusers are not preferred over wide angled diffusers for practical applications.

Overall, the concave and convex geometric tuning parameters are very useful for to tune and improve the efficiencies of the diffuser for valveless micropump applications.

#### **2.2.4. Experimental verification**

Though the analytical modeling of the microdiffuser behavior provides a lot of details about the performance of the diffuser element, it is essential to validate the simulated results by comparing with the experimental data.

Also, all the simulations were carried out in 2D. COMSOL microfluidics module takes into account the depth of the microchannel, and the flow parameters were also defined based on the computation of the Reynolds number. Experimental verification is also a method to understand the real-time behavior of the diffusers. However, it is difficult to explain several phenomena of the diffuser behavior through experiments alone, for example the flow separation for higher diffuser angles cannot be studied without suitable flow visualization. Therefore, to obtain confidence in the simulated results, it is essential to validate with suitable experiments under conditions as close to the simulation environment as possible.

The experiments on the diffuser were carried out to study the pressure coefficient of the nozzle and the diffuser for different diffuser angles for a given Reynolds number. For the present experiments, the value of beta for each diffuser angle that gave the maximum efficiencies at  $Re = 100$  were chosen for the experiments.

#### ***2.2.4.1 Fabrication of microdiffuser devices***

For the present experiments, the microdiffuser channels were fabricated on PDMS and bonded with PDMS-spun-on-glass as the base layer. The process starts with the fabrication of the mould for the PDMS on silicon. A negative photoresist SU8-2 was spun on silicon and lithography as carried out with a photomask which is the negative of the intended features to be replicated on the PDMS. After lithography and curing of the photoresist, the wafers were etched by Deep Reactive Ion Etching (DRIE) to obtain a depth of 100  $\mu\text{m}$ .

The silicon mould was then silanized, i.e. vapor phase silanization was carried out by heating the mould in a closed chamber with 1 ml of (Tridecafluoro-1,1,2,2-Tetrahydrooctyl)-1-Trichlorosilane (United Chemicals Inc., USA) at 60  $^{\circ}\text{C}$  for 4 hours. The silane forms a monolayer on the surface of the silicon and thus prevents the adhesion of PDMS with the substrate. 10:1 ratio of PDMS pre-polymer and the curing agent (Sylgard 184, Dow Corning) was mixed well and degasified. The mixture was then poured onto the silicon mould and baked at 80  $^{\circ}\text{C}$  for 4 hours. After curing, the PDMS was subsequently removed by peeling off the substrate from the silicon mould. In this way, the patterns on the silicon mould are transferred on the PDMS.

Before sealing the microdiffuser channels, ports were created to fit the microfluidic tubes. Separate inlet and outlet ports were created for the main fluid flow from the syringe pump and the reservoir. Two ports were created very close to the diffuser inlet and outlet respectively, for fitting the tubes to be connected to the pressure sensors. In this way, the



pressure drop is measured only across the diffuser avoiding other possible pressure losses in the system such as bending losses, entrance losses, pipe friction losses etc.,.

For the present experiments, the microdiffusers were bonded to the glass by the method of semi-curing PDMS. PDMS was spun on the glass substrate and was cured partially. After the semi-curing, the device layer was brought in contact with the PDMS-on-glass so as to form a strong bonding and prevents any leakage in the channel. It must be mentioned that the reason for not using oxygen plasma bonding of PDMS and glass for the present experiments, is twofold. Firstly, the exposure of PDMS chips to oxygen plasma would render the surface hydrophilic, which would increase the surface friction and thus, the frictional pressure loss in the diffuser. Secondly, in a few initial experiments it was observed that as PDMS ‘ages’ after oxygen plasma treatment, the uneven surface affinity would make it extremely difficult to prime the channel well, thereby leading to the possibility of small cavities. The intermediate cavities in the flow stream along the microdiffuser could disrupt the study of the pressure variation across the diffuser. Figure 2.10 (a) gives the SEM image of the microdiffuser and the microdiffuser as seen under the microscope is shown in Figure 2.10(b).

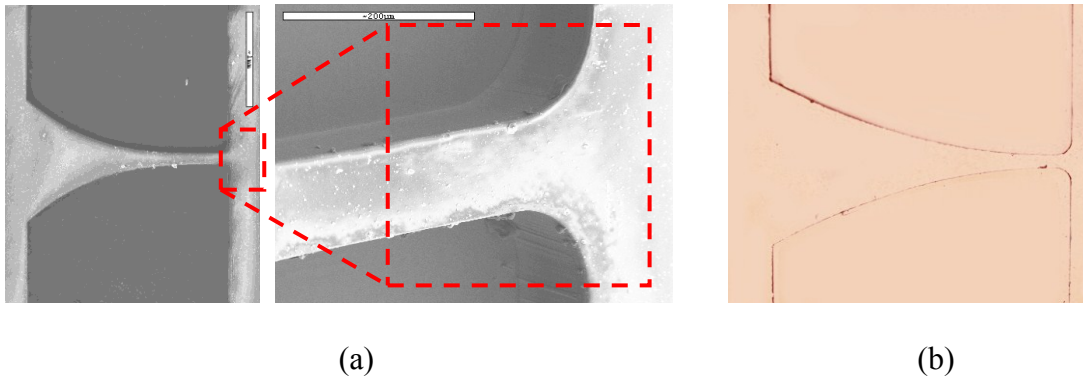


**Figure 2.10:** (a) SEM image of the Silicon mould for a concave PDMS microdiffuser with  $\beta = 1.5$  (b) Fabricated PDMS microdiffuser chip as seen under the microscope.

#### 2.2.4.2 Experimental Setup

The schematic of the experimental setup is as shown in Figure 2.11.

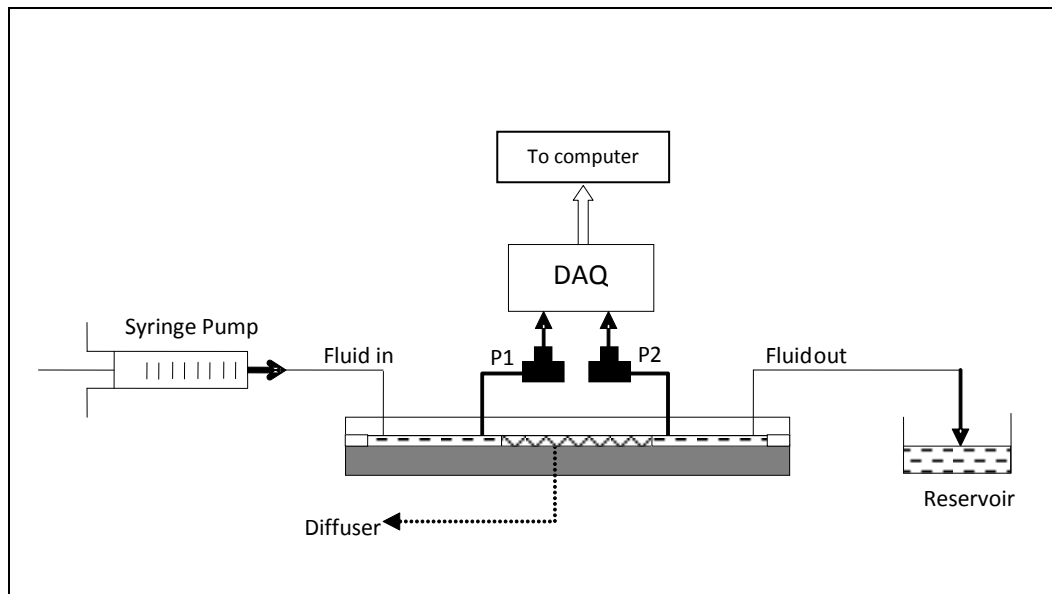


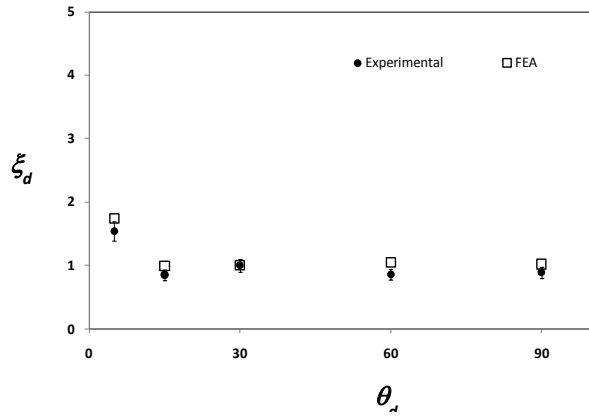
**Figure 2.11:** Schematic of the diffuser experimental setup

A programmable syringe pump (KDS 200, GeneQ Inc., Montreal) is filled with deionized water and provides a steady precision flow rate through the chamber and the diffuser. The flow rate of the pump was set as 600  $\mu\text{l}/\text{min}$  for  $\text{Re} = 100$ . The uncertainty of the flow rate is less than  $\pm 1\%$ . The pressure across the diffuser was measured using pressure sensors (Fujikura). The measurement of the pressure was done through a Data Acquisition (DAQ) system, to which the pressure sensors P1 and P2 were connected. The fluid from the diffuser outlet is discharged into a reservoir. Prior to the experiments, the pressure sensors were extensively calibrated (Hossain 2010) against standard flow systems and known pressures, The results of the pressure sensors were within 5% deviation thereby providing confidence in using the pressure sensors for the present diffuser analysis. The variation of the pressure in the chamber due to the height of the water column in the reservoir is infinitesimally small and is neglected.

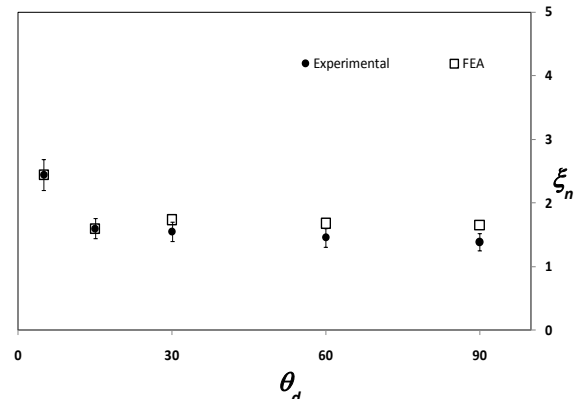
#### ***2.2.4.3 Results***

The experiment is performed by passing water with the syringe pump into the diffuser and measuring the pressure difference across the diffuser. The pressure was calculated in terms of voltage with a Data Acquisition system, and was converted into Pascals using suitable conversion formulas. Since the inlet and the outlet reservoirs were designed symmetric, for the flow in the nozzle direction, the inlet and the outlet were switched and the flow rate was maintained constant for both the nozzle and diffuser directions of flow. Assuming a continuous flow, the velocity at the throat of the diffuser is taken calculated from the flow rate and the cross-sectional area of the diffuser. Therefore, knowing the pressure difference and the flow velocity, the pressure coefficients in both the nozzle and

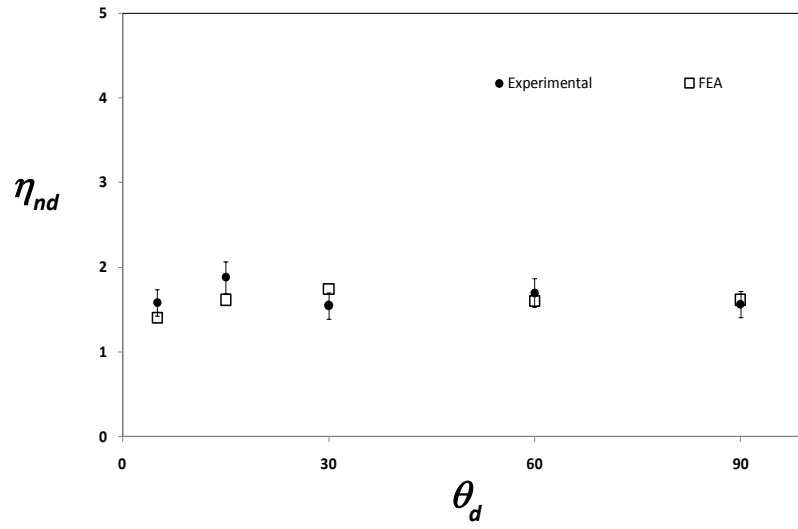
the diffuser directions were calculated from relation 16. The diffuser efficiency is then obtained by taking the ratio of the pressure coefficients in nozzle and diffuser directions respectively, as given in equation 8. The comparison of the experimental and the theoretical pressure coefficients for convex diffusers are as shown in Figure 2.12. The performance of the concave diffusers were also studied experimentally; the efficiency of the concave diffusers was computed from the experimental nozzle and diffuser pressure coefficients for diffuser angles  $30^\circ$ ,  $60^\circ$  and  $90^\circ$ . The value of  $\beta_{cv}$  which exhibit the best efficiency for each diffuser angle was chosen for the experiment. The results are as shown in Figure 2.13.



(a)



(b)



(c)

**Figure 2.12:** Comparison of the experimental and simulated pressure coefficients, and the diffuser efficiencies for convex diffusers with maximum efficiency at  $Re_d = 100$  for different diffuser angles.

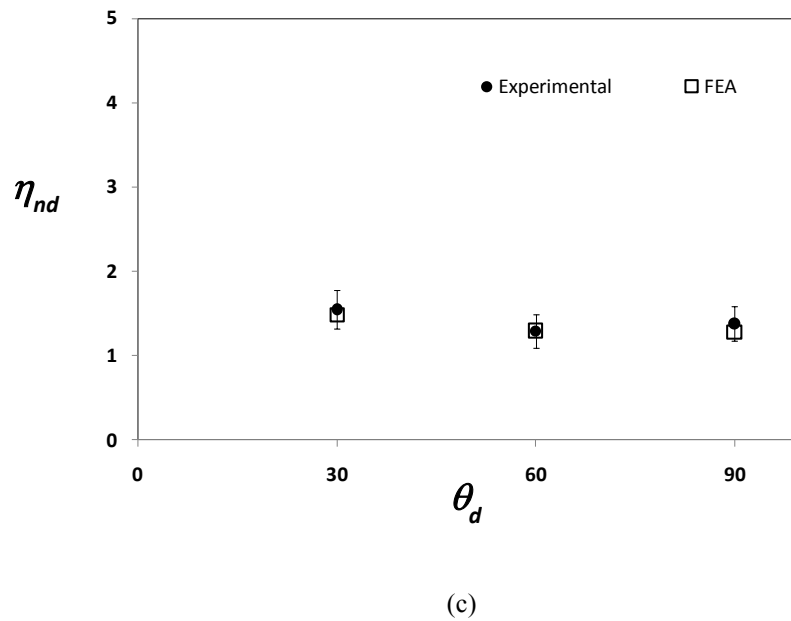
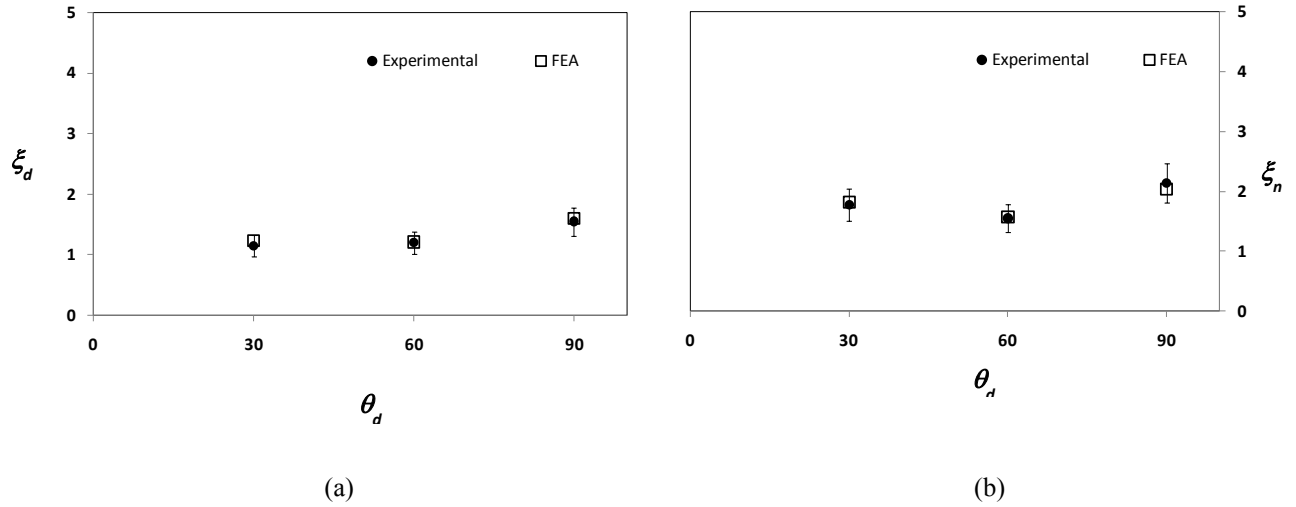


**Figure 2.13:** Comparison of the experimental and simulated pressure coefficients, and the diffuser efficiencies for concave diffusers with maximum efficiency at  $Re_d = 100$  for wide angled diffusers.

There is an excellent agreement between the predicted pressure coefficients in the nozzle and the diffuser directions and the experimental values obtained, for both concave and convex diffusers. The maximum standard deviation observed for the theoretical and

experimental diffuser efficiencies is 0.16. Considering a possibility of 5 – 15 % error between simulation and experiments (Wang et al. 2009), the pressure coefficients obtained from the experiments are well within the tolerance. For all the diffuser angles, the experimental values of the pressure coefficients are marginally lesser than or equal to the predicted value. This may be caused because the actual flow velocity in the diffuser may be slightly lesser than the expected velocity, due to several reasons such as bending losses, flow instability, or stagnated flow in the connecting tubes etc. Another possible reason for the deviation could be the geometric tolerances and the deviation of the feature sizes of the diffuser, due to lithographic imperfections or thermal expansion during the process of curing the PDMS microdiffusers, due to which the actual flow velocity at the throat of the diffuser is slightly different from the expected value. This could also lead to incorrect measurement of the pressure difference across the diffuser. For higher diffuser angles, in the converging wall direction, the deviation is higher which suggests the possibility of slight anomaly in the flow behavior from the FEA predictions. However, there is a good agreement between the experimental and the simulated results for the diffuser efficiency, which shows that the slight anomaly in the results obtained for individual pressure coefficients are due to the flow behavior which is observed in both the positive and the negative direction of flow.

The best diffuser efficiencies obtained with concave and convex tuning for diffuser angles  $30^\circ$ ,  $60^\circ$  and  $90^\circ$  were compared and as predicted by FEM, the experiments confirm that convex diffusers perform better than concave diffusers to increase the diffuser efficiency, as shown in Figure 2.14.

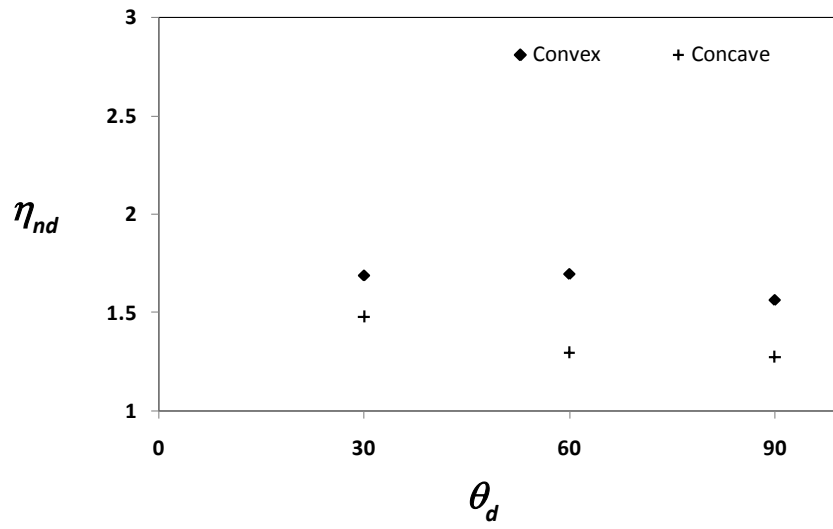


**Figure 2.14:** Comparison of best diffuser efficiencies obtained with convex and concave tuning for wide angled diffusers

**2.2.5. Conclusion**

A power law geometry tuning method has been presented herein and this method can be used to improve the efficiency of microdiffuser/nozzle for valveless micropumps, which can be used in several MEMS applications. This geometry tuning method is simple and is compatible with all microfabrication processes and soft lithography techniques, without the need to modify the existing setup. By this method, the geometry of the microdiffuser can be tuned with a single variable parameter, by which the pressure coefficients can be varied over a wide range, which is useful for valveless micropumping in real-time microfluidic and nanofluidic applications. The results achieved the 2D Finite Element Analysis are very useful to increase the qualitative understanding of the diffuser element flow and are accurate enough to be used for design optimization of diffusers for valveless



micropump applications. Further analyses include the study of the effect of flow velocity on the performance of the geometry conditioned microdiffusers and to study further modifications to the geometry tuning to improve the performance of the microdiffusers. Further analyses include the study of the effect of flow velocity on the performance of the geometry conditioned microdiffusers, consideration of viscoelastic effects of the fluids, effect of geometric tuning with non-Newtonian fluids, analysis of geometric tuned microdiffusers with multiphase fluids and to study other possible modifications to the geometry tuning to improve the performance of the microdiffusers.

### **2.3. Influence of Reynolds number on diffuser performance with geometric tuning**

It is clear from the FEM and experimental results presented in the previous section that geometric and microfluidic flow parameters play a significant role in influencing the performance of a microdiffuser for valveless micropumping, and that under favourable conditions, geometric tuning even helps in improving the efficiency of the micropump significantly. In order to design a microdiffuser element to be used for flow rectification in valveless micropumps, it is essential to study the diffuser performance in terms of its pressure coefficients for a wide range of operating conditions. For microdiffusers used in micropump applications, flow rectification is highly dependent on the Reynolds number ( $Re$ ). Most of the present data available in the literature are available for the friction coefficients and the losses in the diffuser elements are for macro diffuser elements, however, the performance of the microdiffuser at different Reynolds numbers is vastly different. For example, the transition  $Re$  is much less in a microdiffuser than a macro diffuser. Hence, the performance study of the microdiffuser elements at different Reynolds numbers need a separate investigation in order to understand the mechanism of geometric tuning over a wide range of Reynolds numbers.

Literature has in it many contradictory results regarding the pressure loss characteristics and the performance of microdiffusers with respect to the Reynolds numbers have also been reported. For example, Gerlach and Wurmus (1995) have suggested that flow rectification in a nozzle/diffuser element is not achievable in laminar flow, while Singhal et al. (2004) reported that flow rectification is indeed achievable in a nozzle/ diffuser

element for laminar flow. However, there have also been a few significant observations such as, the dependency of flow rectification on Reynolds number, particularly in the laminar region, and the effect of converging/diverging angle in the case of the nozzle/diffuser structure, as reported by Olsson et al. (2000), Gamboa et al. (2005), Yang et al. (2004), Wang et al. (2009), Singhal et al. (2004), Chen et al. (2008), and Olsson et al. (1995). Jiang et al. (1998) showed that the loss coefficient and the efficiency of conical diffusers exhibit very different trends with diverging angle at very low ( $Re < 50$ ) and high ( $Re > 10^5$ ) Reynolds numbers. More recently, Rosa and Pinho (2006) showed that the diffuser loss coefficient quoted from the literature are only valid for turbulent flows and may lead to significant errors when flows are laminar. There is also an agreement on the capability of the diffuser element to direct the flow (Olsson et al. 2000), (Jiang et al. 1998). For the range of Reynolds numbers in this study, the assumption of laminar flow is questionable because previous experimental observations of the Reynolds number at transition from laminar to turbulent flow in micro-channels are inconsistent and contradictory. Peng et al. (1994) predicted an early laminar-to-turbulent transition for the Reynolds number of 200–700 and Mala and Li (1999) have considered the transition Reynolds number in the range of 600–900. Possible reasons for the inconsistency of the experimental data with the conventional theory (Hetsroni et al. 2005), (Kohl et al. 2005), include experimental uncertainties, error or underestimation of the actual roughness of the channel walls, and unaccounted entrance effects of the channel. Given that the maximum Reynolds number of most diffuser micropumps ranges from 10 to  $10^3$ , there is a definite paucity in relevant experimental data and analytical expressions for the pressure loss characteristics in the low Reynolds number flow regime, since all the pressure loss

analyses used for designing the diffuser valve have been based mainly on the empirical data obtained at Reynolds number higher than 30,000 (Wang et al. 2009).

Thus, it is evident that the design of the diffuser for micropump applications is in need of of good analytical studies corroborated with suitable experiments, for the study of the microdiffuser performance over a wide range of Reynolds numbers for micropumping applications. Consequently, the potential of developing a multifunction valveless microfluidic system based on Reynolds number for micropump applications has not been fully explored (Fadl et al. 2009). Pressure coefficients in diffuser and nozzle directions vary drastically with the flow velocity.

The present analysis presents the modeling of the microdiffusers over a wide range of Reynolds numbers for variation in angle and also geometry tuning parameter. The following sections of this chapter present a detailed study of the performance of the microdiffusers based on the variation of geometry through concave and convex betas and the flow velocity (Chandrasekaran and Packirisamy, 2011)

### 2.3.1 Finite Element Modeling

The effect of geometry tuning on the performance of the microdiffuser at different flow velocities was studied using Finite Element Modeling (FEM). The computational domain consists of a large inlet chamber, a diffuser, and an outlet reservoir exactly the same as described in Section 2.2. The widths of the inlet and the outlet chambers are taken as the same. FEM was carried out with COMSOL v3.5 and ANSYS/FLUENT 12.0. The basic differencing schemes are central differencing for the diffusion terms and quadratic upwind interpolation for the convective terms (the QUICK scheme). The pressure–velocity coupling is based on the SIMPLE algorithm. Convergence criterion set as that the normalized norm of the residual for each variable is less than  $10^{-6}$ . A uniform velocity is applied at the chamber inlet and the gauge pressure at the outlet of the reservoir is set as zero. No-slip boundary conditions are imposed on the walls of the diffuser elements.

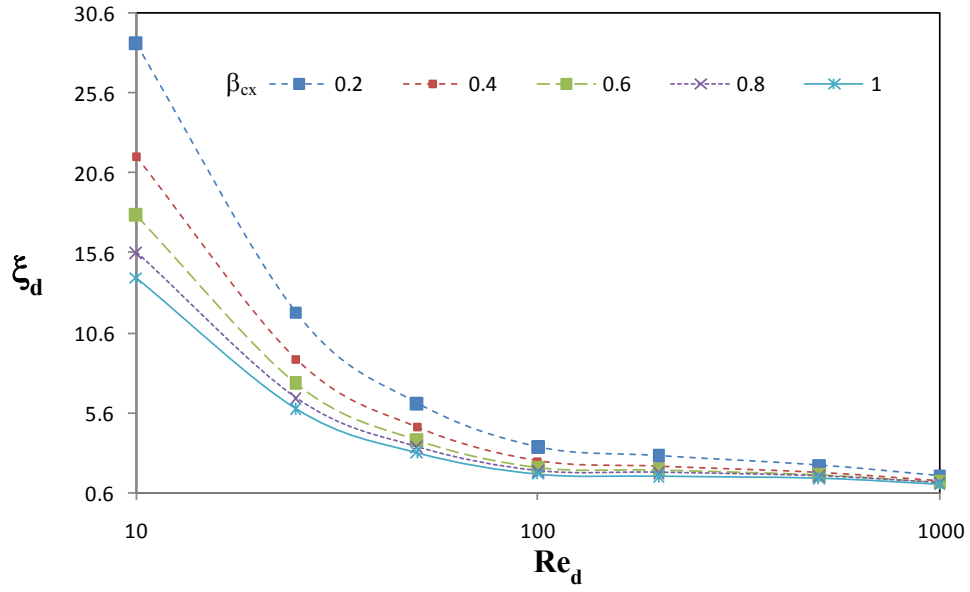
Here, the inlet boundary condition is defined by flow velocity and the outlet boundary condition was set by gauge pressure. The flow velocity was considered based on the Reynolds number at the neck of the diffuser. The Reynolds number is given here with respect to the velocity of the fluid at the neck of the diffuser. If  $D_h$  is the wetted perimeter at the neck of the diffuser, the Reynolds number  $Re_d$  for the flow is defined as

$$Re_d = \frac{\rho u D_h}{\mu} \quad \dots 2.12$$

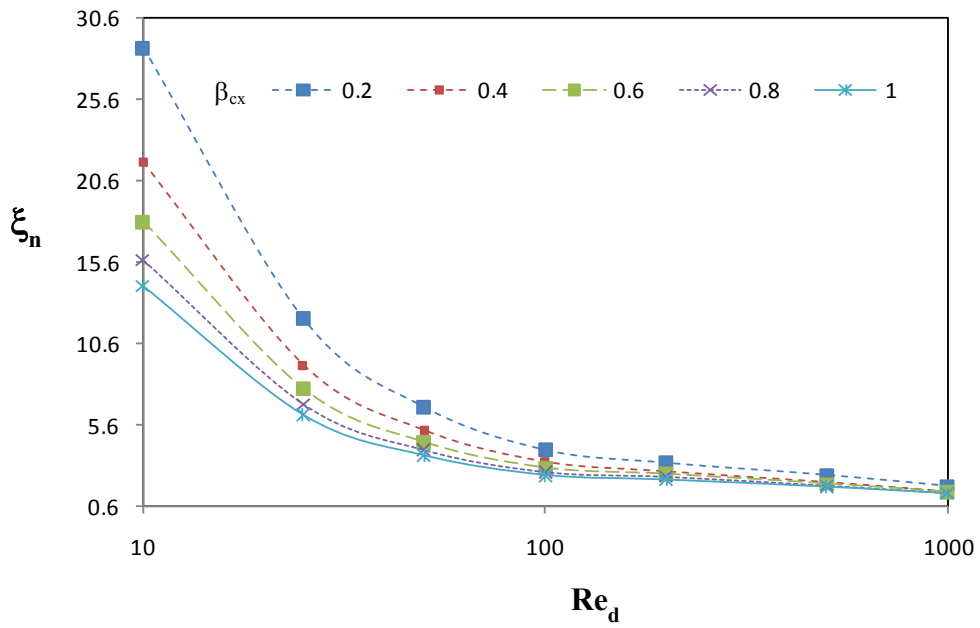
For a typical operational range for valveless micropumps for microbiological applications, the flow Reynolds number lies between 10 and 100 (Fadl et al. 2009). The present analysis considers flow Reynolds numbers of 10, 25, 50, 100, 200, 500 and 1000.

The boundary conditions for the diffuser are the same as described before. The flow is considered incompressible and laminar. For the present study, the transition Reynolds number was considered as 400. For  $Re \geq 200$ , FEM was carried out with ANSYS/FLUENT because of the problem with convergence in using COMSOL at higher Reynolds numbers for the present problem. However, in order to ensure the similarity of results with both softwares, the results of diffuser performances at lower Reynolds numbers were analysed with the previously published results (Wang et al. 2009) and the discrepancy between the results obtained from both the softwares was found to be less than 2%.

The results of the Finite Element Analysis of the diffuser behavior for different angles at different Reynolds numbers with geometric tuning are presented by plotting the variation of the pressure coefficients with convex and concave geometric tuning, as shown in Figures 2.15.1 - 2.15.5 and 2.16.1 - 2.16.5 respectively.

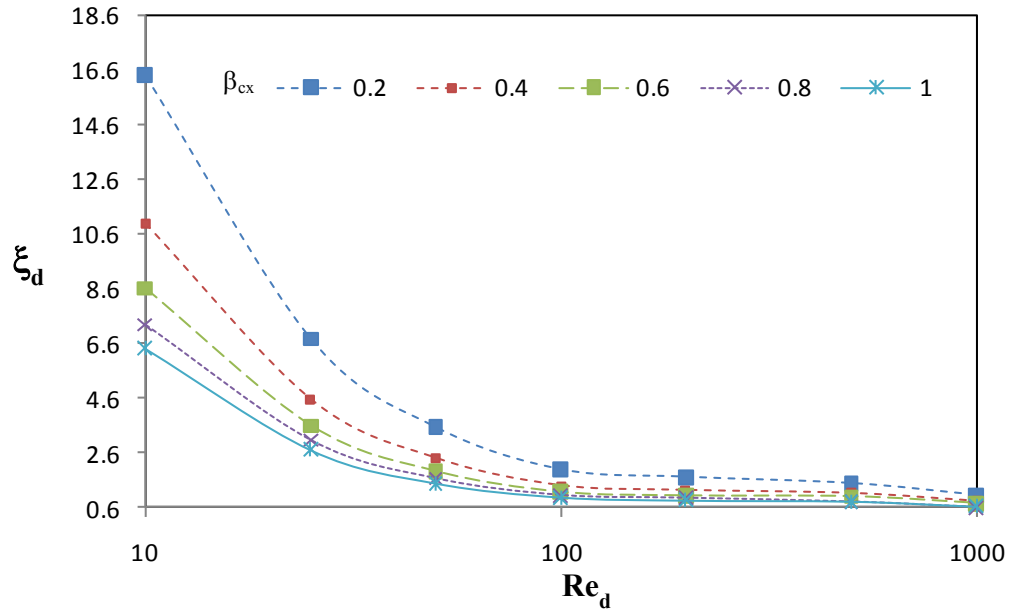


(a)

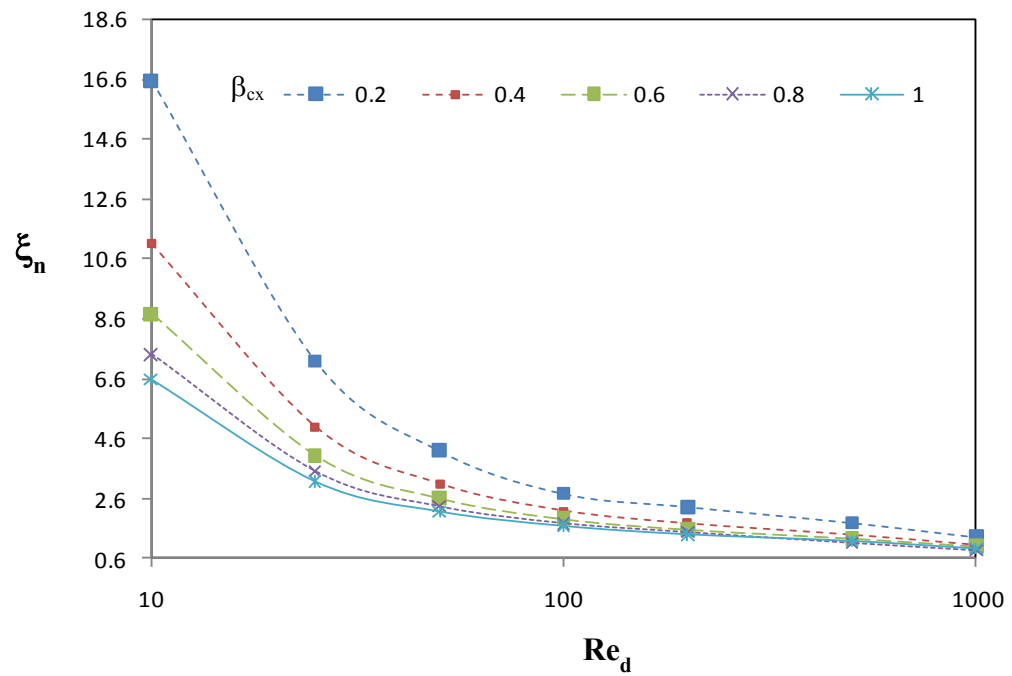


(b)

**Figure 2.15.1:** Variation of pressure coefficients (a)  $\xi_d$  and (b)  $\xi_n$  with the diffuser Reynolds number ( $Re_d$ ) for diffusers with convex tuning ( $\beta_{cx}$ ) for  $\theta_d = 5^\circ$



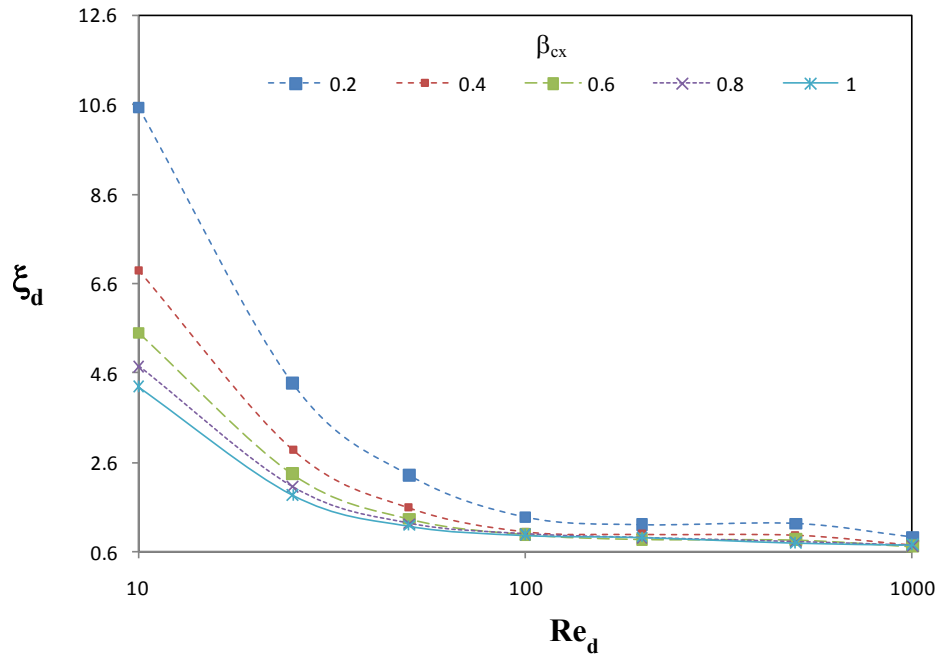
(a)



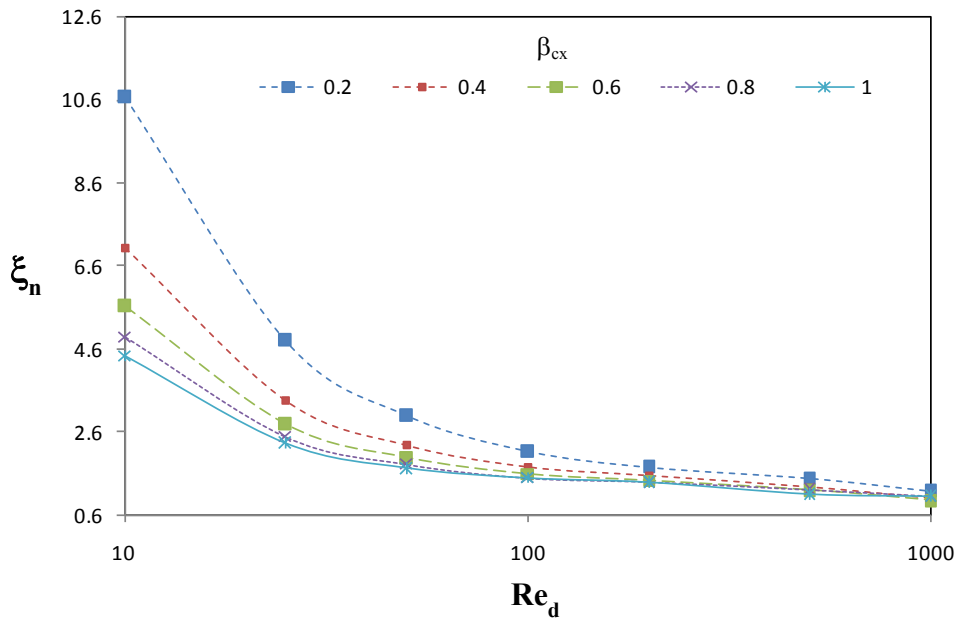
(b)

**Figure 2.15.2:** Variation of pressure coefficients (a)  $\xi_d$  and (b)  $\xi_n$  with the diffuser Reynolds number ( $Re_d$ ) for diffusers with convex tuning ( $\beta_{cx}$ ) for  $\theta_d = 15^\circ$



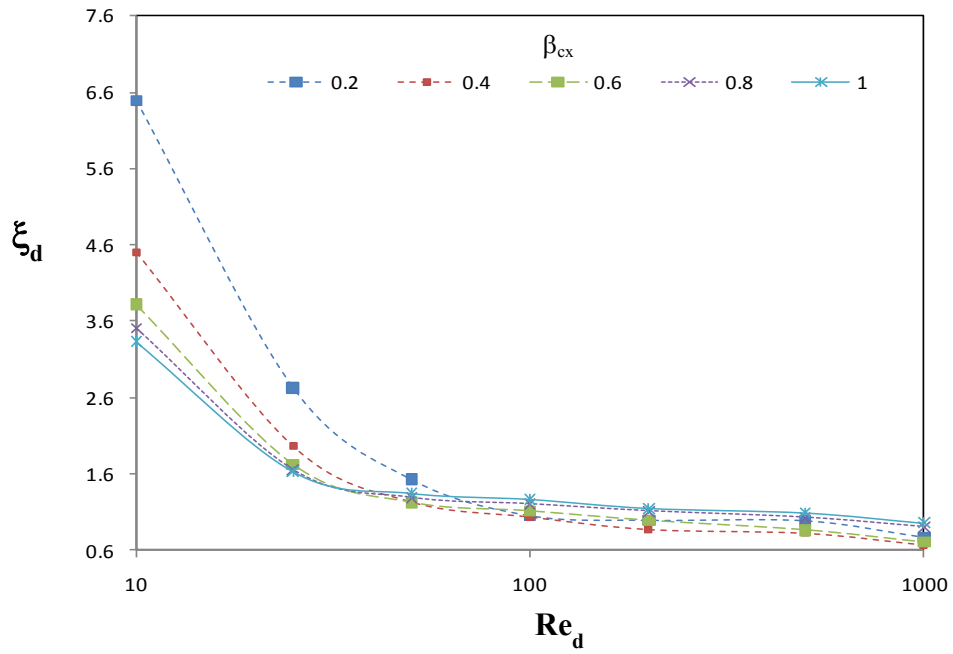


(a)

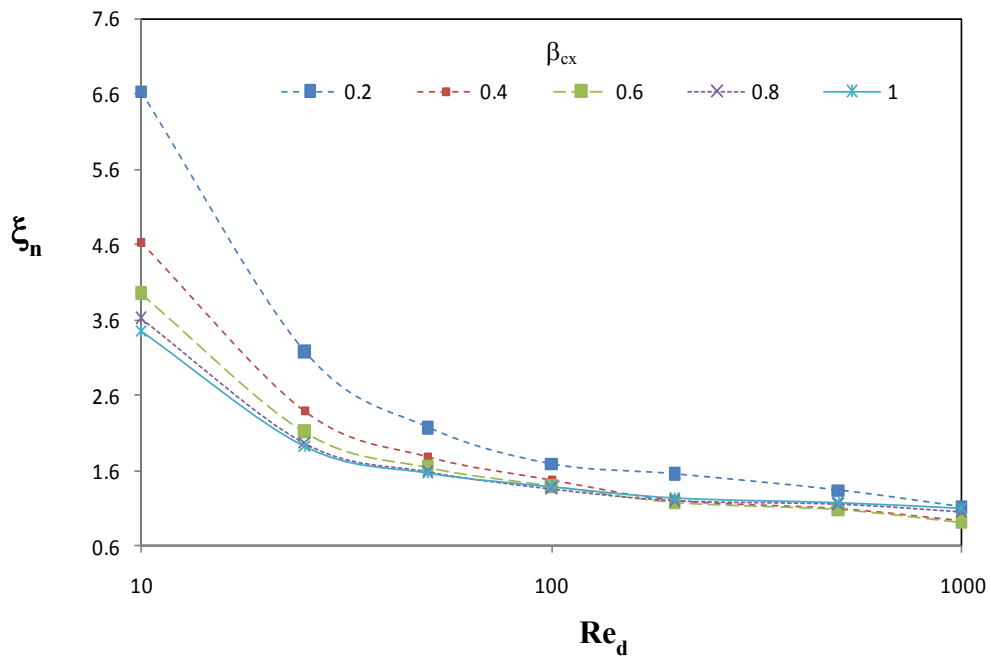


(b)

**Figure 2.15.3:** Variation of pressure coefficients (a)  $\xi_d$  and (b)  $\xi_n$  with the diffuser Reynolds number ( $Re_d$ ) for diffusers with convex tuning ( $\beta_{cx}$ ) for  $\theta_d = 30^\circ$

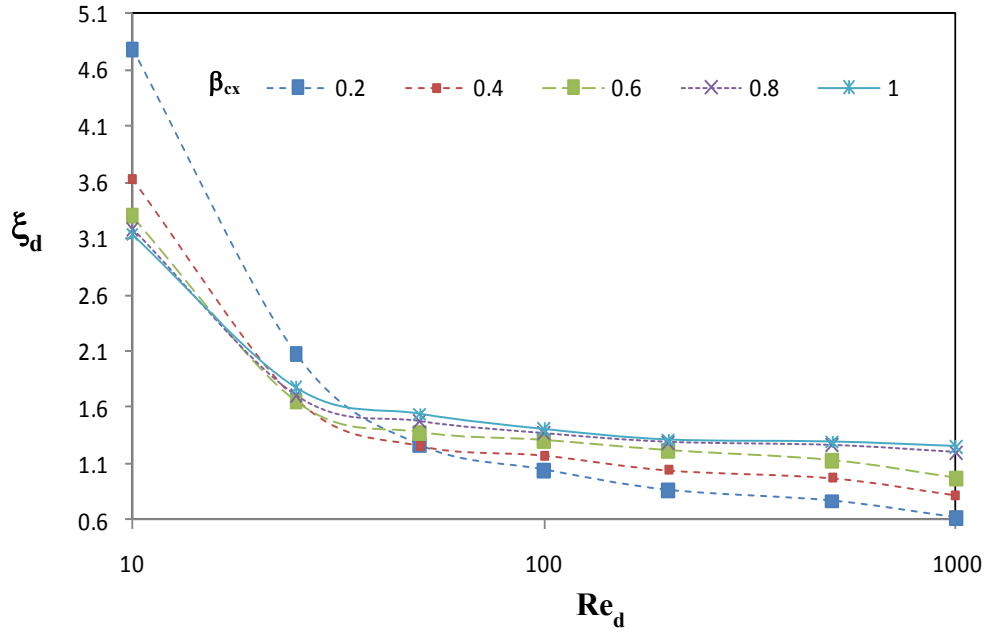


(a)

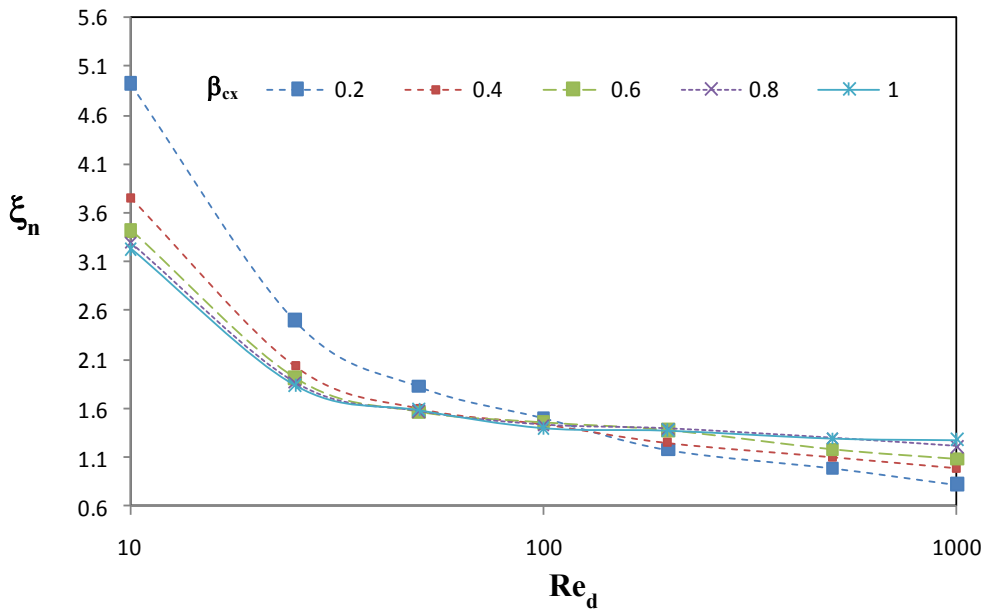


(b)

**Figure 2.15.4:** Variation of pressure coefficients (a)  $\xi_d$  and (b)  $\xi_n$  with the diffuser Reynolds number ( $Re_d$ ) for diffusers with convex tuning ( $\beta_{cx}$ ) for  $\theta_d = 60^\circ$

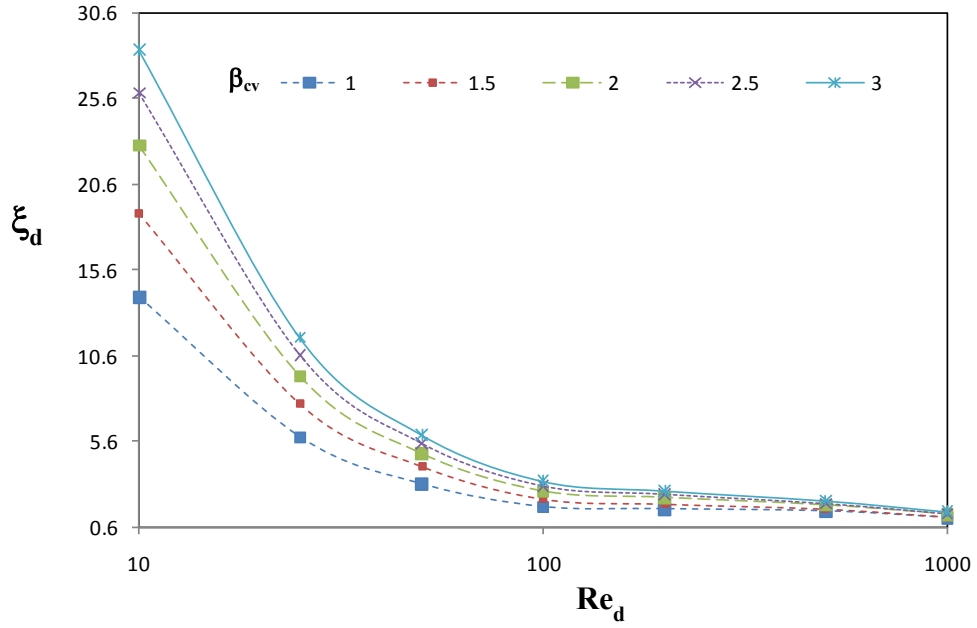


(a)

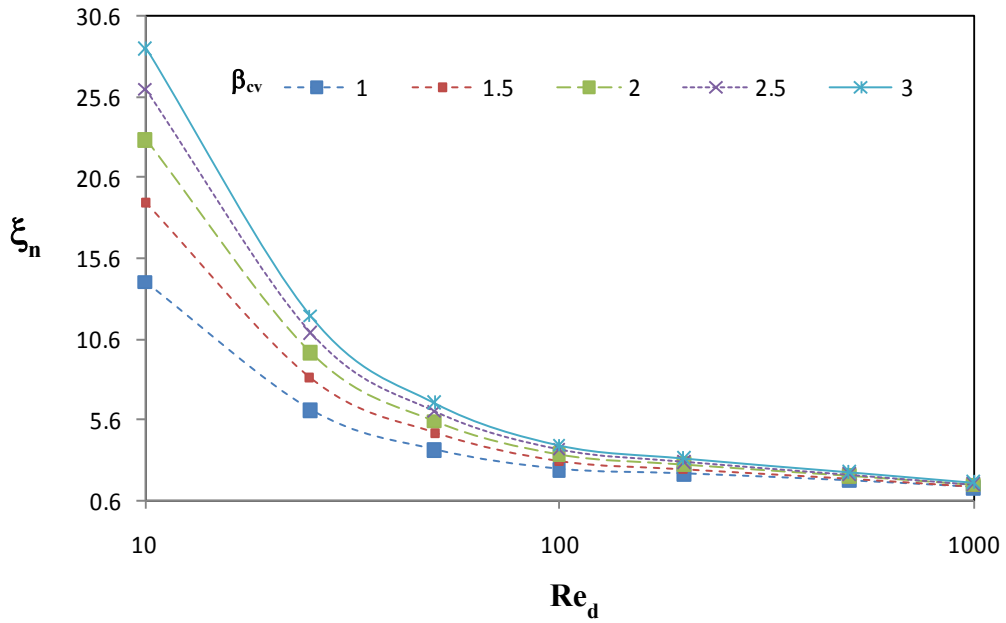


(b)

**Figure 2.15.5:** Variation of pressure coefficients (a)  $\xi_d$  and (b)  $\xi_n$  with the diffuser Reynolds number ( $Re_d$ ) for diffusers with convex tuning ( $\beta_{cx}$ ) for  $\theta_d = 90^\circ$

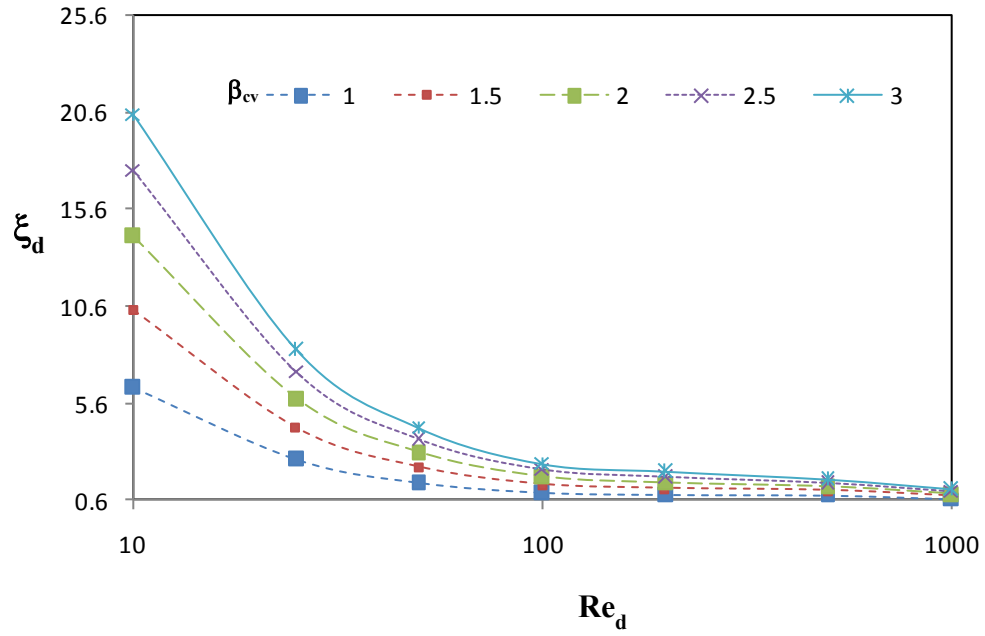


(a)

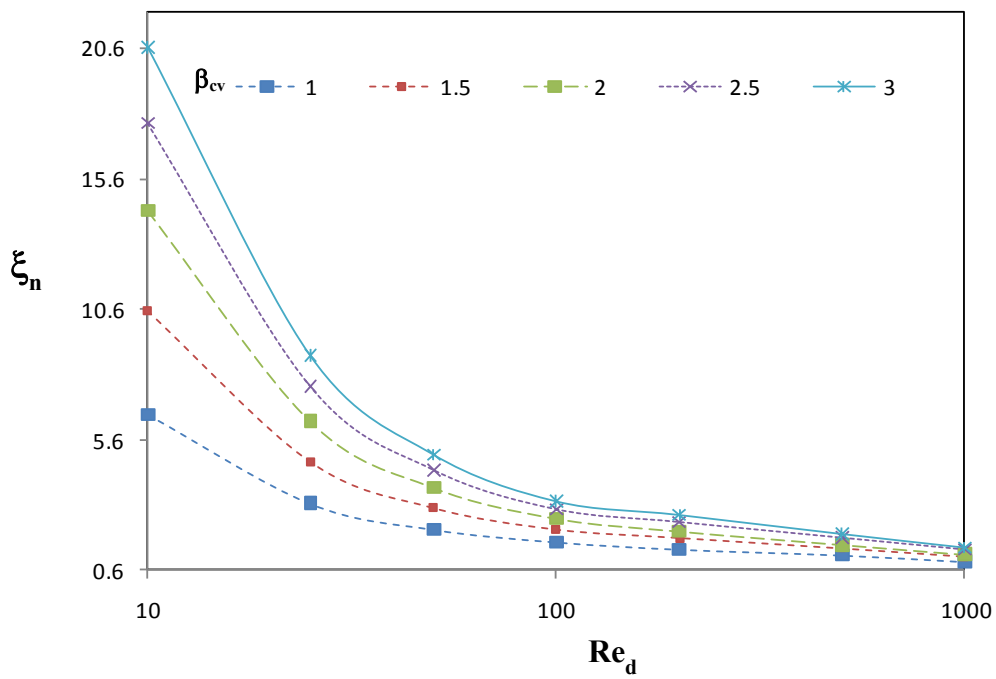


(b)

**Figure 2.16.1:** Variation of pressure coefficients (a)  $\xi_d$  and (b)  $\xi_n$  with the diffuser Reynolds number ( $Re_d$ ) for diffusers with Concave tuning ( $\beta_{cv}$ ) for  $\theta_d = 5^\circ$

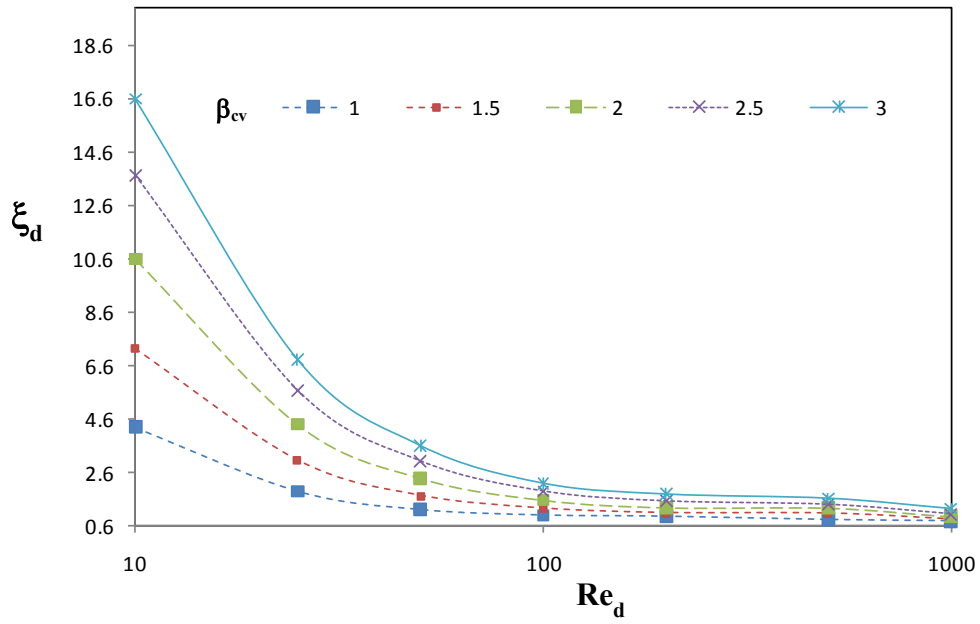


(a)

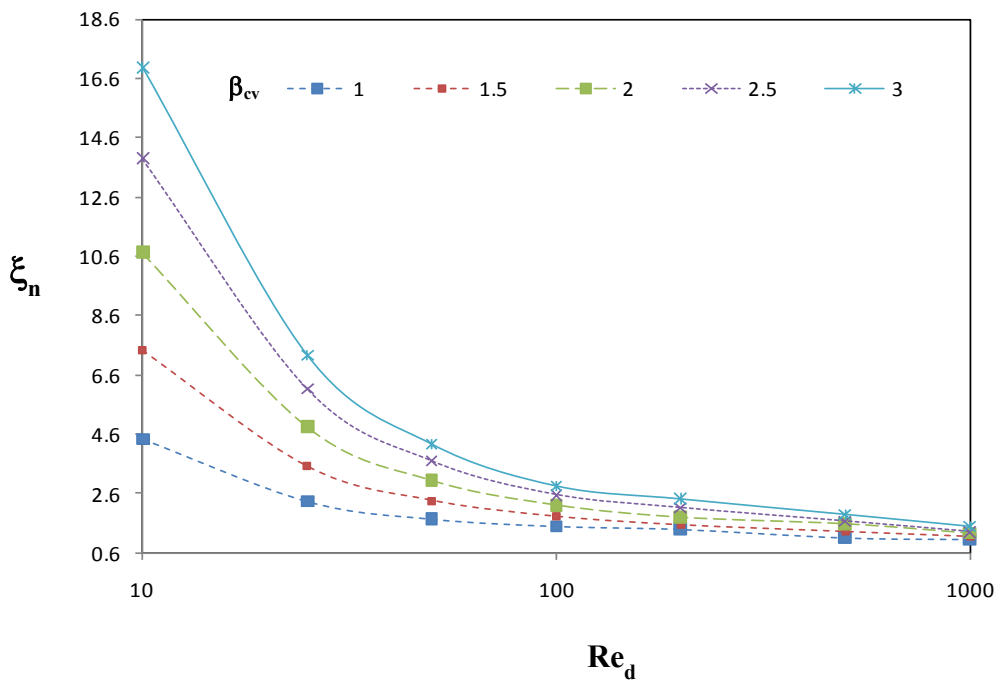


(b)

**Figure 2.16.2:** Variation of pressure coefficients (a)  $\xi_d$  and (b)  $\xi_n$  with the diffuser Reynolds number ( $Re_d$ ) for diffusers with Concave tuning ( $\beta_{cv}$ ) for  $\theta_d = 15^\circ$

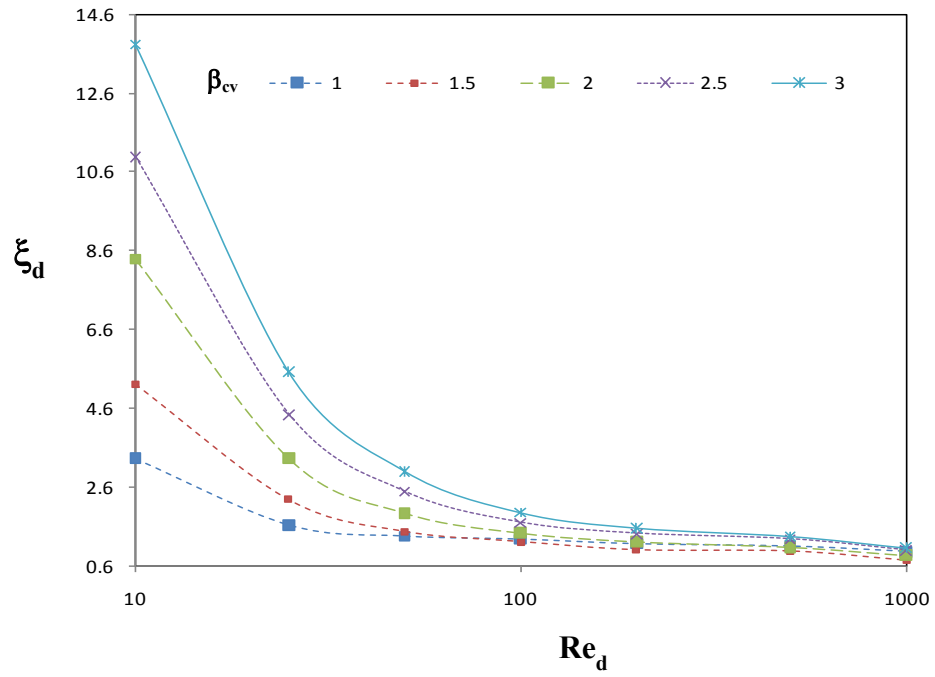


(a)

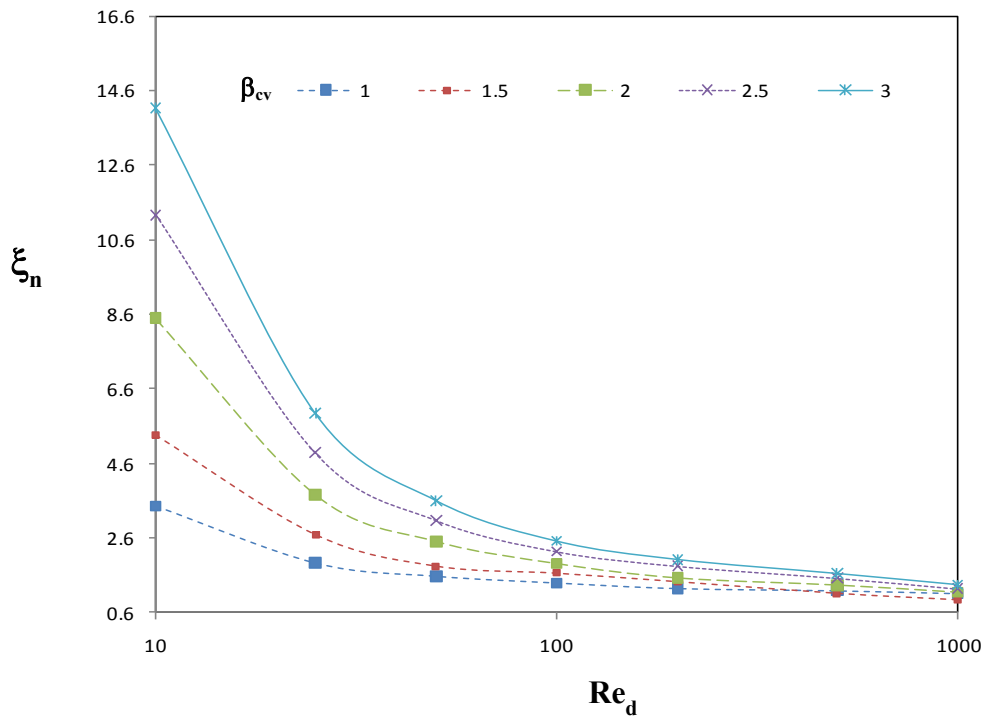


(b)

**Figure 2.16.3:** Variation of pressure coefficients (a)  $\xi_d$  and (b)  $\xi_n$  with the diffuser Reynolds number ( $Re_d$ ) for diffusers with Concave tuning ( $\beta_{cv}$ ) for  $\theta_d = 30^\circ$

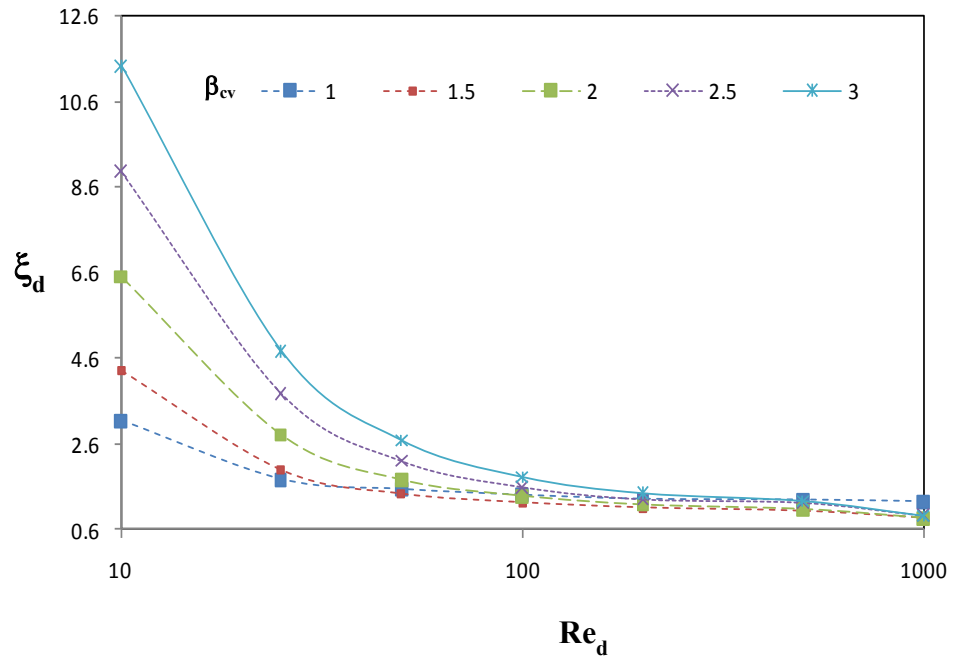


(a)

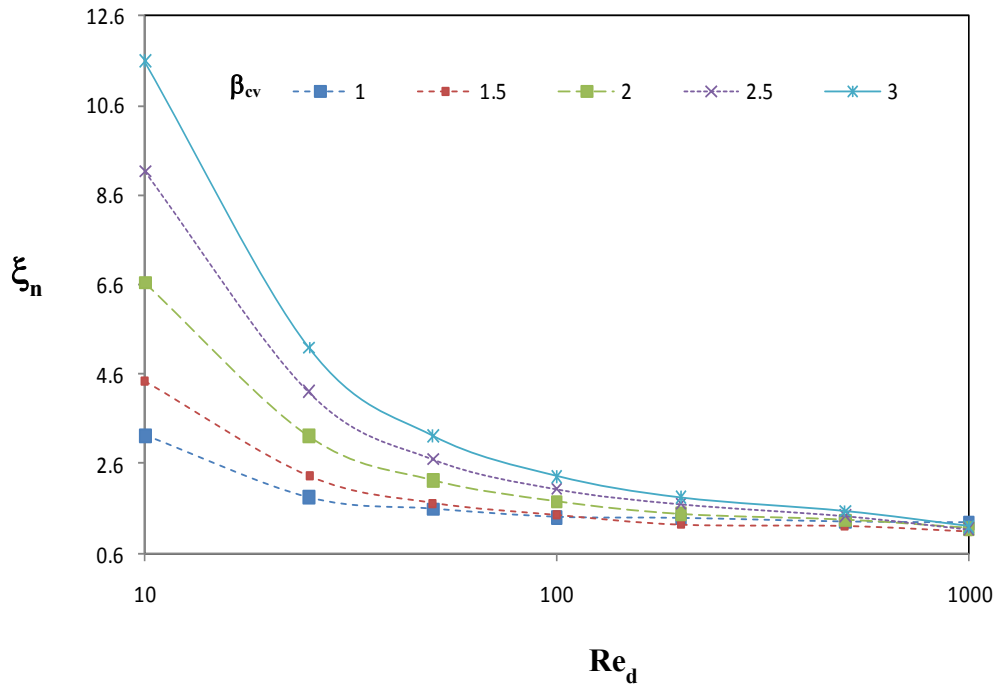


(b)

**Figure 2.16.4:** Variation of pressure coefficients (a)  $\xi_d$  and (b)  $\xi_n$  with the diffuser Reynolds number ( $Re_d$ ) for diffusers with Concave tuning ( $\beta_{cv}$ ) for  $\theta_d = 60^\circ$



(a)

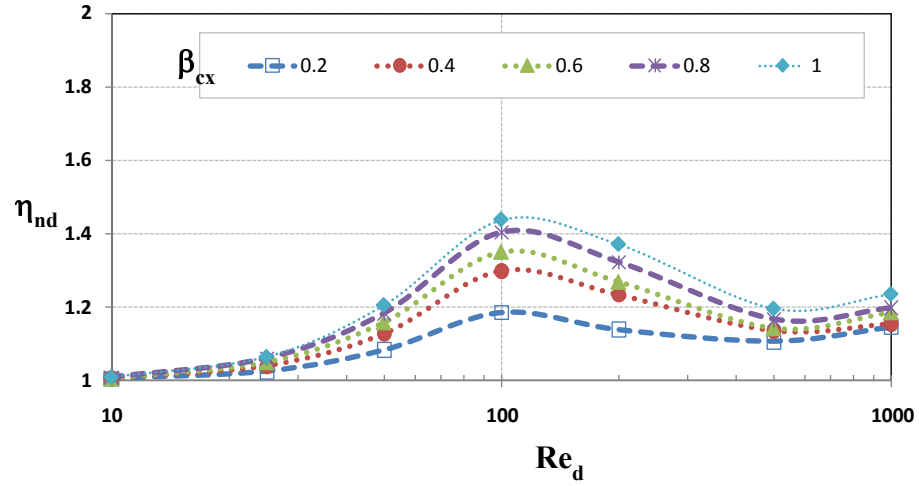


(b)

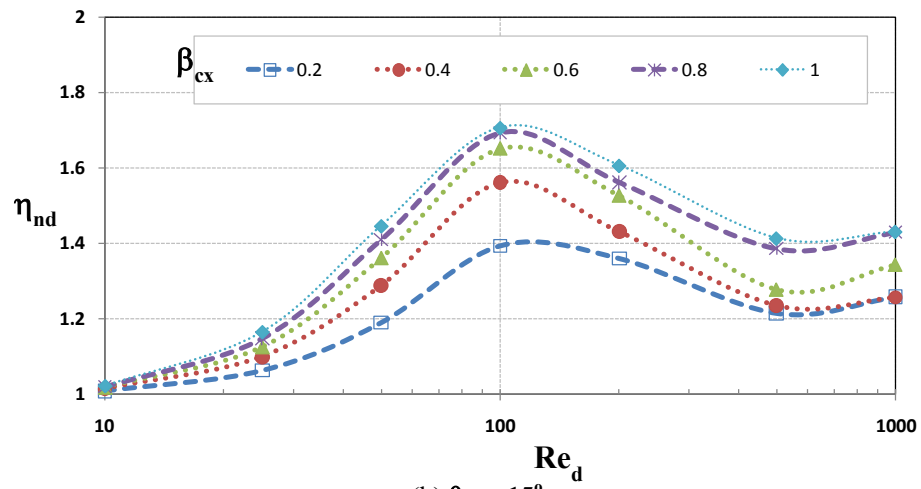
**Figure 2.16.5:** Variation of pressure coefficients (a)  $\xi_d$  and (b)  $\xi_n$  with the diffuser Reynolds number ( $Re_d$ ) for diffusers with Concave tuning ( $\beta_{cv}$ ) for  $\theta_d = 90^\circ$



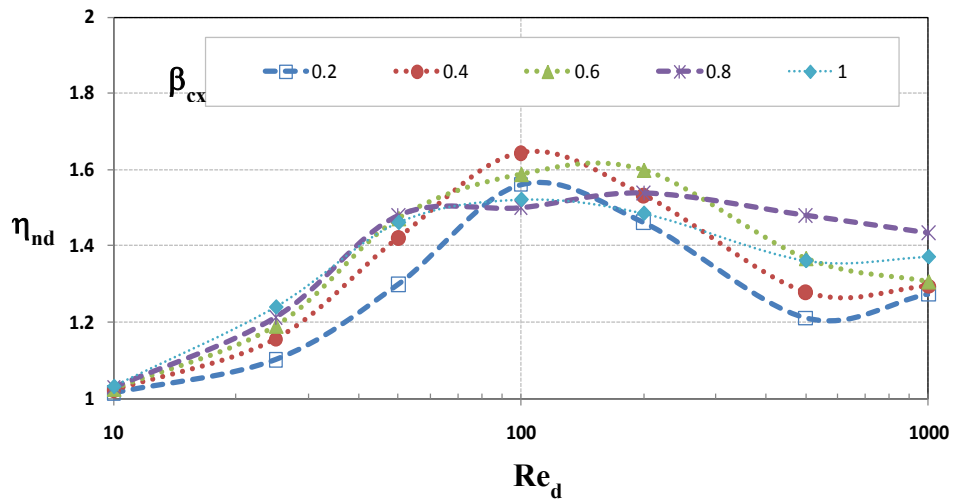
The plots shown in Figures 2.15 and 2.16 show that there is a clear dependence of the pressure coefficients on the flow velocity and the conditioning parameter, for any given diffuser angle. From the pressure coefficients in the nozzle and the diffuser directions, the diffuser efficiency was calculated by taking the ratio of the  $\xi_n$  over  $\xi_d$  for all the diffuser angles. The plots of variation of diffuser efficiencies with Reynolds number for convex diffuser geometries are shown in Figure 2.17. Similarly the diffuser efficiencies of the concave diffusers for different Reynolds numbers are shown in Figure 2.18.



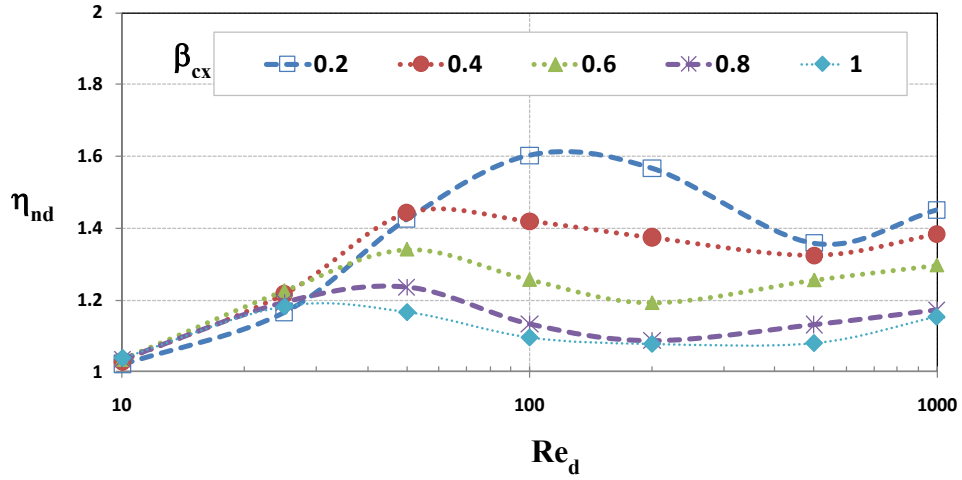
(a)  $\theta_d = 5^\circ$



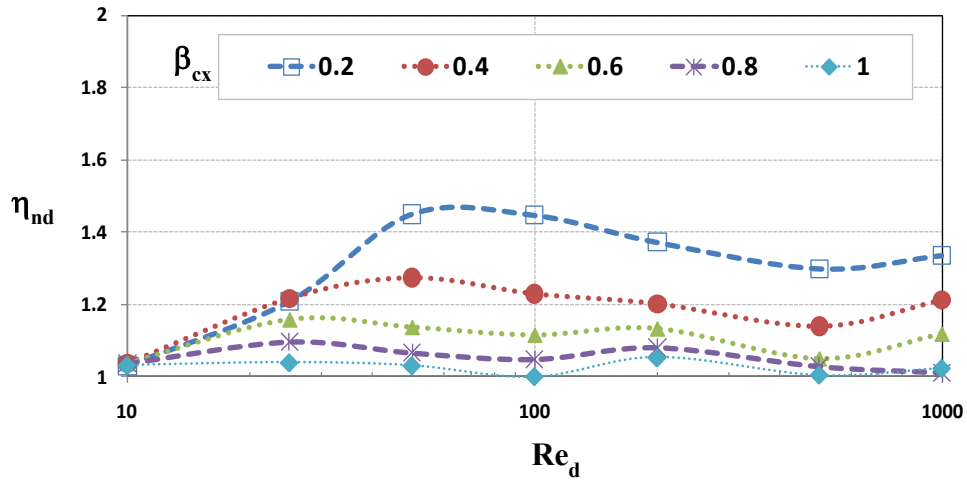
(b)  $\theta_d = 15^\circ$



(c)  $\theta_d = 30^\circ$

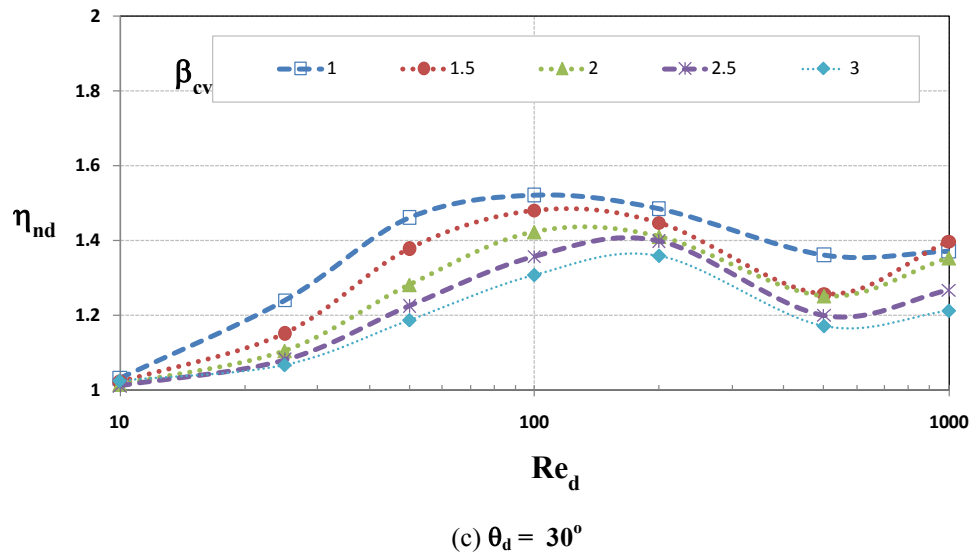
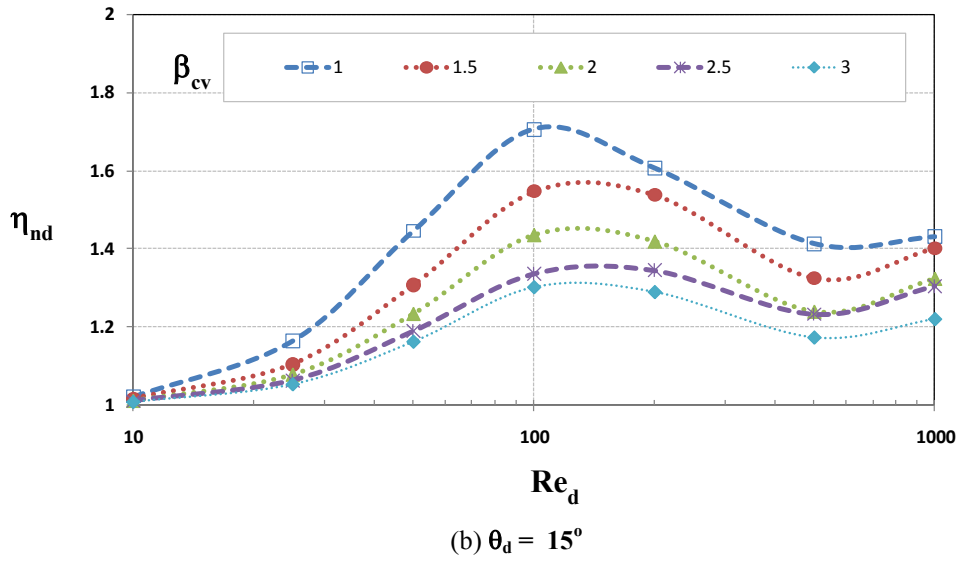
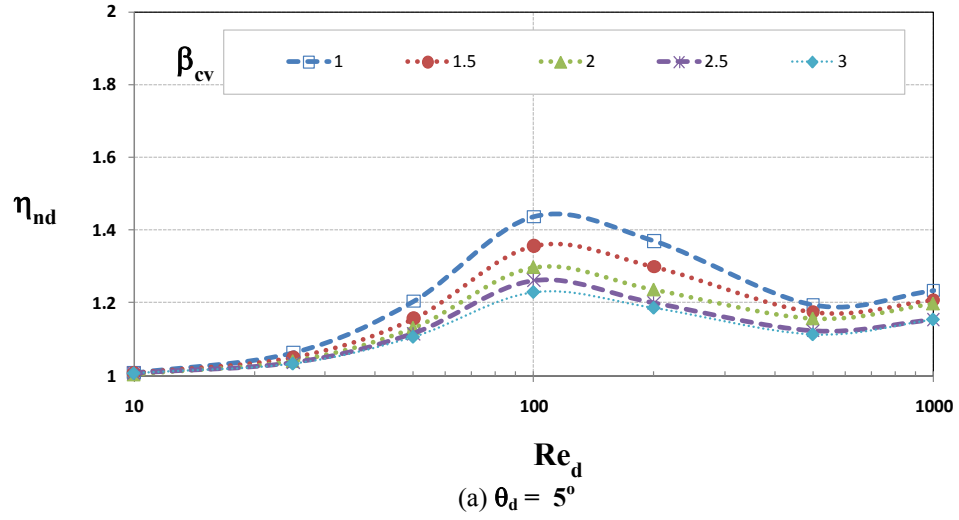


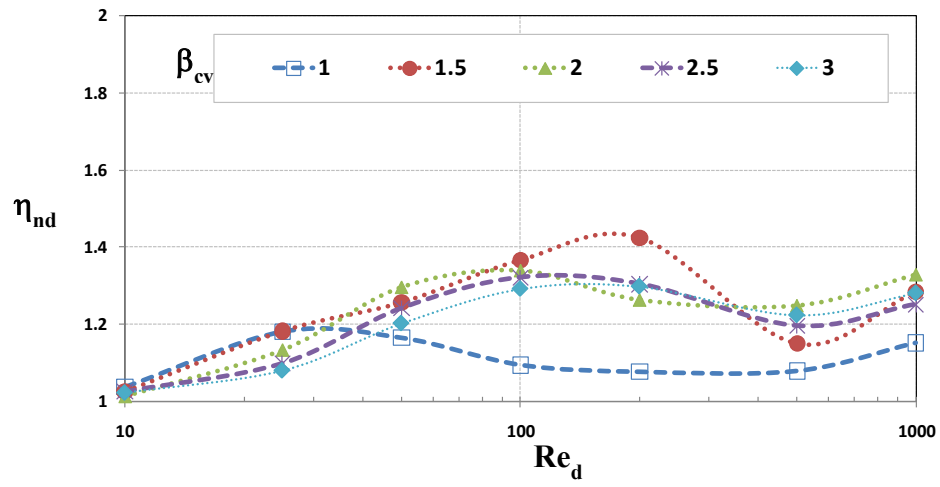
(d)  $\theta_d = 60^\circ$



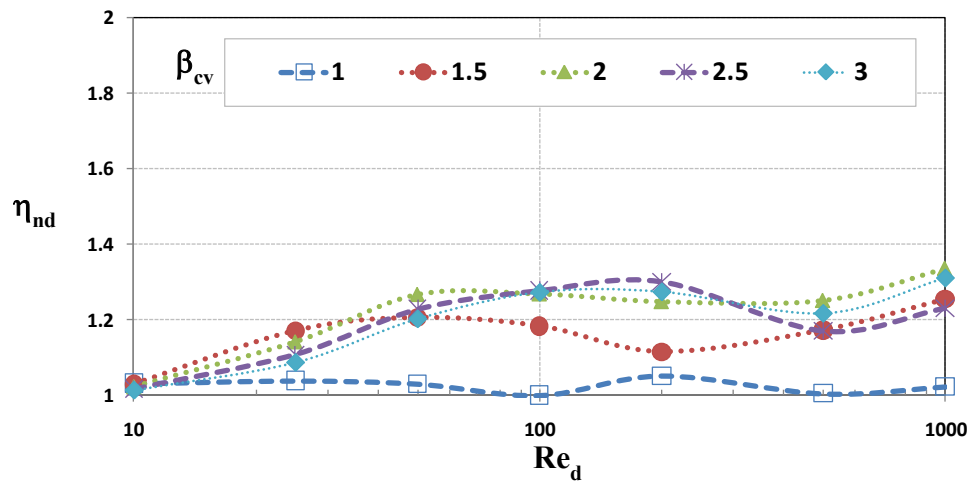
(e)  $\theta_d = 90^\circ$

**Figure 2.17:** Variation of Diffuser efficiencies with Convex geometric tuning and Reynolds numbers for different diffuser angles





(d)  $\theta_d = 60^\circ$



(e)  $\theta_d = 90^\circ$

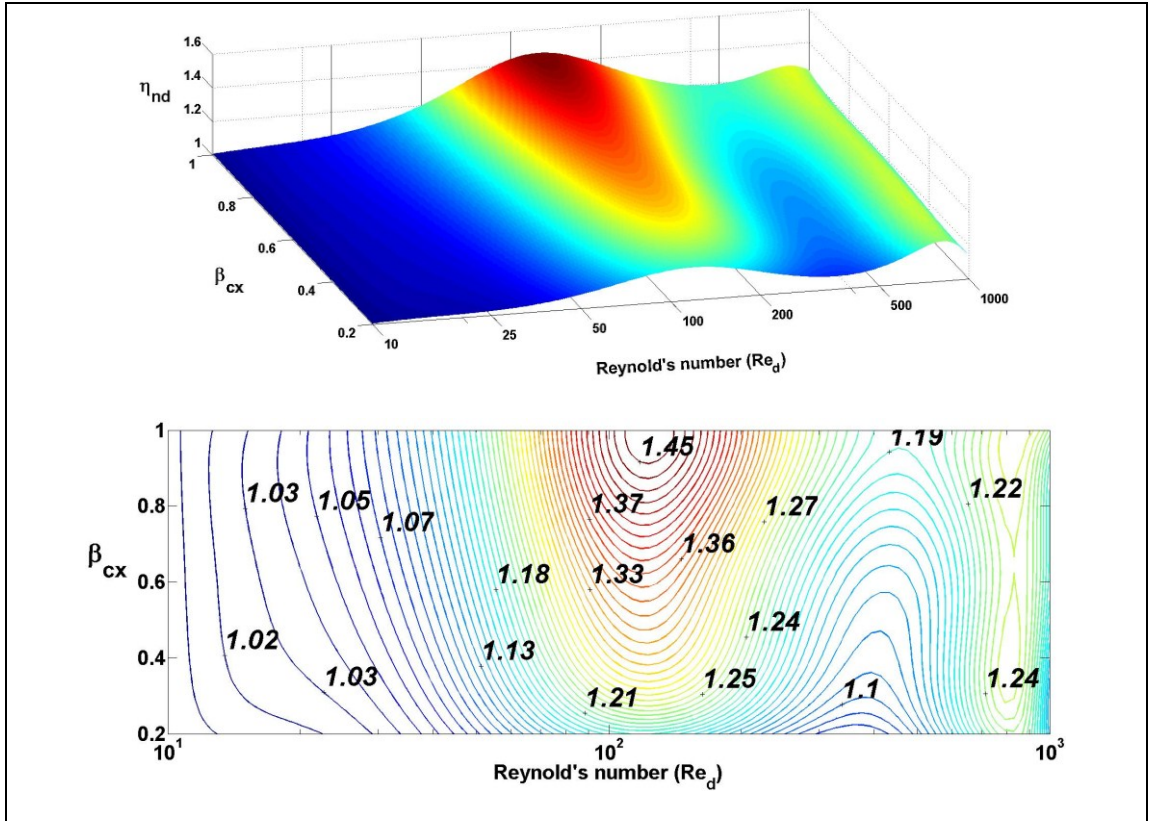
**Figure 2.18:** Variation of diffuser efficiencies with Concave geometric tuning and Reynolds numbers for different diffuser angles

Since, the number of diffuser angles considered for the present analysis is limited, it is important to interpolate the data for the pressure coefficients and the diffuser efficiencies at other diffuser angles using the present result, in order to have complete information for the diffuser behaviour. In that way, it is also possible to exactly choose the diffuser dimensions required for a particular micropump application from a wide range of data available. The plots for the pressure coefficient variations confirm that there is a definite relationship between the Reynolds number and the diffuser coefficients. Therefore, using suitable curve fitting methods, it is possible to interpolate the data within the available data points.

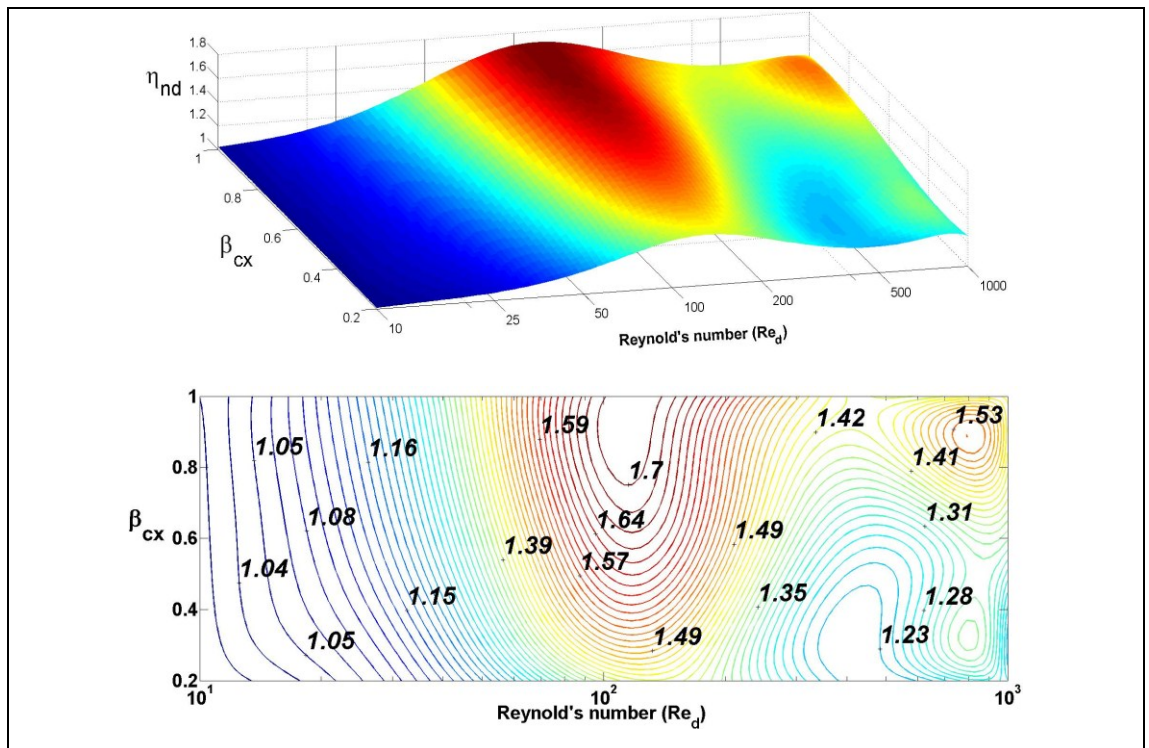
For each of the curves in the plot, the equation of the curve is found out with MATLAB programming and the curve is fit. For the respective  $x$  and  $y$  coordinates, by finding the coefficients of a polynomial  $F(x)$  of degree  $N$  that fits the data such that  $F(x_i) \cong y_i$ , in a least-squares sense and evaluating the polynomial at the required points, the pressure coefficients were calculated for all the diffuser angles. The best fit of the plot is determined by the minimum Residual sum of squares, also known as squared sum of errors (SSE). The best fit of the curve with respect to the original plot was verified by the norm of the residual ( $\mathfrak{R}_n$ ) which is given as  $\mathfrak{R}_n = \sqrt{SSE}$

Therefore, using this curve fitting principle, the equation of all the curves in Figures 2.16 and 2.17 were found, and thus the interpolated values of the diffuser efficiencies were obtained by taking the ratio of nozzle coefficient over diffuser coefficient at each of the interpolated points which were not considered for the Finite Element Analysis.

For all the curve fitting, the best fit curve was obtained for which the  $\mathfrak{R}_n$  is of the order of  $10^{-12}$ . Therefore, for the prediction of the pressure coefficients of the diffuser and the nozzle, the interpolated relation between  $\xi_d$ ,  $\xi_n$  and  $\eta_{nd}$  and the flow velocity is accurate to more than 99%. The interpolated plots of the variation of diffuser efficiencies with flow velocity for different diffuser angles and geometric tuning is presented through surface and contour plots as shown in Figure 2.19. Similarly for the convex diffusers, the variation of the diffuser efficiencies with Reynolds numbers and tuning parameter is shown in Figure 2.20.

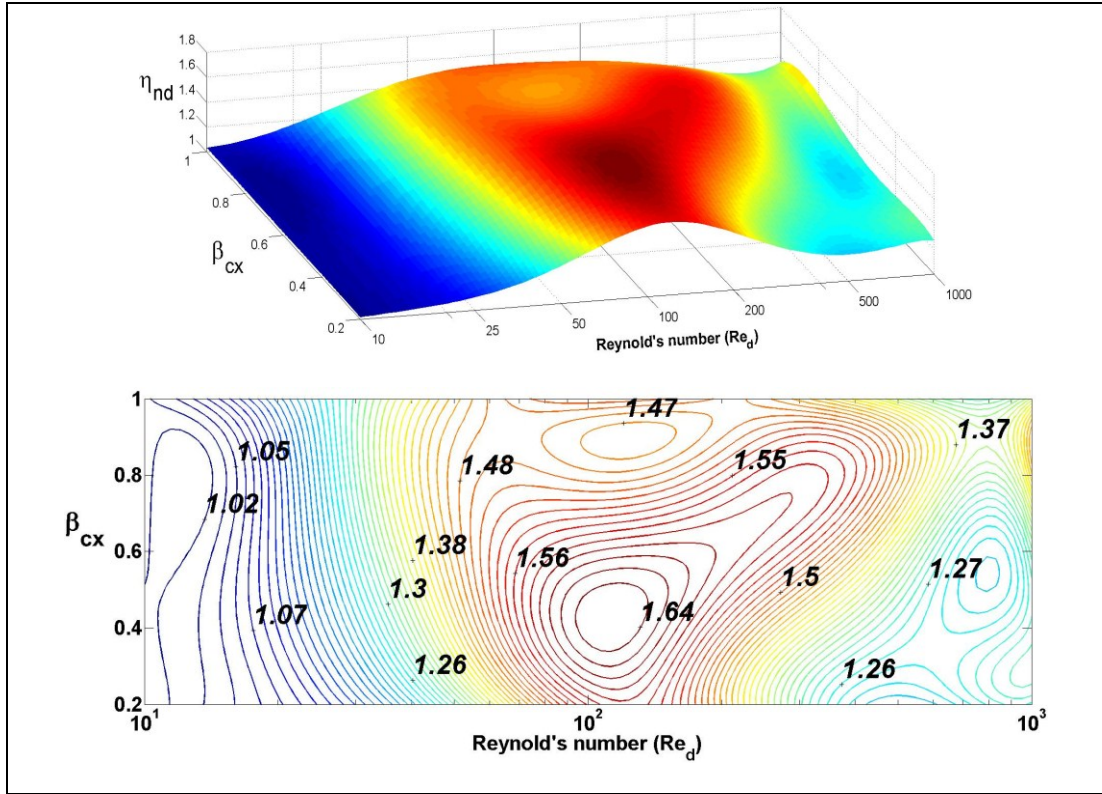


(a) Convex tuning with  $\theta_d = 5^\circ$

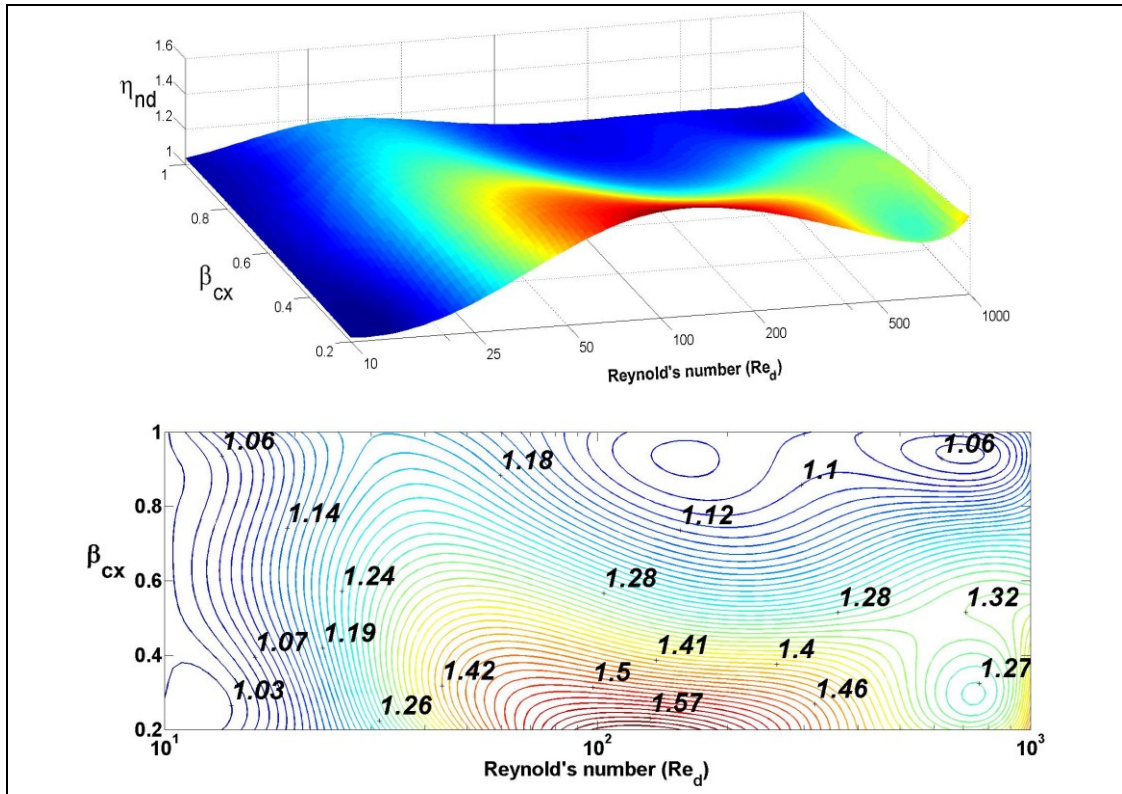


(b) Convex tuning with  $\theta_d = 15^\circ$

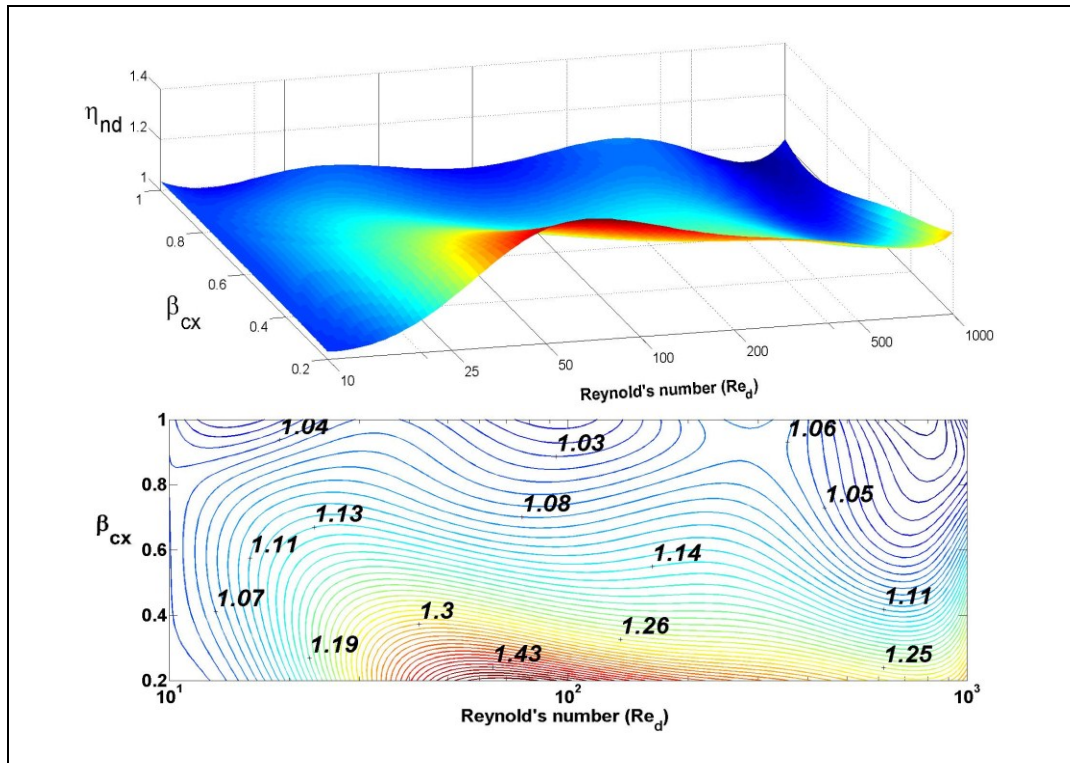




(c) Convex tuning with  $\theta_d = 30^\circ$

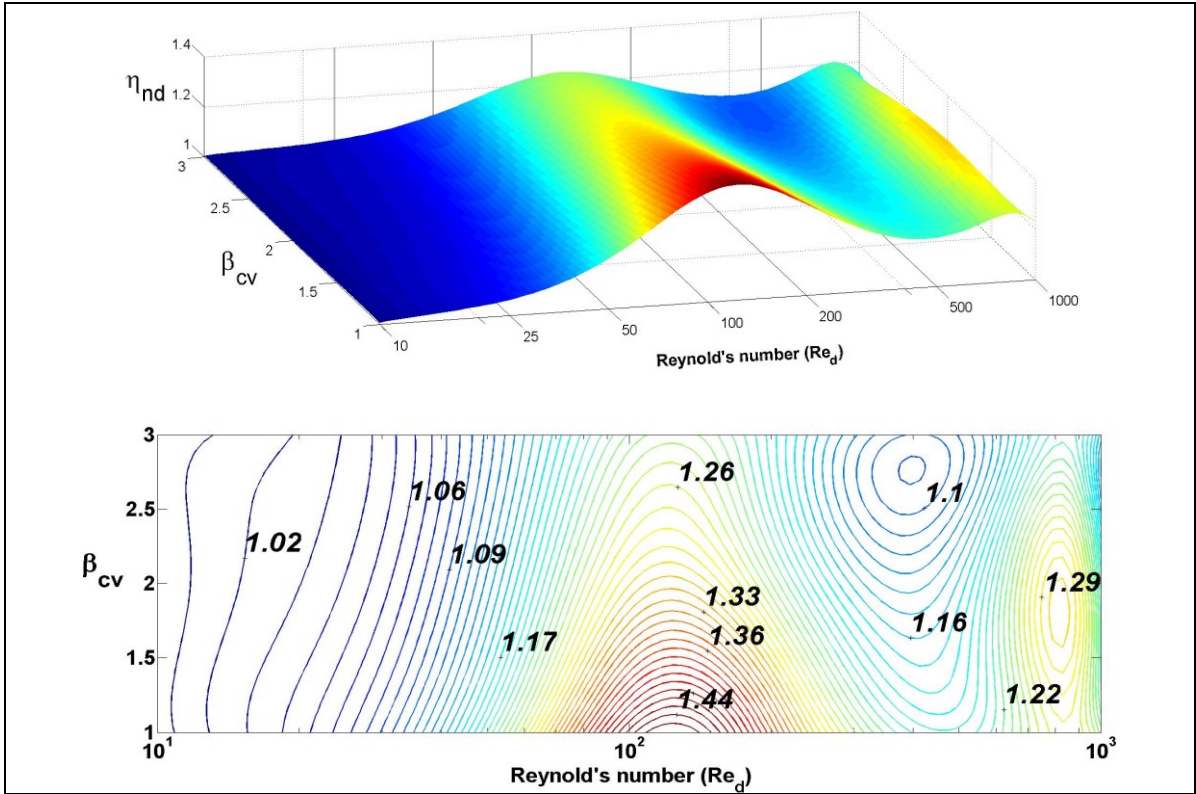


(d) Convex tuning with  $\theta_d = 60^\circ$

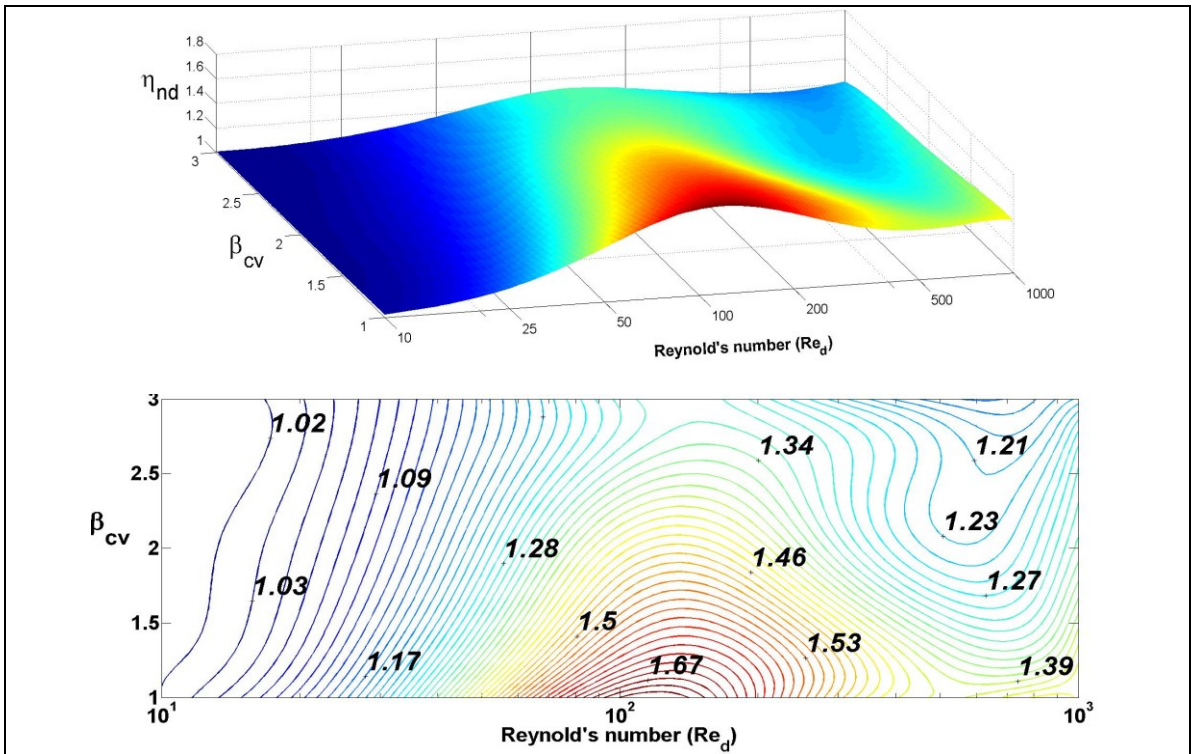


(e) Convex tuning with  $\theta_d = 90^\circ$

**Figure 2.19:** Variation of the diffuser efficiencies with Reynolds numbers for convex tuned diffusers of different diffuser angles

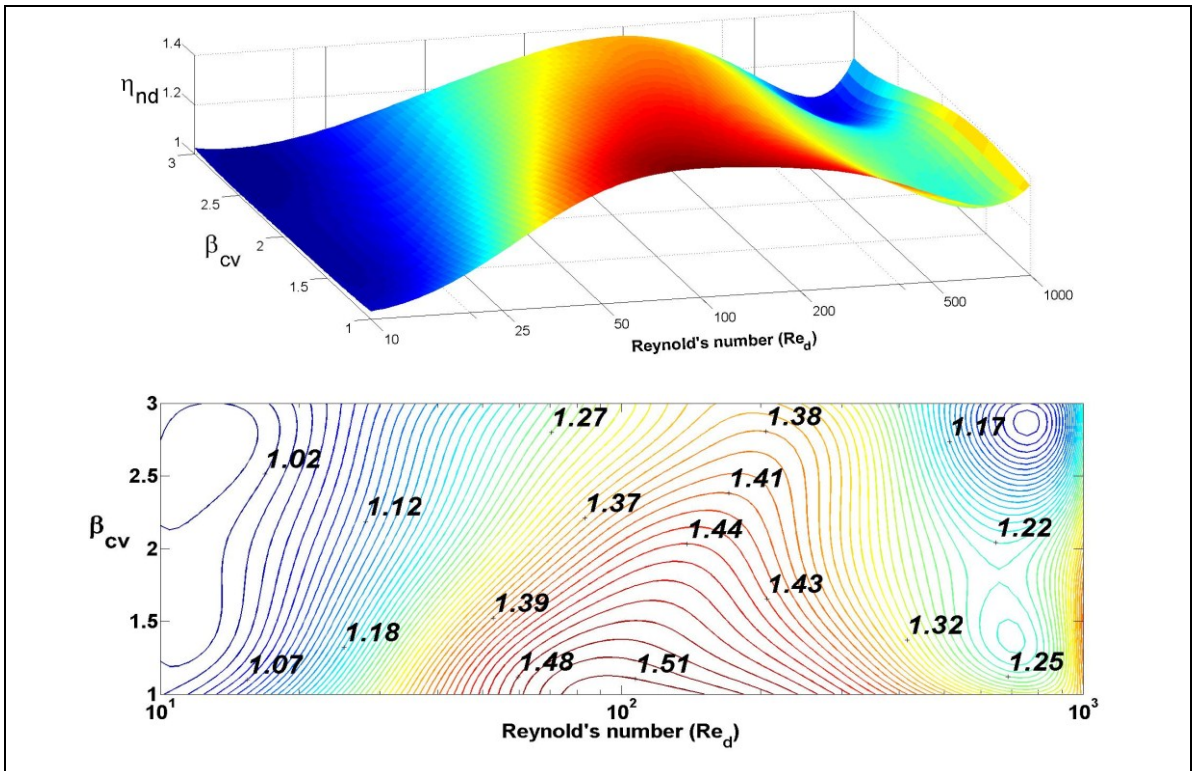


(a) Concave tuning with  $\theta_d = 5^\circ$

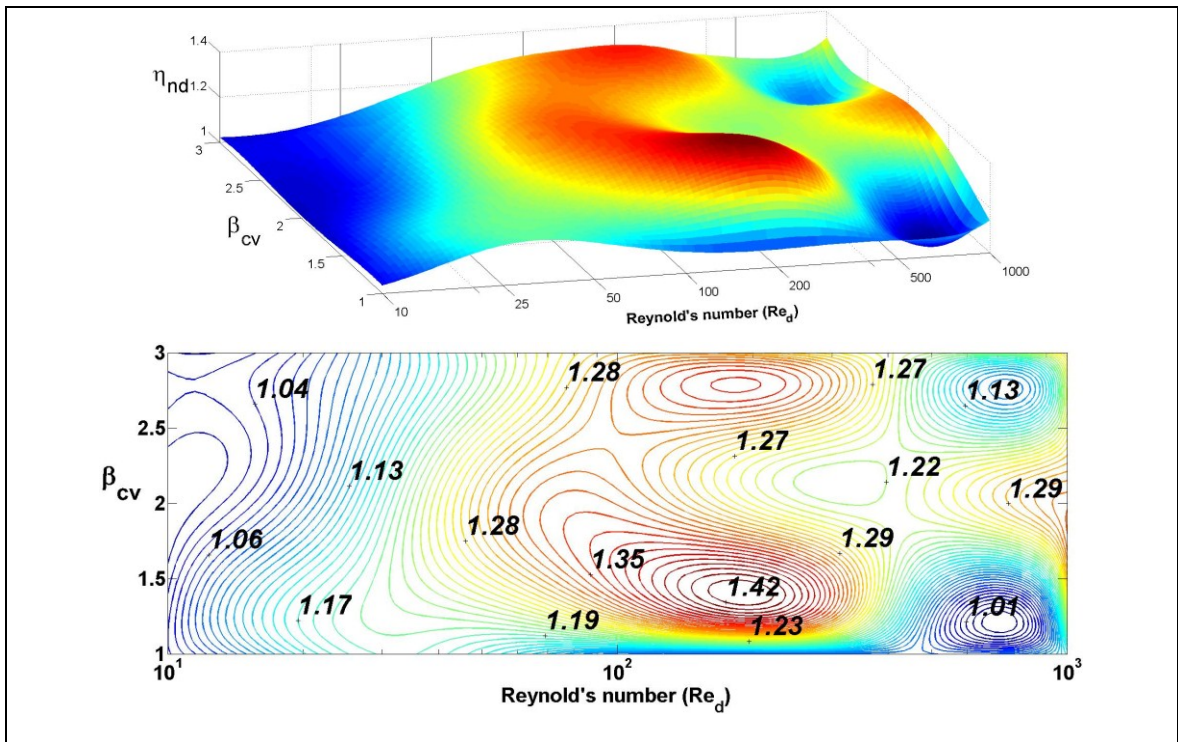


(b) Concave tuning with  $\theta_d = 15^\circ$

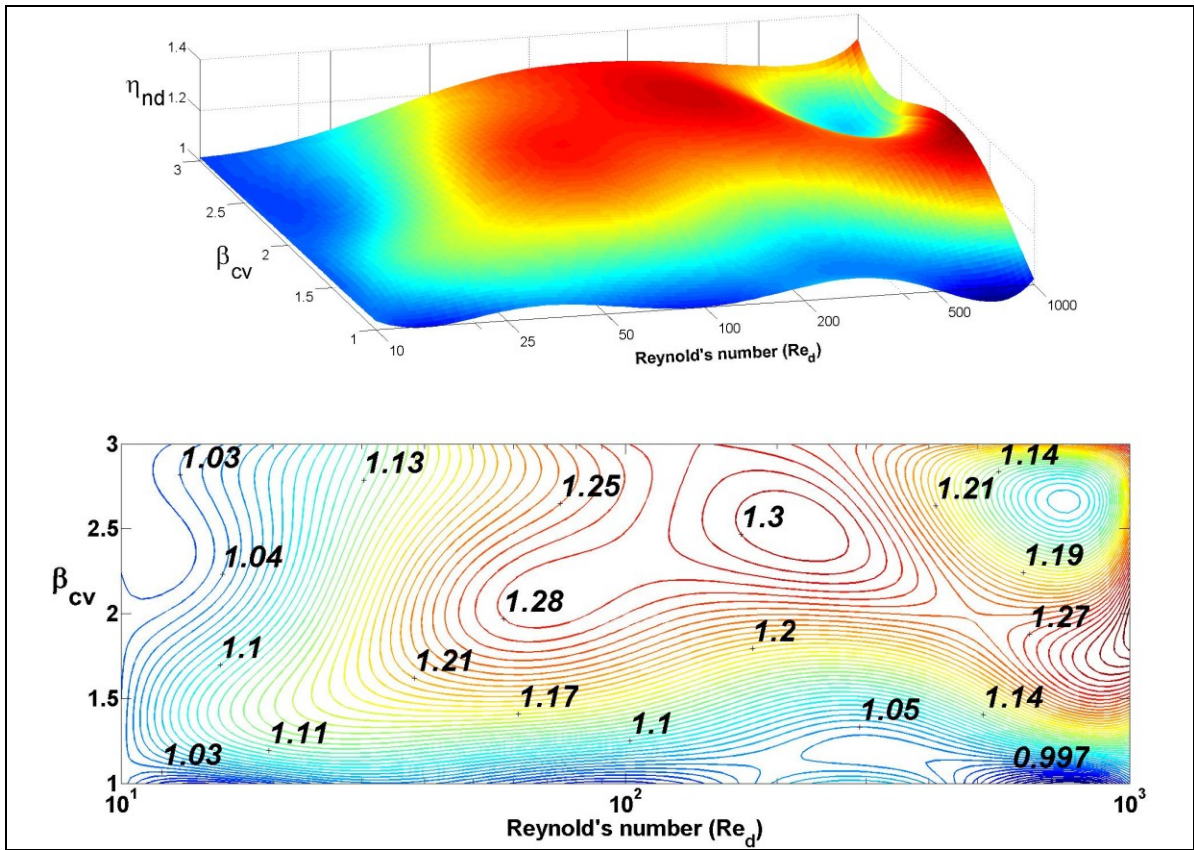




(c) Concave tuning with  $\theta_d = 30^\circ$



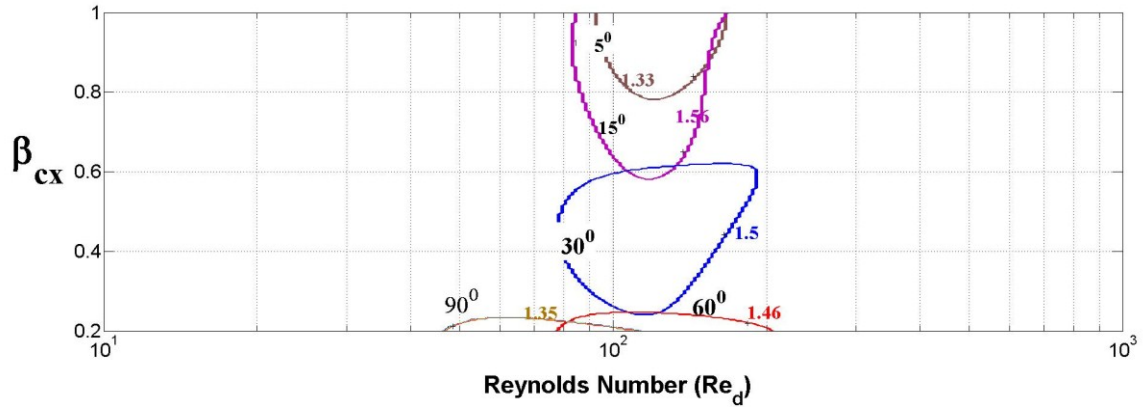
(d) Concave tuning with  $\theta_d = 60^\circ$



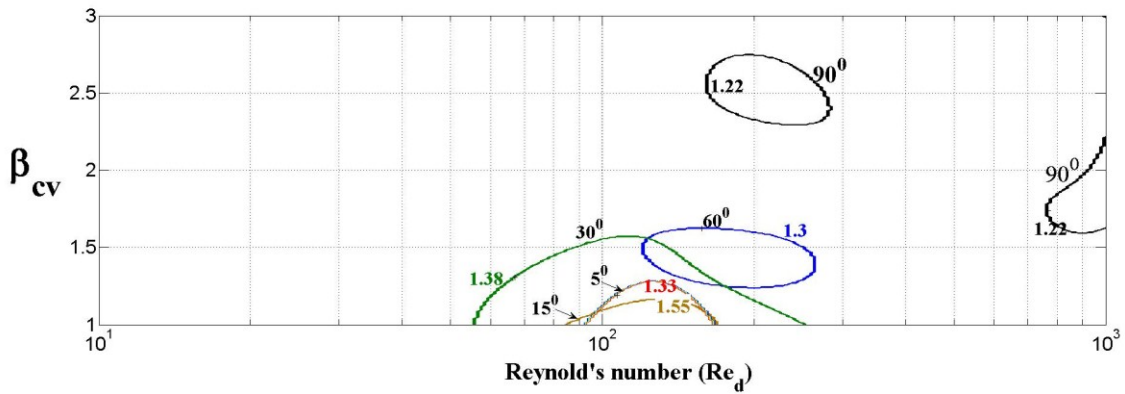
(e) Concave tuning with  $\theta_d = 90^\circ$

**Figure 2.20:** Variation of the diffuser efficiencies with Reynolds numbers for concave tuned diffusers of different diffuser angles

From the plot of the diffuser efficiencies, the zones of maximum diffuser efficiencies were identified. The best 3% efficiency of the concave and the convex diffusers were identified and the zones of the maximum diffuser efficiencies with Reynolds numbers were obtained. The plot is as shown in Figure 2.21.



(a)



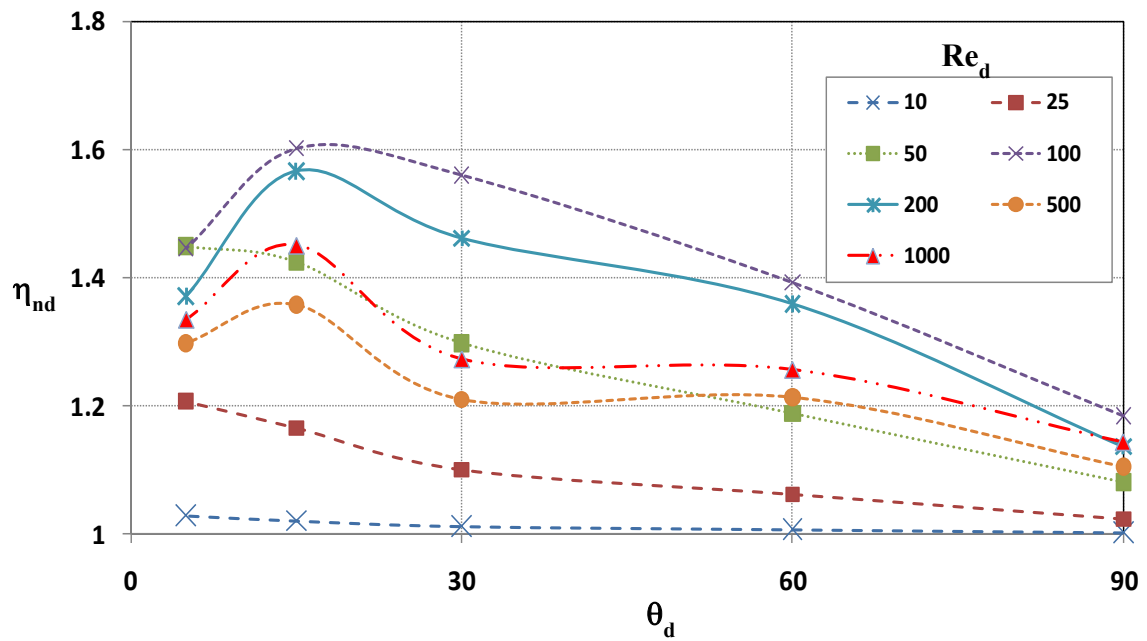
(b)

**Figure 2.21:** Plot of the variation of the best efficiency zones with (a) convex and (b) concave geometric tuning for each diffuser angle

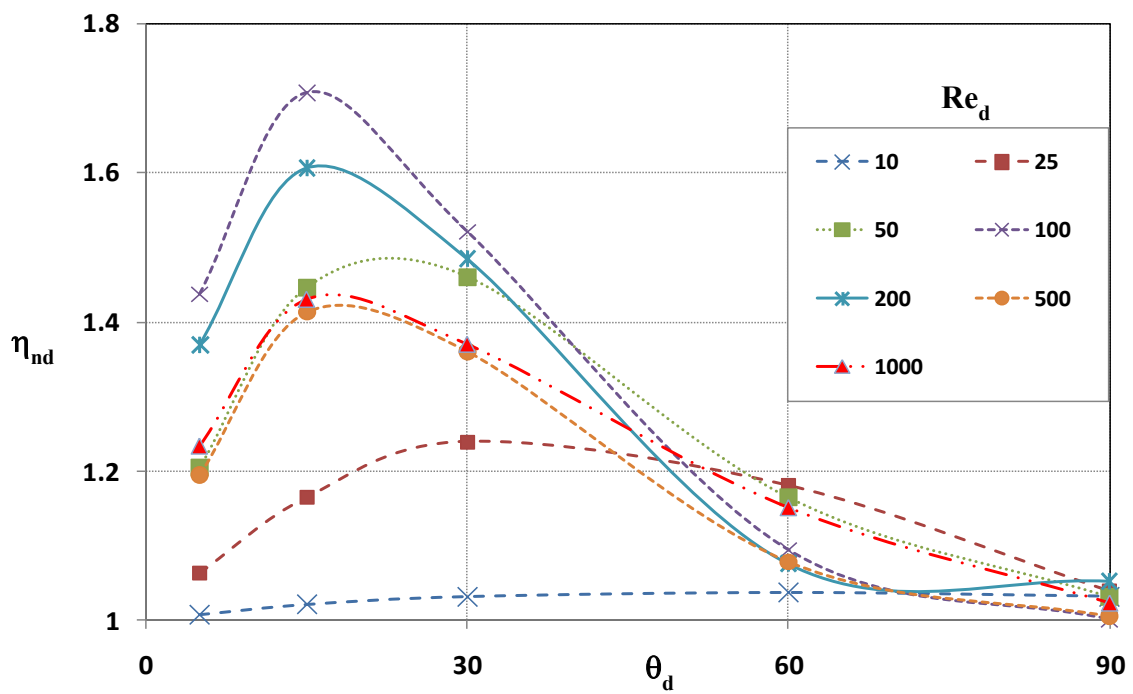
Thus, to achieve the maximum diffuser efficiency, it is important that the flow across the diffuser is operated at this speed. Therefore, the choice of the actuating mechanism should be able to deliver a flow velocity in the range shown for the maximum diffuser efficiency.

In order to further understand the relationship between the diffuser angle and the geometric tuning at different Reynolds numbers, the diffuser efficiencies were plotted for maximum convex tuning and maximum concave tuning and compared with straight

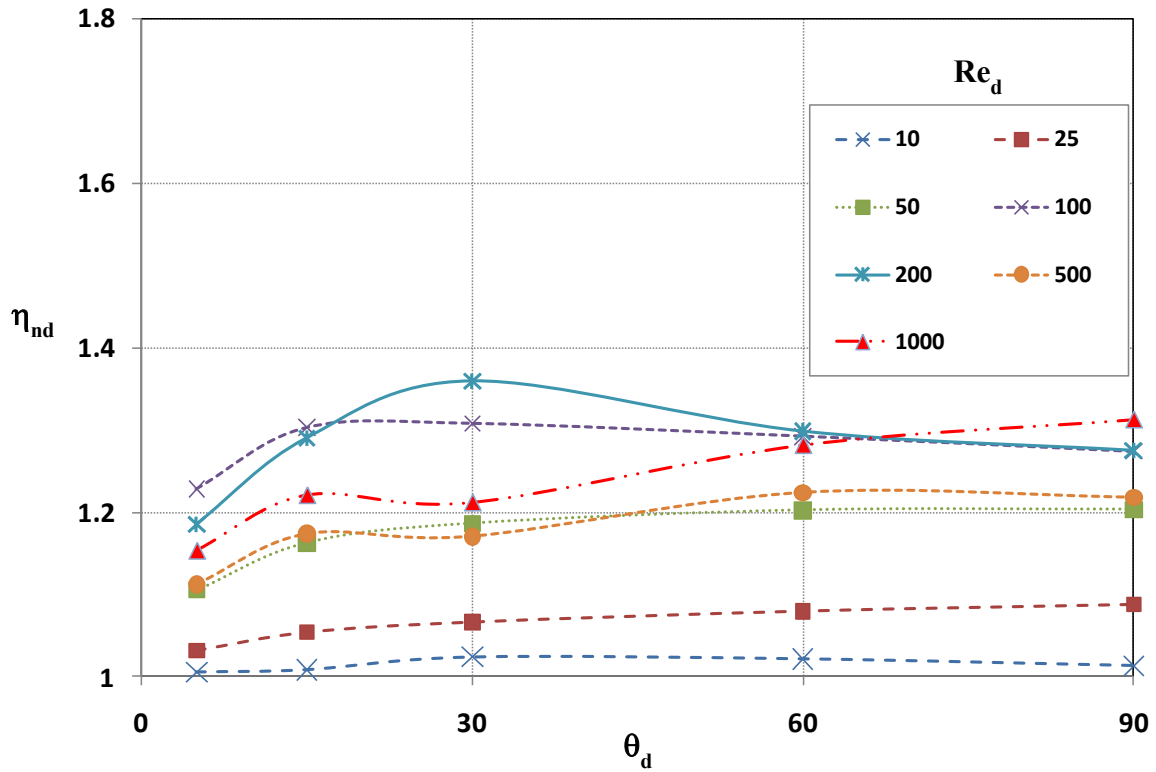
diffusers. The variation of diffuser efficiencies with diffuser angle at different Reynolds numbers is as shown in Figure 2.22 for the extreme geometric tuning



(a) Convex  $\beta_{cx} = 0.2$



(b)  $\beta = 1$



(c) Concave  $\beta_{cv} = 3$

**Figure 2.22:** Comparison of the variation of diffuser efficiencies for (a) Convex tuning (b) Straight diffuser (c) Concave tuning

For straight angled diffusers, the efficiency drops drastically with increase in diffuser angle. Whereas for very low Reynolds number, the effect of diffuser angle on the diffuser efficiency is very less, except for the straight ones.

Though convex tuning increases the diffuser efficiency, the increase in diffuser angle also causes a decrease in the diffuser efficiency and this trend is observed for all Reynolds numbers. However, for concave tuning, the efficiency increases slightly with increase in the diffuser angle. This diffuser efficiency is steady over a wide range of diffuser angles for a given Reynolds number.



The performance of the microdiffuser needs to be studied in conjunction with the operation of a micropump. In a micropump, the flow velocity across a diffuser varies according to the displacement of the actuator. When the flow velocity is high, for straight diffusers, the overall efficiency reduces with the increase in the diffuser angle, due to the onset of flow separation and recirculating zones in the positive diffuser direction of the fluid flow. But it is possible to improve the efficiency in such cases through geometry tuning with convex and concave  $\beta$ 's, as seen in Figure 2.23 (a) – (c). In cases where steady flow velocity can be obtained across the diffusers, convex tuning helps in the achievement of high flow efficiency. However, when the flow velocity across the diffuser varies drastically, in order to obtain a steady flow rectification, concave diffusers can be used. But irrespective of the nature of geometric tuning, for wide angled diffusers, concave and convex diffusers offer higher flow rectification efficiency than straight angled diffusers, for all Reynolds numbers.

### **2.3.2 Summary of FEM results**

The present analysis offers a lot of insight into the functioning and the mechanism of flow rectification in a microdiffuser. Through geometric tuning, a vast number of unrestricted permutations in geometric modifications are possible to the microdiffuser configurations, and several number studies can be carried out based on parametric variations. The present study also poses many interesting questions and motivates further analyses into a few more microdiffuser problems. For example, the pressure loss coefficients for a transient flow may be different from the steady-state values presented here, as it can be

seen that the pressure coefficients depend strongly on the Reynolds number of the fluid flow. Therefore, in applications to micropumps, where the flow velocity across the diffusers vary according the actuation, one can also carry out prediction of the dynamic micropump efficiency to compute the overall pump efficiency. Another interesting study that could be carried out is to study the combined effects of the fluid density and viscosity on the behaviour of the microdiffusers with geometric tuning. It is also possible to vary the performance of a micropump by designing non-similar inlet and outlet diffuser configurations to achieve better flow rectification. In such cases, it is also possible to define the conditioning parameter for one of the diffusers as a function of the other. Therefore, the present analysis opens up the feasibility of carrying out a lot of studies based on the geometric tuning to achieve improved performance of the microdiffuser for micropump applications and in that regard, the present study is by no means exhaustive. However, in comparison with previously available data, if one were to design a diffuser configuration for a micropump taking into consideration the results presented herein, it is now possible to choose an appropriate geometry tuning parameter to achieve improved performance, which is a very significant contribution for applications with integrated micropumping.

## **2.4 Experimental verification**

The Finite Element Analysis provides a lot of information regarding the behavior of the diffuser for different geometries and flow velocities. However, practical behavior of the diffusers will vary drastically. The reasons attributed to the possible differences between

the analytical and experimental results include the non-uniform slenderness and the inlet aspect ratio of the fabricated diffusers, which have been proven to significantly affect the diffuser performances (Olsson et al. 1997). Also, in practice, the pressure loss across a diffuser is not only contributed by the static pressure drop due to the diffusing action of the diffuser valve, but also from other components, such as inlet and outlet channels, sudden expansion and contraction, frictional losses, bends, etc. These parameters, which contribute to the total pressure loss across a diffuser element have neither been clearly described nor analysed (Wang et al. 2009). Therefore, the actual behavior of the diffuser can be identified only through suitable experiments. In this study, the diffuser performance was experimentally studied by measuring the pressure drop across the diffuser elements for different configurations, in order to validate the results of the theoretical predictions.

#### **2.4.1 Fabrication of diffuser channels**

Several material platforms such as silicon, metal, plastic etc. have been explored in the past for the fabrication of diffuser elements. Herein, the microdiffusers were fabricated on PDMS platform. There are several advantages of using PDMS for the present application. Apart from the transparency of the substrate that helps in flow visualization, PDMS also offers a lot of packaging options for the integration of microfluidic tubes for external fluidic circuitry. The bonding techniques and surface chemistry for PDMS are well defined and this makes it easier to bond PDMS with other substrates for leak-proof

sealing of the microchannels. PDMS also offers a cost-effective and easily microfabricable alternate to other substrates, especially for testing purposes.

The design of the diffuser channels consists of inlet port, inlet chamber, diffuser element, outlet chamber and the outlet port for fluid ejection. The pressure drop due to the diffuser is measured by measuring the pressure difference between the inlet chamber and the outlet chamber. For this reason, the inlet and the outlet chambers are isolated from the inlet and the outlet fluidic ports respectively, so that the pressure difference between the inlet and the outlet chamber is not affected by the flow pattern at the inlet and the outlet microfluidic ports. .

According to the Equation 2.12, the Reynolds number of fluid at the throat of the diffuser is influenced by the wetted perimeter, area of cross-section and the flow velocity. It is possible that due to lithographic or fabrication imperfections, the profile of the diffuser at the throat may slightly be altered thereby leading to errors in the calculation of the above mentioned parameters. Square cross-section at the diffuser throat, with the width being the same as the channel depth offers a lot of advantages in terms of calculation of the wetted perimeter and hence the computation of the velocity of the fluid at the throat of the diffuser in terms of Reynolds number. Therefore, the depth of the diffuser channels was fixed as 100  $\mu\text{m}$ . The glass chrome photomask (Fineline Imaging, CO) was used for lithography, as shown in Figure 2.23.

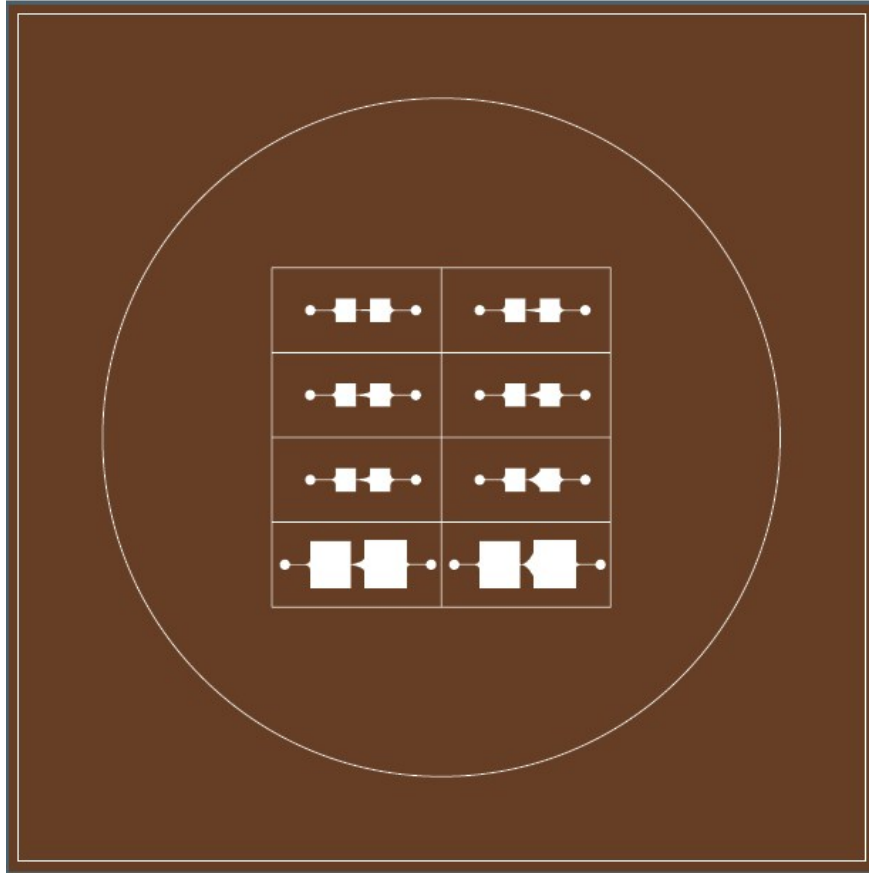


**Figure 2.23:** Layout of the photomask used for SU8 lithography of microdiffusers, obtained from Fineline Imaging

The fabrication of PDMS microdiffusers has been explained briefly in Section 2.2.4.1. For the fabrication of diffuser channels on PDMS with a depth of 100  $\mu\text{m}$ , a two step fabrication method was employed with SU8 lithography and Deep Reactive Ion Etching (DRIE) of silicon substrate. There are several advantages of using silicon mould fabricated by DRIE over SU8 mould formed by lithography method for the fabrication of microdiffusers:

(i) *Precise control of etch depth:* Lithography process is subjected to several variable parameters, such as spin-coating speed, and hence it is not possible to control the depth of the channels precisely. This problem can be overcome through DRIE.

(ii) *Uniformity of channel depth*: The aspect ratio and also the uniformity of the etch depth can be better controlled using DRIE than with photolithography of SU8 mould.

(iii) *Difficulty in handling SU8*: Higher channel depths using lithography can only be obtained with higher viscosities of SU8, which is difficult to handle due to surface adhesion and formation of gas bubbles during the transfer of SU8 photoresist onto the substrate, baking processes etc. This renders SU8 mould lithography process time consuming and also very elaborate.

In the process of fabricating silicon mold, silicon is etched using DRIE method after patterning with SU8. Prior to the photolithography, the silicon wafers were initially cleaned with acetone and Piranha solution. Photolithography was carried out on silicon wafer using the mask design shown in Figure 2.24. The following specifications, as given in Table 2.4, were used for patterning SU8-2 photoresist on silicon.

<b>Operation</b>	<b>Specifications</b>
Pre-baking of Si	95 °C for 600 s
Spin Coating	1000 rpm, 30 s
Soft baking	95 °C , 180s
UV exposure	Lamp power 150 mJ/cm <sup>2</sup> , 10 s
Post-Exposure Baking	95 °C, 240 s
Developing	180 s
Hard baking	100 °C , 900 s

**Table 2.4:** Photolithography parameters for SU8 patterning for silicon mould fabrication using DRIE.

Under these conditions, the thickness of the photoresist obtained in this process is 2 µm. After the SU8 was patterned on the silicon wafer, the substrate was etched using DRIE. An etch rate of 3 µm/min was obtained with DRIE.

Once the silicon moulds were fabricated, the wafers were silanized. Vapor phase silanization was carried out on the moulds, by heating them in a closed chamber with 1 ml of (Tridecafluoro-1,1,2,2-Tetrahydrooctyl)-1-Trichlorosilane (United Chemicals Inc., USA) at 60 °C for 4 hours. The silane forms a monolayer on the surface of the silicon and thus prevents the adhesion of PDMS with the substrate. 10:1 ratio of PDMS pre-polymer and the curing agent (Sylgard 184, Dow Corning) was mixed well and degasified. The mixture was then poured onto the silicon mould and baked at 80 °C for 4 hours. After curing, the PDMS was subsequently removed by peeling off the substrate from the silicon mould. In this way, the patterns on the silicon mould are transferred on the PDMS.

For external tube connections, ports of 2 mm diameter are created on the PDMS channels after removing from the mould. In order to seal the PDMS microdiffuser channels, a glass slide was spun coated with the degasified prepolymer-curing agent mixture at 1500 rpm and the setup was semi-cured at 90 °C for 4 minutes. The substrate is then brought into contact with the semi-cured PDMS-on-glass and slight pressure is applied over the surfaces in contact. The setup is then cured again for 5 minutes at 90 °C thereby forming a permanent bond between the device substrate and the PDMS-on-glass. The unpackaged microdiffuser channel device is shown in Figure 2.24.

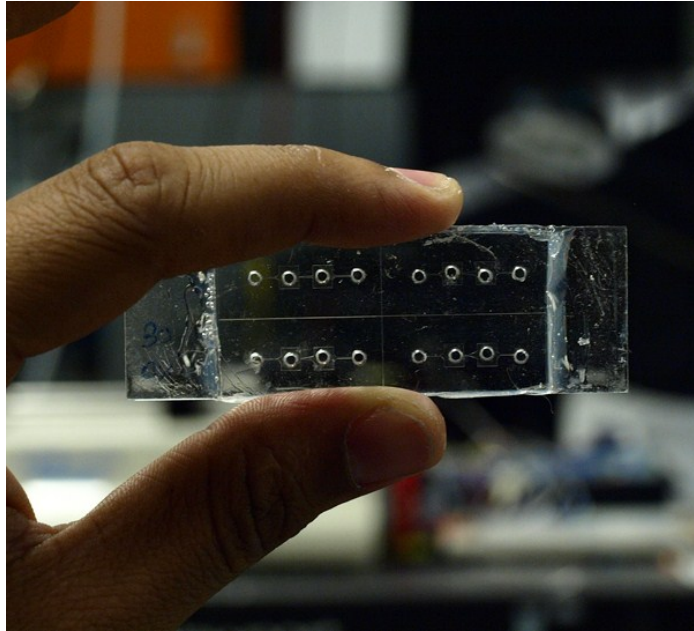


**Figure 2.24:** Fabricated diffuser chip with ports after bonding of the device layer with PDMS-on-glass substrate

Silicone tubes of 0.5mm inner diameter (Gilson) were then connected with the ports of diameter ~2mm. Since the tubes are of slightly larger diameter than the ports, when they are fit into the ports, they are pressed against the inside of the hole, thereby creating mechanical pressure. This pressure seals the ports, thereby preventing any leakage of the fluid. In some cases, in order to ensure leakproof fit, a thin layer of PDMS is applied around the tube so that the gaps are sealed perfectly. After the use of the device, the tubes can be changed by simply removing the tubes from the port and replacing it with another. Thus, the present method of packaging provides a ‘Plug-n-Play’ (Peroziello et al. 2008) option to use the diffuser chip repeatedly.



### 2.4.2 Experimental setup

For the FEM, it was assumed that the outlet of the nozzle/diffuser is at atmospheric pressure and the velocity was specified as input boundary condition. However, for the experiments, the assumption that the outlet of the diffuser is at zero gauge pressure is no longer valid because of the fluidic interconnections at the outlet. Therefore, it is important to measure the pressure difference between the inlet and the outlet of the diffuser in order to know the pressure drop due to the diffuser valve alone.

A schematic of the experimental setup is the same as shown in Figure 2.11 in Section 2.2.4. The experimental setup is as shown in Figure 2.25. Two pressure sensors P1 and P2 were used, each at the inlet and the exit of the diffuser so that the pressure difference across the diffuser element can be found out. The pressure sensors were integrated with a Data Acquisition (DAQ) system, and thereby the pressure changes were measured in terms of voltage. The entire setup including the pressure sensors and the microfluidic chip was translated on a circuit board and the setup was made as rugged as possible. Thus, with the present setup, it was possible to carry out repetitive measurements on multiple microfluidic devices by merely changing the interconnections reversibly. The frictional pressure losses in the interconnection tubes were negligible.

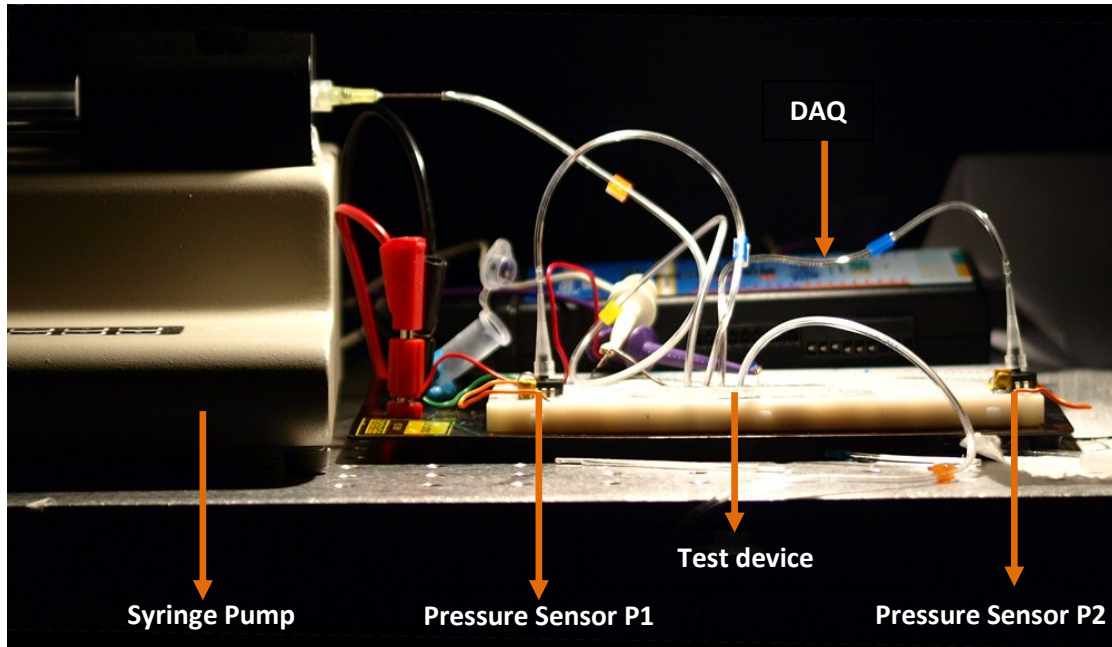


**Figure 2.25:** Experimental setup for measuring the pressure across diffuser microchannels.

### 2.4.3 Results

The net pressure loss across a diffuser element is given by the relation

$$\Delta p_{net} = \xi_{n,d} \frac{1}{2} \rho v_{din}^2 + \Delta p_{ff} \quad \dots 2.15$$

where

$v_{din}$  = Average velocity at the neck of the diffuser given by  $Q / A_{din}$  with  $Q$  being the flow rate of the syringe pump

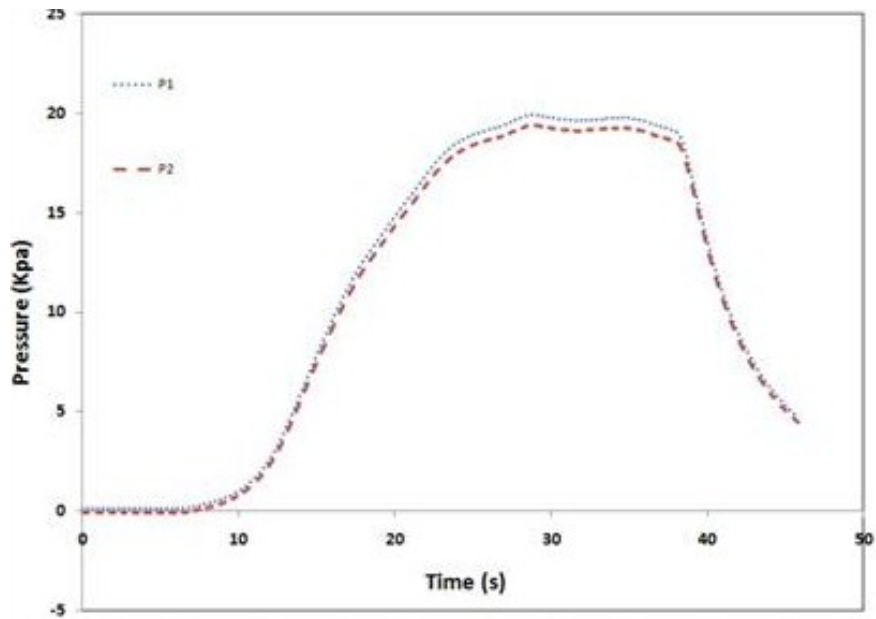
$\Delta p_{net}$  = The total pressure drop measured across the diffuser.

$\Delta p_{ff}$  = The frictional pressure loss in the diffuser element and the connecting channels.

In the present case, given the aspect ratio of the channels, frictional pressure loss in the diffuser was negligible (i.e  $\Delta p_{ff} = 0$ ). Therefore, Equation 2.4 can be written as

$$\xi_{n,d} = \frac{\Delta p_{net}}{\frac{1}{2} \rho v_{din}^2} \quad \dots 2.16$$

The pressure was calculated in terms of voltage. The output of the pressure sensor using the DAQ was converted into Pascals using suitable conversion formulas.  $\Delta p_{net}$  was then calculated by the computing the pressure difference between the pressure measured in P1 and P2. A typical curve obtained for measuring the pressure difference is as shown in Figure 2.26(a). The trend of pressure variation at the inlet and outlet of the diffuser is schematically represented in Figure 2.26 (b) for discussion.



(a)

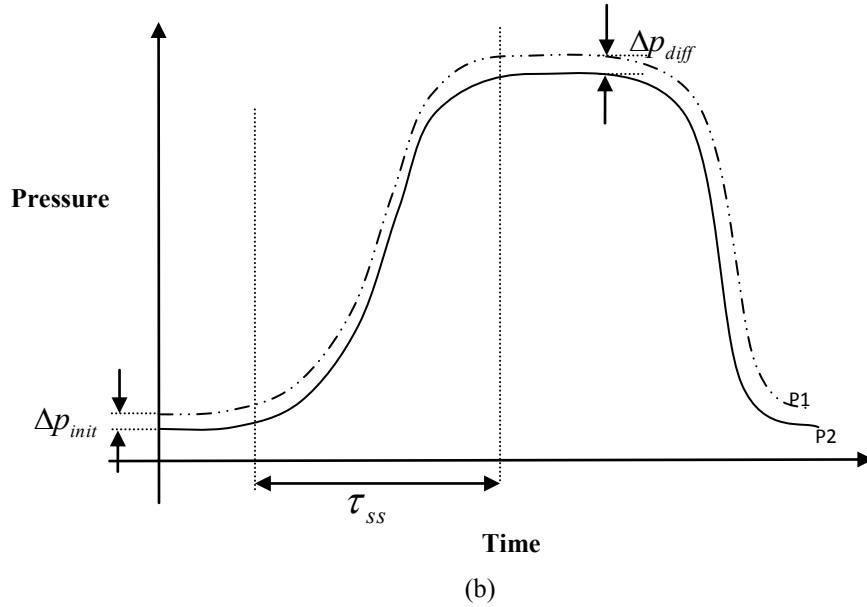
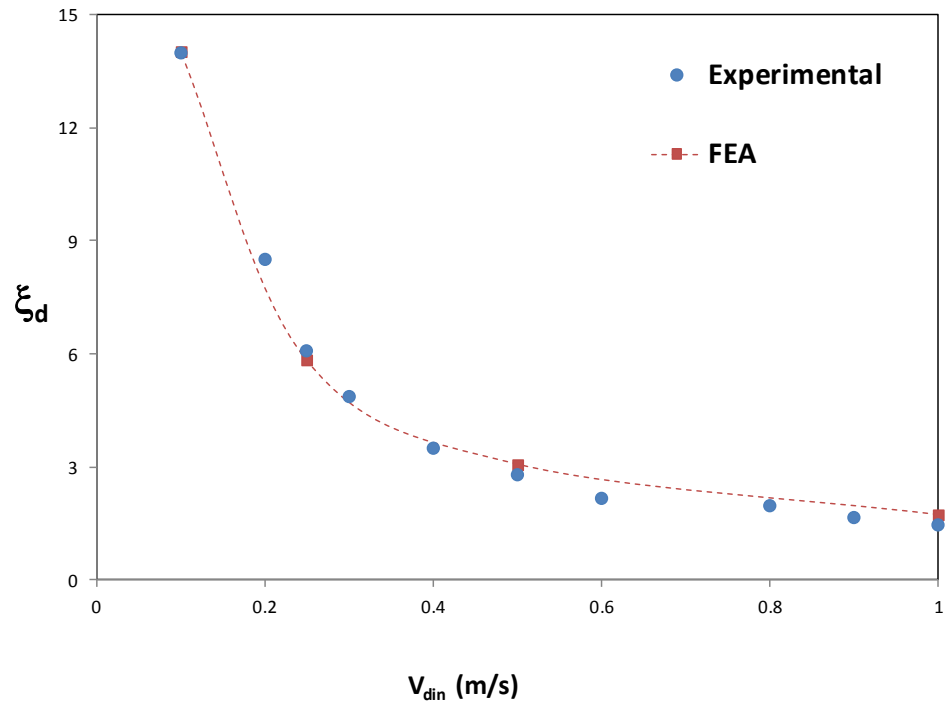


**Figure 2.26:** (a) Variation of pressure at the inlet and outlet of the microdiffuser for Reynolds number 100. (b) Schematic of the pressure variation inside the microdiffuser channels

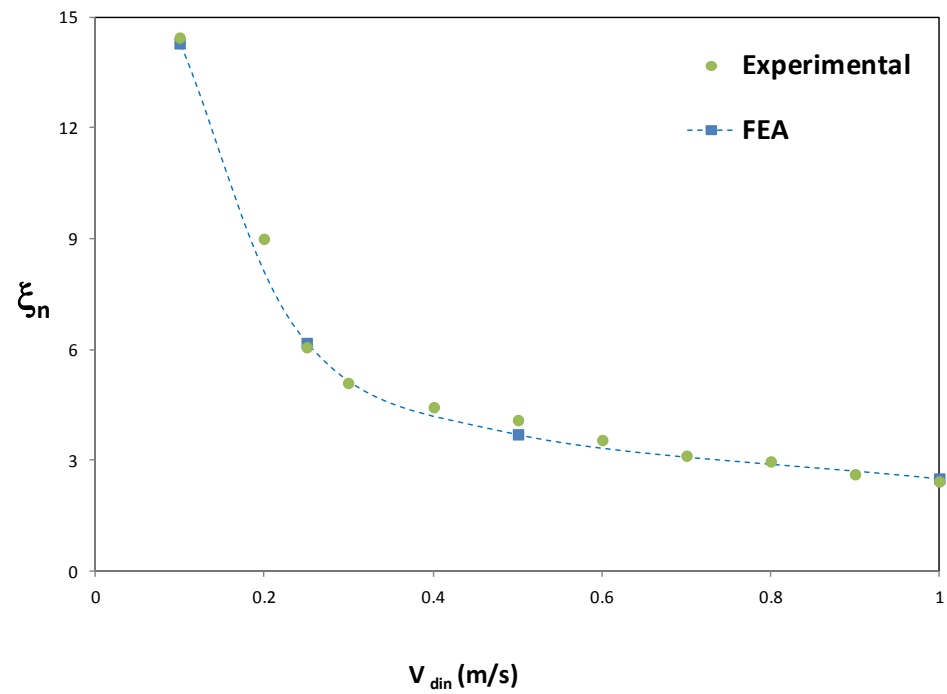
The initial pressure difference,  $\Delta p_{init}$ , is obtained because of the difference in height between the inlet syringe pump and the microchannel. After the flow is initiated in the channel, the flow reaches the steady state after a particular time, given by  $\tau_{ss}$ . This  $\tau_{ss}$  is a property of the system and it depends on several parameters, which includes flow velocity and the diffuser geometry as well. Under steady state, the pressure drop across the diffuser,  $\Delta p_{diff}$ , is obtained by measuring the pressure difference between the pressure sensors P1 and P2. Therefore, the net pressure difference across the diffuser  $\Delta p_{net}$  is given by

$$\Delta p_{net} = \Delta p_{diff} - \Delta p_{init} \quad \dots 2.17$$

The results for the computation of the pressure coefficients are as shown in Figures 2.27.1 – 2.27.5.

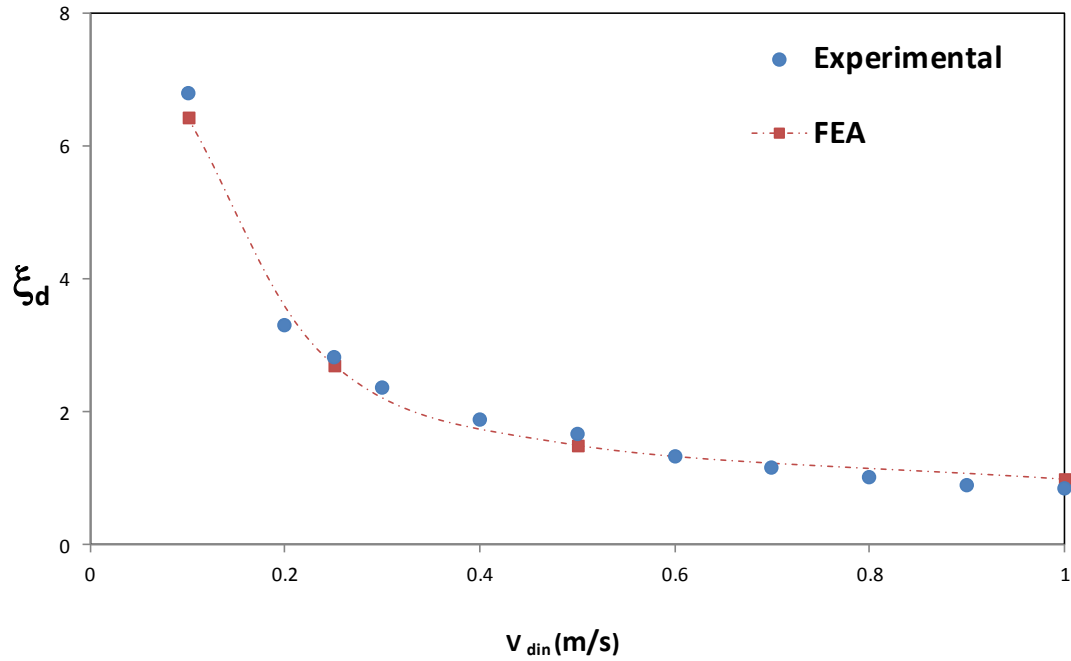


(a)

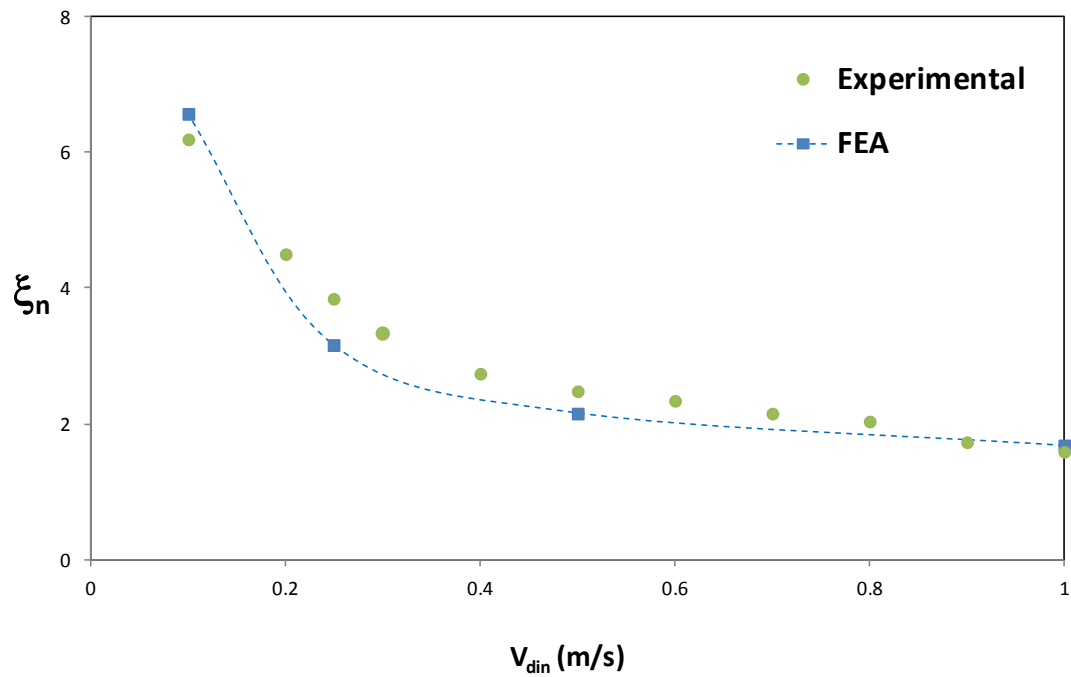


(b)

**Figure 2.27.1:** Variation of pressure drop coefficients (a)  $\xi_d$  and (b)  $\xi_n$  with the throat velocity of the diffuser ( $v_{din}$ ) for  $\theta_d = 5^\circ$   $\beta = 1$

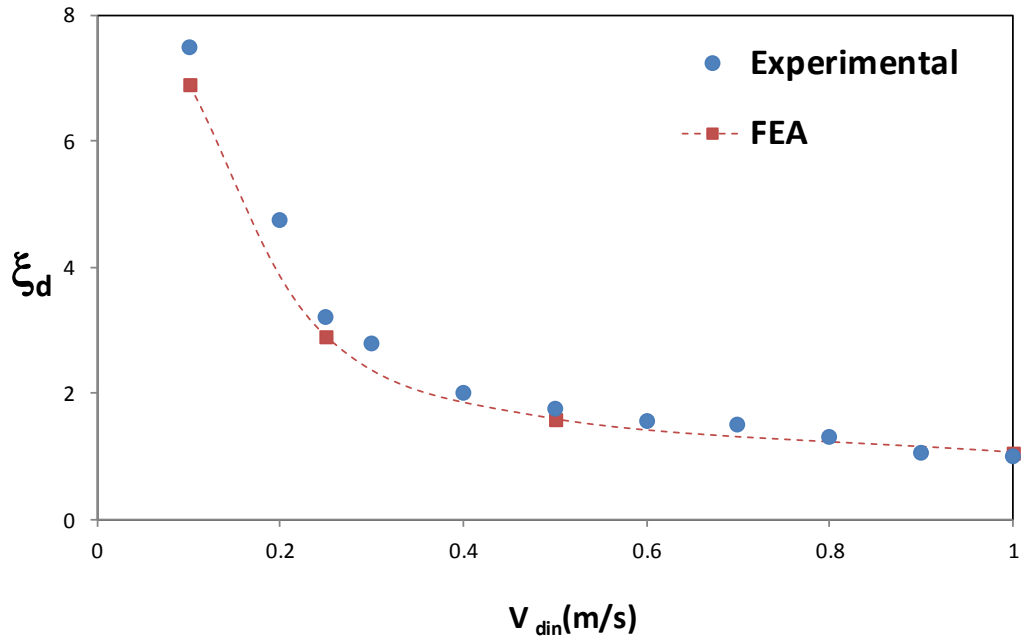


(a)

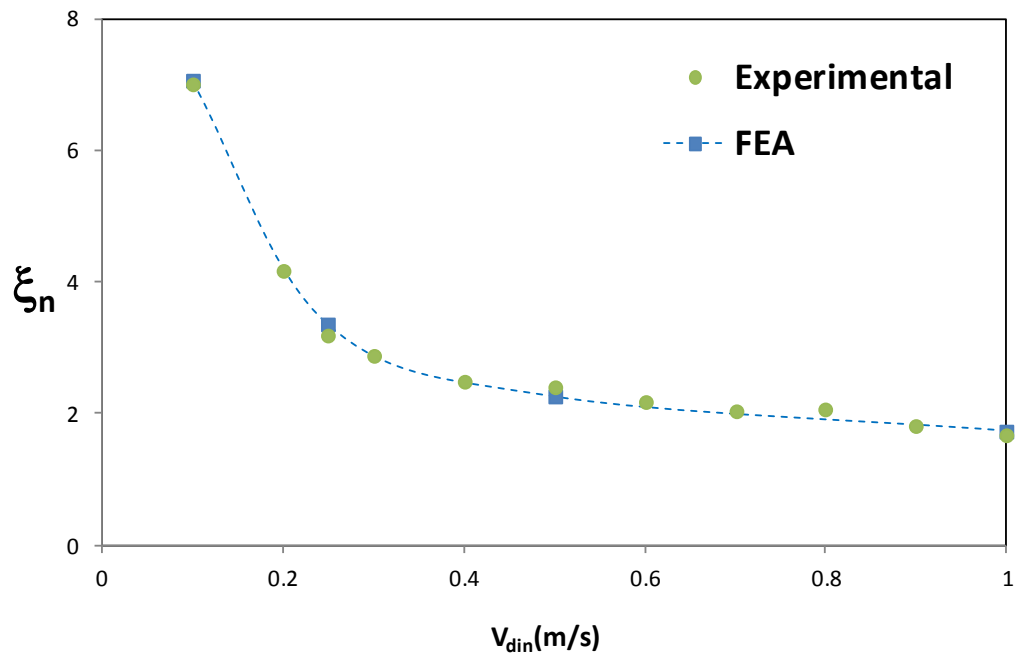


(b)

**Figure 2.27.2:** Variation of pressure drop coefficients (a)  $\xi_d$  and (b)  $\xi_n$  with the throat velocity of the diffuser ( $v_{din}$ ) for  $\theta_d = 15^\circ$   $\beta = 1$

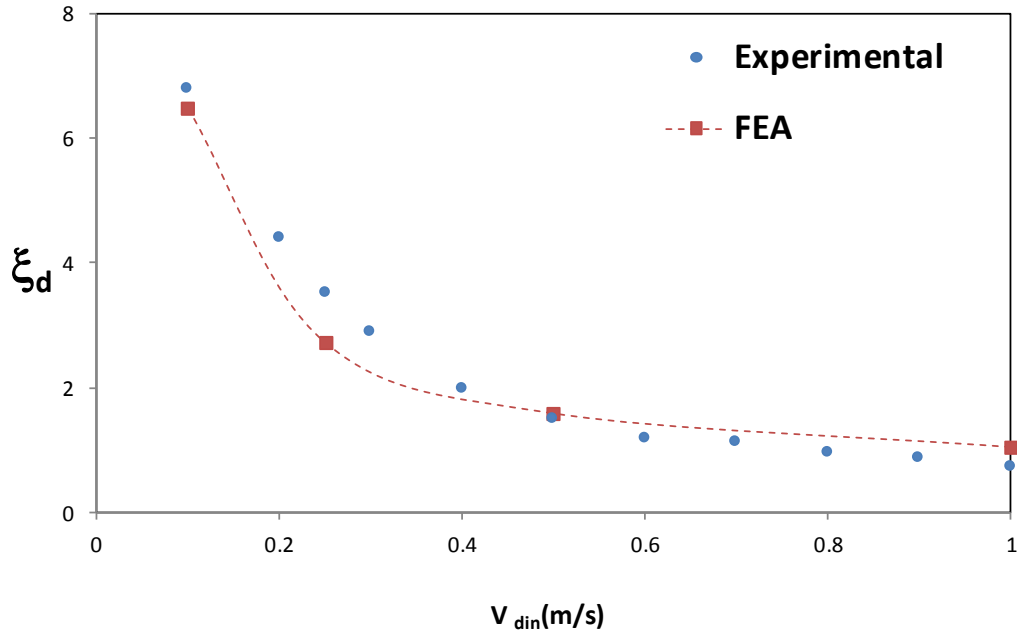


(a)

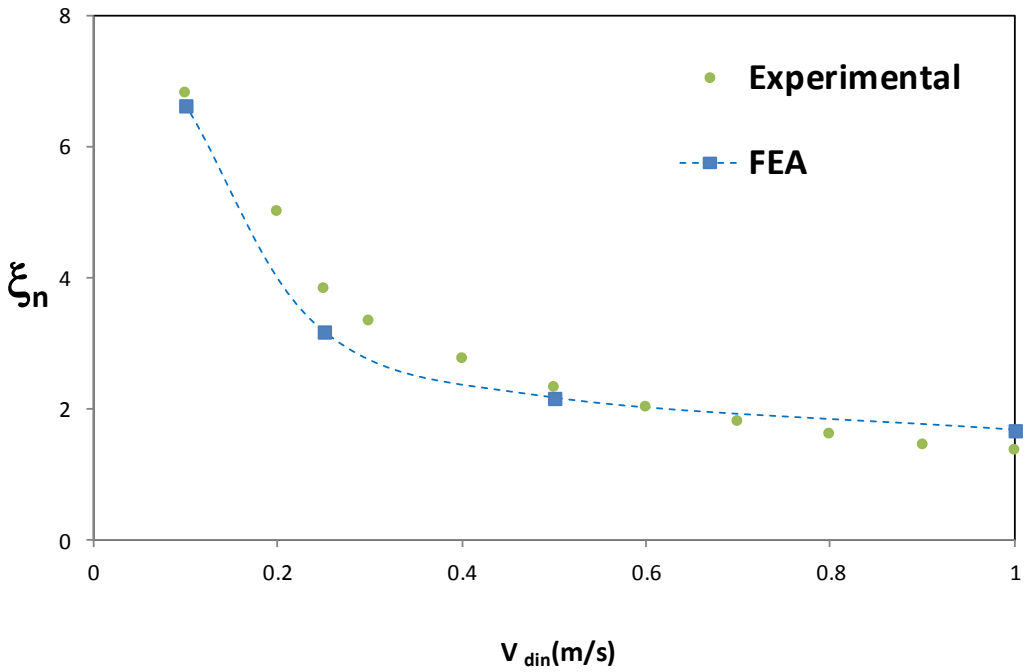


(b)

**Figure 2.27.3:** Variation of pressure drop coefficients (a)  $\xi_d$  and (b)  $\xi_n$  with the throat velocity of the diffuser ( $v_{din}$ ) for  $\theta_d=30^\circ$   $\beta_{cx}=0.4$



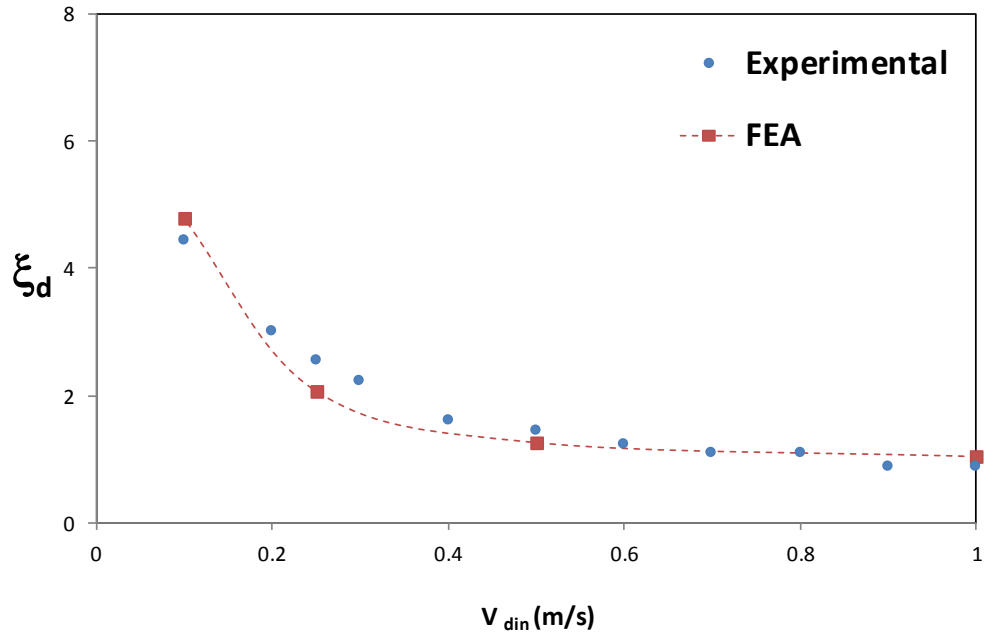
(a)



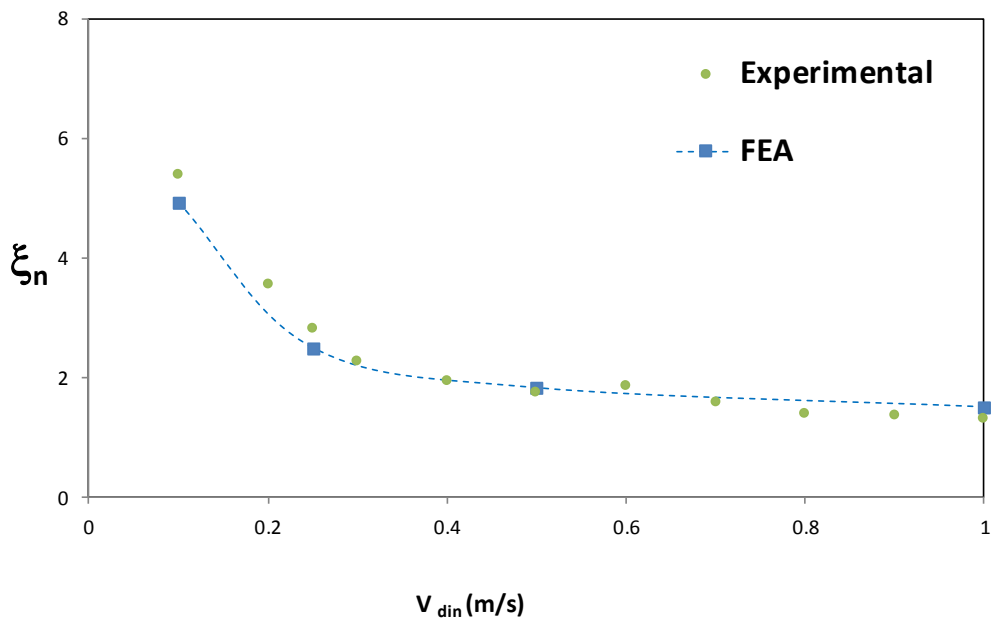
(b)

**Figure 2.27.4:** Variation of pressure drop coefficients (a)  $\xi_d$  and (b)  $\xi_n$  with the throat velocity of the diffuser ( $v_{din}$ ) for  $\theta_d=60^\circ$   $\beta_{cx}=0.2$





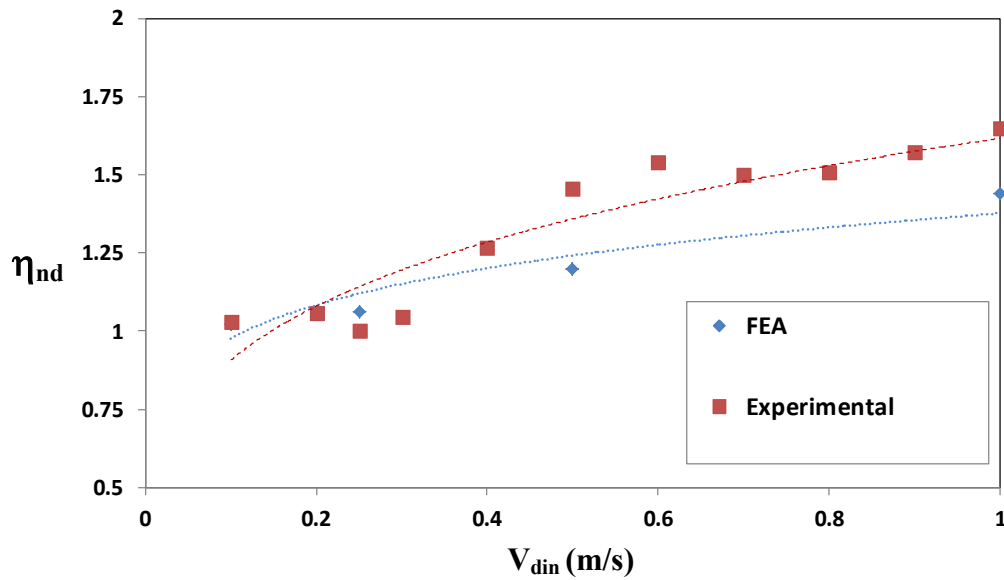
(a)



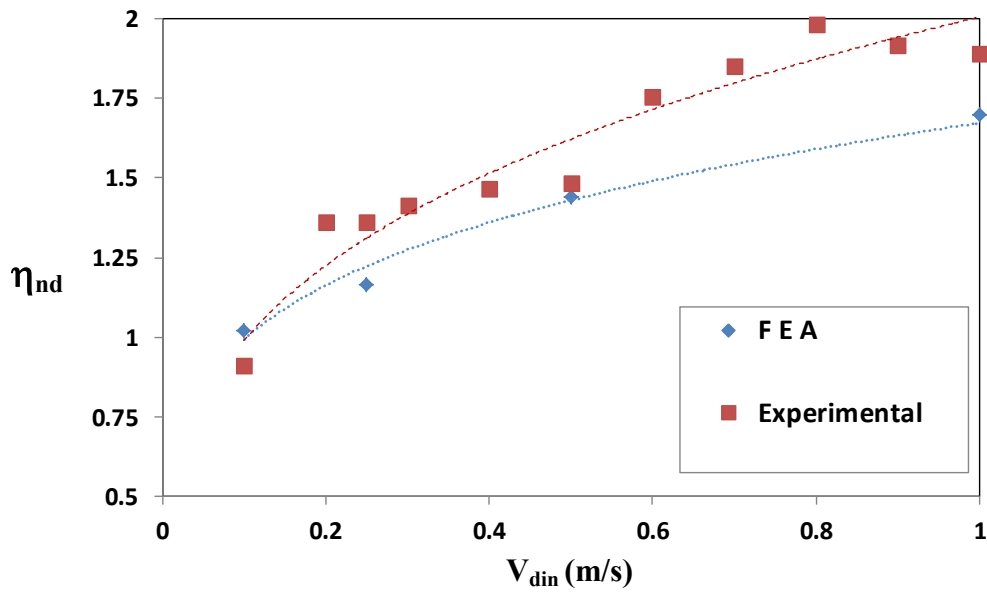
(b)

**Figure 2.27.5:** Variation of pressure drop coefficients (a)  $\xi_d$  and (b)  $\xi_n$  with the throat velocity of the diffuser ( $v_{din}$ ) for  $\theta_d = 90^\circ$  and  $\beta_{cx} = 0.2$

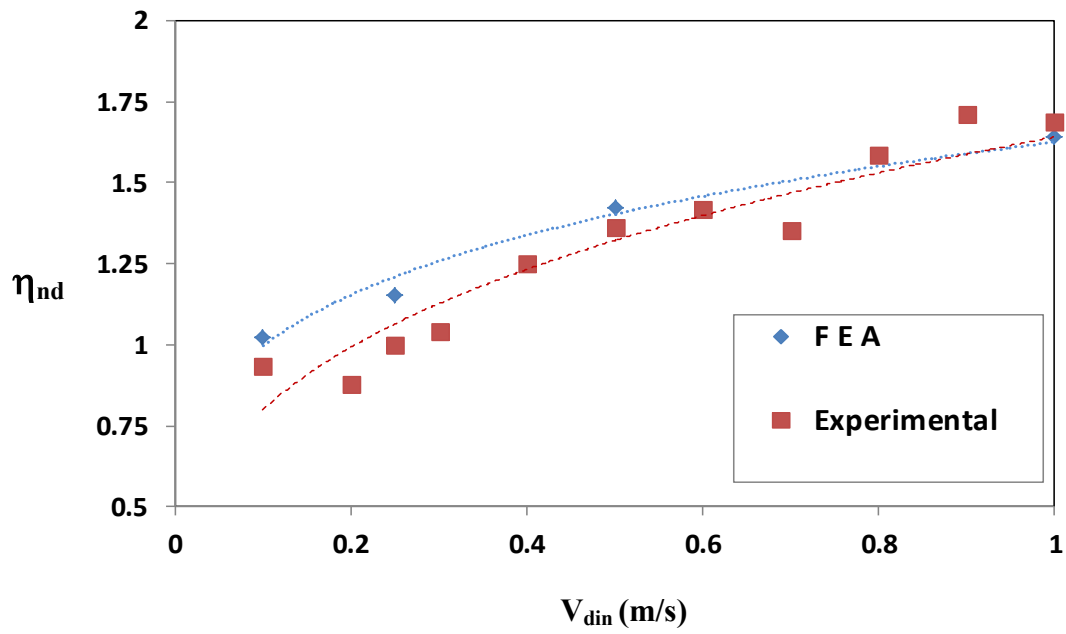
From the experimental pressure coefficients obtained for the nozzle and the diffuser, the diffuser efficiency was calculated. Figure 2.28 shows the variation of experimental and theoretical diffuser efficiencies, along with their trend lines, with flow velocity for different diffuser angles.



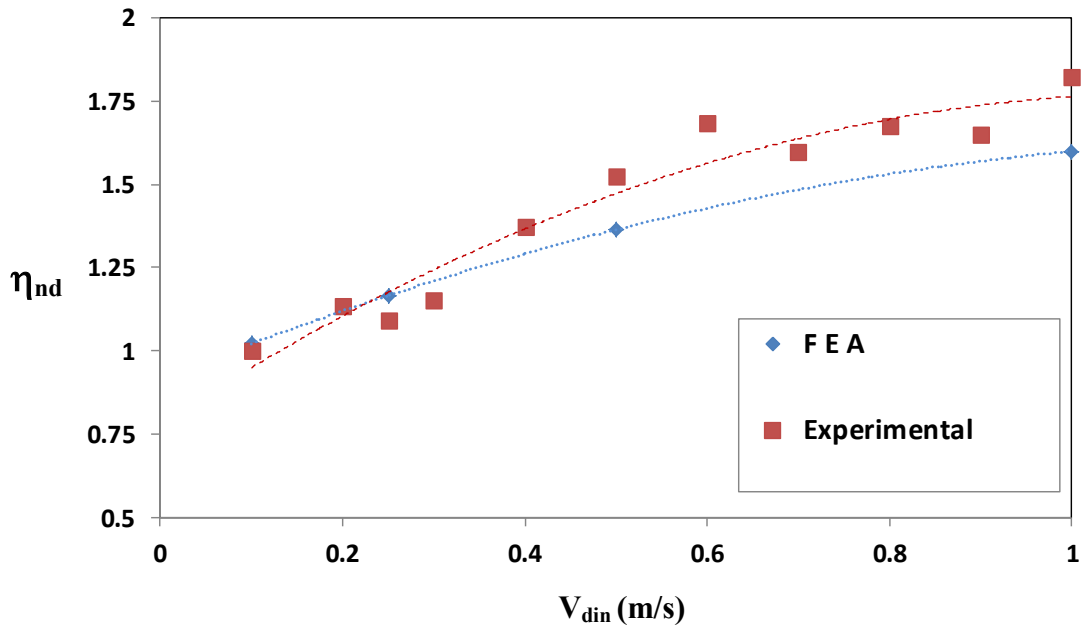
(a)  $\theta_d = 5^\circ, \beta = 1$



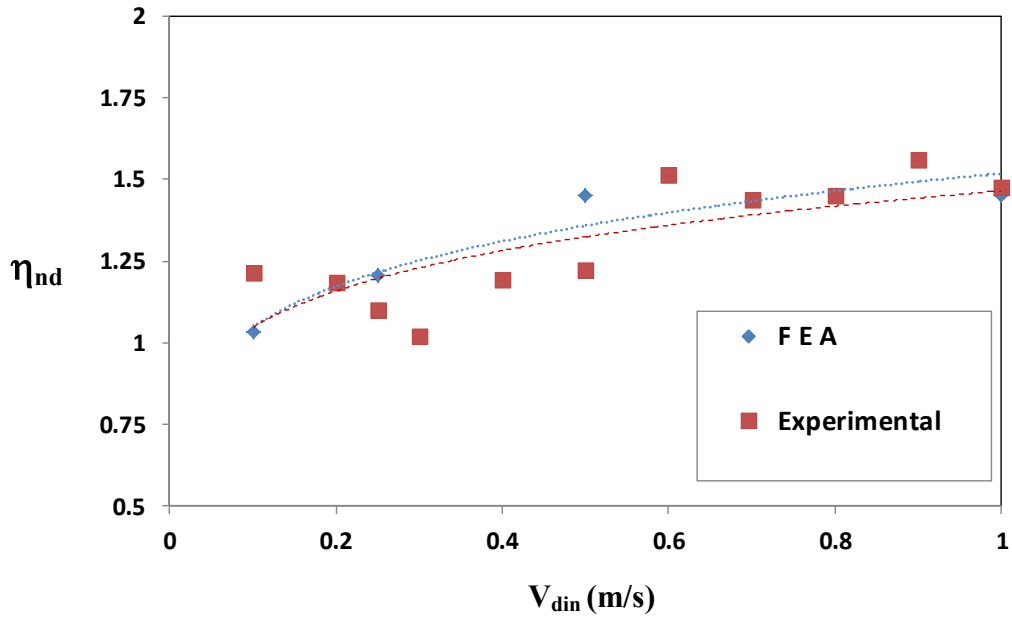
(b)  $\theta_d = 15^\circ, \beta = 1$



(c)  $\theta_d = 30^\circ$ ,  $\beta_{cx} = 0.4$



(d)  $\theta_d = 60^\circ$ ,  $\beta_{cx} = 0.2$



(e)  $\theta_d = 90^\circ$ ,  $\beta_{cx} = 0.2$

**Figure 2.28:** Plot of variation of the predicted and the experimental diffuser efficiency for different diffuser angles

It can be seen that the performance of the microdiffusers at different Reynolds numbers is very close to the predicted behaviour. A significant deviation is observed for 5 degree diffuser, with the experimentally obtained diffuser efficiency much higher than the predicted value. Though the plots of the diffuser and nozzle pressure coefficients are very close, the increased diffuser efficiency suggests that for smaller diffuser angles, there is also a significant pressure loss inside the diffuser, possibly due to the frictional loss due to the shear with the narrow side walls.

## 2.5 Influence of friction on the pressure loss of microdiffuser

For shallow channels, friction contributes to the pressure loss across the diffuser and the microfluidic channel elements across which the pressure difference is calculated.

Considering the positive flow in the x-direction, the frictional pressure drop across a rectangular channel along the channel length is given by the expression (Yang et al. 2004)

$$\Delta p_{ff} = \int_0^L \frac{2f_f \rho v(x)^2}{D_h(x)} dx \quad \dots 2.18$$

where  $f_f$  is the Fanning frictional factor and  $D_h(x)$  and  $v(x)$  are respectively wetted perimeter and the fluid velocity at position  $x$ . Harnett and Kostic (Hartnett, Kostic 1989) proposed a simplified polynomial to describe the friction factor for laminar flow through a rectangular channel that is accurate to 0.05%. The expression is given as

$$f_f = \frac{24(1 - 1.13553Y_d + 1.9467Y_d^2 - 1.70128Y_d^3 + 0.964Y_d^4 - 0.2537Y_d^5)}{Re_d} \quad \dots 2.19$$

where  $Y_d$  is the aspect ratio of the channel given by  $h_c/w_c(x)$  where  $w_c(x)$  is the width of the channel at  $x$ .

The pressure coefficient from the friction factor is given by

$$\kappa_{ff} = \left( \frac{\Delta p_{ff}}{\frac{1}{2} \rho v_{din}^2} \right) \quad \dots 2.20$$

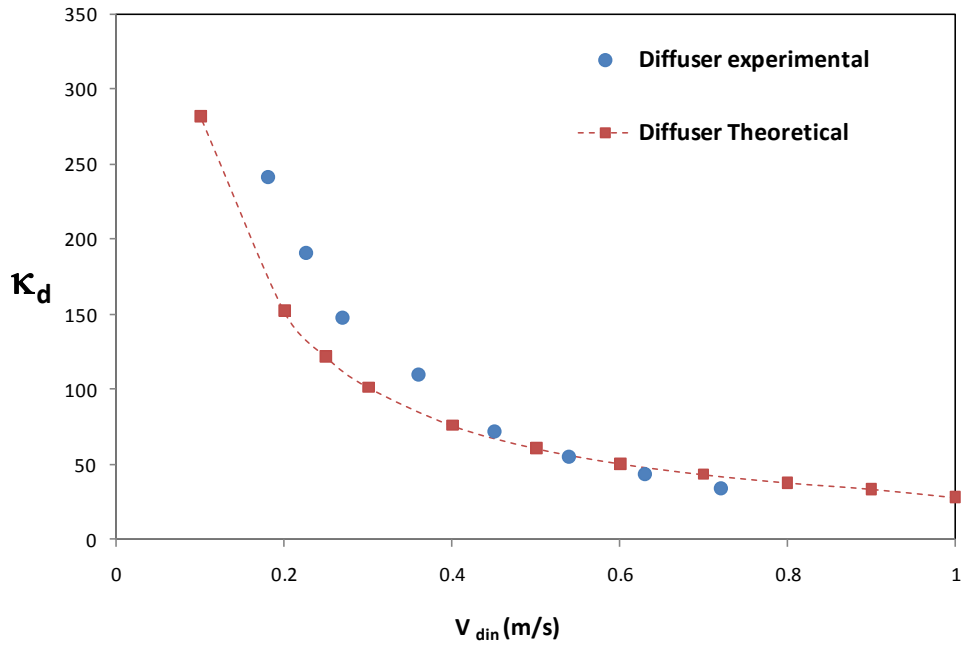
Thus, from equations 2.4 - 2.7, the total pressure loss coefficient  $\kappa_{n,d}$  is given by

$$\kappa_{n,d} = \frac{\Delta p_{net}}{\frac{1}{2} \rho v_{din}^2} = \xi_{n,d} + \kappa_{ff} \quad \dots 2.21$$

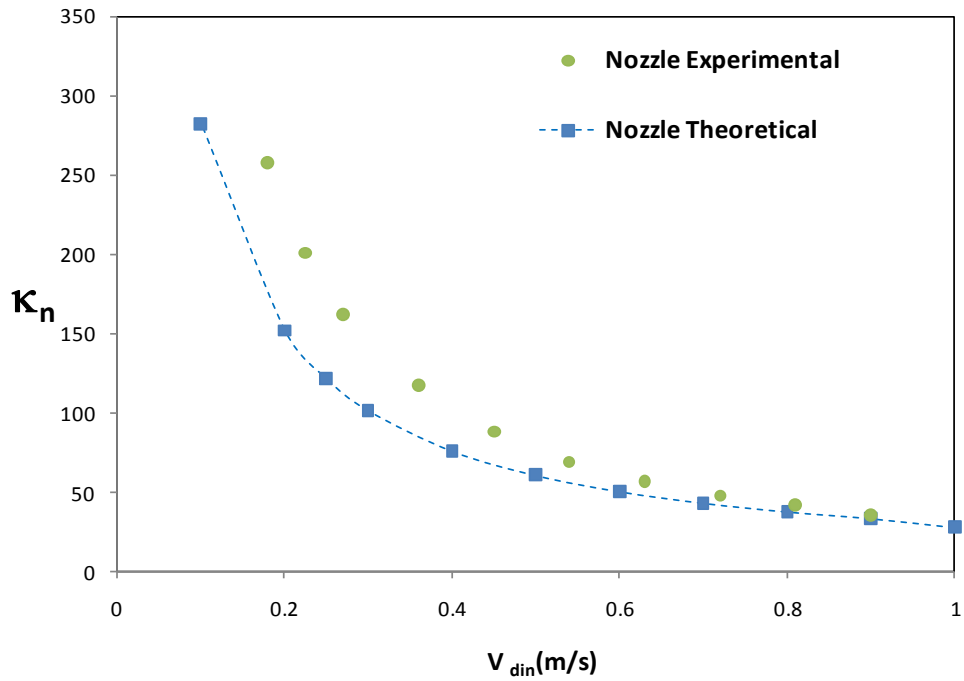
The effect of friction on the diffuser performance was studied using 20 mm diffuser channels. The chip was prepared using same procedure explained in the previous sections, wherein, the silicon mould was fabricated only with 20  $\mu\text{m}$  SU8 substrate. The height of the SU8 is controlled by spin coating. SU8-2015 purchased from Microchem, USA was used for the present application. After the preparation of the PDMS chip from the mould and the creation of microfluidic ports, packaging was done with the PDMS-on-glass substrate as explained before. However, the packaging method was slightly tricky with the 20  $\mu\text{m}$  diffuser, because when bonding the PDMS diffuser chip with the semicured PDMS-on-glass, if the curing is not good, then the chances of the diffuser channels sealing with the bottom substrate is high due to high forces of attraction between the bottom PDMS and the top substrate. Therefore

### **2.5.1 Experimental results of variation of diffuser coefficients with friction**

The variation of the pressure loss coefficients in the 20  $\mu\text{m}$  deep diffusers is given in Figure 2.29.1-5. It can be seen that the pressure loss coefficients due to friction are much higher than the drop coefficients of the nozzle and diffusers, for all diffuser angles.

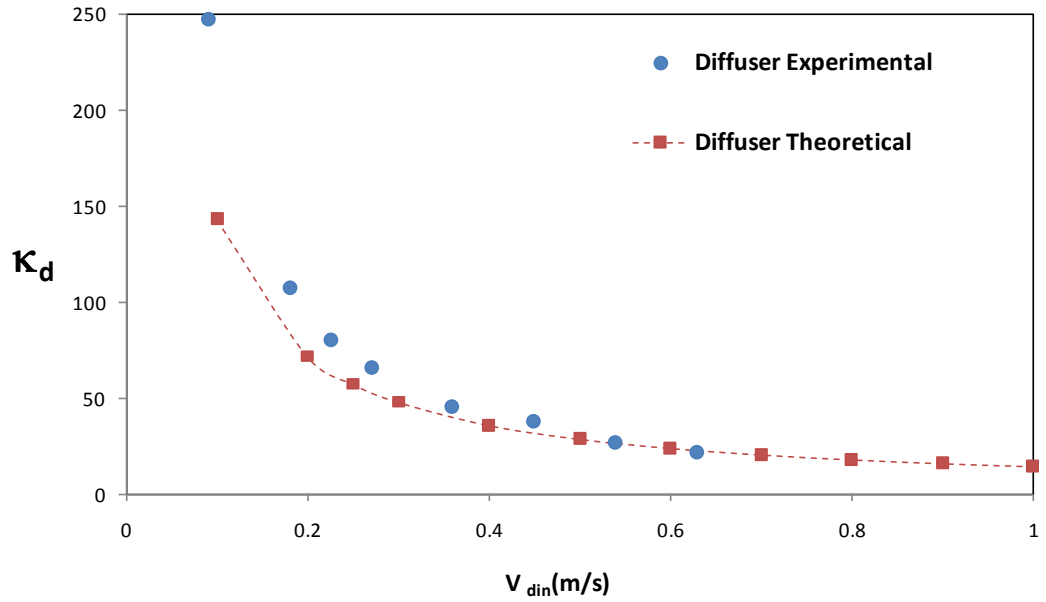


(a)

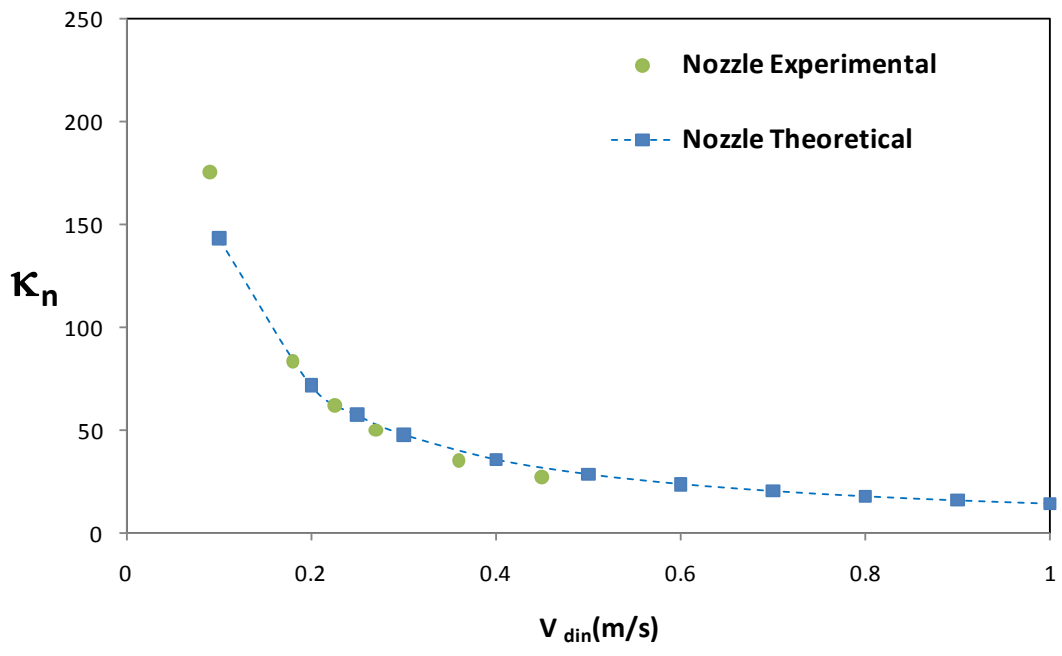


(b)

**Figure 2.29.1:** Variation of pressure loss coefficients (a)  $\kappa_d$  and (b)  $\kappa_n$  with the throat velocity of the diffuser ( $v_{din}$ ) for  $\theta_d 5^\circ$   $\beta = 1$



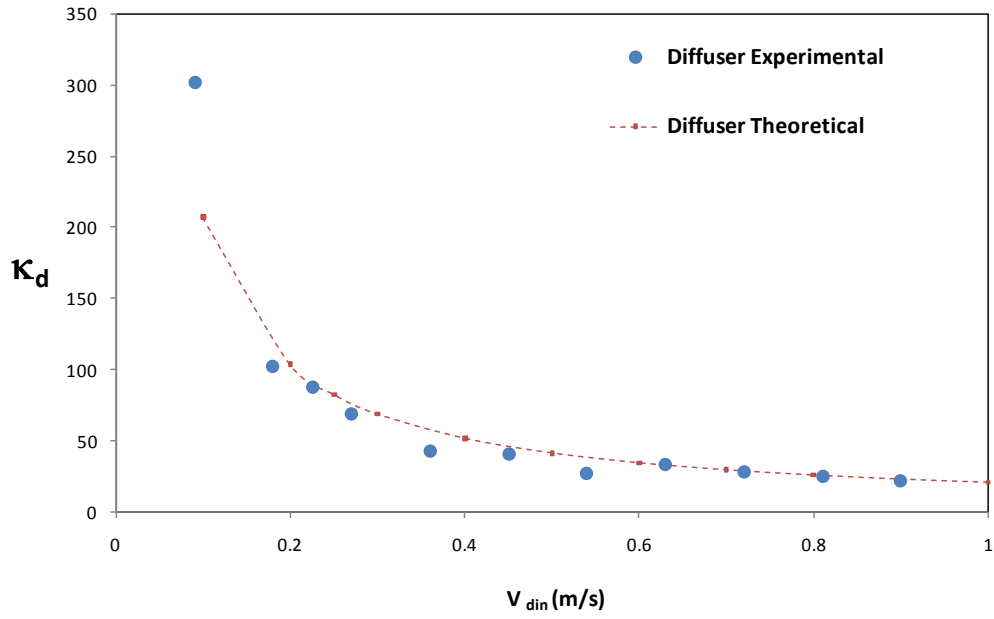
(a)



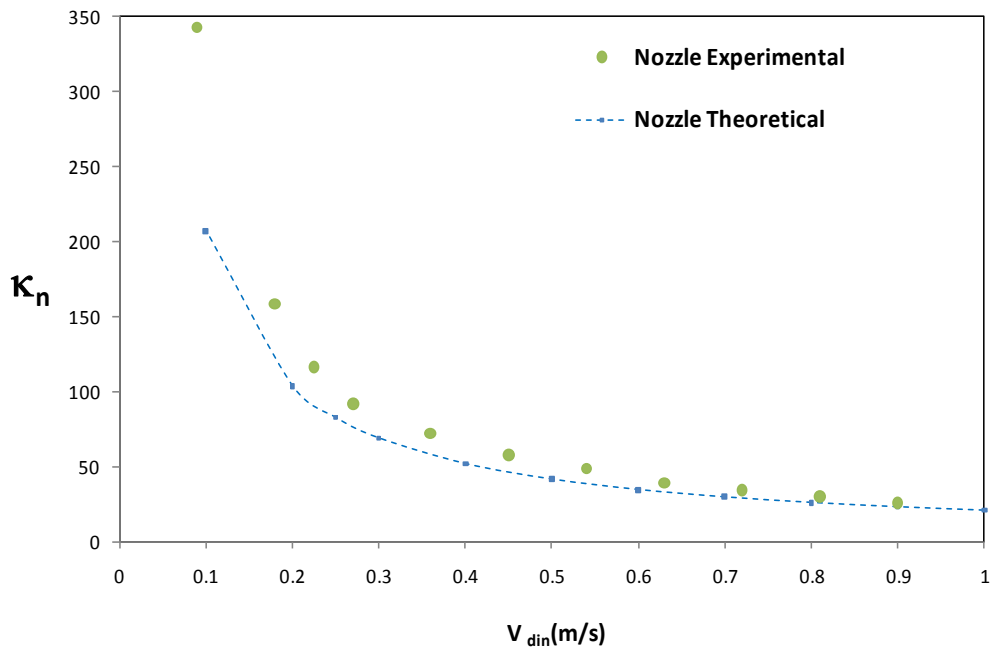
(b)

**Figure 2.29.2** : Variation of pressure loss coefficients (a)  $\kappa_d$  and (b)  $\kappa_n$  with the throat velocity of the diffuser ( $v_{din}$ ) for  $\theta_d=15^\circ$   $\beta = 1$



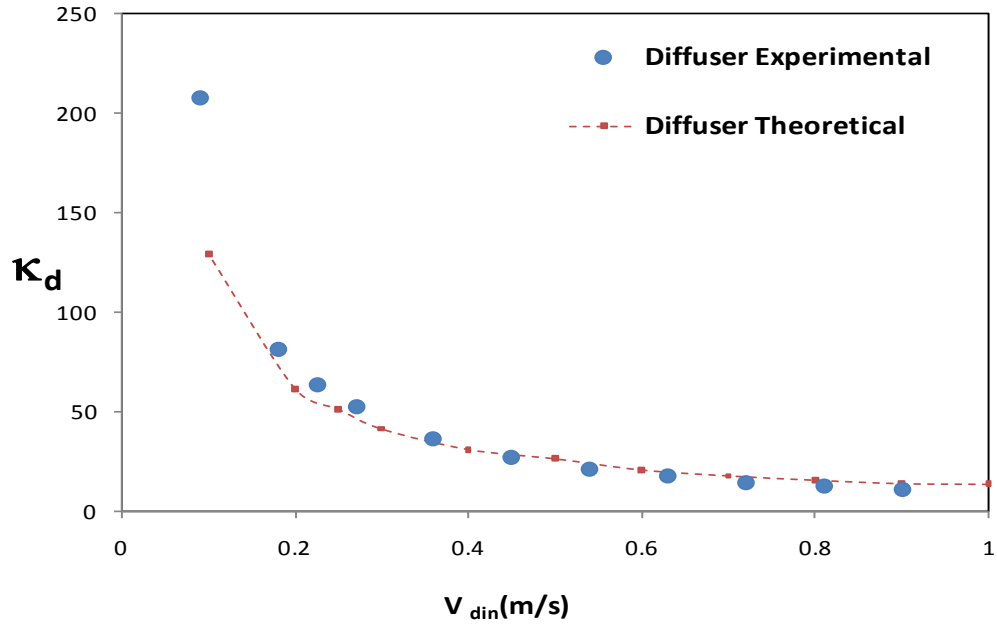


(a)

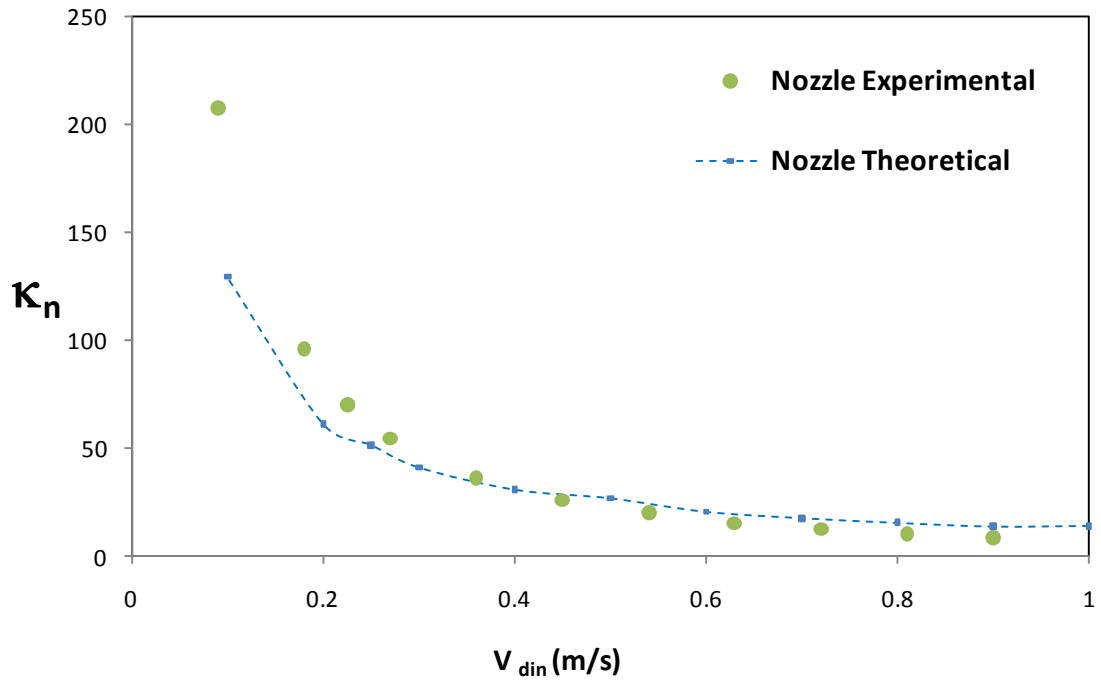


(b)

**Figure 2.29.3:** Variation of pressure loss coefficients (a)  $\kappa_d$  and (b)  $\kappa_n$  with the throat velocity of the diffuser ( $v_{din}$ ) for  $\theta_d=30^\circ$   $\beta_{cx}=0.4$

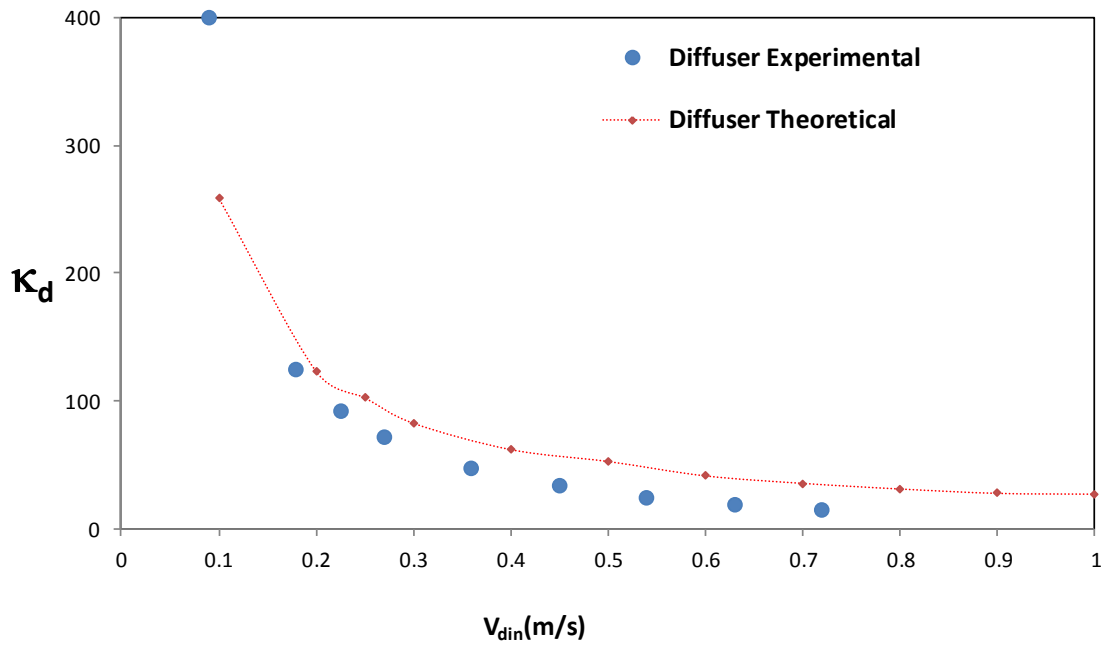


(a)

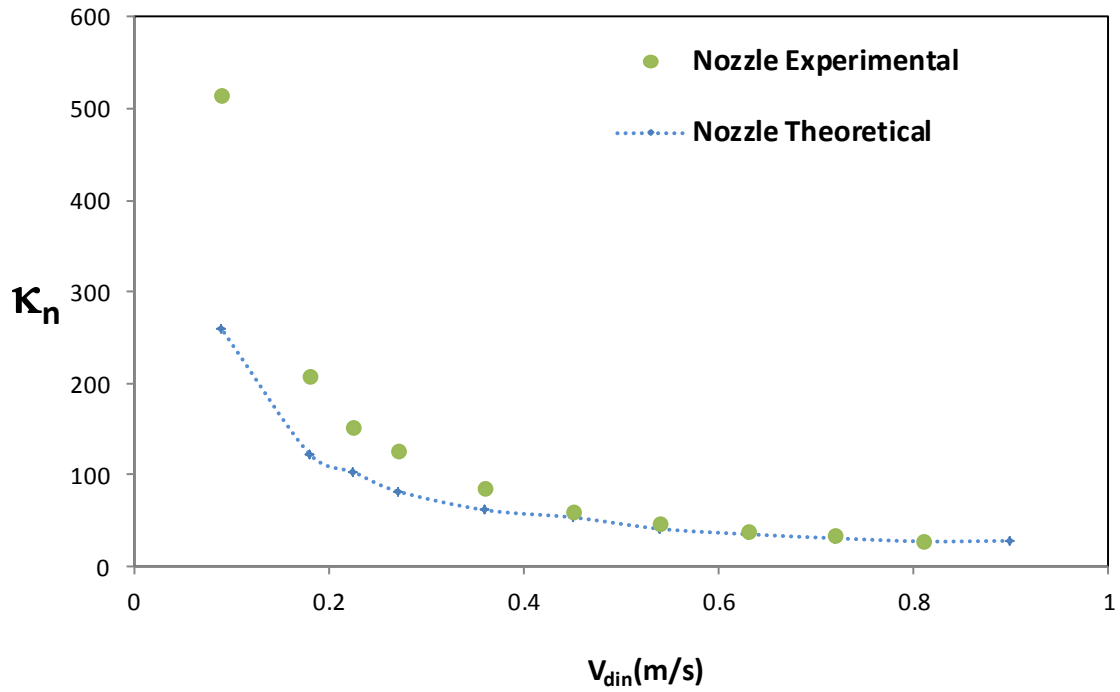


(b)

**Figure 2.29.4:** Variation of pressure loss coefficients (a)  $\kappa_d$  and (b)  $\kappa_n$  with the throat velocity of the diffuser ( $v_{din}$ ) for  $\theta_d=60^\circ$   $\beta_{cx}=0.2$



(a)



(b)

**Figure 2.29.5:** Variation of pressure loss coefficients (a)  $\kappa_d$  and (b)  $\kappa_n$  with the throat velocity of the diffuser ( $v_{din}$ ) for  $\theta_d=90^\circ$   $\beta_{cx}=0.1$

### 2.5.2 Discussion

When friction factor comes into effect, the pressure coefficient for the nozzle and the diffuser is much higher than the pressure coefficients without friction. The nozzle and diffuser pressure coefficients for all diffuser angles at all flow velocities are almost equal. Therefore, the effect of the diffuser behaviour for micropumping is greatly nullified. As from Equation 2.8,  $\kappa_{ff} \gg \xi_{n,d}$ ,  $\therefore \kappa_{n,d} \cong \kappa_{ff}$ . Also from the results it can be seen that there is a significant deviation between the experimental and the theoretical values especially at low Reynolds numbers, wherein, the experimentally obtained values are much greater than the theoretical values.

Few possible reasons can be attributed to the deviation of the diffuser and nozzle pressure coefficients from the predicted values. One important factor is the calculation of the velocity at the neck of the diffuser. It is assumed that the channel depth of the diffuser is 20  $\mu\text{m}$ . However it is possible from minor lithographic errors and from the packaging imperfections that the height of the channel is not always as assumed. The lithography specifications with SU8 (<http://www.microchem.com>) show that, for the parameters used, the thickness of the SU8 would be  $\sim 22 \mu\text{m}$ , the SEM image shown in Figure 2.30 clearly shows that the height of SU8 is  $\sim 19.6 \mu\text{m}$ . Such discrepancies could lead to errors in the computation of the flow velocity at the neck which in turn affects the experimental results. Especially at lower Reynolds numbers, the neck velocity assumes a fairly large significance and consequently, the pressure coefficients are extremely sensitive to such minor variations in the calculations of the flow velocities.

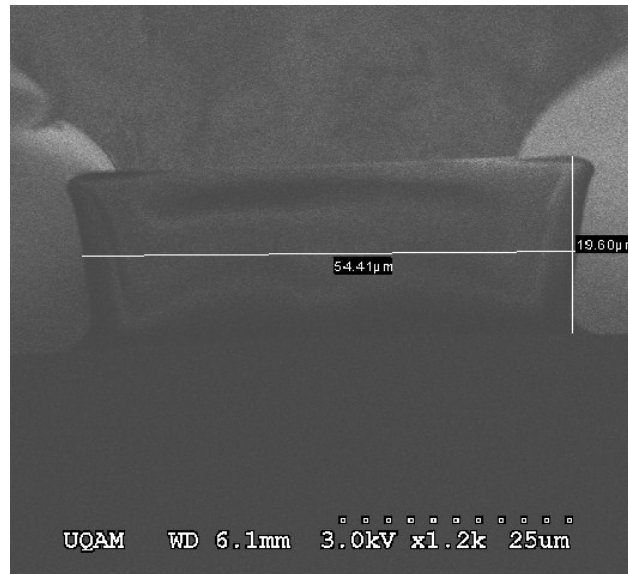


**Figure 2.30:** SEM of the SU8 mould, the thickness obtained from the lithography is 19.6  $\mu\text{m}$

For the present pressure measurement configuration, it is also important to accurately predict the length of the microchannel between the fluid tube coupled to the pressure sensor and the diffuser. Also since the integration of the tube is done manually, it is very difficult to accurately predict the height of the tubes over the surface of the microchannel, and this affects the computation of the frictional loss in the fluidic port for the portion of the microchannel which is closed with the tube. Hence it is extremely difficult to corroborate the experimental results with the predicted frictional loss. However, when taken alone, the experimental results present a clear picture of the behavior of the diffuser

However, the trend of the plots for the experimental results shows that the analytical predictions for the relationships between the diffuser efficiencies hold good.

Thus, from the above discussions, it is very clear that frictional losses can be highly significant in contributing towards the total pressure loss across the diffuser. The effect of friction can nullify the pressure drop coefficients completely and therefore, it is extremely important to take into consideration the effects of friction when designing a microdiffuser.

As the depth of the channel is reduced, the frictional loss obtained in the channel increases tremendously. Under such conditions, smaller angle diffusers cannot be used for micropumping since the loss is high which necessitates the use of wide angle diffuser. Through the geometric tuning presented herein, it is possible to obtain enhanced diffuser performance of the diffuser and hence improve the performance of micropumping

## **2.6 Summary**

This chapter presented the design and experimental validation of microdiffusers for integration with valveless micropump system. One of the most important and the most novel contributions of this work is the geometry conditioning of diffusers to improve the flow rectification efficiency for valveless micropump applications. It is now possible to tune the geometry of the diffuser to obtain the maximum according to the Reynolds number.

FEM was carried out to study the performance of the diffusers based on the pressure drop coefficients in the nozzle and the diffuser flow directions, with geometry tuning for different flow velocities. The FEM was carried out using ANSYS/FLUENT and

COMSOL software package. The results of the FEM showed that there is a clear dependence between the pressure coefficients of the diffusers and the flow velocity for a particular geometry. Thus, one can select a particular conditioning parameter in order to maximise the diffuser efficiency.

Experimental validation of the diffuser behavior was also carried out and the results are in agreement with the predicted diffuser performance. The effect of friction was also studied on the diffusers and one must also take friction effects into consideration when designing the micropump.

# Design, Fabrication and Testing of Piezoelectric -Actuated Valveless Micropump for $\mu$ TAS

### 3.1. Introduction

Micropump applications are found in a large number of technologies and science domains such as biology, medicine, electronics and space air crafting. In the field of chemical and biotechnology, they are used in micro total analysis systems ( $\mu$ TAS), portable DNA testing devices, electronic refrigeration systems and portable medication delivery appliances such as insulin dispensing, among others. As a rule, micro-pumps are designed and microfabricated to meet a set of requirements that vary with the application. For this reason, micropumps designed for different applications are required to pump different types of fluid with high controllability, while also taking into account some other important issues such as reduced size, low power consumption and biocompatibility (Hernandez et al. 2010). Therefore, it is very common to find significant differences in the performance from one micropump to another, depending upon each application.

In order to design a micropump, it is important to choose the right type of actuating mechanism to drive the fluid. Piezo actuation is one of the most common actuating principles used in micropumping which is useful to achieve a vast range of flow rates.



Advantageous properties such as ease of integration in micro-systems and high speed response make piezo-actuation a very good choice for micropump applications. In comparison to devices with different actuation principles, piezoelectric micro-pumps can be designed to work at very high frequencies which translate into increasing flow rates, an advantage which is not available for a few other actuation methods such as pneumatic or shape memory alloy actuation (Hernandez et al., 2010). In addition, other advantages of piezoelectric actuator over other types of actuators such as electromagnetic, thermopneumatic, magnetohydrodynamic, etc. is the capacity to generate large forces and the ability of being synthesized and shaped at very small scale thereby enabling the fabrication of robust micropump devices and easy integration with  $\mu$ TAS. However, despite these remarkable advantages, the main drawback of piezoelectric actuators is the low magnitudes of deformation which translates to a very small displacement of the micropump.

Among several microfluidic bases used for piezoelectric micropumps, silicon has been one of the most commonly used material platforms (Olsson et al. 1997), (Olsson 1998). Silicon offers a lot of packaging flexibilities, but other factors such as high fabrication cost and the requirement of cleanroom based micromachining facilities have led to the development of alternate material platforms such as PDMS, PMMA and other polymers for low-cost micropumping applications. Packaging of micropumps is also very important for the successful synthesis of a micropump. For mechanical piezoelectric actuated micropumps, apart from the microfluidic channel substrate, it is equally important to choose the right type of material platforms for the diaphragm and suitable bonding

techniques for the attachment of the piezo element with the micropump, which also offers material transparency for the visualization of flow behaviour within the micropump that is useful for the characterization of micropump behaviour.

Since the micropump system analysis is a sophisticated multi-disciplinary problem with various field couplings, numerous scientific and engineering researches have been conducted in the past decade to optimize micropump working parameters (Ahmadian and Mehrabian 2006). There have been several mathematical models developed for estimating the performance of valveless micropumps (Ullmann and Fono, 2002) (Ullmann, A. et al., 2001). The effect of geometry and working conditions on flow rectification achieved by the micropumps has been investigated by several researchers. Olsson et al (1998) used lumped mass model to study flat walls diffuser micropumps to simulate numerically the pressure limit, piezoelectric excitation level and flow performance of micropump in single and double chamber micropumps. Experimental works have also been reported about shape optimization of micropump valves (Gamboa et al. 2005) in the literature. Fan et al. (Fan et al. 2005) numerically studied the performance of a piezoelectrically actuated valveless micropump with the consideration of the three-way electro-mechanical-fluid coupling. Pan et al. (Pan et al. 2003) have obtained analytical solution for a valveless micropump in order to investigate the dynamic response of coupled membrane-fluid system with respect to piezoelectric actuation. Nguyen and Huang (2001) studied the effect of membrane deflection and actuation frequency on flow rate and found that flow rate increases by increasing membrane deflection at low frequencies. The mathematical relation for the valveless micropump behaviour with single (Eames et al. 2009) and

double pump chambers (Azarbadegan et al. 2009) were also carried out, based on the flow asymmetry produced during one operating cycle and compared with the results obtained by Stemme and Stemme (1993). However, though several studies have been carried out, the working of a micropump is still not clearly understood, as an intercoupled Fluid-structure interaction physics is involved in its operation.

This chapter presents the design, fabrication, testing, and characterization of a Piezo-actuated valveless micropump on PDMS platform for facilitating further integration with the  $\mu$ TAS. The performance of the micropump is evaluated against several working parameters such as operating frequency, inlet pressure head, and geometry of the microdiffuser. The effect of surface wettability on the flow rate and the bubble generation characteristics of the micropump are also analyzed and the results presented in this chapter.

### **3.2. Understanding the behavior of valveless micropumps**

In a valveless micropump with microdiffuser/nozzle configuration, the flow characteristics are determined by the combination of a volumetric change to the pump chamber and the asymmetric pressure drop across the diffuser/nozzle elements with the direction of the flow. Thus, when the pump membrane is deflected in compression and expansion modes, the pressure drop across the nozzle and diffuser elements become different and thus, the diffuser elements act as a passive valve. The schematic of the valveless micropump is as shown in Figure 3.1.

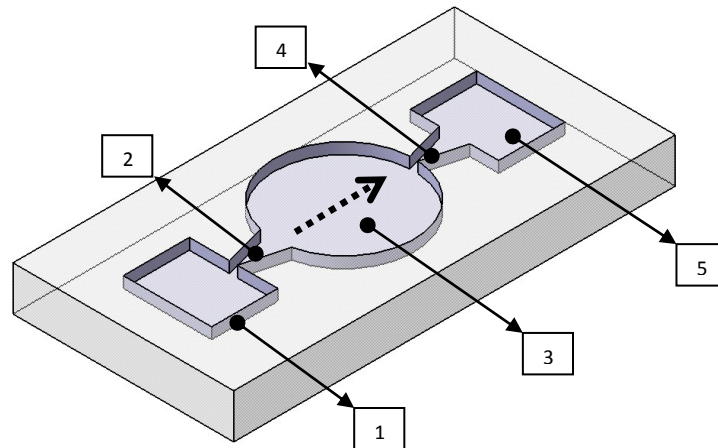


**Figure 3.1:** Schematic of the valveless micropump. The following segments have been labeled 1- Inlet channel, 2- Inlet diffuser  $D_i$ , 3-Micropump chamber, 4-Outlet diffuser  $D_o$ , and 5- Outlet channel  
 .....➤ Indicates the direction of net positive flow

An alternating piezoelectric actuation of the micropump operation results in basically two strokes of the diaphragm, i.e the suction stroke in which the upward motion of the diaphragm causes the suction of the fluid into the chamber, and the compression stroke, in which the downward motion of the diaphragm displaces the fluid from inside the chamber. The stroke ratio is defined as the ratio of the maximum stroke length to the depth of the channel, which can be varied by the variation of the operating frequency and the applied voltage.

The flow is always considered positive from the inlet to the outlet. The schematic of the working principle of a valveless micropump during suction and compression strokes is as shown in Figure 3.2

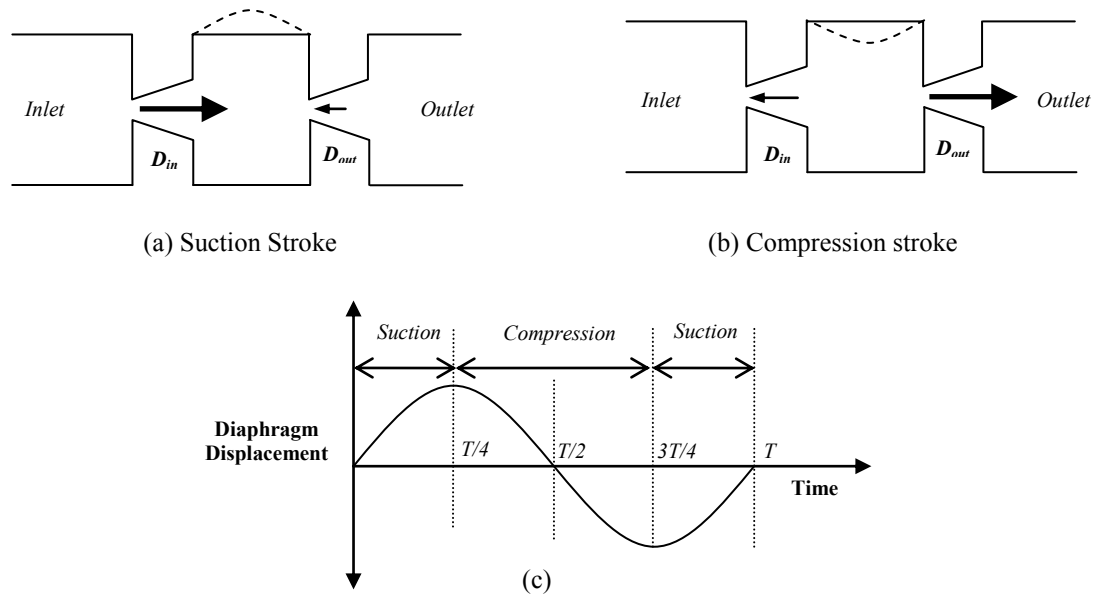


**Figure 3.2:** Schematic of the flow rectification due to the diffuser/nozzle configuration under (a) Suction strokes (b) Pump stroke. The arrow indicates the direction of fluid flow through the diffusers during each pump stroke and the size of the arrow indicates the relative magnitude (not to scale) of the volume of fluid. (c) Variation of pump stroke with sinusoidal diaphragm deflection in one oscillation cycle of time period  $T$ .

The rectification in flow is brought about by the presence of the nozzle/diffuser pair at the inlet and the outlet of the chamber, which produces asymmetric pressure drops across the nozzle and diffuser during one operating cycle of the micropump. The working principle of the valveless micropump under consideration can be summarized as below.

In all the design considerations carried out for the nozzle and the diffuser, as seen in the previous chapter, the net pressure drop of flow in the diffuser direction is always lesser than the nozzle direction. Therefore, during the suction stroke of the pump, fluid flows in from both the inlet and the outlet of the micropump chamber,  $D_{in}$  acts as diffuser to the flow whereas  $D_{out}$  forms the nozzle. Since greater pressure drop is experienced by the fluid in the nozzle direction, more resistance is offered to the fluid by  $D_{out}$  than  $D_{in}$  and hence a greater volume of the fluid flows into the pump chamber from  $D_{in}$ . Similarly,

during compression stroke, the fluid is pushed out from the chamber through both  $D_{in}$  and  $D_{out}$ , however in this case,  $D_{in}$  acts as a nozzle to the flow whereas  $D_{out}$  acts as a diffuser. Hence, greater flow occurs in the diffuser direction towards the outlet. Thus, the net flow is always positive from the inlet to the pump chamber during the suction stroke and from the pump chamber to the outlet during the compression stroke, thereby producing a rectified mean flow towards the outlet.

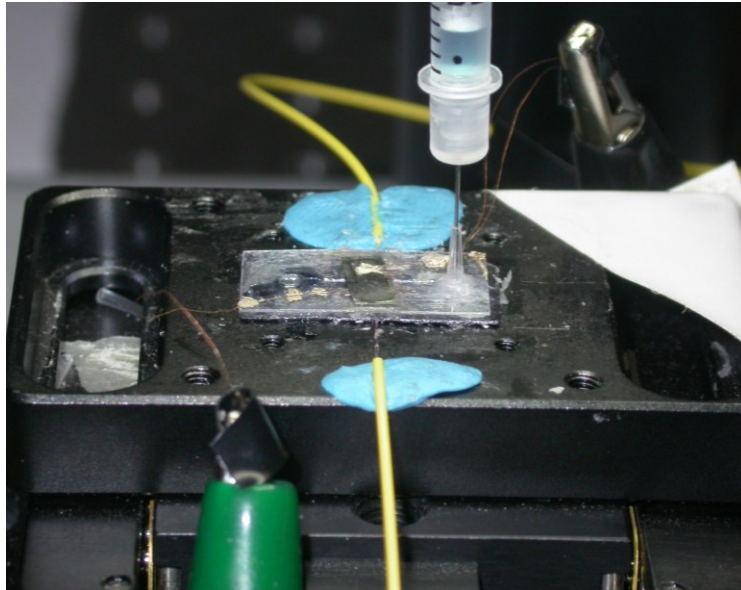
The flow efficiency of the valveless micropump is governed by the efficiency of diffuser and the frequency of oscillation of the diaphragm. For a similar configuration of the nozzle and diffuser at the inlet and outlet, Stemme and Stemme (1993) have calculated the net flow based on the diffuser efficiency and the pump frequency, which was described in Section 2.2. Thus, the performance of the piezo actuated valveless micropump is characterized by its flow rate, which can be varied by the following factors, namely, variation of the actuation properties such as frequency and operating voltage, fluid properties, and the geometric configuration of the pump chamber and the rectifier elements and the available pressure heads.

### **3.3 Design and fabrication of valveless micropump**

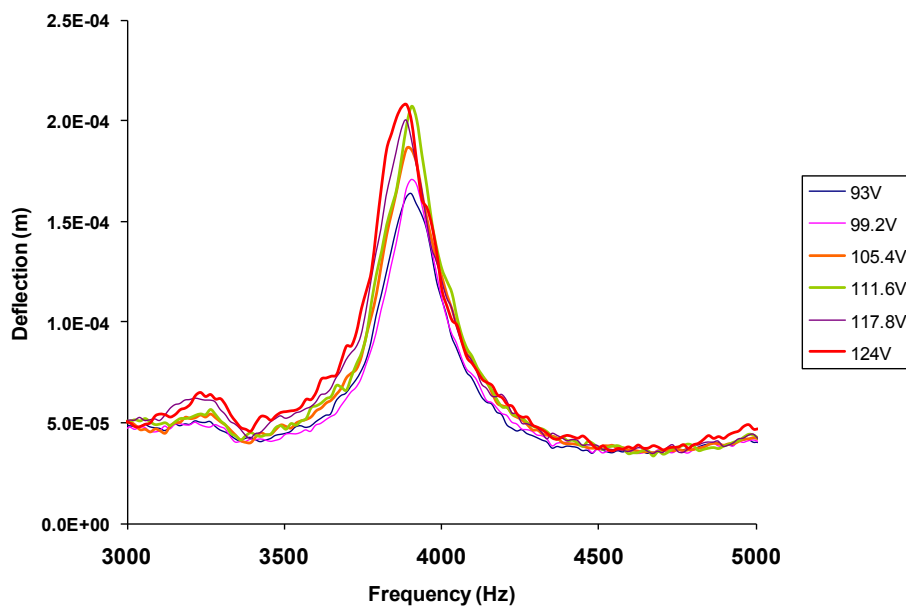
In order to design a micropump, it is essential to understand the working of the micropump clearly. All the relations derived for obtaining the volumetric efficiency of the micropump so far has been under the assumption that the flow through the diffuser element is of constant velocity. In practice, the flow velocity across the throat of the

diffuser would follow the actuation scheme, i.e., for a sinusoidal actuation with the piezo actuator, the flow velocity across the diffuser would also be sinusoidal. Therefore, the classical relations do not entirely hold good for the prediction of the pump performance. Also it must be noted that the pump efficiency would also depend on other parameters such as viscosity of the fluid, depth of the channel and friction factor which, as seen from the previous chapter, plays a significant role in determining the efficiency of the diffuser. Therefore, modeling of the micropump system would necessarily have to take into consideration the above mentioned factors as well. Also, all the micropumps that have been studied through both analytical modeling and experiments have been stand alone systems. Not many studies have been carried out so far for micropumps integrated in a  $\mu$ TAS. Given the difficulties and the multiphysics involved in such a computation, the reliable and possible method to study the performance of the micropump for integration with the  $\mu$ TAS is through experimental verification of their behavior under different flow and actuation conditions. Therefore, it is imperative that the performance of the micropump have to be studied thoroughly through carefully orchestrated experiments.

Preliminary investigations for the synthesis of a piezo actuated micropump were carried out by testing PVDF thin films for micropump actuation. PVDF films were used as the actuating membrane, because of several advantages such as ease of integration, greater actuating amplitudes, low operating voltages, etc. The performance of PVDF actuated micropump was also verified for optical integration on a silicon platform (Chandrasekaran and Packirisamy, 2009b). The setup is as shown in Figure 3.3(a) and the dynamic characteristics of the PVDF membrane is as shown in Figure 3.3(b).



(a)



(b)

**Figure 3.3:** (a) Setup of the PVDF integrated micropump fabricated on silicon (b) Plot of the spectral response of the deflection of the PVDF membrane obtained at various excitation voltages using LDV



It can be seen, in Figure 3.3 (b), that at the natural frequency, the maximum deflection obtained with the PVDF actuation is  $\sim 200 \mu\text{m}$  for the applied voltage of  $\sim 100 \text{ Vpp}$ . This shows that, the major advantage with the PVDF membrane actuation is that high stroke ratio for the micropump can be obtained. However, one of the major disadvantages of using thin films for actuation is that packaging is extremely difficult due to the lack of rigidity. In order to provide support to the PVDF film, the thin films were bonded with solid substrates. In such cases, the pressure generated by the oscillation of the thin film with the solid was not enough to drive the fluid. The fabrication was difficult because of the difficulty in handling the PVDF for bonding and integration with other materials. Also, one had to be careful to not expose the PVDF directly with the medium. Nevertheless, experiments were carried out with PDVF actuated micropump and the feasibility of performing integrated optical detections was studied (Chandrasekaran and Packirisamy, 2009b). However, these above mentioned drawbacks necessitated the development of a more robust piezo actuation system, and therefore, given the difficulties of handling a piezoelectric thin film, the micropump was fabricated using Lead Zirconate Titanate (PZT) disc as the actuator.

PZT has been one of the most common Piezo-materials used for actuation in micropump applications. Herein, the Piezo disc was bonded to a glass diaphragm which forms the enclosing layer for the microfluidic chamber. Even though significantly smaller displacement amplitude was achieved using this method, the main advantage of using PZT-Glass diaphragm is that the system is robust and the packaging is repeatable. Also, through this method of packaging the liquid being transported in the channel does not

come into contact with Piezo substrate and thus the actuation system is inert to the nature and the physics of the liquid that is being transported.

### **3.3.1 Design of the micropump**

The design and the geometry of the chamber is based on three criteria:

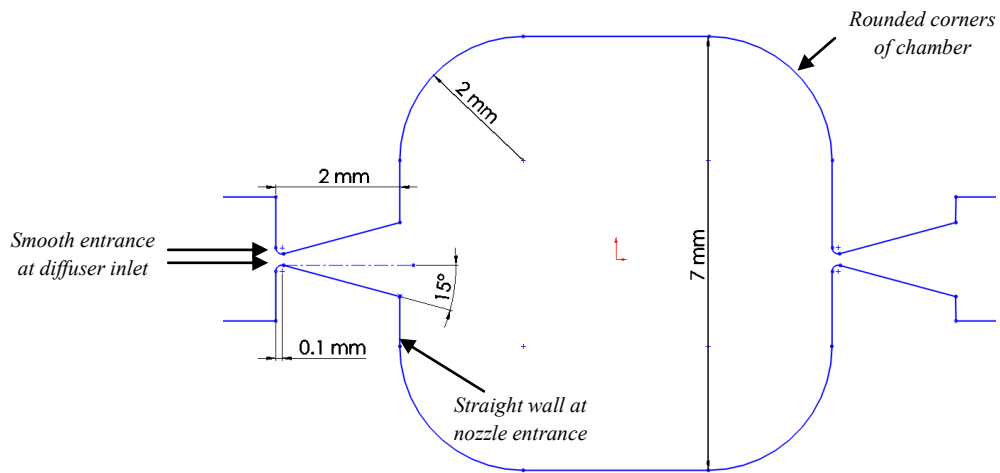
- *The design of the diffuser for maximum flow rectification:* In Chapter 2, it was seen that for obtaining the maximum diffuser efficiency, the diffuser coefficient should be as low as possible whereas the nozzle coefficient should be higher. The pressure drop in the diffuser direction can be reduced by providing a smooth entrance. Therefore, an inlet curvature is provided at the neck of the diffuser. Whereas, for the flow in the nozzle direction, a straight wall at the entrance assists in creating a greater pressure drop. Thus, the diffuser was designed with a smooth radius of 100  $\mu\text{m}$  at the diffuser inlet and a straight wall at the exit. The inlet diffuser width used for the micropump is 100  $\mu\text{m}$  while the length of the diffuser is 2000  $\mu\text{m}$ . In the initial design, a diffuser angle of  $30^\circ$  was used.

- *Non-stagnant flow within the chamber:* In order to achieve maximum flow rate, from the pump it is important to remove any recirculating or stagnant flow behavior within the micropump. Though it is possible to create a variety of micropump chamber geometries, it must be ensured that the geometry also meets the above two mentioned criteria, namely,

Therefore, the corners of the chamber were rounded off, in such a way that the stagnant zones of the flow were removed and at the same time, the flow in the nozzle direction is provided with a straight walled entrance for maximizing sudden pressure drop. In the present design, the total chamber size is  $7 \times 7 \text{ mm}^2$  and the corners are rounded off to a radius of 2 mm.

- *The dimension of the PZT actuator:* The diameter of the PZT actuator determines the maximum obtainable deflection of the membrane. Commercially available PZT actuators are of standard sizes and hence, it must be ensured that the chamber of the micropump is designed in such a way so that the boundary conditions of the vibration of the disc support maximum disc deflection. Hence, the size of the chamber was made greater than the size of the actuator in order to obtain a higher deflection and also accommodate minor misalignments during the process of bonding the piezo disc with the membrane. This would result in more elastic boundary condition resulting in higher deflection of the diaphragm.

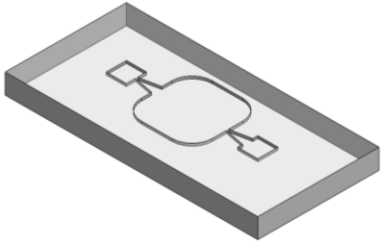
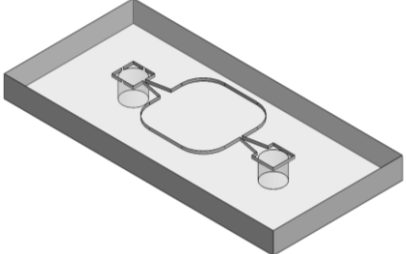
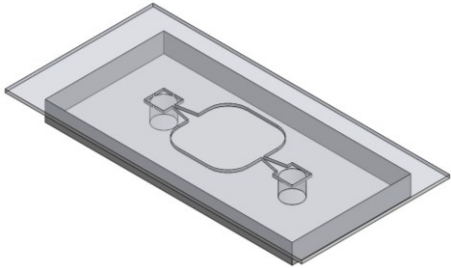
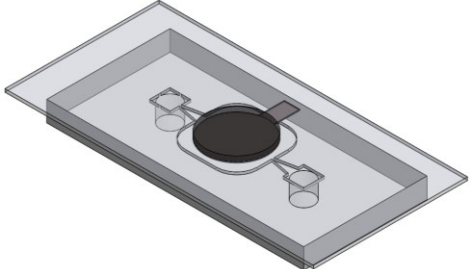
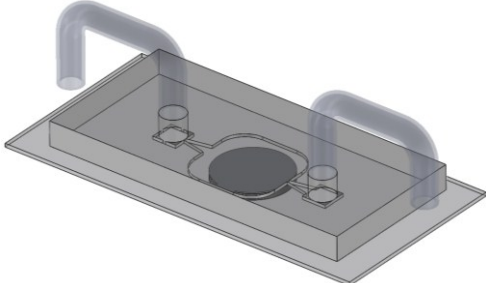
The schematic of layout of the microfluidic base for the micropump, consisting of the pump chamber and the diffusers is as shown in Figure 3.4.



**Figure 3.4:** Layout of the diffuser/nozzle and the micropump chamber

### 3.3.2 Micropump fabrication and assembly

The micropump was fabricated on PDMS platform with the glass membrane forming the diaphragm, which is actuated by a piezo disc. The description of the fabrication of substrates using PDMS substrates was presented in Chapter 2. PDMS micropump base which houses the microfluidic channels, diffusers, and the micropump chamber was fabricated using soft lithography technique using the mold fabricated on silicon with SU8 and DRIE was carried out in order to achieve a total depth of 100  $\mu\text{m}$ . Upon the fabrication of the micropump base, the steps to develop the fully packaged micropump are as described in Table 3.1.

Step #	Process	Schematic
1.	PDMS removal from mould and dicing	
2.	Creation of microfluidic ports	
3.	Bonding with glass cover with semicured PDMS	
4.	Attaching Piezoactuator with the glass diaphragm with conductive epoxy	
5.	Integration of microfluidic interconnection tubes	

**Table 3.1** Fabrication steps for PDMS-Glass Micropump

It is important to follow exactly the same sequence of the packaging procedure as mentioned in Table 3.1. After the fabrication of the PDMS micropump base, ports are created at the inlet and the outlet for the integration with the microfluidic tubes. Thereafter, the microfluidic channels are sealed by attaching a thin glass membrane (Corning cover glass) which is spun with PDMS and allowed to semicure for 3 minutes at 80 °C. Different techniques have been cited in the literature for bonding and integration of the micropump diaphragm. For example, Chen et al. (Chen et al., 2009) have bonded PZT disc with stainless steel which is bonded with PDMS through UV ozone bonding for actuation. However, for all convenient purposes, glass has been the most common packaging material, used with PZT discs for acting as the pump diaphragm. The Piezo-actuating disc (T216-A4NO-173X) to be integrated with the micropump was purchased from Piezosystems Inc., USA. The piezo disc is attached with the glass diaphragm using conductive epoxy. In order to connect the electrical leads to the bottom side of the PZT disc, the conductive epoxy is extended outside the pump region and a thin conducting copper wire is attached using conductive epoxy. The top of the PZT disc is also attached with thin wire with conductive epoxy which forms the other electrode.

The microfluidic tubes are then inserted into the microfluidic ports. Thus, in the micropump assembly, the electrical connections are completely isolated from the microfluidic connection. Polycarbonate sheet was cut to the 2 x 2 in<sup>2</sup> and a hole of 9/16” was drilled. The micropump assembly was then bonded to the polycarbonate support with a double sided adhesive tape. The fully packaged assembly of the micropump is as shown in Figure 3.5.

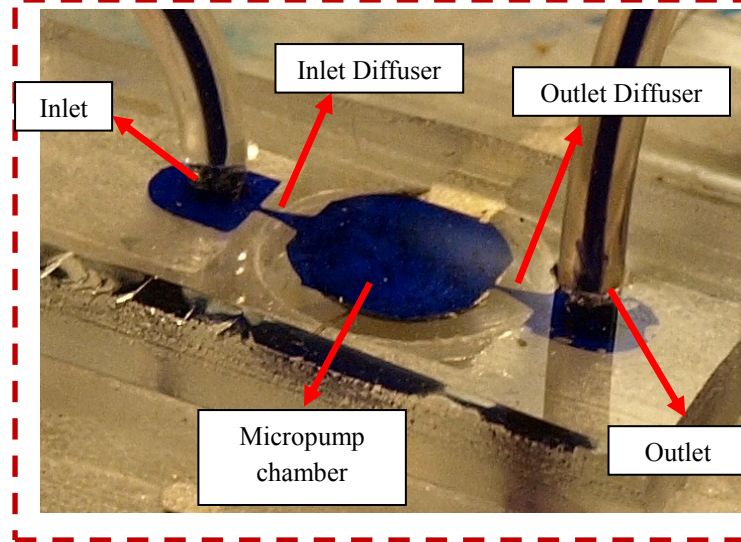
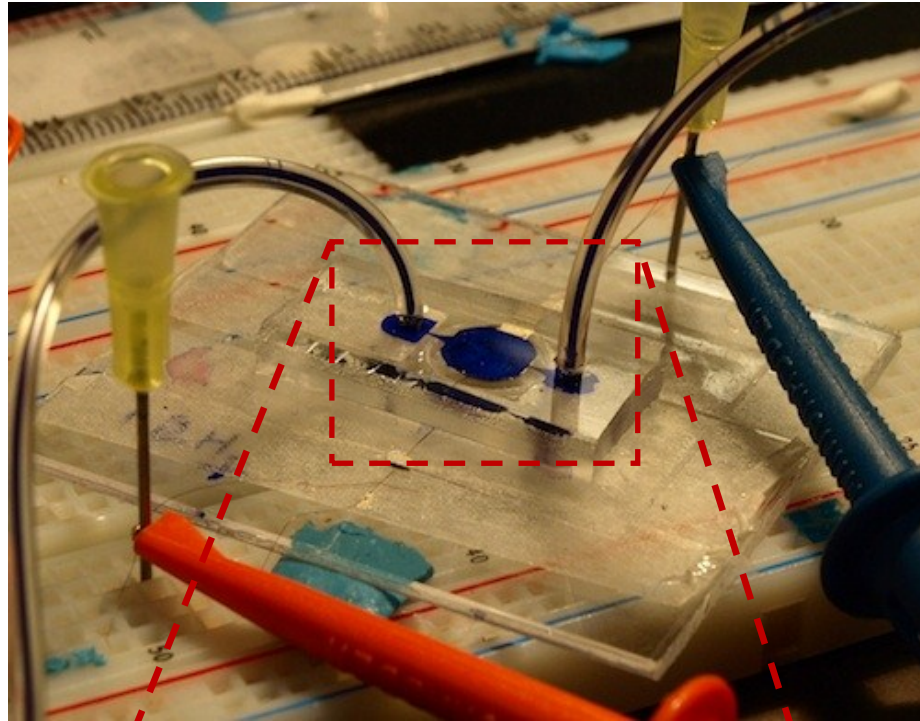


**Figure 3.5:** Fully packaged micropump assembly

### **3.4 Testing of micropump performance**

Experiments carried out to study the performance of the micropump were based on the measurement of the flow rate at different operating conditions, such as the operating frequency, back pressure, and applied voltage. For most of the experiments, DI water was used as the working fluid. The pump pressure generated by the oscillating diaphragm was also measured with respect to frequency and operating voltage and also was calibrated against the measured flow rate.

#### **3.4.1 Experimental setup**

The simplest schematic of the experimental setup for the combined micro-electromechanical integrated microfluidic testing is as shown in Figure 3.6. The experimental setup is classified into three major subsystems integrated with the micropump, namely, the micropump actuation system, the dynamic characterization system and the microfluidic flow measurement system.



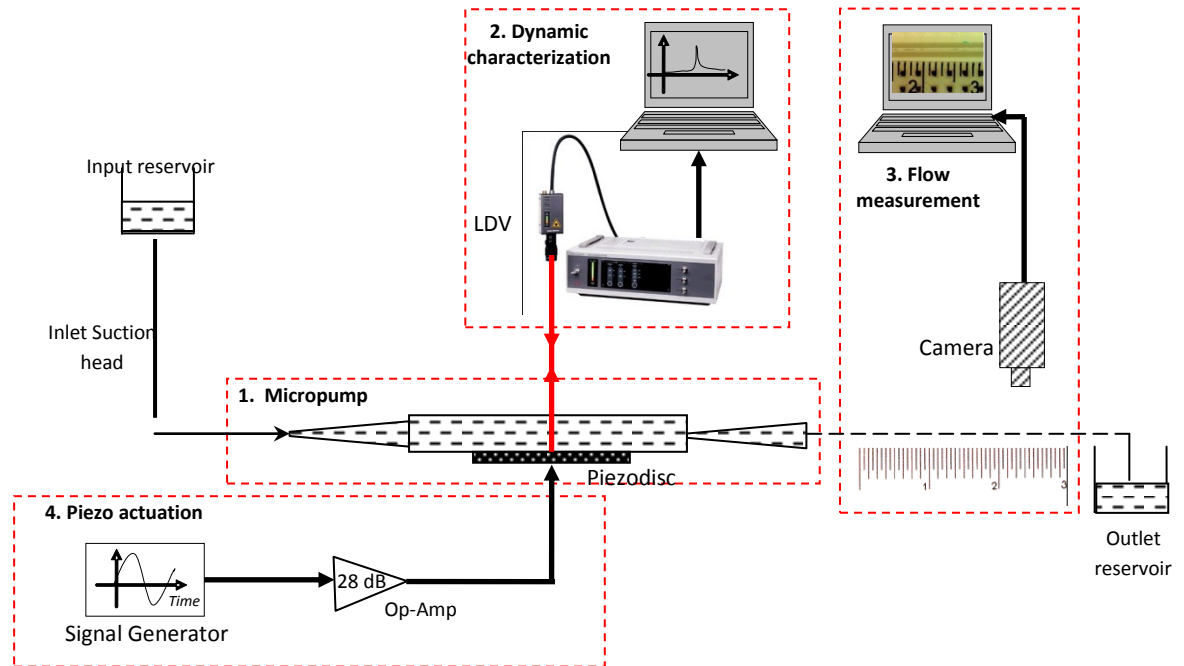


**Figure 3.6:** Schematic of the experimental setup for characterization of the valveless micropumps

### 3.4.1.1 High voltage amplifier system

In order to amplify and deliver a high voltage output to actuate the piezo device, a high voltage AC amplifier was designed (Agudelo, 2008) and used in the circuit. The high voltage amplifier deviates greatly from the ideal electrical characteristics of operational amplifiers. The most important aspect affected is the output resistance of the linear amplifier, which increases considerably, generally exceeding the hundreds of ohms. Therefore, if in a given operation point the low impedance load becomes comparable to the output resistance, there will be a drop in the output voltage of the amplifier.

The high capacitance intrinsic to the piezoelectric material which results in a low impedance load that is very hard to drive at high voltages. Furthermore, since the

impedance varies with the frequency, the driving circuit has to cope up with the bandwidth required by the operation of the piezoelectric device. Also, since the piezoelectric device requires high voltage, a relatively low current implies a large power amplifier. Present amplifier technology usually provides a maximum output of a few *milliAmperes*, which may not be sufficient to comply with the piezoelectric device requirements. The effect of the relatively high output amplifier impedance can be somewhat alleviated by using alternative feedback circuit configurations, however, the basic requirement for an improved actuation performance is the use of a more ideal high voltage amplifier suitable for the present application. Therefore, in order to provide sufficient current to the piezoelectric pump at any frequency without letting the actuation voltage drop, for the stable operation of the micropump, a high voltage AC amplifier circuit as was designed and used for the present setup. The circuit diagram (Agudelo, 2008) for the amplifier is as shown in Figure 3.7. Another motivation to develop the amplifier is that, whereas commercially available amplifiers are bulky, the present setup can be packaged suitably and integrated into a portable system. For the present amplifier, the gain obtained was  $\sim 30$ .

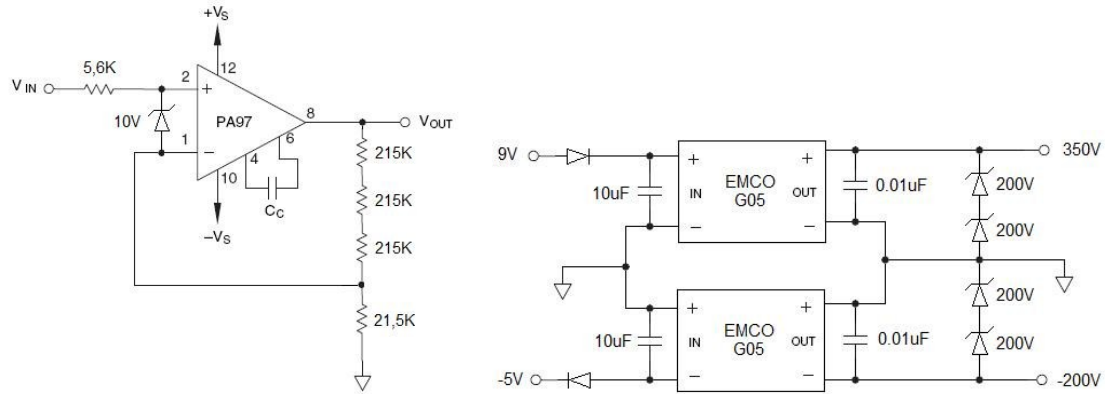
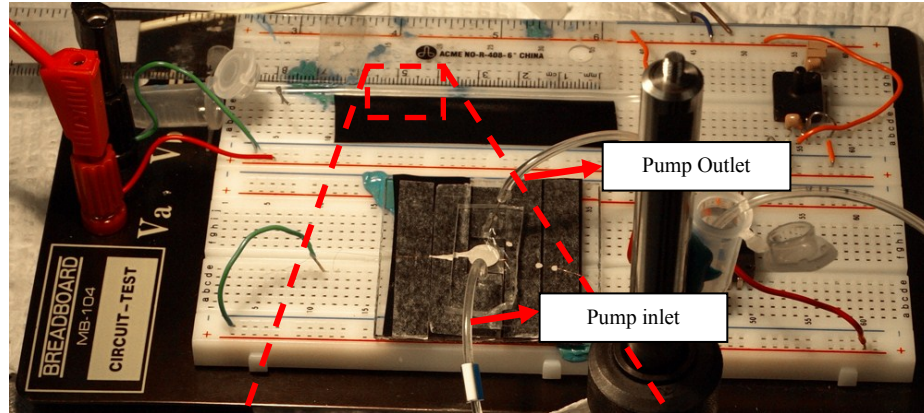


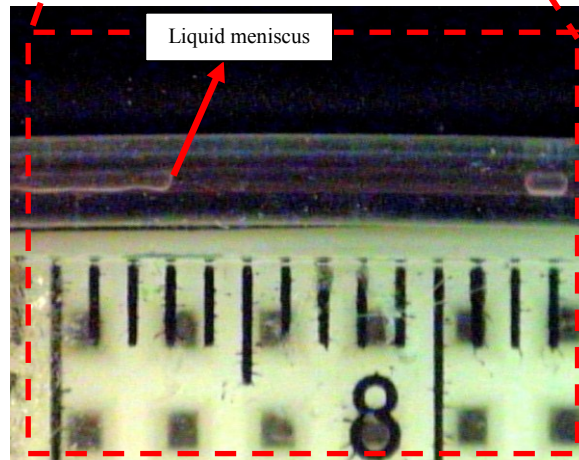
**Figure 3.7:** Circuit diagram of the high voltage amplifier circuit for the actuation system (Agudelo, 2008)

### 3.4.1.2 Flow measurement and dynamic characterization setup

Initial flow characterizations were carried out with the flow meter attached at the exit of the outlet tube from the micropump. However, during subsequent experimentations it was found that the integration of the flow meter caused an additional back pressure to the system, thereby reducing the flow drastically. Therefore, the flow was measured from the outlet tube of the micropump by tracing the movement of the liquid meniscus against a calibrated scale. The setup is as shown in Figure 3.8. Since the tube at the outlet is open, there is no additional back pressure to the flow of the liquid inside the system. The mean average flow is taken over a period of time, by measuring the distance travelled by the lower meniscus of the liquid in the tube, and since the inner diameter of the tubes are known, the total volume of the fluid that is pumped during the process is calculated.



(a)



(b)

**Figure 3.8:** (a) Experimental setup for flow measurement at the micropump outlet (b) Tracking the movement of the liquid meniscus inside the microfluidic tube against a calibrated reading

The dynamic characterization of the micropump behaviour was carried out using a single point Laser Doppler Vibrometer (LDV). The principle of the LDV is that the laser light back scattered from the actuating diaphragm device goes through a shift in frequency by an amount proportional to the velocity of the surface. Thus, the study of the frequency modulated signal is directly a function of the direction of velocity of the surface under investigation. This system can thus be used for the measurement of natural frequency and the deflection amplitude of the actuator. The dynamic characterization setup is as shown

in Figure 3.9. The tests were carried out on a vibration isolation table in order to reduce the effects of external vibrations on the system.

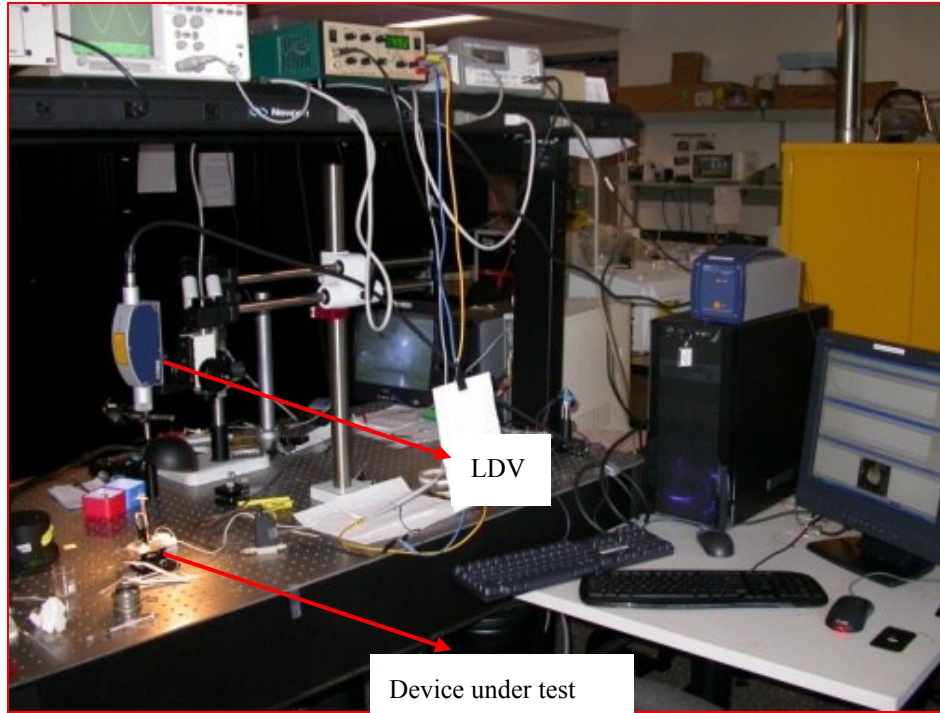


**Figure 3.9:** Experimental setup for dynamic characterization of the micropump

### 3.5 Experimental results

The following sections present the results of the measurement and characterization of the flow rate and dynamic behavior for the valveless micropump under different working conditions.

### 3.5.1 Dynamic behavior of the micropump

Before measuring the flow rate of the valveless micropump, it is important to know the natural frequencies of vibration of the disc and also the relationship between deflection of PZT disk and applied voltage frequency. The frequency sweep plot is as given in Figure 3.10. The natural frequency of oscillation was measured as  $\sim 77$  kHz.

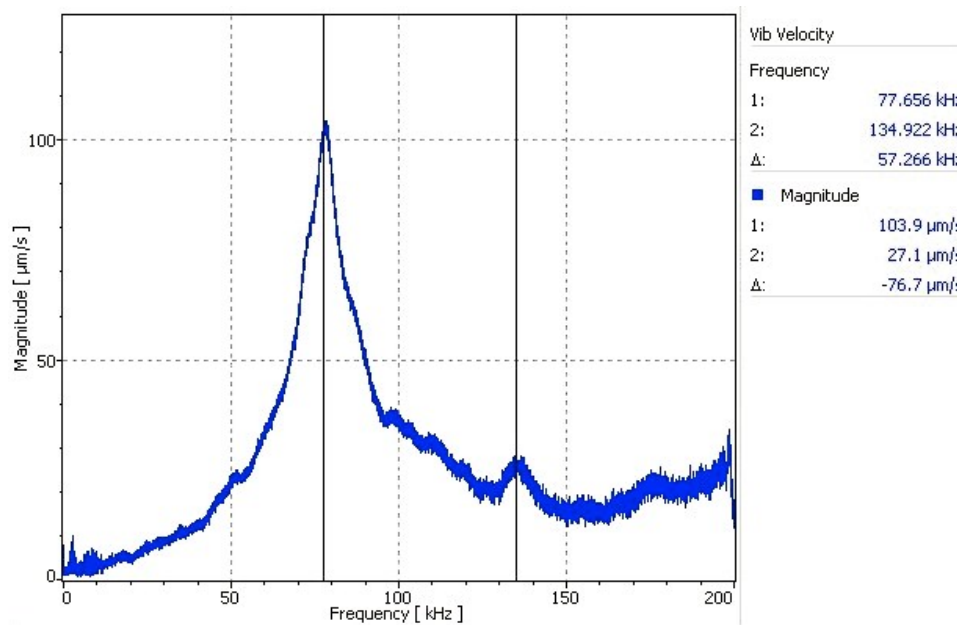


**Figure 3.10:** Plot of the spectral response of the surface velocity for the piezo-actuated micropump

Finite Element Analysis of the system was carried out with ANSYS v13.0 and the results are presented in Table 3.2. There is a very close agreement in the values of the measured natural frequencies for the first and second modes and the simulated results.

	<b>Experimental</b>	<b>FEA</b>	<b>Error</b>
<b>I Mode</b>	77.65 kHz	76.8 kHz	2 %
<b>II Mode</b>	134.92 kHz	137.34 kHz	2.2 %

**Table 3.2:** Comparison of the predicted and the experimental I and II natural frequencies of the micropump

The experiment and the FEA show that the natural frequency of the system is much higher than the operating frequencies of the micropump. Therefore, within the operating frequency range of the micropump, the change in frequency is expected to affect only the flow properties of the fluid and the minor changes in the deflection of the diaphragm due to change in frequency can be neglected.

Measurement of the diaphragm central deflection was carried out with the LDV setup in the voltage range of 120-200 Vpp and a frequency range from 5 Hz to 2500 Hz. Subtracting the external noise at lower frequencies due to external vibrations, the deflection was measured in the frequency range within which the micropump is operated. The average deflection of the micropump at different applied voltages is given in Figure 3.11. At lower voltages, very small deflection is observed till around 120 Vpp, which is not enough to drive the fluid. Also, beyond 200 Vpp, the increase in deflection is not significant, and also, the micropump operation was restricted to less than 200 Vpp, since a very high applied voltage caused electrical breakdown of the system at high frequencies. The deflection of the micropump diaphragm was measured with air and water inside the chamber, as shown in Figure 3.11.

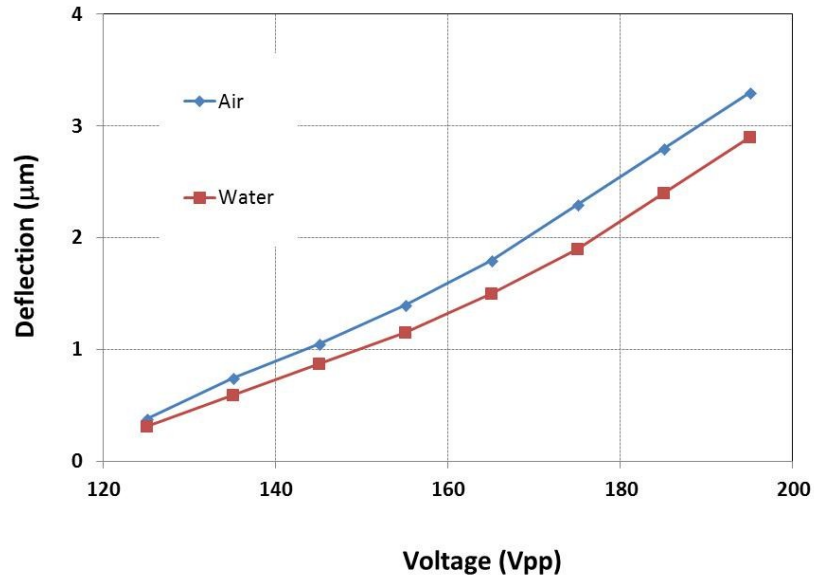


**Figure 3.11:** Plot of the variation of the pump deflection with applied voltage.

### 3.5.2 Measurement of micropump flow rate

The performance of the micropump is determined by its flow rate. The flow rate of the micropump is a characteristic of the rectification produced by the diffuser, pump deflection, operating frequency and the back pressure (i.e the pressure exerted by the system on the liquid moving forward). In most of the mechanical micropump systems, the back pressure to the fluid flow is created by the friction produced in the channels and the outlet tube connection, and the pressure head due to the height of the liquid column at the outlet. It is important to carry out the study of flow rate at zero inlet pressure, which would be close to the real-time application of the device when integrated with the  $\mu$ TAS.

The drive frequency of the micropump is defined as the frequency at which maximum flow rate is obtained. The flow rate ( $\dot{Q}$ ) at zero inlet head, i.e, when there is no pressure exerted at the inlet, was measured for different operating frequencies. The experiments



were repeated three times and the average values of the flow rates were recorded. The results of the flow rate measurements are as shown in Figure 3.12. Maximum flow obtained with the micropump was  $\sim 55$  nL/min for a driving frequency of 2 Hz with an applied voltage of 200 Vpp. The flow rate was also studied by varying the applied voltage at the driving frequency. The variation of flow rate with applied voltage is as shown in Figure 3.13. It can be seen that the flow rate varies significantly for the change in the diaphragm deflection due to the change in voltage. Very insignificant flow rate was obtained for voltage less than 150 Vpp.

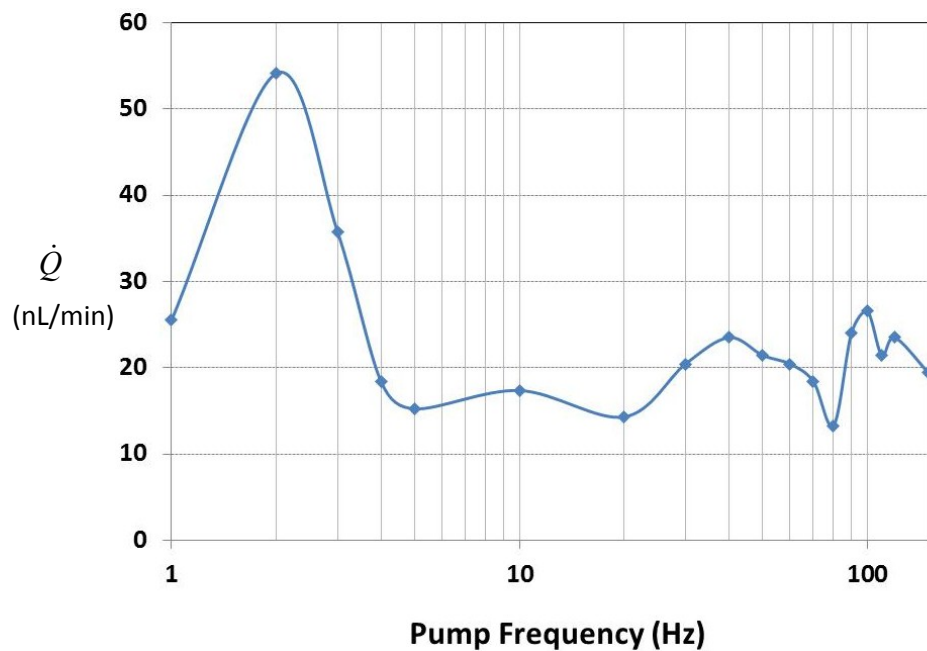


**Figure 3.12:** Plot of variation of flow rate with pump operating frequency

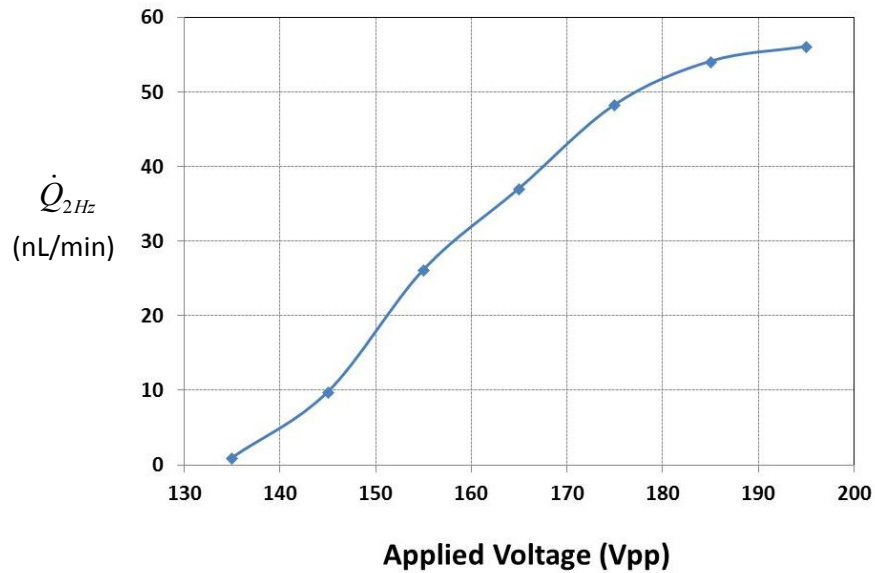


**Figure 3.13:** Plot of variation of flow rate with applied voltage

In most of the micropumps studied so far, the flow rate is calculated against back pressure. The back pressure is defined as the pressure that is exerted at the delivery side, or the outlet of the micropump, against the net forward flow of the liquid. Obviously, as the back pressure increases, the flow rate decreases. In that way, the performance of the micropump is usually calibrated against the maximum workable back pressure.

However, when the micropump is integrated within a  $\mu$ TAS, the back pressure remains constant in such a system and the flow rate is not expected to vary much due to the change in the back pressure. In such a system, in order to overcome the back pressure applied to the micropump flow, the flow rate can be increased only by increasing the pressure head due to the water column at the suction side, i.e. the inlet of the micropump. The schematic of the system is as shown in Figure 3.14.

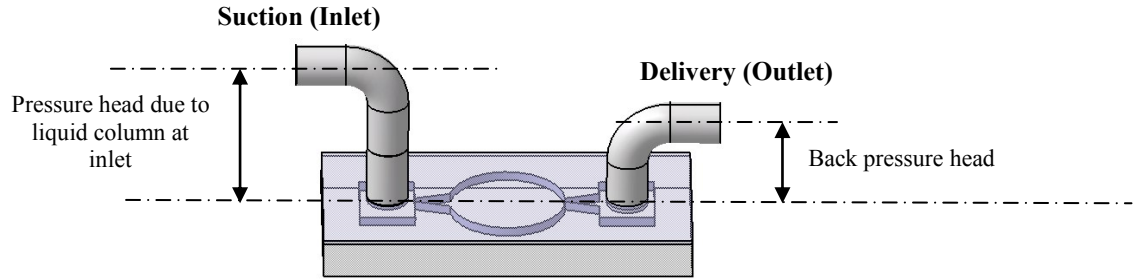


**Figure 3.14:** Schematic of the micropump inlet and outlet pressure heads

For this system, without the application of external pressure, the pressure head can be varied only by the variation of the pressure exerted by the height of the liquid column available at the inlet,  $h_{in}$ .

Thus, the pressure due to the liquid column at the inlet is given as

$$P_{in} = \rho g h_{in} \quad \dots 3.1$$

where  $\rho$  is the density of the liquid and  $g$  is the acceleration due to gravity.

For the present micropump, the flow rate was calculated by varying the pressure available at the inlet of the micropump. The variation of the flow rate with pressure head due to the liquid column at the inlet,  $P_{in}$ , is as shown in Figure 3.15. The flow rate increases linearly as  $P_{in}$  increases.

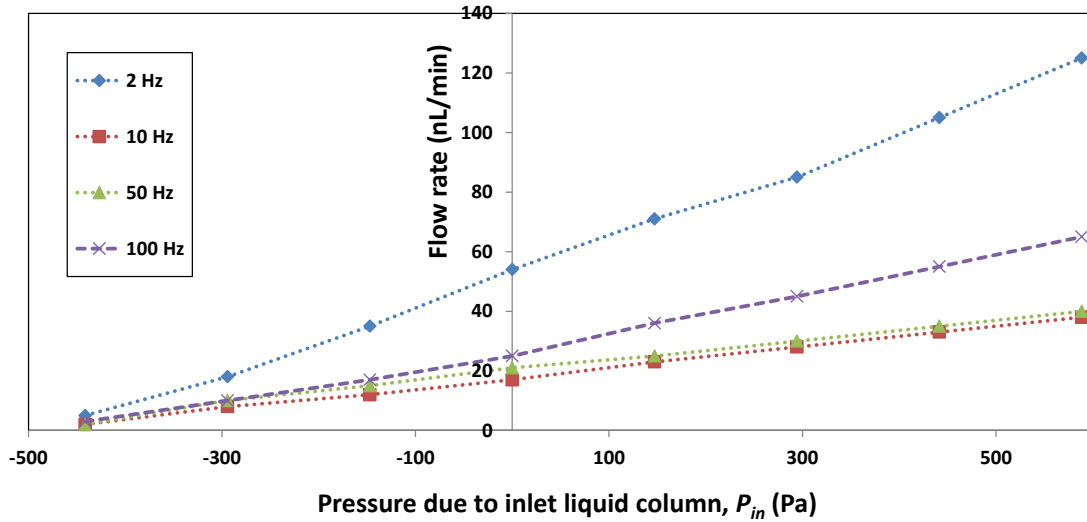


**Figure 3.15:** Variation of the pump flow rate with pressure head due to water column at the micropump inlet, at different operating frequencies.

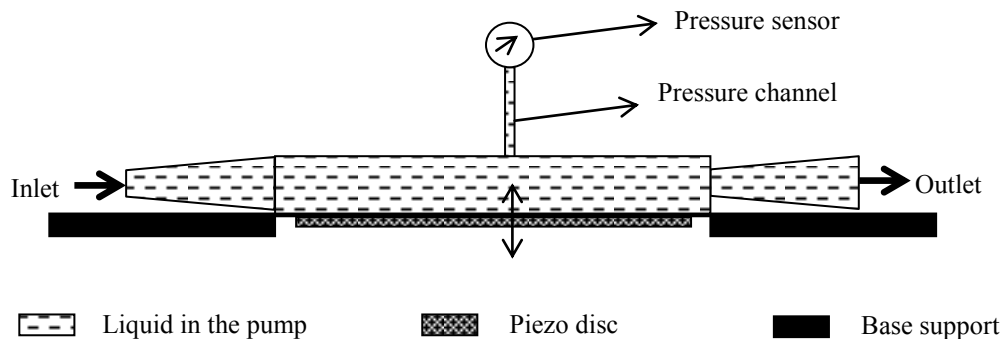
It can also be seen that the maximum pressure that can be overcome by the micropump to produce a forward flow is  $\sim 0.8$  kPa.

### 3.5.3 Measurement of micropump chamber pressure

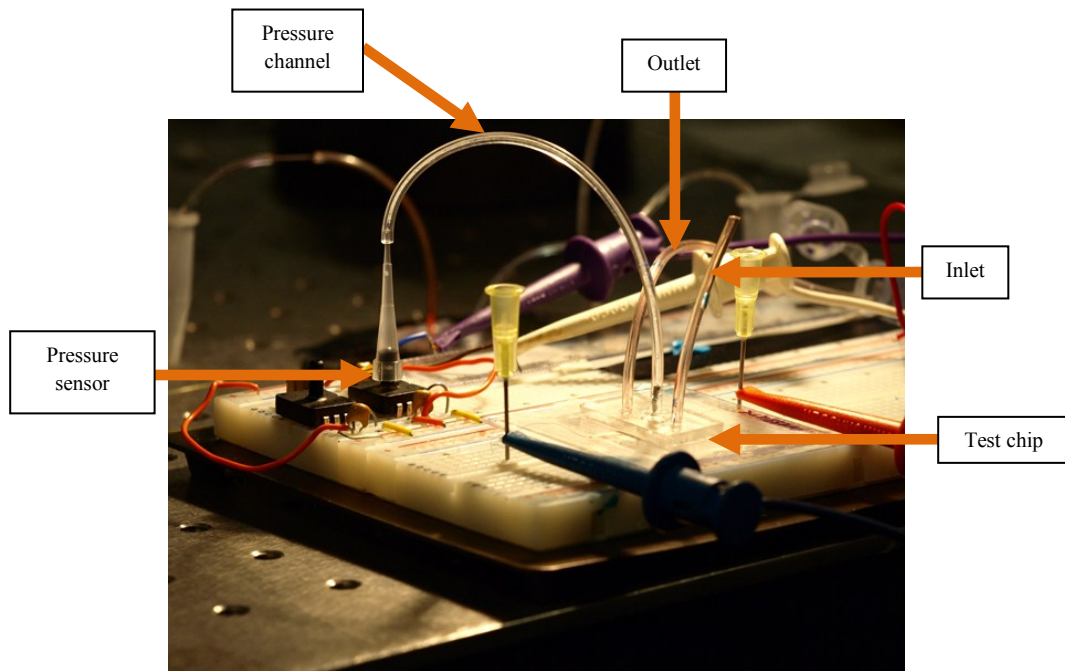
From the previous study, it was seen that the flow rate varies with operating frequency. In order to study the pressure generated by the oscillating diaphragm and its effect on the flow rate at different frequencies, it is important to measure the variation of chamber pressure with the operating frequency.

The schematic of the micropump chamber pressure measurement is as shown in Figure 3.16(a) and the experimental setup for the pressure measurement in the micropump

chamber is as shown in Figure 3.16(b). For the pressure measurement, an independent pressure channel was connected at the top of the micropump chamber to the pressure sensor (Fujikura), as shown in Figure 3.16(b). Prior to connecting the pressure channels, the microfluidic tubes used as the pressure channels were tested for inherent frictional losses, and it was found that the frictional pressure loss in the pressure channels were negligible. Therefore, the pressure sensor directly measures the pressure inside the chamber of the micropump. Also, the pressure channels were integrated with the micropump system in such a way that the setup enables the measurement of chamber pressure without disrupting the main flow stream. The entire assembly of the pressure measurement system, which consists of microfluidic pressure sensor circuit connected with the data acquisition system, was made on a circuit board so as to make a rigid setup.



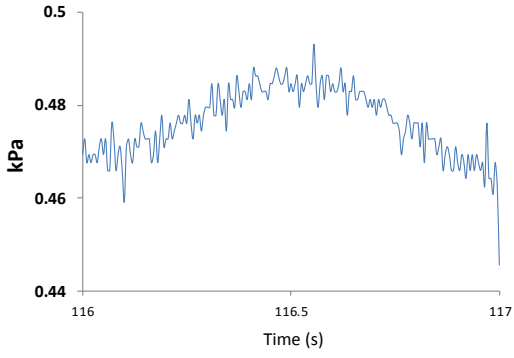
(a) Schematic of the micropump pressure measurement setup



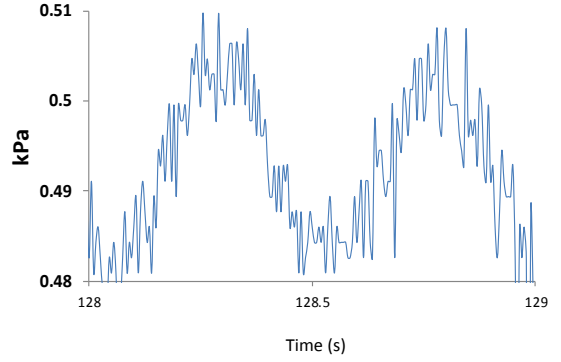
(b) Test setup

**Figure 3.16:** (a) Schematic of the micropump pressure measurement setup (b) Experimental setup for the micropump chamber pressure measurement

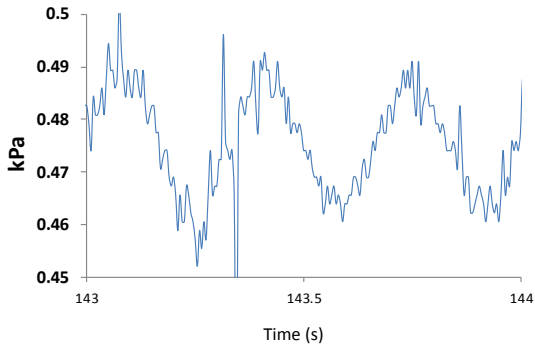
The results of the variation in the chamber pressure at different operating frequencies are as presented in Figure 3.17. The y-axis represents the pressure in kPa and the x-axis represents the arbitrary time of the micropump operation in seconds.



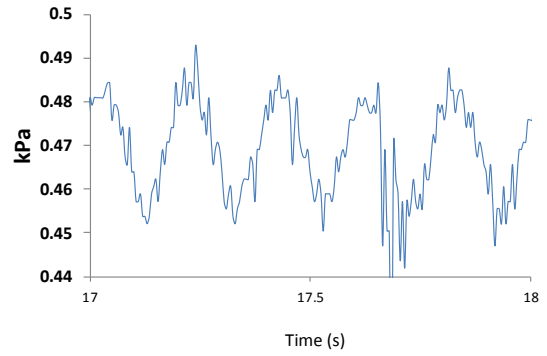
(a) 1 Hz



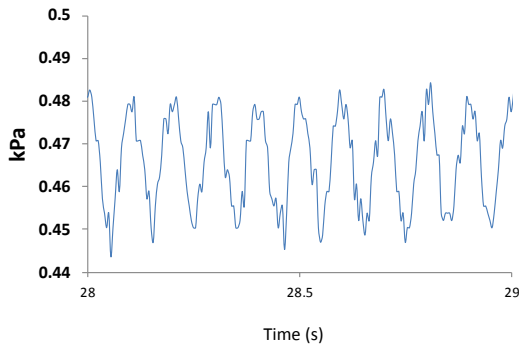
(b) 2 Hz



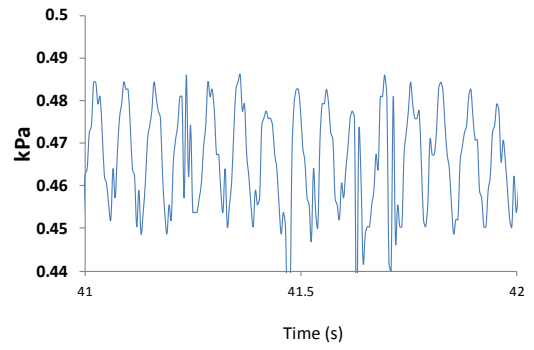
(c) 3 Hz



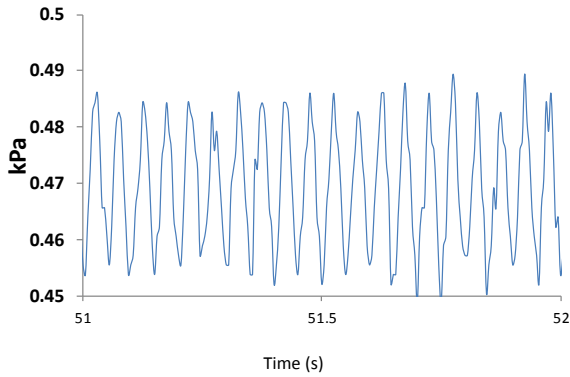
(d) 5 Hz



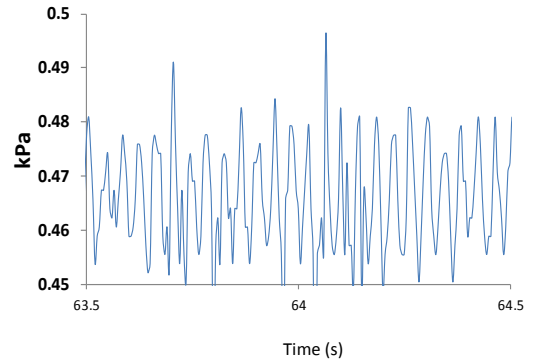
(e) 10 Hz



(f) 15 Hz



(g) 20 Hz



(h) 25 Hz

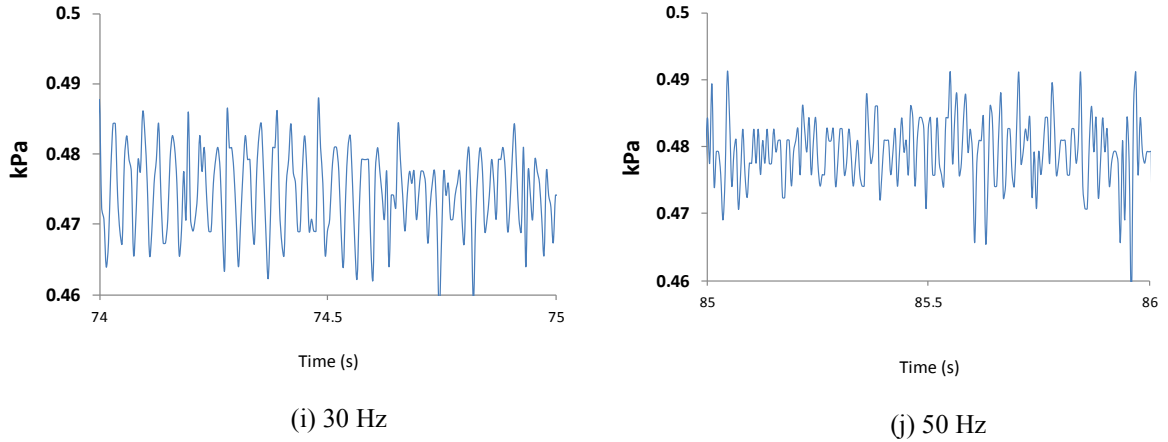


**Figure 3.17:** Plot of variation of micropump chamber pressure for different actuation frequencies

During pumping, the micropump chamber pressure can be defined by the relation

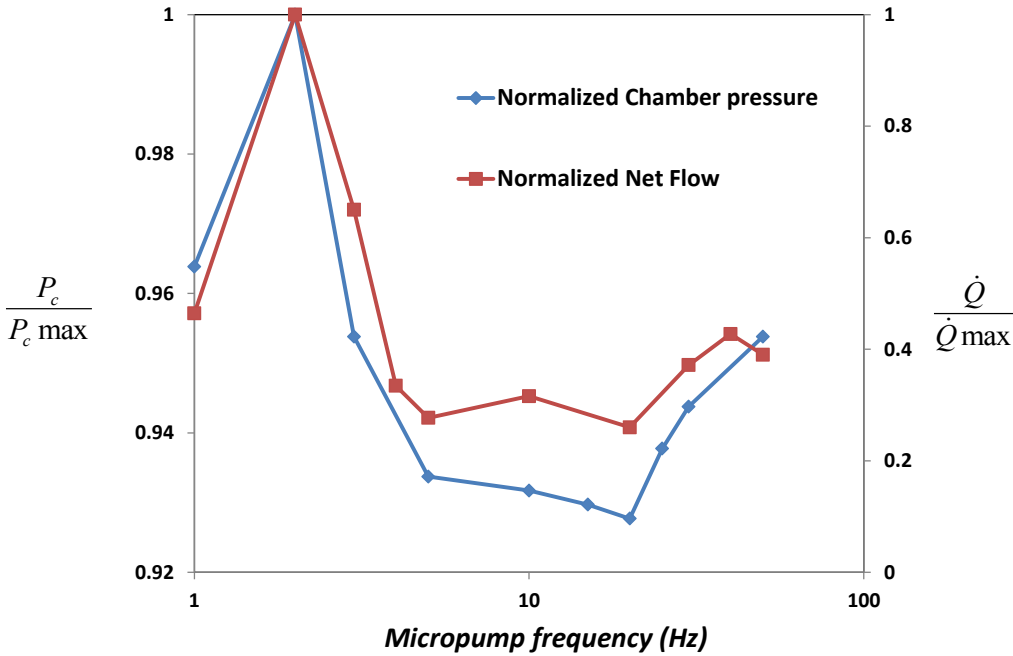
$$P_o = P_c + dP_c \text{Sin}(\omega_p t) \quad \dots 3.2$$

Where  $P_c$  is mean chamber pressure and the  $dP_c$  is the amplitude of pressure variation due to the sinusoidal oscillation of the diaphragm.  $P_c$  causes the net forward flow of the fluid, the  $dP_c$  accounts for the oscillatory motion of the fluid.

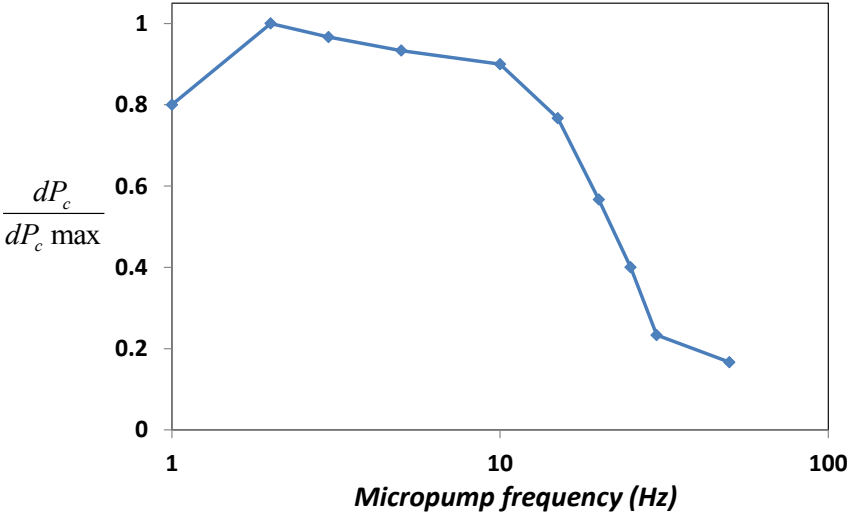
The plot of variation of  $P_c$  and  $dP_c$  with micropump frequency is shown in Figure 3.18. Herein, the chamber pressure and the pressure variation amplitude have been normalized with respect to the maximum values. It can be seen that the maximum chamber pressure is obtained at the frequency of 2 Hz. A plot of normalized flow rate shows that the behavior of the flow rate is very similar to that of the chamber pressure. Thus the driving frequency of the pump is 2 Hz, when the maximum flow rate is obtained due to the generation of maximum pump pressure. It can also be seen that, at the driving frequency, the amplitude of pressure variation is the maximum due to the sinusoidal motion of the



diaphragm, thereby producing the maximum fluid to flow across the diffuser during one cycle, which therefore enables better flow rectification from the diffusers.



(a)



(b)

Figure 3.18: Variation of pressure rise and flow rate with pump operating frequency

### 3.5.4 Effect of diffuser geometry on micropump flow rate

In order to study the effect of the diffuser geometry on the performance of the micropump, the micropump flow rate was studied for different diffusers with different geometric tuning (Chandrasekaran and Packirisamy, 2011). Three different configurations for the micropump was chosen, namely the convex with  $\beta_{cx} = 0.4$ , concave with  $\beta_{cv} = 1.5$  and the straight walled diffuser. The flow rate was measured for all the three designs. The inlet pressure head and the back pressure water head were maintained at zero. In this way, it was ensured that the variation in the flow rate is due to the effect of diffuser alone. The results of the flow rate measurement are as shown in Figure 3.19.

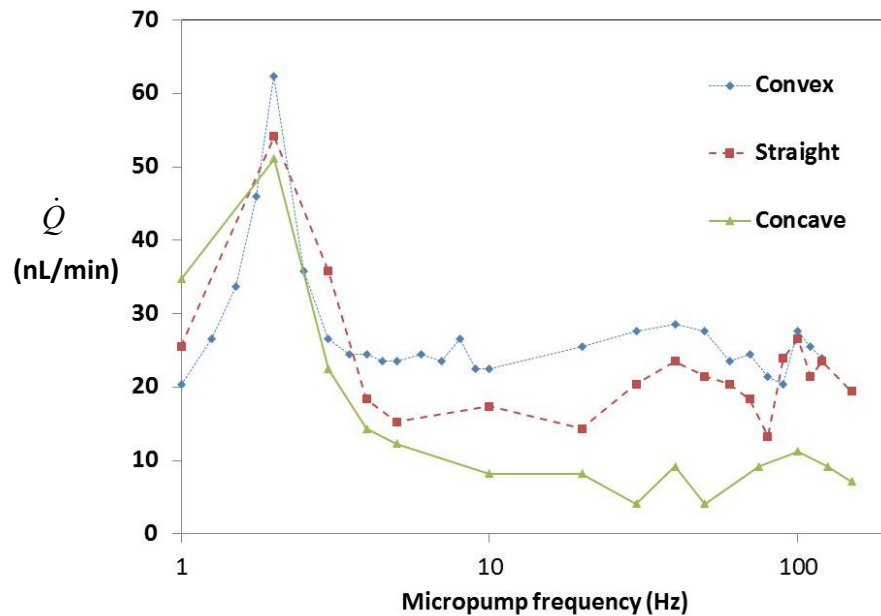


**Figure 3.19:** Plot of the flow rate as a function of driving frequency for micropump with different diffuser configurations

As seen in chapter 2, the finite element analysis results show that, the pressure coefficients of the convex diffuser is always greater than straight diffuser, which is greater than concave diffuser. In the above experiment, the operating frequency was increased continuously. It was also seen from the pressure measurements that the pressure generated is maximum at the driving frequency. It is possible for frequencies less than the driving frequency not enough pressure is generated for flow rectification by the diffusers, and hence the diffuser configuration with least pressure drop, which in this case is the concave diffuser (Chandrasekaran and Packirisamy, 2011), offers greater flow.

At the driving frequency, once the base pressure is reached, the micropump with convex diffuser gives the maximum flow rate, and the straight diffuser performs better than the concave diffuser. The same trend is also observed at higher frequencies and the difference in the flow rates due to flow rectification of the different diffusers increase significantly with operating frequency.

This shows that there is a clear relationship between the diffuser configuration of the valveless micropump, and the Reynolds number of fluid, which is influenced by the diaphragm deflection, and its operating frequency, in order to obtain a significant flow rate in the micropump. For any given micropump, there exists an optimum pressure distribution depending upon the combination of the micropump geometry, operating conditions and fluid parameters, which favors the maximum flow. For the chosen micropump configuration, this occurs at an operating frequency of 2 Hz.

### **3.5 Effect of surface affinity on micropump flow**

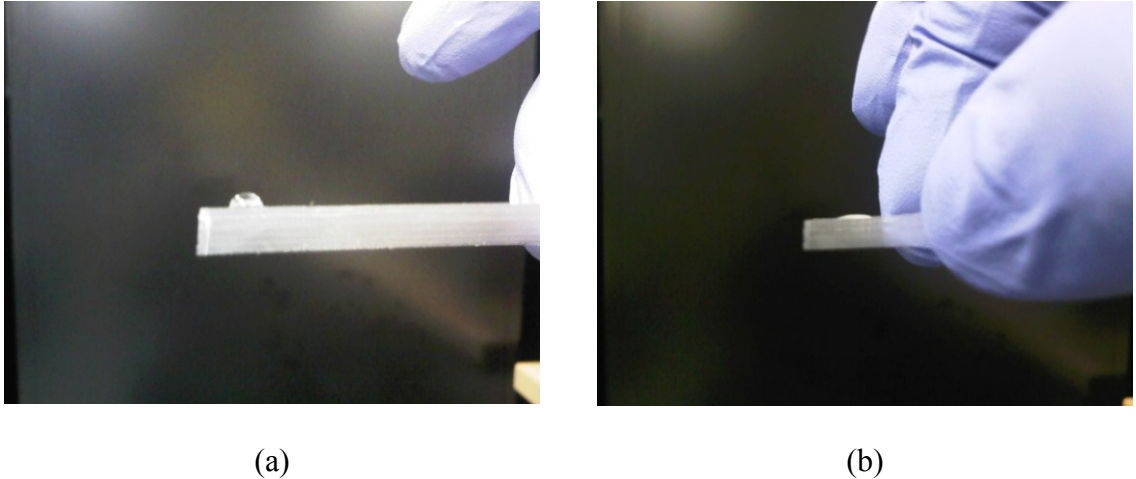
As mentioned in Section 3.1, early works on mechanical micropumps have been carried out with silicon due to its high performance. However, with the high fabrication costs, silicon based micropumps have been replaced with micropumps based on polymers such as PDMS. The experiments carried out on PDMS based micropumps, as presented in the previous sections, have shown that PDMS micropumps have the potential for low cost, fabricable devices, for easy integration with the  $\mu$ TAS.

From the experiments carried out so far, it is also clear that several other factors such as self-priming, bubble tolerance, high flow and pressure capabilities of the micropump need to be addressed effectively in order to obtain a significant flow rate from the micropump. Wearing of the surface has been one of the prime issues with PDMS based micropumps (Woiass 2005) which therefore restrict the performance of the system. Most of the PDMS used are treated under oxygen plasma for rendering the surface hydrophilic. However, the properties of the surface changes with ‘aging’ and the resulting differential surface wettability could affect the performance of the microfluidic system. Another major problem with the PDMS based micropumps is the release of small gas bubbles which deteriorate the flow rate of the micropump tremendously (Shen, Liu 2008). The main aim of this work is to study how the performance of the PDMS micropump is affected by the wettability properties of the micropump surfaces, and to understand if the performance of the PDMS micropump can be improved through surface modification techniques.

In order to study the effect of surface wettability on the micropump performance, two types of micropump chamber surfaces were prepared. Herein, the effects of hydrophilic and hydrophobic micropump surfaces are studied, on the flow rate and the bubble generation capabilities. The nascent PDMS is by itself hydrophobic. Therefore, in order to render the micropump hydrophilic, oxygen plasma treatment of the surface was carried out on the fabricated PDMS micropump chip prior to the packaging of the micropump which is described in Section 3.2.

The PDMS sample to be treated with oxygen plasma was cleaned with DI water and dried with inert gas. The sample was then placed inside the chamber of the plasma cleaner (Harrick Plasma) and vacuumized. When the pressure inside the chamber reaches  $\sim 100$  mTorr, a flux of Oxygen gas is introduced into the chamber for 60 sec in the RF oscillating electric field of power of 29.6 W generated in the gas region. This process changes the surface from hydrophobic to hydrophilic.

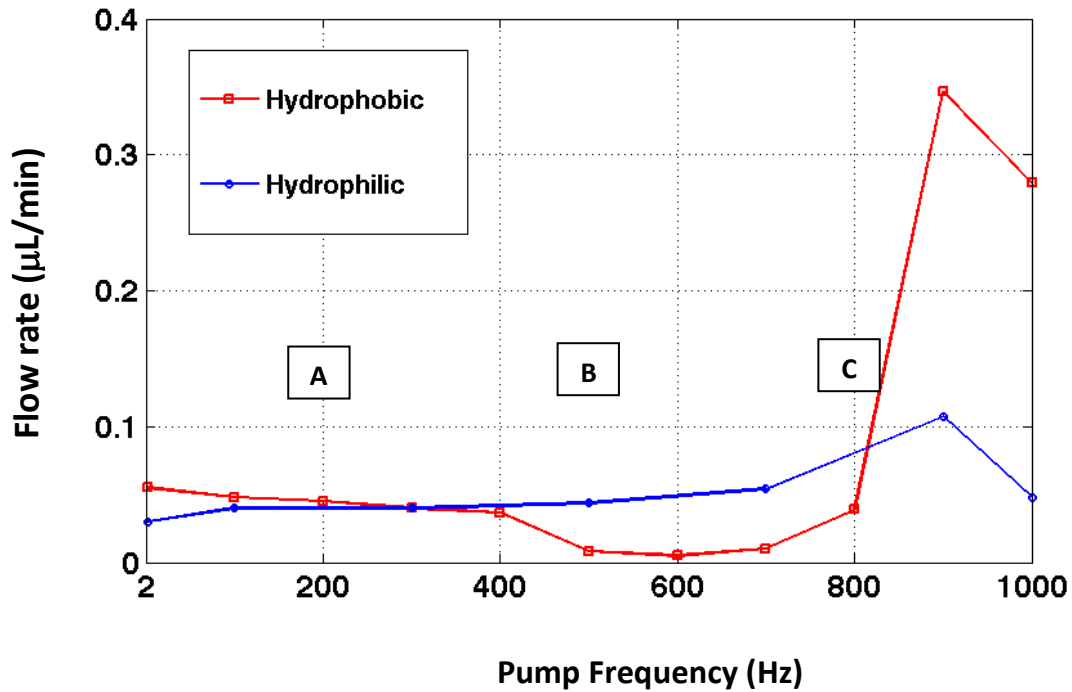
The contact angles of the hydrophilic and the hydrophobic channels are as shown in Figure 3.20. It can be seen that the contact angle made by water with the hydrophilic surface after oxygen plasma treatment, is around  $5^\circ$  as compared to the contact angle made by water drop with the original PDMS sample used without plasma treatment, which is around  $90^\circ$ .



**Figure 3.20:** Demonstration of contact angle of water droplet on PDMS with (a) Hydrophobic PDMS (b) Hydrophilic PDMS

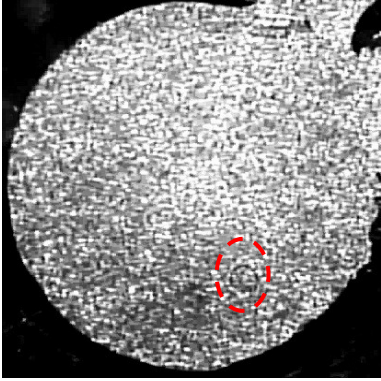
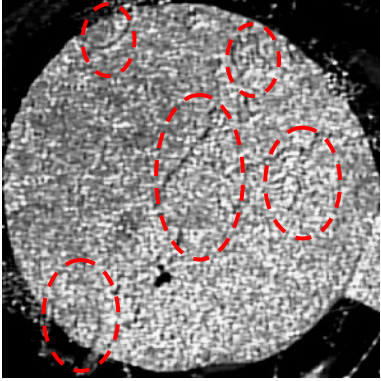
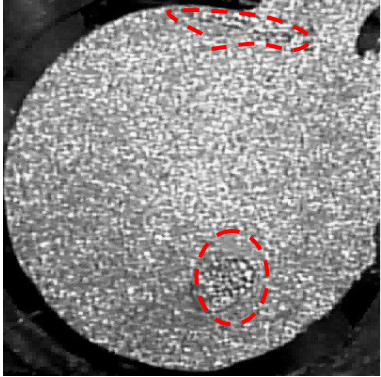
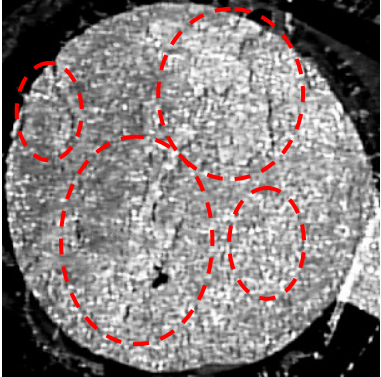
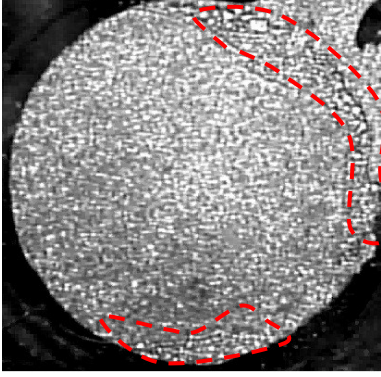
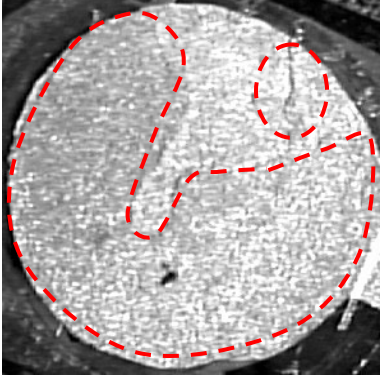
In order to measure the flow rate from the hydrophilic and the hydrophobic micropumps, the systems were primed with DI water and the pumps were operated with increasing operating frequencies. The setup for measuring the flow rate is the same as described before, i.e by tracing the movement of the water meniscus at the outlet tube. It is important that both the hydrophilic and the hydrophobic micropump systems operate with similar pressure at the inlet and back pressures.

The results of the flow rate measurement and the images taken of the micropump chamber which show the generation of the bubbles at different stages, are as shown in Figure 3.21 and Figure 3.22 respectively.



**Figure 3.21:** Plot of variation of the net flow with the pump frequency for hydrophilic and hydrophobic micropumps

For frequencies less than 200 Hz, the flow rate of the hydrophobic micropump is higher than the hydrophilic micropump. However, as the frequency is increased, the flow rate obtained with hydrophobic micropump decreases. The decrease in the flow rate for hydrophobic micropumps also coincides with the inception of cavitation bubbles in the pump chamber. For hydrophilic micropumps, there is a slight increase in the flow rate with increase in frequency till 700 Hz. Figure 3.23 shows the bubbles formed with hydrophilic and hydrophobic micropumps, at different stages of micropumping indicated in Figure 3.22. The regions of micropump chamber occupied with bubbles are indicated with dotted lines.

Stage	Hydrophilic	Hydrophobic
A		
B		
C		

**Figure 3.22:** Images of the micropump chamber at different stages of pumping indicated in Figure 3.21, for hydrophilic and hydrophobic micropumps



The formation of bubbles inside the micropump chamber was quantified using *bubble fraction*. Herein, the bubble fraction is defined as the ratio of the area of the micropump chamber that is occupied by the bubble to the total chamber area. Thus, the tendency of the micropump to generate bubbles inside the chamber is denoted by its bubble fraction. The plot of the variation of the bubble fraction with operating frequency, for both hydrophilic and hydrophobic pumps, is as shown in Figure 3.23.

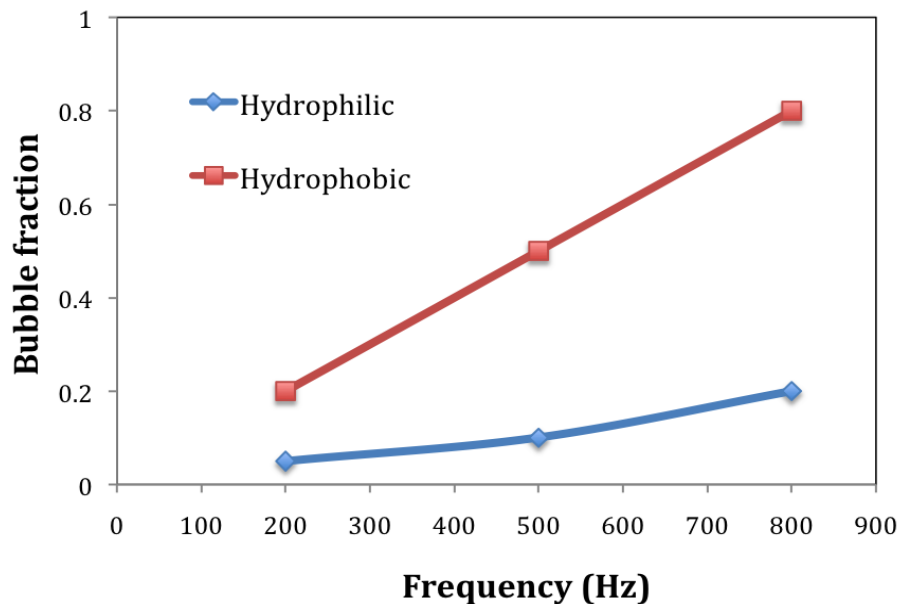


**Figure 3.23:** Plot of variation of the bubble fraction with micropump operating frequency for hydrophilic and hydrophobic micropumps

At lower frequencies, the tendency of hydrophilic surface to generate bubbles in the chamber is very less, whereas hydrophobic surface generates significant amount of bubbles to choke the flow. One possible explanation for the choking of the flow due to the generation of gas bubbles is that much of the energy from the micropump diaphragm is

taken up for the compression and expansion of the bubbles, which therefore retards the flow. As the operating frequency is increased, it can be seen that while more bubbles are generated with the hydrophobic micropump to decrease the flow rate tremendously, hydrophilic surface exhibits the least tendency to form gas bubbles. However since more energy from the micropump is available, there is a slight increase in the flow rate for hydrophilic micropumps with increase in operating frequency.

At higher frequencies, the cavitation bubbles formed in the chamber collapses. In that process, the energy released during the cavitation bubble collapse pushes the liquid out of the chamber. Since the hydrophobic surface repels water, the net flow obtained with the hydrophobic micropump is much larger than the hydrophilic micropump.

Therefore, from the surface wettability point of view, the hydrophobic surface improves the flow rate. This observation matches well with the observations of Cho et al. (2006). A possible explanation for this phenomenon is that, the contact angle made by the water drops with the surface is larger in hydrophobic surfaces and hence it is possible that the chances of occurrence of voids between the liquid drops and the surface increases, thereby producing more cavitation bubbles. The bubble generation in the hydrophobic micropumps retards the flow and decreases the flow rate tremendously. For hydrophilic micropump surface though, there are no bubbles generated, the flow rate slightly increases with the pumping frequency. Therefore, this shows that there is a very strong relationship between the flow rate and the generation of cavitation bubbles in the micropump, which warrants further detailed study.

### 3.6 Conclusion

In this chapter, the design, fabrication and testing of a Piezoelectric Actuated Valveless Micropump (PAVM) was presented. The micropump was fabricated on PDMS platform with a piezo disc actuating a glass diaphragm. Flow rectification is brought about by the diffuser pair for the micropump. The micropump performance was studied by the measurement of flow rate under different operating conditions. At zero inlet pressure, a flow rate of 55 nL/min was produced at a driving frequency of 2 Hz.

This chapter also presents the pioneering method to measure the pressure of the micropump chamber due to the oscillating diaphragm and it can be clearly seen that the net flow produced by the micropump is highly dependent on the pressure generated by the oscillating diaphragm. The diffuser geometry has a significant effect over the performance of the micropump and there is a very strong relationship between the flow rectification due to the diffusers and the mechanical behavior of the actuator, namely deflection and operating frequency.

The effect of surface wettability on the performance of the micropump was also studied. At driving frequency, hydrophobic micropumps perform better than their hydrophilic counterparts. It was found that hydrophobic micropumps offered better flow than hydrophilic micropumps. It is also well known that oxygen plasma treated PDMS surface slowly reverts back to the hydrophobic state with time, due to 'aging'. Therefore, during this transition, given that some of the portions of the micropump chamber surface retain

their hydrophilicity for longer, an uneven surface wettability develops due to which priming of the pump becomes difficult as the liquid prefers hydrophilic zones of the micropump than the hydrophobic. It was observed during the experiments that insufficient priming tremendously reduces the flow rate of the system as the liquid oscillates within the chamber itself. This is another reason for preferring hydrophobic PDMS micropump over hydrophilic.

During the study on the effect of surface wettability on the micropump performance, it was observed that the flow rate increases significantly as the frequency is increased. This phenomenon also corresponds to the collapse of the bubbles formed due to cavitation in micropump. It is very important to mark a clear distinction between flow due to pumping and impulsive flow induced due to cavitation. Kim et al. (2004) have reported on the observation of two peaks in the flow rates with varying frequency. It can also be observed that in that report, the second peak is observed at a much higher frequency (2.5 kHz) than the first peak, despite the deflection of the diaphragm being much smaller at higher frequency. Though the systems under comparison are not quite similar, and the working fluid used by Kim et al. is methanol than water, a similar trend is observed for the flow rate obtained with the micropump with increasing frequencies. It was also found that the collapse of the bubbles caused an impulsive flow out of the micropump chamber. This warrants further study on the behavior of cavitation and bubble formation in micropumps. More results on the cavitation behavior in the micropumps are presented in the next chapter.

# Study of Cavitation Behavior in Valveless Micropumps

### 4.1. Introduction

Among the different types of micropumps (Laser, Santiago 2004) used in Micro-Total Analysis Systems ( $\mu$ TAS), mechanical valveless micropumps that work on the principle of oscillating diaphragms with nozzle/diffuser flow rectification elements, as described in Chapter 3, have several advantages such as simplicity of implementation, immunity to the nature of liquid transported, generation of high flow rates, lack of fatigue induced failure, among others, which make them very suitable for biological applications such as biofluidic transport, targeted drug delivery, etc. One of the important factors that affect the performance of a mechanical micropump is cavitation.

Cavitation is referred to the formation of the vapor bubbles and their subsequent collapse due to the drop in the localized pressure below the vapor pressure of the liquid under amicable conditions favoring such a phenomenon. In reciprocating diaphragm micropumps, the effect of cavitation is coupled with the mechanical vibration behavior of the oscillating diaphragm. Thus, the cavitation could have a significant effect due to the higher velocities associated with oscillation of the micropump diaphragm, thereby affecting the performance of the micropump drastically and alter the flow behavior. Though cavitation is a common occurrence in micropumping, this is one of the least

understood of all pumping phenomena, and very limited progress has been made to study the behavior of cavitation in micropumps. Cavitation can also occur in all liquids, including biological fluids and therefore, it is important to study the phenomenon of cavitation in detail for micropumps and consider the effects of cavitation for all mechanical micropump designs for biological applications.

Cavitation phenomenon has been extensively studied and researched upon during the last few decades in fluid machinery and macroscale pumping systems. The occurrence of cavitation has been reported in several works on valveless micropumps (van der Wijngaart et al. 2000), (Eames et al. 2009), (Olsson et al. 1997). However, there has been no dedicated study on cavitation in micropumps and its effects on the performance of the micropump. This chapter presents the study of cavitation behavior in mechanical valveless micropump, extending the macroscale pumping principles as applicable in the microscale. The aim of the present work is to analyze the cavitation behavior in micropumps, to identify the cavitating flow patterns for different operating conditions of the micropump, and to study the effects of cavitation on the performance of the micropump. The following sections of this chapter present the theory of cavitation in valveless micropumps, experimental investigation of the different stages of cavitation in valveless micropumps from the cavitation inception to the growth and collapse of cavitation and the phenomenon of supercavitation in micropumps., effects of cavitation in micropumps and also some of the chemical and biological applications of cavitation which can be used for  $\mu$ TAS.

## **4.2. Cavitation theory for micropumps**

The valveless micropump system described herein basically consists of a pump chamber with an oscillating diaphragm forced by a piezoelectric device and a microdiffuser/nozzle pair. Piezoelectric actuation is proposed for present system due to many advantages, such as very short response time, high actuation, and feasibility of operating at higher frequencies among others. The flow occurs from the suction side to the delivery side through the micropump chamber, and the pulsating flow is translated into a unidirectional flow by the combination of a volumetric change to the pump chamber and the asymmetric pressure drop across the microdiffuser diffuser/nozzle elements during one operating cycle (Wang et al. 2009).

Therefore, the main parameters on which the performance of the mechanical valveless micropump depends upon are the dynamic properties of the actuator, viz. deflection and operating frequency, back pressure, geometry of the microdiffuser pair, properties of the working fluid and the internal resistance offered to the fluid flow by the system components and connecting tubes.

During cavitation, the classical theory for flow in valveless micropump will not be valid as the system transforms itself into dual phase flow. Therefore, in order to study the behavior of the micropump during cavitation, the classical macroscale cavitation theory for pumps is applied in the microscale to the present micropump configuration. The

schematic of the energy level diagram of the valveless micropump system under an open loop configuration is as shown in Figure 4.1.

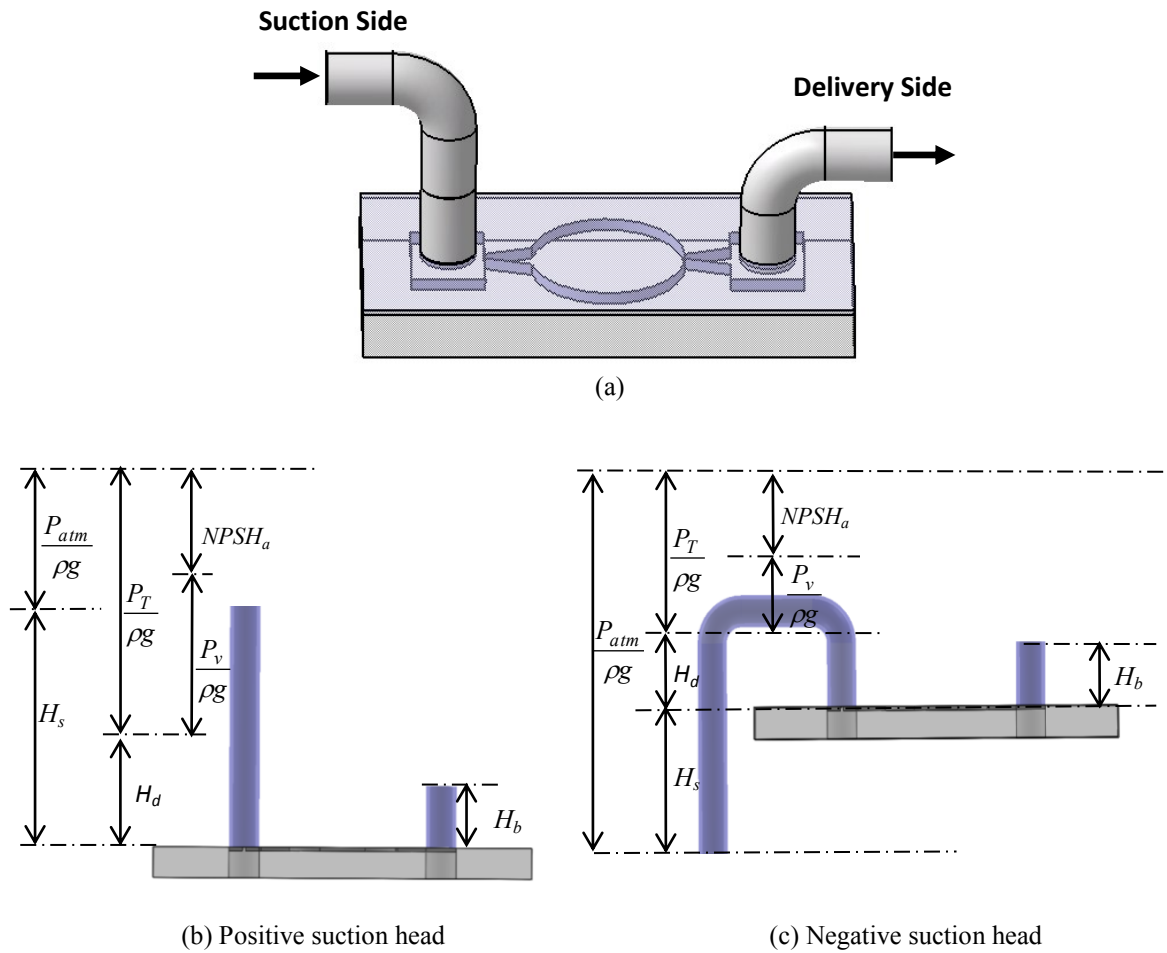


**Figure 4.1:** Schematic of the energy level diagram in a valveless micropump

Here,

$\frac{P_{atm}}{\rho g}$  - Atmospheric pressure head

$H_s$  - Suction head available at the entrance of the micropump

$\frac{P_v}{\rho g}$  - Vapor pressure head of liquid corresponding to the operating temperature



$H_d$  - Dynamic pressure loss in the suction line, which includes the pressure drop across the diffuser/nozzle

$H_b$  – Static head in the delivery side

$\frac{P_T}{\rho g}$  - Total head available at the entrance of the pump.

Where  $\rho$  is the density of the liquid and  $g$  is the gravity acceleration. By convention, the suction head ( $H_s$ ) is taken positive if the inlet reservoir is higher than the pump chamber and the suction head is negative if the inlet reservoir is below the pump chamber. Similarly, since the static head in the delivery side,  $H_b$ , is against the flow of the liquid out, the pressure head is taken as negative. In most of the  $\mu$ TAS applications, the system is integrated with other complimentary modules and therefore, the pressure at the delivery section,  $H_b$ , is constant, which is defined as the back pressure.

In the case of a closed system, the atmospheric pressure is replaced by the chamber pressure. For reference, the chamber pressure in a symmetric micropump is represented by the pressure at the center of the diaphragm. The chamber pressure for the micropump is defined as the pressure inside the micropump chamber. Cavitation in the micropump chamber would occur when the pressure falls below the vapor pressure of the liquid at any location inside the chamber. Under no flow condition, the chamber pressure is given as the average pressures at inlet and outlet of the micropump.

The available Net Positive Suction Head of the micropump ( $NPSH_a$ ) is defined as the total pressure head available, above the vapor pressure head, for the micropump on the suction side, which is given by the relation

$$NPSH_a = \frac{P_{atm}}{\rho g} + H_s - H_d - \frac{P_v}{\rho g} - H_b \quad \dots 4.1$$

where  $H_s - H_b$ , the difference in pressure head between the inlet and the outlet.

The actuation of the micropump induces the fluid motion, which leads to dynamic pressure losses in the system due to pressure drop across the microdiffuser/nozzle elements and frictional pressure losses in the fluid lines. The frictional loss in the microfluidic channels is estimated using the Fanning friction factor.

Considering the positive flow in the x-direction, the frictional pressure drop across a channel with rectangular cross-sectional area along the channel length is given by the expression (Yang et al. 2004)

$$\Delta p_{ff} = \int_0^L \frac{2f_f \rho v(x)^2}{D_h(x)} dx \quad \dots 4.2$$

where  $f_f$  is the Fanning frictional factor and  $D_h(x)$  and  $v(x)$  are respectively the hydraulic diameter and the fluid velocity at position  $x$ . The micropump channel can be considered as a series of rectangular cross-sectional ducts of varying channel widths. Harnett and Kostic (1989) proposed a simplified polynomial to describe the friction factor for laminar flow through a rectangular channel that is accurate to 0.05%. The expression is given as

$$f_f = \frac{24(1 - 1.13553Y_d + 1.9467Y_d^2 - 1.70128Y_d^3 + 0.964Y_d^4 - 0.2537Y_d^5)}{\text{Re}_d} \quad \dots 4.3$$

where  $Y_d$  is the aspect ratio of the channel given by  $h/w(x)$  where  $w(x)$  is the width of the channel at  $x$ , and  $h$  is the depth of the channel.

Similarly, the maximum pressure drop across the diffuser (Eames et al., 2009) is given as

$$\Delta P_{diff} = \rho \left( \frac{V_0 \omega_p}{A_{din}} \right)^2 \frac{\xi_n}{\left( \sqrt{\left( \frac{\xi_n}{\xi_d} \right) + 1} \right)^2} \quad \dots 4.4$$

Where  $\xi_n$  and  $\xi_d$  are the nozzle and the diffuser pressure drop coefficients respectively and  $A_{din}$  is the area of cross-section at the throat of the diffuser.

Therefore, the total dynamic head,  $H_d$ , can be written as the sum of the frictional pressure loss and the pressure drop across the diffuser at the inlet, expressed by the equations 4.3 and 4.4, respectively.

The Net Positive Suction Head required ( $NPSH_r$ ) is defined as the dynamic pressure head required for the fluid to flow under the oscillating diaphragm of the micropump, which is mainly the kinetic head of the liquid entering the micropump chamber and the head needed to overcome the losses encountered inside the micropump chamber. The acceleration of the liquid due to the continuous oscillation of the diaphragm converts the pressure energy to kinetic energy.

As seen in Figure 4.1a, the pump chamber is formed typically by a cylindrical cavity and the diaphragm enclosing the chamber is excited to oscillate vertically. During the oscillation, for a micropump chamber with the depth  $D_p$ , the chamber volume,  $V_p$ , at any given time  $t$  during the pump operation can be written as

$$V_p = V_c - V_0 \sin \omega_p t \quad \dots 4.5$$

where  $V_0$  is the amplitude of volume variation due to the deflection of the diaphragm and  $V_c$  is the initial volume of the chamber. The angular frequency  $\omega_p$  is given as  $2\pi f_d$ , with  $f_d$  being the frequency of diaphragm oscillation. If  $R_c$  is the radius of the oscillating diaphragm, then the volume variation amplitude can be approximated by the relation

$$V_0 = \alpha_p \pi R_c^2 \delta_p \quad \dots 4.6$$

Where  $\alpha_p$  is a dimensionless coefficient which characterizes the shape of the deformed planar surface and  $\delta_p$  is the maximum deflection at the center of the diaphragm. The rate of change of volume of the fluid flow inside the pump chamber can be given as

$$\left| \phi_p \right| = \left| \frac{dV_p}{dt} \right| = \left| V_p \omega_p \cos(\omega_p t) \right| \quad \dots 4.7$$

For a sinusoidal oscillation of the diaphragm, with the period of oscillation denoted by  $T$ , the suction and the pumping stroke is effected by the upward and downward motion of

the diaphragm, as schematically shown in Figure 3.2. Thus, the volume of the fluid inside the pump during one cycle of pumping is given as

$$V_{net} = \int_0^{\frac{T}{4}} -\phi_p dt + \int_{\frac{T}{4}}^{\frac{3T}{4}} \phi_p dt + \int_{\frac{3T}{4}}^T -\phi_p dt = 4V_0 \quad \dots 4.8a$$

The mean value of the volume flux  $\phi_{av}$  of the micropump operated for a time period of  $\tau_p$  is given

$$\phi_{av} = \frac{1}{\tau_p} \int_T^{T+\tau_p} \frac{4V_0\omega_p}{2\pi} dt \quad \dots 4.8b$$

If  $A_{av}$  average area of cross-section of the micropump chamber can be then, the kinetic energy of the fluid inside the pump chamber is given by the expression

$$KE = \alpha_{ke} \frac{1}{2} \rho \left( \frac{\phi_{av}}{A_{av}} \right)^2 = \alpha_{ke} KE_{av} \quad \dots 4.9a$$

where  $\alpha_{ke}$  is the kinetic energy correction factor that can be expressed by the relation

$$\alpha_{ke} = \frac{1}{A_c} \int_{A_c} \left( \frac{V_f}{(\phi_{av}/A_{av})} \right)^3 dA_c \quad \dots 4.9b$$

with  $V_f$  being the actual velocity of the fluid and  $A_c$  being the area of the chamber. Thus, the  $NPSH_r$  for the micropump is given by the relation

$$NPSH_r = \xi_p \alpha_{ke} \left( \frac{KE_{av}}{\rho g} \right) = \frac{\xi_p \alpha_{ke}}{2g} \left\{ \frac{\frac{4V_0 \omega_p}{2\pi}}{\frac{1}{R_c} \int_0^{R_c} h \sqrt{R_c^2 - r^2} dr} \right\}^2 \quad \dots 4.10$$

Here,  $\xi_p$  is the cavitation parameter, which is defined as the ratio of the inlet suction head to the kinetic energy head at the inception of cavitation. Assuming a laminar flow of the fluid inside the microchamber, the kinetic energy correction factor is taken as 2 (Fester et al. 2008). For a given micropump configuration, the cavitation parameter is only dependent upon the Reynolds number (Brennan 1995). Therefore, the cavitation parameter can also be expressed as

$$\xi_p = \xi_p^* \cdot Re_{av} \quad \dots 4.11$$

with  $Re_{av}$  denoting the average Reynolds number. The probability of occurrence of cavitation for a liquid is higher for higher values of  $\xi_p$ . However, the material property of a liquid (e.g. viscosity, lubricating property, particle content, corrosiveness) also impacts the cavitation parameter.

The manner in which the pump head drops as  $NPSH_a$  is reduced below  $NPSH_r$  depends very much on the type and geometry of the micropump. As the head of the pump varies widely with  $NPSH_a$ , the pump suction head is normalized with respect to the  $NPSH_c$  or critical  $NPSH$  i.e the  $NPSH$  at which cavitation incepts. Thereby, it is easier to compare the development of cavitation in terms of the drop in the pump head with cavitation. The cavitation number ( $\sigma_c$ ) for the micropump is defined as the ratio of the available suction head over the critical  $NPSH_c$ , and is expressed by the relation

$$\sigma_c = \frac{NPSH_a - NPSH_c}{NPSH_c} \quad \dots 4.12$$

At the inception of cavitation,  $NPSH_a$  is equal to  $NPSH_c$  and therefore, the cavitation number is 0, which is referred to as the critical cavitation number. The occurrence and the extent of cavitation in a micropump system depend mainly upon the absolute value of the minimum static pressure head available and the required dynamic head of the micropump. In other words, when the locally lowest static pressure of the liquid inside the micropump chamber is close to the vapor pressure at the prevailing temperature, local boiling of the liquid occurs resulting in the formation of vapor bubbles. Therefore, to prevent cavitation, it is important to operate the micropump such that the  $NPSH_r$  is always less than  $NPSH_a$ . For a given micropump under operation, the different stages of cavitation can be defined with through the cavitation number as

$$\sigma_c = \begin{cases} \sigma_c > 0, & \text{No Cavitation} \\ 0, & \text{Cavitation inception} \\ \sigma_c < 0, & \text{Under Cavitation} \end{cases} \quad \dots 4.13$$

The prediction of micropump cavitation parameter  $\xi_p$  and cavitation number  $\sigma_c$  using  $NPSH_r$  and  $NPSH_a$  is very important to study the performance of a micropump and to understand its cavitation behavior. Any macroscale pumping system would include the listing of  $NPSH_r$  and other cavitation terms, whereas pumping in microscale lacks these important specifications. The remainder of this chapter presents the experimental study of the cavitation behavior in valveless micropumps.

### 4.3. Experimental investigation of cavitation behavior in micropumps

As discussed in Section 4.2, the phenomenon of cavitation involves several parameters. Several works on micropumps have reported the occurrence of cavitation behavior, however the phenomenon of cavitation is still not understood well. Though the fluid pressure relations described in the previous section explain the phenomenon of cavitation, it is still important that suitable experiments are carried out in order to practically realize the cavitation behavior and better understand the fluid pressure relationships described in Section 4.2. Therefore, experiments were suitably designed so as to induce cavitation in micropumps and to study the cavitation behavior for the different cavitation parameters. Suitable conditions favorable for cavitation in a micropump can be created by any one of the following methods:

- *Increasing the dynamic head:* For a given micropump configuration with fixed channel depth, chamber area, and inlet suction head, the higher the value of  $NPSH_r$ , means greater the tendency to cavitate. The dynamic head of the micropump can be increased by increasing either the amplitude of volume variation of the micropump or the frequency of oscillation or both.

- *Decreasing the inlet suction head:* In cases where the micropump operating parameters are fixed, then the inducing of cavitation is possible only through the variation of the available static pressure heads at the inlet side of the micropump. The pressure equations described in the previous section clearly suggest that  $NPSH_a$  can be decreased by



decreasing the inlet pressure head. Alternately, the  $NPSH_a$  can also be decreased by increasing the back pressure. The backpressure is defined as the total pressure available along the microfluidic circuit that resists the forward flow of the fluid that is pumped. Most works on micropumps study the pump behavior with respect to the variation in backpressure. However, taking into consideration that in most of the applications of micropump, the device is integrated with complimentary modules and therefore in such cases, the back pressure available in the system is fixed. Therefore, for the present experiments, the variation in  $NPSH_a$  is carried out through the alteration of the inlet pressure head available at the suction side of the pump, while holding the system back pressure constant.

The experiments presented here take into consideration both the above mentioned effects in order to study the cavitation behavior. Table 4.1 gives the specifications of the valveless micropump considered for the present experiments.

Parameter	Value
Diffuser angle, $\theta_d$	30°
Diffuser length, $L_d$ ( $\mu\text{m}$ )	2000 $\mu\text{m}$
Inlet diffuser width, $w_d$	100 $\mu\text{m}$
Microchamber depth,	100 $\mu\text{m}$
Micropump chamber diameter	7 mm
Inner diameter of connecting tubes	500 $\mu\text{m}$

**Table 4.1:** The different geometric parameters for the valveless micropump used for cavitation experiments

The fabrication of the micropump on PDMS platform with glass actuating diaphragm and PZT actuator is already described in Chapter 3. The plot of variation of the micropump deflection with the actuation voltage is as shown in Figure 4.2. Since the fabrication procedure and the configuration of the micropumps used in all the following cavitation

experiments are the same, the deflection-voltage characteristics shown in Figure 4.2 are also not expected to vary for every micropump device.

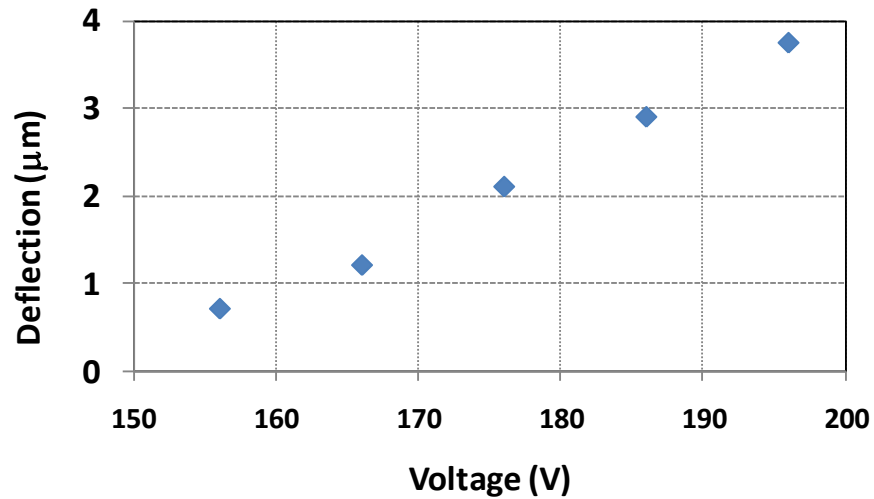


**Figure 4.2:** Plot of variation of average diaphragm deflection with applied voltage for the micropumps used in cavitation experiments with water.

For all the experiments, the outlet conditions are maintained constant. In order to alter the inlet suction condition, a long inlet tube is provided, as shown in Figure 4.3(a) so that the height of the liquid column can be adjusted in order to vary the inlet suction head,  $H_s$ . The inlet reservoir of the micropump is attached to a movable scale as shown in Figure 4.3(b), and thus its height is controlled. The micropump outlet is connected to a reservoir which is always at the same level as the micropump chamber, such that  $H_b$  is always zero.

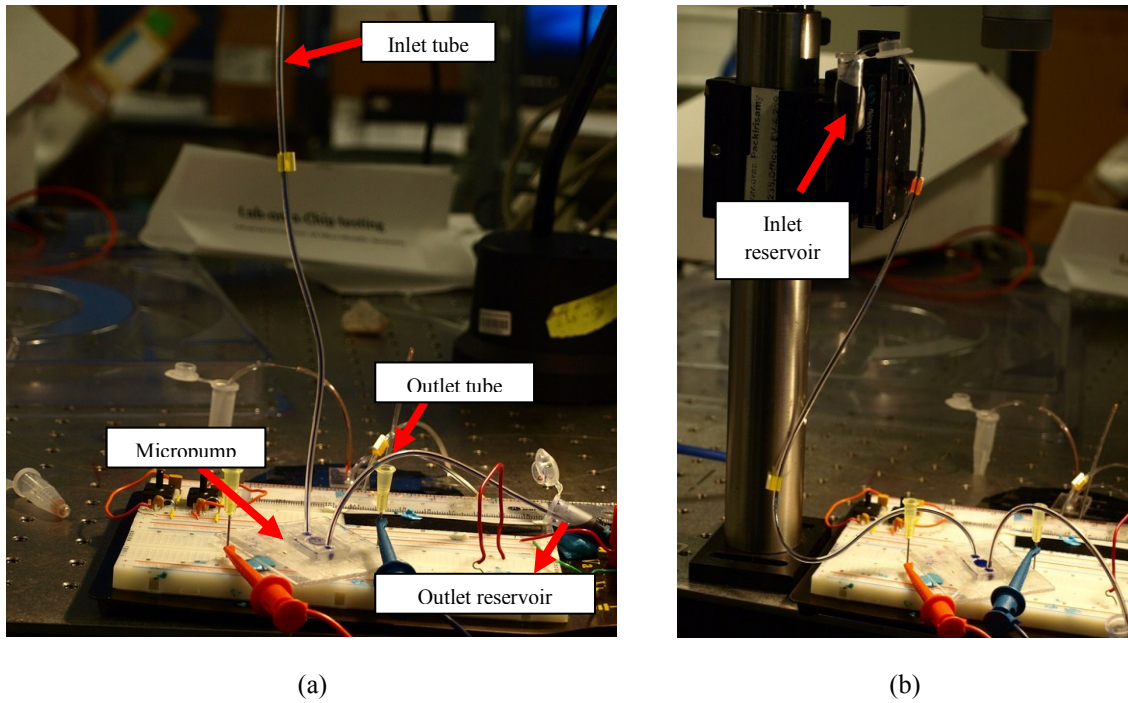


**Figure 4.3:** Experimental setup for study of cavitation

The experimental setup that comprises of the micropump actuation system, the dynamic characterization and flow visualization system and the microfluidic flow measurement system, is the same as shown schematically in Figure 3.6 in Chapter 3. The experiments were carried out with deionized water (DI water) as the working fluid. In some experiments, a dye was used with water in order to aid better flow visualization. Initially, the system is well primed with 99% Ethanol continuously to remove air in order to improve the filling of the chamber with water. DI water is introduced into the micropump through a syringe. All the experiments have been conducted at the room temperature of 20°C.

#### **4.4. Experimental results**

The experiments were carried out under favorable hydrodynamic conditions that facilitate cavitation by varying one or more of the following three parameters, namely, the diaphragm displacement, operating frequency, and the inlet suction head. Cavitation behavior in micropumps reveals the different stages of cavitation, which are similar to the cavitation behavior observed in other microfluidic channel mechanisms. Once the cavitation incepts, the images of cavitation with the chamber associated flow patterns are recorded using the camera/microscope combination unit. Image processing is then carried out to produce images from the video files.

The studies showed that distinct stages of cavitation are observed with micropump cavitation, namely, the cavitation inception, growth and subsequent collapse of cavitation bubbles, and supercavitation. The cavitation behavior is also affected by the presence of impurities or dissolved gases in the liquids and flow disturbances in the micropump chamber such as sharp corners.

##### **4.4.1 Cavitation inception**

The origin and the formation of the cavitation bubbles is still unclear. However, it has been researched upon that there are several effects that can modify the cavitation inception. Most important among them is the availability of cavitation nuclei which comprises of undissolved gas bubbles and impurities in the bulk liquid flow or trapped on

the crevices of the device surface. It is also possible that cavitation originates from undissolved gas nuclei existing in the interstices in the container's wall rather than from free cavities in the liquid (Tarantino, Mongiovi 2001). As a result, the cavitation incepts even when the static pressure is above than the vapor pressure. But, two important considerations are necessary regarding the inception site of the cavitation in the present valveless micropumping system. Firstly, in the present configuration of a micropump, the maximum velocity of the fluid is in proximity to the oscillating diaphragm within the microfluidic circuit, the point of the highest velocity will be at the peak of the oscillating diaphragm. Secondly, in microfluidic devices, it has been argued that because of the very short residence time of bubbles in the low pressure region and the availability of only small bubbles, the surface nuclei are increasingly more important than stream nuclei (Singh, Peles 2009). Therefore, the nuclei attached to the surface of the oscillating diaphragm, also known as the surface nuclei are expected to be the main source for the cavitation inception. Additionally, given that practically it is difficult to achieve a fool proof priming of the system, the resulting air pockets within the chamber also add to the probability of inception and development of cavitation. Thus, the presence of dissolved gases, impurities or flow disturbances like sharp corners facilitate the inception of cavitation even when the static pressure is above the vapor pressure.

Another important factor that gives rise to the cavitation is the fluid response to the oscillation of the diaphragm. At lower frequencies of diaphragm oscillation, the fluid flow due to pumping takes predominance. As the frequency of oscillation is increased, due to the inertial effects of the fluid, the flow rate is decreased. This also creates a void between

the oscillating diaphragm and fluid layer, leading to the formation of more crevices thereby facilitating the development of cavitation. If the viscosity of the fluid is high, the ability of the fluid to move along with the oscillating diaphragm reduces. This leads to discontinuities in the fluid thereby leading to pockets in the fluid medium, which facilitates the formation of vapor bubbles during the operating cycle.

The inception of cavitation occurs during the accelerating phase of the suction stroke, when the pressure inside the chamber falls below the atmospheric pressure. At lower operating frequencies, however this cavitation is not sustained as the fluid fills in to the chamber. In the case of diffuser based valveless micropump, cavitation occurs due to high oscillating velocities of the diaphragm, low static pressure and flow curvatures (Olsson et al. 1996). Thus, the pump performance is then drastically affected due to cavitation. At higher operating frequencies, high velocities of the oscillating diaphragm cause a severe pressure drop immediately, thereby facilitating cavitation inception. After the inception of cavitation, with further pumping, the vapor bubbles are also subjected to compression and expansion along with the operating fluid, as the diaphragm oscillations. Thus, the kinetic energy of the diaphragm used for the pumping of fluid is distributed to the bubbles as well and the bubbles are sustained in the fluid, which is the reason why the pump efficiency is reduced tremendously with the inception of cavitation. Thus, cavitation also restricts the maximum pump diaphragm excitation frequency and high flow rates.

Cavitation inception is defined as the first appearance of bubbles in the chamber. The inception of cavitation can be identified only through flow visualization methods.

However, for the present micropump system, since the flow visualization is carried out from the top of the oscillating diaphragm and due the transparency of the substrates (PDMS and glass diaphragm), the precise identification of the origination and the nucleation site of the cavitation bubble inside the chamber presents a considerable challenge. Therefore, the cavitation bubbles were allowed to grow until bubbles grow and occupy 1% of the total area of the oscillating diaphragm, and suitable image processing was carried out.

The inception of cavitation also provides details about the micropump characteristics and its behavior for the liquid being pumped. When  $\sigma_c = 0$ , the micropump cavitation parameter  $\xi_p$  can be given by the relation

$$\xi_p = \frac{NPSH_a \cdot \rho g}{\alpha_{ke} \cdot KE_{av}} \quad \dots 4.14$$

The critical cavitation frequency ( $\nu_c$ ) is defined as the minimum frequency of operation of the micropump required in order to cavitate. In other words, critical cavitation frequency is the pump frequency at which  $\sigma_c = 0$ .

In order to identify the inception of cavitation, in the first experiment, the diaphragm deflection was varied and the critical cavitation frequency was found out. Herein, the suction head available at the inlet (i.e height of the liquid column at the inlet) is kept zero, and the deflection of the pump was varied by changing the actuation voltage. The critical frequency is identified for each deflection by increasing the frequency of the micropump

and identifying the frequency at which cavitation bubbles appear in the micropump chamber. The experimentally obtained values of the critical cavitation frequency of the micropump for different micropump deflections are as shown in Figure 4. 4. The images of the different cavitation inception stages also show that the nucleation site of the cavitation is random.

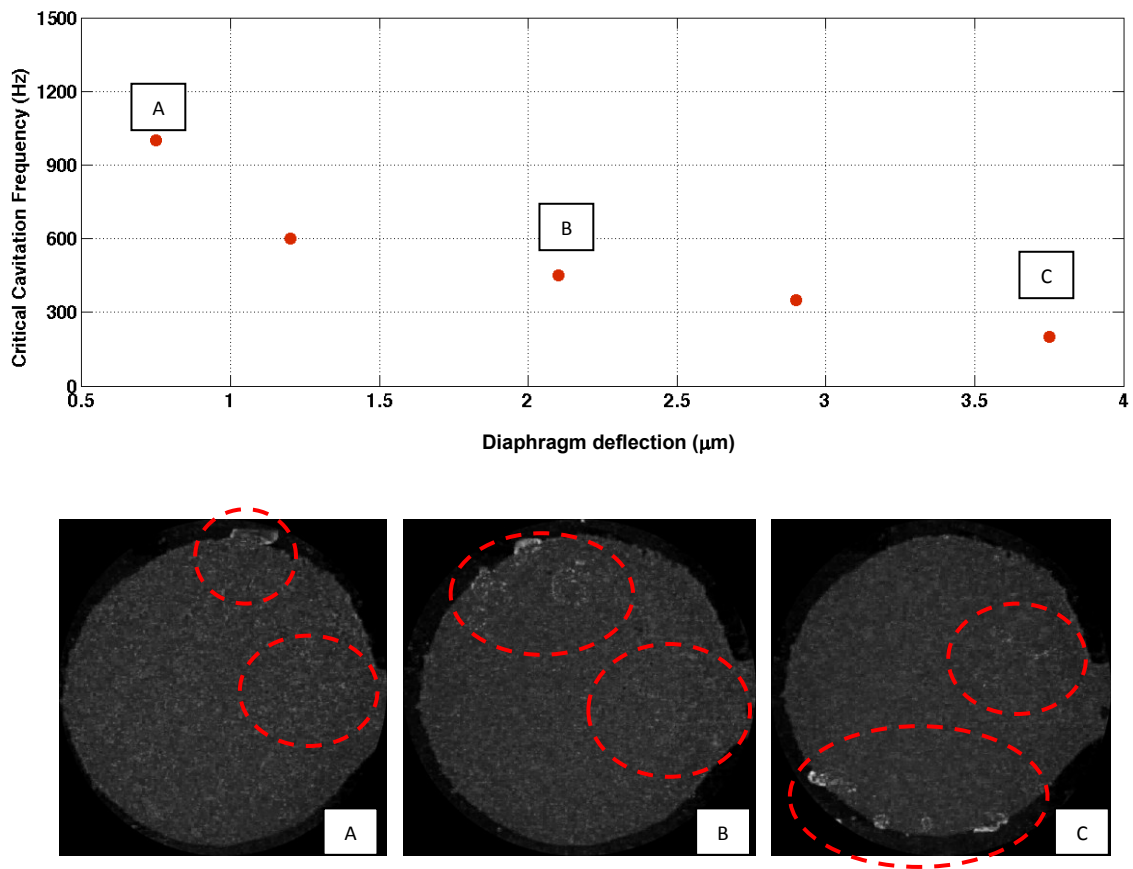


**Figure 4.4:** Experimentally obtained values for the critical cavitation frequencies for different micropump deflections for  $H_s = 0$

In order to find out the cavitation parameter, for a constant diaphragm deflection inlet suction head was varied and the critical cavitation frequency was studied. The deflection



of the micropump was maintained at  $3.75 \mu\text{m}$  obtained with an actuation voltage of 195 Vpp. The height of the liquid column at the inlet was varied using the setup shown in Figure 4.3. The variation of critical cavitation frequency with inlet suction head is as shown in Figure 4.5.

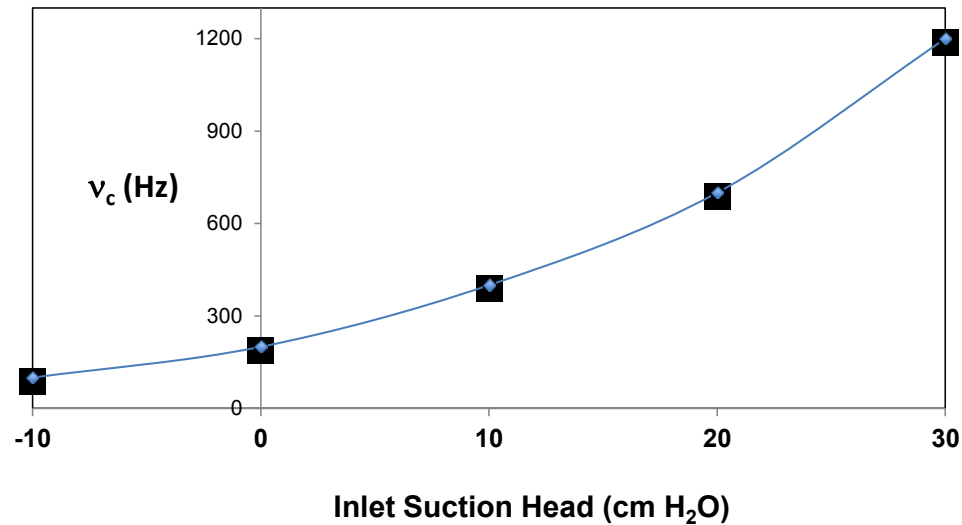


**Figure 4.5:** Variation of critical cavitation frequency with inlet suction head for constant micropump diaphragm deflection

Herein, the negative suction head refers to the inlet column below the level of the micropump diaphragm, as shown schematically in Figure 4.1. At zero suction head the critical cavitation frequency is 200 Hz. As the inlet head is increased, the critical cavitation frequency increases. However, for a given micropump, it is not possible to calculate the cavitation parameter by directly applying Equation 4.14. Therefore, the cavitation parameter was computed by calculating the change in the critical cavitation frequency for corresponding change in inlet suction head ( $\Delta H_s$ ), taken with respect to the lowest suction head ( $-10 \text{ cm H}_2\text{O}$ ). Thus, between two inlet suction heads  $H_{S1}$  and  $H_{S2}$

$$NPSH_{a1} = \frac{\xi_p \alpha_{ke} KE_{av1}}{\rho g} ; NPSH_{a2} = \frac{\xi_p \alpha_{ke} KE_{av2}}{\rho g} \quad \dots 4.15(a)$$

$$NPSH_{a1} - NPSH_{a2} = \frac{\xi_p \alpha_{ke}}{\rho g} (KE_{av1} - KE_{av2}) \quad \dots 4.15(b)$$

$$\text{Therefore, } \xi_p = \frac{\rho g \Delta H_s}{\alpha_{ke} (\Delta KE_{av})} \quad \dots 4.15(c)$$

The plot of variation of the cavitation parameter with change in inlet suction head difference is as shown in Figure 4.6.

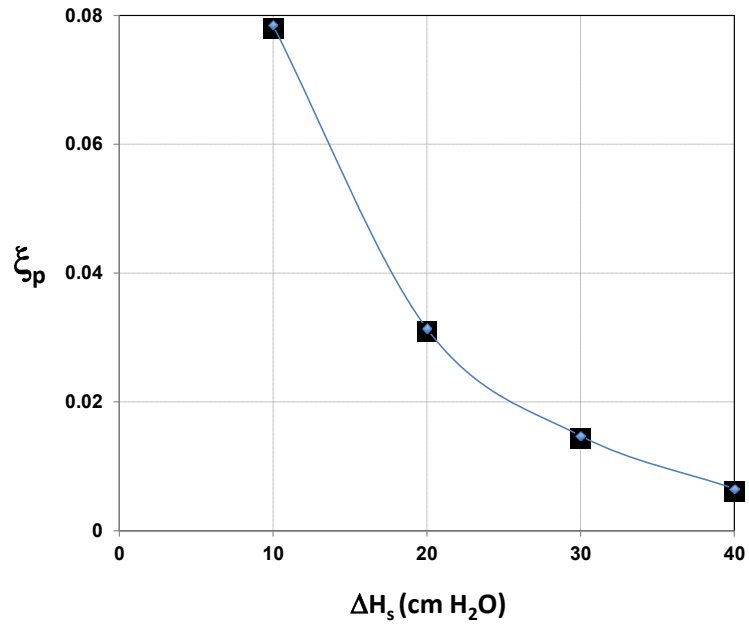


**Figure 4.6:** Variation of cavitation parameter with inlet suction head for constant micropump diaphragm deflection of 3.75  $\mu\text{m}$

Thus, for a given micropump, it is clear based on the experimental results and the theoretical formulation that the probability of occurrence of cavitation in the micropump chamber increases with the following parameters only, i.e, increase in the micropump deflection, increase in actuation frequency and decrease in inlet suction head.

#### **4.4.2 Growth of cavitation bubbles**

After the inception, the rate of growth of cavitation bubbles, the maximum volume of the bubble growth, the bubble distribution and its lifetime depend in a complex way on the channel geometry and the energy distribution inside the chamber (Ory et al. 2000), (Yuan et al. 1999). The presence of nucleation sites and the randomness also add to the complexity of the cavitation growth phenomenon. However, the contributing factors for growth of the cavitation bubbles within the chamber are the variation of the chamber pressure inside due to the oscillation of the diaphragm and the energy supplied to the cavitation bubble by the diaphragm due to pumping. The combination of the two factors is expected to cause the growth and the subsequent collapse of the cavitation bubbles. The expansion of the vapor bubble inside the micropump chamber is schematically shown in Figure 4.7. It is to be noted that the diffuser elements shown in the suction and the delivery side do not represent the cross-sectional view and are purely presented for illustrative purposes only.

In the case of rotodynamic pumps, energy is continuously transformed from the impeller to the fluid along the direction of flow that always occurs from the inlet and the outlet. As a result, the location of inception, growth and the collapse of the cavitation bubbles always occur at nearly the same place on the mechanical element due to the uni-direction of flow. But, in the case of reciprocating diaphragm type micropump, the flow changes directions with respect to the diaphragm oscillation. As a result, the inception of

cavitation occurs at the locally lowest static pressure supported by the presence of cavitation nuclei, such as microcrevices, airpockets, dissolved gases, sharp corners, etc.

In the case of diaphragm type micropump, the lowest static pressure would occur at the point of highest velocity corresponding to the central peak location of the oscillating diaphragm. Once the bubbles are initiated, the growth and collapse of the bubbles depend upon the rate of energy transfers between diaphragm – bubble ( $E_{db}$ ), diaphragm – fluid ( $E_{df}$ ) and bubble – fluid ( $E_{bf}$ ), schematically shown in Figure 4.7. These energy transfers depend upon the inlet suction condition ( $NPSH_a$ ), static pressure distribution inside the chamber, flow velocity and the oscillating velocity of the diaphragm.

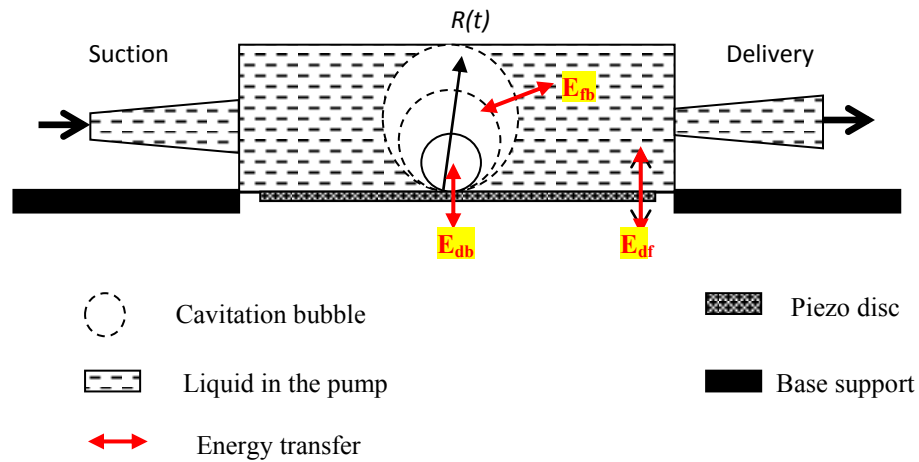


**Figure 4.7:** Schematic of the cavitation bubble growth inside the micropump chamber

Hence, the pattern of bubble growth is complex depending upon the geometries of the microchambers, nozzle/diffusers, and the shape of the diaphragm. Once the bubble is initiated, the growth behavior and the collapse depend on the relative energy transfer across bubble, fluid and diaphragm. Hence, one could influence the growth behavior and

the collapse of cavitation bubbles by modifying inlet suction condition, pump frequency, diaphragm deflection and geometry of the micropump chamber.

Under cavitating conditions, the vapor bubbles expand, displacing an equivalent volume of liquid from the micropump chamber. Also, as the bubbles grow, the pressure exerted by the growing bubbles will drive the fluid out of the micropump chamber. Therefore, the growth of cavitation bubbles can be studied by two methods, namely the pressure measurement inside the chamber and also the cavitation induced flow. As mentioned earlier, one could influence the cavitation growth behavior and the collapse behavior by modifying any of the dynamic parameters (oscillating frequency and diaphragm deflection), the inlet suction condition, and the geometry of the micropump. In order to reduce the complexity of the studies, in this work, the growth of cavitation bubbles is studied with respect to the change in cavitation frequency only.

#### ***4.4.2.1. Pressure measurement under cavitation growth***

As it is difficult to measure the static pressure inside the chamber and inside the bubble due to the micro nature of the device, the growth of the bubble is monitored indirectly through the rise in pressure of stagnant fluid compressed by the growing bubble. The trapped flow inside the stagnant chamber is compressed by the growth of the bubble and the increase in pressure becomes indicative of the growth rate of the bubble. The schematic of the pressure measurement to monitor the growth of cavitation bubbles is as shown in Figure 4. 8.

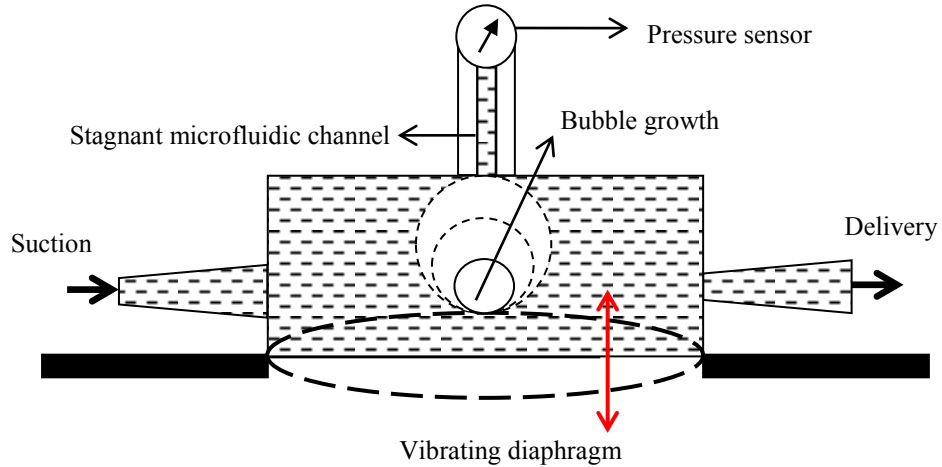


**Figure 4.8:** Schematic of the pressure measurement due to bubble growth using stagnant microfluidic channel

The pressure-growth relationship of the cavitation bubbles is denoted by the bubble pressure ratio,  $\sigma_p$ . If the pressure exerted by the bubble at any time  $t$  during the operation of the pump is denoted as  $P_b(t)$ , then the bubble pressure ratio is given as

$$\sigma_p = \frac{P_b(t)}{P_b(\tau_g)} \quad \dots 4.15$$

where  $\tau_g$  is the total time taken for the maximum bubble growth before collapse. The maximum bubble pressure is obtained at  $t = \tau_g$ . The plot of the variation of  $\sigma_p$  with time for different cavitation frequencies is as shown in Figure 4.9. Since there is no bubble formed in the chamber when the pump is not operated, at time  $t = 0$ ,  $\sigma_p$  is set to 0. The increase in the pressure indicates the expansion of the bubbles inside the micropump chamber. Usually, the collapse time for the bubble is very short, of the order of a few milliseconds (Kuiper 1981), the volume attained by the expanding vapor bubbles is

maximum at  $t = \tau_g$ . For lower frequencies, the time taken for the bubbles to expand and reach the maximum volume before collapse is longer. As the pumping frequency is increased, the time taken for the bubble to attain the maximum pressure reduces, which indicates that the rate at which the bubble growth is faster at higher frequencies. After attaining a maximum pressure at  $t = \tau_g$ , the decrease in  $\sigma_p$  indicates the beginning of collapse of the cavitation bubbles. The overall volume occupied by the bubbles inside the chamber reduces as the bubbles collapse, and thus the pressure exerted by the bubbles reduces.

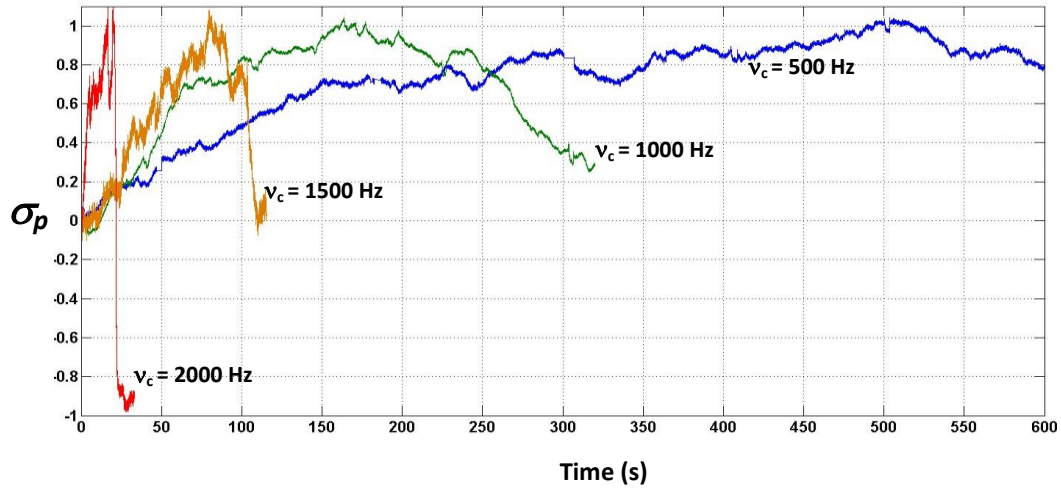


**Figure 4.9:** Plot of the variation of the bubble pressure ratio with time for different frequencies

#### 4.4.2.2 Cavitation growth induced flow

The flow in the micropump due to the bubble growth is as a result of the vapor bubbles displacing an equivalent volume of liquid through the outlet ports of the micropump. The resulting velocity of the fluid is called the expansion velocity which is distinct from the pumping velocity, as expansion velocity of the fluid is observed only with an increase in micropump frequency after the cavitation inception. After the inception of cavitation, the

flow is choked, as the nascent vapor bubbles block the flow. The subsequent increase in the flow velocity in the outlet with increase in the frequency is purely due to the growth and collapse of the cavitation bubbles. The bubble expansion flow for the micropump was experimentally verified by calculating the flow at the outlet of a fully primed pump in the first 60 s of operation, at different frequencies with the inlet suction head and the outlet static pressure head being zero. Figure 4.10 presents the measured variation of the flow rate with the pumping frequency. As can be seen, after the inception of cavitation, the flow is choked and the flow rate decreases. The increase in the flow rate in the outlet indicates the flow due to the growth of the bubbles, also referred to as the bubble expansion flow.

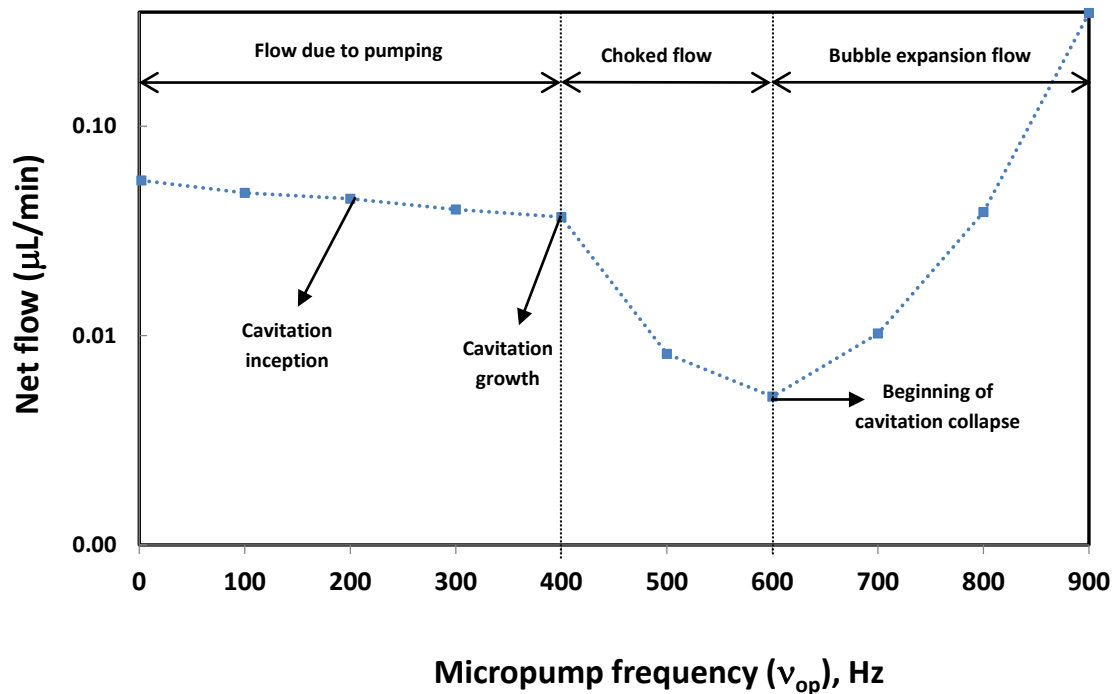


Figure 4.10: Measured variation of flow rate of the pump with operating frequency



In order to study the bubble expansion flow, the micropump cavitation shape number ( $\sigma_{sh}$ ) (Packirisamy, 1990) is defined as

$$\sigma_{sh} = \frac{\left(\frac{\omega_p}{2\pi}\right)\sqrt{Q_p}}{(g \cdot NPSH_c)^{0.75}} \times 1000 \quad \dots 4.16$$

Here,  $Q_p$  is the discharge from the micropump at the delivery side due to the expansion of cavitation bubbles. For a constant pumping frequency, the variation of shape number depends on the discharge produced.

The direction of the cavitation induced flow depends upon  $\Delta H_s$  i.e the difference between the available pressure heads at the inlet and the outlet plus the dynamic pressure heads within the microfluidic channel. When the pressure heads available at the inlet and the outlet are equal, then the direction of the cavitation induced flow is governed only by the dynamic pressure losses across the suction and the delivery sides of the micropump. At lower pumping frequencies, the growth rate of the bubble and the pressure exerted therein is less. Under such conditions, the growth of the bubble pushes the fluid out of the diffuser i.e the delivery side of the micropump, since the pressure drop across the diffuser is lesser than the nozzle. However, as the pumping frequency is increased, the pressure drop in the pump chamber would become quite different favoring the flow both in suction and the delivery sides of the pump. Therefore, in order to maintain a unidirectional flow through the delivery side, it is important that the inlet suction head is always greater than the pressure exerted by the bubble growth  $P_b(t)$ . For lower inlet suction heads, increase in the pumping frequency causes the cavitation induced flow to occur both the nozzle and

the diffuser due to the high pressure induced by the cavitation bubble growth. However, as the inlet suction head is increased, the resulting increased flow of the liquid into the micropump chamber acts as a feeder for creating more cavitation bubbles inside the micropump chamber thus resulting in a tremendous increase in the flow though the delivery side of the micropump. The characterization of the flow under such conditions is also limited with the existing setup.

Figure 4.11 shows the plot of the variation of micropump shape number with time for different pumping frequencies. The increase in the shape number indicates the growth of the cavitation bubbles and the decrease in the shape number indicates the collapse of the cavitation bubbles.

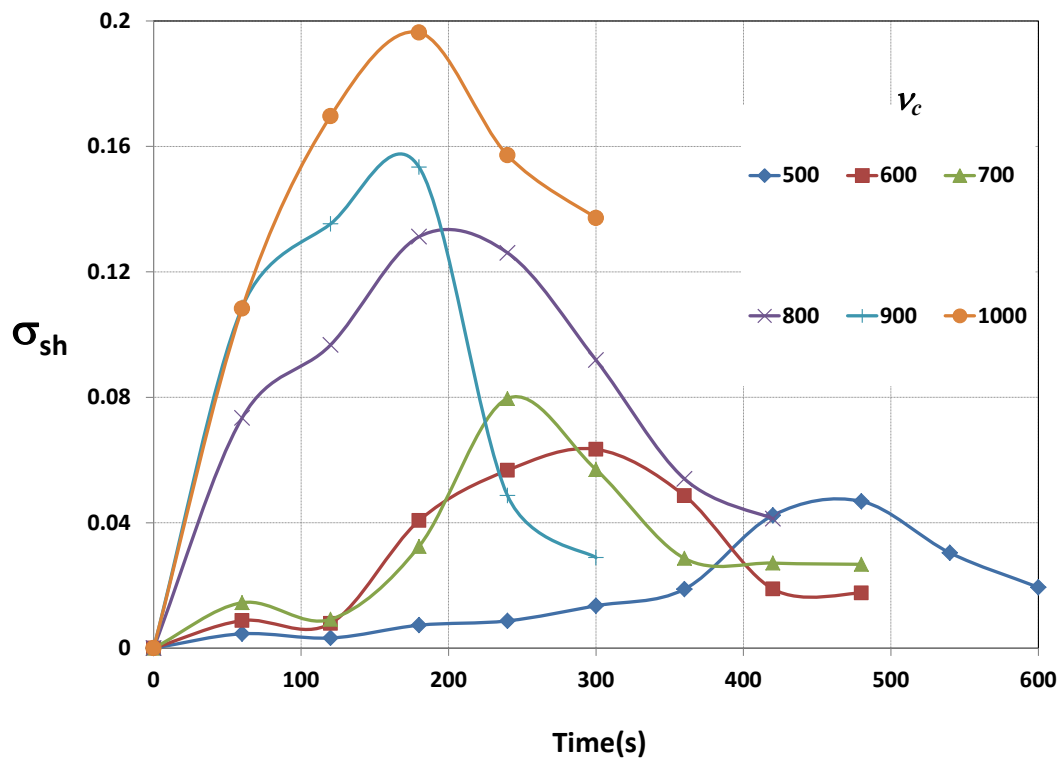


**Figure 4.11:** Plot of variation of the micropump shape number with time at different pumping frequencies.

#### ***4.4.2.3 Comparison of pressure and flow measurements***

From the pressure and flow measurements, it is clear that the growth of the bubble is indicated by the rate of increase of pressure and the shape number. Once the maximum volume for the equilibrium state of the bubble is reached, the bubbles start to collapse and this causes the decrease in pressure as well as the shape number. The time taken for the maximum bubble growth,  $\tau_g$  was calculated from the variation of cavitation induced pressure and shape number, as shown in Figure 4.9 and 4.11 respectively.  $\tau_g$  was also calculated from the visualization of the cavitation growth inside the micropump chamber. The plot of variation of  $\tau_g$  with  $\nu_c$  for all the three methods of estimation is shown in Figure 4.12. The growth time,  $\tau_g$ , reduces rapidly with increase in the pumping frequency. The estimated growth time for the cavitation bubbles is in close agreement for all the three methods. From the results presented in Figure 4.9, 4.11 and 4.12, the time taken for the maximum cavitation growth inside the micropump chamber for operating frequencies outside the tested range can be predicted by extrapolation.

Therefore, it is safer from cavitation to work under low pumping frequency, while it is faster to induce cavitation induced flow at higher pumping frequencies. This study emphasizes that the effect of cavitation has to be considered in the design of valveless micropump and to determine its operating frequency.

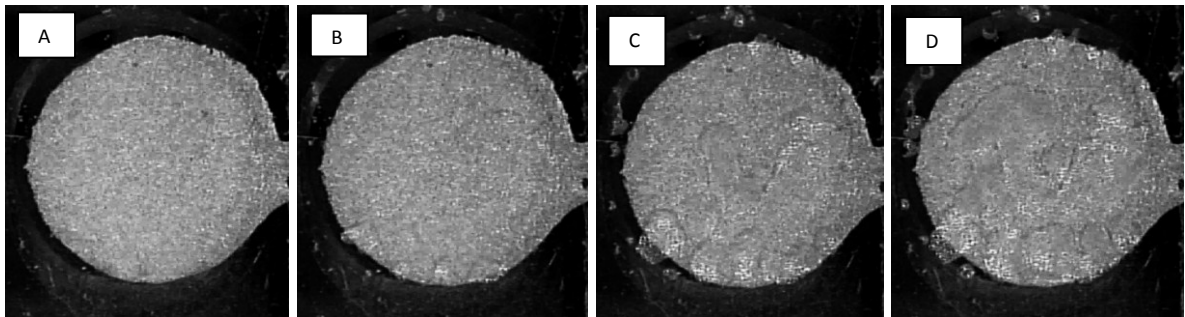
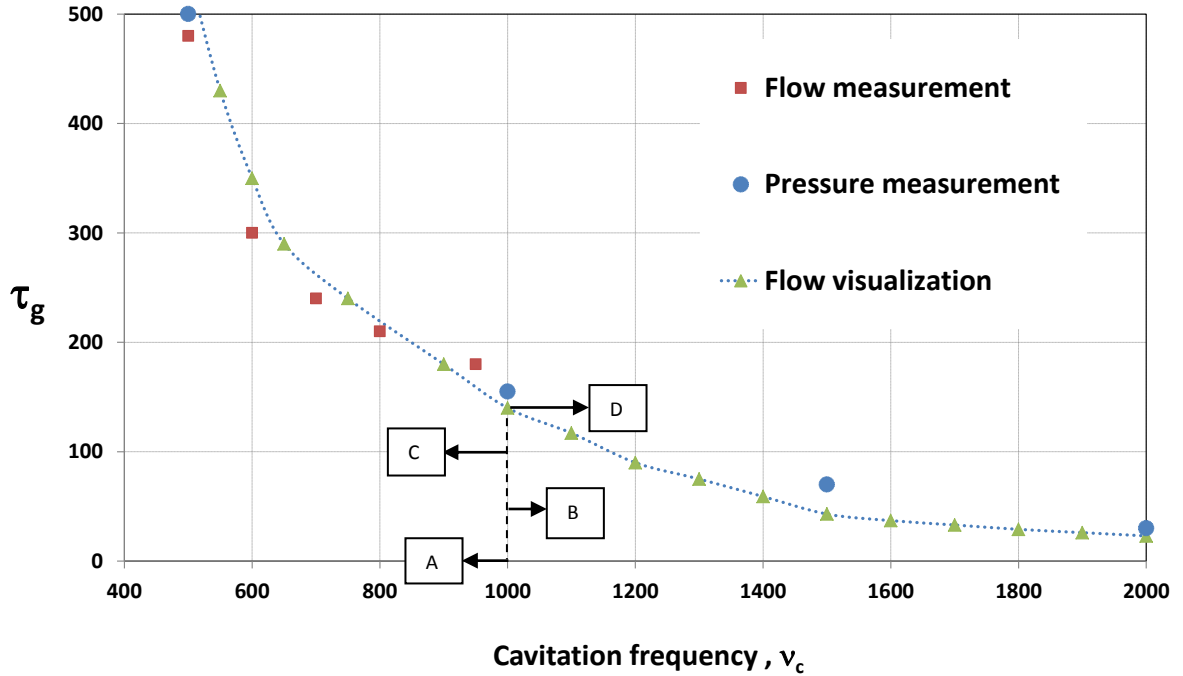


**Figure 4.12:** Plot of variation of bubble growth time with cavitation frequency as identified by cavitation growth induced flow measurement, chamber pressure measurement due to cavitation bubble growth and visualization of cavitation growth inside micropump chamber.

#### 4.4.3 Cavitation collapse

The collapse of cavitation bubbles is an important phenomenon because of the noise and material damage that can be caused by the high velocities, pressures, and temperatures that result from that collapse. Cavitation bubble collapse is sometimes accompanied by shock and vibrations that can potentially be severely damaging to the micropump.

The reason for cavitation bubble collapse is the alternating shrinking and the expansion of the bubbles leading to the bursting of the bubbles. The energy released during the collapse of a few bubbles is also utilized for the collapse of neighboring bubbles. However, the intensity of the collapse of cavitation bubbles depends purely upon the energy supplied from the oscillating diaphragm. When the cavitation number is high under low micropump frequency, the kinetic energy imparted to the oscillating bubble is low leading to slower collapse. As the cavitation number decreases under high operating frequencies, the kinetic energy of the system is high which facilitates high energy transfer to the bubble leading to the collapse of the bubbles drastically. Under very high velocities of pump operation, the collapse of the cavitation bubbles start even during the growth phase and is difficult to distinguish.

As seen from the previous experiments, the cavitation bubble collapse can be identified by the drop in the expansion velocity of the fluid identified through the shape number, and also a decrease in the pressure exerted by the bubbles. Since the number of bubbles that can be formed during the cavitation process is random, the collapse of cavitation bubbles can be characterized only through the total time taken for all the bubbles to collapse. Cavitation collapse time is easier to be characterized through flow visualization methods. Alternately, the cavitation collapse time can also be computed from the pressure measurements, which is denoted by the time taken for the pressure to reach the initial pressure after the collapse of the bubble starts. In case of higher cavitation numbers, the time taken for all the bubbles to collapse is high.

In order to study the cavitation collapse, separate experiments were carried out to induce cavitation and to calculate the time taken for the bubbles to start collapsing. The kinetic energy of the oscillating diaphragm was varied by changing the pump deflection through supply voltage and the operating frequency. Cavitation experiments were carried out under various diaphragm deflections and frequencies. It is known that  $NPSH_r$  is strongly dependent on the peak diaphragm velocity. The tested variation of the total time taken for the bubbles to collapse,  $\tau_c$ , for different peak deflection of the diaphragm obtained with different applied peak voltages, is as shown in Figure 4.13. It can be seen that the  $\tau_c$  decreases with increase in operating frequency and the deflection. Another interesting observation is that the collapse time  $\tau_c$  is always lesser than the maximum cavitation growth time  $\tau_g$ . This shows that the collapse of the cavitation bubbles commences in certain pockets of the micropump chamber even as the bubbles continue to grow in other regions.

The experiments were repeated several times and a very high repeatability was obtained for the cavitation collapse time,  $\tau_c$ . The time taken for the collapse of the cavitation bubbles for micropump frequencies outside the tested range can also be predicted through extrapolation.

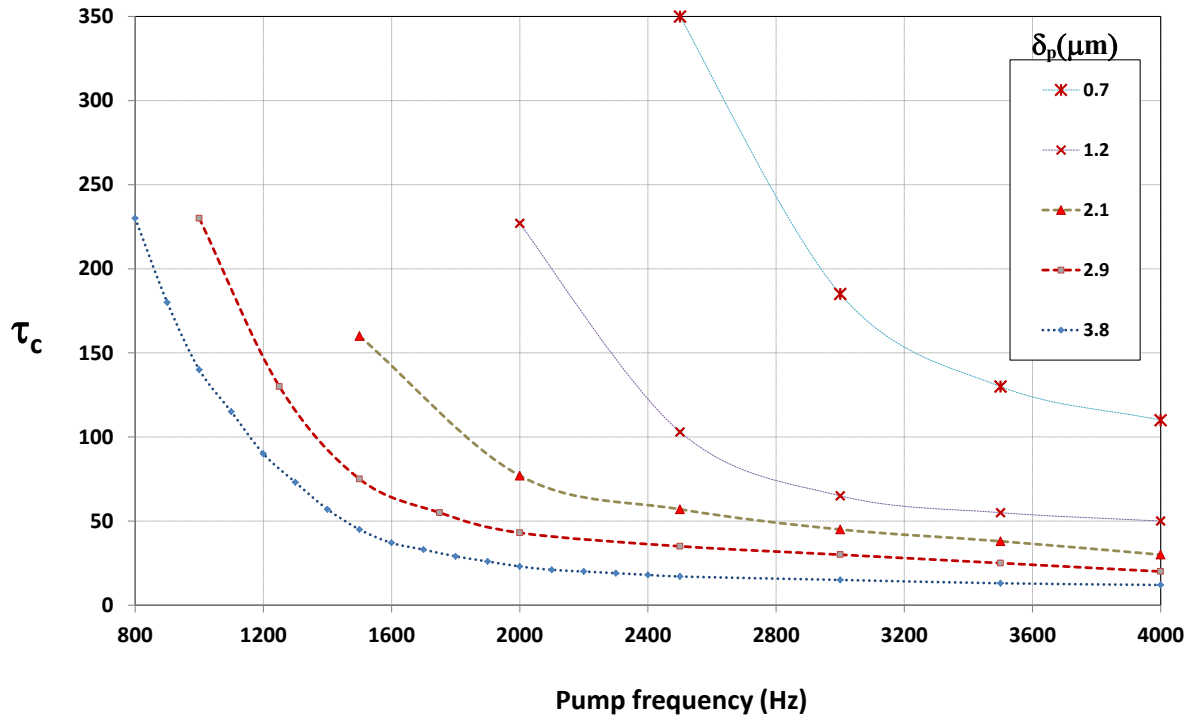


Figure 4.13: Plot of the time taken for cavitation collapse with frequency for different pump deflections

#### 4.4.4 Supercavitation

Under certain favorable conditions, such as very low suction head or high diaphragm velocity, the cavitation bubble grows continuously occupying large volume of the micropump chamber thereby disrupting the continuous flow behavior from the inlet to the outlet. However, flow of fluid from inlet into the micropump chamber can still occur if sufficient pressure is provided at the inlet, either externally or by increasing the height of the inlet water column. In such cases, the flow of liquid into the cavitating micropump chamber acts like a feeder for further cavitation to take place, with the fresh influx of liquid being converted into vapor bubbles and subsequently collapsed.

However, when there is no flow of liquid from the input into the chamber during cavitation process, the continued operation of the pump causes all liquid inside the micropump chamber to cavitate and subsequently collapse thereby leaving the chamber void at one point. Such a condition is referred to as the supercavitation condition for the micropump, wherein all the liquid present inside the entire micropump chamber cavitates.

Once cavitation is initiated, for a given inlet pressure head, the cavitation collapse and the subsequent supercavitation is dependent only upon the kinetic energy of the oscillating diaphragm (i.e frequency and deflection). The plot of the variation of pressure exerted by cavitation bubble in the micropump chamber at different pump frequencies is as shown in Figure 4.14. The pressure exerted by the cavitation bubble increases with increase in frequency which indicates the cavitation growth. The drop in pressure indicates the collapse of the cavitation bubbles. The pressure reaches zero when all the bubbles inside the chamber collapse. The onset of supercavitation is indicated by the drop in the relative change in pressure in the chamber to zero.

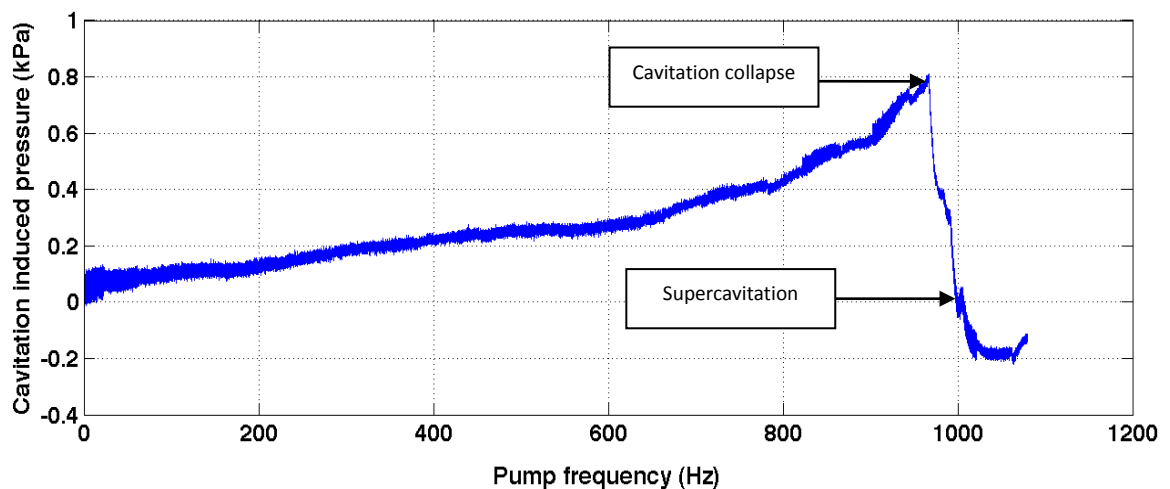


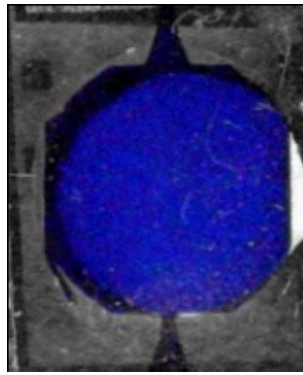
**Figure 4.14:** Variation of cavitation induced pressure with frequency



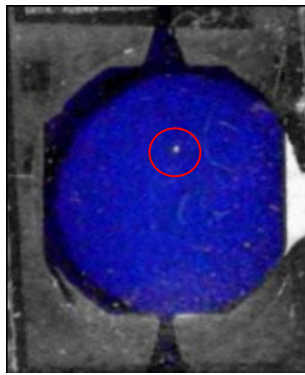
Alternately, when the dynamic properties of the oscillating diaphragm (i.e the frequency and the deflection) is maintained constant, the occurrence of supercavitation depends only upon the available inlet suction head of the micropump. Thus, for different inlet pressure heads, when the diaphragm deflection is maintained constant, the micropump operating frequency at which supercavitation occurs changes. This frequency is called the supercavitation frequency.

As seen from Figure 4.14, when supercavitation sets in, the relative pressure rise inside the chamber reaches zero and sustained operation of the micropump also causes the pressure to drop below zero. Therefore, if the operation of the pump is stopped immediately after the onset of supercavitation, since the pressure at the inlet and the outlet is higher than the pressure inside the chamber, the liquid is driven back into the chamber through both inlet and outlet. This phenomenon of reverse flow is observed only under supercavitation conditions when the relative pressure inside the chamber becomes negative. Thus, one can also use the reverse flow technique in order to determine the onset of supercavitation in micropumps.

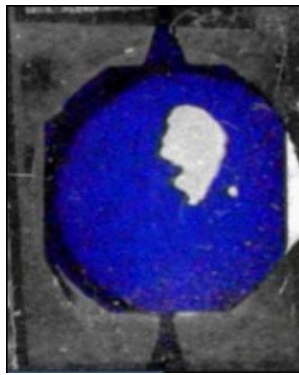
The different stages of cavitation in a micropump chamber, leading to supercavitation is as shown in Figure 4.15. For clarity of flow visualization, a colored dye was used with water in order to identify the cavitation.



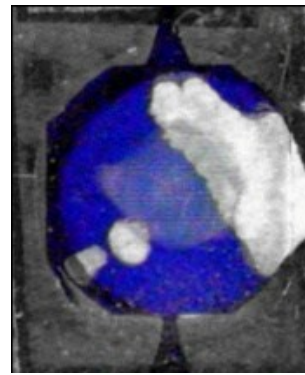
I. Before cavitation inception



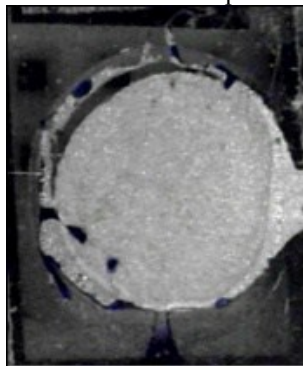
II. Cavitation inception



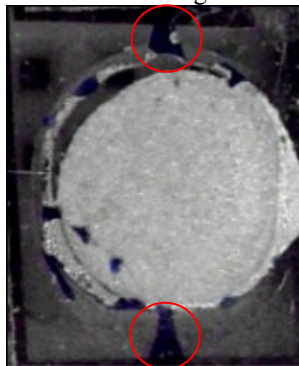
III. Cavitation growth



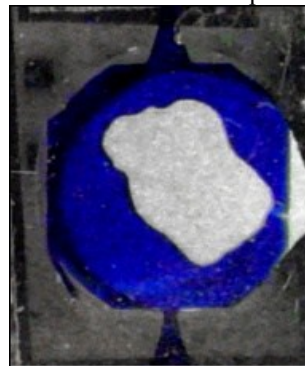
IV. Cavitation collapse



V Supercavitation – Pump stopped



VI Chamber refill begins



VII. Fluid refills in chamber

**Figure 4.15:** Images of different stages of cavitation in micropump leading to supercavitation, and the subsequent filling of the fluid inside the micropump chamber after stopping the micropump

For the present micropump, in order to study the phenomenon of supercavitation, the method of reverse flow was employed by monitoring the change in direction of flow of the liquid at the micropump outlet after the micropump was stopped at different frequencies. The supercavitation frequency,  $\nu_{sc}$ , is denoted as the frequency at which the reverse flow occurs. The inlet pressure head was varied by changing the height of the water column at the inlet, and the change in the supercavitation frequency with inlet pressure head was recorded. The plot of variation of  $\nu_{sc}$  with inlet pressure head,  $H_s$  is shown in Figure 4.16.

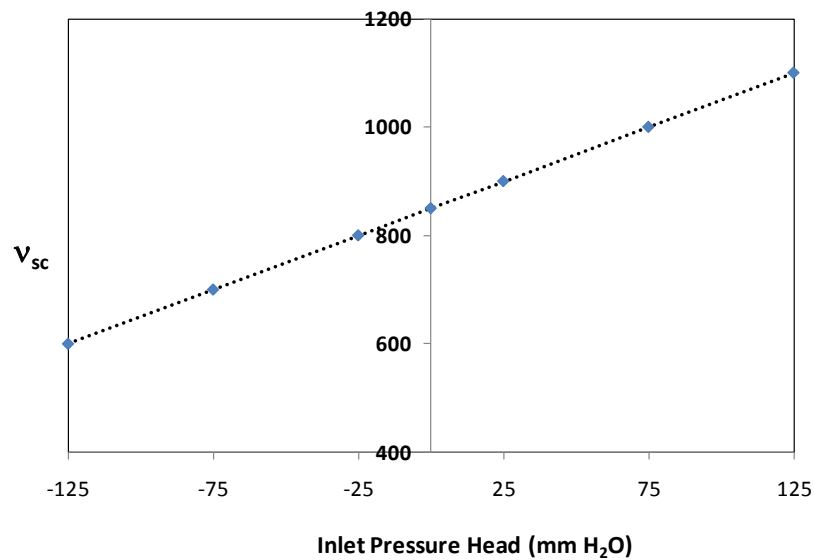


**Figure 4.16:** Plot of the variation of supercavitation frequency with inlet pressure head based on reverse flow calculation

When the supercavitation sets in a micropump, the pressure inside the chamber is so low, and flow is disrupted such that the net flow due to pumping in any direction is not possible. The low pressure region present in the micropump chamber extends into the

inlet/outlet channels and tubes. The expansion of the bubbles inside the channels further pushes the fluid from the tubes. Under these conditions, the growth of bubble is continuously favored, leading to continuous growth of the bubbles inside the connecting microfluidic tubes without collapse.

This phenomenon causes a tremendous increase in the rate at which the fluid is pushed out of the system due to the expansion of the cavitating liquid inside the tubes, after all the liquid inside the chamber is converted into vapor bubbles and subsequently collapse. Figure 4.17 shows the outlet of a micropump subjected to supercavitation, it can be seen that the cavitation spreads into the outlet channels. After supercavitation, it can be seen that there is a thick layer of vapor bubble deposition is formed on the microfluidic tubes, as shown in Figure 4.18.

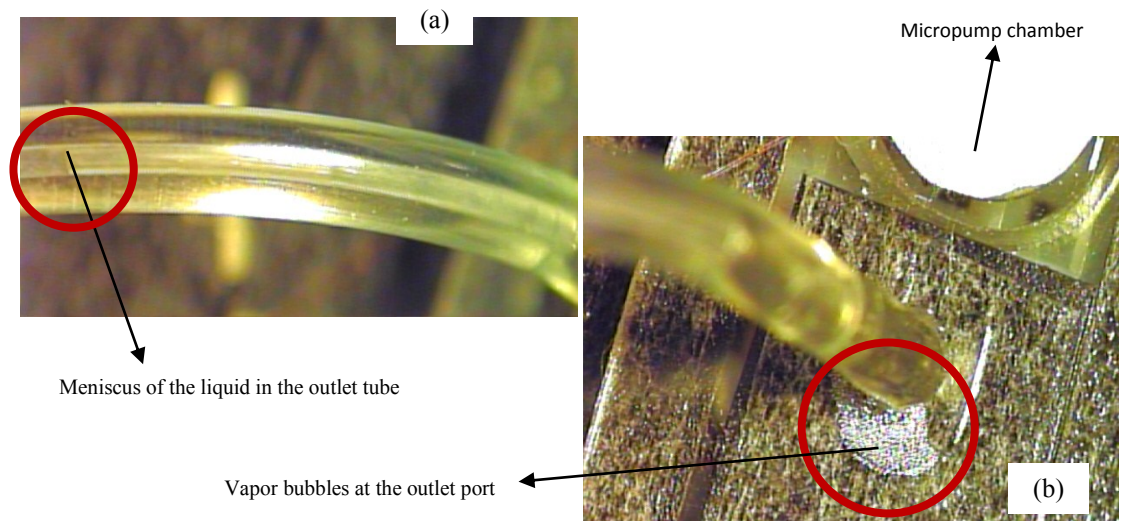


**Figure 4.17:** (a) Expansion of the cavitation bubbles into the outlet channel and (b) Formation of the vapor bubbles at the outlet port of the micropump after supercavitation

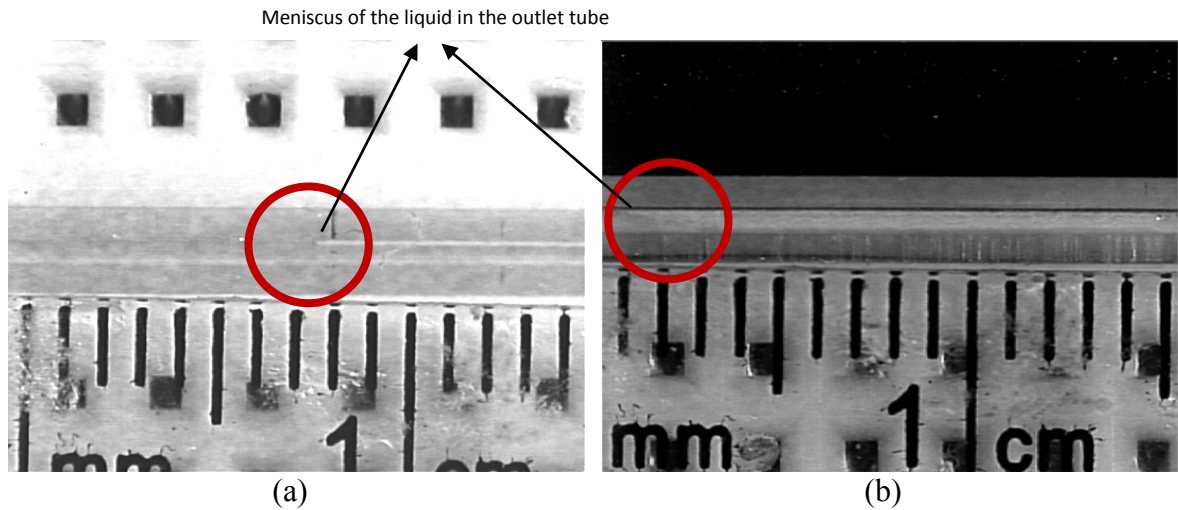


**Figure 4.18:** The outlet tube of the micropump (a) before supercavitation and (b) after supercavitation. The thick layer of vapor deposited on the tube due to supercavitation makes it extremely difficult to distinguish the meniscus of the flowing liquid visually, despite having a contrasting background.

#### 4.5. Summary of cavitation phenomenon in micropumps

Cavitation in a micropump chamber is initiated when the  $NPSH_a$  is equal to  $NPSH_r$ . With further increase in the  $NPSH_r$ , the cavitation bubbles grow until the energy is transferred to the bubble leading to the collapse of the bubbles. The cavitation growth is found to be dependent on several factors such as the presence of nucleation sites, microcrevices, dissolved gases, flow configuration, oscillating frequency, inlet suction head, deflection of the diaphragm etc.

Though initial cavitation stagnates the flow in the micropump due to the formation of bubbles that provides resistance to the flow, the flow was induced due to further

expansion of cavitation bubbles. In one of the earlier works (Wang et al. 2004), microfluidic actuation based on the induction of bubbles has been explored by laser induced cavitation. In the present case, the growth of the vapor bubbles caused due to the diaphragm oscillation, results in an increase in the pressure exerted by the cavitation bubbles. The direction of the fluid flow due to the expanding vapor bubbles depends upon the static heads available at suction and delivery sides.

When there is no flow of liquid from the input into the chamber during cavitation process, the continued operation of the pump causes all liquid inside the micropump chamber to cavitate leaving the chamber void, thereby inducing supercavitation. Under supercavitation, the growth of cavitation bubble is continuously favored, leading to continuous growth of the bubbles inside the tubes without collapse. The expansion of the cavitation bubbles inside the microfluidic tubes push the fluid at tremendous rate, thereby leading to a high Reynolds number flow.

#### **4.6. Effects of cavitation in micropump**

Inception, growth and collapse of cavitation bubbles are generally accompanied by a number of effects that influence the dynamics of the bubbles generated. In general, cavitation bubbles tend to collapse exceedingly fast, emitting pressure waves and even light (sonoluminescence).

With the growth of cavitation bubble inside the micropump chamber, tremendous pressure is exerted on the oscillating diaphragm. When the cavitation bubbles collapse, high pressure waves are created and these waves induce loading on the diaphragm and the actuator. As a consequence, sometimes severe sparks are observed, which results in the charring and burning down of the electrical circuit thereby leading to device failure. Therefore one needs to monitor the growth of cavitation in order to avoid electrical loading on the actuator. Figure 4.19 shows spark produced due to the overload on the actuator during cavitation.



**Figure 4.19:** Sparks due to electrical overload on the actuator caused by growth and collapse of cavitation bubbles

Typically, when the cavitation bubbles collapse, an audible ‘pop’ sound similar to a ‘cracking of the knuckle’ is emitted from the micropump. In some cases, if the noise is too loud, the shock waves are also strong enough to damage the oscillating diaphragm.

Figure 4.20 shows a crack in the oscillating diaphragm caused due to a repeated collapse of cavitation bubbles.

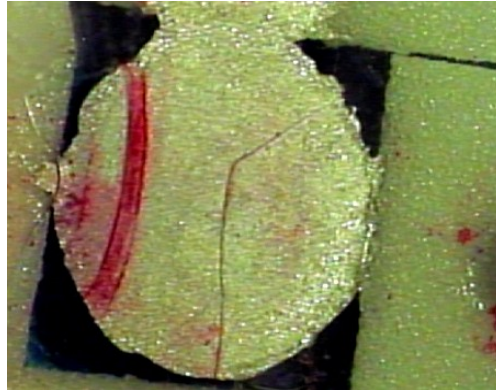
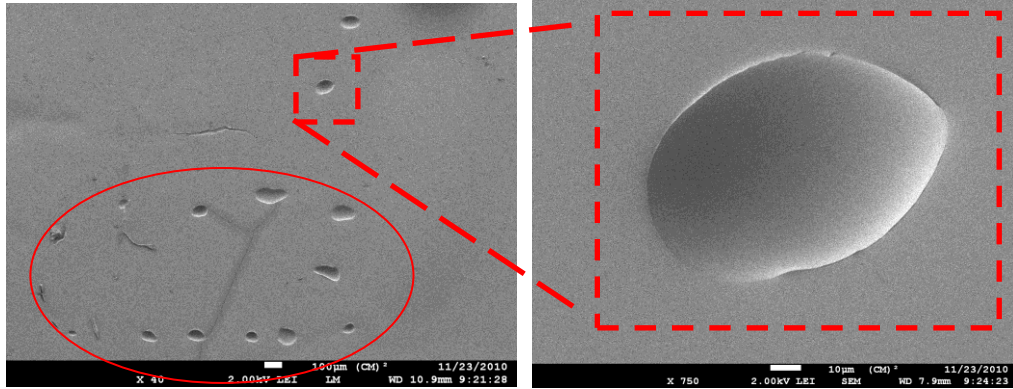


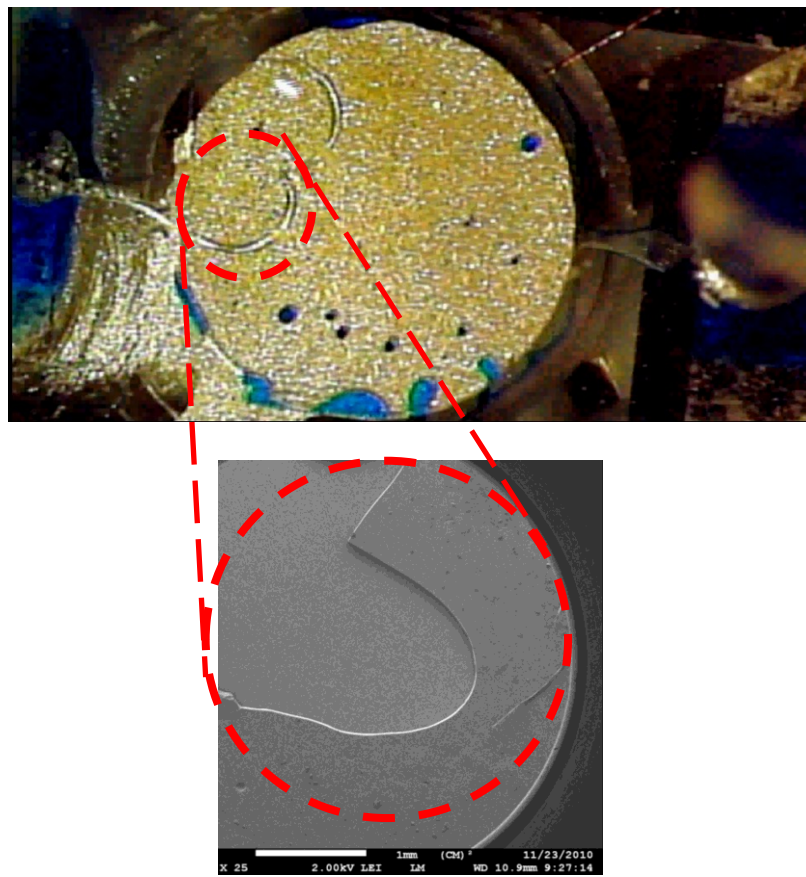
**Figure 4.20:** Crack observed in micropump diaphragm caused by repeated collapse of cavitation bubbles.

In the case of developed cavitation, if the relative velocities between the liquid and the solid walls are high, cavitation can also lead to the *erosion of these walls*. Research has shown that when a cavitation bubble collapses near a solid boundary, which in the present case is the moving diaphragm, the direction of the micro jet will almost always be towards that boundary. In other words, the entire energy of collapse is directed at a microscopic area of the surface of the diaphragm which leads to the formation of micro-erosion on the diaphragm surface. The SEM image of a few micropits formed due to low intensity cavitation bubble collapse is as shown in Figure 4.21(a). At higher frequencies, as more nuclei are joined, the cavitation collapse is more drastic and huge craters are also created on the chamber surface, as shown in Figure 4.21(b).





(a) Micropits



(b) Erosion of micropump surface

**Figure 4.21:** (a) Micropits created by the collapse of cavitation bubbles on the micropump diaphragm  
 (b) Crater crated by a cavitation bubble collapse on the micropump chamber surface

Therefore, it is very important that one should know to control the occurrence of cavitation inside the micropumps, so as to constructively exploit the phenomenon for different applications, without damaging the micropump.

## **4.7 Applications of cavitation**

Some of the useful applications of cavitation in micropumps, which were explored during the experiments, are presented in the following sections.

### **4.7.1 Improving micropump performance using cavitation**

Though cavitation poses several detrimental effects, controlled cavitation is very useful to improve the performance of the micropump for many applications.

#### ***4.7.1.1 High Reynolds number flow***

As seen in Section 4.4, supercavitation causes the vapor bubbles to expand rapidly inside the micropump chamber and this pushes the fluid out of the chamber at a tremendous rate. Cavitation induced flow is a highly attractive alternative to achieve high flow rates in valveless micropump applications which require high Reynolds number flow. The maximum flow rate obtained with supercavitation induced flow is more than 100 times greater than the flow obtained with valveless micropumping. Thus, cavitation can be used in high Reynolds number microfluidic test beds.

#### ***4.7.1.2 Enhanced priming of micropump***

During the operation of micropumps, it is possible that a significant volume of air bubbles get trapped inside the chamber and the diffusers. Given the complex geometries of the microfluidic channels, it is extremely difficult to purge the air bubble. In some cases, the air bubbles are trapped in the corners of the micropump chamber. And in such cases, it is not easy to fill the micropump chamber with full inherent air bubbles. (Kim et al., 2005). The presence of air bubbles drastically reduces the performance of the micropump, and the flow rate produced by the pump drops significantly. Therefore, it is very important that all the air bubbles are purged so as to achieve a better micropump performance.

One of the methods of removal of air bubbles is the continuous priming of the micropump chamber with fluids. This is done by inducing a microjet of high velocity liquid, into the micropump chamber which purges the bubbles, and thereby helping in removing them. However, there are two disadvantages of the technique of microjet induced purging. Firstly, it is extremely difficult to remove the air bubbles trapped near the boundaries of the micropump chamber, since the flow velocity of the microjets are very less near the walls of the chamber. Secondly, introducing microjets at higher velocities also sometimes cause damage to the adhesion between the glass diaphragm layer and the PDMS channel layer, and thus the bonding fails. Thus, the practical applications of the micropump require an extensive degasification process which includes alternate filling and emptying of the micropump chamber at low fluid velocity. This is a tedious, time consuming process and also is not always effective.

One of the practical benefits and advantages of low frequency cavitation is the feasibility of collapsing the air bubbles that are trapped inside the micropump chamber, thereby assisting in better priming. During the cavitation experiments, it has been found that low frequency induced cavitation is one of the easiest ways of removing the air bubbles that are trapped inside the chamber. By inducing cavitation inside the micropump chamber at a very low frequency, the air bubbles inside the microchamber expand and then subsequently collapse, thus aid in better priming of the system. Thereafter, using the reverse flow technique after supercavitation, it was possible to fill the channel completely only with the operating fluid and thus prime the chamber well for further experiments. The fully primed micropump chamber before and after supercavitation is as shown in Figure 4.22. It can be seen that the air bubbles trapped inside the micropump collapse during cavitation enabling better priming of the micropump.

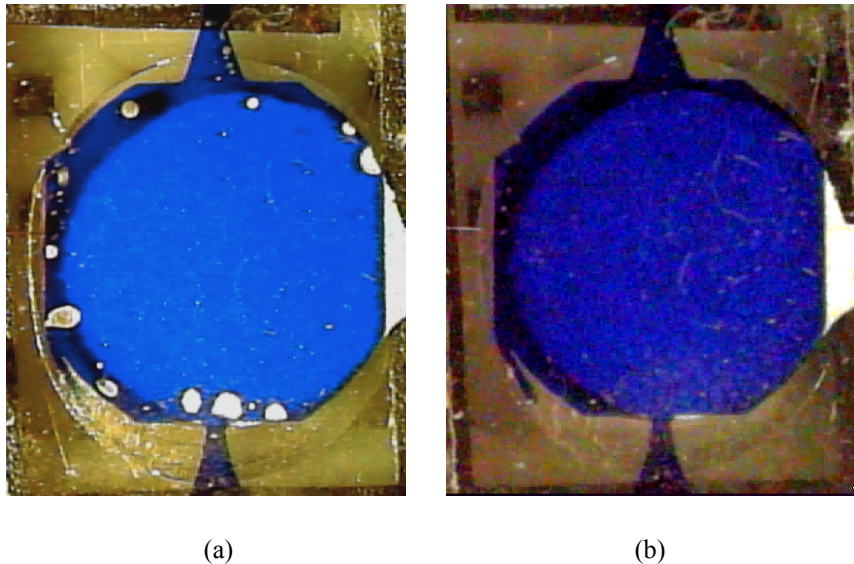


**Figure 4.22:** Priming of micropump chamber (a) before and (b) after supercavitation

#### **4.7.2 Cavitation assisted mixing of liquids**

Mixing in microfluidics is challenging and is difficult to achieve due to the low Reynolds number of fluid flow. When Reynolds number is small, then hydrodynamic instabilities and turbulence are almost nonexistent (Tabeling, 2005). Most of the mixing techniques presented in the literature points out to the use of passive mixing, wherein the micro chamber geometry is suitably modified to increase the area of contact between the fluids. One of the ideas of mixing in micro chambers is micro-mixers based on size reduction. In this method the size of the system decreases in order to reduce the diffusive mixing time (Pabit and Hagen, 2002). Ring-shaped micro mixers, developed by Scherer and Quake (2000) are another type of mixer used and the herringbone micro mixer, which is passive chaotic mixer was created by Strooke et al. (2002).

Among the different types of mixing in the micro regime reported, the most common type of mixing involves diffusion mixing. However, since one does not have a control over the diffusion inside a channel, it is extremely difficult to achieve the desired level of mixing or to alter the mixing properties by this technique. Therefore, active mixing is employed in microfluidic applications wherein a part of the microfluidic channel is moved or external force like pressure or electric field is applied so as to create necessary conditions for mixing.

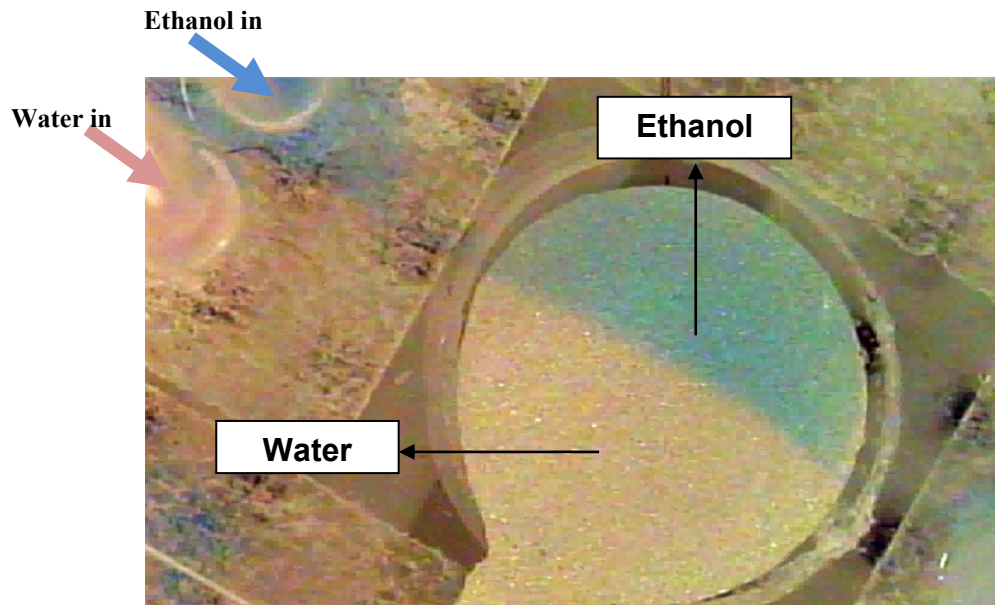
Herein, a cavitation induced mixing mechanism is proposed, where it is possible to mix two fluids by the creation of suitable cavitating conditions inside the micropump

chamber. Mixing with cavitation has been studied with laser induced cavitation before (Hellman et al., 2007), wherein the bubble expansion and subsequent collapse within the channel disrupt the laminar flow of the parallel fluid streams and produces a localized region of mixed fluid. Using similar principle, one can take advantage of cavitation effects in the micropump to induce mixing of two fluids in the chamber and use it for further analyses.

In order to achieve mixing it is necessary that atleast two fluids are input into the micropump chamber. However given the extremely laminar nature of flow within, it is not possible to use a single input, without the formation of recirculating microfluidic systems (Chandrasekaran and Packirisamy, 2006). Therefore, it is essential that the two fluids are transported into the system through two separate microfluidic ports. Hence, for this experiment,  $\mu$ TAS with two inlet ports was fabricated. This also calls for the integration of two microfluidic tubes at the inlet of the micropump. It is important that the microfluidic tubes are exactly similar in length and dimensions in order to prevent any back flow that could happen from one tube to another due to backpressure.

Before inducing cavitation, the flow based passive mixing was verified by passing two highly miscible fluids, namely water and ethanol, which are input into the system, as shown in Figure 4.23. In order to distinguish between the fluids, a blue dye was added with ethanol and a red dye was added with water. In order to simultaneously inject the fluids into the system, two inlet ports were made in the micropump. The fluids were passed simultaneously into the micropump chamber using a double channel syringe

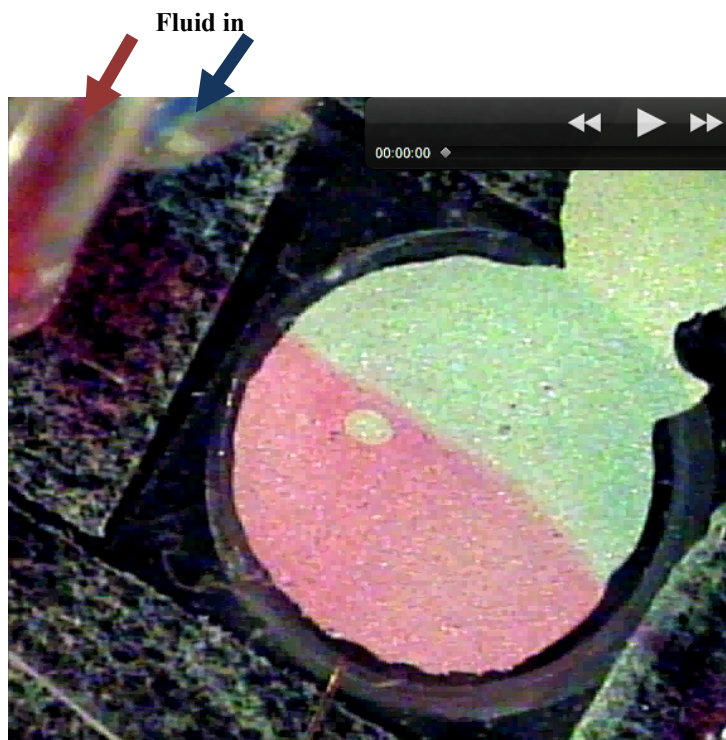
pump. It can be seen that, without the actuation of the micropump, the flow is perfectly symmetric inside the micropump chamber and there is absolutely no mixing of the fluid within any part of the system, including at the inlet, narrow diffuser neck (100  $\mu\text{m}$ ) and the outlet.



**Figure 4.23:** Flow of ethanol and water inside the micropump chamber. Without the micropump operation no mixing occurs inside the chamber.

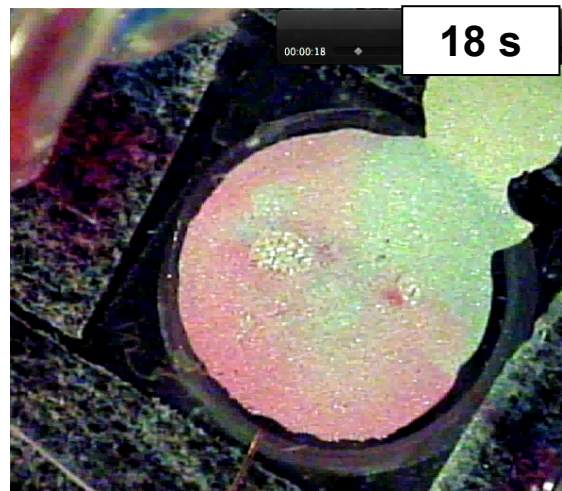
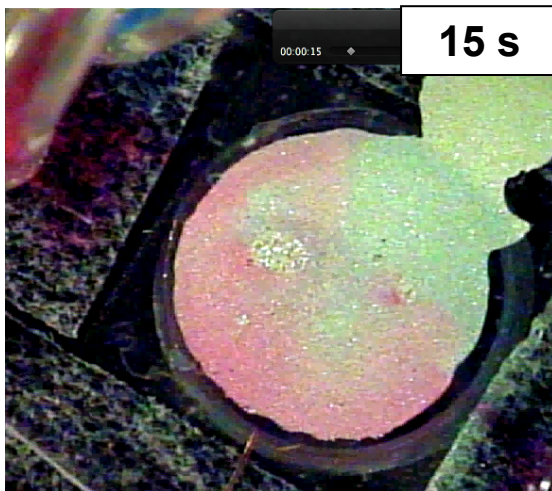
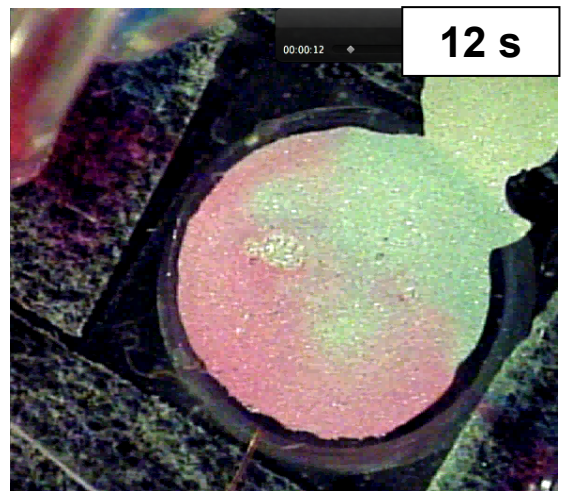
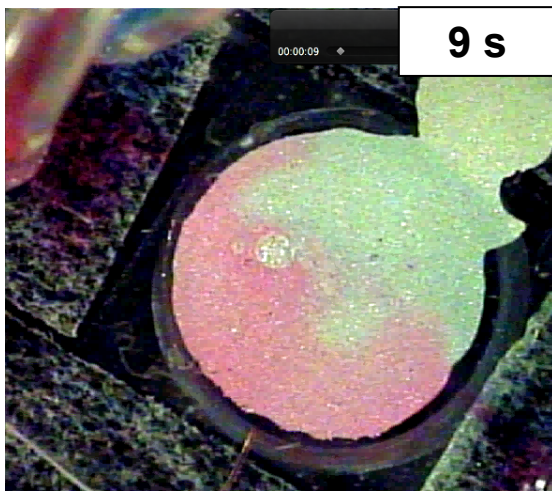
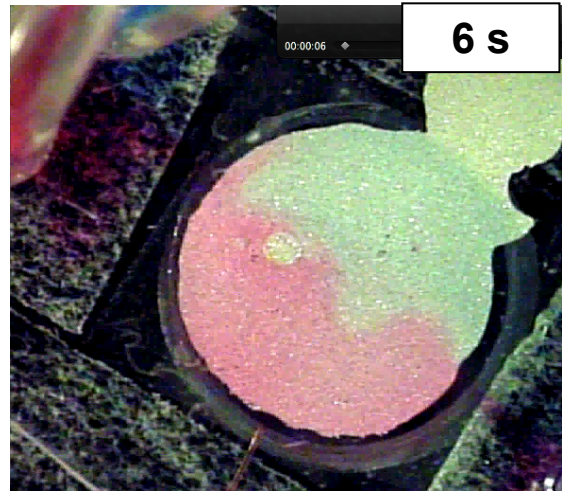
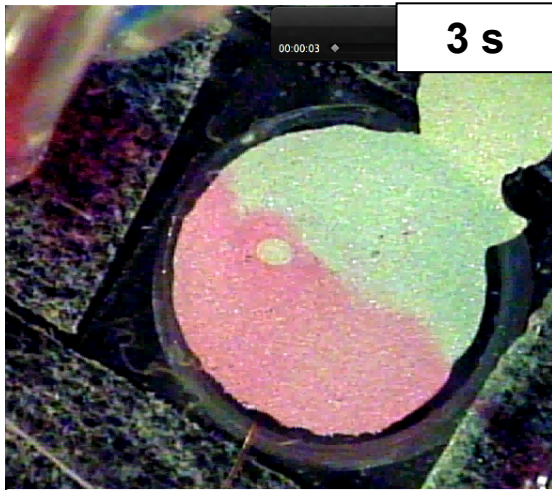
To demonstrate the phenomenon of cavitation induced mixing, higher concentrations of red and blue dyes were added to water and ethanol respectively in order to enable better visualization of mixing inside the micropump chamber, and the liquids were injected into the micropump using the syringe pump. As seen in Figure 4.24, before the start of the micropump, there is no mixing between the liquids. Thereafter, the micropump was operated at 1000 Hz, in order to create cavitating conditions inside the chamber. The

results of the experiment are as shown in Figure 4.25 which shows the cavitation based mixing at different times, after the start of the micropump operation.



**Figure 4.24:** Two fluids remain unmixed before starting of micropumping.







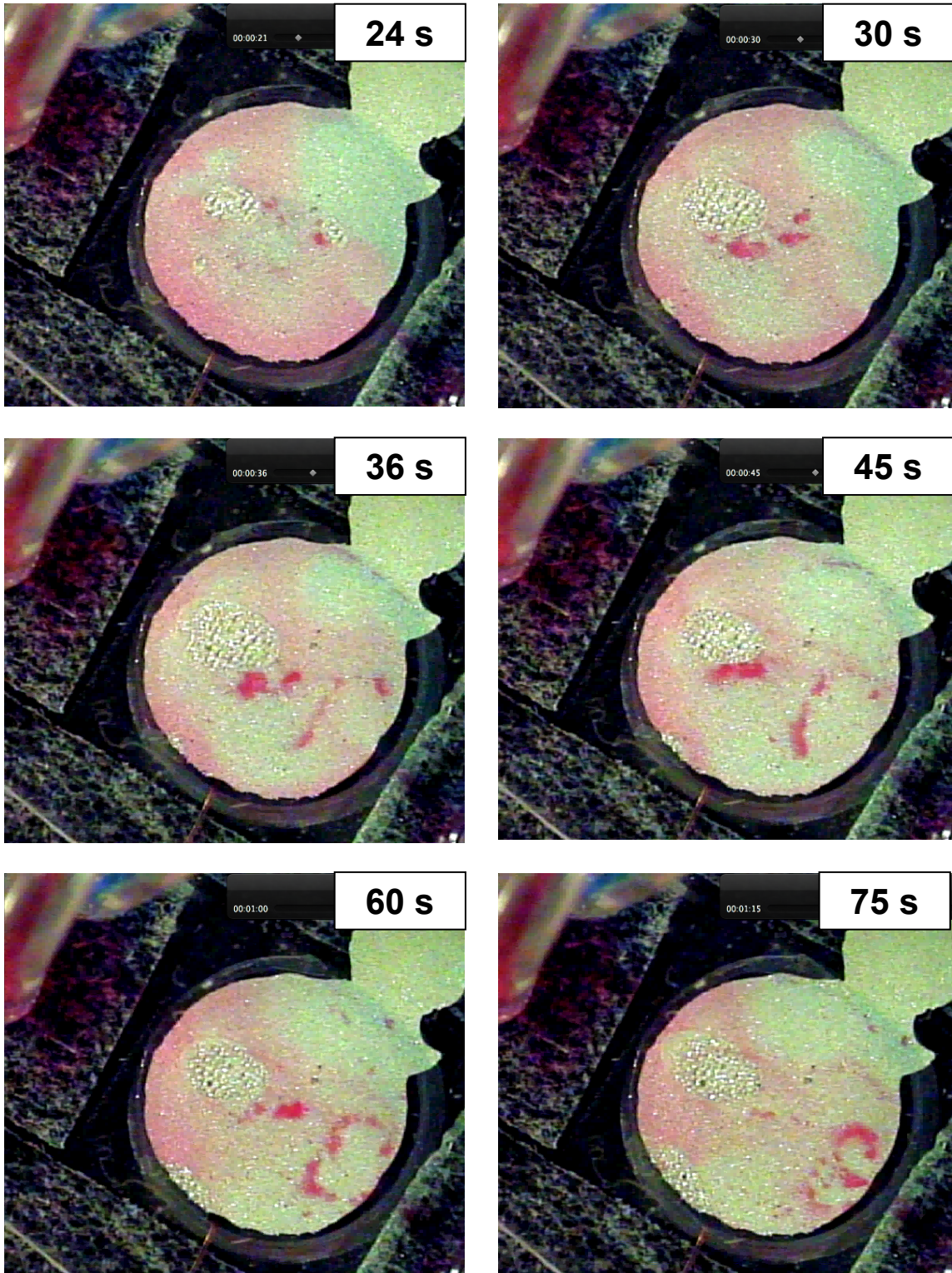


**Figure 4.25:** Progress of cavitation induced mixing in the micropump chamber at different stages

At the end of mixing, it can be seen that there is a cavitation pit that is developed inside the micropump chamber, which acts as an obstacle for fluids to flow through. However, when the two fluids were input into the channel again, and streamlined laminar flow is observed as shown in Figure 4.26, when there is no pumping.



**Figure 4.26:** Laminar flow with subsequent input of fluids after cavitation induced mixing

From the Figure 4.25, it is very clear that cavitation assists mixing tremendously. However, it can be seen that at the end of the experiment, there is a large void created inside the micropump chamber, which is due to the cavitation induced damage that results in the formation of a large crater on the micropump. Therefore, it is important that the cavitation induced mixing is carried out at a lower frequency which assists the mixing, but which does not cause any damage to the surface of the micropump during the cavitation collapse. It is also possible to use a series of cavitation micropumping for thorough mixing.

### 4.7.3 Cavitation assisted fluid separation

It is known from the cavitation experiments and the results presented in Section 4.4 that, after the initiation of cavitation, the liquid is converted to vapor bubbles as the pressure inside the chamber drops below the vapor pressure of the liquid. This phenomenon can be used to separate two liquids, with different physical properties and vapor pressure.

In order to demonstrate this, two immiscible liquids were passed into the micropump chamber separately and cavitation was induced, such that liquid with a higher vapor pressure cavitates and is pushed out of the chamber due to the phenomenon of supercavitation. For this experiment, rotary pump oil (Fomblin) which has an extremely low vapor pressure of  $\sim 10^{-7}$  Torr and water, with a vapor pressure of 17.5 Torr at 20 °C were chosen, and were injected into the micropump chamber. In order to distinguish the two liquids, a blue dye was added to water. The images of the micropump chamber at different stages of cavitation are as shown in Figure 4. 27



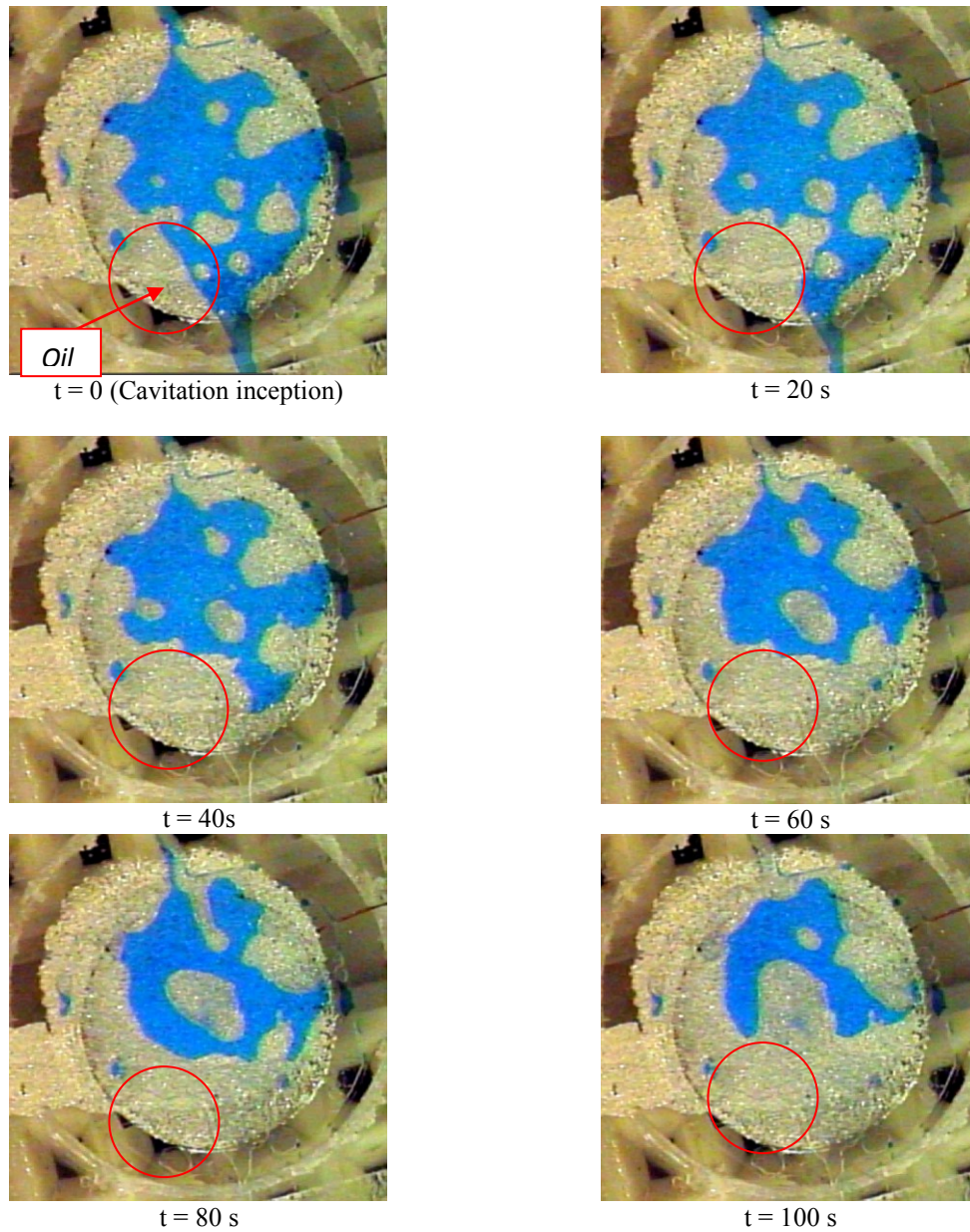


**Figure 4.27:** Different stages of cavitation assisted separation of water and oil.

Due to the high viscosity of oil, it was not possible to prime the pump uniformly with oil. Subsequent input of water occupied the voids inside the micropump chamber. The regions occupied by oil are marked at  $t = 0$ . It can be seen that during cavitation, the oil remains

inside the micropump chamber, whereas the water (indicated by the blue dye) cavitates and is pushed out of the chamber, as shown in Figure 4.28.

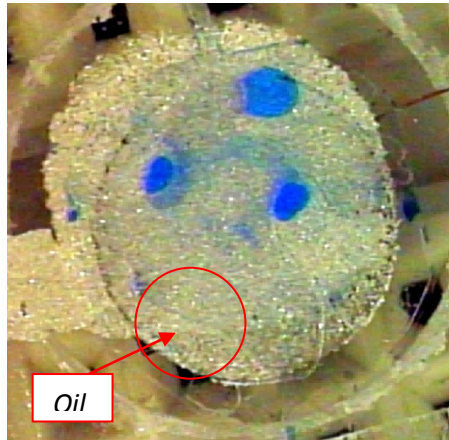


**Figure 4.28:** Image of the micropump chamber after separation of oil and water.

Thus, cavitation was used for separation of two liquids based on different vapor pressures. The same principle can be extended to the separation of other immiscible liquid - liquid, or solid-liquid mixtures, using the phenomenon of cavitation.

#### ***4.7.3.1 Blood fractionation using cavitation***

Using a similar principle described above for fluid separation, cavitation phenomenon was also explored for blood fractionation application, for the separation of blood plasma and blood cells. This phenomenon was a purely accidental discovery, as a result of a minor injury when working in the laboratory.

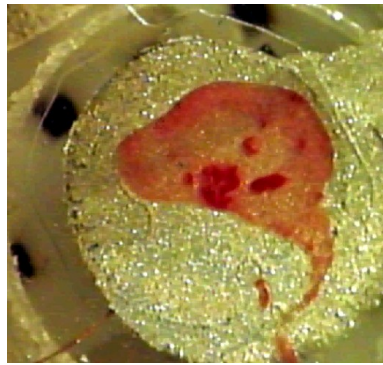
A drop of blood was placed at the inlet port of the micropump, as shown in Figure 4.29, and was pushed into the micropump chamber when the connecting tube was plugged at the port.



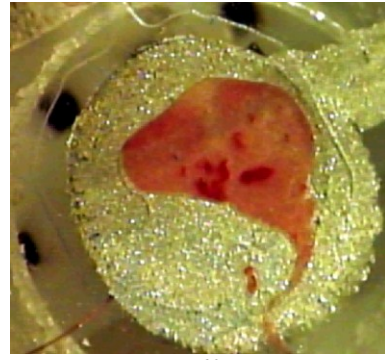
**Figure 4.29:** Input of blood sample into the micropump

The micropump was operated at supercavitation frequency of 2000 Hz and the effect of cavitation on the blood drop was studied. The images of the micropump chamber during supercavitation of blood are shown in Figure 4.30.

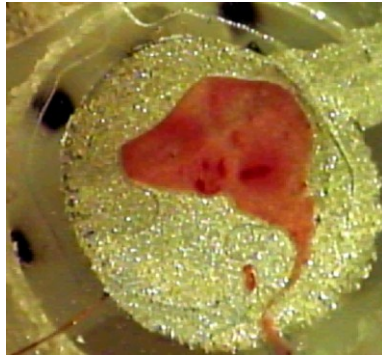




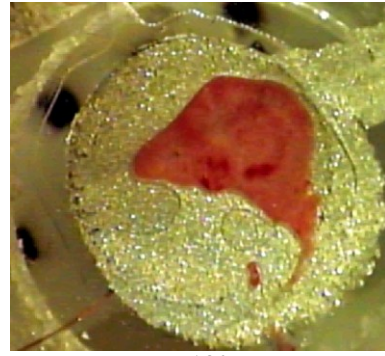
t = 0 s (Supercavitation inception)



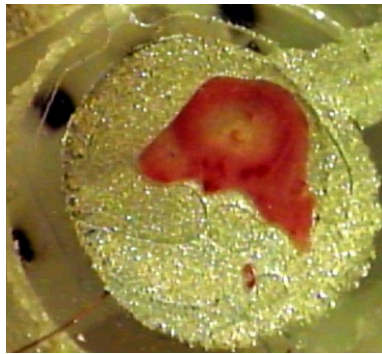
t = 60 s



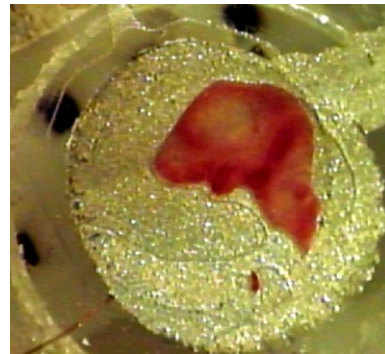
t = 120 s



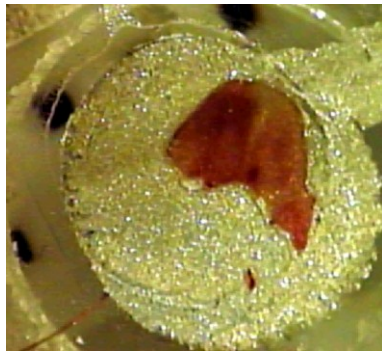
t = 180 s



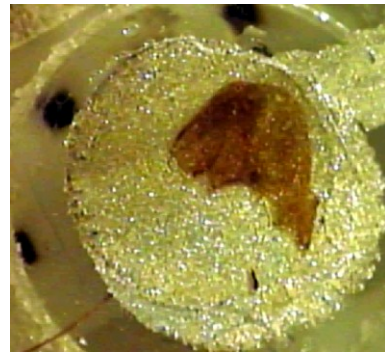
t = 240 s



t = 300 s



t = 360 s



t = 420 s

**Figure 4.30:** Different stages of supercavitation assisted separation of blood plasma from blood cells



The liquid blood plasma is converted to vapor bubbles and is separated from the other constituents of the blood. The cells, i.e the Red Blood Cells (RBC) and the White Blood Cells (WBC), were retained inside the micropump chamber itself. Thus, the plasma can be collected separately as shown in Figure 4.31. Thus, cavitation enables the separation of blood plasma from the blood cells, thereby enabling the possibility of carrying out further clinical diagnostics using the plasma alone. This process is called as blood fractionation.

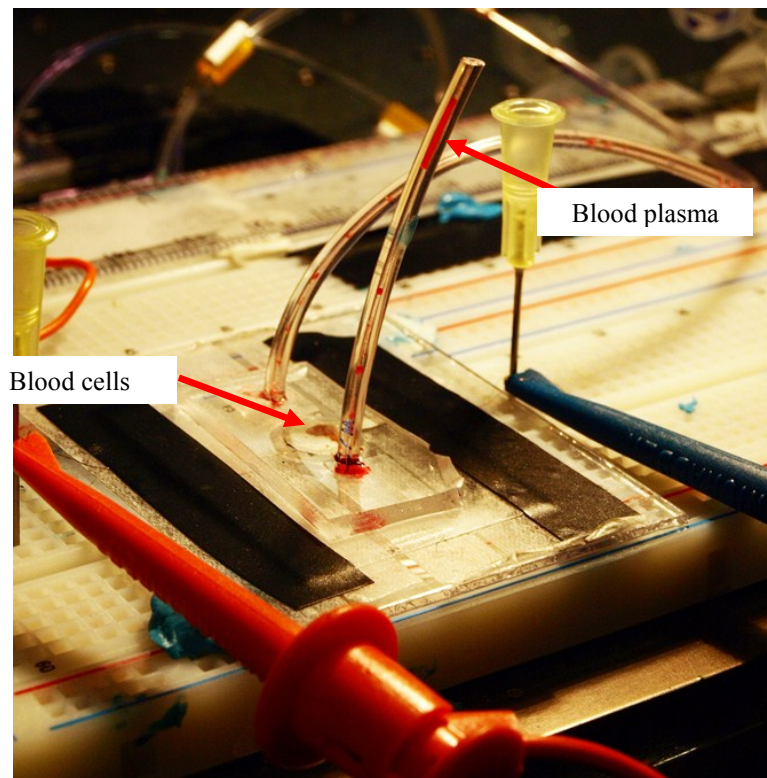
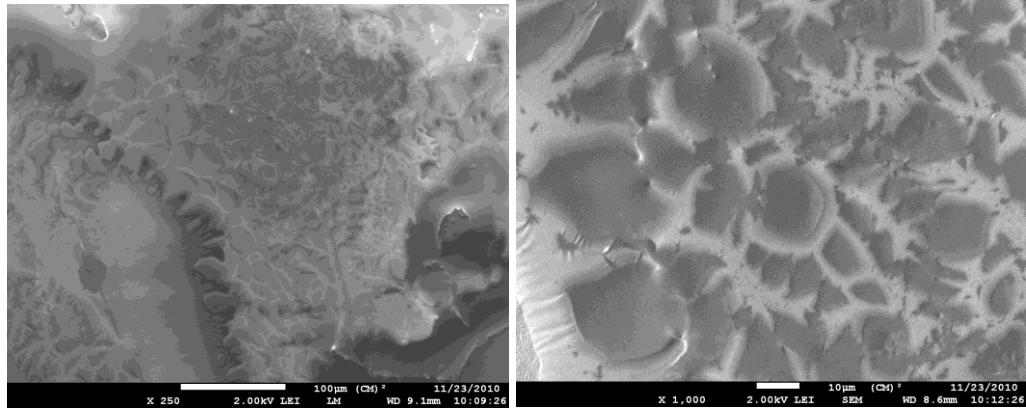


**Figure 4.31:** Separation of blood plasma from blood cells

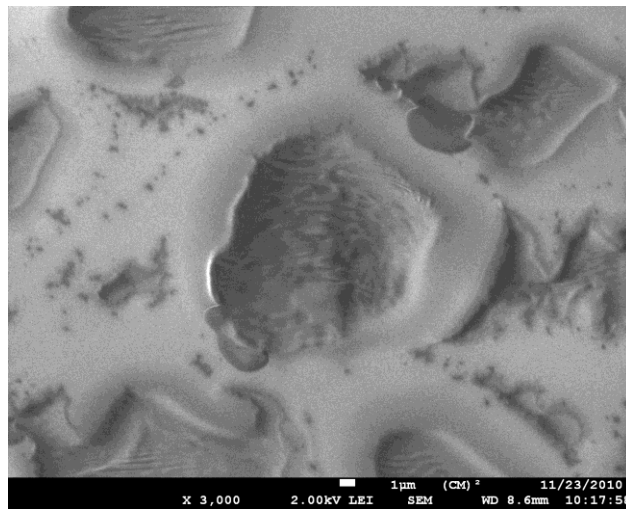
A short study on the constituents of the blood show that RBC's are biconcave disks, which are supposed to be extremely deformable. The viscosity ratio between the inner

fluid of RBC and the suspending medium partly characterizes the behavior of the RBC in its environment. It has been reported that RBCs exhibit different behaviors and even take different shapes depending on the Reynolds number and the degree of shear force. At a relatively high Reynolds number and viscosity ratio, but in the laminar regime, RBCs flip around themselves; this movement is often referred to as tumbling. At a lower Reynolds number and viscosity, however, the cells follow a tank-treading movement in which the membrane of the cell alone is rotating around the centre of the mass. A cell, which tank-treads, maintains a stationary orientation with the flow (Abkarian and Viallat 2008). Finally, a third transitional regime was found by Abkarian et al. (2007), and is named swinging. In this regime the cell tank-treads but undergoes oscillations around its stationary orientation.

Therefore, cavitation flow assists in all the above mentioned mechanisms, and since the RBC is extremely deformable, the motion of the oscillating diaphragm causes the compression of the cells. Therefore, these cells are not transported out the of micropump chamber due to supercavitation. However, only the blood plasma is converted to vapor bubbles during cavitation and thus is transported out of the chamber, as shown in Figure 4.31. The SEM images of the blood cells collected in the micropump chamber is as shown in Figure 4.32



(a) Red Blood cells (RBC)



(b) White Blood Cell (WBC)

**Figure 4.32:** SEM image of the Red Blood Cells and the White Blood Cells that were separated inside the micropump chamber

Centrifugation and filtration are the two conventional techniques for blood plasma separation in laboratories. Both methods are time-consuming, relatively expensive and might damage cells if not used carefully (Sallam, 1984).

For the present experiment, as seen in Figure 4.29, only one drop of blood of a few tens of microlitres was used. Thus, the present experiment proves that with better design and fabrication of the micropump, separation of small volume measured quantity of blood can be carried out easily and transportation can also be carried out into the microfluidic system. The blood plasma can be used for various pathogenic studies for detection and analysis of several important molecules present in it.

The experiment was stopped at that stage and no further analyses were carried out. Thus, the accidental injury was very useful in carrying out real-time experiment with human blood, which is otherwise restricted at the Optical-Bio Microsystems Laboratory.

#### **4.7.4 Cavitation assisted cell lysing**

For biological applications, cavitation phenomenon can be tuned to the advantage of the user, either to lyse a cell or to transport a cell faster without doing any harm to it. Cell lysing is one of the important applications of cavitation, as has been reported in the literature. However, most of the reports discuss about cavitation at ultrasonic frequencies of ~50 kHz. However, high powers are often damaging and can sometimes destroy the biological substrates making them not useful for further analyses. Hence, for such applications, low frequency mechanically generated cavitation as described in this work is more useful in biological applications.

With the present system, the feasibility of cavitation for cell lysing was verified using Human Embryonic Kidney (HEK293) cells. One of the disadvantages of the present system was that with the growth of the cavitation bubble, the cells transported into the micropump chamber were pushed out of the system and thus were not subjected directly to the shock induced by the cavitation bubble collapse. However, with suitably designed cell trapping system within the micropump chamber, it is believed that cell lysing with the system is definitely possible.

#### **4.7.5 Cavitation induced chemical cleaning**

In experiments which used oil as the working fluid, the subsequent removal of the oil from the micropump chamber was difficult despite continuous priming. In such cases, ethanol was injected into the system and a low frequency cavitation was induced. Ethanol mixed with oil and the cavitation phenomenon pushed the liquid out of the chamber without damaging the system. In a few experiments in which the ink was used, the ink particles adhered onto the surface of the microfluidic channel as shown in Figure 4.33(a). The attractive forces between the ink and the micropump surface are believed to be due to the attraction of their dipole bonds. In order to release these bonds and remove the contaminants from adhering onto the channel surface, the chamber was treated with milk.

Milk is an emulsion which contains both polar and non-polar substrates, which therefore dissolves most of the solute types. In order to clean the ink particles off the micropump surface, the chamber was initially primed with commercially available milk as shown in

Figure 4.33 (a), so that the milk bonds weakly with the contaminants. Thereafter, mild cavitation was induced inside the chamber. The collapse of cavitation bubbles caused the removal of the ink particles from the channel surface, as shown in Figures 4.33(b) and 4.33(c), thereby helping in cleaning the micropump chamber surface. The subsequent supercavitation induced flow helps in carrying the contaminant particles away so that they do not reattach to the surface.

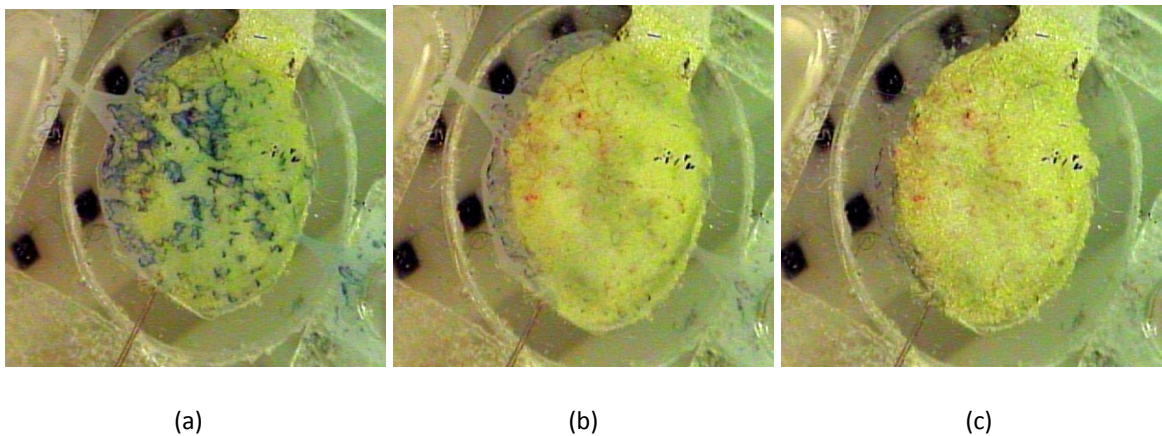


**Figure 4.33:** Images of the micropump chamber (a) Before cleaning (b) After one time cavitation assisted chamber clean with milk (c) After cleaning with water

#### 4.8. Conclusion

This chapter presents the study of behavior of cavitation in a mechanically actuated valveless micropumping system. The principles of cavitation in macroscale pumping have been extended to the microscale and the cavitation parameters for micropumping have been defined. For any given micropump, cavitation occurs when the  $NPSH_a$  is less than  $NPSH_r$ .

Experimental investigation was carried out to study the behavior of cavitation in micropumps. Four stages of micropump cavitation, namely, cavitation inception, cavitation growth, collapse of cavitation bubbles and supercavitation were observed during cavitation in micropumps. Cavitation induced flow and pressure measurements were carried out during each stage of cavitation, by varying dynamic parameters of the micropump and inlet suction head. These results were also supported by flow visualization experiments.

Cavitation poses a few detrimental effects on the micropump performance. However, in this work, cavitation has also been explored for the following applications:

- Mixing of fluids
- Fluid separation
- Blood fractionation
- Cell lysing
- Chemical synthesis
- High Reynolds number microfluidic applications
- Cleaning and enhanced priming of micropump chamber

Thus, micropump cavitation is an important phenomenon, which needs to be well understood for the design and operation of the micropump, as it can significantly affect device performance. At the same time, controlled cavitation can be exploited for several chemical and biological applications in  $\mu$ TAS.

# Development of External Hybrid Integrated Optical Detection System for $\mu$ TAS

### 5.1. Introduction

As discussed in Chapter 1, optical sensing system has a lot of advantages for the detection and analysis of chemical and biological species in a  $\mu$ TAS. With the need to analyze individual particles or molecules for biosensing, and to detect smaller sample volumes, it is important to develop a high sensitive optical detection platform. Given the important functions of microfluidics and micropumps in a  $\mu$ TAS, it is important that the optical detection system is suitably integrated with the microfluidics ensemble in order to carry out high sensitive biodetections with smaller sample volumes. Of chemical and biological substrates the two main factors that affect optical detection in a  $\mu$ TAS are sensitivity and scalability to smaller dimensions. While in macro scale, optical components such as lenses and filters are used in traditional bioanalytical devices. The major challenge in a  $\mu$ TAS is to integrate the external optical ensembles with microfluidics for efficient biosensing through coupling of optical signals in and out of device, without compromising on the sensitivity of the system.

Therefore, the integration of optics, microfluidics and biology into MEMS forms the backbone for the successful implementation of the  $\mu$ TAS for several biomedical



applications at the micro and nano levels for Point-Of-Care Testing (POCT) and in-situ biomedical detections for carrying out rapid, precise and high throughput biodetections.

## **5.2 Classification of Opto-microfluidic integration**

Several works have been carried out for the integration of microfluidics and microphotronics and different types of Opto-microfluidic integration are possible for the realization of a  $\mu$ TAS, as discussed in Chapter 1. Some of the novel integration technologies for micro-optics and microfluidics use a filled microfluidic channel as a liquid-core waveguide (Demetri Psaltis et al. 2006). However, literature suggests that broader classification of the different methods of traditional optical microfluidic integration leads to two types, namely hybrid integration and monolithic integration.

Monolithic integrated optical microfluidic systems (Lien et al. 2003), (Cohen et al. 2004), (Friis et al. 2001), (Leeds et al. 2004) have a lot of advantages, for  $\mu$ TAS applications. Through the monolithic optical microfluidic integration, the problem of efficient coupling have been used such as pig-tail coupling of optical fibers to the microchip, or hybridized micro optical systems with laser diodes and in addition to the light source, the other optical and fluidic components have also been aligned through proper definition of the lithographic method itself (Balslev et al. 2005)

However, monolithic integrated systems also have their own disadvantages, mainly due to the optical losses incurred in the system. For systems in which the coupling of light from

the source to the optical system poses a problem with mode mismatch losses and other insertion losses. Some of the monolithic integrated devices also suffer from lithographic imperfection related optical losses due to scattering and surface roughness (Splawn, Lytle 2002). This calls for the necessity of developing a hybrid integrated system with optical fibers in order to minimize optical losses.

Among the hybrid integrated optical microfluidic systems, two types of integration feasibilities are possible, namely the External “off-chip” hybrid integrated system and Internal “On-Chip” hybrid integrated system. As the name suggests, both the above mentioned types of hybrid integration are distinguished in the manner in which the optical fiber is integrated with the microfluidic domain. External hybrid integrated systems are those in which the optical components such as light sources, fibers, photodetectors, and spectrometers are integrated outside the microfluidic regime, through suitable fixtures and setup.

The internal hybrid integrated system, the optical components and the microfluidics are hybridly integrated onto the same chip. The advantage with internal hybrid integrated devices is that the system is more rugged and most of the optical losses experienced with the external hybrid integrated system such as material absorption loss, minor misalignment losses, sensitivity etc are reduced. However in comparison with the external hybrid integration system, the internal hybrid integration suffers from lack of manoeuvrability of components, which therefore suggests that the system is not flexible .

Most of the integrated optical microfluidic systems referred in the literature are developed through hybrid integration, externally or internally. In this chapter, the feasibility of carrying out controlled biodetection on an externally hybrid integrated microfluidic platform has been presented. The feasibility of optical detection has been demonstrated through demonstrated the method of laser induced fluorescence and optical absorption. Different material platforms have been used and the compatibility of absorption and fluorescence detections has been demonstrated through integrated biomicrofluidic experiments.

### 5.3 Development of external hybrid integrated System

The feasibility of the external hybrid integration was demonstrated on silicon platform for the detection of antigen-antibody interaction through the method of fluorescence (Chandrasekaran et al. 2007). The schematic of the external hybrid integrated setup is as shown in Figure 5.1

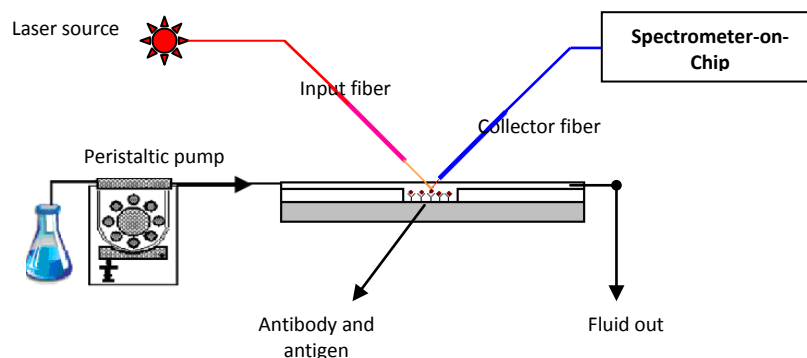


**Figure 5.1:** Schematic of the external hybrid integrated fluorescence detection setup (Chandrasekaran et al. 2007).

In this work, the fibers were externally integrated with the microfluidic system. Important aspects of the present work include flow velocity controlled passive immobilization of the antigen molecules onto the surface of the silicon microfluidic channels without the need for specialized surface treatments through simple and inexpensive microfluidic packaging techniques with pyrex and polycarbonate materials, which could be applied in standard packaging technologies for silicon based microfluidic chips. Hence, the hybrid integration of silicon based microfluidic chip and silica-on-silicon based spectrometer-on-chip opens up the feasibility of fabricating a monolithically integrated Lab-on-a-chip type device that could be used for in-situ biomedical applications and Point-of-Care testing (POCT) for rapid pathogenic detections and for other chemical and biological sensing.

However, one of the main limiting factors for the presented hybrid integrated system is the inability of the silicon microfluidic channel system, to offer optical transparency in the visible wavelength range. The optical transparency of the microfluidic channel is important so that the biological reactions taking place within the system can be monitored optically, through optical measurements and also through flow visualization, thus making the platform suitable for carrying out more than one type of optical detection. Also, it is important to develop suitable microfluidic system to facilitate proper biointeraction. Aside from fluorescence detections, in other forms of bio-optical detections which calls for biological interactions such as protein-protein interactions, enzyme-ligand interactions, or antigen-antibody binding, it is important to create the appropriate conditions of microfluidic mixing for enhancing bio-interactions.

Therefore, in order to address the above issues, a glass based external hybrid integrated system was fabricated to carry out optical absorption and fluorescence detections. Through proper design of the microfluidic channels, appropriate molecular interaction and controlled mixing, is also realized, and the optical transparency of the glass microfluidic system also offers compatibility with optical detection in the visible wavelength range and flow visualization.

### **5.3.1 Design of recirculating microfluidic system for external hybrid integration**

Among the important and critical issues which need to be addressed for the successful development of a microfluidic platform for hybrid integrated biosensing and biodetections, mixing of fluids within microfluidic channels, immobilization of the biomolecules onto the surface, the control of the amount of fluid used and localization of the area of interaction of the biomolecules within the microfluidic channels . There are two prime concerns with regard to immobilization of biomolecules, primarily, the proper binding of the specific biomolecule site during immobilization and secondly, the retention of the bioactivity of the molecules after immobilization. Within a closed microfluidic channel, one does not have a control over proper immobilization of biomolecules onto the surface and therefore, it is essential to employ a suitable method to trap the biomolecules within the area of scrutiny without disrupting their physical and biological properties and enable passive mixing for bio-interaction, so as to carry out successful biosensing on microfluidic platform. In cases where the detection of bio-interactions has to be carried out under continuous microfluidic flow, the biosensing would be rendered difficult

especially at high flow velocities. Hence, it is important to develop a microfluidic technique in which one can enhance the time of interaction of the biomolecules and hence increase the throughput even at higher flow velocities, thereby creating a scope for several potential applications in biological and chemical sensing.

In this work, a recirculating microfluidic platform has been developed for carrying out optical biodetection. The present device can be used for passive mixing of the biological species within the microfluidic channel without immobilization, through appropriate design and flow control. The schematic of the recirculating microfluidic chamber is given in Figure 5.2. The microfluidic channel design consists of a single input port which branches into two output channels from the recirculation chamber. The Recirculation zone or R-Zone is the region of the chamber, in which fluid recirculates, as shown in Figure 5.3(a). The different channel geometries used in the present work were as follows: Recirculation chamber of  $1500 \times 1500 \mu\text{m}^2$ , width of input /output microfluidic channels is  $150 \mu\text{m}$ .

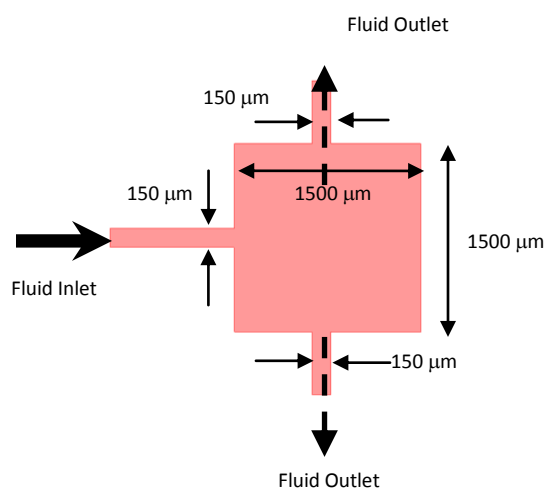


**Figure 5.2:** Design parameters for recirculating microfluidic chamber.

In order to understand the flow behavior within the chamber, finite element modeling of the fluid flow within the recirculating chamber was carried out. The continuity and Navier Stokes equations given in Equations (5.1) and (5.2) were solved, assuming a 2-dimensional flow that is invariant with respect to the height. The boundary conditions used for the modeling are constant fluid velocity at the inlet and ambient pressure at the outlet. The incompressible and Navier-Stokes continuity equations for Newtonian fluid are given as

$$\nabla \cdot \vec{u} = 0 \quad \dots 5.1$$

$$(\vec{u} \cdot \nabla) \vec{u} = \frac{-\nabla p}{\rho} + \gamma \nabla^2 \vec{u} \quad \dots 5.2$$

wherein,  $\vec{u}(x,y)$  is the velocity vector of the fluid,  $p$  is the pressure,  $\rho$  is the fluid density,  $\gamma$  is the kinematic viscosity and  $\nabla \equiv i \frac{\partial}{\partial x} + j \frac{\partial}{\partial y}$ . Boundary conditions for ideal liquid flows are always assumed to be at no slip.

Finite Element Analysis was carried out to solve Equations (5.1) and (5.2) for the selected chamber geometry, using commercial software COMSOL. The formation of the recirculation zone within the chamber was studied from the Finite Element Modeling of the flow behavior within the recirculating zone using COMSOL. The predicted flow behavior within the flow chamber is as shown in Figure 5.3(a). The flow within the chamber consists of optical measurement zones in three flow regimes, namely, the flow zone,  $F^*$  containing only the forward main flow, the recirculating zone or the R-Zone consisting of only recirculating or trapped flow and the overlap zone,  $O^*$  which borders

both forward and recirculating flows as shown in Figure 5.3(b). The velocity profile of the liquid along the positive x-axis at different sections of the R-Zone is as shown in Figure 5.3(b). It can be seen that the velocity of the fluid in the x-axis is very high at the inlet and the velocity drops down as the fluid enters the R-Zone

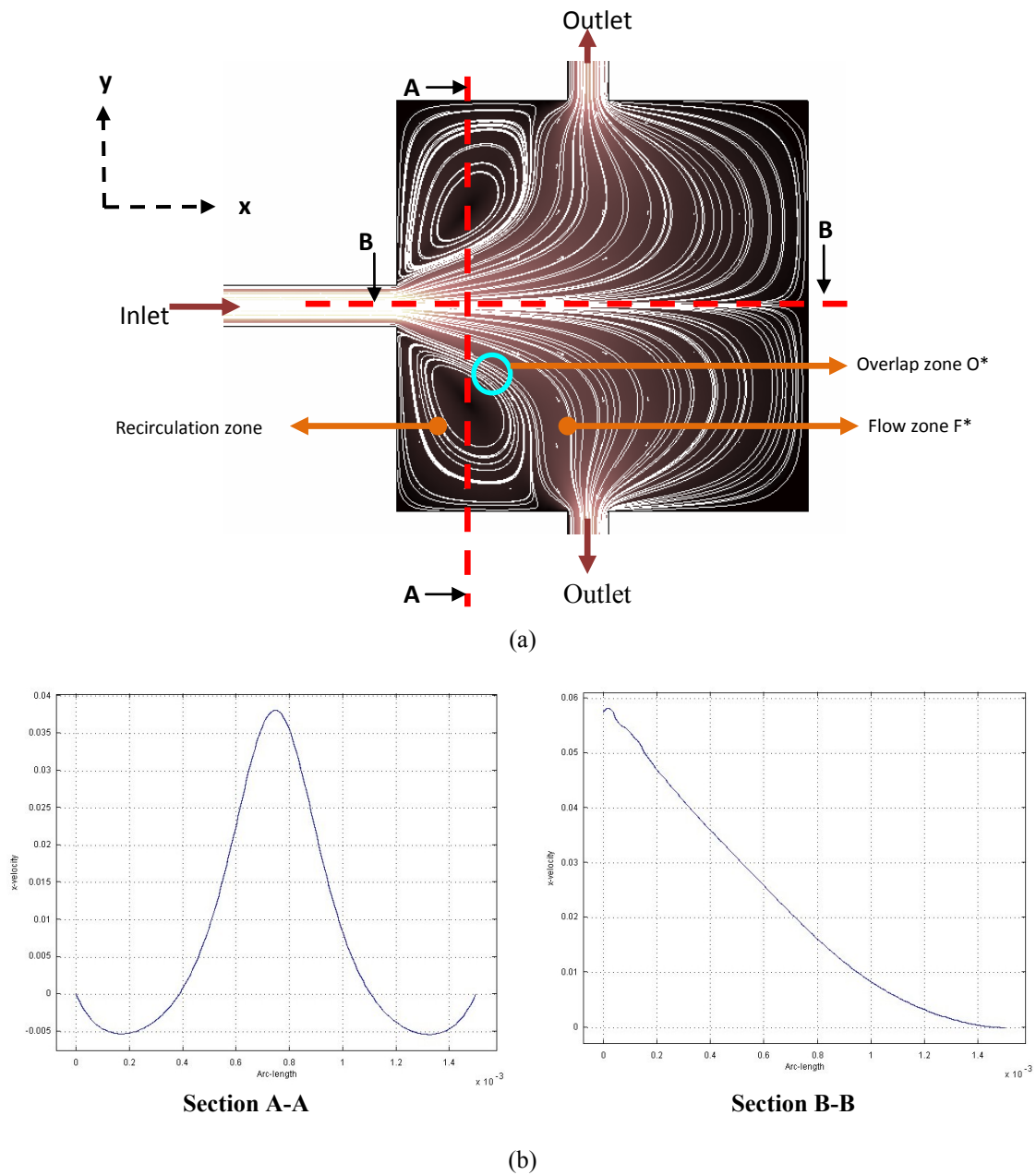


**Figure 5.3:** (a) Predicted flow behavior within in the recirculating microfluidic chamber (b) x-velocity profile of the fluid flow across sections A-A and B-B in the R-Zone. The unit for the velocity is ‘m/s’ and the length of the R-zone is measured in ‘m’.



The presence of the recirculating zone is dependent upon the flow velocity and the chamber geometry. By controlling the fluid flow velocity and the dimensions of the microfluidic channels and the chamber, the amount of biological specimen involved in the reaction within the R-zone is also controlled, resulting in a more reliable biointeraction. In order to study the influence of flow velocity on the recirculating flow, the fluid behavior within the chamber was studied for different inlet velocities of the fluid.

The predicted streamlines inside the chamber at Reynolds numbers of 0.1, 1 and 10 are presented in Figure 5.3. The Reynolds number (Re) herein is defined as

$$\text{Re} = \frac{\rho D_h \bar{u}}{\mu} \quad \dots 5.3$$

where

$\rho$  – density of the fluid

$\bar{u}$  – average flow velocity at the inlet

$D_h$  – characteristic length or hydraulic diameter

$\mu$  – dynamic viscosity of the fluid

One can observe the development of recirculation zone with the increase in the Reynolds number in Figure 5.3. The amount of fluid trapped depends upon the size of the recirculating zone. In order to study the size of the recirculation zone, the co-ordinates of the centre or the eye of the recirculating flow region,  $(\Psi_x, \Psi_y)$  were identified as shown in Figure 5.4 and the change in the position of the eye was estimated with respect to the variation in the Reynolds number of the fluid flow.

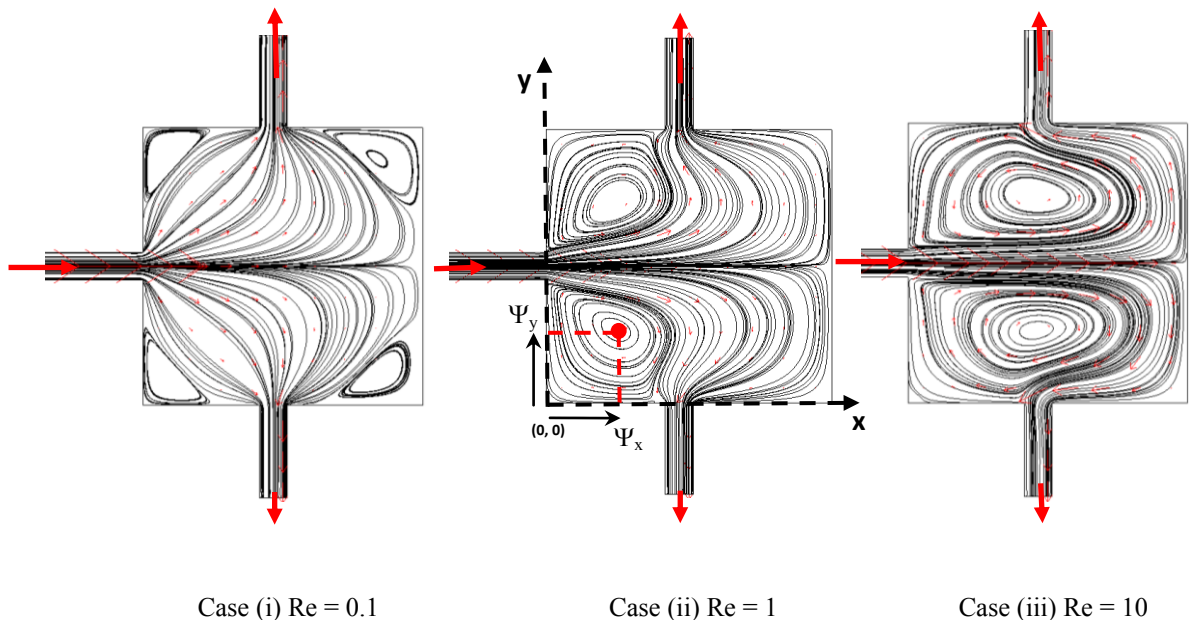


**Figure 5.4:** The development of recirculation with Reynolds number.

The position of  $\Psi_x$  and  $\Psi_y$  are used to represent the size of the recirculation zone. The variation of the position of the centre of the recirculating zone with respect to the flow Reynolds number is given in Figure 5.5. This figure indicates the increase in position of the recirculation eye leading to increased recirculation area with Reynolds number, until it reaches a steady value.

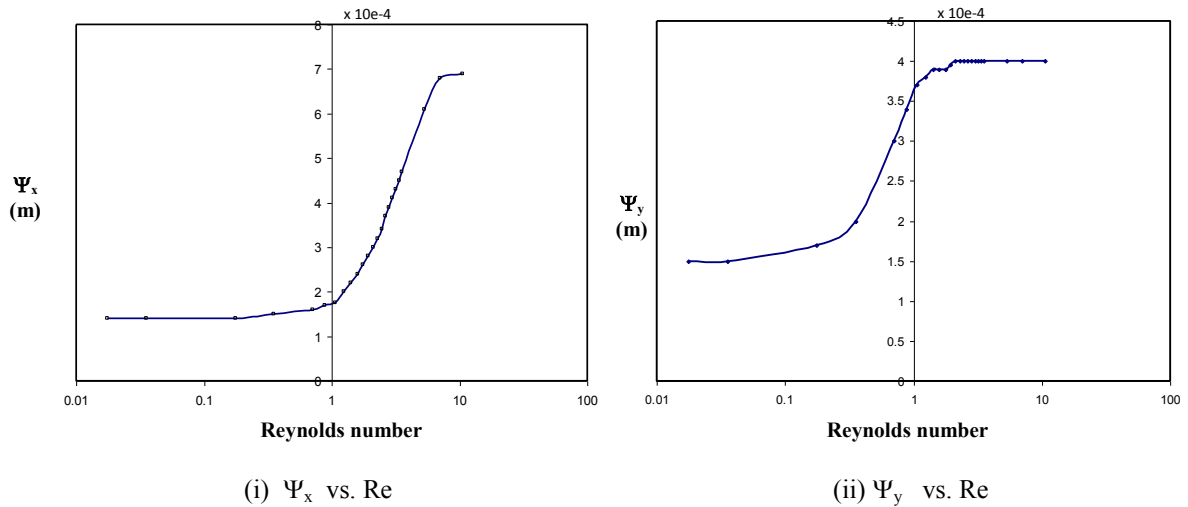


**Figure 5.5:** Variation of recirculation center with Reynolds number

For very low Reynolds number (Re), i.e. less than 0.35, a very small recirculation region was formed closer to the walls of the chamber and any increase in the flow velocity did not have an effect in the increase of the recirculation flow volume. It can be seen in Figure 5.4 that the increase in flow velocity does not have a significant effect on  $\Psi_x$  and  $\Psi_y$  for low Reynolds number of less than 0.35. As the velocity of flow was gradually increased, i.e. for Re higher than 0.35, the onset of significant recirculation zone was observed, until the Re is 1. Further increase in Re increased the volume of fluid within the recirculation zone, as seen in Figure 5.5. As  $\Psi_x$  increases, the quantity of the fluid trapped in the recirculating zone increases, until it reaches a definite volume beyond which there is no further increase in the recirculating fluid volume because of the geometric constraint of the chamber.

Since the fluid flow is laminar in the input channels, the chemical reaction between the reacting fluids can occur only in the R-Zone. A small flux input of the fluid displaces a portion of the fluid previously present in the R-Zone, while a good amount of the previously existing fluid is flushed out of the R-zone only after some time with prolonged and continuous fluid injection. This phenomenon could be used to create the condition necessary for the chemical reaction between two reacting fluids injected into the same channel, thereby ensuring that the reaction happens only in the R-Zone thus enabling the real-time characterization of reaction inside the microreactor. Thus, by the implementation of such a design, for the present mono-input microfluidic system, R-zone forms the region of reaction of the biofluids through carefully monitored and controlled fluid input.

If the biodetection involves immobilization, then the continuous flow method for biodetection will only be useful in the flow zone  $F^*$ . Within the overlap zone  $O^*$ , biodetection is possible only when a rapid reaction takes place between the two sequentially input fluids. In certain situations, delayed or instantaneous interaction of biomolecules is possible without the need for immobilization or chemical reactions. In such cases, continuous flow method with recirculation can still be employed for biodetection. At lower flow velocities, there is no significant recirculating zone formed; leading to no fluid entrapment within the chamber. Hence, continuous flow detection of biomolecules would not be possible without immobilization of the molecules with the surface. But, at slightly higher velocities, the developed recirculating zone facilitates the delayed interaction between the samples already existing within the recirculating zone

with subsequently input fluid, and creates better conditions for bio-interaction. At high velocities, it must be noted that the time available for interaction and detection is also significantly reduced. Therefore, an appropriate choice of flow velocity is essential to allow enough interaction between the sequentially passed biological samples and to have significant detection time.

Thus, with the help of recirculating microfluidic design, the impingement jet from the inlet would mix and react with the fluid already present in the R-Zone. The flow behavior also shows a recirculating region in the R-Zone, as expected, which would help in better mixing of the input fluid with the previously existing fluid. As the flow is pressure driven, it is possible to change the length of the impingement jet and obtain different degrees of mixing in the chamber. The advantage of this impingement mixing method is the feasibility of using only one inlet port and one outlet port for microfluidic sample mixing, even though the present device consists of one input port and two outlet ports. In the impingement flow mixing with single inlet port, one has to use intermittent flow of the samples. In this way, it is also possible to mix many fluids in the same chamber effectively without many inlet ports.

### **5.3.2 Fabrication of microfluidic chips**

The possibility of fabricating microfluidic channels on glass has been demonstrated by wet etching on a 50 mm × 25 mm Corning microscopic slide using a buffered HF solution (Jacobson et al. 1994). In this work, the microfluidic channels were fabricated using the

Protolyne process technology (Micralyne Inc., Canada), offered to the Canadian Universities through the Canadian Microelectronics Corporation (CMC). This technology enables the user to develop a network of bulk- micromachined channels and features with 8 reservoirs in glass substrate for microfluidic applications.

The microfluidic chip consists of two plates of Schott Borofloat glass which are fusion-bonded together. The top plate has eight 2 mm diameter reservoirs which are used for fluidic channels. The bottom plate has the designed microfluidic channel pattern and the etch pads bulk etched into it. These etch pads consist of 1.5 mm diameter circular pad to be connected to the etched channels and are also used to align the top and bottom plates. The depth of the microfluidic channel is 20  $\mu\text{m}$ . Figure 5.6 shows an unpackaged microfluidic chip.

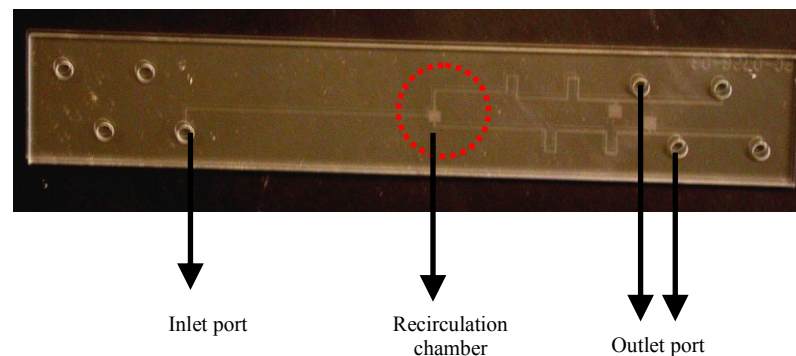


**Figure 5.6:** Unpackaged microfluidic chip fabricated by Protolyne process technology

In order to characterize the flow behavior within the microfluidic chip, flow visualization through the recirculation chamber was carried out using an epifluorescence microscope setup. 5  $\mu\text{m}$  spheres which fluoresce at the wavelength of 610 nm for an excitation of

wavelength 540 nm, were passed through the channel and the flow behavior was recorded through the epifluorescent microscope. The recirculation zone observed visually from the flow visualization experiments is shown in Figure 5.7(a). Herein, the velocity of the fluid flow was controlled using the peristaltic pump which was used as input. As predicted by the FEM analysis, it was also observed that the recirculation zone was formed only for fluid velocities, higher than 0.016 m/s corresponding to Reynolds number of 0.564. Given the limitations of the flow visualization setup, the maximum fluid velocity for which the visualization could be carried out was at  $Re = 0.7$ . It can also be seen that the flow behaviour within the chamber, as predicted by the Finite Element Modeling corroborates well with the streamlines observed with the flow visualization experiment, as shown in Figure 5.7(b)

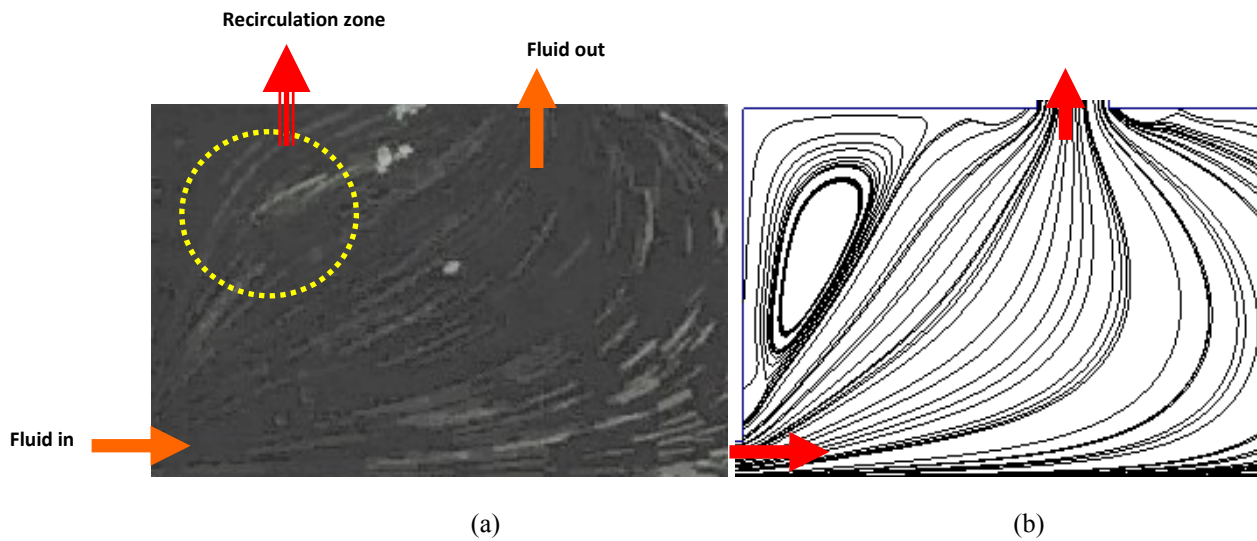


**Figure 5.7:** (a) Flow visualization carried out with fluorescent particles using epifluorescence microscope at  $Re=0.7$  (b) Flow behavior at  $Re = 0.7$  predicted through FEM.

#### 5.4 Demonstration of optical absorption using external hybrid integration

In order to demonstrate the feasibility of biophotonic absorption detection for micro and nano level species with microfluidic device, enzyme Horse Radish Peroxidase (HRP) was chosen. HRP is a redox enzyme (biochemical catalyst) with a molecular weight of approximately 40 kDa ( $1 \text{ Da} = 1.660540 \times 10^{-27} \text{ kg}$ ). It structurally resembles glycoprotein with one mole of protohaemin. These enzymes exhibit different isotropic forms and are generally isolated from the roots of horseradish (Jeetender et al. 2005). The size of the HRP molecules is of the order of a few angstroms to a few nanometers (Leung et al. 2004). The size of the molecule is an important factor here because, when the molecular size is comparable to that of the microfluidic channel, there is a risk of clogging in the channel during flow.

When HRP comes into contact with  $\text{H}_2\text{O}_2$ , the reaction causes the reduction of the latter compound. This reaction is spontaneous, within around 200  $\mu\text{s}$  (Tanaka et al. 2003). When the enzyme is added on the antibody, it produces superoxide or the ROS (Reactive Oxygen Species) by the reduction of Hydrogen Peroxide. Due to this phenomenon,  $\text{H}_2\text{O}_2$  clings on to HRP and forms like a “cotton structure” (DiNello, Dolphin 1981). The main advantage of using HRP for testing is that its optical activity can be easily monitored and the activity is fairly stable in organic or inorganic solvents (Lu et al. 1997). Figure 5.8 shows the molecular structure of HRP and the change in structure upon reaction with  $\text{H}_2\text{O}_2$ .



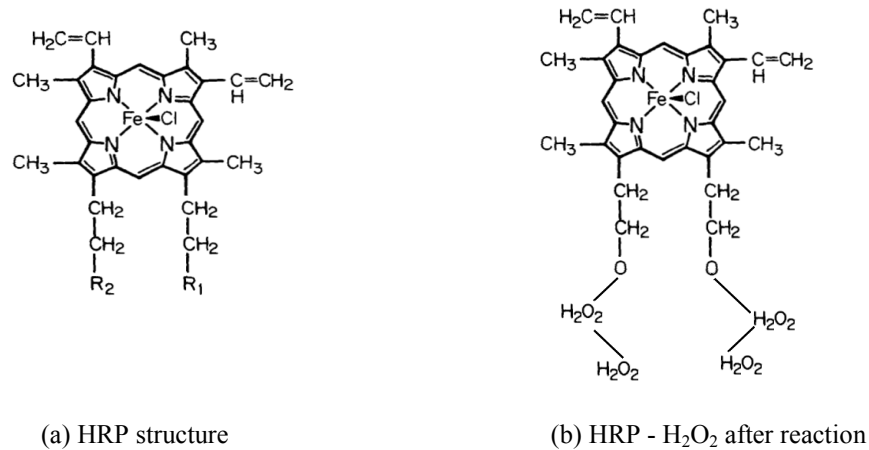


**Figure 5.8:** Molecular structure of (a) HRP and (b) HRP-H<sub>2</sub>O<sub>2</sub> after reaction (DiNello, Dolphin 1981)

HRP used in the experiments is a commercial grade 9003-99-0 bought from Sigma, St. Louis, USA and Hydrogen Peroxide is the standard grade bought from Sigma, USA. The concentration of the enzyme used was 1% to the active ingredient in aqueous solution while the H<sub>2</sub>O<sub>2</sub> used was 30% by weight solution.

Initially, the Potassium Phosphate buffer solution is prepared. Potassium hydrogen Phosphate (K<sub>2</sub>HPO<sub>4</sub>) is a white powder in appearance whose molecular weight is 174.18 gram per mol. In order to prepare 0.1 M buffer, i.e, 0.1 mole of Potassium Phosphate in 1 litre of the solution, 8.71 g of Potassium Phosphate is added to 500 ml of water. A slightly hazy colorless solution of PBS is produced and this solution is diluted with strong hydrochloric acid (HCl) in order to obtain a buffer solution with a pH of 6.0.

Solid HRP is taken in a pan and weighed in physical balance. The buffer solution is added to HRP to get a liquid solution of the enzyme with a pH of 6.0. A clear amber brown solution of HRP is obtained at 10 mg per 1 ml of 0.1M potassium phosphate. The activity of HRP is measure in terms of ‘units’. In the present case, 1 mol HRP reacts with 1 mol H<sub>2</sub>O<sub>2</sub> to form 1 mol of water and ½ mol of oxygen. The reduction reaction is given as per the equation



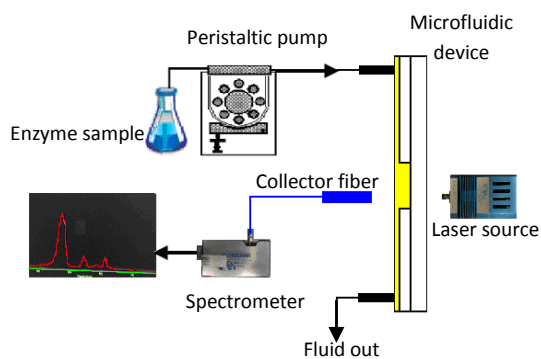
The oxygen released during this reaction is made to react with another specimen to form a separate compound through an oxidation reaction. By knowing the number of moles of the newly formed compound, the number of moles of oxygen released during the reaction is obtained, which is equivalent to the number of moles of HRP reacted with H<sub>2</sub>O<sub>2</sub>. For the sample prepared in the procedure mentioned as above, an enzymatic activity of 250 to 330 units per mg solid HRP is obtained (Jeetender et al. 2005).

#### **5.4.1 Experimental setup**

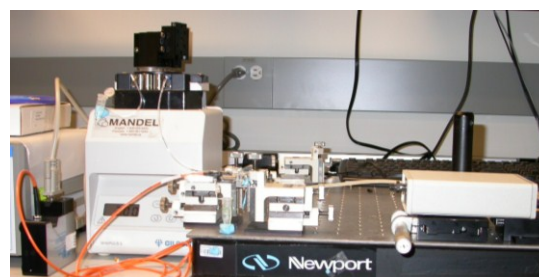
Figure 5.9 (a) shows the schematic representation of the experimental setup used for carrying out the absorption characterization and the testing setup is as shown in Figure 5.9(b). A peristaltic pump (Gilson) was used to pump in the fluid through the channel. The set up for the experiment with the visible light consisted of a pulsed xenon light

source (Ocean Optics) at 470 nm and a broadband light source (Ocean Optics) for wavelengths from 300 nm to 700 nm.

The input light was beamed at the microfluidic channel and was collected in SMA fiber with the diameter of the core 50  $\mu\text{m}$ , aligned with respect to the R-Zone of the microfluidic device as shown in Figure 5.8(a). The microfluidic device was placed on two micropositioners in order to carefully align the R-Zone with respect to the position of the collector fiber. The output from the fiber was coupled onto a spectrometer (USB 2000, Ocean Optics) in order to study the spectral variations due to the flow and the fluid reaction in the microfluidic channel and hence study the absorption characteristics of the sample. In order to avoid any optical noise from external sources, the entire experiment was carried out in the dark thereby ensuring that the performance or the signal-to-noise ratio of the device was not affected due to external disturbances.



(a) Schematic experimental setup



(b) Experimental setup

**Figure 5.9:** Experimental setup for measuring the recirculation flow aided optical absorption.

The absorbance measured by the spectrometer is given by the formula

$$A_{\lambda} = -\log_{10} \left( \frac{S_{\lambda} - D_{\lambda}}{R_{\lambda} - D_{\lambda}} \right) \quad \dots 5.3$$

Where

$\lambda$  - Wavelength of light used

$A_{\lambda}$  - Absorbance

$S_{\lambda}$  - Intensity of light passing through the sample

$D_{\lambda}$  - Dark Intensity

$R_{\lambda}$  - Intensity of light passing through a reference medium.

#### **5.4.2 Results of absorption detection**

The optical absorption experiments with HRP and H<sub>2</sub>O<sub>2</sub> were carried out in two stages. In the first experiment, the absorbance was measured using blue light at 470 nm. The variation of optical absorbance recorded by the spectrometer, according to the different fluids present in the channel, is as shown in Figure 5.10. The stepwise experimental procedure is given in Table 5.1. It must be remembered that the time taken by the fluid to reach the R-Zone is approximately 100 s, as calculated from the flow analysis carried out initially.

The main idea of introducing HRP again in step 8 is to confirm that the randomness observed in the absorbance values are due to the reaction between HRP and H<sub>2</sub>O<sub>2</sub>. Since there is no reaction between water and HRP, the transition of absorbance value recorded

by the spectrometer is smooth after (6) as shown in Figure 5.10. The channel was subsequently flushed with water for some time so that HRP and H<sub>2</sub>O<sub>2</sub> molecules present in the channel were removed. From this experiment, one can estimate the individual absorbance values of water, HRP and H<sub>2</sub>O<sub>2</sub>. The absorbance values exhibited by water and H<sub>2</sub>O<sub>2</sub> are nearly the same ~0.01 and for HRP, the absorbance value is ~0.035.

Step #	Process description
Step 1	Water is passed through the channel and reference absorbance is measured
Step 2	H <sub>2</sub> O <sub>2</sub> is passed for 120 s so that R-Zone is filled with water
Step 3	At t = 0, HRP is passed into the channel
Step 4	At (1), HRP enters R-Zone and reaction between HRP and H <sub>2</sub> O <sub>2</sub> starts
Step 5	At (2), HRP flushes out the reactants to solely occupy the channels
Step 6	At (3), H <sub>2</sub> O <sub>2</sub> is passed into the channel
Step 7	At (4), beginning of reaction between H <sub>2</sub> O <sub>2</sub> and HRP present in the R-Zone, now the H <sub>2</sub> O <sub>2</sub> is replaced by water.
Step 8	At (5), water replaces the reactants in the R-Zone, now HRP is passed again.
Step 9	At (6) HRP enters the R-Zone and the absorbance is recorded without reaction

**Table 5.1:** Experimental procedure for enzymatic absorption study at 470 nm

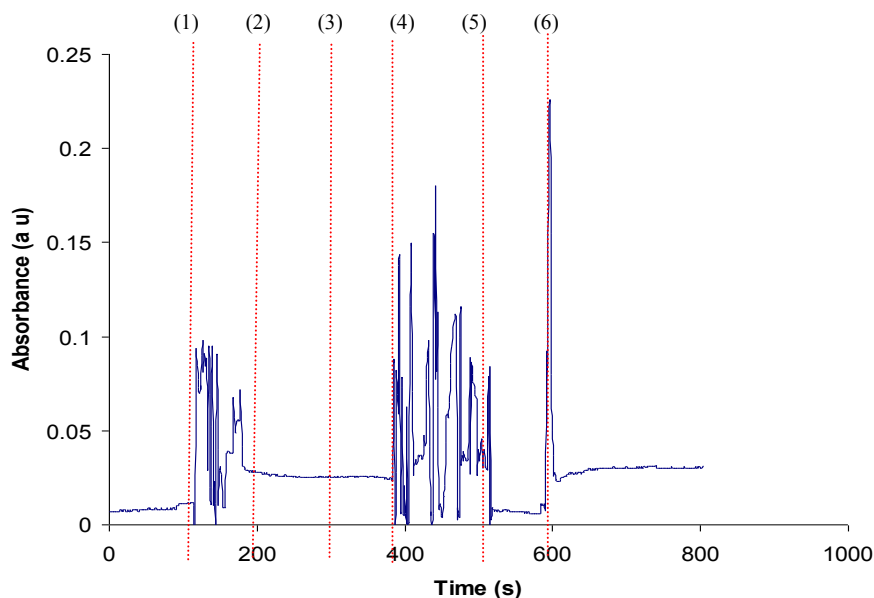


**Figure 5.10:** Spectral absorption characteristics due to HRP and H<sub>2</sub>O<sub>2</sub> in the microfluidic channel at 470 nm.

In order to estimate the absorption spectrum over a wider wavelength range, a second experiment was carried out by replacing the blue light with a broadband light source having the wavelength ranging from 400 nm to 800 nm due to the randomness observed due to the random mixing. Though the previous experiment was useful in precisely determining the absorbance values of the individual liquids, it was not possible to calculate the absorbance due to the reaction of the fluids in the real time. This problem was overcome in this experiment, wherein the absorbance was recorded for individual fluids and the reaction product. Three distinct wavelengths were chosen for the absorption study of the liquids, namely, 485 nm, 530 nm and 630 nm. The result of the experiment is as shown in Figure 5.11, and the different stages of the experiment have been segregated appropriately. Initially, the reference absorbance was measured by passing water through the channel. The sequence in which the experiment has been carried out is explained in Table 5.2 with reference to the Figure 5.11. The initial reference measurement for absorbance was taken by passing water into the channel.

<b>Step #</b>	<b>Process description</b>
Step 1	Pass water for 300s and note the reference absorbance
Step 2	Pass H <sub>2</sub> O <sub>2</sub> for 120 s, absorbance of H <sub>2</sub> O <sub>2</sub> is almost the same as water
Step 3	At t = 420 s, pass HRP.
Step 4	At (I), t = 520 s, pass H <sub>2</sub> O <sub>2</sub> again, to flush the HRP present in the tubes and channel
Step 5	At (II), t = 620 s, pass water. The randomness in the absorbance value is due to the reaction between H <sub>2</sub> O <sub>2</sub> and the remnant HRP.
Step 6	At (III), t = 700 s, Pass HRP for 30 s and immediately pass H <sub>2</sub> O <sub>2</sub>
Step 7	At (IV), t ~ 830 s, HRP enters R-Zone. At (V), t ~900 s, H <sub>2</sub> O <sub>2</sub> enters the R-Zone. The pump is stopped.
Step 8	After 240 s, at (V), pump is started again and H <sub>2</sub> O <sub>2</sub> flushes the reactants previously present.
Step 9	After 30 s, water is passed and the channels are flushed.

**Table 5.2:** Experimental procedure for enzymatic absorption study using broadband light source

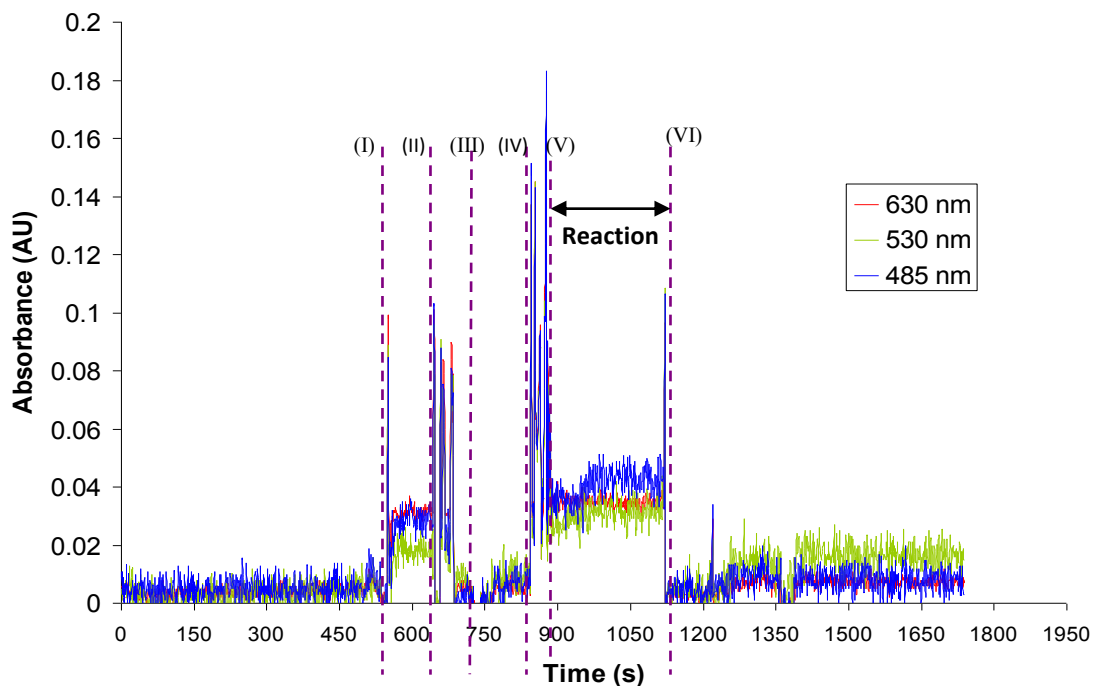


**Figure 5.11:** Spectral absorption characteristics due to HRP,  $\text{H}_2\text{O}_2$  and their reaction in the microfluidic channel at different times.

In step 5, water is passed into the channel so as to flush the R-Zone slightly before carrying out the absorption measurement during the actual reaction. The reaction between HRP and  $\text{H}_2\text{O}_2$  started at  $t = 900$  s and was allowed to proceed in the R-Zone for 240 s. The absorbance increase due to the reaction recorded at the different wavelengths is as shown in Figure 5.12. A significant increase in the absorbance was observed due to the reaction between HRP and  $\text{H}_2\text{O}_2$  for 485 nm and 530 nm. However, in case of absorbance at 630 nm, though an increase is observed during the reaction, it is not very pronounced as the intensity of light at 630 nm using the broadband light source is considerably less compared to the light coming out at 485 nm and 530 nm. A trend line added through the data points shows the time taken for the absorbance to reach a steady state, which

indicates that the reaction to complete is approximately 240 s. This reaction time is the same as predicted by Jeetender et al. (2005).

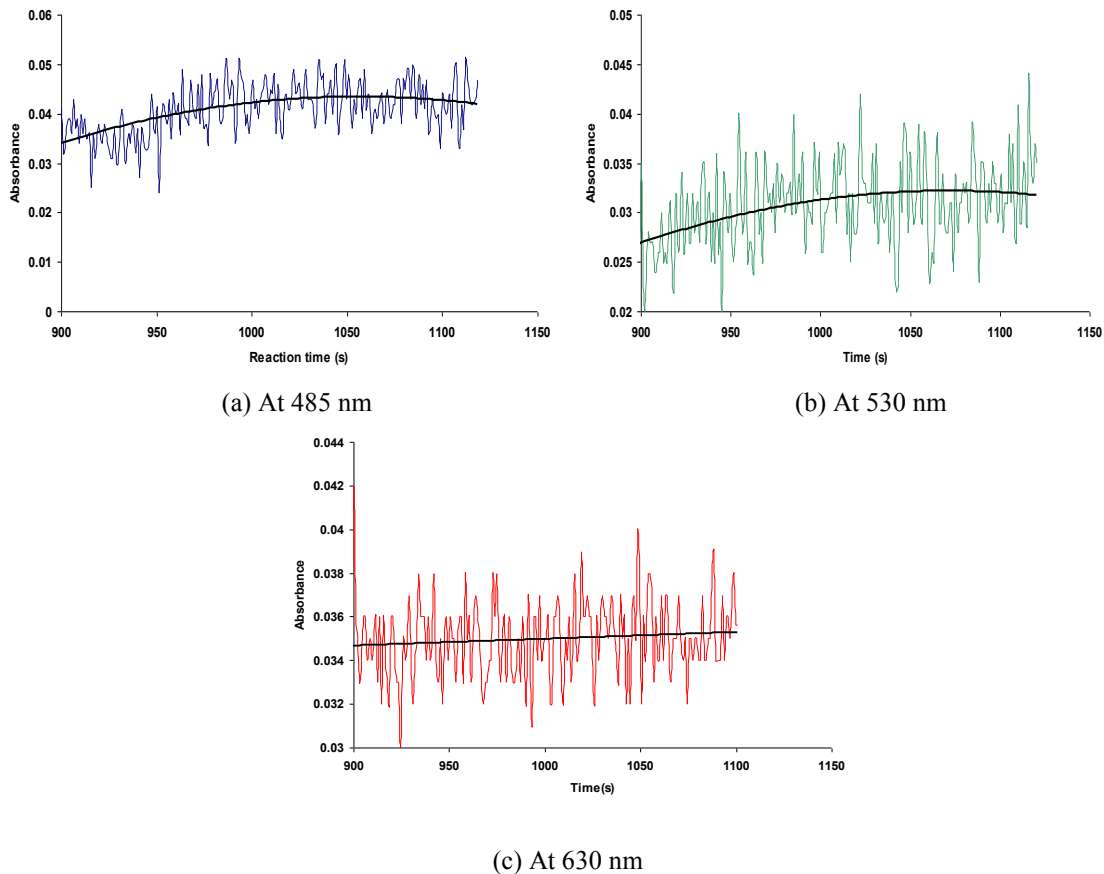


**Figure 5.12:** Absorbance measurement during HRP-H<sub>2</sub>O<sub>2</sub> reaction

Thus, using this method, characterization of an enzymatic reaction can be performed through optical absorption technique. The volume of liquid used for the real inspection under the optical beam is approximately 0.03 nanolitres. It is thus evident that even with such low sample volume, it is possible to accurately study the enzymatic reaction using this method. This method can now be easily extended to carry out time-dependant reaction studies of other micro and nano level biological reactions for a  $\mu$ TAS.

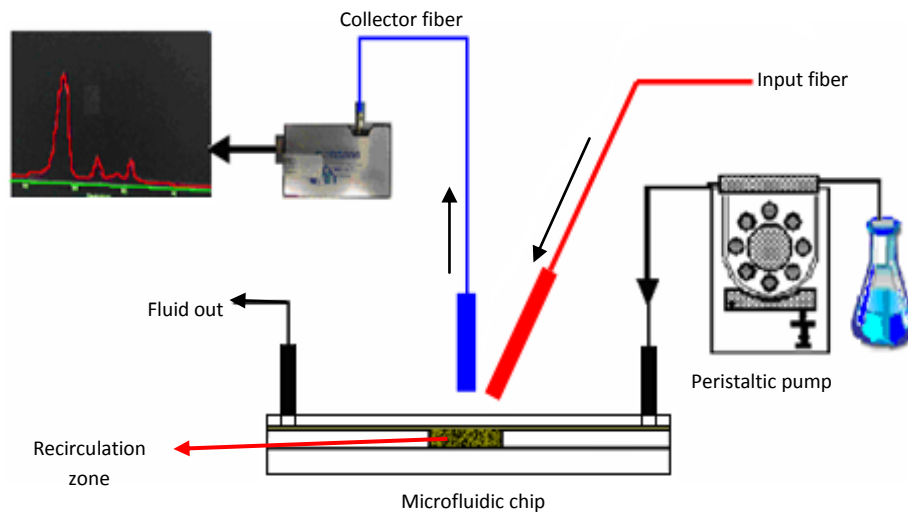


## **5.5 Demonstration of external hybrid integrated fluorescence detection**

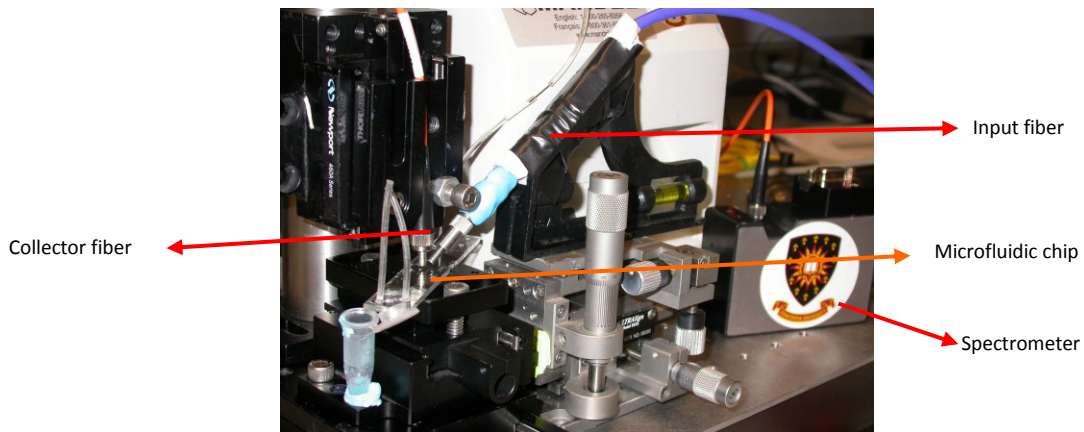
The main objectives of the experiments carried out in order to study the feasibility of fluorescence detection using external hybrid integrated setup

- (i) To demonstrate the application of recirculating microfluidic system for fluorescence based hybrid integrated biodetection
- (ii) To develop a suitable control mechanism for the bio-interaction of involving fluorophore tagged antibody for fluorescence based bioetection.
- (iii) To study the recirculation flow behavior and particle mixing of the fluorophore tagged antibody under continuous and intermittent flow conditions.

The feasibility of fluorescence based biodetection using hybrid integrated system has been demonstrated with Antisheep Antibody (AB) tagged with Alexafluor 647 (AF647) fluorophore particles. By controlling the fluid flow through the recirculating microfluidic system, it was possible to isolate AB separately into a recirculation zone within the microfluidic channel, thereby enabling qualitative and quantitative biodetection. Finite Element Modeling of the flow behavior has been carried out and the results were similar to the results of flow visualization obtained with tagged antibody particles. The schematic for the bio-optical microfluidic test setup for external hybrid integrated fluorescence detection is shown in Figure 5.13(a) and the experimental setup is shown in Figure 5.13(b).



(a) Schematic of optical microfluidic setup



(b) Optical microfluidic experimental setup

**Figure 5.13:** (a) Schematic and (b) Experimental setup of the optical microfluidic testing setup

The input fiber was fixed on a  $45^\circ$  platform clamped onto an adjustable positioner. The output fiber was positioned vertical with respect to the recirculation chamber. The microfluidic chip was placed on a 2D adjustable platform so that the position could be adjusted with respect to the collector fiber. Initially, the collector fiber was positioned appropriately with respect to the recirculation zone and the distance between the input

fiber and the chamber was adjusted in order to obtain sufficient excitation for optimum fluorescence detection. The collector fiber was coupled onto a spectrometer for carrying out the spectral analysis.

The experiments for fluorescence detection using the present setup were carried out with Antisheep Antibody (AB) tagged with Alexafluor-647 (AF647), which gave a fluorescence emission at 670 nm upon excitation with a light of 640 nm wavelength. 6.6% by volume AB was prepared by diluting the stock sample with Phosphate Buffer Solution (PBS) appropriately. The flow velocity for fluid injection for all experiments was maintained at 0.0583 m/s, which corresponds to a Reynolds number of 2.05.

### **5.5.1. Experimental results**

The behavior of the recirculation zone was initially studied under continuous fluid flow conditions. Thereafter, in a later study, the flow was stopped after the particles reached the recirculation zone, and its effect on the recirculating fluid behaviour, diffusion of molecules and particle mixing was studied. Finally, in order to investigate the difference in the fluid behavior in the recirculating zone and the flow zone, fluorescence measurements were carried out from the fluorophore tagged antibody particles present in the non-recirculating flow zone. These experiments are detailed in the following subsections and the results have been presented.

### 5.5.1.1 Recirculating development under Continuous flow (CFR)

The continuous flow experiment has been carried out in order to verify the recirculating fluid behavior and to study the control of fluidic mixing with appropriate intermittent fluidic input. It has been demonstrated that by suitably controlling the time of the input of the fluid, or the supply time, the reaction time can be precisely controlled. It is also possible to control the mixing time and the mixing intensity of a fluid present in the recirculation zone with the subsequently input fluid through supply time and the rinsing time of the fluids.

The sequence in which the experiment was carried out is given in Table 5.3. Herein, an intermittent flow technique has been observed, wherein tagged antibody was passed for short durations of 30s and 60s respectively and the fluorescence measurements were carried out. The fluorescence observed was only due to the antibodies which are trapped in the recirculation zone under continuous fluidic input. The results of the CFR experiment are presented in Figure 5.13, in accordance to the sequential procedure explained in Table 5.3.

<b>Step #</b>	<b>Procedure</b>
<i>1</i>	<i>Pass AB for 30 s</i>
<i>2</i>	<i>AB enters RC, pass water</i>
<i>3</i>	<i>Rinsing by water begins</i>
<i>4</i>	<i>Pass AB for 60 s</i>
<i>5</i>	<i>AB enters RC, start passing water</i>
<i>6</i>	<i>Rinsing by water begins</i>

**Table 5.3:** Sequential procedure of continuous flow fluorescence detection experiment using AF647 tagged Antisheep Antibody

The gradual increase in fluorescent intensity at positions marked as 2 and 5 in Figure 5.14 proves that the fluorophore tagged antibodies take some time to displace the previously

existing fluid from the recirculation zone. The residence time, i.e, the life time of the fluorescent molecules within the recirculating zone, and hence the mixing intensity, can thus be controlled very well by controlling the supply time of the fluid. It can also be observed that decrease in the fluorescence due to the rinsing of the antibody particles with water is also gradual, due to the time taken by water to displace and rinse the antibody from the recirculation zone. The results are further discussed in Section 5.5.2.

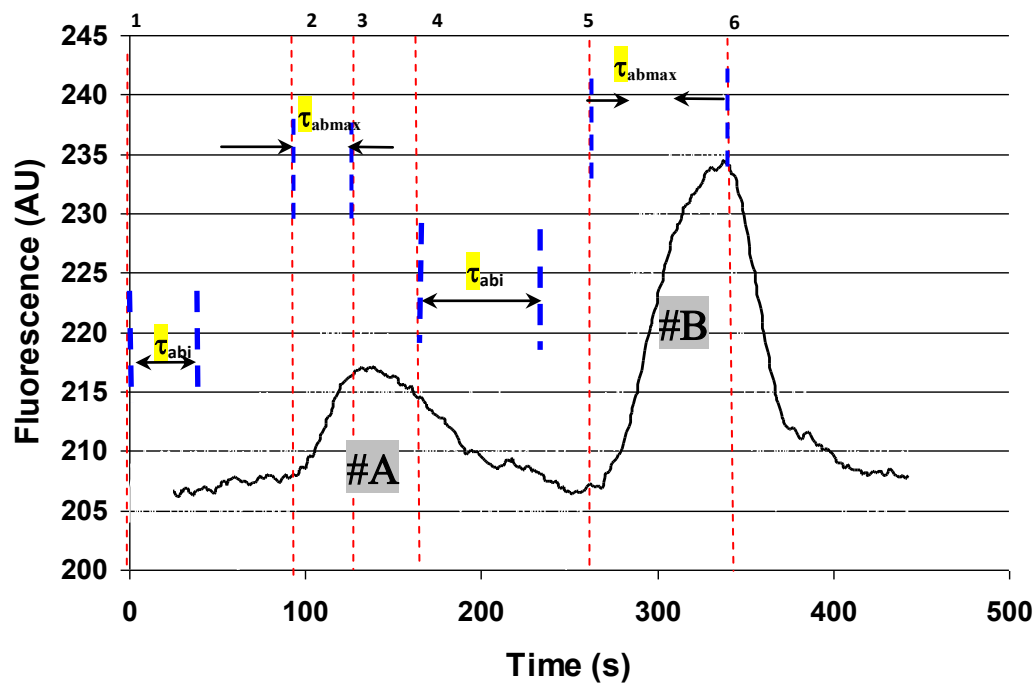


Figure 5.14: Continuous flow fluorescence detection in the recirculation chamber for AF647 tagged AB

### 5.5.1.2 Diffusion of recirculating fluid under stopped flow (SFR)

In order to study the effect of diffusion of molecules present within the recirculating zone, a stopped flow experiment was carried out. In this experiment, the effect on the miscibility of fluid trapped within the recirculation zone with the fluid present in the non-recirculating region was studied. Herein, the tagged antibodies were passed into the channel till a steady state of fluorescence was reached, and water was then passed into the

channel. The non-covalent interaction of the antibody particles with water through diffusion and mixing was studied and the results are presented in Figure 5.15 in accordance to the experimental sequence tabulated in Table 5.4.

<b>Step #</b>	<b>Procedure</b>
<i>1</i>	<i>Pass AB</i>
<i>2</i>	<i>AB enters RC</i>
<i>3</i>	<i>Pass water</i>
<i>4</i>	<i>Rinsing begins</i>
<i>5</i>	<i>Stop flow</i>
<i>6</i>	<i>Start pumping fluid again</i>

**Table 5.4:** Sequential procedure of stopped flow fluorescence detection in the RC using AF647 tagged AB (Refer Figure 5.14)

The flow was stopped briefly during rinsing indicated as step 5 in Figure 5.15. At that stage, one can observe a decrease in the fluorescence with lesser slope, due to the diffusion of the remnant tagged AB present within the recirculation zone, with the neighboring water molecules present in the non-recirculating flow zone. Once the flow is re-started again, a marginal increase in the fluorescence can be observed (Step 6 in Figure 5.145). The maximum fluorescence obtained once the flow is re-started, is the same as the fluorescence intensity when the flow was stopped at step 5, suggesting that the diffused antibody molecules re-enter the recirculation zone before being rinsed with water completely. The results are further discussed in Section 5.5.2.

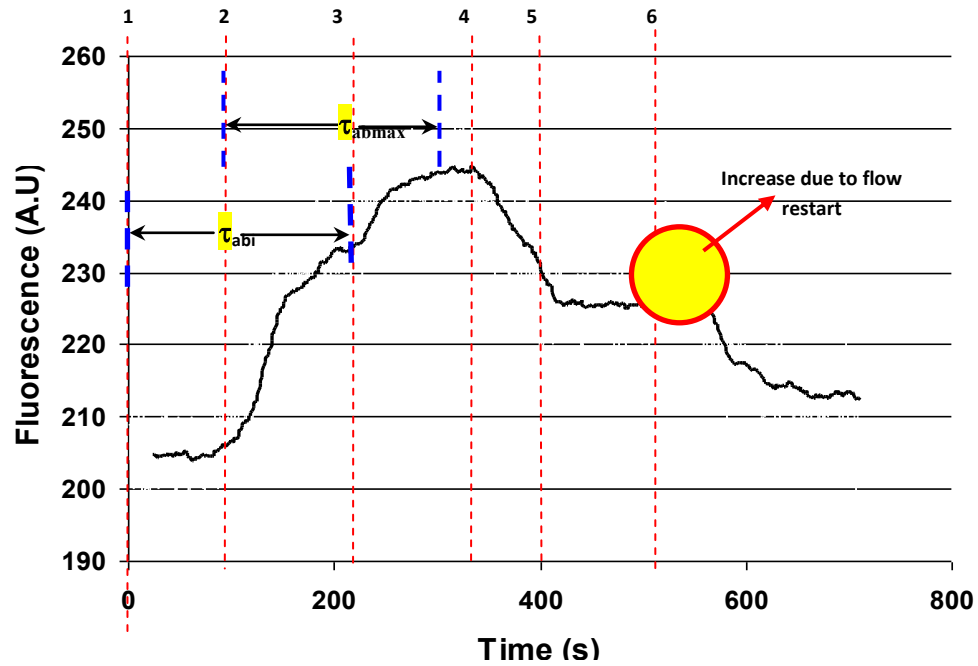


**Figure 5.15:** Results of the stopped flow fluorescence detection experiment

### 5.5.1.3 Continuous flow fluorescence detection in non-recirculating flow zone (CFF)

Finally, in order to verify the results of the above experiments, and to distinguish the flow behavior of the tagged antibody particles from the recirculation zone and the non-recirculating flow, a simple experiment was carried out in which the antibody was passed for 60s and the fluorescence readings were recorded from the non-recirculating flow zone of the RC. The sequence of the experimental procedure is given in Table 5.5 and the results are presented in Figure 5.16.

Step #	Procedure
1	<i>AB enters RC</i>
2	<i>Rinsing begins</i>

**Table 5.5:** Sequential procedure of continuous flow fluorescence detection in the flow zone (Refer Figure 5.16)

An immediate increase in the fluorescence was observed when the antibody enters the RC at step 1 in Figure 5.16. The drop in fluorescence is also immediate during rinsing of the antibody with water indicated by step 2 in Figure 5.16, unlike the previous experiments wherein the fluorescence was observed within the recirculating flow zone with gradual increase or decrease of fluorescence

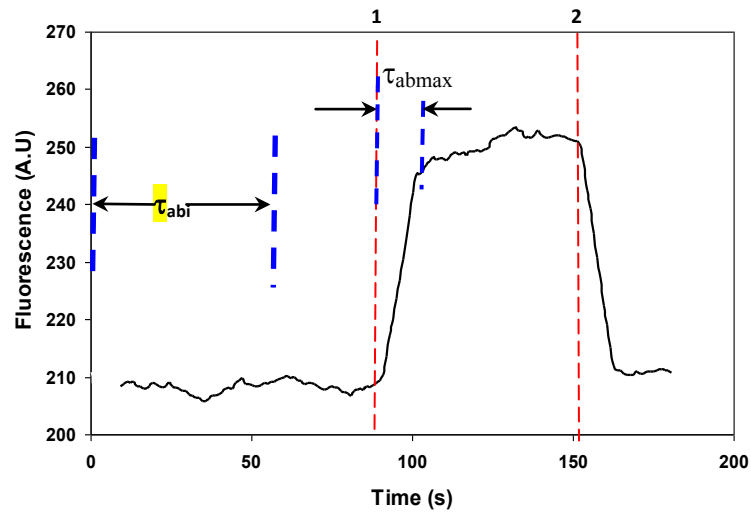


**Figure 5.16:** Fluorescence observed in the flow zone of the RC in a continuous flow system

### 5.5.2 Discussion

From the results of the above experiments, the following parameters considered for analysis, defined as:

$\tau_{abi}$  - Total time for which antibody is passed



$\tau_{abmax}$  - Time taken for the antibody to attain maximum fluorescence emission, measured from the time of particle entry of the particle into the RC

$\varpi_f$  - Ratio of the total time of the input of fluid to the time taken to attain maximum fluorescence, i.e  $\varpi_f = \tau_{abi}/\tau_{abmax}$

$\Omega_{fi}$  - Rate of fluorescence increase i.e.  $\Omega_{fi} = dF/dt$ , where dF is the change in fluorescence increase in the particular time interval dt.

In all the above experiments, the time taken for the antibody particles and water to reach the RC is  $\sim 95s$ .

Exp #	Ref. Fig.	$\tau_{abi}$ (s)	$\tau_{abmax}$ (s)	$\varpi_f$	$\Omega_{fi}$ (dF/dt)
#A – CFR	5.13	30	30	1	0.4
#B – CFR	5.13	60	60	1	0.4
SFR	5.14	210	210	1	0.33
CFF	5.15	60	7	0.12	3

**Table 5.6:** Comparison of the time taken for tagged antibody to exhibit maximum fluorescence in the recirculation flow zone and non-recirculating flow zone

From Table 5.6, it can be seen that for immediate increase in fluorescence, value of  $\varpi$  is very small, as seen from the CFF experiment. When the time taken for attaining maximum fluorescence is equal to the time of input of the fluid as seen in experiments CFR and SFR,  $\varpi_f$  is 1, which is the maximum.

The parameters  $\varpi_f$  and  $\Omega_{fi}$  are significant in understanding the recirculating flow behavior. While  $\varpi_f$  is high for recirculating flows, the value of  $\varpi_f$  is significantly low in the non-recirculation flow zone. On the other hand, the experimental results suggest that while drastic increase in fluorescence is achieved ( $\Omega_{fi} = 3$ ) for non-recirculating fluid flow for a given concentration the fluorescence increase is gradual for fluid present in the

recirculation zone ( $\Omega_{fi} = 0.33\sim 0.4$ ). Thus, by tuning the parameters  $\varpi_f$  and  $\Omega_{fi}$  through appropriate selection of the flow injection time and velocity, one could control the time of interaction of the fluid particles present within the recirculating zone, with the subsequently injected particles. Based on the values of  $\varpi_f$  and  $\Omega_{fi}$ , one could determine the nature of biodetection that could be employed for a particular microfluidic channel design. High  $\varpi_f$  and lower  $\Omega_{fi}$  would be suitable for enhanced bio-interaction through recirculation. Conversely, the microfluidic channel zones with low  $\varpi_f$  and high  $\Omega_{fi}$ , with shorter duration of biomolecular interaction, would not be suitable for biodetection without immobilization.

Thus, with the help of parameter  $\varpi_f$  and  $\Omega_{fi}$ , the phenomenon of recirculating flow has been clearly demonstrated using the present microfluidic channel design for studying fluorescence based biosensing.

## 5.6 Conclusions

As outlined at the beginning of the chapter, there are several advantages of hybrid integration of optics and microfluidic system for biodetections. Integrated opto-microfluidics offers a lot of advantages to carry out high throughput analysis for various biomedical applications. The hybrid integrated optical microfluidic platform based on single inlet impingement mixing with intermittent flows on a recirculating microfluidic platform has been designed, fabricated and tested successfully for the detection of both

individual molecules and enzymatic reactions through fluorescence spectroscopy and optical absorption methods respectively.

The intermittent flow control method using recirculating microfluidic system of trapping the fluid in localized regions of the fluid system enables bio-interactions and overcomes the need for bio-immobilization under continuous flow environment. Thus, the recirculating microfluidic design addresses the problem of biosensing involving two species on a microfluidic platform with single input channel, through a simple implementation of flow control. This technique is simpler, faster and easy to handle as compared with other processes of particle isolation and subsequent interaction, such as electro-osmosis, electrophoresis, dielectrophoresis, magnetic particle separation etc. In most of the microfluidic based system, it would not be possible to study the gradual reaction of two species because of the introduction of mixing channels which would prevent the ab-initio study of the biochemical reaction. This problem was overcome in the present work, through suitable channel design and accordingly modified experimental procedure. The other main advantage of using intermittent flow based recirculating microfluidic platform is that the amount of fluid injected can be precisely controlled which gives distinct advantages in handling smaller sample volumes and drug delivery systems.

The hybrid integrated microfluidic system has been developed for simple and rapid sensing, wherein the principle and feasibility of biodetection with fluidic recirculation have been demonstrated successfully. Though micro-vortex formation in microfluidic

channels have been previously reported in the literature (Shelby et al., 2003) the present work explores the feasibility of using the recirculating fluid behavior for achieving enhanced bio-interactions for optical detections with a hybrid integrated setup. Through this method, biodetection with two or more species can be made possible without the need for immobilization, which is otherwise difficult to implement within microfluidic channel environment. Another main advantage of the present system is that the biosensing with this microfluidic device can be employed for more than one optical detection techniques. Enhancements to the microfluidic chamber design could result in better achievement of fluid recirculation and thereby would enable better biomolecular interaction. Thus, the hybrid integrated microfluidic system provides a platform for carrying out in-situ biomedical detections and can be used for several important applications in the field of medicine, biotechnology, and chemical sensing.

Thus, through external hybrid integration, the bio-opto-microfluidic detection feasibilities have been verified and this provides confidence in fabricating a more integrated setup for integration with the  $\mu$ TAS.

# Improving Sensitivity of Hybrid Integrated Systems and Internal Hybrid Integrated $\mu$ TAS

### 6.1 Introduction

The external hybrid integration of the optics and microfluidics, presented in the previous chapter, is a very important step in developing a prototype towards the synthesis of a fully integrated Micro – Total Analysis Systems. The system proves that it is possible to integrate optics and microfluidics and also ensure that the functionalities of each of the components are not affected by the other supporting module. Therefore, as a next step, it is important to improve the sensitivity of the hybrid integrated system in order to improve the throughput.

Despite the capability of carrying out integrated microfluidic biosensing, the main disadvantages of external hybrid integrated systems are sensitivity and optical alignment, which restricts the use of such systems in real-time biological applications. External hybrid integrated systems suffer from optical losses as a result of packaging. Material absorption losses at the interface of where the light from the external fiber is coupled into the microfluidic channel are inevitable. Especially for fluorescence detection, the coupling of optical signal from the biomolecules into the collector fiber needs to be as high as possible. In the case of absorption detection with external hybrid integrated

systems, wherein the light from the input fiber is coupled coaxially into the collector fiber through the biological specimens present in the microfluidic channel, the system also suffers from misalignment losses due to the lack of robustness of the setup. Due to these restrictions, the external hybrid integrated system requires bulky positioners which need to be integrated with the optical detection system, thereby limiting the portability of the device. Also, the recirculating microfluidic platform of external hybrid integrated system limits the extension of biosensing applications to optical detections carried out perpendicular to the plane of the fluid flow. This calls for the integration of optics and microfluidics to fabricate a three dimensional  $\mu$ TAS, which is complex.

Therefore, considering the above mentioned disadvantages, it is important to develop integrated optical microfluidic systems with improved sensitivity and optical alignment, for increasing the throughput of integrated biosensing. This chapter focuses on the methods to improve the sensitivity of the hybrid integration by overcoming the sensitivity and the optical alignment problems. The sensitivity of the external hybrid integrated device is improved in two stages. Firstly, a method of selective integration of reflectors with microfluidic channel is proposed. In the next work, in order to obtain a more robust optical alignment, the optical fibers are directly integrated with the microfluidic channels and the improved sensitivity of biodetection has been demonstrated through the internal “on-chip” hybrid integration. The proposed opto-microfluidic system would enable the improvement of optical coupling efficiency and also minimizing the optical losses, such as material absorption loss, scattering loss, etc., thereby creating a robust system. In both stages, the improved sensitivity is demonstrated for fluorescence based biodetection

technique only. However the internal hybrid integration method can be applied to other forms of biodetections also.

## **6.2 Enhanced fluorescence based bio-detection through selective integration of reflectors in microfluidic Lab-on-a-Chip**

The following sections present the excerpt of the paper published in the journal *Sensor Review* (Chandrasekaran and Packirisamy, 2008)

In most of the practical applications of a biosensor, the amount of an enzyme present in a sample is low and the hence, the fluorescence produced upon the interaction of enzyme with the fluorophores-tagged antibody is very small. In such conditions, it is possible that the fluorescence spectroscopy may not yield satisfactory results. A simple method to overcome this problem is to tag more fluorophores to the antibody. But the disadvantage is that, increasing the number of the fluorescence tagged antibody molecules would result in the increase in the size of the particles flowing across the channel which sometimes may result in clogging of the microfluidic or nanofluidic channels. Therefore, in order to carry out significant fluorescence detection using hybrid integrated optical microfluidic device, it is very essential to amplify the fluorescent signal emitted out from single molecules after taking into consideration some of the possible fluorescence diminishing factors.

Therefore, to improve the sensitivity of fluorescence detection, a simple and cost effective technique to integrate a reflector surface with microfluidic and nanofluidic channels is

presented for the enhancement of fluorescence produced by the fluorophores within the microfluidic channels. The schematic of the reflector integration to improve fluorescence is as shown in Figure 6.1. When the microfluidic channel surfaces are integrated with mirrors, the fluorescent signals reflect off the surfaces resulting in enhanced fluorescence detection efficiency due to increased sensing area. When the surface of the microfluidic channel is reflecting, the fluorescence signal is reflected off the surface, thereby enabling better sensing of the signal through the detector, thus improving the detection and the coupling efficiency. Thus, the microfluidic channel surfaces can be made to act like micromirrors through selective integration of reflector onto the channel surfaces. However, when the channel surface is non-reflecting, much of the fluorescence signal emitted in the direction of the channel is absorbed and only the small part of fluorescence from the fluorophore will be sensed by the detector.

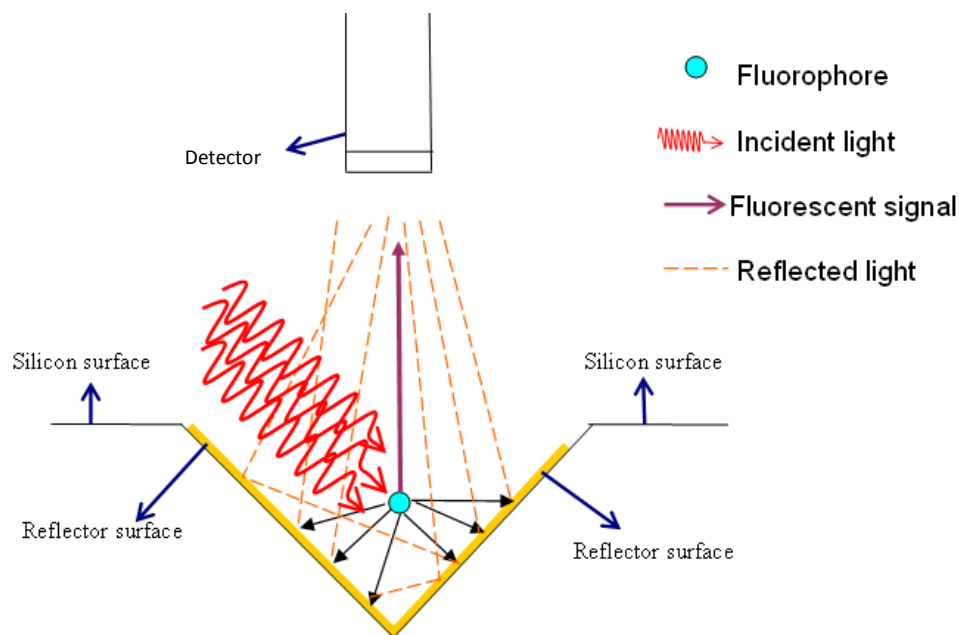


**Figure 6.1:** Schematic representation of fluorescence amplification through partial gold sputtering on the microfluidic channel



### 6.2.1 Design, Fabrication and Bonding of microfluidic chip

The microfluidic system basically consists of a single inlet and outlet port, and an rhombus shaped microfluidic chamber, as shown in Figure 6.2. Fluid from the inlet enters the Microfluidic chamber, wherein the study of fluorescence could be carried out before the fluorophores are rinsed out through the outlet channel. Finite Element Modeling (FEM) of the flow behavior within the Microfluidic chamber and the microfluidic channels was carried out for pressure driven flow with no-slip. The possible stagnation zones for the proposed channel configurations were analyzed. Based on the FEM results, appropriate modifications were carried out in the geometry and the microfluidic channel dimensions. Optimized parameters for the microfluidic channel geometry and dimensions were determined for fabricating the microfluidic channels on silicon.

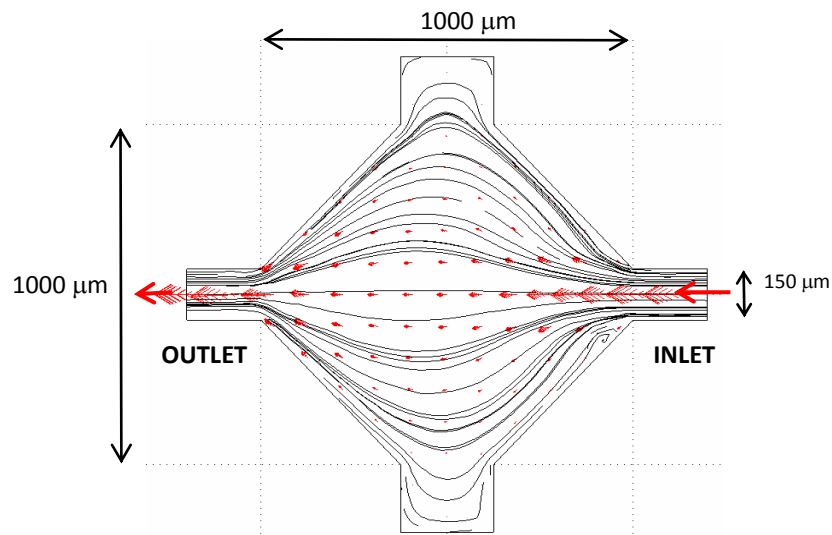


**Figure 6.2:** Design of the microfluidic chamber with simulated flow streamlines

The several methods of fabrication of silicon based microchannel systems include isotropic dry etching using  $\text{XeF}_2$  (Chen et al. 2006), anisotropic wet etching with chemical etchants such as Tetra Methyl Ammonium Hydroxide (TMAH) (Lee et al. 2008), Potassium Hydroxide (KOH) (Emerson et al. 2006), Ethylene Diamine Pyrocatechol (EDP) (Li 2006) etc., Deep Reactive Ion Etching (DRIE) etc. A Hybrid micromachining technique involving isotropic dry etching using Xenon difluoride ( $\text{XeF}_2$ ) followed by controlled anisotropic etching has been demonstrated by Chandrasekaran et al. (2006)

The microfluidic chips that have been used in the present work were fabricated through anisotropic etching with Tetra Methyl Ammonium Hydroxide (TMAH) (Chandrasekaran and Packirisamy, 2005). Oxidized Silicon wafers were initially patterned by standard lithographic process and the oxide layer in the exposed region was selectively removed using 1:5 ratio of Hydrofluoric acid (HF) and DI water. The samples were then loaded on a Teflon holder and etched for 6 hours at  $80^\circ\text{C}$  in a closed TMAH etch setup and under these conditions the etch rate obtained was  $\sim 25\ \mu\text{m/h}$ . After etching, the samples were rinsed with DI water and introduced in HF again in order to remove the oxide layer completely before carrying out further post processing for selective gold deposition.

Packaging of microfluidic chip, involves sealing the microfluidic channel with a top cover and its interconnection with external fluidic circuit. This process attenuates the amount of detectable fluorescence in an external hybrid integrated optical microfluidic system due to

various factors like the type of bonding between the top cover and the substrate, thickness of the cover used, its compatibility to biological specimen that is passed through the microfluidic channel etc. Also, in hybrid integrated optical microfluidic systems, it is essential that the alignment position of the output fiber be optimized in order to detect the fluorescence efficiently. For cases involving single molecule or low concentration of fluorophores, given the optical loss of fluorescent light through the packaging medium, the fluorescent fiber must be very precisely positioned with greater proximity to the channels, which is practically difficult to achieve. Therefore, through the method of reflector integration with the microfluidic channel, it is possible that the fluorescence signal measured is enhanced with the principle schematically depicted in Figure 6.1, thereby improving the sensitivity of the system.

A number of factors such as reflectivity, microfabrication capability with silicon, affinity with biomolecules etc. determine the choice of reflector surface to be integrated with the microfluidic chip. In this work, the partial reflector deposition was carried out using metallic gold. Gold is ideally suited for the present application as the average reflection of gold, as shown in Figure 6.3, is more than 98 % in the wavelength range near 650 nm (Melles Griot Inc.), due to which the metal forms a very good reflector material of the fluorescent signals produced in that range.

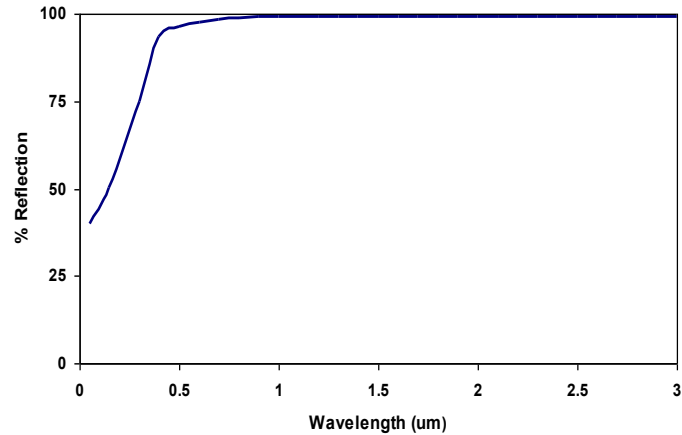
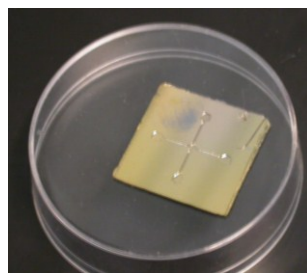
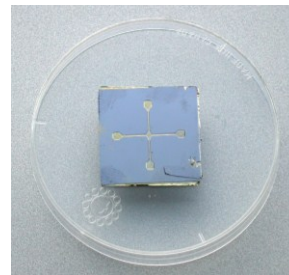


**Figure 6.3:** Reflection curve for gold at different wavelengths (Melles Griot Inc.)

The fabricated microfluidic chips were sputtered with gold (Edwards) at a pressure of 0.3 mbar for 180 s. The initial gold coating was carried out over the entire surface of the microfluidic chip as shown in Figure 6.4(a). However, during adhesion characterization of the microfluidic chip packaging, it was found that gold sputtered silicon surface does not bond properly with Pyrex with the bond failing at gold-silicon interface. Therefore, the gold coated chips were further processed carefully to remove the gold layer only from flat top surfaces and produce partially gold integrated microfluidic chips, as shown in Figure 6.4(b).



(a)



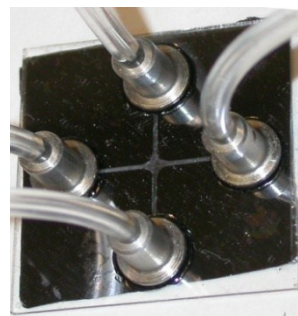
(b)

**Figure 6.4:** (a) Fully Gold-coated microfluidic chip (b) Selectively gold integrated silicon chip after post-processing

Two different microfluidic bonding feasibilities have been explored herein, namely with Pyrex and polycarbonate as microfluidic channel sealant. The optical transmittance properties and the bioaffinity of both the packaging materials were initially verified and were found to be similar. The partially gold integrated silicon chips were packaged with a transparent polycarbonate top cover (these chips are called SGP - Silicon-Gold-Plastic chips). Microfluidic tubes were inserted into the holes drilled on the polycarbonate top cover and the assembly was fixed onto gold integrated chips with epoxy glue. The non gold sputtered chips were packaged with Pyrex top cover (called SiPy -Silicon-Pyrex chips), wherein, suitable designed steel metal connectors fabricated with CNC machining that fit perfectly into the holes on the Pyrex top cover were glued to the Pyrex wafer and connected to the external microfluidic circuit so as to form a compact microfluidic package. The packaged SGP and SiPy chips are as shown in Figure 6.5.



(a) SGP

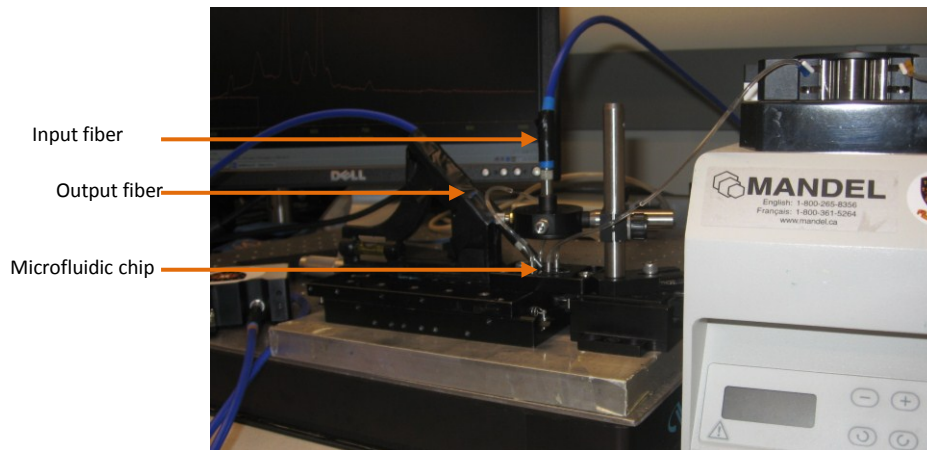


(b) SiPy

**Figure 6.5:** SGP and SiPy microfluidic chips with fluidic interconnects

### 6.2.2. Test setup and experiment

The bio-optical testing setup consists of a standard SMA end connectorized input fiber mounted on an inclined platform rigidly clamped on a movable positioner. A laser diode source (OZ Optics) was used as the input light source emitting light at 635 nm. The microfluidic chip was mounted on a nano-positioner so that the position of the chip with respect to the input fiber could be finely adjusted. The fluorescent signals were collected by a standard SMA fiber of 50  $\mu\text{m}$  core diameter, and this fiber was coupled with a multi modal spectrometer (Ocean Optics) at the other end in order to carry out further spectral analysis. Controlled fluid injection into the microfluidic channel was achieved using a peristaltic pump (GILSON, ON).



(b) Experimental setup

**Figure 6.6:** External Hybrid integrated Fluorescence detection setup

The fluorescence based bio-detection has been demonstrated using Alexafluor 647 tagged anti-sheep antibody (2 mg/ml, pH 7.5 in 0.1 M NaP and 0.1 M NaCl, with 5 mM azide

tagged with Alexafluor 647), which was used as the fluorophore particle. Three different concentrations of the antibody were prepared: 1%, 2%, and 5%, by diluting the antibody with Phosphate Buffer Solution (PBS). Isopropyl Alcohol (IPA) and DI water were used to rinse the microfluidic channel and clean the biomolecules after the fluorescence measurements.

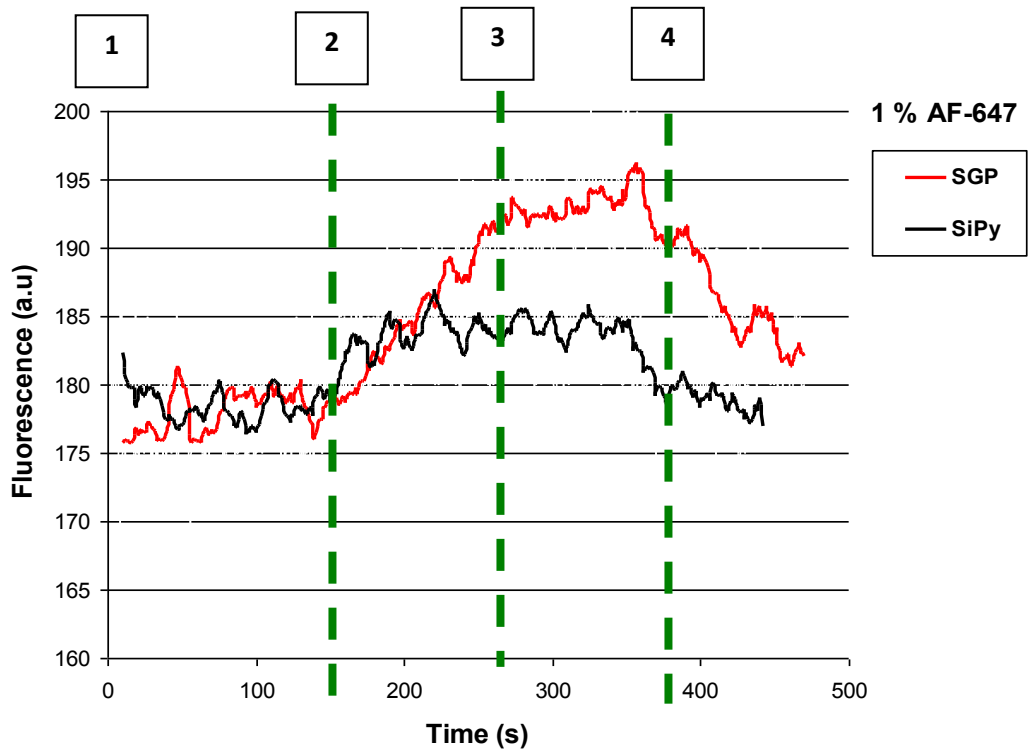
### 6.2.3. Experimental results

The sequence in which the experiment was carried out is listed in Table 6.1. Initially, fluorophore was passed into the microfluidic channel at a Reynolds number of 1. At this fluid injection speed, the time taken for the fluorophores to reach the Microfluidic chamber,  $\tau_i$ , is around 125 s. As soon as a spike was observed in the fluorescence, water was passed into the channel, and the rinsing was carried out. Once the fluorophores were cleaned from the microfluidic channel surface by water, IPA was passed so as to remove any remnant fluorophores that could have immobilized with the channel surface.

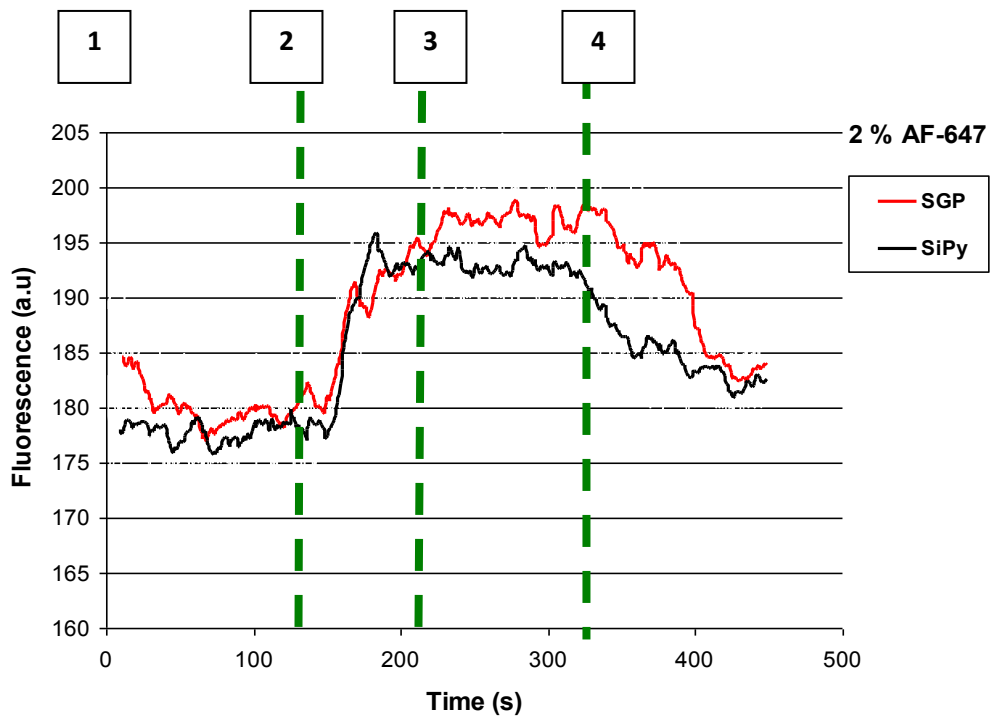
Step #	Procedure
1.	Pass AF647 into the microfluidic channel
2.	AF647 enters Microfluidic chamber
3.	Pass water
4.	Rinsing of the fluorophores begin.

**Table 6.1:** Sequential experimental procedure for fluorescence detection in SGP and SiPy

The moving average results for the fluorescence study on the SGP and the SiPy for different concentrations of the fluorophore particles are shown in Figure 6.7.

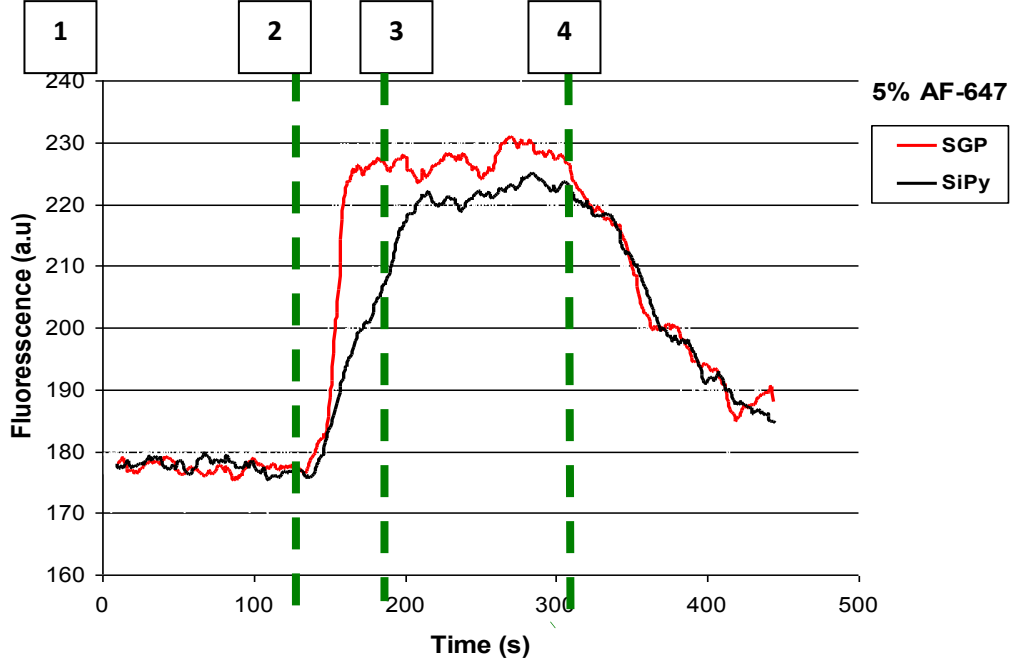


(a) Fluorescence detected for 1 % AF647



(b) Fluorescence detected for 2 % AF647





(c) Fluorescence detected for 5% AF647

**Figure 6.7:** Fluorescence detected for different concentrations of AF 647 with and without gold integrated microfluidic channels

From the results shown in Figure 6.7, it can be seen that for all the concentrations of the fluorophores used, gold integrated microfluidic channels show higher fluorescence than the bare silicon channels. Thus, enhanced fluorescence was obtained using the method of partial gold integration with the microfluidic channels.

In order to understand the phenomenon of enhanced fluorescence, a parameter called fluorescence compensation factor  $Z_c$ , was defined. Herein,  $Z_c$  is defined as the difference between the respective maximum fluorescence values observed in the SGP and the SiPy microfluidic channels, normalized with respect to the maximum fluorescence discrepancy observed between them. Therefore,

$$Z_c = \frac{\{F_{SGP} - F_{SiPy}\}}{\text{Max.}(F_{SGP} - F_{SiPy})} \quad \dots 6.1$$

wherein,

$F_{SGP}$  = Maximum fluorescence measured from the SGP channels

$F_{SiPy}$  = Maximum fluorescence measured from the SiPy channels

From the results obtained above, the value of  $Z_c$  was plotted with respect to different concentrations of the fluorophores, as shown in Figure 6.8.

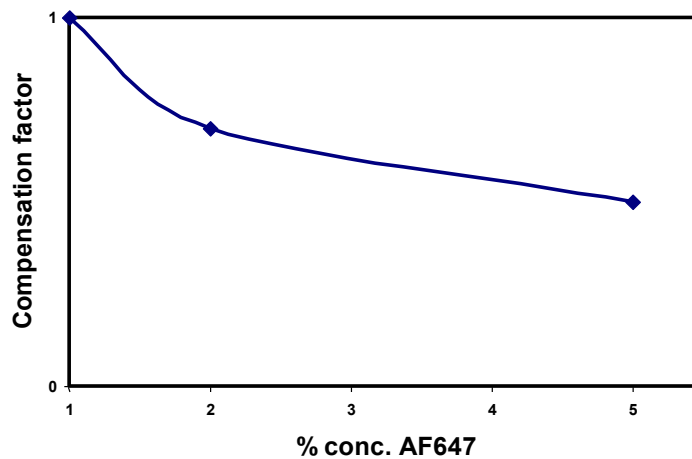


**Figure 6.8:** Plot of the compensation factor for the different concentrations of the fluorophores

For low concentrations of fluorophores, the compensation factor was higher, which means that greater amplification of fluorescence was obtained. As the concentration of the fluorophore was increased, the compensation factor decreases, indicating that the amplification in fluorescence was reduced. This is because, as the concentration of the fluorophores is increased, the number of fluorophore molecules which immobilize on to

the surface of the microfluidic channel also increases, the phenomenon which has been observed as better for silicon microfluidic channel surface than on gold (Chandrasekaran et al., 2007). Therefore, enhanced fluorescence is observed from the immobilized molecules than the fluorophore molecules that are present within the microfluidic channel under continuous flow conditions, as shown in the schematic in Figure 6.2. Thus, it is important to note that the integration of gold within the microfluidic channels for fluorescence amplification is more successful for very low concentration of the fluorophores, which is essential in real-time analysis of antigen-antibody binding.

### **6.3 Integrated Microfluidic Biophotonic chip for Laser Induced Fluorescence Detection**

The following section presents the excerpt from the paper titled the same as the section title, published in the *Journal of Biomedical Microdevices* (Chandrasekaran and Packirisamy 2010)

Integrated Lab-on-a-Chip or Micro-Total Analysis Systems offer several advantages for the detection of active chemical and biological species. In this work, an integrated microfluidic biophotonic chip is proposed for carrying out laser induced fluorescence detection. A Spectrometer-On-Chip device, specifically designed for multiple fluorescence detections at different emission wavelengths is integrated with the opto-microfluidic chip fabricated on Silicon-Polymer hybrid platform. The input fiber from the laser source, and output fiber coupled with a Spectrometer-on-Chip were integrated with the microfluidic channel so as to make a robust setup. Fluorescence detection was carried

out using Alexafluor 647 tagged antibody particles. The experimental results show that the proposed biophotonic microfluidic device is highly suitable for high throughput detection of chemical and biological specimens.

### **6.3.1. Introduction**

Lab-on-a-Chip or Micro-Total Analysis Systems ( $\mu$ TAS) (Jakeway et al. 2000), (Reyes et al. 2002), (Auroux et al. 2002), (Vilkner et al. 2004), (Dittrich et al. 2006), as they are sometimes referred to as, offer several advantages for health monitoring, Point-of-Care Testing (POCT), rapid detection of biological and chemical species and bio-security, by virtue of miniaturization, portability, improved signal-to-noise ratio and the ability to carry out in-situ medical detections. Integrated Lab-on-a-chip devices that rely on optical techniques for high sensitivity biodetection are also known as biophotonic chips (Bettioli et al. 2006). Depending upon its application and functionality, several components can be integrated within a biophotonic chip. However, microfluidics is an essential unit of biodetection because it not only introduces the biological environment into the system but also enables convenient handling of smaller sample volumes, transportation of the fluids into the detection units and the ejection of wastes after analysis.

Monolithic integrated systems such as the device demonstrated by Burns et al. (Burns et al. 1998) are highly suitable for biophotonic chip applications. But the requirements of some macro-scale operating units, such as microfluidic pumps, lasers, spectrum analysers etc make it impossible to fabricate the ensembles monolithically, and therefore a hybrid integrated package is required to cluster such macroscale components with microfabricated devices (Krulvitch et al. 2002).

In the past, research has been carried out on the integration of micro-optical ensembles, (Seo, Lee 2004), (Leistiko, Jensen 1998), (Yegnanarayanan et al 2007), (Ruano et al. 2003), (Chabinyk et al. 2001), (Irawan et al. 2006), (Su et al. 2008) within biophotonic Lab-on-a-Chip devices for various types of detection. Several biophotonic detection methods such as fluorescence (Webster et al. 2001), absorption (Balslev et al. 2006), refractometry (White et al. 2007), evanescent wave spectroscopy (Jiang et al. 2008), etc. have also been reported in the literature. Among the different biodetection techniques, Laser Induced Fluorescence (LIF) spectroscopy is one of the most common techniques used for biosensing owing to its high sensitivity, selectivity, and the ability to carry out instantaneous detection. Among other advantages, the potential for applications in biophotonic Lab-on-a-Chip systems are numerous (Thrush et al. 2003).

In this work, an optical microfluidic platform hybrid integrated with Spectrometer-on-Chip is presented for fluorescence based biodetection. The proposed system incorporates a novel silicon-polymer microfluidic channel platform integrated with optical waveguides within the channels. Spectrometer-on-Chip designed specifically for the detection of particular wavelengths of fluorescence emissions has been integrated with the opto-microfluidic chip for biophotonic detections. In order to understand the feasibility of hybrid integration for fluorescence spectroscopy using the Spectrometer-on-Chip, an external hybrid integrated device (Chandrasekaran et al. 2007) was proposed initially for the biodetection, wherein, the optical assembly, i.e., the excitation fiber from the laser and the collector fiber to the spectrometer was hybrid integrated outside the microfluidic domain and the device was used to detect sheep antigen with antisheep antibody tagged

with Alexafluor647. However, the major drawbacks of the externally hybrid integrated device were the optical losses and fiber misalignments, thereby leading to reduced efficiency of fluorescence detection for lower concentrations of the biomolecules.

Even though monolithic fabrication of the waveguides with the microfluidic channels is feasible (Lien et al. 2003), (Cohen et al. 2004), (Friis et al. 2001), (Leeds et al. 2004), optical losses (Splawn, Lytle 2002) incurred in the systems due to scattering, insertion and surface roughness would be detrimental for the detection of low concentration of biomolecules. Therefore, for the present application, the fibers were directly integrated with the microfluidic chip in order to improve the performance of the hybrid integrated system. The proposed opto-microfluidic chip would enable in the improvement of optical coupling efficiency, Q-factor of the fluorescence emission and also in minimising the optical losses, such as material absorption loss, scattering loss, etc., thereby creating a robust biophotonic system.

The following sections of the paper give a detailed description of the design and synthesis of the biophotonic chip along with the results of the fluorescence detection experiments.

### **6.3.2. Modeling and design**

The schematic illustration of the proposed Lab-on-a-Chip system is as shown in Figure 6.9. The opto-microfluidic chip basically consists of independent optical and microfluidic channels. The microfluidic setup comprises of inlet/outlet ports and fluidic channels with a detection chamber. In the optical channel, the input fiber from the laser terminates at the

detection chamber of the microfluidic channel, to illuminate the fluorescent biomolecules. A collector fiber, which is coupled with the input channel to the Spectrometer-on-Chip, is integrated with the channel at a coupling distance  $D$  from the input fiber. It can also be noted that there is a definite offset distance ( $\delta_f$ ) between the microfluidic channel surface and the core of the optical fibers. Therefore, for a pressure driven flow, when the pressure difference is low between the inlet and the outlet of the channels, flow velocities would be reduced thereby increasing the possibilities of passive immobilization of the biomolecules onto the microfluidic channel surface. It is important to avoid this behaviour as it would hinder biodetection because of the difficulties in the excitation and the emission of fluorescence. Hence, it is very essential that the present biophotonic chip setup has no stagnation flow of biomolecules through suitable microfluidic chamber design.

The Spectrometer-on-Chip, with its size being less than  $4 \text{ cm}^2$ , is very suitable for integration with the microfluidic device for biophotonic detections. The Spectrometer-on-Chip was designed based on Echelle grating fabricated with Silica-on-Silicon platform (Janz et al. 2004). Herein, the set of input channels, specifically designed for a particular wavelength, terminate at the boundary of slab waveguide region where the light diverges in the waveguide plane and illuminates the grating. Light is diffracted back from the concave grating and is focused onto the output waveguides, which are arrayed along the Rowland circle with a spacing chosen to give the desired channel separation.

One of the novelties of the present work is the wavelength specific configuration of the Spectrometer-on-Chip (Packirisamy and Balakrishnan, 2008) as against the arrangement of a standard spectrometer. Herein, each output channel is designed for specific wavelength of tunable bandwidth targeting fluorescence of a particular band. As there are many output channels available, multiple wavelengths can be detected simultaneously thereby enabling multi-analyte detection. A typical spectral response of a Silica-on-Silicon Spectrometer-on-Chip is given in Figure 6.10, in which simultaneous fluorescence at five different wavelengths is detected with as many output channels. In general, the Spectrometer-on-Chip could be designed for many combinations of wavelengths and bandwidths depending upon the application. Hence, the advantage of the Spectrometer-on-Chip is that simultaneous detection of different fluorescent emissions is possible through the different output channels of the chip.

Using similar principle, a 16-channel Spectrometer-on-Chip was designed targeting the fluorescence outputs at specific wavelengths listed in Table 6.2. The design was carried out with a bandwidth of 5-10 nm depending upon the wavelength. For reference, the different channels of the Spectrometer-on-Chip are as listed below, in Table 6.2.

<i>Channel Label</i>	<i>Purpose</i>
<i>Channel 4</i>	<i>Input</i>
<i>Channel 5</i>	<i>Emission at 570 nm(Cy3)</i>
<i>Channel 8</i>	<i>Emission at 550 nm</i>
<i>Channel 9</i>	<i>Emission at 532 nm</i>
<i>Channel 11</i>	<i>Emission at 670 nm (Cy5)</i>
<i>Channel 13</i>	<i>Emission at 650 nm</i>
<i>Channel 14</i>	<i>Emission at 640 nm</i>
<i>Channel 15</i>	<i>Emission at 633 nm</i>

**Table 6.2:** Different channels of the Spectrometer-on-Chip and their functions



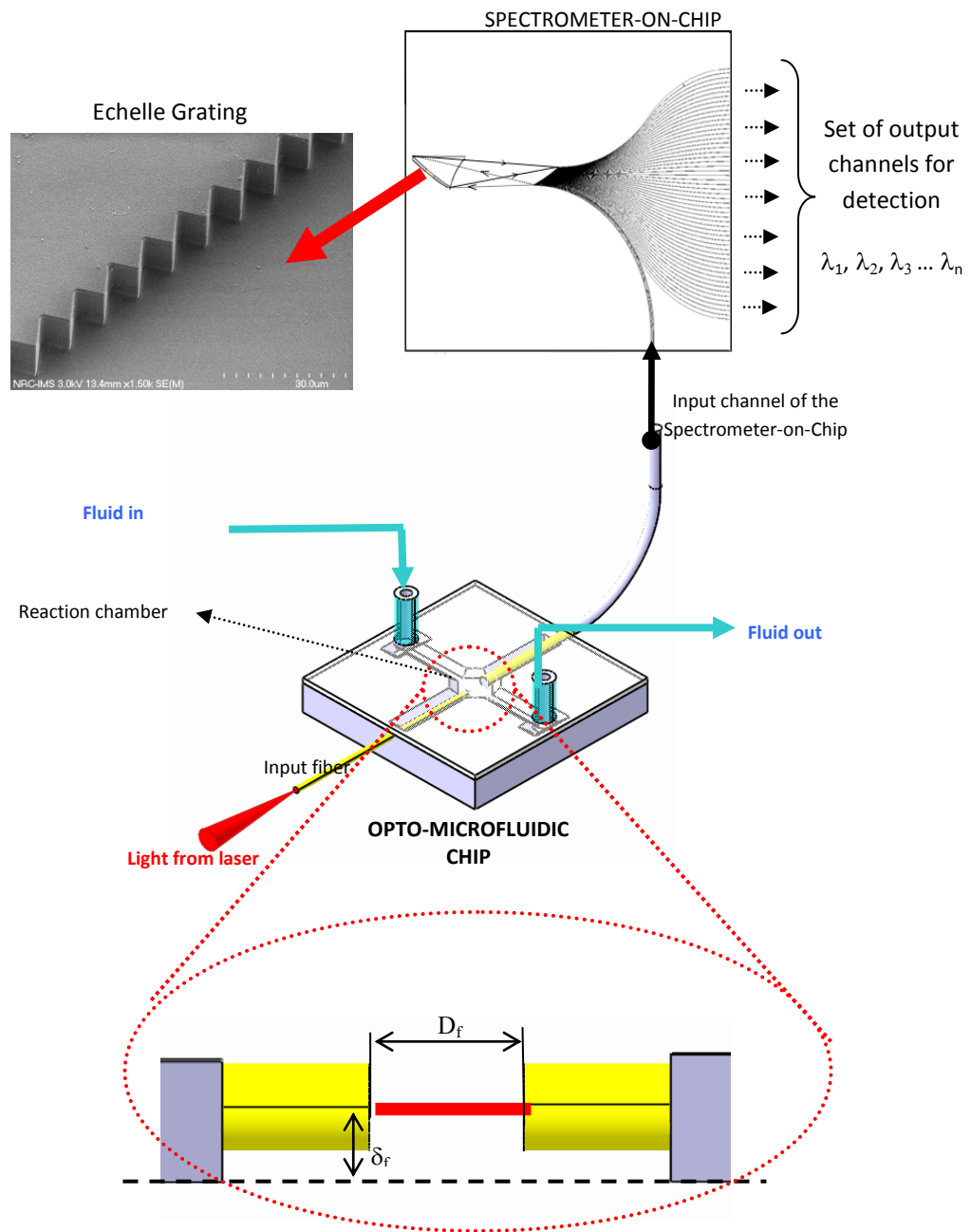


**Figure 6.9:** Schematic illustration of the opto-microfluidic chip integrated with the Spectrometer-on-chip.

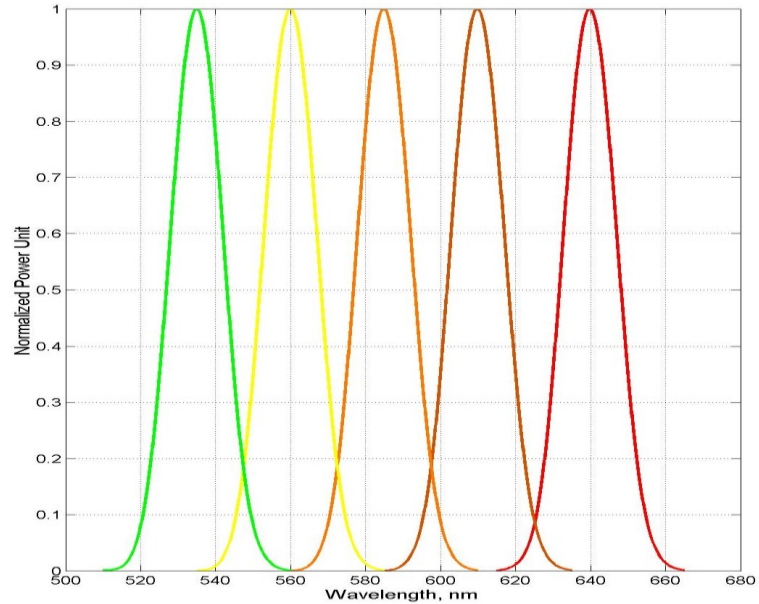


**Figure 6.10:** Typical response from the different output channels of the Spectrometer-on-Chip (Packirisamy and Balakrishnan, 2008)

For the design of the opto-microfluidic chip, several microfluidic channel configurations were considered and Finite Element Analysis (FEA) was carried out for flow behaviour within the microfluidic chambers. Different geometries of microfluidic channels and detection chambers were modeled using commercial software COMSOL v3.4 for the Finite Element Analysis by solving the Navier-Stokes equation. Effectively, the modeling and design of the chambers were based on the following criteria:

1. Non-stagnant flow and ease of rinsing
2. Ease of mask preparation for lithography and chip fabrication
3. Relative simplicity of the geometry
4. Ease of integration of optical channels with the microfluidic chip.

Finite Element Modeling of the flow behaviour was carried out for different microfluidic chamber configurations and the results of the analyses showed recirculation of fluid around sharp corners of the chamber under high pressure difference. Hence, optical channels were designed to be away from the fluidic channels with obtuse-angled boundaries. Both these design criteria were satisfied with the selected rhombus geometry of the microchamber.

In the present work, anisotropic etching technique using Tetra Methyl Ammonium Hydroxide (TMAH) was proposed for the fabrication of the opto-microfluidic chip for the following reasons: (i) Ease of fabrication to obtain the desired microchamber geometry, (ii) Feasibility of the formation of V-channels for the robust alignment and integration of the optical fibers and (iii) Reduced surface roughness. However, this method of fabrication would render an anisotropic chamber geometry due to development of fast etch corners. Therefore, the design of the microchannels and the chambers was carried out in such a way that the micromachined geometry of the chamber is close to the desired shape of the microchamber.

FEA of the flow behaviour within the rhombus chamber were compared with the anisotropic chamber of geometry expected to be obtained using TMAH silicon etching. The results are shown in Figure 6.11. It can be seen that the streamlines of flow in both the chambers are very similar.

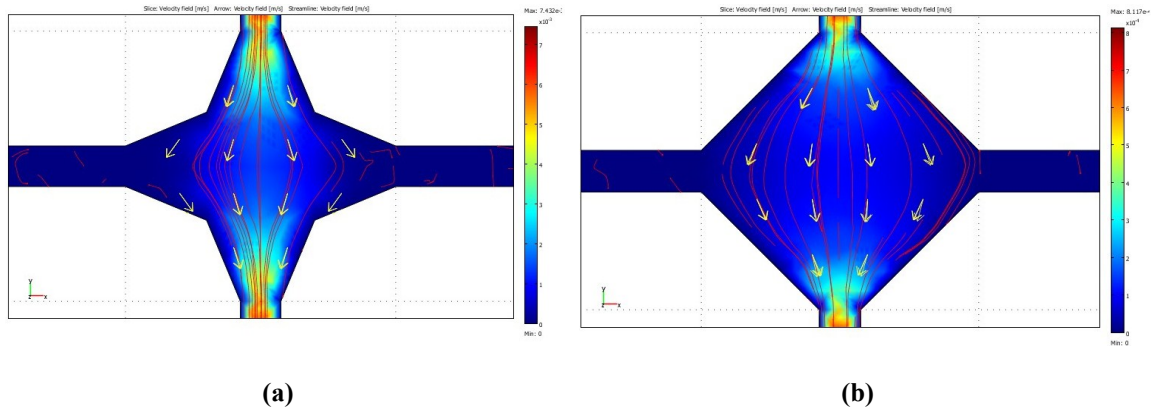


**Figure 6.11:** Results of the Finite Element Analysis of the flow behavior within (a) anisotropically etched chamber and (b) rhombus chamber.

The flow velocity at the detection zone along the mid streamline,  $V_{\min}$ , within the microchamber was calculated and results were compared for the anisotropic chamber and the rhombus chamber, assuming a pressure driven flow across the channels. From the graph shown in Figure 6.12, it can be seen that there is a very negligible difference between the flow velocities in the stagnant flow zones of rhombus and anisotropic chambers. Thus, through careful design of the chamber, the advantages of the anisotropic etching are utilized without compromising on the flow behavior.

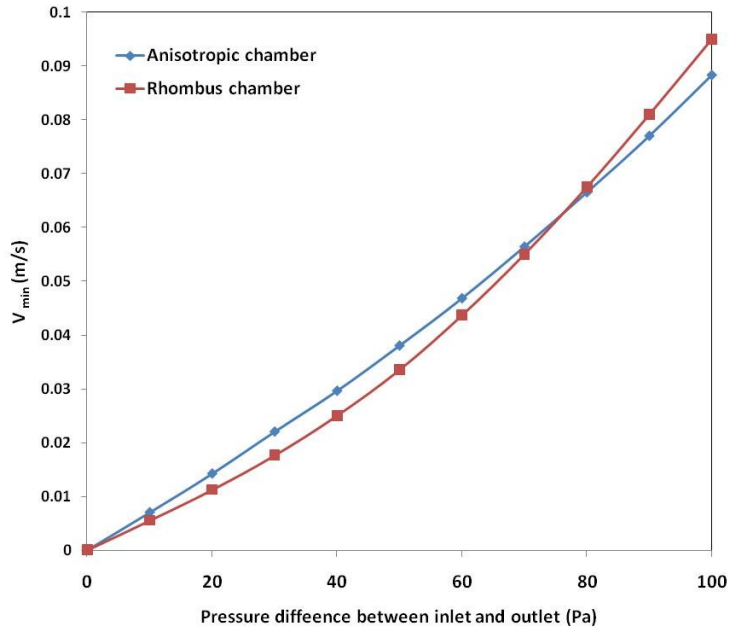


**Figure 6.12:** Comparison of  $V_{min}$  in the detection zone of anisotropically etched chamber with rhombus chamber.

### 6.3.3. Opto-Microfluidic chip synthesis

Different steps involved in the synthesis of the opto-microfluidic chip include fabrication of the microfluidic chamber, integration of the optical units with the channel, and packaging of optical and microfluidic systems, so as to enable integrated microfluidic-bio-photonic detection. In this work, a novel Silicon-Polymer (Polydimethylsiloxane or PDMS) hybrid platform has been developed for the integration of photonic and microfluidic units.

### 6.3.3.1 Fabrication

The feasibilities and advantages of TMAH anisotropic microfabrication for the present work have been outlined in the previous section. In line with those discussions, the following design parameters have been considered for the fabrication of opto-microfluidic chip:

Width of the optical channel,  $W_o = 250 \mu\text{m}$

Width of the microfluidic channel,  $W_m = 150 \mu\text{m}$

Width of the opto-microfluidic chip = 25 mm

Wafer thickness = 500  $\mu\text{m}$

Etch time,  $t$ : 6 hours

Etch rate of 25% TMAH at 80°C along {100},  $ER = 25 \mu\text{m/hr}$

Angle made by the fast etch planes with {100} plane,  $\theta = 22.5^\circ$

Under Etch Rate (UER) at  $\theta$ ,  $UER_{\text{max}} = 58 \mu\text{m/hr}$  (Landsberger et al., 1996)

The mask design for the microfluidic chamber and the evolution of the chamber geometry during the etching process is as shown in Figure 6.13. O is the convex corner in the mask design and O' is the etched corner during etching. From the design, it can be calculated that under etch rate along OO' is given by

$$UER_{OO'} = \{UER_{\text{max}} / \text{Cos } \theta\} \quad \dots 6.2$$

$$OO'_t = t \times UER_{OO'} \quad \dots 6.3$$

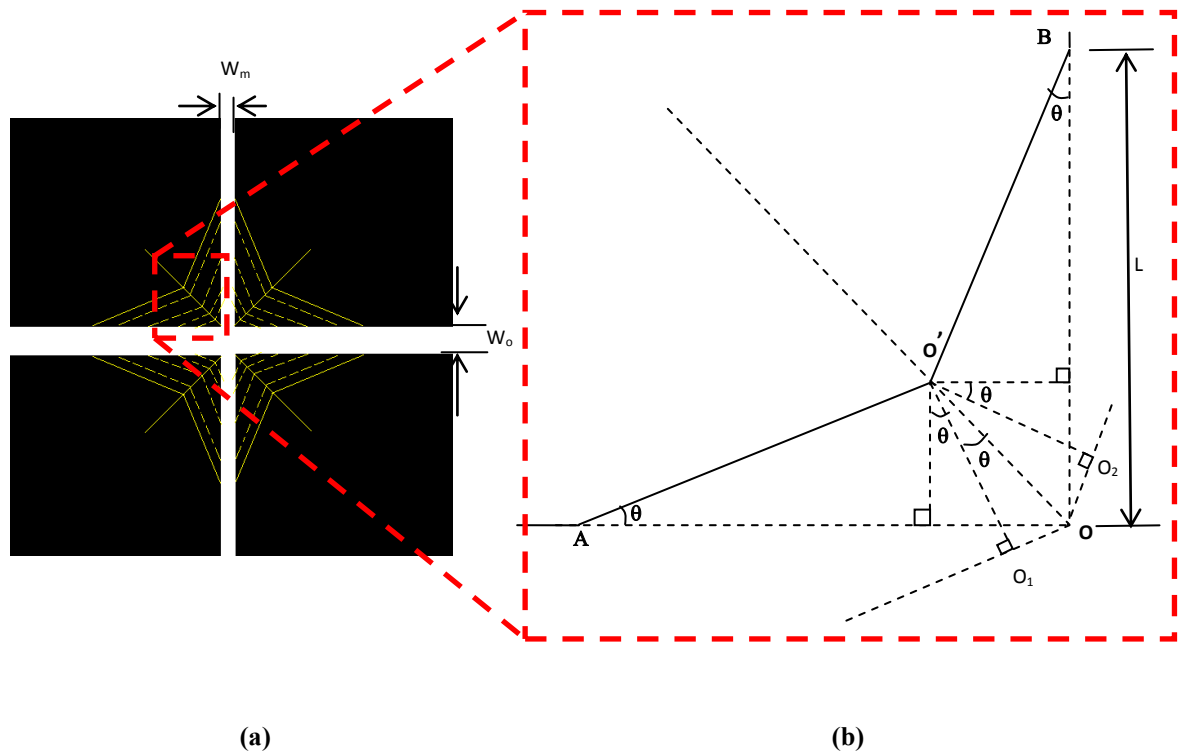


**Figure 6.13:** Schematic diagram showing the etch progress of microchamber. (a) Etch mask indicating the etch fronts at four convex corners (b) Detailed view of propagation of etch front at a convex corner:  $O$  is the convex corner and  $AO'$  and  $BO'$  are the etch fronts

Thus, during the etching process the guide length,  $L$ , developed for the specified etch time,  $t$  is given by

$$L = O'O_1 / \sin \theta = (UER_{\max} \times t) / \sin \theta \quad \dots 6.4$$

For fabricating the chip, 500  $\mu\text{m}$  thick Silicon (100) wafer with an oxide layer thickness of  $\sim 500$  nm was initially cleaned with Piranha solution made of a 3:1 conc. sulfuric acid ( $\text{H}_2\text{SO}_4$ ) with hydrogen peroxide ( $\text{H}_2\text{O}_2$ ) for 5 minutes. Positive photoresist S1813 was spun coated and patterned with a photomask. After developing and post-baking the

photoresist, oxide layer was developed with Buffered Oxide Etchant (BOE, 1:6 of 49% HF and 40% NH<sub>4</sub>F by volume).

The wafer was then etched in 25% TMAH at 80 °C and an etch stop was used for the prevention of back-side etching. The etch rate of <100> silicon obtained under these conditions was 25 μm/hr. The wafer was etched for 6 hours and thereafter, rinsed thoroughly with DI water. Oxide layer was subsequently removed. The SEM of the fabricated chamber geometry is as shown in Figure 6.14(a). After the fabrication of the chip, the edges were diced as shown in Figure 6.14(b) in order to facilitate the integration of fibers with the optical channels.

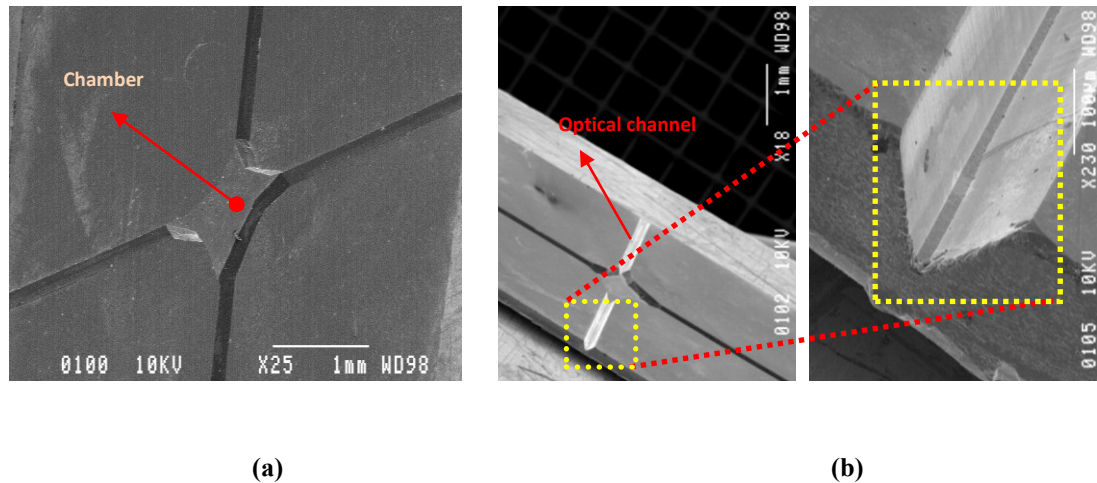


**Figure 6.14:** SEM images of (a) fabricated microfluidic chip (b) V-slots for fiber integration.

### 6.3.3.2 Integration and packaging

FC connectorized tapered lens ended fiber (OZ Optics, ON) connected to a laser was used as the input excitation fiber. Fiber strippers and precision cleavers (Newport, USA) were



used to remove buffer layer and cladding around the fiber. The input excitation fiber from the laser source and the output collector fiber coupled to the input channel 4 of the Spectrometer-on-Chip were positioned on the optical channels and supported well so as to isolate them from buckling or bending stresses. In order to determine the coupling distance between the fibers, fiber positioning was carried out under a microscope. The position of the output collector fiber was finely adjusted using a micropositioner for acquiring the maximum optical signal. The fibers were integrated within the optical channel slots using index matching gels and PDMS as shown in Figure 6.15, which not only bind the fiber with silicon, but minimize optical losses and also block the channel, thereby preventing leakage of bio-fluid through the optical channels. After the fibers were positioned, UV curable index matching gel (Norland Optical Adhesive 63) was injected into the optical channels and the setup was then cured with UV for 45s. To complete the sealing, PDMS gel was then coated on top, to enable the bonding of top PDMS cover with the opto-microfluidic chip.

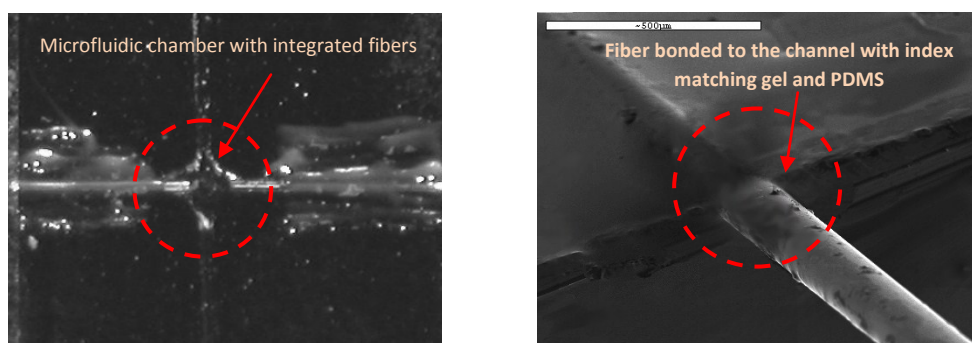


**Figure 6.15:** Integration of fibers with the microfluidic channels

PDMS was chosen as the top cover for the microfluidic channels due to the ease of bulk fabrication, cost-effectiveness and hydrophobicity, which is advantageous for microfluidic lid in order to repel the bio-fluid from adhering onto the surface (Chang et al. 2003). Herein, PDMS was prepared to the required geometry of microfluidic chip by standard soft-lithography process (McDonald et al. 2000). It was then cleaned in HCl: H<sub>2</sub>O solution in the volumetric ratio of 1:5 for 5 minutes. Two ports (2 mm diameter) were created on the PDMS to form the inlet and outlet of the microfluidic channel. Microfluidic tubes (250 μm inner diameter) were then fitted on the PDMS ports and the setup was again cured at 60 °C for 2 hours. A thin epoxy layer was coated on the PDMS; it was then aligned with the microfluidic channel and reversibly bonded with the silicon. Another layer of epoxy was then coated around the PDMS silicon interface so that the bonding is leak proof. Figure 6.16 shows the fully packaged microfluidic chip with integrated input/output waveguides.

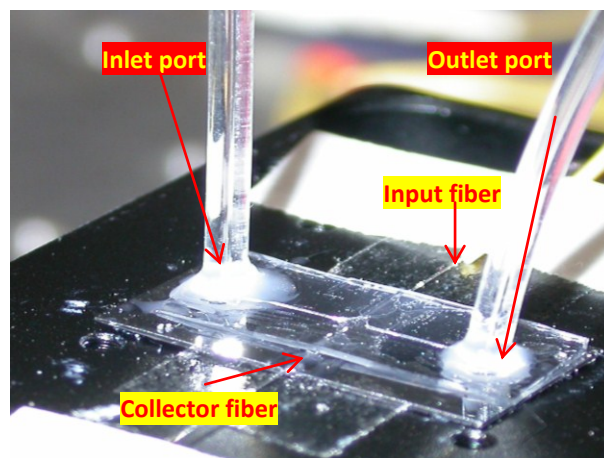


**Figure 6.16:** Fully packaged hybrid optical microfluidic chip.

#### 6.3.4. Spectrometer-on-Chip testing

In order to obtain confidence in the packaging of the Spectrometer-on-Chip with the opto-microfluidic chip, to measure the losses incurred in the system, and to prove the feasibility of using the Spectrometer-on-Chip with the present setup for biological and multi-fluorescence detection applications, the device was tested for the detection of fluorescence from Cy5 dye having an emission peak similar to Alexafluor 647, at 670 nm. This experiment was carried out under static no-flow conditions of the fluorophore.

Cy5 particles were excited using a laser source at 633nm, having an optical spectrum as shown in Figure 6.17(a). The passband of the grating for Cy5 emission was designed to pick out only the Cy5 emission at 670 nm in channel 11 of the Spectrometer-on-Chip, while filtering out wavelengths outside of the passband, including the excitation wavelength. The device response to the fluorescence excitation at 670 nm from channel 11 is as shown in Figure 6.17(b). The measured signal-to-noise ratio is 18.65 dB. From Table 1, it can be seen that channel 15 of the Spectrometer-on-Chip was designed for 633 nm, which is a control channel to confirm the excitation wavelength. Hence, the excitation wavelength at 633 nm was measured from the output channel 15, as shown in Figure 6.17(c). Similarly, any number of wavelengths could be detected by proper design of output channels of the Spectrometer-on-Chip as required in the case of multi-analyte detection. Thus, the device was tested for the simultaneous detection of multiple wavelengths. For multi-analyte detection at other wavelengths, the fluorescence emissions can be measured through the optical channels of respective wavelengths, as listed in Table 6.2. This experiment also provides confidence in employing the Spectrometer-on-

Chip with the hybrid integrated setup for measurements under continuous flow conditions. The spectrometer was designed and fabricated by Enablence Inc., Kanata.

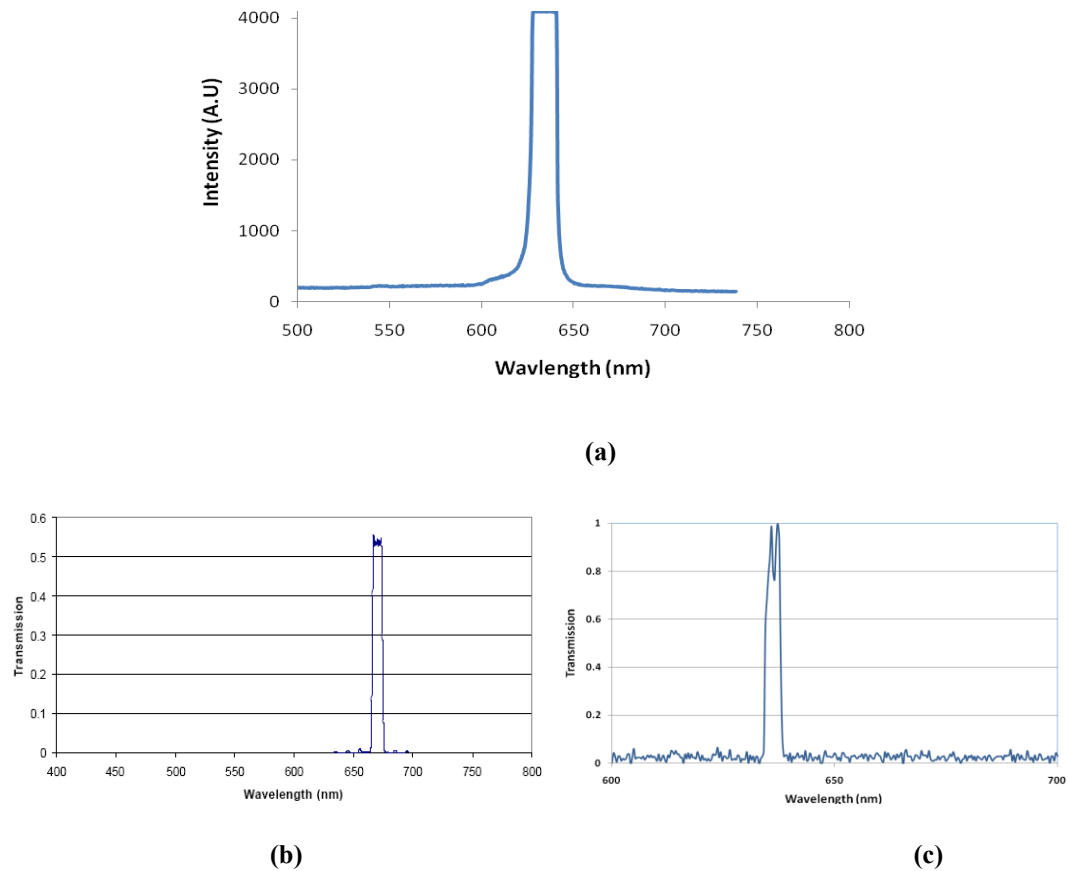


**Figure 6.17:** (a) Excitation spectrum from laser source at the input fiber of the microfluidic channel (b) Response of the Spectrometer-on-Chip at 670 nm from channel 11 (c) Response of the Spectrometer-on-Chip at 635 nm from channel 15

### 6.3.5 Biophotonic testing

The main objectives of carrying out biophotonic experiments using the opto-microfluidic system were as follows:

- (i) To demonstrate the feasibility of real-time biodetection using the integrated microfluidic biophotonic chip
- (ii) To demonstrate the non-stagnant flow through the microfluidic system
- (iii) To examine the accuracy of the optical alignment of the system for maximum collection efficiency

Herein, the fluorescence based bio-detection has been demonstrated using Alexafluor 647 tagged anti-sheep antibody as the fluorophore. 5% antibody (Alexafluor-647, 2 mg/ml, pH 7.5 in 0.1 M NaP and 0.1 M NaCl, with 5 mM azide) was prepared by diluting with Phosphate Buffer Solution (PBS). Isopropyl Alcohol (IPA) was used to rinse the microfluidic channel after biodetection. A peristaltic pump (Gilson Minipuls3) was used for fluid injection into the micro-channels. The experimental setup is as shown in Figure 6.18. The laser source (OZ Optics) was coupled with the input fiber and the collector fiber was coupled with the Spectrometer-on-Chip. AF647 tagged antibody was pumped into the channel with a peristaltic pump.

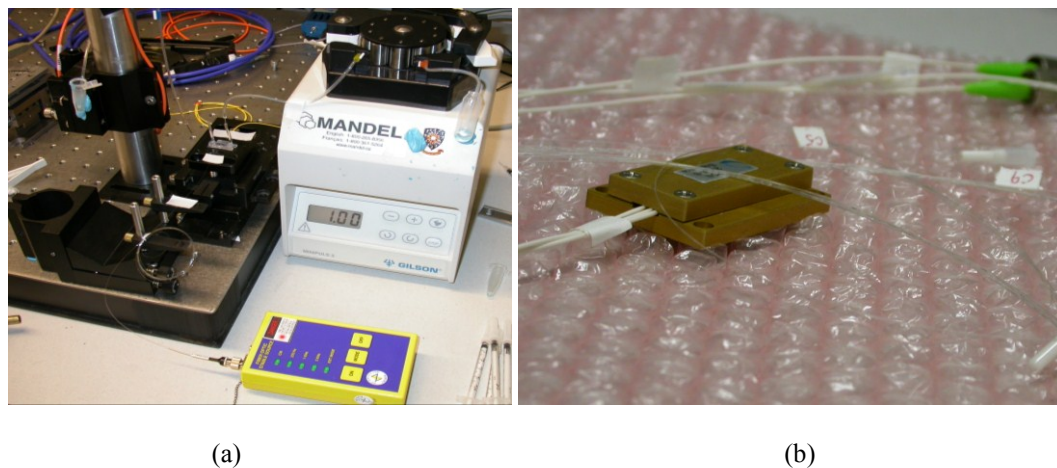


**Figure 6.18:** (a) Biodetection testing setup using the integrated device (b) Spectrometer-on-Chip

The biophotonic testing was carried out in three stages. In the first experiment, the feasibility of biodetection using the integrated system was examined by direct excitation of the fluorophores. Fluorescent signal similar to the signal observed from the Spectrometer-on-Chip for Cy5 was observed, thereby proving that the Spectrometer-on-Chip works well with the integrated opto-microfluidic system. To improve the sensitivity of detection, a multimodal input Spectrometer-on-Chip was used.

The second phase of the biophotonic tests comprised of dynamic microfluidic experiments under flow conditions. These tests were performed in order to demonstrate the feasibility of biophotonic detection using the Spectrometer-on-Chip under continuous flow conditions. In these experiments, a pulsed flow technique was observed wherein, fluorophore tagged antibody molecules were passed into the microfluidic channels for a short duration of 15 s and was rinsed off the channel. The results of the pulsed flow experiments are presented in Figure 6.19. For a Reynolds number of 1, the residence time, i.e. the time taken by the fluorescent particles to reach the detection zone was  $\sim 150$  s. The spike in fluorescence is observed at 150 s after the fluorophore tagged antibody molecules enter the detection zone. The experiment was repeated for a pulsed flow for 30 s and the results are shown in Figure 6.19(b). The sequence in which the experiment was carried out is given in Table 6.3, with respect to the experimental results presented in Figure 6.19.

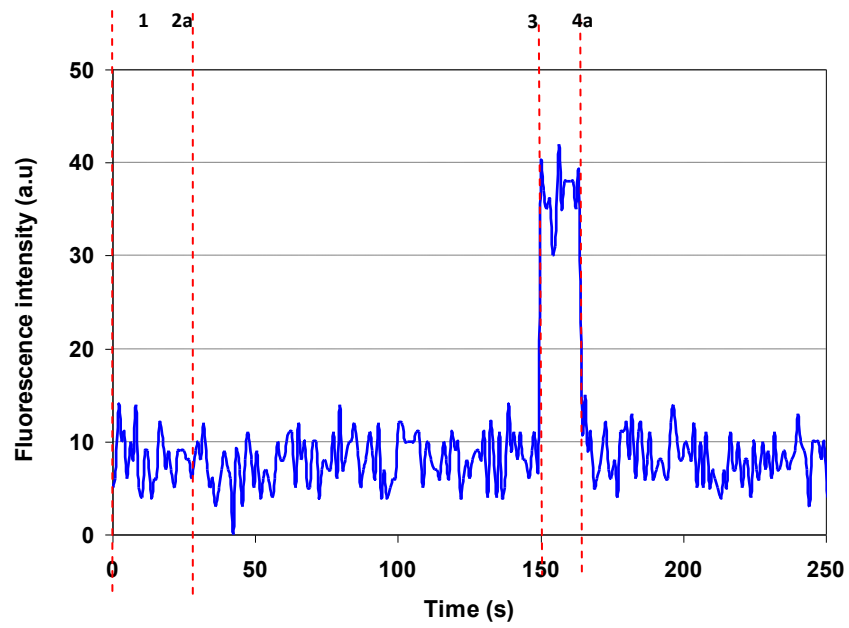
Step #	Procedure
1	Pass Alexafluor 647 tagged antibody
2	Discontinue the flow of AF647 tagged antibody; pass H <sub>2</sub> O
3	Fluorophores enter the reaction/detection chamber
4	Fluorophores exit the reaction chamber/rinsing by water begins

**Table 6.3:** Sequential procedure for pulsed flow fluorescence measurement experiments with respect to the results presented in Figure 6.19.

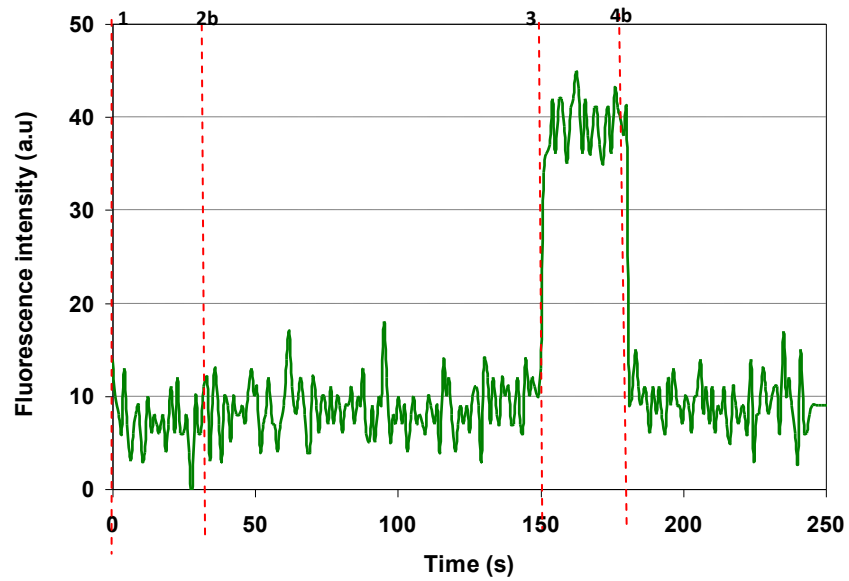
\* a and b in Figure 6.19 indicate the experiments carried out for 15s and 30 s pulses respectively

From the flow experiments, one can observe that there is an immediate increase in the fluorescence signal as soon as the fluorophore enters the reaction chamber at #3 (Figure 6.19). Also, the decrease in fluorescence due to the rinsing of the channels beginning at #4 (Figure 6.19) is immediate, which shows that the flow in the microfluidic channel is continuous. Therefore, the experimental results prove that the present design of the opto-microfluidic chip is appropriate for non-stagnant flow.

The results of the above experiments were verified for increased concentration of the antibody molecules. 10% of 2 mg/ml AF647 tagged antibody was passed continuously through the microfluidic channels using the pulsed flow technique for 15s and 30s respectively, and the fluorescence response was verified. The result of the fluorescence detection with higher concentration of AF647 is as shown in Figure 6.20. Higher pulse durations were tested for the biodetection feasibilities, however it was observed that for very long pulses, some residual fluorescence was observed.



(a) 15s pulsed flow



(b) 30s pulsed flow

**Figure 6.19:** Results of pulsed flow tests with Alexafluor 647 tagged antisheep antibody



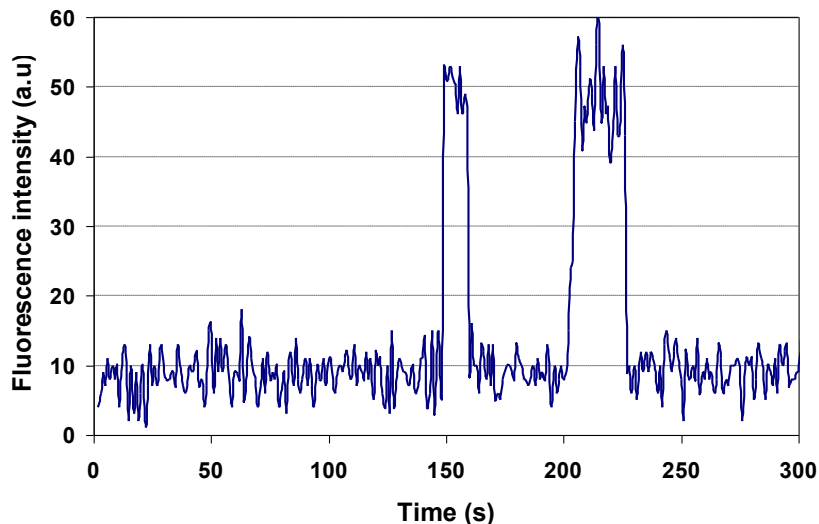


**Figure 6.20:** Results of dynamic tests with 10% of 2 mg/ml AF 647 tagged antisheep antibody

In order to determine the efficiency of the system for different coupling lengths between the fibers using the same setup, the distance between the input and collector fibers ( $D$ ) was varied from 250  $\mu\text{m}$  to 2000  $\mu\text{m}$ . The positioning and the integration of the fibers within the microfluidic chip were carried out under a microscope, and the distance between the fibers was measured under two optical magnifications, based on the field of view. As per the least count of the microscope measurement scale, the positioning precision for the coupling distances of upto 500  $\mu\text{m}$  is  $\pm 5 \mu\text{m}$  and for coupling distances of greater than 500  $\mu\text{m}$ , the positioning precision is  $\pm 10 \mu\text{m}$ .

5% of 2 mg/ml AF647 was passed between the fibers in the microfluidic channel and the fluorescent signals at different coupling distances between the fibers were recorded. The amplitude of the fluorescence signal for each value of  $D$  was normalized with respect to the maximum fluorescence observed at a coupling distance of 250  $\mu\text{m}$ .

If  $\chi_f$  is the coupling of fluorescent signal into the collector waveguide at any moment, the loss in the system due to the increase in coupling distance is given as

$$\text{Optical loss, } \beta_{ih} \text{ (dB)} = -10 \log_{10} \left( \frac{\chi_f}{\chi_{f \max}} \right) \quad \dots 6.5$$

Here,  $\chi_{f \max}$  is the maximum fluorescent signal at  $D = 250 \mu\text{m}$  and  $\tau$  is the fluorescent signal obtained at any other coupling length. Thus, for the increase in the coupling length from  $250 \mu\text{m}$  to  $2000 \mu\text{m}$ , the fluorescence loss in the system is 1.1 dB.

The variation of normalized fluorescence with respect to the coupling distance is shown in Figure 6.21.

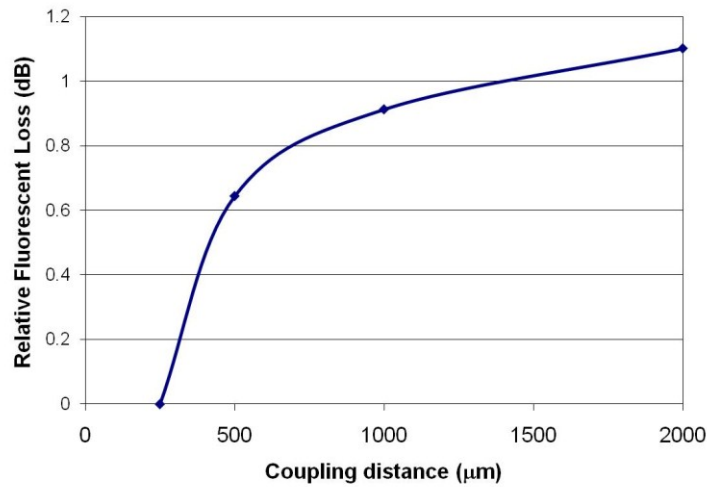


**Figure 6.21:** Variation of the fluorescence loss for different coupling distance between the fibers

The biophotonic experimental results provide confidence in the packaging methods for the synthesis of the integrated device. Through the internal hybrid integration method proposed in this work, low concentration of biomolecules can be detected, which is a

major advantage compared with the external hybrid integrated method. The Spectrometer-on-Chip device has enabled in the increase of the quality factor for the fluorescent signals, and the experimental results, shown in Figures 6.17, 6.19 and 6.20 prove that the device is sensitive for no-flow and continuous flow testing. It is evident that even for an eight fold increase in the coupling distance between the fibers, the relative fluorescent loss is low. This proves that the optical alignment and the optical integration in the system are robust. Also, the Spectrometer-on-Chip is highly suitable for the integrated microfluidic device for carrying out biophotonic fluorescence detections and can be used in real-time applications for chemical and biological detections.

#### **6.4. Conclusion**

In this Chapter, an on-Chip hybrid integrated optical microfluidic platform was developed for biophotonic detection of absorption and fluorescence using a Spectrometer-on-Chip.

The feasibility of fluorescence biodetection has been demonstrated through the successful detection of Alexafluor 647 tagged antibody molecules. The important novelties of the present work are the integration of the Spectrometer-on-Chip with the Optical microfluidic device.

There are several advantages of using silicon, however from the feasibility of cost-effective microfabrication of the system-on-chip and integration with micropump, PDMS offers more potential advantages than silicon.

The On-chip optical microfluidic integration was demonstrated with a hybrid silicon-polymer device. The success of the hybrid integrated setup opens up the feasibility of monolithic integration of silicon based microfluidic channel with Silica-on-Silicon based Spectrometer-on-Chip. Other important advantages of the proposed biophotonic system are independence of each module in terms of functionality, multi-analyte detection, rapid, precise and discriminating results with wavelength specific Spectrometer-on-Chip configuration, low background/high signal-to-noise ratio, lack of moving parts, robust, portability, and feasibility of bulk fabrication. Thus, the proposed device is highly suitable for in-situ biomedical detections of chemical and biological specimens. Further modifications to the present system would involve monolithic attachment of microfluidic chip and spectrometer to increase the coupling efficiency and study of variation of different microfluidic parameters for improved flow behavior.

Also, as an extension of the previous study, the feasibility of integration of fibers with PDMS was verified. Herein, the input and the output optical fibers were integrated with PDMS microfluidic channel, and the bonding was done using PDMS itself, so that the fibers are completely embedded into the PDMS substrates.

For this process, the mould for the PDMS was made on metal and was fabricated by precision milling. After the PDMS device is fabricated, ports were created for fitting the microfluidic tubes. In order to insert the optical fibers, the slots in the optical channels were opened in the PDMS chip. The positioning of fibers within the optical channels was done using fiber positioners. This process was carried out under the microscope so that

the distance between the fibers can be monitored to a greater precision. Two different configurations of the optical-microfluidic chip were studied, i.e straight fiber configuration and orthogonal fiber configuration, as shown in Figure 6.22.

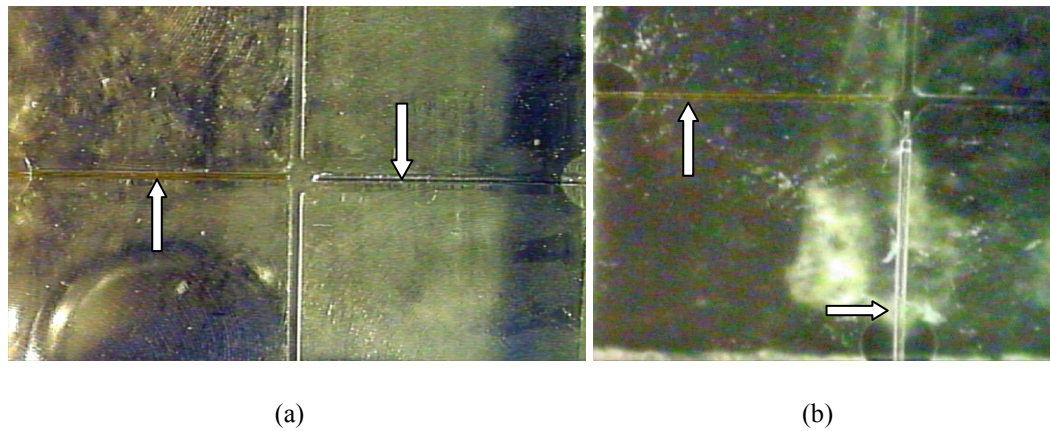


**Figure 6.22:** Fibers positioned in the optical channel during the on-chip opto-microfluidic integration with (a) straight coupled and (b) orthogonal coupled fiber configurations.

In the straight coupled fiber configurations, the input and the collector fiber were positioned along the same axis, so that light can be directly coupled onto the output fiber. Once the fibers were positioned, the optical alignment was verified by passing light through the fiber and studying the collection intensity, fine alignment adjustments were made so that the light coupled into the collector fiber is maximum. For the orthogonal fiber configuration, the input and the output fibers were positioned orthogonal to each other. This was carried out to avoid direct light coupling for laser induced fluorescence testing as shown in Figure 6.23. It can be seen that for orthogonal fiber configuration, there is no direct light being coupled into the collector fiber.

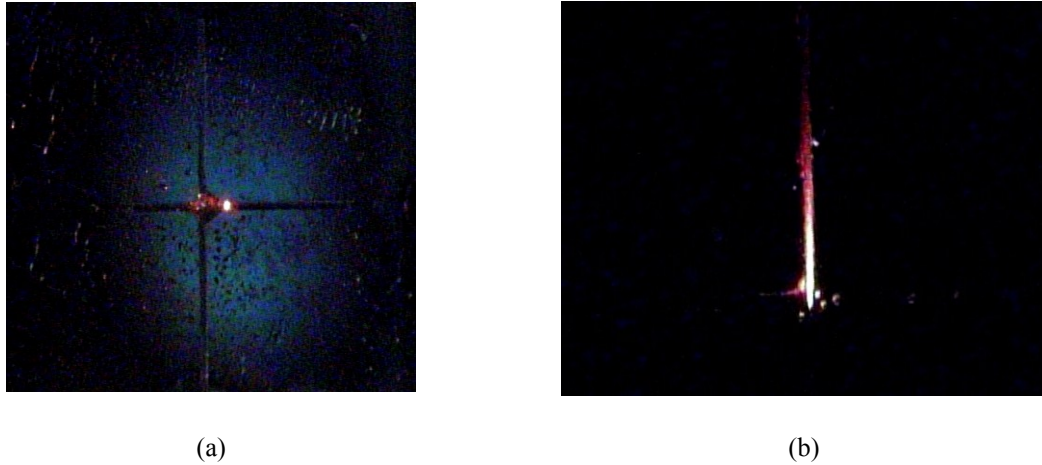


**Figure 6.23:** Trace of light seen for (a) direct fiber coupling (b) orthogonal fiber coupling

Once the fiber alignment was done, the ends of the optical channels were sealed using PDMS. This process not only binds the optical fibers securely with the PDMS channel but also seals the ends so as to prevent the leakage of fluid from the microfluidic chamber. During the initial few trials, it was found that during the process of sealing the optical channels, PDMS filled into the microfluidic chamber due to capillary force and thus blocked the microfluidic flow. Therefore, in the subsequent trials, the prepolymer-curing agent mix was allowed to cure at room temperature for 4 hours before sealing the optical channel so that the flow of the PDMS due to capillary is avoided. The top cover for the system was also fabricated with PDMS and using semicured PDMS, the top cover was attached with the optic chip thereby forming a completely sealed chip. Ports were also created in the microchannel and hybrid integrated bio-opto-microfluidic testing with micromechanical pumping was also carried out by the integration of a separately fabricated micropump, by creating a supercavitation induced flow. However, the experiments were restricted to only qualitative studies and no further analysis of the results was done.

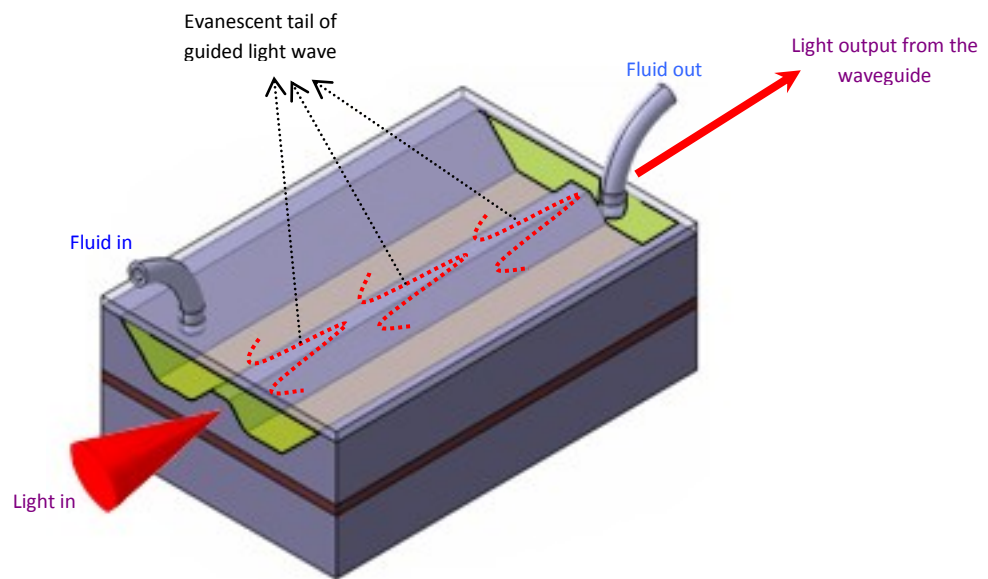
# **Modeling, Fabrication and Testing of Nano-integrated Evanescence Waveguide Detection System**

### **7.1 Introduction**

While sensitivity is the key for developing optical detection system which can be able to detect very low concentrations of biological specimens, the greatest challenge is to suitably integrate this system with the  $\mu$ TAS without compromising on the high signal to noise ratio for real-time biosensing applications. It is well known that biomarkers and labeling of biomolecules can structurally and functionally interfere with an assay. They may not be specific, and may be very difficult to conjugate. These problems are often encountered in single molecule detection systems (Vollmer, Arnold 2008). This calls for the application of label free biodetection system in a  $\mu$ TAS which is also very sensitive to detect the presence or concentration or activity of biological specimens.

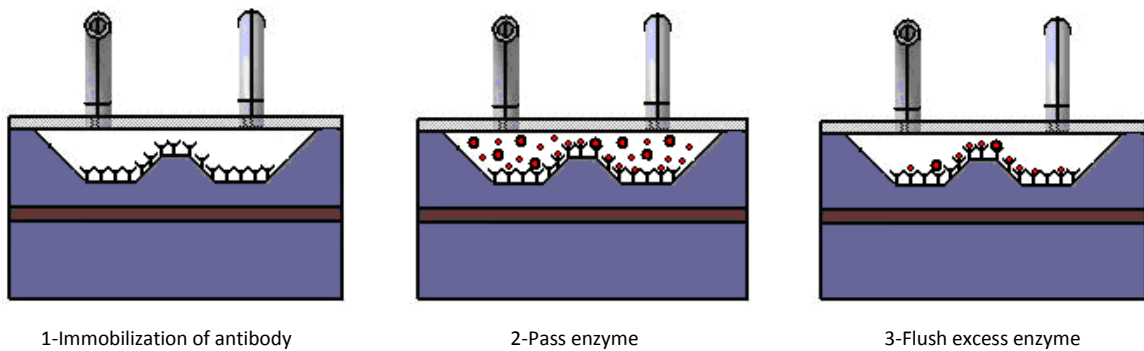
One of the methods of label free biodetection is the evanescent wave sensing (Jiang et al. 2008),(Chandrasekaran and Packirisamy, 2009) which is based on the bio-optical interaction between the evanescent tail of a planar waveguide mode and the surrounding media, resulting in the perturbation of optical mode propagated through the waveguide. The schematic of the evanescent wave detection is as shown in Figure 7.1(a). The technique to carry out chemical and biosensing using evanescent wave detection

technique with integrated microfluidics is schematically depicted in Figure 7.1(b). A receptor layer is immobilized onto the surface of the waveguide using passive immobilization technique (Chandrasekaran et al., 2007). The exposure of this functionalized surface to the complementary analyte molecules subsequently passed through the microfluidic channels and the resulting biochemical interaction between them, induces a local change in the bio-optical interaction between the specimens and the evanescent field. This change is detected through the change in the properties of the guided light and its amplitude can be correlated to the concentration of the analyte, thereby yielding a quantitative measurement of the interaction. Thus, with the integration of microfluidics, since it is possible to precisely meter the quantity of biological substrate which is immobilized onto the waveguide surface and the amount of antibody which reacts with the immobilized specimens and hence, precise measurement of the bio-optical interaction through evanescence can be made possible.



(a) Schematic of evanescent based arrangement with integrated microfluidics





(b) Evanescence based biodetection with integrated microfluidics

**Figure 7.1:** (a) Schematic illustration of evanescence wave phenomenon and (b) Evanescent wave detection using integrated microfluidics.

Recently, a lot of work has recently been focused on the development of evanescent field sensors for biological sensing. Evanescence based detection has been implemented in different forms such as surface plasmon resonance (SPR), which is one of the most successful label-free techniques widely employed for the determination of many types of interactions (Homola et al. 1999) and porous silicon based biosensors (Lin et al. 1997). Furthermore, integrated optical biosensors based on slot-waveguide resonators (Barrios et al. 2008), Mach-Zehnder interferometers (Prieto et al. 2003), directional couplers (Luff et al. 1996), micro-ring (Yalcin et al. 2006), and resonant cavity (Blair and Chen, 2001) resonators have also been demonstrated to be very sensitive for label-free biosensing, based on the principle of evanescent wave detection. Though, evanescence detection has been commonly used and cited in the literature, surprisingly, this biodetection principle has not been much investigated on a  $\mu$ TAS (Densmore et al., 2006). Therefore, it is very

important to develop a suitable evanescent wave sensing platform which can be integrated with microfluidics for successful implementation in a  $\mu$ TAS.

Evanescent wave detection is a surface phenomenon, i.e, the detection method can be used for sensing any chemical or biological activity that takes place on the surface of the waveguide, due to the direct interaction of the biological specimens with the optical field. Therefore, this method is very sensitive to the identification of the presence or activity or reactions of chemical and biological specimens present in the bio-optical interaction zone. However, as seen with hybrid integrated systems, the sensitivity of the evanescence based detection system is also bound to be affected due to the integration with other complimentary functionalities, due to material losses caused by packaging, mis-alignment losses, absorption losses etc. Therefore, it is also important to improve the sensitivity of evanescence based biodetection, which will be useful for detection of very low concentration of chemical and biological specimens upon the integration of the evanescence system with microfluidics.

In this work, a novel method of Nano-Enhanced Evanescence detection Technique (NEET) is proposed (Packirisamy and Chandrasekaran, 2010) for integration with the  $\mu$ TAS for the detection of active chemical and biological specimen. This technique includes the integration of nanoparticles on the surface of the waveguide which would thereby facilitate better bio-optical interaction, between the evanescent field of light and the chemical/biological substrates.

The NEET system can be employed through the integration of nanofeatures, such as nanotubes, nanospheres, nanocavities, nanorods, etc. in order to influence the evanescence of light and thereby potentially improve the sensing efficiency. The nanofeatures could be fabricated with the same material (eg. Silica, Silicon, GaAs, InP, SU8, PDMS, other optical materials, optical polymers etc) in a single lithography step or different nano-materials (for eg. Carbon Nanotubes, Gold Nanorods, Silver nanoparticles etc.) as well and integrated subsequently with the waveguide. While features like nanocavities and nanopillars can be fabricated on the same material platform as the waveguide as a part of the waveguide fabrication process, other features such as nanocolloids, nanospheres, nanorods, nanotubes etc. could be integrated from other materials also. Nanofeatures of different material that are used for NEET will have different refractive index than the material of the waveguide. One of the ideas of the NEET is that evanescence can be controlled by varying the properties of the nanofeatures according to the biological specimen to be tested. The other advantage of the NEET is that it is operable in both the visible and infrared (IR) spectra depending upon the material platform selected, which therefore is useful for integration with the  $\mu$ TAS.

The following sections of this chapter present the modeling of Nano-integrated evanescent system, and the experiments carried out in order to demonstrate the feasibility of NEET.

## 7.2 Modeling of nano-integrated evanescence system

In order to study the effect of Nano-enhanced evanescence, it is essential that a suitable model be built and the feasibility of NEET be studied theoretically. Literature suggests that several works have been carried out on the modeling of nanophotonic systems through various computational methods (Scarmozzino et al., 2000). Herein, a Finite Difference Time-Domain (FDTD) study (Szabo et al., 2006), was carried out, in order to study the effect of integrating nanofeatures on the evanescence behavior of light being guided through a waveguide. The FDTD technique is a widely used propagation solution technique in microphotronics, especially for computations involving photonic bandgap devices, for which the standard Beam Propagation solutions are inadequate and is not suitable for the geometry. The only disadvantage of this method is that it is computationally demanding requiring a fairly dense grid of points at which all three vector components of both the electric and the magnetic fields must be maintained and thereby resulting in the usage of large memory storage and long computation times.

The Finite Difference Time Domain (FDTD) modeling of nano-integrated waveguides was carried out by solving the Maxwell's curl equation which can be written in Cartesian coordinates as simple scalar equations.

$$\frac{\partial H_x}{\partial t} = -\frac{1}{\mu_{em}} \left( \frac{\partial E_y}{\partial z} - \frac{\partial E_z}{\partial y} \right) \quad \dots 7.1(a)$$

$$\frac{\partial H_y}{\partial t} = -\frac{1}{\mu_{em}} \left( \frac{\partial E_z}{\partial x} - \frac{\partial E_x}{\partial z} \right) \quad \dots 7.1(b)$$

$$\frac{\partial H_z}{\partial t} = -\frac{1}{\mu_{em}} \left( \frac{\partial E_x}{\partial y} - \frac{\partial E_y}{\partial x} \right) \quad \dots 7.1(c)$$

$$\frac{\partial E_x}{\partial t} = -\frac{1}{\varepsilon_{em}} \left( \frac{\partial H_z}{\partial y} - \frac{\partial H_y}{\partial z} \right) \quad \dots 7.2(c)$$

$$\frac{\partial E_y}{\partial t} = -\frac{1}{\varepsilon_{em}} \left( \frac{\partial H_x}{\partial z} - \frac{\partial H_z}{\partial x} \right) \quad \dots 7.2(a)$$

$$\frac{\partial E_z}{\partial t} = -\frac{1}{\varepsilon_{em}} \left( \frac{\partial H_y}{\partial x} - \frac{\partial H_x}{\partial y} \right) \quad \dots 7.2(b)$$

Where  $E$  and  $H$  represent the electric field and the magnetic fields respectively and the constants  $\mu_{em}$  and  $\varepsilon_{em}$  represent the permeability and the permittivity of the medium respectively. Maxwell's equations describe a situation in which the temporal change in the  $E$  field is dependent upon the spatial variation of the  $H$  field, and vice versa. The FDTD method solves Maxwell's equations by first discretizing the equations using central differences in time and space and then numerically solving these equations in software.

The FDTD simulations were carried out with Full WAVE (RSoft v8.0, <http://www.rsoft.com>). Due to the large computation times, a full three-dimensional simulation of even simple problems like planar, evanescent splitter can be nearly impossible. Therefore, in the present work, the FDTD simulations were carried out only for a sample section of the waveguide, and the results are extended to estimate the evanescent influence over an entire waveguide length.

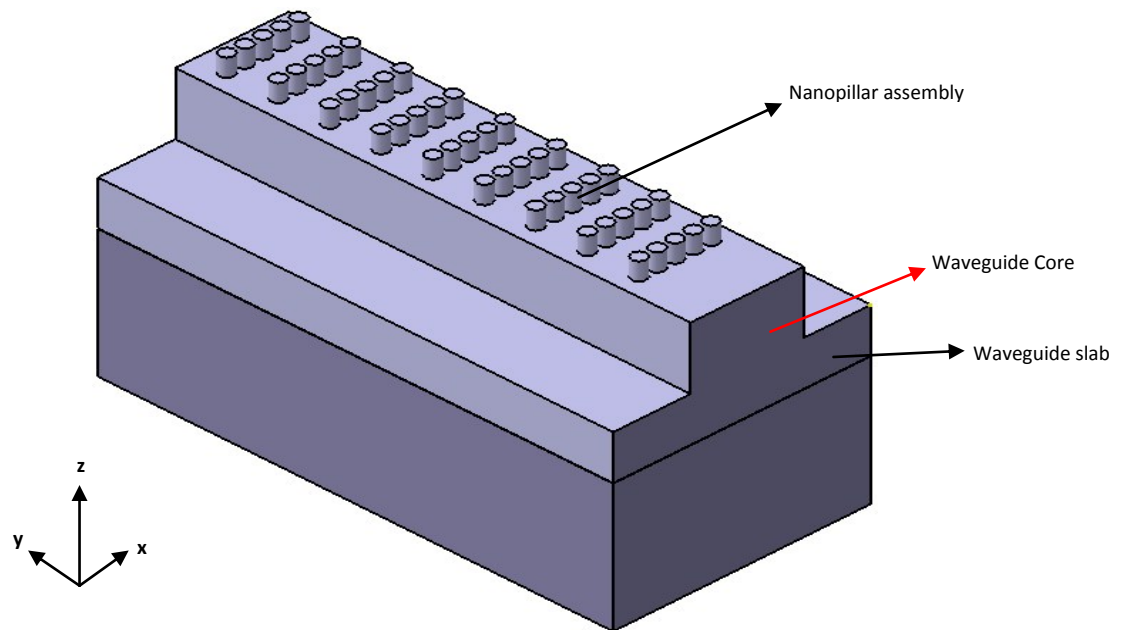
For light being propagated through a given waveguide, the total evanescent loss was calculated by calculating the total power in the evanescent field, normalized with respect to the input power of the light. The optical power in the region of interest is calculated by defining a time monitor along the nano-integrated region of the waveguide, which measures the total evanescent field strength. The power flow through the monitor domain as a function of time,  $S(t)$ , is defined as

$$S(t) = \frac{1}{S_0} \operatorname{Re} \left( \int_{A_m} [E(t) \times H^*(t)] dA_m \right) \quad \dots 7.3$$

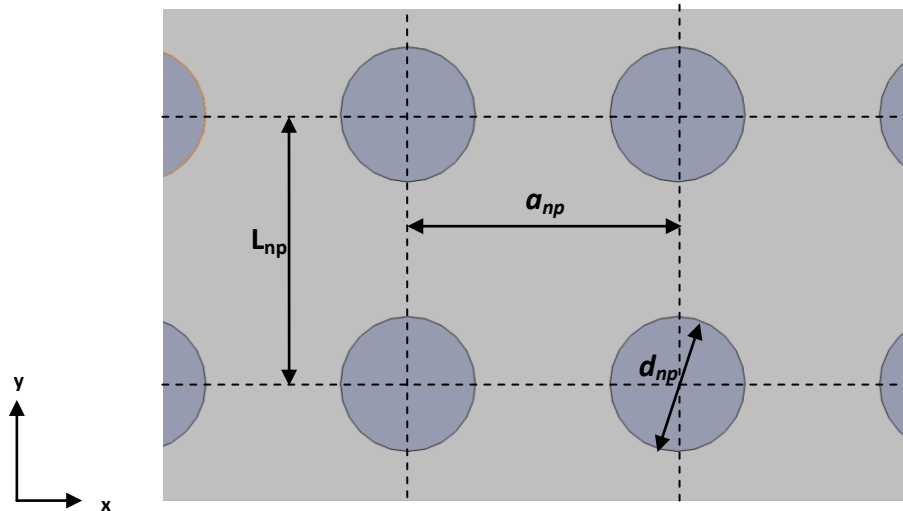
Where  $S_0$  is the launch power, and  $A_m$  is the area defined by the monitor. The monitor measures the power flow through all surfaces of the monitor volume defined by its width, height and length. The relative Nano-enhanced evanescent loss,  $\chi_{ev}$ , is defined as the difference between the total power of the evanescent field with integrated nanoparticles and the power of the evanescent field of a plain waveguide without nanofeatures. The motivation of the present modeling is to study the variation of  $\chi_{ev}$  for different evanescent conditions, simulated by varying the geometry and the layout of the nanoparticles on the surface of the waveguide. Herein, three different nanofeatures have been studied, namely, with nanopillars, nanocavities and nanospheres. While nanopillars and nanocavities can be integrated only on top of the waveguide surface, nanospheres could be integrated on both the top wall and the sidewalls of the waveguide.

### 7.2.1 Implementation of NEET with nanopillars

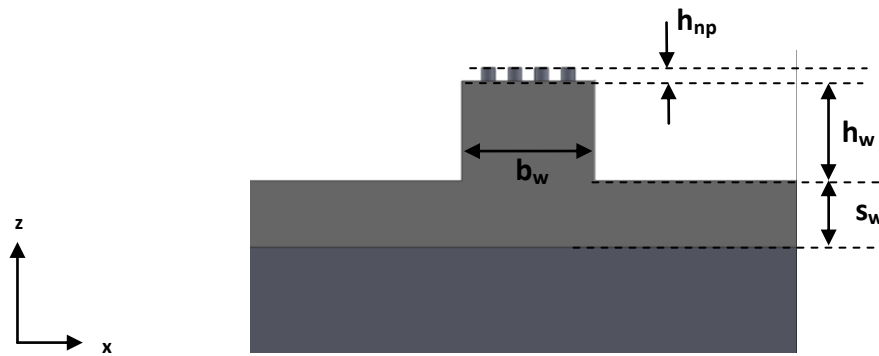
The waveguide system was modeled on a rectangular rib waveguide with integrated nanopillars as shown in Figure 7.2. The optical rib waveguide shown in Figure 7.2 is implemented on silicon platform and includes a waveguide slab, a rib waveguide core and a plurality of nanopillars implemented on a top side wall of the rib waveguide core. The plurality of nanopillars is arranged in ordered arrays/rows along the length of the waveguide core. A single array consisting of 5 nanopillars, each separated by a distance,  $L_{np}$ , was modeled on the waveguide. The pitch between nanopillars in an array is denoted as  $a_{np}$  and the height of the nanopillars is denoted by  $h_{np}$ . The number of arrays of nanopillars is denoted by  $N_{np}$ . The dimensions of the rib waveguide and the integrated nanopillars, considered for the present modeling is as given in Table 7.1



(a)



(b)



(c)

**Figure 7.2:** Schematic of the silicon waveguide with integrated nanopillars

Feature	Dimension
Waveguide core width, $b_w$	$1\ \mu\text{m}$
Waveguide core height, $h_w$	$0.9\ \mu\text{m}$
Waveguide slab height, $s_w$	$0.1\ \mu\text{m}$
Diameter of nanopillars, $d_{np}$	$100\ \text{nm}$
Pitch between nanopillars, $a_{np}$	$100\ \text{nm}$
Height of the nanopillars, $h_{np}$	$100\ \text{nm}$
Distance between nanopillars arrays, $L_{np}$	$500\ \text{nm}$

**Table 7.1:** Waveguide and nanopillars dimensions used for FDTD modeling



The wavelength of light considered was 1550 nm Transverse Electric (TE) mode, and the refractive index of silicon is taken as 3.45. Two different substrates for the surrounding medium, namely air and water, were considered for the present analysis, The refractive indices (RI) for air and water are taken as RI = 1 and RI = 1.35 respectively, and it is assumed that the refractive index of most of the biological substrates suspended in a solution is close to that of water. The relative nano-enhanced evanescence was studied by increasing the number of nanopillar arrays and the plot of variation of  $\chi_{ev}$  with  $N_{np}$  is as given in Figure 7.3.

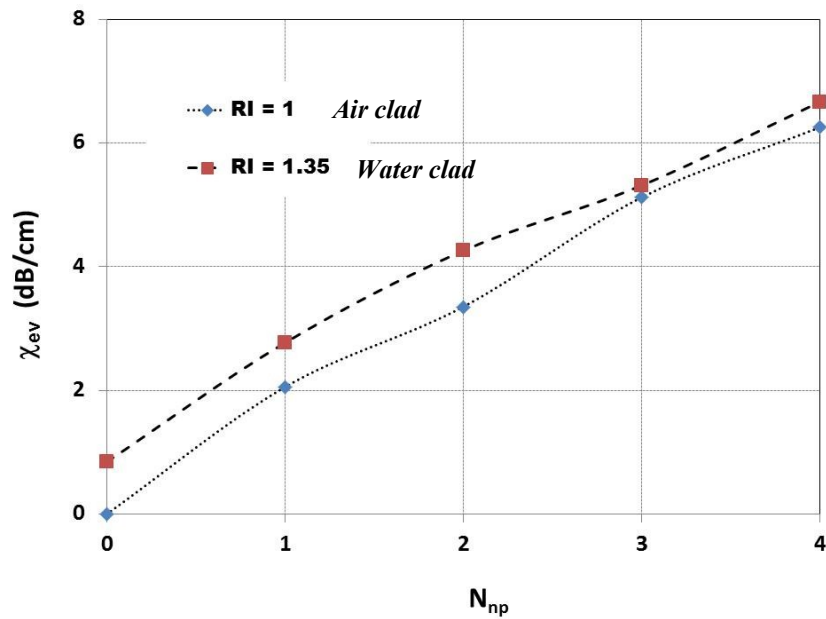


**Figure 7.3:** Plot of the relative Nano-enhanced Evanescent loss on silicon waveguide with integrated nanopillars for different surrounding medium (air and water)

It can be seen that with an increase in the number of nanopillar arrays, there is a clear increase in evanescent loss. Also it can be seen that the evanescent loss is higher in the case of higher refractive index, as noticed with water. The evanescent loss with the addition of 4 nanopillar arrays is almost 6 dB/cm. This shows that there is a significant

increase in evanescence due to the integration of nanopillars with the surface of the waveguide.

In order to study the effect of nano enhanced evanescence on the distribution of the nanopillars on top of the waveguide, the distance between the nanopillars was varied and the effect on evanescence was studied. The distribution of the nanopillars on top of the waveguide is given by the  $d_{np}/a_{np}$  ratio. The diameter of the nanopillars was kept at 100 nm and the distance between each array of nanopillars on the waveguide was 500 nm. The relative evanescence measurements were carried out with respect to the evanescent loss seen when  $d_{np}/a_{np} = 1$ , i.e the nanopillars are clustered together without any separation and the evanescent loss is denoted by  $\chi_a$ . The simulations were carried out for different heights of the nanopillars. The results of the FDTD analysis are as shown in Figure 7.4.

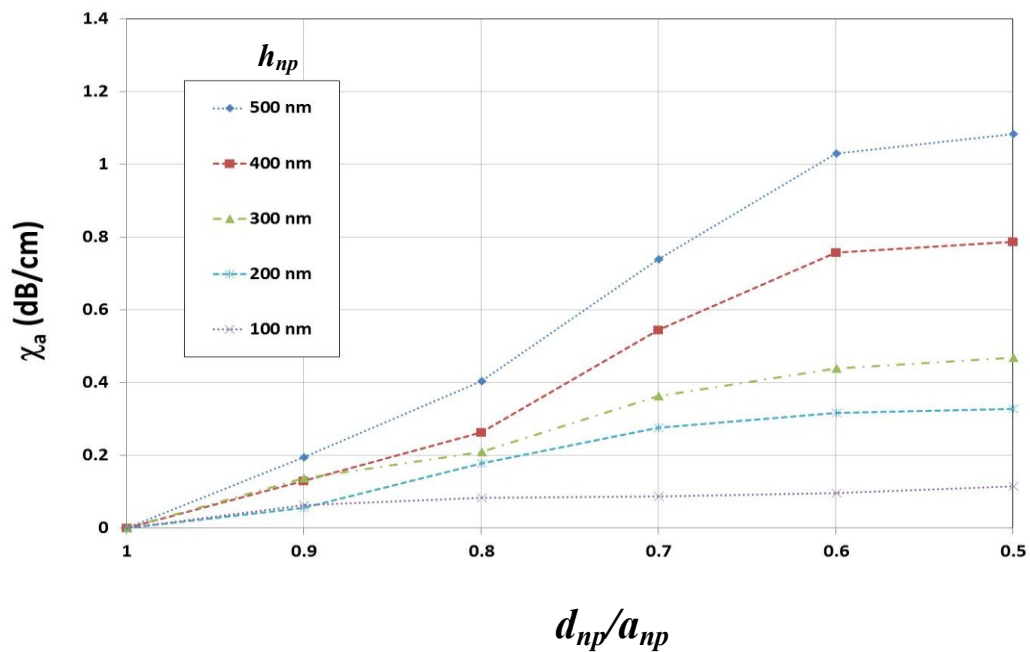


**Figure 7.4:** Plot of variation of relative evanescence with  $d_{np}/a_{np}$  ratio of nanopillars integrated on silicon waveguide

From the above results, it can be seen that evanescence improves by distributing the arrangement of nanopillars on top of the waveguide, than clustering them together. Also it can be seen that with the increase in the height of the nanopillars, there is an increase in the evanescent loss, possibly because of the greater surface area of the nanopillars being exposed to the surrounding medium when the height of the nanopillars is increased.

Thus, the integration of nanopillars with the waveguide results in a significant effect improvement of evanescence, as seen from the FDTD analysis.

### **7.2.2 Implementation of NEET with nanocavities and nanospheres**

In continuation of the previous analysis, NEET was also studied on silicon waveguide with integrated arrays of nanocavities. Figure 7.5 shows the schematic perspective view of a waveguide having a plurality of nanocavities integrated thereon in accordance with the NEET. The waveguide is implemented on a waveguide slab and includes a rib waveguide core. The plurality of nanocavity each of diameter 100 nm are integrated on top of the waveguide core with in ordered arrays/rows along the length of the rib waveguide core. The waveguide dimensions are the same as used in the previous model. The depth of the nanocavities used for the present modeling is 500 nm.

The nanocavities are distributed on top of the waveguides in such a way that the pitch between each of the nanocavity is 200 nm and the length between each array of nanocavities is 500 nm. The number of arrays of nanocavities is denoted by  $N_{nc}$ . The

relative evanescent loss upon the integration of nanocavities,  $\chi_{ev}$ , estimated with respect to the plain waveguide without nanocavities, is shown in Figure 7.6.

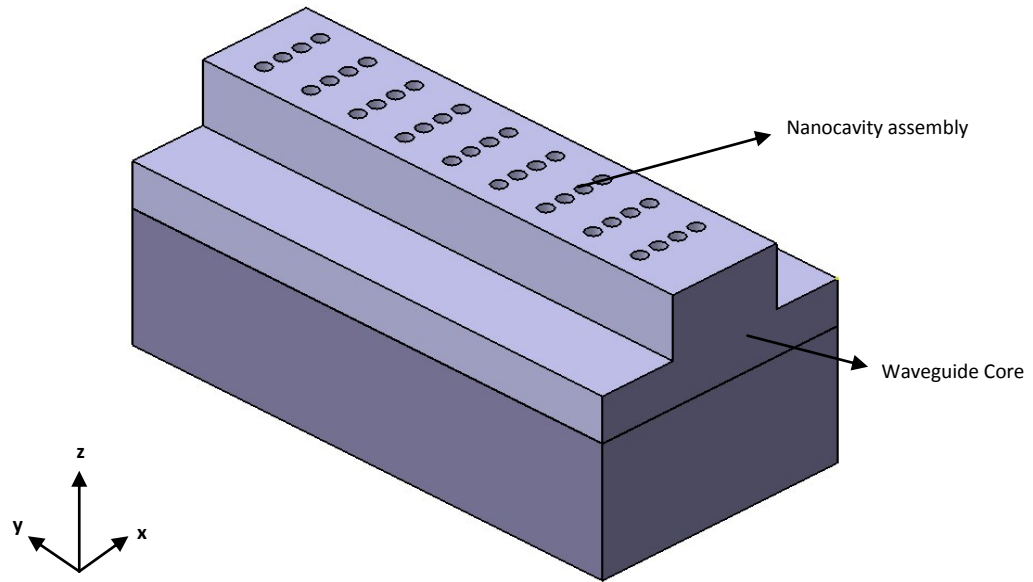


Figure 7.5: Schematic of the SOI waveguide with nanocavities.

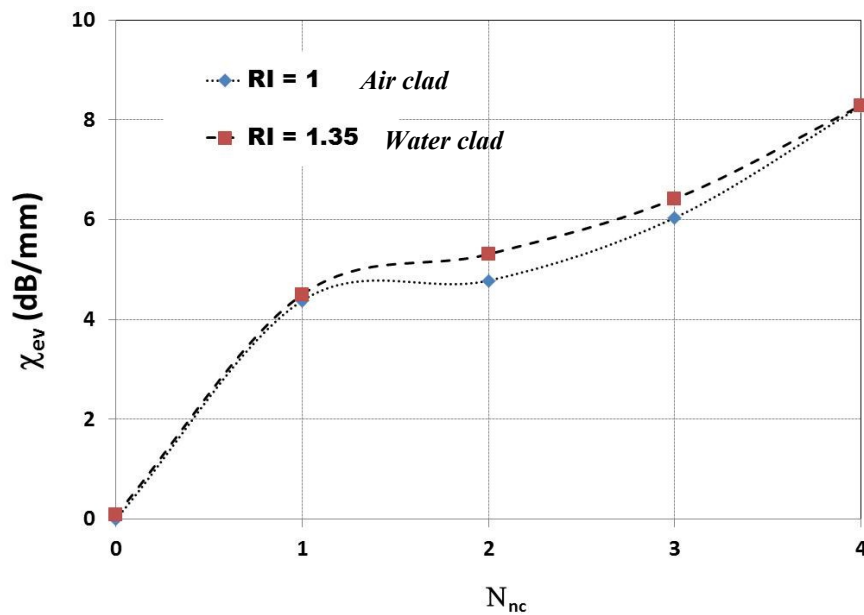
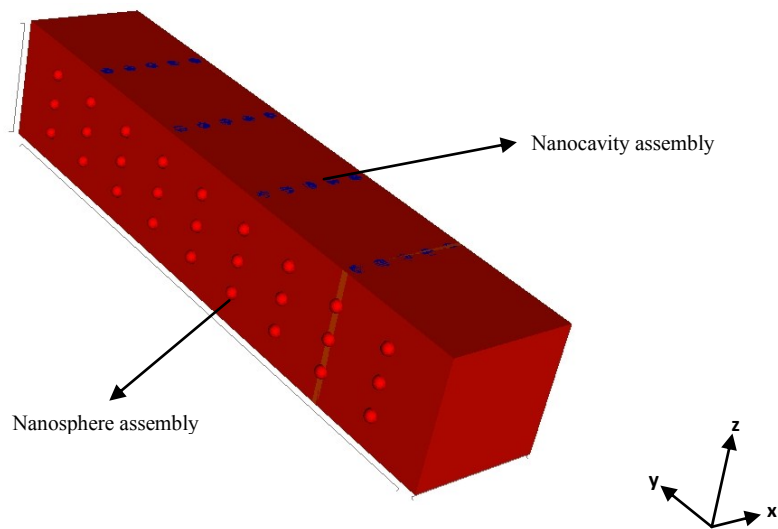


Figure 7.6: Relative Nano-enhanced evanescence loss from silicon waveguide with integrated nanocavities for different surrounding medium (air and water)

The relative evanescent loss with the nanocavities is much higher than with the nanopillars. This is probably because the nanocavities directly interfere with the mode of the propagating wave inside the core of the waveguide, which causes greater perturbation and hence a greater evanescent loss, whereas the nanopillars present outside the waveguide core can only affect the bio-optical interaction of the evanescent field from the core.

However, it can also be seen that there is a very little difference between the evanescent loss due to the change in the refractive index of the surrounding medium. It is possible that the total surface area of the nanocavities exposed to the surrounding medium is much lesser compared to the nanopillars, and hence a significant difference is not observed due to the change in the RI of the medium.

In order to study the evanescence from the sidewalls of the waveguides, the system was modeled with silicon nanospheres integrated on the sides of the waveguide, which has nanocavities on the top surface. The schematic waveguide design is as shown in Figure 7.7.



**Figure 7.7:** Schematic depiction of a silicon waveguide core strip integrated with nanospheres and nanocavities

Herein, a temporal power monitor was defined in the region of the nanospheres (region of interest) and the effect of nanospheres on the evanescent behavior of the waveguide was studied. The total evanescence in the monitor region for waveguides with nanospheres and without nanospheres was compared and the results are as shown in Figure 7.8. It can be seen that greater evanescence loss is observed from waveguides whose sidewalls are integrated with nanospheres, than plain sidewalls.

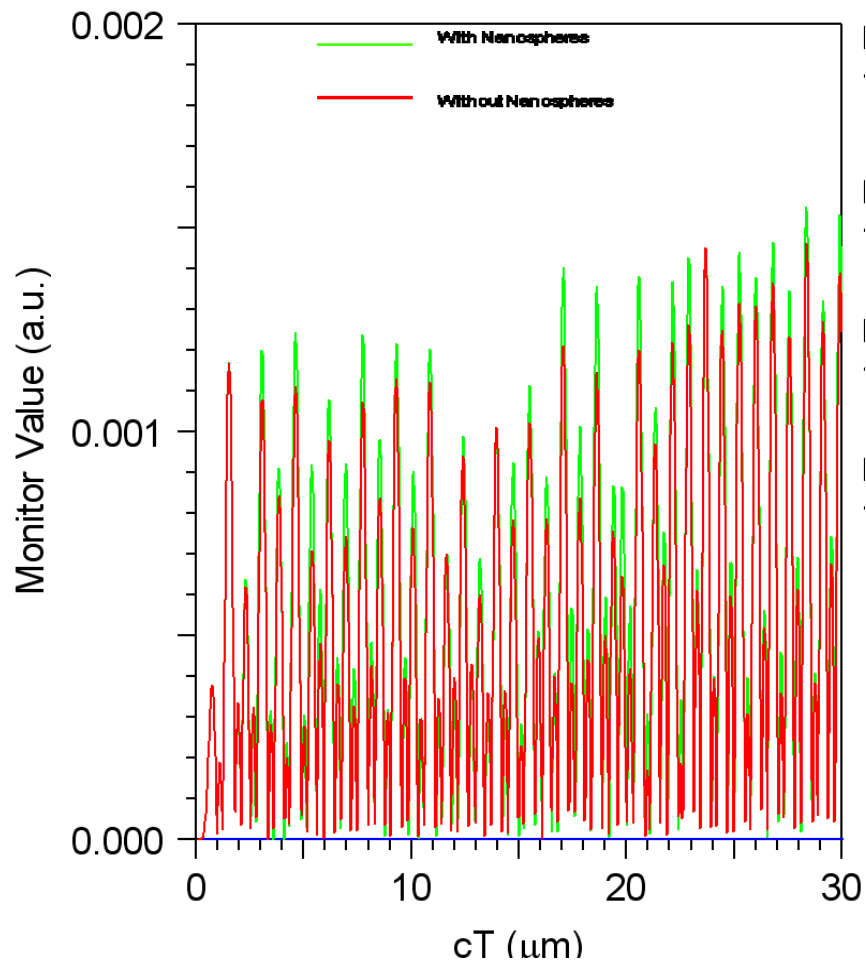


**Figure 7.8:** Results of FDTD analysis of evanescence loss from the side walls of the silicon waveguide with and without integrated nanospheres .

### 7.2.3 Discussion

From the FDTD, analysis, it can be inferred that increasing the number of nanopillars and nanocavities, increased the evanescence of light from the waveguide thereby validating the concept of NEET. As the nanopillars and nanocavities can be implemented only on top of the waveguide, the integration of nanospheres on the waveguide side walls was modeled and it is clear that evanescence improves due to the nanointegration along the waveguide sidewalls also.

Though the Figures 7.2, 7.5 and 7.7 are schematic representations of the real system, the nanofeatures need not be necessarily integrated in an ordered manner on the waveguide. Randomized distribution of the nanoparticles on the surface of the waveguide also would result in scattered evanescence due to NEET. The choice of the dimension and arrangement of the nanofeatures on the waveguide, can be controlled by the fabrication and integration techniques, depending upon many factors such as wavelength of light, dimensions of the waveguide, sensitivity of the system, physical properties of the biological specimen to be tested for, etc. The present modeling has been carried out on silicon waveguides, however, this method can also be extended for other waveguide substrates such as polymers, GaAs, InP, etc.

Apart from the integration of nanoparticles to improve the evanescence, it is expected that the evanescent loss is greater with the addition of other lossy components to the waveguides such as taper, bends. The evanescence can be appropriately tuned by defining the number of nanofeatures, nanocavities and nanopillars or a combination of both, on the

waveguide. Evanescence can also be increased by defining nanofeatures along the sidewalls of the waveguide and also along the slab of the waveguide.

### **7.3 Experimental investigation of evanescence with nano-integrated waveguide system**

The evanescence detection experiments were carried out, with the following motivation:

(i) Implementation of the concept of NEET: As mentioned before, the feasibility of external hybrid integrated evanescence detection has already been demonstrated on SOI platform (Chandrasekaran and Packirisamy, 2009a). However, it is important to prove the concept of NEET and to verify the feasibility of the implementation of NEET for integration with the  $\mu$ TAS.

(ii) Demonstration of NEET with visible wavelength: Previous evanescence measurement experiments were carried out on SOI waveguides using infrared wavelength of light. Also the FDTD modeling was carried out on silicon waveguide. Therefore, through the present experiments, it was aimed to prove the concept of NEET with polymer waveguide, using visible wavelength of light. Herein, the evanescence was measured using input light of 632 nm wavelength.

(iii) Development of integrated optical detection platform for  $\mu$ TAS: The experiments also provide a platform for the development of an optical detection system based on Nano-enhanced evanescence in the visible wavelength range that can be integrated with microfluidics.



Though the modeling was carried out with Silicon waveguides, in order to perform NEET experiments in the visible wavelength, it is important to choose a proper choice of the waveguide material that facilitates light propagation and evanescence in the visible wavelength. It is also important that the chosen material platform be suitable for integration with the  $\mu$ TAS. Hence, the waveguides for the evanescent detection was fabricated on SU-8 (Yang et al. 2009). SU-8 is a negative photoresist, which has shown good optical properties and it is mechanically and chemically stable (Borreman et al. 2002). SU8 is transparent for wavelengths above 400 nm, and has an index of refraction of  $\sim 1.56$ , which makes it a suitable material for waveguiding.

### **7.3.1 Fabrication of SU8 Waveguides**

For the present experiments, the waveguides were fabricated on SU8-on-Silicon platform. The schematic of the waveguide cross-section is as shown in Figure 7.9. It consists of the SU8 waveguide core,  $40 \times 50 \mu\text{m}^2$ , and a bottom cladding SU8 of lesser refractive index than the core (Ong et al., 2006). In order to have a guided mode in the SU8 layer, the SU8 must be surrounded by a suitable cladding material of a lower index. But it is not possible to use silicon itself as a cladding, because it has a higher index than SU8. This problem can be avoided only by oxidizing the silicon substrate before the SU8 is deposited.

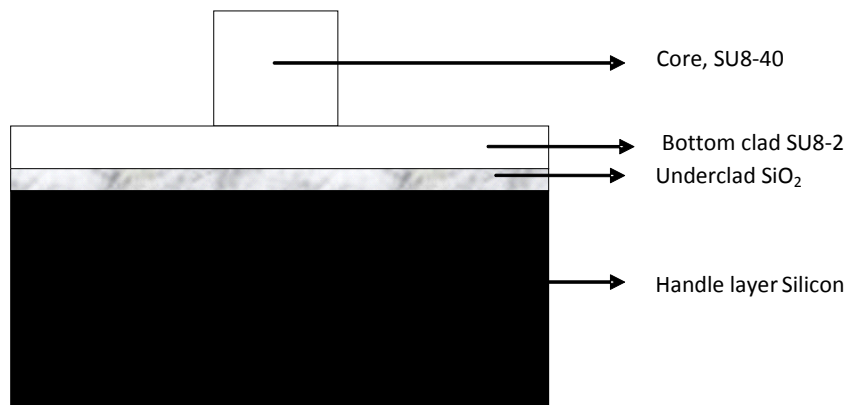


**Figure 7.9:** Schematic of the SU8-on-Silica waveguide cross-section

The process starts with the deposition of oxide of thickness 300 nm on top of the silicon wafer using Plasma Enhanced Chemical Vapor Deposition process (PECVD). Initially, a less viscous SU8-2 photoresist was spin coated on Silica-on-silicon wafer at a spin speed of 500 rpm, and cured for 30 minutes at 60 °C. The purpose of using this SU8 layer is twofold, i.e, the SU8 intermediate layer acts as a bottom clad to the waveguide core, and also this layer is used to improve the adhesion between the SU8 core and the substrate, since the Silica substrate is hydrophobic, which therefore repels the photoresist hence making it difficult to achieve good uniform bonding of the core layer onto the silica substrate.

Thereafter, SU8-40 layer of 40 μm thickness was spun coated on the SU8-2 coated wafer and using suitable photomasks, photolithography was carried out to obtain straight waveguide core structures of width ranging from 50 – 200 μm, with a refractive index of ~1.59 at 630 nm (Microchem Inc.). The refractive indices of the bottom clad SU8 and the

core was controlled by the pre-exposure baking time, it was found that increase in the pre-exposure baking time increased the refractive index (Ong et al. 2006). Therefore, the core SU8 was baked for longer duration before UV exposure than the bottom clad. The thermally grown oxide layer on silicon acts as the second underclad layer to the SU8 waveguide system.

### **7.3.2 Nano-integration with SU8 waveguides**

Though the feasibility of NEET was studied theoretically using nanopillars and nanocavities, the fabrication method is expensive and also rigorous. Hence, in this work, the nano-enhanced evanescence is studied with Multi Walled Carbon Nanotubes (MWCNT).

Nanotubes were adsorbed on the surface of the waveguide and evanescence measurements were carried out. Initially, CNT-water mixture was prepared, by the addition of 0.5 mg CNT (Walled Carbon Nanotube) with 1 mL of water. The CNT remains suspended in water and do not dissolve to form a solution. CNT based NEET was studied in two different experiments, with water alone and secondly with CNT suspended in water. The experimental setup is shown in Figure 7.10. The setup consists of independent three-axis stages in which the input fiber, the waveguide device and the output fibers were positioned independently. The input and the output fibers were butt coupled with the waveguide device and their positions were adjusted precisely so as to maximize the coupling efficiency. The open setup of the system enables ease of addition

of the specimens on top of the waveguides for evanescence sensing, and their subsequent cleaning.

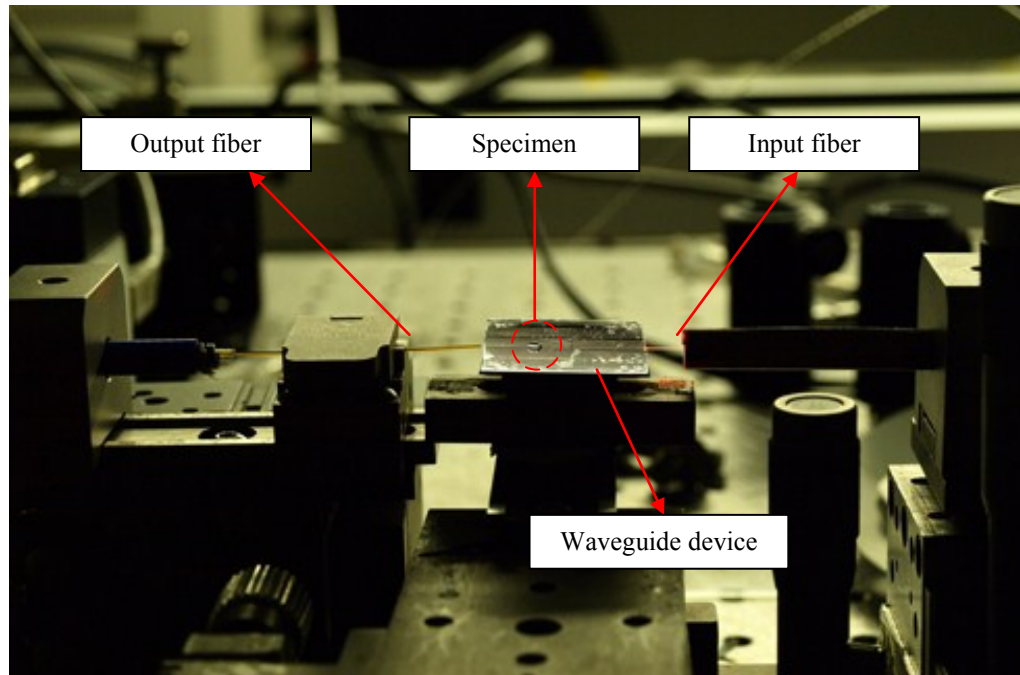


**Figure 7.10:** Experimental setup for evanescence detection using SU8-on-Silica waveguide

### 7.3.3 Experimental Results

The results of evanescence with water and water suspended with CNT are as shown in Figure 7.11, which gives the evanescent loss with time. An increase in evanescent loss is observed immediately after the addition of the substrate on top of the waveguide. The subsequent reduction in the loss is due to the evaporation of the liquid from the waveguide surface. At the end of the evaporation of the liquid, the remnant loss is due to the adsorbed CNT on the surface of the waveguide. In case of evanescence test with

water alone, the total evanescent loss is the same as before the addition of water medium. However, by the addition of CNT with water, the evanescent loss is higher at the end of water evaporation.

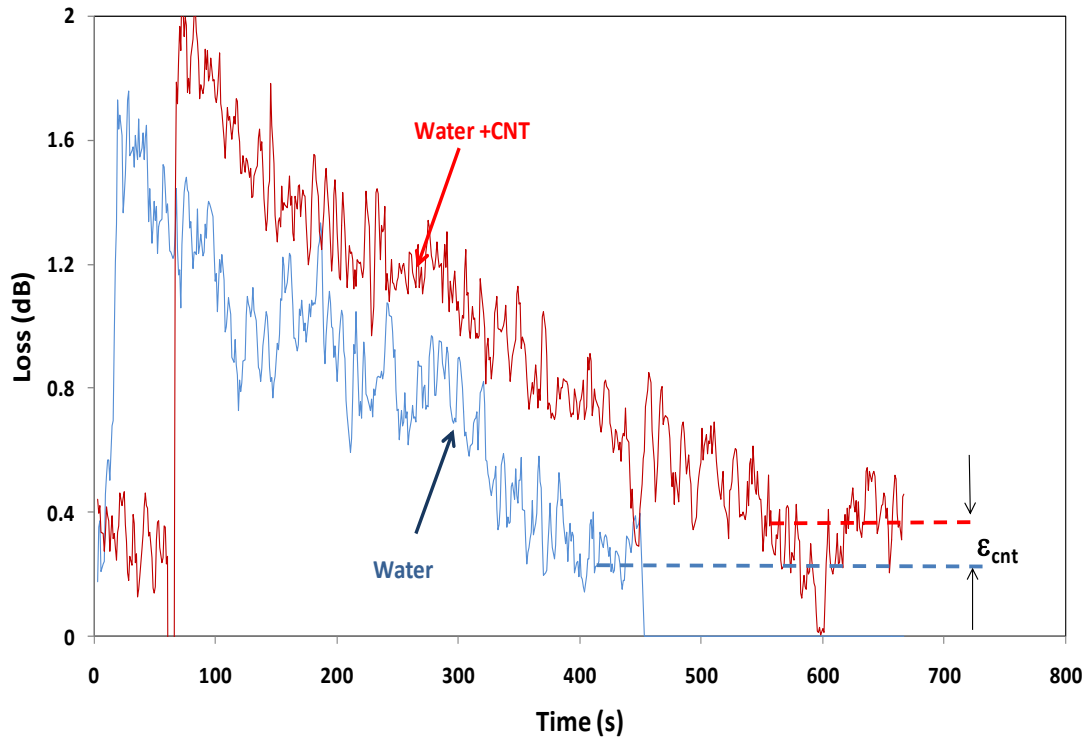
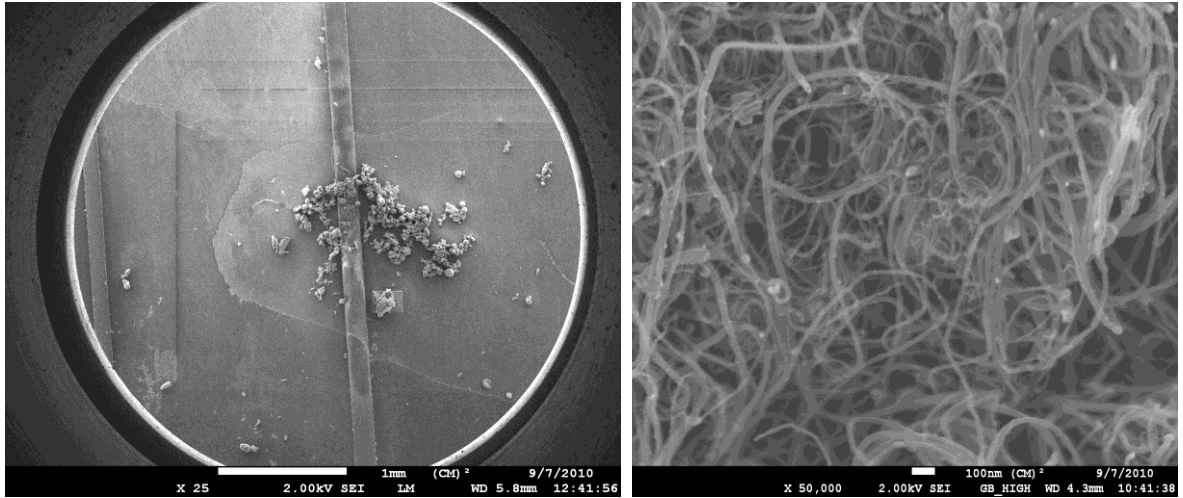


**Figure 7.11:** Plot of evanescent loss with time for water suspended with and without MWCNT

Also, the time taken for the evaporation of liquid from the waveguide surface is nearly equal for both the experiments. This shows that the total volume of the substrate added to the waveguide is the same in both cases. And hence, the increased evanescent loss after the evaporation of all water is due to the adsorption of CNT onto the waveguide surface. The SEM images of the CNT deposited on the waveguide after water evaporation are as shown in Figure 7.12.



(a)

(b)

**Figure 7.12:** SEM image of (a) CNT deposited on the waveguide after water evaporation (b) close up of the carbon nanotubes

In the next test, powder CNT was directly deposited on top of the waveguide surface and the evanescent loss was measured. The plot of the evanescent loss with time is as shown in Figure 7.13. It can be seen that the resultant evanescent loss upon the addition of the MWCNT does not decrease with time, thus proving that the decrease in evanescence with time shown in Figure 7.12 is definitely due to the evaporation of liquid from the waveguide surface.

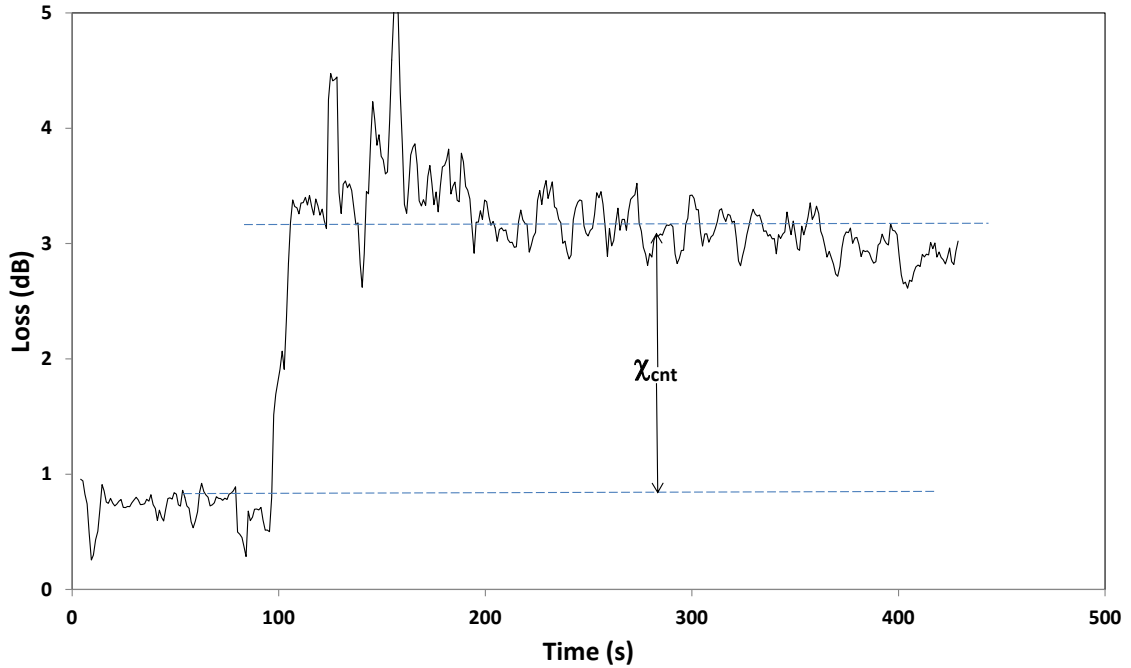


**Figure 7.13:** Plot of evanescent loss with time for MWCNT deposited directly on the waveguide.

The results of the experiments with the CNT are summarized in Table 7.2. Here  $\chi_{\text{cnt}}$  is the evanescent loss due to the integration of the Carbon Nanotubes alone on the waveguide.

Concentration of CNT	Evanescent loss due to CNT, $\chi_{\text{cnt}}$ (dB)	Evanescent field length (mm)	Evanescent loss (dB/cm)	Evanescent coefficient ( $\text{cm}^{-1}$ )
0.05~0.07 mg/mL	0.2	2	1	0.23
Pure CNT powder	2.1	3	7	1.61

**Table 7.2:** Evanescent coefficient for the CNT enhanced evanescence tests carried out with SU8-on-silicon waveguide at 632 nm.

One can modify the NEET based loss by increasing the evanescent length and concentration of the nano features. Though the present experiments were carried out using Carbon Nanotubes, it is also possible to apply the concept of NEET through other nano

features such as gold and silver nanocolloids. Thus, the concept of NEET has been experimentally verified with Carbon Nanotubes. NEET offers a lot of promise for improving the sensitivity of chemical and biodetection for  $\mu$ TAS applications.

#### **7.4 Conclusion**

Evanescence based biodetection is a very useful label free optical detection technique which has a lot of potential applications when integrated with the  $\mu$ TAS for carrying out highly sensitive chemical and biodetection. In order to improve the sensitivity of the system, a method of integration of nanofeatures with the evanescence detection is proposed, through Nano-Enhanced Evanescence Technique (NEET). The NEET is a very novel and pioneering technique which has not been explored or implemented before.

Some embodiments of the NEET include integration of nanofeatures, such as nanopillars, nanocavities, nanorods, nanotubes, nanoparticles etc., and microphotonic elements on any suitable material platform, to provide a cost effective solution to the needs of in-situ chemical and biomedical detection and Point-of-Care Testing (POCT) devices. Through the Nano-enhanced evanescence detection system, it is now possible to detect biological and chemical interaction in the IR as well as visible spectra of light. Different standard micromachining techniques can be used in order to microfabricate NEET incorporated biosensor system on several material platforms. The proposed Nano-Enhanced Evanescence integrated Technique (NEET) significantly improves the efficiency of the



sensor system. Now, one could foresee vast application potentials with the proposed nano-enhanced evanescence detection integrated with a  $\mu$ TAS.

FDTD simulations were carried out in order to prove the concept of NEET. It should be noted that the simulation and measurement results provided herein are provided for illustrative purposes only, and other simulations and/or measurements under the same or different conditions may result in the same or different results. Though the preliminary investigation of the feasibility of evanescence detection was carried out on Silicon-on-Insulator waveguides using HRP and  $H_2O_2$  (Chandrasekaran and Packirisamy, 2009a) this chapter also presented the fabrication and testing of SU8 polymer based waveguide system, which is useful for hybrid integration with  $\mu$ TAS. The experiments carried out with MWCNT on SU8-on-Silica waveguide validate the concept of NEET, as the evanescence observed with nano-integrated waveguides is higher than waveguides without nanointegration.

The principle of NEET is in no way limited to implementations in conjunction with a system or sensors that reflects the example simulation and/or measurement conditions described herein. The studies were provided as examples for demonstration purposes only, and should not be construed as limiting the scope of the present method.

# Fabrication and Assembly of Hybrid Integrated $\mu$ TAS

### 8.1 Introduction

The major challenge towards the development of  $\mu$ TAS is the integration of microfluidics with the three optical detection systems, namely, absorption, fluorescence and evanescence for simultaneous detection. While it is known that for absorption and fluorescence detection the microfluidic channel need to be in-plane with the waveguides, but for the evanescent detection system a separate microfluidic layer needs to be integrated on top of the waveguide thereby forming a three dimensional system. Thus, the integrated evanescent detection system alone presents an exciting challenge for fabrication and bonding, and more than one fabrication technique is needed to fabricate both the waveguides and the microfluidics. It would be more convenient to incorporate all of these functionalities into a single device, by using the configuration of clustered optical microfluidic system. One such method to develop a clustered optical microfluidic setup is to create a multilayered system (Zellner et al. 2010), however, such a system needs precise alignment and suitable bonding techniques for the different layers, which is difficult to achieve. Therefore, the only alternate solution is to develop a suitable on-chip hybrid integrated optical microfluidic system, which is capable of integrating all the three detection systems with microfluidics, without affecting the functionality of each other.

As with any optical based analysis, it is important that the bio-optical interaction carried out with the  $\mu$ TAS results in a high signal to noise ratio. For this purpose, the internal hybrid integrated system has several advantages over the external hybrid integrated system, as seen from Chapter 6. However, one of the disadvantages of such a system is the lack of maneuverability of the fibers which are integrated directly with the microfluidic channel platform and sealed so as to form a packaged setup. Also, alignment of fibers using etched grooves makes the sealing in microfluidic channels difficult, as the fibers need to be perfectly placed in plane with the microfluidic channel and also level with the top of the substrate. A more straightforward and interesting approach to such a hybrid integration process is to use a filled microfluidic channel as a liquid-core waveguide (Schueller et al. 1999), in which fluids with different refractive indices form the waveguide. This approach has tremendous flexibility, but does not lend itself to the full functionality that  $\mu$ TAS applications require (Sheridan et al. 2009). In that way, the use of optical fiber to guide the light into the microfluidic channels provides a better solution. Therefore, the direct integration of optical waveguides with microfluidic channels appears to be an agreeable alternative, in order to address the problems of waveguide–channel alignment and reduce complexity of packaging. In this way, the optical fibers could be attached and detached from the integrated waveguides, without disturbing the alignment between the waveguide and microfluidic channel, and also without needing to disturb the microfluidic packaging. Therefore, the waveguides are directly integrated with the microfluidic channels in the chip and the fibers are attached to the waveguides externally to the chip for the proposed  $\mu$ TAS.

It is also important to choose the correct material platform for the fabrication of the integrated optical microfluidic device. With low material and fabrication costs, the  $\mu$ TAS fabricated on PDMS platform have the potential to be manufactured in large quantities. PDMS platform can also be disposable, eliminating the problems associated with contamination in medical applications where devices are usually cleaned and reused. Therefore, the prototype for the integrated  $\mu$ TAS is proposed to be fabricated on PDMS material platform.

The following segments of this chapter present the method of design, fabrication and integration of the on-chip hybrid integrated Micro-Total Analysis System..

## **8.2 Design of the integrated $\mu$ TAS**

The schematic of the proposed hybrid integrated  $\mu$ TAS is as shown in Figure 8.1. The hybrid integrated  $\mu$ TAS consists of three segments:

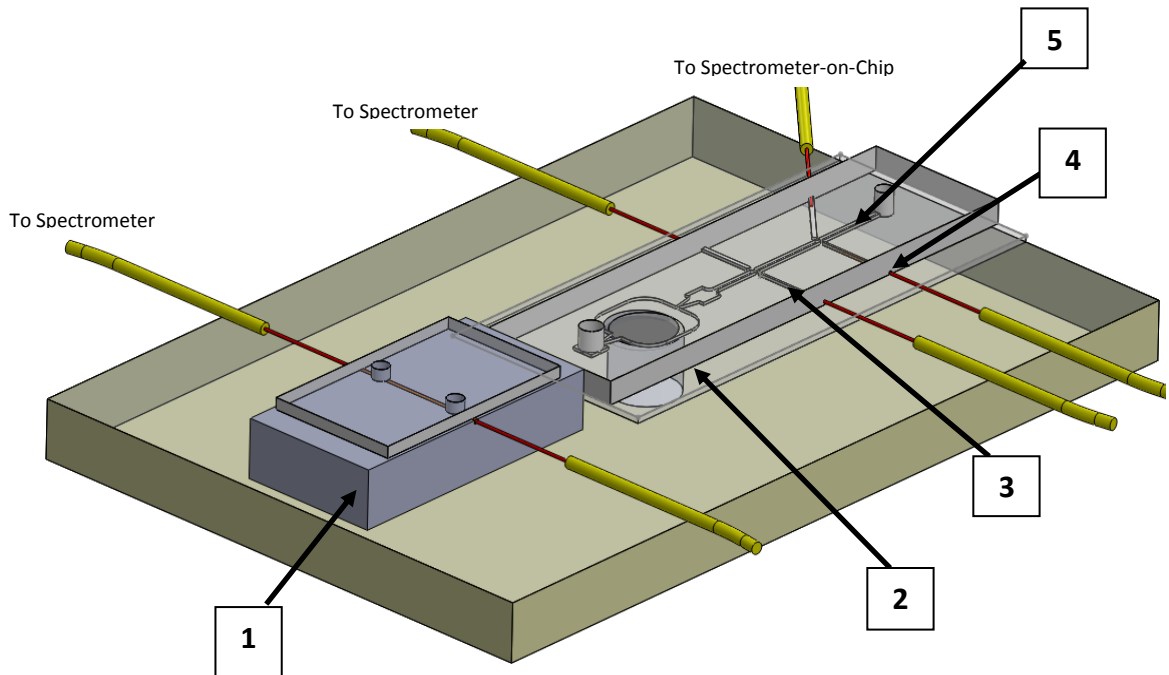
[1] The nano-integrated evanescent sensing system which consists of a microfluidic channel integrated on top of the waveguide thereby forming a three dimensional system.

[2] The valveless micropump zone, which consists of the micropump chamber, the nozzle/diffuser pair, and the piezoelectric actuator system. The motion of the fluid through the microfluidic channel in both the evanescent sensing system and the absorption-fluorescence system, is caused due to the pumping

[3,4] The integrated waveguide system for optical absorption and fluorescence, in which the waveguides are integrated with the microfluidic channels in such a way that the

optical path is intercepted by the microfluidic channel to bring about the bio-optical interaction.

[5] Microfluidic channel for the transportation of the fluids.



1 – Nano integrated Evanescent detection system

2- Piezo-actuated valveless micropumping system

3- Absorption detection system

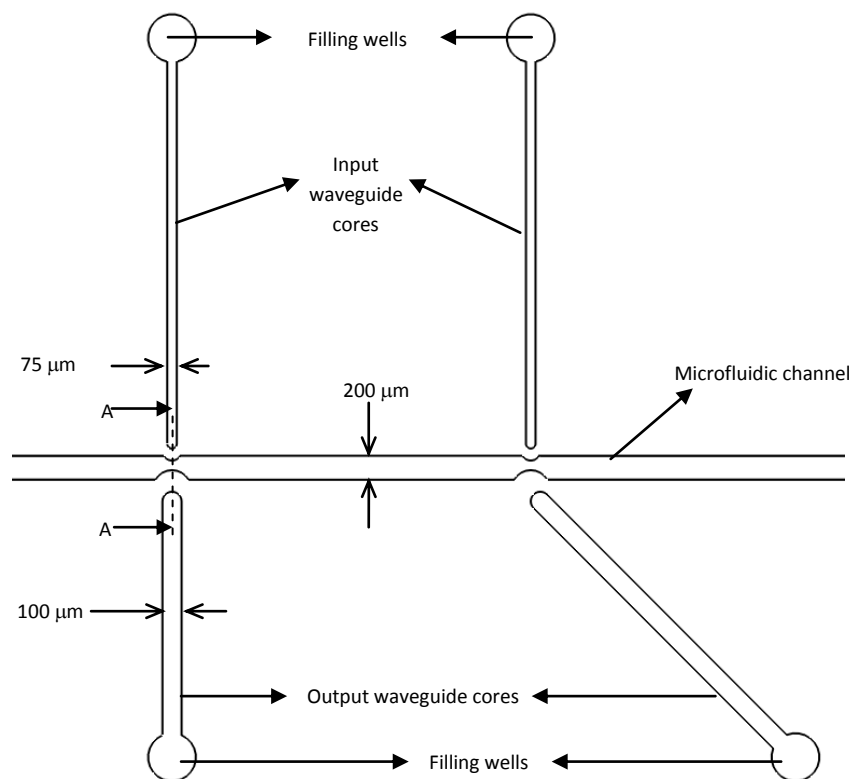
4- Fluorescence detection system

5- Microfluidic channel

**Figure 8.1 :** Schematic of the proposed hybrid integrated  $\mu$ TAS

The waveguide detection system for optical absorption and fluorescence is designed to be highly sensitive, using an in-plane direct excitation configuration in which the input

waveguides intersect the microfluidic channel orthogonally. The design of the optical waveguide system is as shown in Figure 8.2. The waveguide system consists of an input waveguide which is orthogonal to the microfluidic channel. The output waveguide was designed depending upon the type of detection. For absorption detection, the output waveguide is designed coaxially with the input waveguide. However, for fluorescence detection, the output waveguide was designed at an angle of  $15^\circ$ , so that the incident light does not get coupled into the output waveguide, as shown in Figure 8.2.



(a)

### Cross-section A-A

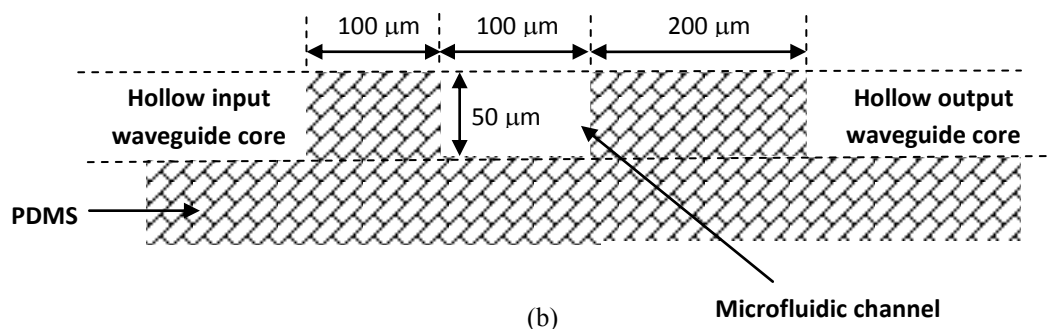


**Figure 8.2:** (a) Design of the optical waveguide system for absorption and fluorescence detection (b) Cross sectional view of the hollow waveguide

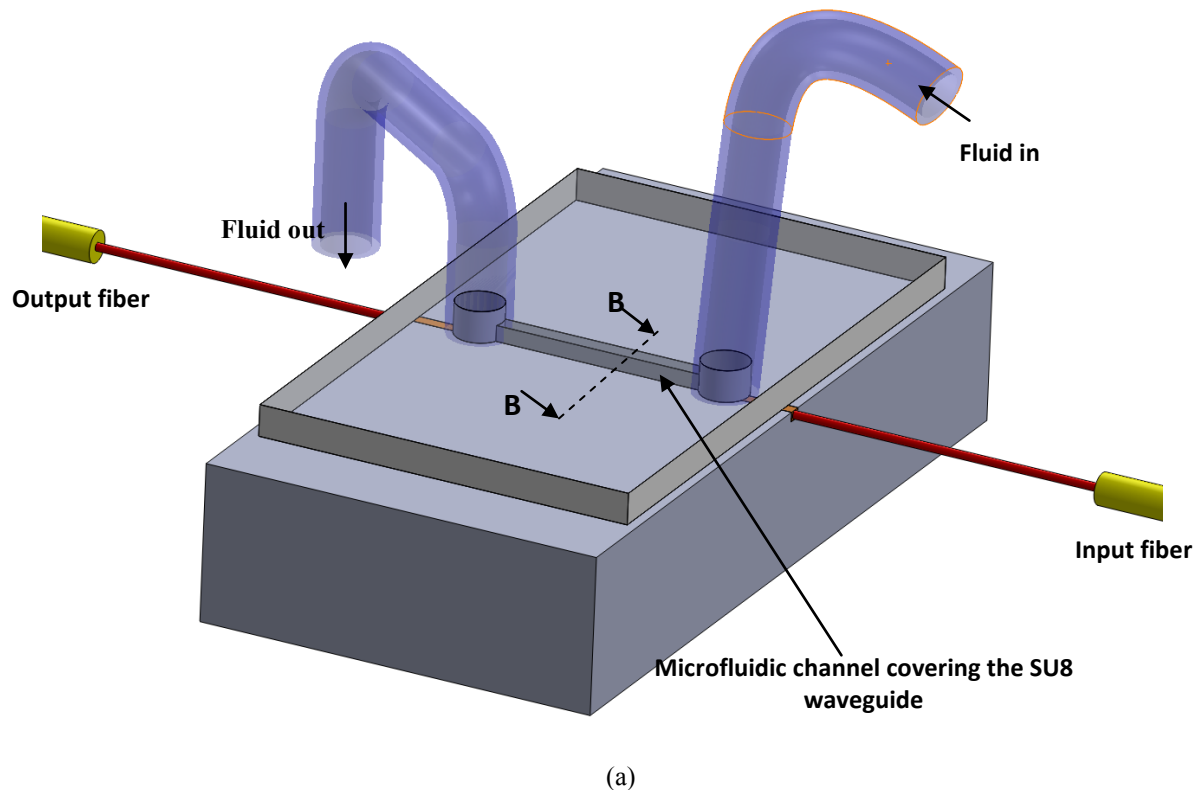
The width of the microfluidic channel at the waveguide section is 100 μm. The ends of the waveguides are made spherical in order to maximize light coupling into the waveguide and to converge the light. The distance between the output waveguide and the microfluidic channel is 200 μm and the distance of the microfluidic channel from the input waveguide is 100 μm. Each waveguide is provided with a well at the outer ends which will be used to fill up the hollow part of the waveguide with core material that would be moved into the waveguide through capillary effect. The tip of the waveguides are separated from the microfluidic channels for two purposes,

- To prevent the adhesion of biomolecules at the ends of the waveguides
- To prevent blockage the microfluidic channel, in case of overflow of the waveguide core.

For the microfluidic channel, the width of the channel from the micropump is 200 μm. The larger microfluidic channel width reduces the back pressure to the flow of the fluid

from the micropump. However, the width of the microfluidic channel at the waveguide cross section was made 100  $\mu\text{m}$ , in order to achieve better bio-optical interaction. In order to overcome the sudden pressure drop in the fluid due to the change in the channel width in the constriction area, a smooth curvature is provided for the microfluidic channel at the waveguide cross-section.

The schematic of the evanescent detection system with integrated microfluidic tubes is as shown in Figure 8.3. The evanescent detection system consists of straight waveguides and the microfluidic channels are integrated with on top of the waveguide. For this system, it is important that the fluid flow takes place in the same direction as the propagation of light. Hence the microfluidic channels are integrated along the same axis as the waveguide.





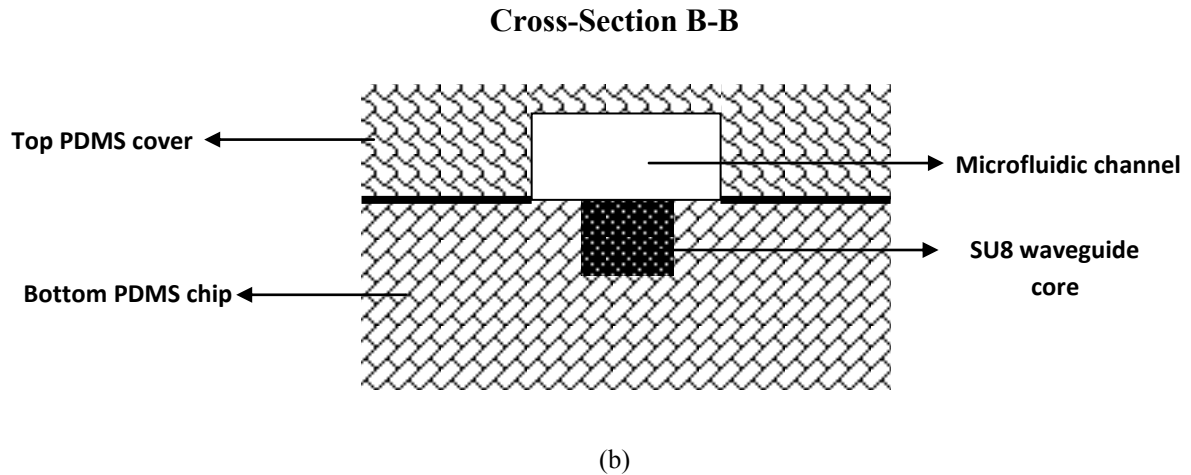


**Figure 8.3:** (a) Schematic of the evanescence detection system (b) Cross-section view of the integrated microfluidic waveguide system

The nanoparticles are integrated on top of the waveguide in order to improve the sensitivity of detection. The waveguide designed for the evanescent sensing was a straight waveguide with a core width of  $100\ \mu\text{m}$  and a core height of  $50\ \mu\text{m}$ . The length of the waveguide is  $1\ \text{cm}$ , in order to allow a large area of bio-optical evanescent field interaction. The width and the height of the microfluidic channel on top of the waveguide is  $500\ \mu\text{m}$  and  $100\ \mu\text{m}$  respectively. The large width of the microfluidic channel not only ensures that the fluid in the channel covers the entire area of the waveguide, but also reduces the back pressure offered to the flow during pumping.

### 8.3 Fabrication of integrated optical microfluidic chip

For the optical waveguides, SU8 is proposed as the waveguide core material that will be embedded within the PDMS, which acts as the clad. There are several advantages of using SU8 as the waveguiding material. Compared to the refractive index of clad PDMS

(~1.44), the RI for SU8 is ~1.58 which gives a high index contrast useful for the confinement of the light. Also, SU8 is both photopatternable and at the same time, in the liquid form, can be used as a fillant. SU8 curing can be done either with UV exposure or thermal curing and it also has a low polymer shrinkage rate of 7.5% after curing (Lee et al. 2003a). These properties make SU-8 an excellent candidate for waveguiding.

The SU8 used for waveguiding purpose was bought from Microchem. SU8-2 is used because of its low viscosity (45 cSt). Figure 8.4 shows the absorbance characteristics of the SU8-2 in the visible wavelength (Microchem Inc.)

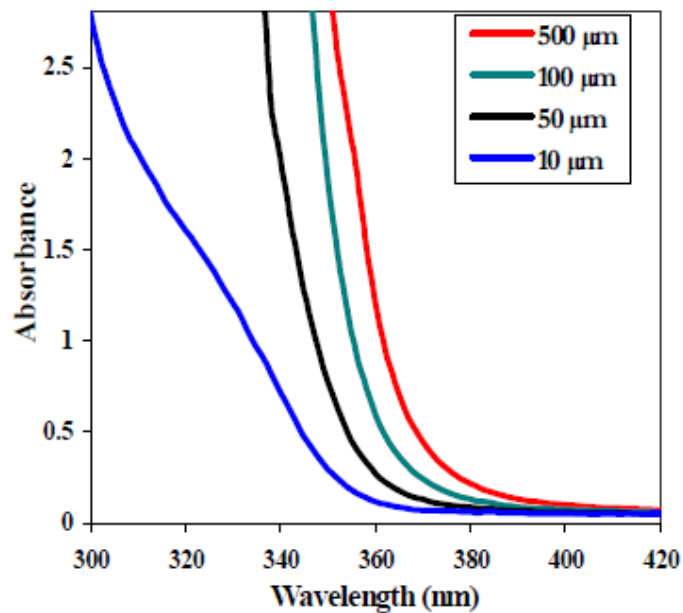
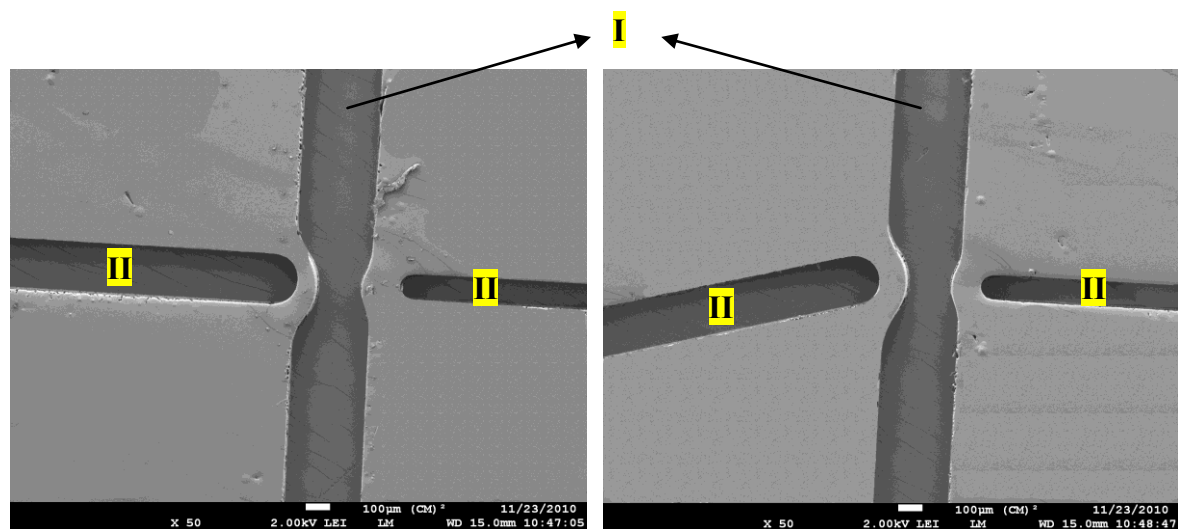


**Figure 8.4:** Absorbance characteristics of different film thickness of SU8 with visible wavelength (Microchem Inc.)

It can be seen that the absorbance of SU8 at visible wavelengths is almost zero. Therefore, SU8 is the perfect waveguiding material for the present application.

The different steps which are involved in the fabrication of the optical microfluidic chip is shown in Table 8.1.

The silicon mould for the PDMS was fabricated by DRIE, and the fabrication procedure is the same as described in the previous chapters. It is extremely important that the microfluidic ports are created in the PDMS at the first step after the preparation of the mould itself. The SEM images of the waveguide slots with integrated microfluidic channel fabricated with the PDMS substrate is as shown in Figure 8.5.



(a)

(b)

I – Microfluidic channel

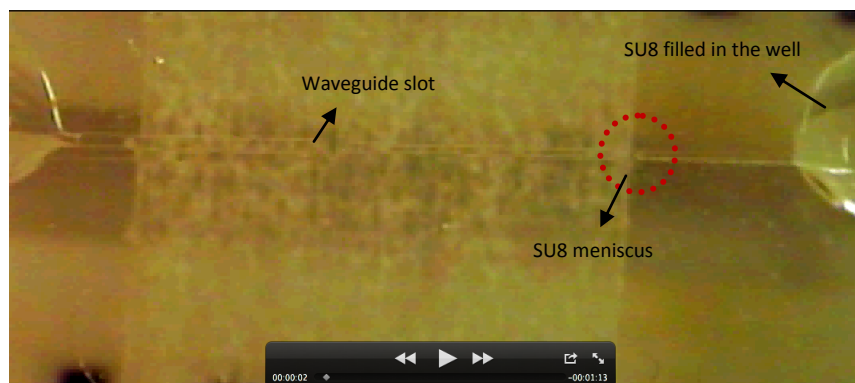
II- Channel forming the core of the waveguide

**Figure 8.5:** SEM image of the waveguide slot with the microfluidic channel for (a) Absorption detection system and (b) Fluorescence detection system

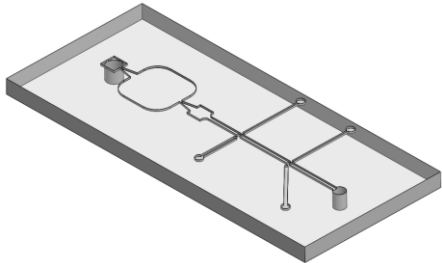
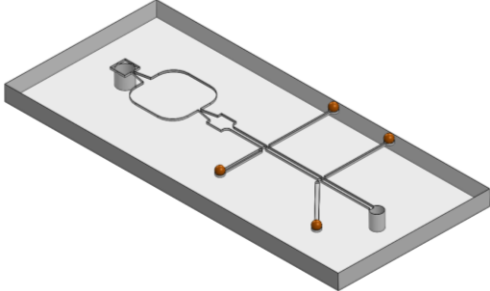
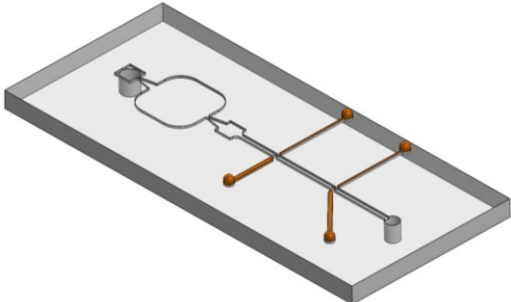
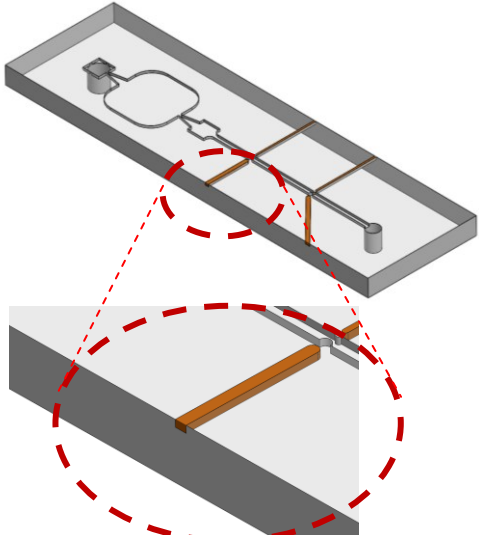
Prior to filling the waveguide slots with SU8, the photoresist was taken in a small beaker and was de-gassed in a vacuum dessicator, in order to remove dissolved gases. The

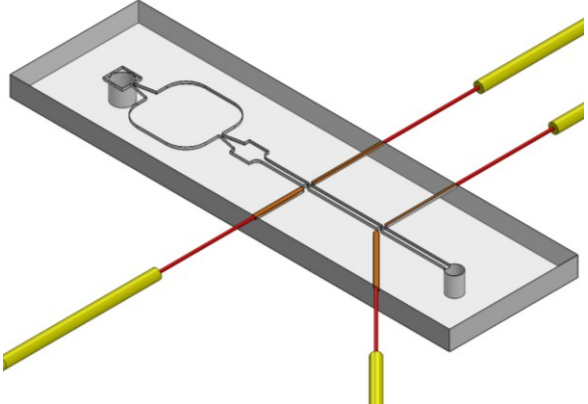
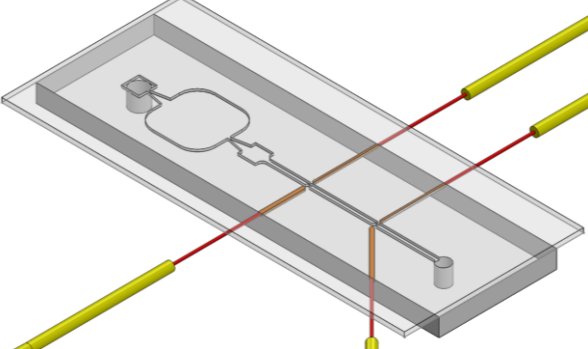
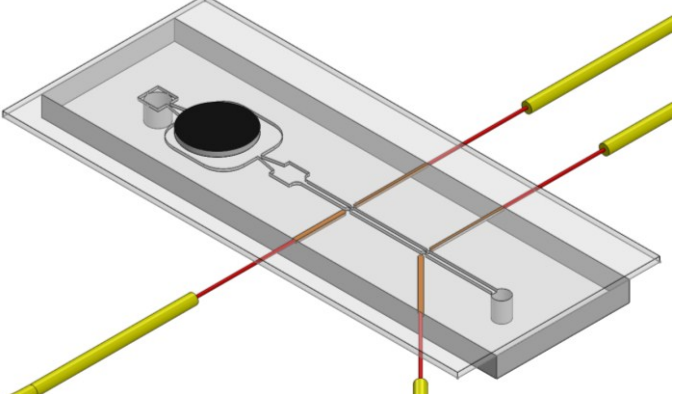
SU8 photoresist was then heated at 60 °C for 10 minutes in order to reduce the viscosity that enables capillary effect in the waveguide slot. 20  $\mu\text{L}$  of SU8 was then taken in a pipette and was carefully filled in the well. The capillary force in the channel draws the SU8 into the channel and thus fills up to form the waveguide core, as shown in Figure 8.6.

It must be noted that since the surface of a fresh PDMS sample is hydrophobic, it repels SU8. Therefore, any excess SU8 present on the PDMS does not spread on the surface. Instead, only SU8 is filled in the channels, due to the capillary action. The excess SU8 is removed by using a wipe. If the surface of the PDMS is rendered hydrophilic, then the SU8 adheres to the surface and it becomes extremely difficult to clean the surface after use, or to remove the SU8 in case of any mistakes during the process.



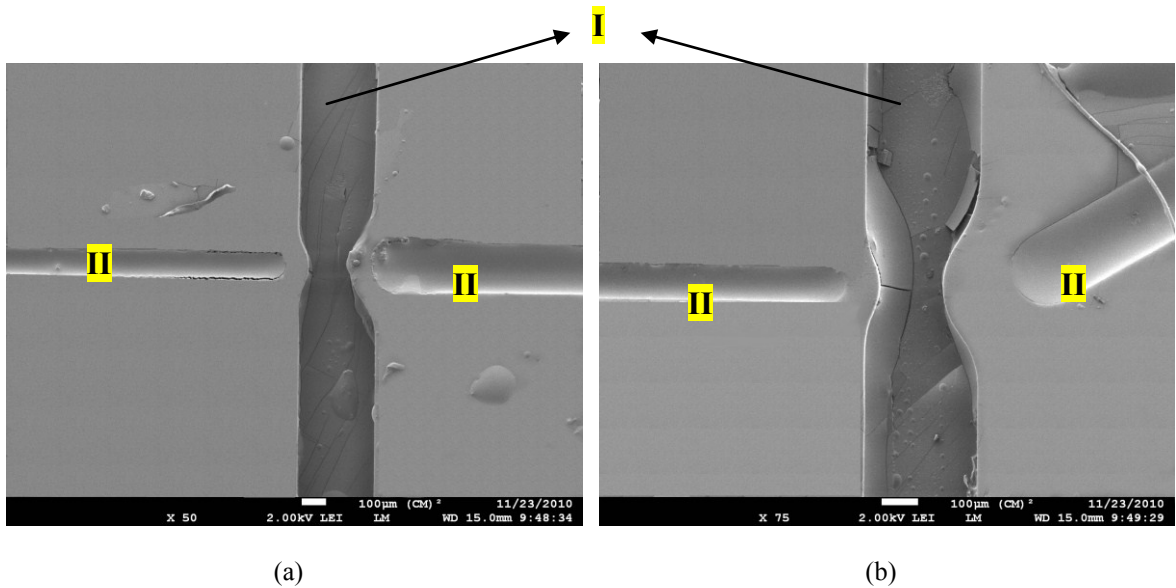
**Figure 8.6:** Filling of the channels with SU8 for waveguide core as seen under the microscope

Step	Action	Schematic
1.	Preparation of PDMS chip	
2.	Filling of well with SU8 photoresist	
3.	Filling waveguide core through capillary	
4.	Wafer dicing to remove SU8 wells	

5.	Integration of optical fiber	
6.	Glass cover bonding	
7.	Attachment of Piezo actuator with conductive epoxy	

**Table 8.1:** Fabrication steps for the optical microfluidic chip with integrated micropump, absorption and fluorescence optical detection systems

The SEM image of the SU8 waveguides and the microfluidic channels is as shown in Figure 8.7.



I – Microfluidic channel      II- Channel forming the core of the waveguide

**Figure 8.7:** SEM image of the SU8 waveguide and the microfluidic channel. The debris in the microfluidic channel is from the fluid flow in between the channels

### 8.3.1 Fiber integration

A tapered lens ended fiber (OZ optics, ON, Canada), which gives a spot size of  $5\ \mu\text{m}$  at a distance of  $26\ \mu\text{m}$ , was used as the input fiber. One end of the fiber was an FC-PC connector and the other end was the tapered lens through which light is emitted into the waveguide. The input fiber was connected with the light source (OZ Optics, Canada) of wavelength  $632\ \text{nm}$ . The output fiber was SMA end connected which was coupled with the Spectrometer. In order to couple the fiber with the waveguide, the fiber was stripped of the jacket to a length of  $\sim 10\ \text{cm}$  and the bare fiber was butted against the waveguide. For the fluorescence detection setup, the channel 4 from the Spectrometer-on-chip was connected to the output fiber coupled to the output waveguide.

Both the tapered lens fiber and also the waveguide device were mounted on individual xyz micropositioners so as to enable separate alignment of each module. The setup for the passive alignment is as shown in Figure 8.8. The fibers were aligned on the V-grooves and the input and the output fibers were positioned in a five axis fiber positioner. The optical microfluidic chip was placed in a separate positioner, so that each of the fibers and also the waveguides can be maneuvered and positioned accurately. Maximum optical light coupling into the fiber was ensured by fine tuning the position of the fiber and by observing the maximum optical coupling of the incident light from the output fiber coupled into the spectrometer. Thereafter, UV index matching gel (Norland NOA60) was applied at the tip of the fiber and the setup was exposed to UV for 60 s. This process bonds the fiber with the waveguide.

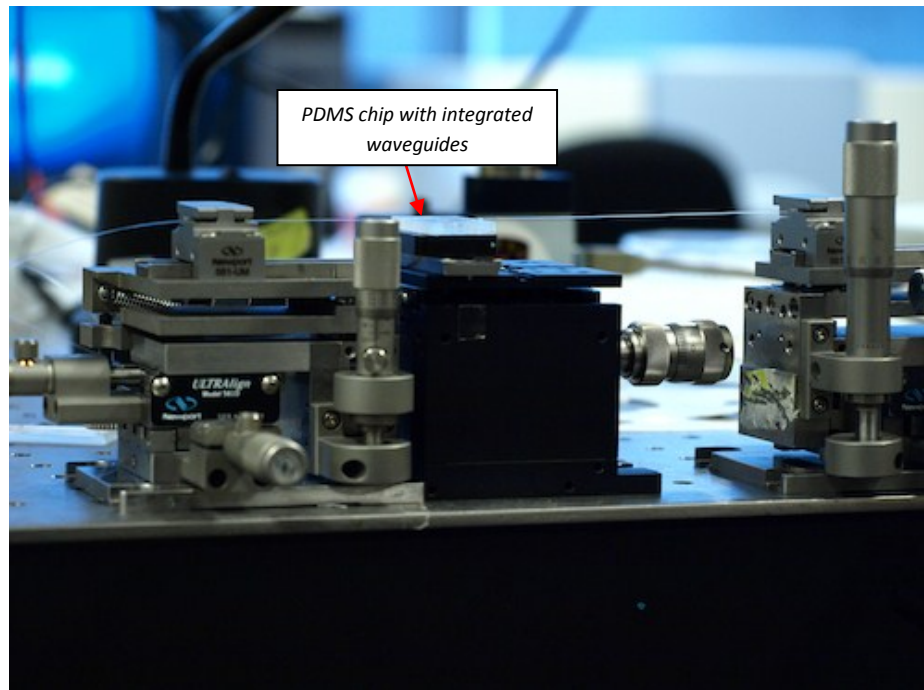


**Figure 8.8:** Assembly of the fibers placed on the positioners



Since the amount of UV epoxy is very less, the fiber is bonded with the waveguide over a small surface area which results in decreased bond strength. In order to maximize the bond strength between the fibers and the waveguides, a second coating of UV epoxy is added on top of the waveguide and the setup is cured again.

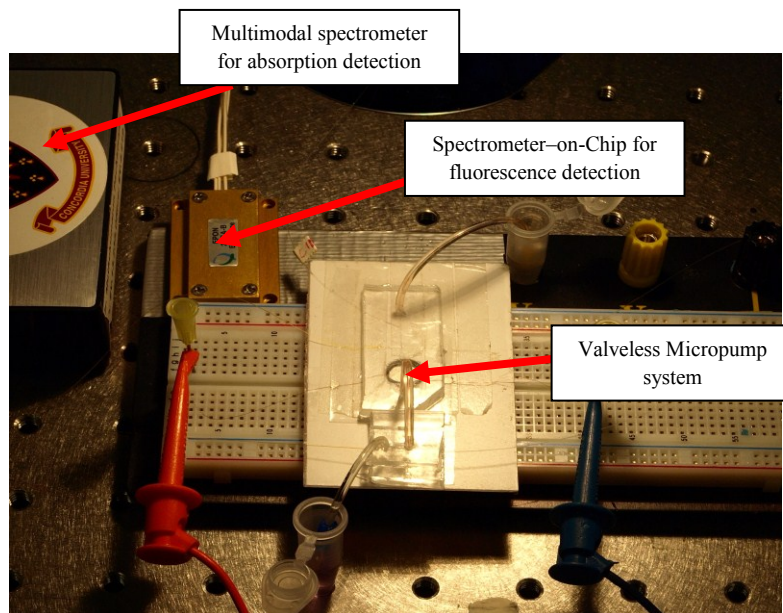
### **8.3.2 Micropump integration**

Once the optical chip is fabricated, the micropump is integrated very similar to the procedure explained in Chapter 3. The thin Corning glass slide is used as the deflecting diaphragm and also a cover for the microfluidics. PDMS was spin coated on the glass cover and semicured at 60 °C for 3 minutes, Thereafter the glass is bonded on top of the waveguide layers. This glass also forms the seal-top for the microfluidic channels. Using silver conductive epoxy, the PZT actuator is bonded on top of the glass diaphragm and the wires are attached.

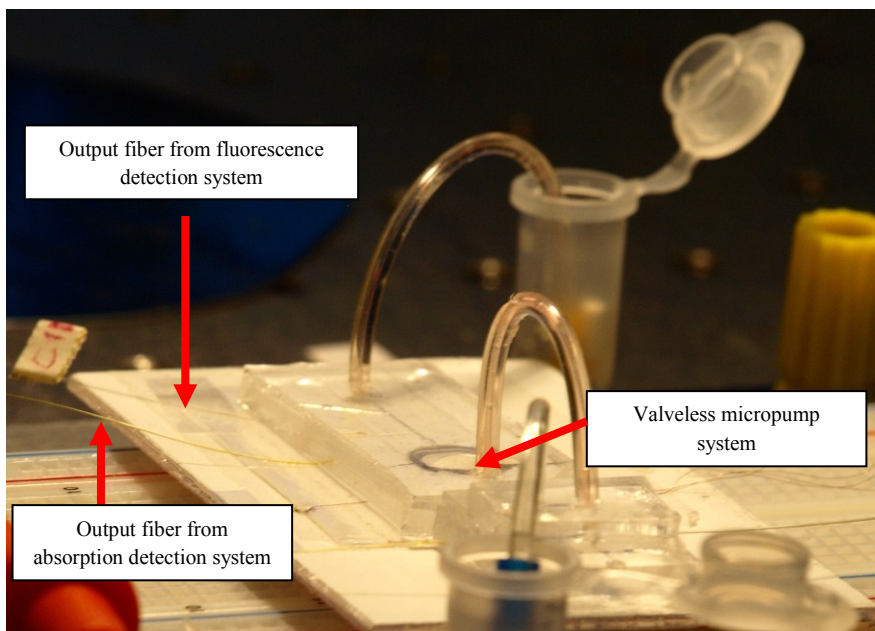
The entire system is then inverted and attached with a polycarbonate support using a double sided adhesive tape. Care must be taken during this process as it is possible that sometimes the fibers are damaged. A hole of ¼” was drilled on the polycarbonate support in order to fit the piezo actuator inside, and thus the glass diaphragm stays flat and well sealed with the polycarbonate support.

With this arrangement of the optical microfluidic chip, the micropump module does not interfere with the optical ensembles and the functionalities of all the components of the

system remains independent. The integrated absorption-fluorescence detection system is as shown in Figure 8.9



(a)

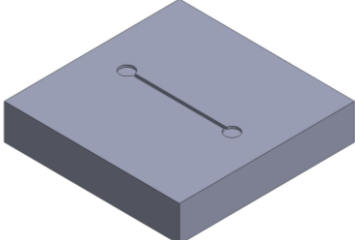
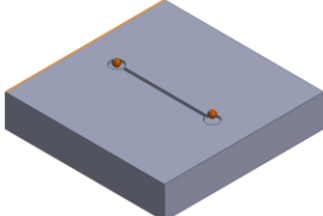
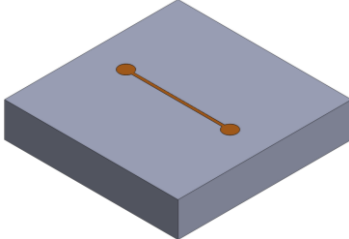
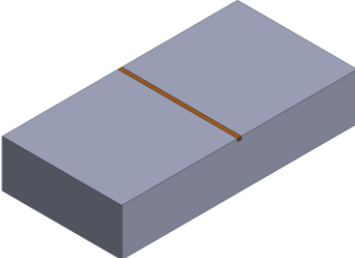


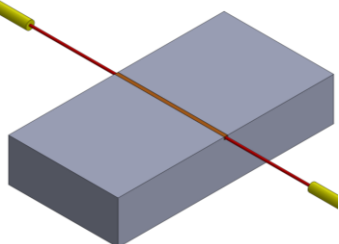
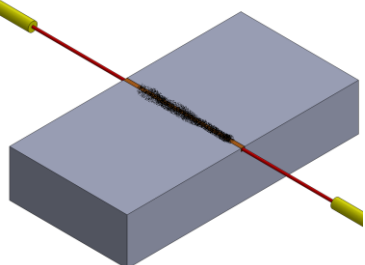
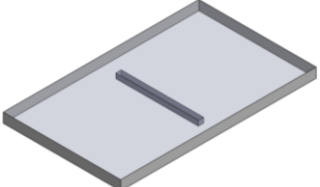
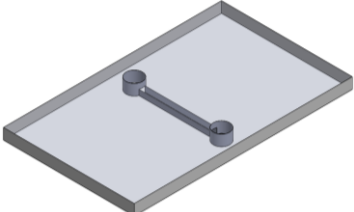
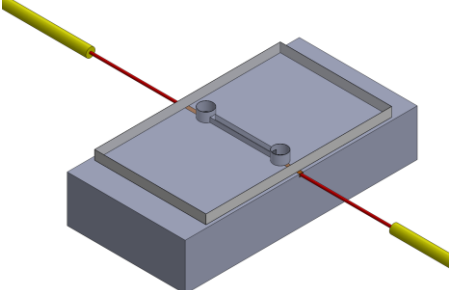
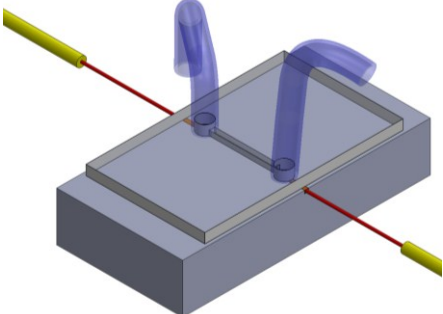
(b)

**Figure 8.9:** Integrated optical-microfluidic setup with absorption-fluorescence detection system and valveless micropump

### 8.4 Fabrication of nano-integrated evanescent waveguide system

The schematic of the evanescence detection system was shown in Figure 8.3. The sequential procedure for fabrication of the nano-integrated evanescence detection system is given in Table 8.2.

Step	Action	Schematic
1.	Fabrication of base PDMS chip with hollow waveguide core	 <p>A 3D perspective view of a rectangular PDMS chip. A thin, dark grey line representing a hollow waveguide core is embedded within the chip, extending from one side to the other.</p>
2.	Filling of well with SU8 photoresist	 <p>A 3D perspective view of the chip. The hollow waveguide core is now filled with a brown material, representing SU8 photoresist. The top surface of the chip is also covered with a thin layer of this material.</p>
3.	Filling waveguide core through capillary	 <p>A 3D perspective view of the chip. The hollow waveguide core is now filled with a brown material, representing SU8 photoresist. The top surface of the chip is also covered with a thin layer of this material.</p>
4.	Wafer dicing to remove SU8 wells	 <p>A 3D perspective view of the chip. The hollow waveguide core is now filled with a brown material, representing SU8 photoresist. The top surface of the chip is also covered with a thin layer of this material.</p>

5.	Integration of input and output fibers with SU8 waveguide core	
6.	Integration of Carbon Nanotubes	
6.	Fabrication of PDMS top cover with microfluidic channel	
7.	Creation of ports for microfluidic tubes	
8.	Bonding top PDMS cover with bottom PDMS waveguide substrate	
9..	Insertion of microfluidic tubes	

**Table 8.2:** Fabrication steps for Nano-integrated evanescence detection system

Multi-walled Carbon Nanotubes (MWCNT) was integrated with the SU8 waveguides in order to enhance the evanescence loss (Packirisamy and Chandrasekaran, 2010). Nano-integration with the SU8 waveguide is carried out in two stages. In the first step, after the degasification of the photoresist, 0.5 mg of MWCNT powder was mixed with 1 ml of SU8. The suspended solution was then filled in the waveguide well so that as the SU8 fills the waveguide core through capillary effect and is cured. Suspended nanoparticles also get embedded within the waveguide core. Thereafter, Carbon Nanotubes 0.5 mg of MWCNT powder was mixed with 1 ml of DI water and was spray coated on top of the SU8 waveguide so as to immobilize the nanotubes with the waveguide, which would improve the evanescence from the waveguide surface.

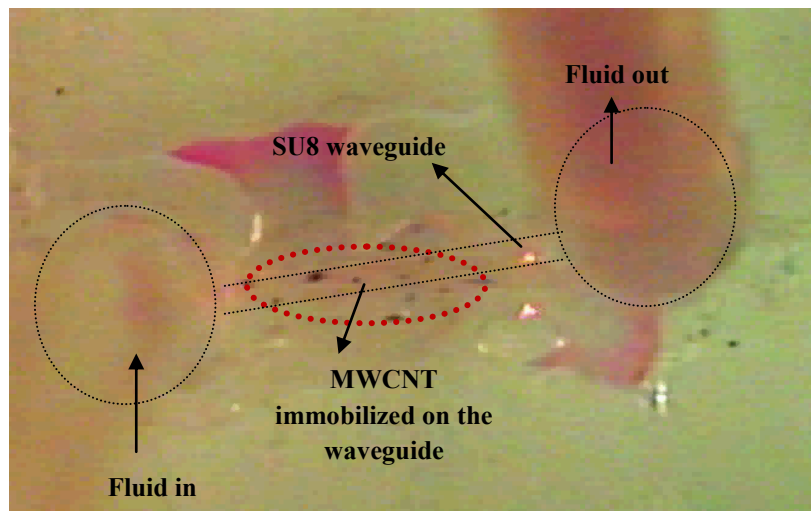
After the fabrication of the nano-integrated waveguide core, the SU8 wells were diced from the corners and the input and the output fibers were integrated with the waveguide ends using the similar procedure as explained in Section 8.3.1. Since for the evanescence detection, the maximization of coupling between the input and the output fiber is not a necessity, passive alignment of the fibers was carried out.

In order to integrate microfluidic channel on top of the waveguide, a separate PDMS chip was fabricated with a straight microfluidic channel of 500  $\mu\text{m}$  width and 100  $\mu\text{m}$  depth. Once the fluidic ports were created in the top PDMS substrate, thin layer of silicone glue was applied on the PDMS and was semicured for 5 minutes. Thereafter, the microfluidic chip was aligned and bonded on top of the fiber-waveguide assembly and pressure was applied during curing. In this way, leak proof bonding was obtained between the fluidic

chip and the waveguide device layer. The nano integrated evanescent waveguide device is as shown in Figure 8.10.



(a)



(b)

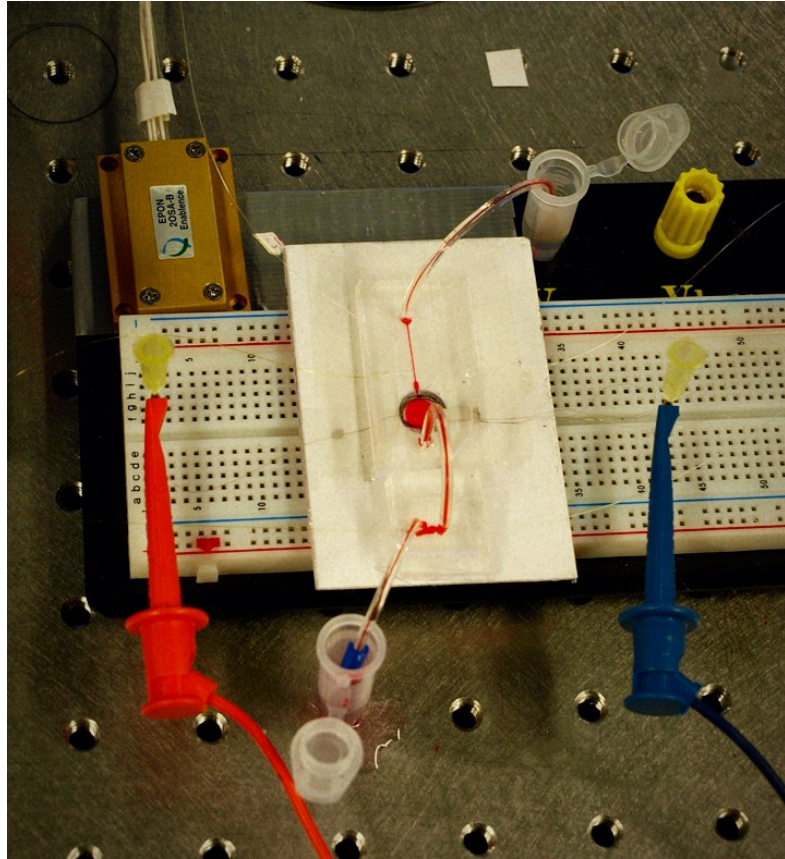
**Figure 8.10:** Integrated microfluidic Evanescence measurement system

## 8.5 Assembly

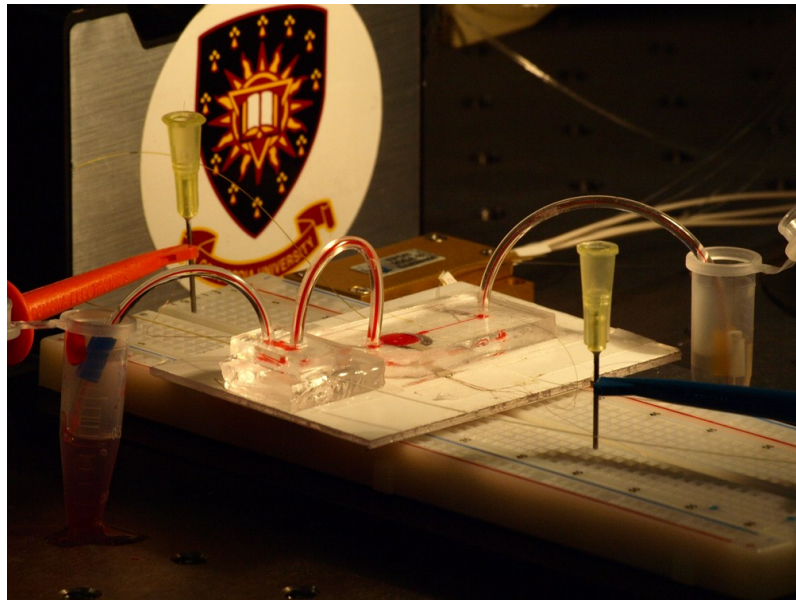
Both the integrated microfluidic evanescent detection system and the micropump integrated absorption-fluorescence optical detection system were fixed rigidly on top of a Polycarbonate support using double sided adhesive tapes in such a way that the axes of the waveguides for both the systems were parallel to each other. In that way, fibers from both the chips did not interfere with each other. However, the microfluidic channel in the evanescent system runs along the waveguide whereas, the channel is orthogonal to the waveguides for the absorption and fluorescence detection. The ports of the chips were connected using microfluidic tubes and were sealed using a thin layer of epoxy. One of the main advantages with this setup is that, since the microfluidic tubes were plugged into the ports of optical microfluidic chip using clearance fit, it was easy to remove and replace the tubes whenever necessary.

The entire assembly was then placed in a bread board which would enable the electrical connection of the micropump leads. The polycarbonate plate was held rigidly onto the bread board using double sided tape. The fully integrated  $\mu$ TAS is as shown in Figure 8.11.





(a)



(b)

**Figure 8.11:** Fully integrated  $\mu$ TAS under testing



# Testing of Integrated $\mu$ TAS

### 9.1 Introduction

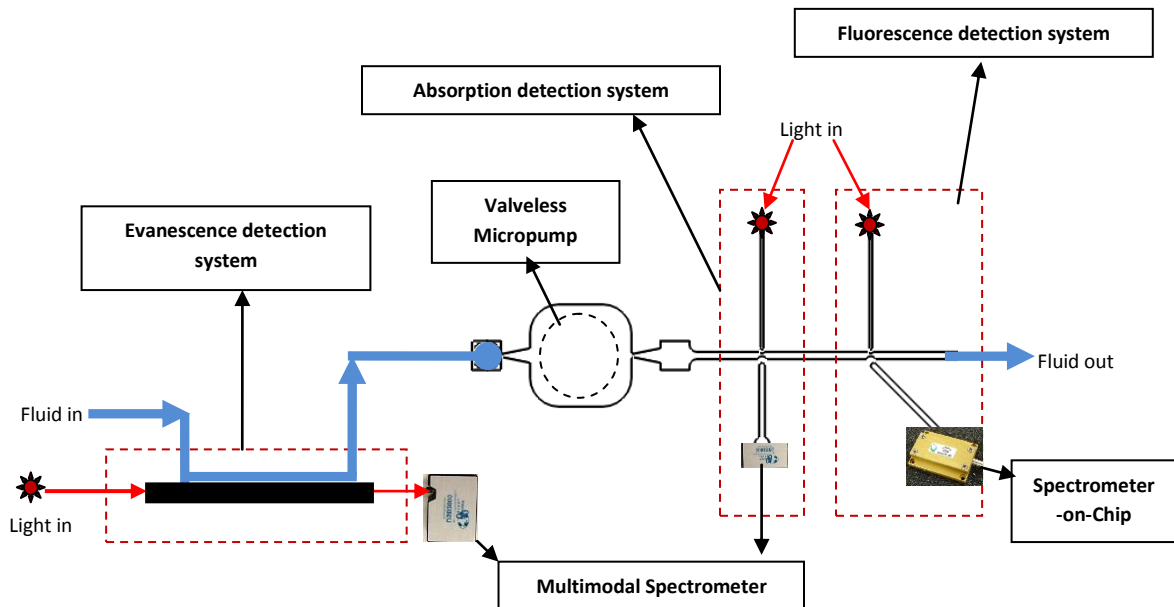
Testing of the  $\mu$ TAS is important to verify the performance of the integrated system in real-time, and to study the deviation in performance characteristics of the individual modules under integrated testing. The individual components of the  $\mu$ TAS, namely the valveless micropump, non-stagnant microfluidic system and the optical detection system that comprises of the absorption, fluorescence and the nano-enhanced evanescence detection have been tested individually and the respective performances established. Thus, the integrated testing involves the verification of the complimentary performance of each of the modules without interfering with the functionality of each other. Through the integrated testing, one could also understand the suitability of the proposed device for biological Point-of-Care applications, and thereby identify a potential real-time chemical and biological application for the  $\mu$ TAS.

The objectives of carrying out the integrated testing with  $\mu$ TAS are:

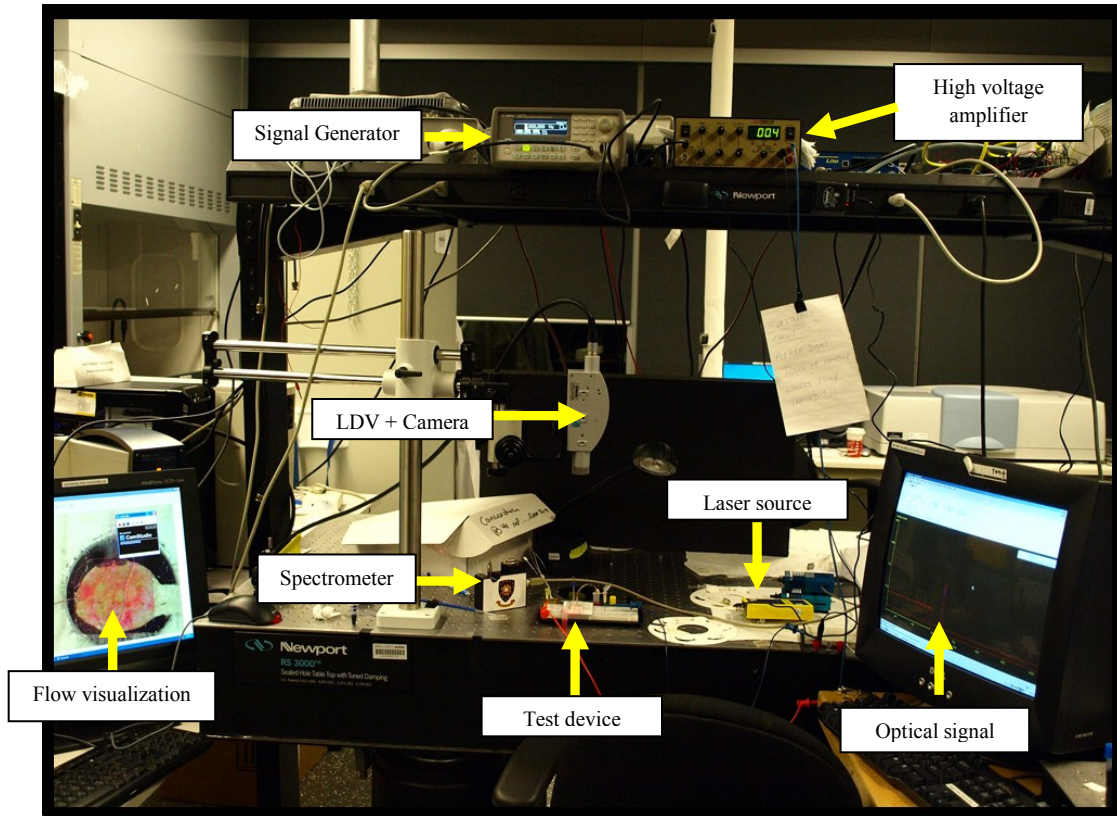
- Testing of integrated functionalities of the  $\mu$ TAS such as micropump, cavitation, optical waveguide based detection system, and non-stagnant microfluidic system.
- Testing of Nano-Enhanced Evanescence detection Technique (NEET) in  $\mu$ TAS environment.

- Testing of applications of cavitation, such as mixing and chemical synthesis, in  $\mu$ TAS

The schematic of the integrated  $\mu$ TAS test assembly is shown in Figure 9.1(a) and the experimental setup for the integrated testing is as shown in Figure 9.1 (b). The optical testing involves coupling of light from the source onto the respective SU8 waveguide, and collecting the light emerging out of the output waveguide at the other end for spectral analysis using the Spectrometer-on-Chip. The input light at 632 nm was used for the tests. Since the electrical wiring of the micropump assembly is very fragile, it is possible to snap the wiring with stress. Therefore, the  $\mu$ TAS test assembly was integrated on a circuit board, in order to provide the high voltage input for the micropump. The micropump actuation setup and the flow visualization setup have already been described in Chapters 3 and 4. The entire setup was tested on a vibration isolation table in order to avoid external disturbances.



(a) Schematic of the integrated  $\mu$ TAS test assembly



(b) Test setup

**Figure 9.1:** (a) Schematic of the integrated  $\mu$ TAS test assembly and (b) Integrated  $\mu$ TAS testing setup

The following sections of this chapter present the nano-integrated evanescence and the absorption measurements that have been carried out using the integrated device.

## 9.2 Integrated nano-enhanced evanescence measurements

In Chapter 7, the feasibility of nano-enhanced evanescence was demonstrated on an external hybrid integrated setup wherein the fluid was added directly on top of the waveguide. With the integrated system, the nano-integrated evanescence measurements were carried out with integrated micropumping. Herein, the feasibility of nano-based

evanescence is demonstrated further with gold nanoparticles. The evanescence measurements were carried out with gold colloid solution. Since the Carbon Nanotubes were immobilized onto the surface of the waveguide during the fabrication process itself, the introduction of gold colloid further enhances the evanescence through NEET.

Gold nanoparticles have been widely used in Surface Plasmon Resonance (SPR) studies and also for Surface Enhanced Raman Scattering (SERS) due to their ability to resonantly scatter visible and near-infrared light upon the excitation of their surface Plasmon oscillation. They can be easily detected in as low as  $10^{-16}$  M concentration (El-Sayed et al., 2005). Gold colloids have also been used to modify the surface to increase evanescence (Tang et al., 2006)

### **9.2.1 Synthesis of gold nanoparticles**

For the preparation of the gold colloid, 28 mg of gold salt  $\text{AuCl}_4\text{H}$  (Alfa Aeser) is diluted in 100 mL of DI water and is heated to boiling at 80 °C. Sodium citrate solution was then prepared by adding 0.5 g of sodium citrate in 50 ml DI water and is added to the gold solution. The color of the solution becomes dark blue. Upon further heating for 15 minutes, the color of solution changes from dark blue to dark red, indicating the formation of Au nanoparticle colloidal solution. The size of the nanoparticle is ~40nm.

### 9.2.2 Experiment

In the first experiment, the feasibility of measurement of evanescence with the integrated setup was measured. As seen from the previous chapter, the setup of the integrated system is such that, the biological liquid is transported from the vial into the evanescent sensing system the output microfluidic port of the evanescence system forms the input to the micropump. In this way, the evanescent path is fabricated at the inlet section of the micropump. Therefore, in order to achieve integrated biosensing, it is necessary that the liquid from the inlet reservoir be pumped into the micropump chamber during which it is possible to carry out the evanescence based biodetection when the liquid flows is pumped through the evanescent path.

So, in order to facilitate this, the nanocolloid solution was filled in the inlet tube of the evanescent sensing system and the micropump was operated. The pump was operated at the driving frequency of 2 Hz, with an applied voltage of 195 V<sub>pp</sub> at which it is expected to produce a deflection of ~3 μm, as seen from the Chapter 3. As the fluid is pumped, the evanescence was measured from the waveguide by measuring the intensity loss at the output of the waveguide. The net evanescent loss is then measured in dB as

$$\text{Evanescent loss, } E_{np} = -10 \log_{10}(I/I_0) \quad \dots 9.1$$

where  $I$  is the time varying intensity of the output light during evanescence and  $I_0$  is the reference intensity used for measurement. Herein,  $I_0$  is taken as the output intensity

measured when there is no fluid in the microfluidic channel. The plot of the time varying evanescent loss micropumping is given in Figure 9.2.

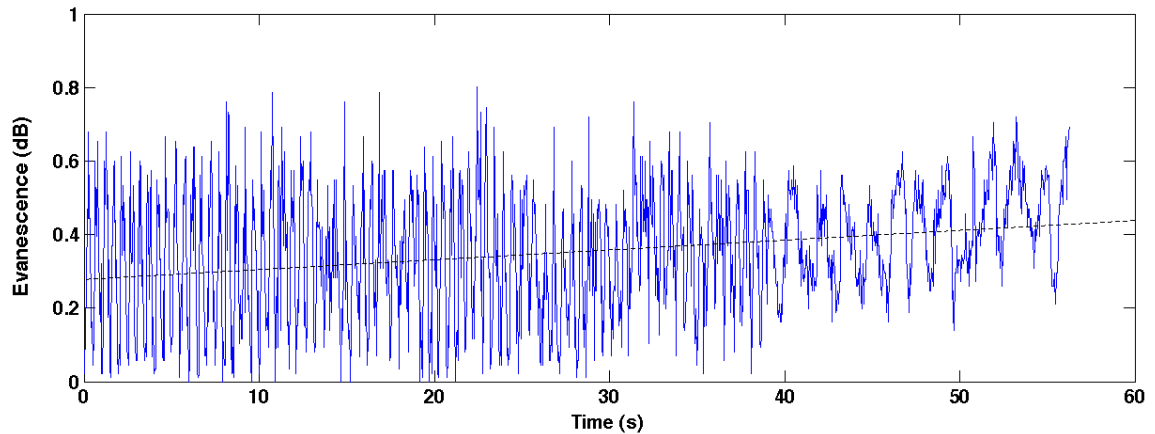


**Figure 9.2:** Plot of variation of evanescence with micropumping

It can be seen that the evanescence varies in phase with the pumping. As the fluid is displaced along the waveguide surface sinusoidally, the variation in evanescence is also observed accordingly, without any phase lag at the same frequency as the operating frequency. The plot also shows that there is an increase in the evanescence with continued micropumping. This net increase in the evanescence over a period of time indicates that the fluid is displaced forward due to the pumping. In order to demonstrate the phenomenon more clearly, the frequency of the micropump was changed to 1 Hz after 40s. The variation in evanescence is also seen to change according to the frequency at which the liquid is pumped.

The next study was conducted in order to study the evanescence along the whole length of the waveguide. As seen from the previous experiment, the rate at which the fluid is

transported over the evanescent length of the waveguide by valveless micropumping is very less. Therefore, in order to expedite the study, the micropump was operated with simultaneous actuation of the fluid with a syringe pump, so that the fluid is pumped all the way along the entire evanescent field length of the waveguide.

The inlet microfluidic tube of the evanescent detection system was connected with the syringe pump and the fluid was filled completely in the tube till the inlet port. Simultaneously when the evanescence measurements are started, the fluid was actuated initially with the valveless micropump, such that the fluid just enters the evanescent field from the microfluidic tube. Thereafter, the fluid is transported along the evanescent field of the waveguide with simultaneous pumping by both the external syringe pump and the micropump. The results of the evanescence measurements are as presented in Figure 9.3 and the sequence in which the experiments were carried out is presented in Table 9.1, with respect to Figure 9.3

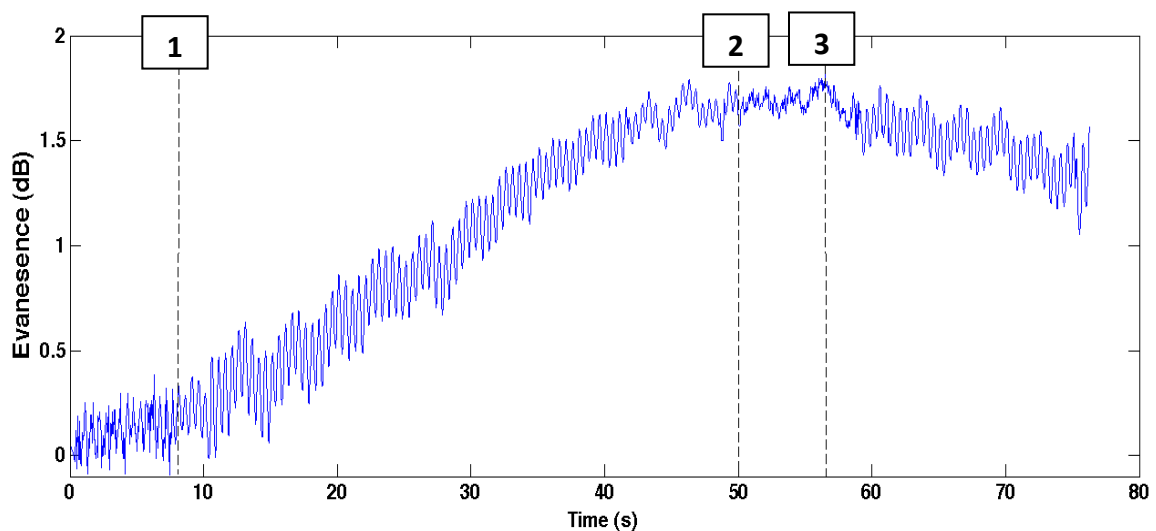


**Figure 9.3:** Plot of variation of evanescence with external syringe pumping and micropumping

Process #	Procedure
1	Begin external fluid actuation with syringe pump
2	Fluid reaches maximum evanescent field length, stop pumping
3	Begin reverse pumping by syringe suction

**Table 9.1:** Different stages of fluid actuation for evanescence detection

Before the fluid is actuated with external syringe pump, it can be seen that the evanescent loss varies due to the oscillation of the pump at the same frequency of operation. There is a slight increase in the evanescence, as observed in Figure 9.2, which shows the forward motion of the gold colloidal solution due to micropumping. At #1, when the syringe pump starts to actuate the fluid inside the system, it can be seen that there is a significant increase in the evanescence, as the evanescent field length of the gold colloidal solution is increased. At the same time, the variation of the evanescent field length at 2 Hz is due to the continued operation of the micropump. At #2, the fluid reaches the maximum evanescent length. Subsequently, it can be seen that the evanescent oscillation stops once the maximum field length is reached. This proves that the time varying variation in the evanescence is caused by the oscillatory motion of the fluid within the micropump. The syringe pump is stopped at #2 and at #3, the fluid is pulled out of the evanescent field by manual syringe suction. It can be seen that as the field length is reduced, the evanescence is also reduced, and it can also be seen that the oscillation in evanescence begins again as the fluid moves sinusoidally in the evanescent field.



### 9.2.3 Calculation of evanescence coefficient

From the evanescence loss observed in the above experiments, the evanescence coefficient of the gold nanoparticles was calculated. In this way, all the evanescence measurements are standardized. The following procedure was adopted in calculating the evanescence loss for the calculation of evanescence coefficient.

For the experiment carried out with micropumping, it is assumed that the maximum flow rate of the pump,  $\dot{Q}$ , is 60 nL/min, as experimentally characterized in Chapter 3. The area of cross section of the microfluidic channel,  $A_{mf}$ , on top of the waveguide is  $\sim 500 \mu\text{m} \times 100 \mu\text{m}$ , where 500  $\mu\text{m}$  is the width of the channel and depth of the channel is 100  $\mu\text{m}$ , which is obtained from the bonding of the top microfluidic covering layer with the waveguide layer. Thus, the net total evanescent field length of the waveguide,  $L_{ev}$ , which is covered with the fluid due to pumping in 60 s is given as

$$L_{ev} = \frac{\dot{Q}}{A_{mf}} = 1.2 \text{ mm} \quad \dots 9.2$$

From the results of the experiments which were carried out with micropumping of gold nanoparticles, and with individual specimen measuring the evanescent loss over the entire waveguide length, the evanescent loss coefficient,  $\alpha_{ev}$ , was computed for each of the specimen. The length of the waveguide was measured to be 1 cm and the specimens were immobilized over the entire waveguide length. Therefore, the evanescence loss,  $\beta_{ev}$ , can be directly measured in dB/cm. Accordingly, the total loss due to evanescence was computed by the following relations.

$$\beta_{ev} = 10 * \alpha_{ev} * \log_{10}(e), \quad \therefore \alpha_{ev} = \beta_{ev} / [10 * \log_{10}(e)] \quad \dots 9.3$$

The mean values of the evanescence coefficient obtained from the above experiments are tabulated in Table 9.2.

Experiment	Average increase in Evanescence	Average Evanescence loss (dB)	Evanescence path length (cm)	Evanescence loss (dB/cm)	Evanescence coefficient (cm <sup>-1</sup> )
Test 1	0.02	0.2	0.12	1.66	0.382
Test 2	0.155	1.55	1	1.55	0.357

**Table 9.2:** Evanescence coefficient for the different tests carried out on the CNT integrated SU8 waveguides with Gold colloidal solution

From both the experiments, the evanescence coefficient obtained is very close. This shows that the evanescent losses measured in both the above experiments are consistent, thus proving the success of carrying out integrated evanescence measurements on SU8 waveguides with integrated microfluidics and micropumping. It must be mentioned that this is the first integrated evanescence measurement experiment carried out with integrated microfluidics in which the biological fluid is actuated by an integrated micropump.

In the above experiments, it is possible to measure the evanescence only from the top surface of the waveguide, however if the waveguide is fabricated in such a way that the microfluidic channel engulfs all the three sides of the waveguide, it is possible to obtain a triple bound evanescence, by immobilization of the specimens along the side walls of the waveguide also.

### **9.3 Integrated optical absorption detection using cavitation assisted mixing in microreactor based $\mu$ TAS**

$\mu$ TAS devices that work with very small volumes of reactive species are often referred to as miniaturized reaction systems or Microreactors (Ehrfeld et al., 2000). These microreactors have found extensive applications in chemical and biotechnologies (Lomel et al. 2006). Areas that have attracted most research on microreactors for chemical technologies have centered on gas and liquid phase reactions covering simple microscale mixing of different fluids to volumetric titrations, heterogeneous and homogeneous catalysis, catalytic oxidation (Walther et al. 2009), heterocyclic synthesis, photochemical reactions (Tung et al. 2000) and micro fuel cell (Pattekar and Kothare, 2004) applications. The miniaturization of these chemical reactors offers a lot of practical advantages for the present generation chemical and pharmaceutical industries.

Optical absorption is one of the most important techniques which have been used to carry out high throughput analysis of miniaturized of chemical assays in microreactors. There are several important advantages of using absorption method for the detection systems in microreactors. Primarily, it is possible to carry out a comprehensive study of time-dependent enzymatic reactions using this method. This technique is simpler, faster and can be used to rapidly detect instantaneous reactions. Thus, in microreactors which work with very small volume reacting fluids, optical absorption technique can be used to precisely detect the biochemical reactions, together with the reaction intensity. Hence, optical absorption method is very convenient to be employed on microreactors and other  $\mu$ TAS devices.

In this work, the feasibility of carrying out integrated optical detection has been demonstrated on a microreactor based  $\mu$ TAS, using cavitation assisted mixing of the reactants. Previously, the study of controlled biosensing through optical absorption method has been carried out using an external hybrid integrated microreactor device (Chandrasekaran and Packirisamy, 2006), wherein the reaction between HRP and  $H_2O_2$  was detected. Herein, taking advantage of the integrated optical detection as well as cavitation induced mixing, the study of controlled chemical synthesis in a microreactor based  $\mu$ TAS is carried out for the detection of the presence of reducing sugars in a sample using Benedict's test.

### **9.3.1 Implementation of chemical synthesis with cavitation induced mixing**

The principle of the Benedict's test is that reducing sugars, which are present in a given sample, react with Benedict's reagent to reduce the blue copper (II) ion to form a brick red precipitate of copper (I) oxide. Thus, the presence of glucose in the specimen is determined by the change in color. The concentration of the specimen is also determined by the change in color. For high concentration, the color of blue vitriol turns green, yellow and then to deep red. Apart from the change in color, the reaction is also characterized by the formation of the precipitate due to the reduction of the glucose. Benedict's test can be used to determine the presence of a wide variety of sugars, which includes all the monosaccharides and disaccharides, lactose and maltose, due to which

this test is critical for many biochemistry applications, including the study of Diabetes Mellitus (Pavri, 2001).

Thus, it is clear that in the Benedict's experiment, it is necessary to create favorable conditions for proper mixing of the Benedict's reagent and the sugar solution, in order to carry out the reduction reaction. Herein, the phenomenon of cavitation induced in the micropump is used for facilitating the mixing between the two samples to induce chemical reaction. The optical absorption studies are then carried out in order to characterize the specimens and the mixing. The change in the optical absorption indicates the extent of Benedict's reaction, which indicates the presence of sugars present in the solution, which can then be calibrated suitably to determine the concentration of the sugars in the sample.

### **9.3.2 Preparation of chemicals for Benedict's test**

The feasibility of carrying out Benedict's test is demonstrated herein by the determination of the presence of glucose in cell culture medium. Glucose is one of the important ingredients of cell culture solution, which is useful for the rejuvenation the cells which are stored in the culture medium. Therefore, for the present experiments, the cell culture medium RPMI 1640 with L-Glutamine (purchased from Wisent Inc.), with a concentration of 2  $\mu\text{g/mL}$  of D-Glucose, was used.

In order to prepare the Benedict's reagent, 10 g of anhydrous Sodium Carbonate is dissolved in 80 mL of DI water taken in a beaker. The mixture is stirred well but not all the salt gets dissolved in the water. Then 17.5 g of Sodium Citrate crystal is added to the solution and the beaker is heated gently and stirred slowly to aid dissolution. The solution is then filtered in order to remove the undissolved salts. In a separate beaker 1.75 g of Copper (II) Sulphate pentahydrate is dissolved in 10 mL of DI water. Thereafter, the Copper Sulphate solution is added to slowly, with continuous and constant stirring. The solution is cooled for sometime, to obtain the Benedict's reagent.

Prior to the experiments, different concentration of the sugar solutions was prepared by diluting the cell culture solution in the volumetric ratios of 1:1 to 1:3 with DI water. The solutions were then mixed with Benedict's reagent and the reaction was observed. The color changes as observed with the mixing of both the solutions are as shown in Figure 9.4. For the lowest concentration of the sugars, the color of the mixture solution is bluish. As the concentration of the sugars is increased, the color changes from blue to bluish green and thereafter slightly yellowish. In this test, undiluted sample gave a reaction mixture which was greenish-yellow in color while the most diluted sample gave a bluish mixture. Upon heating, the greenish solution turns to reddish indicating the presence of sugars. However without external heating, the concentration of sugar solution is determined by the change of color of the solution from blue to green to slightly yellow.

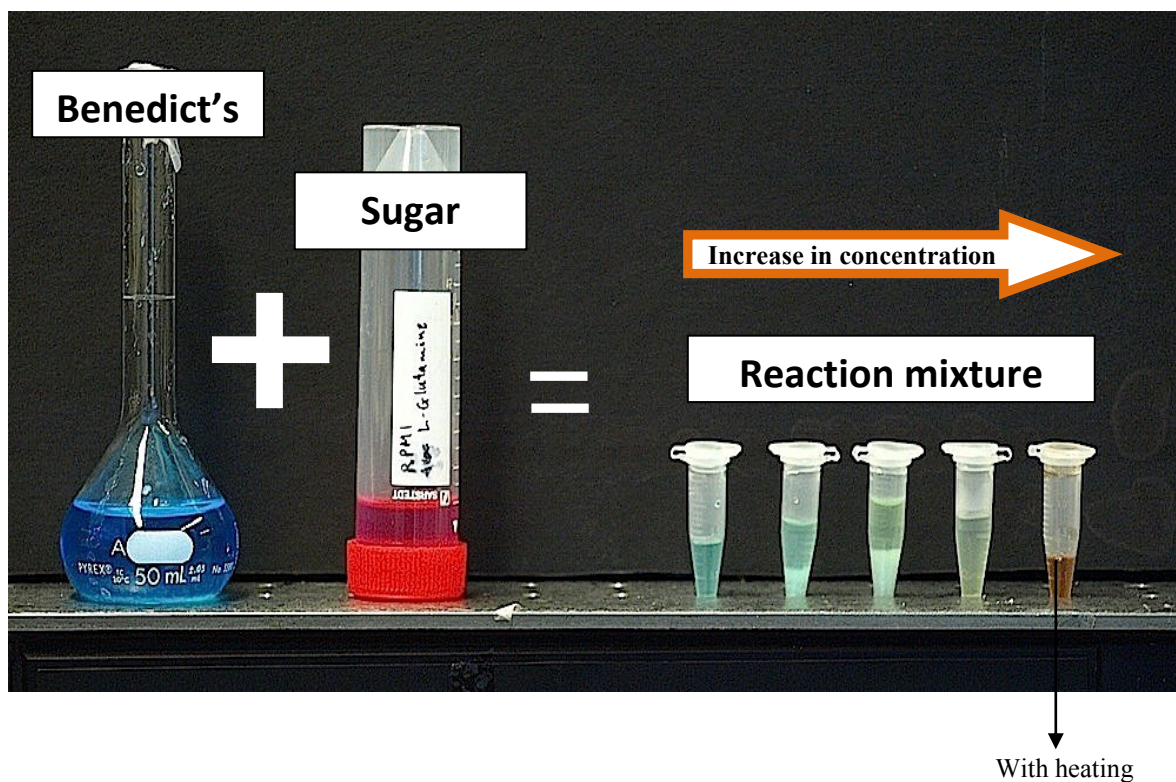


**Figure 9.4:** Different stages of color changes with the concentration of the sugar solution with the Benedict's test. The red colored solution seen at the end is obtained when the solution is heated slightly

One of the other advantages of carrying out optical absorption detection for the Benedict's test is that, due to the formation of the precipitate during the reaction, higher optical absorption in the visible wavelength is expected, which can be detected instantaneously.

### 9.3.3 Experimental setup

The experimental setup for the integrated optical absorption detection is as shown in Figure 9.5. In order to facilitate simultaneous pumping of two liquids into the micropump

chamber, a  $\mu$ TAS was fabricated with two inlet ports at the suction side of the micropump. However, to realise this setup, the evanescence measurement system was temporarily removed from the hybrid integration, though it is still possible to carry out evanescence detection by connecting the evanescent sensing system at the delivery side of the micropump in such a way that the outlet of the micropump forming the inlet to the evanescent sensing system. The Benedict's solution and the cell culture medium were taken in two separate syringes and loaded on the syringe pump. The tubes from the syringe pump were connected with the inlet of the micropump. As mentioned before, in order to maintain similar flow condition from both the syringes, the tubes of similar lengths and the dimensions were used.

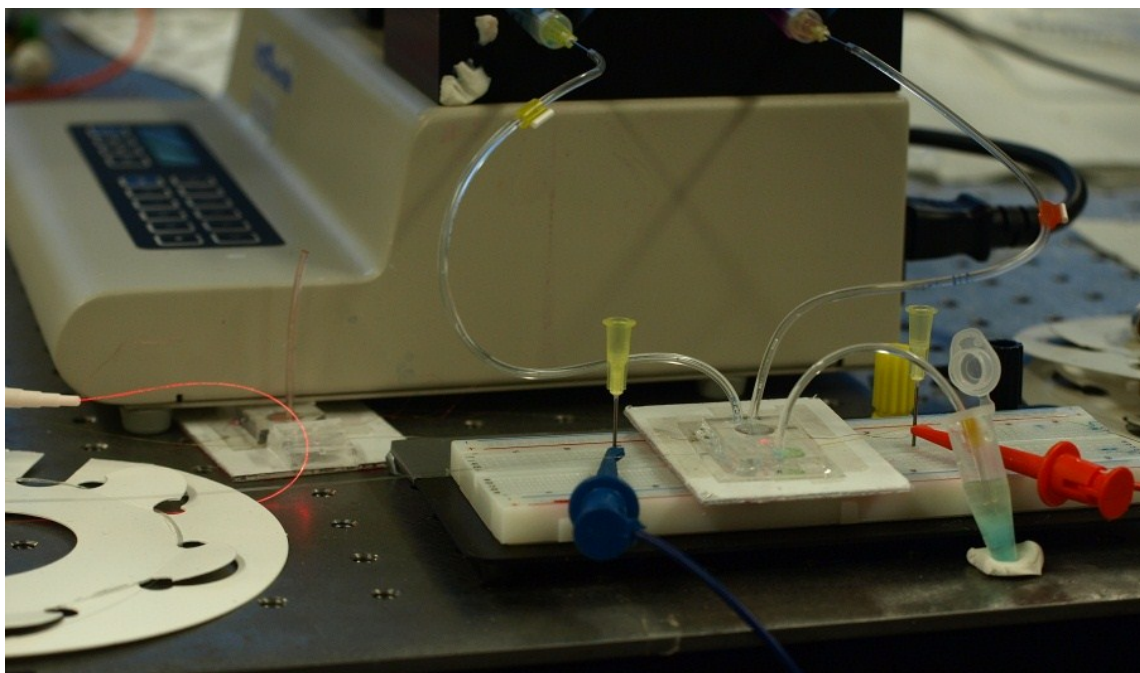


**Figure 9.5:** Experimental setup for integrated optical absorption measurements



As seen from the previous chapter, the optical absorption detection system was integrated on the delivery side of the micropump, just after the outlet diffuser. The optical absorption experiments were performed at 632 nm wavelength. Before measurement of the optical absorption from the Benedict's test, the optical absorptions of the individual specimens were recorded.

Steady simultaneous flow of both the test specimens is obtained using the syringe pumps. In order to induce cavitation, the micropump was operated at a cavitation frequency which is high enough to create the suitable conditions for cavitation to occur, but at the same time, does not cause significant damage to the micropump because, as seen from the qualitative analysis, high frequency cavitation can cause damage to the micropump surface, due to the formation of craters. Therefore, for the present experiment, a low frequency cavitation at 800 Hz was induced in order to facilitate mixing.

#### 9.3.4 Results

The optical absorption was measured by the change in the optical intensity at the waveguide output. The optical absorbance of the specimen measured by the spectrometer is given by the formula

$$A_{\lambda} = -\log_{10} \left( \frac{S_{\lambda} - D_{\lambda}}{R_{\lambda} - D_{\lambda}} \right) \quad \dots 9.4$$

Where

$\lambda$  - Wavelength of light used

$A_\lambda$  - Absorbance

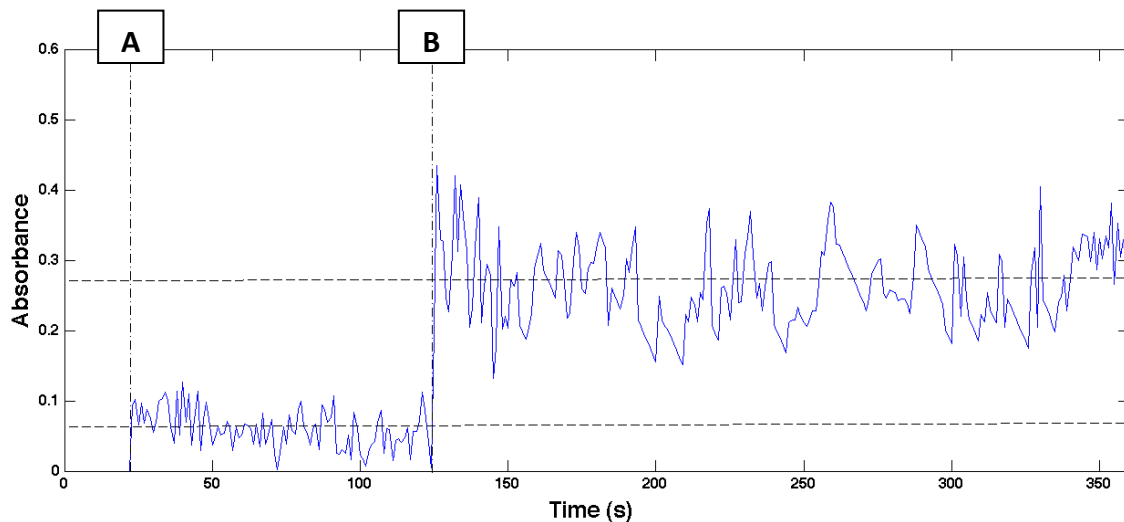
$S_\lambda$  - Intensity of light passing through the sample

$D_\lambda$  - Dark Intensity

$R_\lambda$  - Intensity of light passing through a reference medium.

The reference intensity of the light is taken when there is no fluid between the waveguides in the microfluidic channel. Thereafter, the individual specimens are passed individually into the microfluidic channel, without the operation of the micropump by loading only the respective syringes on the pump and releasing the other, such that flow occurs only from one of the two inlet ports into the micropump chamber. This prevents the flow of the fluid being actuated by the syringe pump into the other channel.

Figure 9.6 shows the dynamic measurement of the optical absorption of the individual chemicals under steady flow.



A – Glucose solution enters detection zone

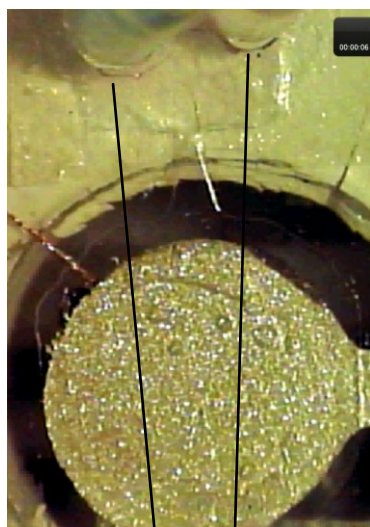
B – Benedict's solution enters detection zone

**Figure 9.6:** Variation of optical absorption under steady state flow with sugar solution and Benedict's solution at 632 nm wavelength

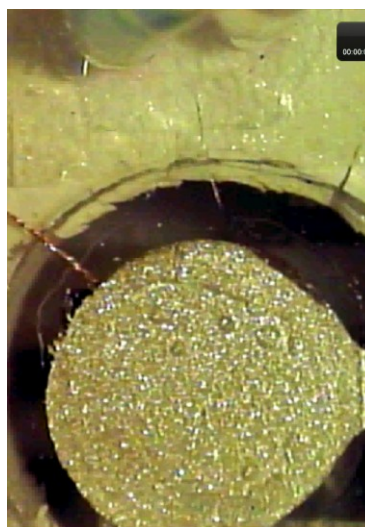
The optical absorption is zero till cell culture solution is passed into the microfluidic channel (A). Immediately, the syringe with Benedict's solution is loaded onto the micropump and is injected into the channel. The increase in the optical absorption is observed at ~125 s (B) due to Benedict's reagent. The Benedict's solution exhibits higher optical absorption than Sugar solution, which is along the expected lines, since it is well known that the blue color of the Benedict's solution is obtained due to its high absorption of wavelengths ~600 nm.

After the measurement of the respective absorbances of the Benedict's solution and sugar solution, the liquids present inside the microfluidic channels were completely removed

with continuous purging and suction in order to perform the integrated tests, and the reference intensity of the light was taken again. Thereafter, the Benedict's and cell culture solutions were injected into the micropump chamber using the syringe pump simultaneously for facilitating the Benedict's reaction, as shown in Figure 9.7.



**Liquids enter the chamber from the microfluidic tubes simultaneously**



**Liquids fill the micropump chamber**

**Figure 9.7:** Benedict's reagent and the sugar solution entering the micropump chamber

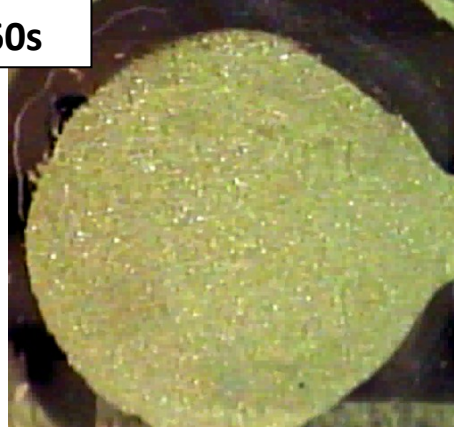
The different stages of formation of the precipitate with cavitation induced mixing is as shown in Figure 9.8.

**Cavitation growth induced mixing**

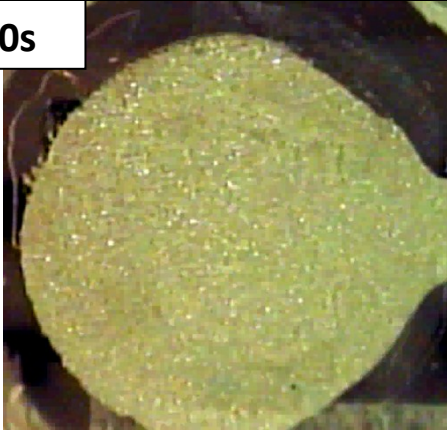
**30s**



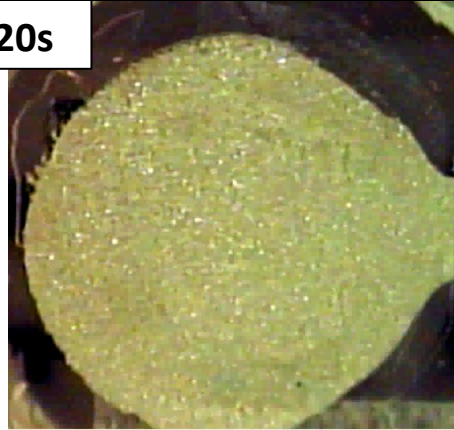
**60s**



**90s**



**120s**



**150s**



**180s**





**Cavitation Collapse Induced Mixing**

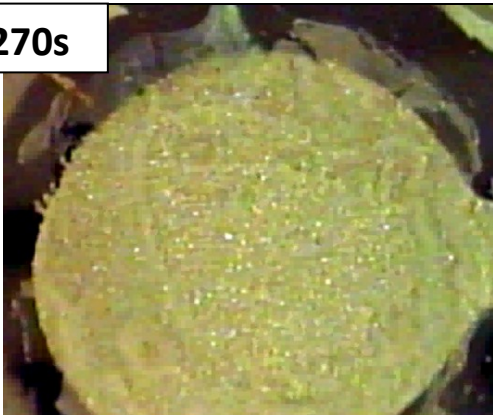
**210s**



**240s**



**270s**



**285s**

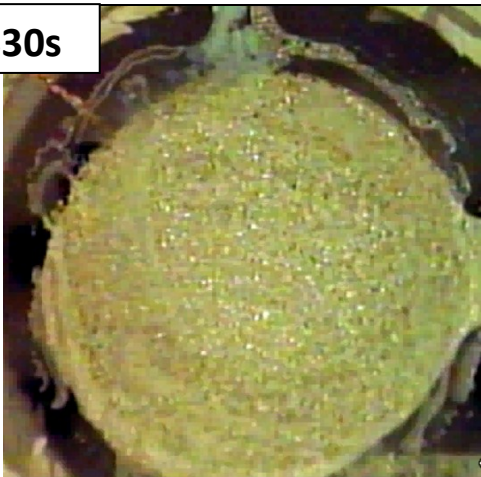


**Supercavitation induced Mixing**

**300s**



**330s**



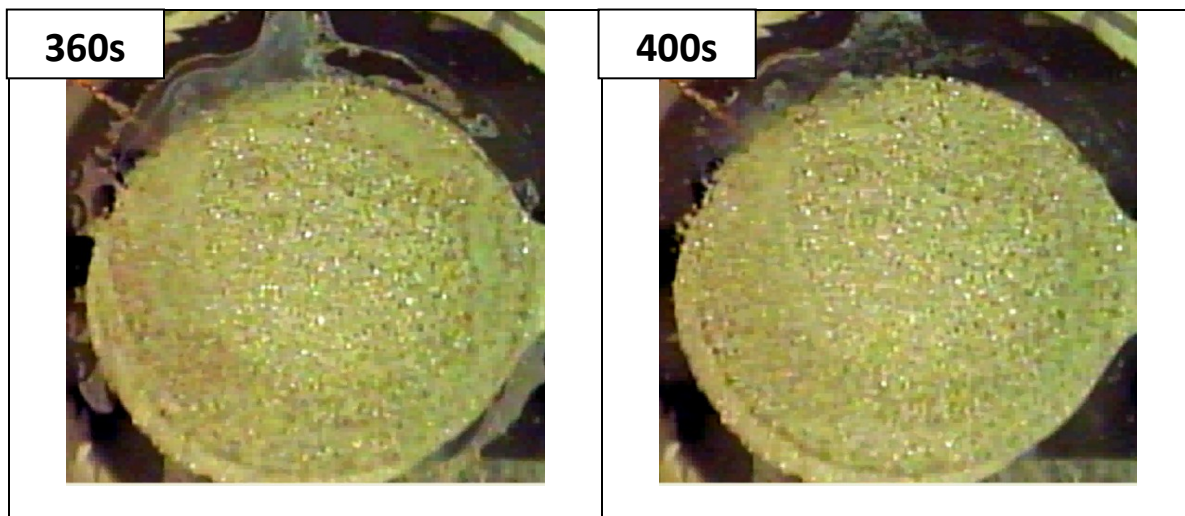


**Figure 9.8:** Different stages of variation induced mixing of Benedict's solution with sugar solution

The micropump was stopped at ~420 s. The reaction mixture present inside the chamber after cavitation is as shown in Figure 9.9.



**Figure 9.9:** Reaction mixture inside the micropump chamber after cavitation

Both Benedict's reagent and the glucose solution are transparent and clear when injected into the micropump chamber. Once the reaction between the fluids commences, there is a definite change in color observed in the micropump chamber. The color of the reaction mixture turns bluish green. As the reaction proceeds, the cavitation assisted mixing of the two liquids also results in the formation of a bluish green precipitate (as seen in Figure 9.4 when the liquids were mixed externally). The formation of the precipitate is also accompanied by the increase in turbidity inside the micropump chamber. Thus, the effectiveness of cavitation assisted mixing of the two fluids is qualitatively characterized by the increase in the turbidity of the reaction mixture with time, as observed at different stages of the reaction in Figure 9.8.

One of the advantages of this system is that, since the cavitation based mixing was carried out at low frequency, the collapse of the cavitation bubbles does not cause a significant damage to the micropump. At low frequency, without the formation of cavitation bubbles, the mixing is not sufficient. But since the system was not fully primed with chemicals, the formation of cavitation in this system is also assisted by the voids present in the chamber. The turbidity of the reaction mixture increases once the cavitation bubbles are formed at ~180 s. The initial mixing happens only at the interface of the two liquids. With sustained cavitation, the mixing is spread throughout the micropump chamber. (t = 210 – 400 s) It can be seen that during initial stages of micropumping, the mixing and the formation of the reaction mixture is influenced only at the inlet, and there is no fluid present at the outlet diffuser before the onset of the cavitation induced flow.



The collapse of the cavitation bubbles occurs at  $\sim 210$  s and this enhances the mixing further homogeneously inside the chamber. At the same time, the reaction mixture is also pushed out of the chamber due to the cavitation collapse, similar to the phenomenon, which was explained earlier in Chapter 4. Once the supercavitation sets in, the fluid is continuously pushed out of the chamber. This facilitates the flow for optical absorption measurement.

The absorption measurement is recorded simultaneously from the instant when the liquids enter the micropump chamber. The result of dynamic measurement of the optical absorption due to the mixture is as shown in Figure 9.10.

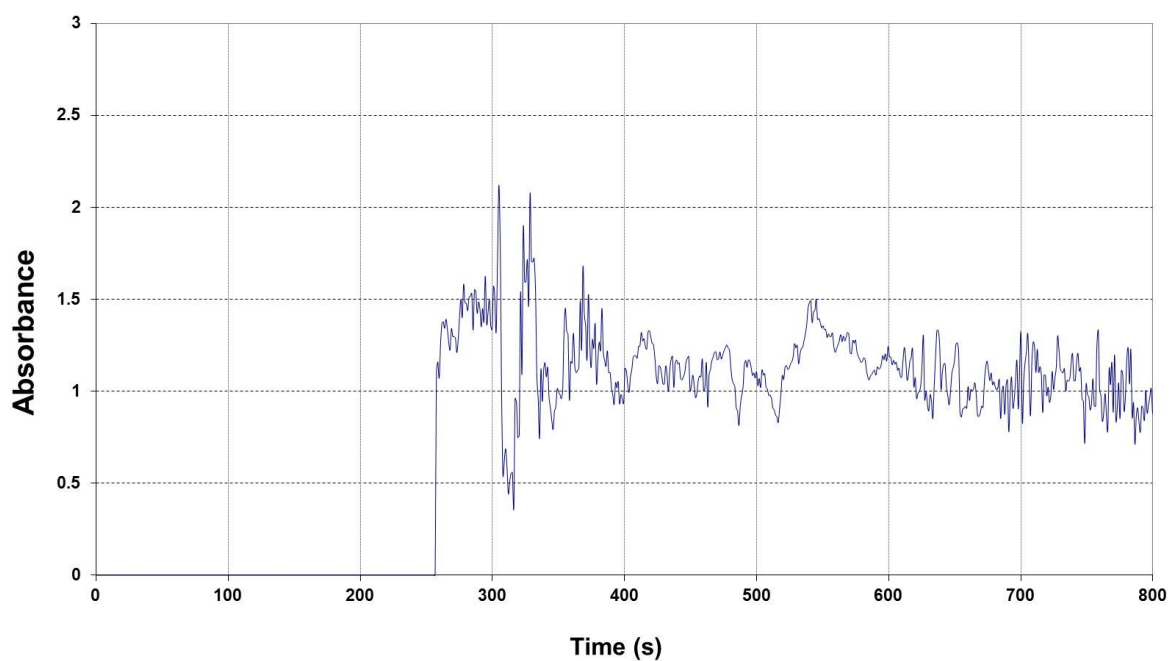


**Figure 9.10:** Variation of Optical absorption of the Benedict's reagent-sugar solution mixture

As expected, the absorbance of the reaction mixture is much higher than the individual specimens. The transportation of the reaction mixture and the precipitate from the micropump chamber is facilitated by the energy released in the process of collapse of the cavitation bubbles. Thus, as the reaction mixture is transported through the optical detection zone, turbidity of the precipitate causes an increase in the optical absorption. As seen in Figure 9.10, spike in the optical absorbance is observed when the reaction mixture enters the optical absorption zone. It can be observed that the total time taken for the increase in the optical absorption ( $\sim 250$  s) is the same time taken for the cavitation collapse inside the micropump chamber as seen in Figure 9.7 ( $\sim 240$  s), which thereby proves that the optical absorption is caused only due to the reaction mixture.

The outlet reservoir is as shown in Figure 9.11. It can be seen that there are two distinct colored layers of the solution at the outlet. The solid precipitate is from the Benedict's test performed externally, shown in Figure 9.4. This is because the cavitation causes the vaporization of the liquid inside the micropump and supercavitation induced flow pushes out only the fluid from the system, while the solute particles are not completely transported out of the system, and they remain immobilized along the sidewalls of the microfluidic channels and the tubes at the outlet. This shows that in order to carry out absorption detection of the reaction mixture, it is essential to integrate the optical detection system as close as possible to the micropump outlet.

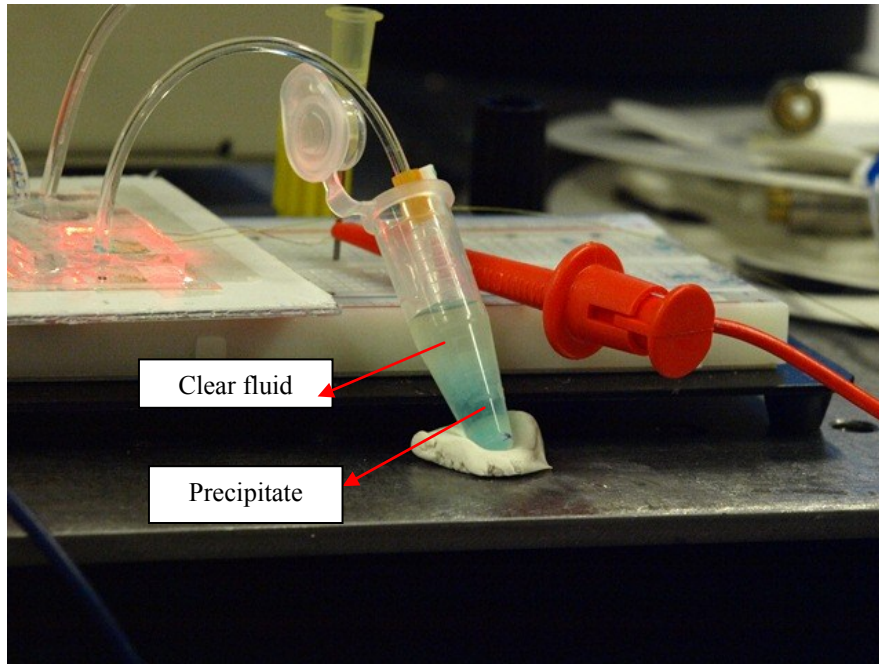


**Figure 9.11:** Distinct layers at the output reservoir after Benedict's test

From the optical absorbance, the absorption coefficients  $\alpha_{ab}$  for each specimen were calculated, using the formula

$$\alpha_{ab} = \beta_{ab} / [10 \log_{10}(e)] \quad \dots 9.5$$

where  $\beta_{ab}$  is the absorption loss in dB

The mean absorption coefficients of Benedict's solution, sugar solution and the reaction mixture is summarized in Table 9.3

Specimen used	Average absorbance	Loss in dB	Absorption coefficient (cm <sup>-1</sup> )
Glucose	0.08	0.8	18.42
Benedict's	0.27	2.7	62.1
Reaction mixture	1	10	230.25

**Table 9.3:** Absorption coefficient for the test specimens and the reaction mixture.

Thus, from the above experiment, the feasibility of carrying out real time biochemical detection on the proposed  $\mu$ TAS platform has been demonstrated successfully. The same setup can also be used for measurement of fluorescence based biointeractions, wherein, it is possible to input two biofluids (which, for fluorescence detection, would be antigen and fluorophore tagged antibody respectively). Upon mixing the two fluids inside the micropump, it is possible that the interaction of antigen and fluorophore-tagged antibody can be facilitated easily, thereby creating a more robust platform for fluorescence detection. Though the feasibility of fluorescence detection has not been explicitly demonstrated using the fabricated sensor, the successful previous studies on hybrid integrated fluorescence detections presented in Chapters 6 and 7 quells any possible doubts over the feasibility of carrying out fluorescence studies with this device as well.

#### **9.4 Conclusion**

In this chapter, the biophotonic testing carried out with the integrated  $\mu$ TAS and the results have been presented. Nano-integrated evanescence was demonstrated using gold colloid solutions and it was shown that the system is highly sensitive to evanescent detection. The immobilization of carbon nanotubes significantly increases the evanescence. Therefore, it is possible that the gold colloid can be used for tagging specific antigens, which can be used for carrying out highly sensitive evanescence detection.

The optical absorption was demonstrated using Benedict's test. The formation of the reaction mixture of Benedict's reagent with sugar solution is facilitated by cavitation induced mixing, and this was detected through change in the optical absorption. One of the real-time applications of this experiment is that using the Benedict's solution, it is possible to determine the presence of sugars in biological samples such as blood and urine. Thus, the fabricated device and the results of the test performed herein can be used for in-vivo determination of the level of diabetes in a person.

The experiments performed on the hybrid integrated  $\mu$ TAS are very unique for the following reasons:

- (i) The first of its kind of experiments to perform combined simultaneous optical detection, for absorption, evanescence, and fluorescence.
- (ii) The pioneering effort to carry out integrated microfluidic evanescence sensing with fluid actuation, and to implement the concept of NEET on the integrated platform.
- (iii) The first experimental work carried out by combining integrated optical detection with high efficiency mechanical valveless micropump based fluid actuation system.
- (iv) The first experimental work to exploit the chemical/biological application of micropump induced cavitation for integrated detection.
- (v) The first work to carry out the study of cavitation assisted chemical synthesis in a  $\mu$ TAS

### 10.1 Summary

In meeting the objectives towards realizing a fully integrated  $\mu$ TAS, this thesis was successful in designing, fabricating and testing valveless pump integrated and optical detection based  $\mu$ TAS for chemical and biological sensing applications. The main components of this  $\mu$ TAS are the Piezo-Actuated Valveless Micropump (PAVM), non-stagnant microfluidic system, and the optical detection system (which consists of waveguide based absorption, fluorescence and evanescence detection units). The  $\mu$ TAS was fabricated on a PDMS platform, and the optical waveguides fabricated using SU8-on-PDMS. The components were hybrid integrated so as to form a robust setup.

Microdiffusers/nozzles are essential components of a valveless micropump in order to create a unidirectional flow. The geometrical tuning of the microdiffuser presented in this work is very useful to enhance the efficiency of valveless micropump through improved flow rectification over a wide range of flow conditions. The flow behavior of different geometry tuned diffusers was studied through Finite Element Modeling (FEM). A test platform was developed for the measurement of pressure coefficients of the diffuser. The results of the experiments and the FEA are in very close agreement. One must necessarily take into consideration the effects of friction while designing the diffusers for valveless micropumps.

The performance of the valveless micropumps has been studied experimentally. The flow rate of the micropump was measured by varying the operating frequency, inlet suction head, and diaphragm deflection (controlled by the operating voltage). The driving frequency of the micropump is 2 Hz and a maximum flow rate of 55 nL/min was obtained for a deflection of 3.7  $\mu\text{m}$ , when the actuation voltage is 200 V<sub>pp</sub>. Pressure measurements were also carried out to measure the chamber pressure, and the maximum pressure is generated by the oscillating diaphragm at the driving frequency of 2 Hz, thereby supporting the results of the flow measurement. The study surface modifications of the micropump show that hydrophobic surfaces are very useful for obtaining higher flow rates than hydrophilic surfaces. However, with hydrophobic surface, there is also the problem of bubble generation at higher actuation frequencies, which lead to the study of the cavitation behavior in micropumps.

Extending the principles of macroscale cavitation, the static and dynamic pressure head relationships of the micropump were formulated in order to understand the cavitation behavior in valveless micropumps. Experimental investigation was carried out, by varying the dynamic parameters of the micropump and the inlet suction head. The results of the experiments, based on flow measurements, pressure measurements and flow visualization, identify four stages of micropump cavitation, namely, cavitation inception, cavitation growth, collapse of cavitation bubbles and supercavitation. Though cavitation is detrimental for the performance of the micropumps, several useful applications of this phenomenon have been explored in this work, such as high Reynolds number flow, fluid

separation, fluid mixing, cell lysing, blood fractionation, chamber cleaning, and chemical synthesis, among others.

As discussed in Chapter 1, research has been on-going to develop highly sensitive optical detection based sensors for real-time Point-of-Care applications. One must remember that in practical applications of a biosensor, the concentration of a particular enzyme present in a sample used for detection is of the order of a few ppm. With the optical detection platform developed herein, consisting of waveguide based absorbance, fluorescence and evanescence detection units, it is possible to carry out many different types of biological and chemical detections when integrated with the  $\mu$ TAS. While absorption detection can be used for the sensing of time-dependent biochemical reactions between two species, fluorescence detection can be used for detection of labeled antigen-antibody interactional studies and evanescence measurement can be used for high sensitive biomolecular and individual specimen detections. In order to realize evanescence based sensors for practical applications, it is essential to improve the sensitivity of the detection system. The integration of nanoparticles and nanofeatures with the evanescent waveguides is very useful for improving the sensitivity of the system, implemented through Nano-Enhanced Evanescence detection Technique (NEET) proposed herein. The NEET was demonstrated through Finite Difference Time Domain (FDTD) studies and experimentally verified by using Multiwalled Carbon Nanotubes (MWCNT) with SU8-on-Silica waveguides.

Significant focus has been applied to the integration of the subcomponents of the  $\mu$ TAS, based on different material platforms. On a truly hybrid integrated scale, this work



provides a comprehensive analysis and study of feasibilities of integrating the different components of  $\mu$ TAS. This includes the micropump, Spectrometer-on-Chip, and the three layer evanescence detection waveguide system with integrated microfluidics. The work presented on hybrid integration – development of external and the internal hybrid integration techniques for the integration of optics and microfluidics, the recirculating microfluidic platform for the hybrid integrated system, and selective micromirror integration with microfluidic channel surface for enhanced fluorescence detection - are simple, easy to implement, and robust.

Fabrication of the hybrid integrated  $\mu$ TAS was carried out on a PDMS platform with SU8 waveguides for the optical detection system. Finally, testing was carried out to demonstrate the integrated functionalities of the device and to explore some chemical and biological applications of the proposed device. NEET with integrated microfluidic actuation was demonstrated using gold nanoparticles on Carbon Nanotubes which were immobilized SU8 waveguides. The feasibility of integrated optical absorption was demonstrated by performing Benedict's test to determine the presence of glucose, wherein, cavitation assisted mixing was employed for facilitating the reaction between the sugar solution and Benedict's solution. Thus, the proposed  $\mu$ TAS is highly suitable for in-situ biomedical applications and Point-of-care testing.

## **10.2 Novelties of the present work**

The most significant novelties of the present work are:

- Geometry tuning of microdiffusers for valveless micropump applications
- Study of micropump performance through pressure measurement
- Research on cavitation in valveless micropumps.
- Implementation of cavitation and supercavitation phenomena for chemical and biological applications.
- Integration of optical absorption, fluorescence and evanescence detection on a single platform.
- Integration of Spectrometer-on-Chip for wavelength specific fluorescence detection.
- Nano-Enhanced Evanescence detection Technique (NEET) and integrated microfluidic evanescence detection.
- Integrated  $\mu$ TAS testing (Integrated Microelectromechanical-Microfluidic-Microphtonic-Biochemical testing)

## **10.3 Scope for further research and development**

Several interesting and significant results have been obtained from the present work. The integration of several modules also gives rise to the possibility of a wide variety of studies that can be carried out in each of the sub- $\mu$ TAS components. Based on the present thesis, some potential areas have been identified for further development. The following list is not exhaustive, but contains proposals for research that could improve the present design.

- *Diffusers for valveless micropumps*: The geometrical tuning method proposed in the present work is based on power law and is controlled by a single variable. However, there are several other microfabrication friendly geometrical modifications, such as the work presented by Izzo et al. 2007, that could be realized for improving the efficiency. Flow resistance through addition of obstacles in the diffusers also helps to increase the pressure coefficients (Lee et al., 2009), and the geometrical tuning techniques can be extended to these obstacles as well. The effect of friction has shown that it is possible to increase the diffuser coefficients significantly with additional flow resistance. One of the ideas to improve the diffuser efficiency through friction is to integrate nanoparticles with the diffusers. The addition of nanoparticles would increase the surface roughness, and depending on the distribution and localization of these nanoparticles, the frictional pressure drop could be increased or decreased in the diffusers to suit the micropump.

- *Micropump*: Though a lot of research has been carried out on valveless micropumps, the working of the micropump is not clearly understood. With powerful multiphysics tools presently available, fluid-structure interaction studies can be carried out to improve the understanding of operation of the micropumps. With piezoelectric actuation, methods to improve the flow rate include the integration of more than one actuator in the micropump. For example, it is possible to develop a micropumping system with parallel diaphragms oscillating out-of-phase. One can also design a micropump based on the arrangement of actuators in series for peristaltic micropumping.

- *Cavitation:* One of the important contributions of the present thesis is the study of cavitation in valveless micropumps. A more detailed study of the cavitation phenomenon would be useful in order to better understand the cavitation mechanism in micropumps. For example, it would be interesting to study the cavitation behavior with respect to the geometry of the micropump chamber, or the effect of the diffuser configurations on the cavitation pattern. Cavitation and supercavitation in valveless micropumps have many biological applications, which have not yet been fully explored in this work. Real-time clinical testing can also be carried out with the present cavitation system, as demonstrated with the blood fractionation experiment.

- *Recirculating microfluidic system:* Recirculating microfluidic systems offer a lot of advantages such as tunable flow structure and independence of many properties of liquids (Lin et al., 2008). In this work, the advantages of recirculating microfluidics have been exploited only for external hybrid integration to create enhanced biointeraction. However, this system can be also used with  $\mu$ TAS and microreactors in several clinical applications and bioassays (Lee et al., 2006). It is now possible to create a high Reynolds number microfluidic test bed for biological applications by combining supercavitation induced high velocity flow with the recirculating flow system.

- *Nano-integrated optics:* The integration of nanomaterials into the realm of photonic technology offers a lot of advantages in improving the detection sensitivity of the system as demonstrated with the evanescence measurement techniques. It is also possible that through advanced fabrication methods, other nano features can be fabricated on the

waveguide-based devices, such as nano-pillars or nano-cavities, which would significantly improve evanescence. Though in the present work only simple straight waveguides were used, the effect of NEET can also be studied on waveguides with different geometries. It is also possible that evanescence testing can be carried out on all directions if suitable microfabrication methods are used.

- *Monolithic integration:* The successful synthesis and testing of a hybrid integrated system provides confidence to carry out further miniaturization of the device for the realization of a chip-sized biosensor. With better alignment and packaging techniques, it is possible to fabricate a 3D  $\mu$ TAS, which helps in miniaturization of the system. It may also be possible to synthesize a well-packaged and fully automated  $\mu$ TAS, by integrating the external modules, such as high voltage amplifier and pressure sensors, on a circuit board base and monolithic integration of Spectrometer-on-Chip with the integrated optical-microfluidic setup.

- *Integrated  $\mu$ TAS applications:* Through the integration of the Spectrometer-on-Chip, it would be possible to carry out specific fluorescence detection of multiple wavelengths, which would enable the feasibility of multi-analyte detection with the  $\mu$ TAS. Also, one of the ideas to extend the application of the present device is to integrate other detection systems such as electrodes across the microfluidic channels, in addition to the optical waveguides. This opens up a lot of feasibility for carrying out biosensing based on the measurement of electrical signals, as demonstrated with bioresistance (Chandrasekaran et al., 2008), which can be used for measuring the activity of biological species such as Heat

Shock Proteins (HSP) useful for cancer detections. In this work, several real-time and Point-of-Care applications have been identified for the application of  $\mu$ TAS, which need to be tested.

#### **10.4 Contributions of the present work**

From the present thesis, the work on nano-integrated evanescence detection has been applied for U.S provisional patent:

*“VIS/IR compatible nano-enhanced evanescence-integrated technique (NEET) based microphotonic device and sample analysis system” U.S. Provisional Patent Application No. 61/242,858.*

The following articles have been published from the work carried out during the course of the PhD.

##### **10.4.1 Journal papers**

- [1] Arvind Chandrasekaran and Muthukumaran Packirisamy, “Geometrical Tuning of Microdiffusers/nozzles for Valveless Micropumps” *Journal of Micromechanics and Microengineering*, vol. 21(4), pp. 045035, 2011.
- [2] Arvind Chandrasekaran, Gino Rinaldi and Muthukumaran Packirisamy, “Label-free Detection of Enzymatic Interaction through Dynamic Behavior of Microstructures”,

- Journal of Advances in Engineering Sciences and Applied Mathematics*, vol. 2(1-2), pp. 1-7, 2011
- [3] Arvind Chandrasekaran and Muthukumaran Packirisamy, “Integrated Microfluidic Biophotonic Chip for laser induced fluorescence detection”, *Journal of Biomedical Microdevices*, vol. 12(5), pp. 923-933, 2010.
- [4] Arvind Chandrasekaran and Muthukumaran Packirisamy, “Experimental Investigation of Evanesence based Infrared biodetection technique for Micro-Total Analysis Systems ( $\mu$ TAS)” *Journal of Biomedical Optics*, Vol. 14, Issue 5, pp. 054050-054050-11, 2009.
- [5] Anas Alazzam, Arvind Chandrasekaran, Muthukumaran Packirisamy, Ion Stiharu, and Rama Bhat, “Bioaffinity limitations for anisotropically etched silicon microfluidics” *International Journal of Abrasive Technologies: Special issue*, vol. 3(2) pp. 122-132, 2010.
- [6] Arvind Chandrasekaran Shanmugasundaram Pakkiriswami, Jian Liang You, Ashwin Acharya, Muthukumaran Packirisamy and Denis Maxwell, “Bioresistive identification of Heat Shock Protein”, *Biomicrofluidics* vol. 2(3) pp 034102:1-10, 2008.
- [7] Arvind Chandrasekaran and Muthukumaran Packirisamy, “Enhanced bio-molecular interactions through re-circulating microflows” *Journal of Nanobiotechnology*, vol. 2(2) pp 39-46, 2008.
- [8] Arvind Chandrasekaran and Muthukumaran Packirisamy, “Microfluidic Lab-on-a-Chip system hybrid integrated with Spectrometer-on-Chip for fluorescence based biodetection” *PHOTONS*, vol. 6(1), pp 31-34, 2008.

- [9] Arvind Chandrasekaran and Muthukumaran Packirisamy, “Enhanced fluorescence based bio-detection through selective integration of reflectors in microfluidic Lab-On-a-Chip” *Sensor review*, vol. 28(1), pp 33-38, 2008. {Highly Commended Award Winner at the Literati Network Awards for Excellence 2009}
- [10] Arvind Chandrasekaran, Ashwin Acharya, Jian Liang You, Kim Young Soo, Muthukumaran Packirisamy, Ion Stiharu and Andre Darveau “Hybrid integrated Silicon microfluidic platform for fluorescence based biodetection” *Sensors- Special issue on optical biosensors*, vol. 7, pp. 1901-1915, 2007.
- [11] Arvind Chandrasekaran and Muthukumaran Packirisamy, “Absorption characterization of enzymatic reaction using optical microfluidics based intermittent flow microreactor system”, *Journal of Nanobiotechnology*, Vol. 153, n 6, pp. 137-143, 2006.
- [12] Arvind Chandrasekaran and Muthukumaran Packirisamy, “Absorption detection of enzymatic reaction using hybrid integrated biophotonic microfluidic system”, *PHOTONS*, vol. 4, Fall issue, pp 27-31, 2006.

#### **10.4.2 Conferences and presentations**

- [1] Arvind Chandrasekaran and Muthukumaran Packirisamy, “A Novel Integrated Biophotonic platform for Micro-Total Analysis Systems”, Photonics North 2010, Niagara, Canada.
- [2] Arvind Chandrasekaran and Muthukumaran Packirisamy, “Piezo-Actuated Valveless Micropumps for Micro-Total Analysis Systems” *ASME 7th International Symposium*



*on Fluid-Structure Interactions, Flow-Sound Interactions, and Flow-Induced Vibration & Noise*, Montreal, Canada, 2010

- [3] Arvind Chandrasekaran and Muthukumaran Packirisamy, “Integrated Micro-Total Analysis Systems for biophotonic enzymatic detections” SPIE Photonics West, San Francisco, 2010, Vol. 7555-49.
- [4] Arvind Chandrasekaran and Muthukumaran Packirisamy, “Integrated biophotonic Micro Total Analysis Systems for flow cytometry and particle detection” Photonics North, Quebec City, Proc. SPIE, Vol. 7386, 738603, 2009.
- [5] Arvind Chandrasekaran, Gino Rinaldi and Muthukumaran Packirisamy, “*Label free detection of enzymatic interaction through dynamic behavior of microstructures*”, International Conference on MEMS (ICMEMS 09), Chennai, India, 2009.
- [6] Arvind Chandrasekaran and Muthukumaran Packirisamy, “*Opto-microfluidic Lab-on-a-Chip for biodetection*”, International Conference on MEMS (ICMEMS 09), Chennai, India, 2009.
- [7] Arvind Chandrasekaran and Muthukumaran Packirisamy, “*Integrated Optical Microfluidic Lab-on-a-chip*” Proc. of SPIE, Vol. **7099**, Photonics North, Montreal, June 2008.
- [8] Arvind Chandrasekaran and Muthukumaran Packirisamy, “*Integrated Photonic Microsystem for biodetection with Spectrometer-on-Chip*” Annual Conference of the Canadian Institute for Photonics Innovations (CIPI), Banff, Alberta, May 2008.
- [9] Arvind Chandrasekaran, Abtin Nobahar and Muthukumaran Packirisamy, “*Finite Element Modeling of intermittent flow molecular sorting system for optical*

*microfluidics based bioassay*”, Photonics North, Ottawa, Proceedings of SPIE, Vol. 6796.

- [10] Arvind Chandrasekaran and Muthukumaran Packirisamy, “*Hybrid Integrated Photonic MEMS device for biodetection with Spectrometer-on-Chip*” Annual Conference of the Canadian Institute for Photonics Innovations (CIPI), Ottawa, 2007.
- [11] Arvind Chandrasekaran, Muthukumaran Packirisamy, Vijay Devabhaktuni, and Subhash Rakheja, “*A hybrid integrated microfluidic Lab-On-a-Chip on silicon platform for high throughput bio-assays*” International Conference on "Emerging Mechanical Technology - Macro to Nano" BITS Pilani, 2007, India.
- [12] Arvind Chandrasekaran, Vahe Nerguizian and Muthukumaran Packirisamy, “*Modeling of SOI based Photonic crystals for far IR applications*” IEEE International Symposium on Industrial Electronics (ISIE 2006), Montreal, 2006, vol. 4, pp 3387–3390.

A few more papers are in pipeline and will be submitted for publication soon...

## References

Abkarian, M., Viallat, A., 2008, "Vesicles and red blood cells in shear flow" *Soft Matter*, 2008, 4, pp. 653-657.

Abkarian, M., Faivre, M., and Viallat, A., 2007, "Swinging of Red Blood Cells under Shear Flow" *Physical Review Letters*, 98, pp. 188302 -188305

Acerro, M., Plaza, J., Esteve, J., Carmona, M., Marco, S. and Samitier, J., 1997, "Design of a modular micropump based on anodic bonding", *Journal of Micromechanics and Microengineering*, 7, pp. 179-182.

Agudelo, C., G., 2008, "Nonlinear control of electrostatic micromirrors" *Masters Thesis*, Ecole Polytechnique de Montreal, Canada

Ahmadian, M. and Mehrabian, A., 2006, "Design optimization by numerical characterization of fluid flow through the valveless diffuser micropumps", *Journal of Physics: Conference Series*, 2006, Institute of Physics Publishing, pp. 379-384.

Ahmed, R. and Jones, T., 2007, "Optimized liquid DEP droplet dispensing", *Journal of Micromechanics and Microengineering*, 17, pp. 1052-1058.

Ahn, C.H., Choi, J.W., Beaucage, G., Nevin, J., Lee, J.B., Puntambekar, A. and Lee, R., 2004, "Disposable Smart Lab on a Chip for Point-of-Care Clinical Diagnostics", *Proceedings of the IEEE*, 92(1), pp. 154-173.

Alderman, B., Mann, C., Oldfield, M. and Chamberlain, J., 2000, "Embedded mask using UV positive resist technology", *Journal of Micromechanics and Microengineering*, 10, pp. 334-336.

Alderman, B., Mann, C., Steenson, D. and Chamberlain, J., 2001, "Microfabrication of channels using an embedded mask in negative resist", *Journal of Micromechanics and Microengineering*, 11, pp. 703-705.

Alm, B., Imke, U., Knitter, R., Schygulla, U. and Zimmermann, S., 2008, "Testing and simulation of ceramic micro heat exchangers", *Chemical Engineering Journal*, 135, pp. 179-184.

Almeida, V.R., Panepucci, R.R. and Lipson, M., 2003, "Nanotaper for compact mode conversion", *Optics Letters*, 28(15), pp. 1302-1304.

Amirouche, F., Zhou, Y. and Johnson, T., 2009, "Current micropump technologies and their biomedical applications", *Microsystem Technologies*, 15(5), pp. 647-666.

Anderson, J.R., Chiu, D.T., Jackman, R.J., Cherniavskaya, O., McDonald, J.C., Wu, H., Whitesides, S.H. and Whitesides, G.M., 2000, "Fabrication of topologically complex

three-dimensional microfluidic systems in PDMS by rapid prototyping", *Anal.Chem.*, **72**(14), pp. 3158-3164.

Andersson, H., van der Wijngaart, W., Nilsson, P., Enoksson, P. and Stemme, G., 2001, "A valve-less diffuser micropump for microfluidic analytical systems", *Sensors & Actuators B: Chemical*, **72**(3), pp. 259-265.

Angelov, A. and Coulter, J., 2008, "The development and characterization of polymer microinjection molded gratings", *Polymer Engineering & Science*, **48**(11), pp.2169–2177.

ANSYS v12, <http://www.ansys.com>.

Armani, D.K. and Liu, C., 2000, "Microfabrication technology for polycaprolactone, a biodegradable polymer", *Journal of Micromechanics and Microengineering*, **10**, pp. 80-84.

Attia, U.M., Marson, S. and Alcock, J.R., 2009, "Micro-injection moulding of polymer microfluidic devices", *Microfluidics and Nanofluidics*, **7**(1), pp. 1-28.

Auroux, P.A., Iossifidis, D., Reyes, D.R. and Manz, A., 2002, "Micro total analysis systems. 2. Analytical standard operations and applications", *Analytical Chemistry*, **74**(12), pp. 2637-2652.

Ayliffe, H., Frazier, A. and Rabbitt, R., 1999, "Electric impedance spectroscopy using microchannels with integrated metal electrodes", *Journal of Microelectromechanical Systems*, **8**(1), pp. 50-57.

Azam, A., Boukadam, M., Izquierdo, R., Acharya, A. and Packirisamy, M., 2008. Integrated multifunctional fluorescence biosensor based on OLED technology, *Joint 6th International IEEE Northeast Workshop on Circuits and Systems and TAISA Conference, 2008.*, pp. 173-176.

Azarbadegan, A., Cortes-Quiroz, C., Eames, I. and Zangeneh, M., 2009, "Analysis of double-chamber parallel valveless micropumps", *Microfluidics and Nanofluidics*, **9**(2-3), pp. 171-180

Balslev, S., Bilenberg, B., Geschke, O., Jorgensen, A., Kristensen, A., Kutter, J., Mogensen, K. and Snakenborg, D., 2004, "Fully integrated optical system for lab-on-a-chip applications", *Micro Electro Mechanical Systems, 2004.17th IEEE International Conference on MEMS*, pp. 89-92.

Balslev, S., Jørgensen, A.M., Olsen, B.B., Mogensen, K.B., Mogensen, K.B., Snakenborg, D., Geschke, O., Kutter, J.P. and Kristensen, A., 2006, "Lab-on-a-chip with integrated optical transducers", *Lab on a Chip*, **6**(2), pp. 213-217.

- Barrios, C.A., Banuls, M.J., Gonzalez-Pedro, V., Gylfason, K.B., Sanchez, B., Griol, A., Maquieira, A., Sohlström, H., Holgado, M. and Casquel, R., 2008, "Label-free optical biosensing with slot-waveguides", *Optics Letters*, **33**(7), pp. 708-710.
- Bartholomeusz, D., Andrade, J. and Frazier, A., 2000, "Bioluminescent based chemchip for point-of-care diagnostics", *1st Annual International Conference On Microtechnologies in Medicine and Biology 2000*, pp. 602-606.
- Bashir, R., 2004, "BioMEMS: state-of-the-art in detection, opportunities and prospects", *Advanced Drug Delivery Reviews*, **56**(11), pp. 1565-1586.
- Becker, H. and Gartner, C., 2000, "Polymer microfabrication methods for microfluidic analytical applications", *Electrophoresis*, **21**(1),.
- Becker, H. and Heim, U., 2000, "Hot embossing as a method for the fabrication of polymer high aspect ratio structures", *Sensors & Actuators: A.Physical*, **83**(1-3), pp. 130-135.
- Beebe, D.J., Moore, J.S., Yu, Q., Liu, R.H., Kraft, M.L., Jo, B.H. and Devadoss, C., 2000, "Microfluidic tectonics: A comprehensive construction platform for microfluidic systems", *Proceedings of the National Academy of Sciences*, **97**(25), pp. 13488.
- Bettioli, A., Teo, E., Udalagama, C., Rao, S.V., van Kan, J., Shao, P. and Watt, F., 2006, "Integrating photonic and microfluidic structures on a device fabricated using proton beam writing", *Proceedings of SPIE*, **6186**, pp. 61860F-1.
- Bhagat, A.A.S., Jothimuthu, P., Pais, A. and Papautsky, I., 2007a, "Re-usable quick-release interconnect for characterization of microfluidic systems", *Journal of Micromechanics and Microengineering*, **17**, pp. 42-49.
- Bhagat, A.A.S., Jothimuthu, P. and Papautsky, I., 2007b, "Photodefinable polydimethylsiloxane (PDMS) for rapid lab-on-a-chip prototyping", *Lab on a Chip*, **7**(9), pp. 1192-1197.
- Bhushan, B., 2006. *Springer handbook of nanotechnology*. Springer Verlag.
- Bilenberg, B., Hansen, M., Johansen, D., Özkapici, V., Jeppesen, C., Szabo, P., Obieta, I., Arroyo, O., Tegenfeldt, J. and Kristensen, A., 2005, "Topas-based lab-on-a-chip microsystems fabricated by thermal nanoimprint lithography", *Journal of Vacuum Science & Technology B: Microelectronics and Nanometer Structures*, **23**, pp. 2944.
- Blair, S., and Chen, Y., 2001, "Resonant-enhanced evanescent-wave fluorescence biosensing with cylindrical optical cavities", *Applied Optics*, **40**, pp. 570-582.
- Borreman, A., Musa, S., Kok, A., Diemeer, M. and Driessen, A., 2002. "Fabrication of polymeric multimode waveguides and devices in SU-8 photoresist using selective polymerization", *Proc. Symp. IEEE/LEOS Benelux Chapter*, 2002, Citeseer, pp. 83-86.

Bourouina, T., Bossebuf, A. and Grandchamp, J.P., 1997, "Design and simulation of an electrostatic micropump for drug-delivery applications", *Journal of Micromechanics and Microengineering*, **7**, pp. 186-188.

Brennan, C., 1995, "Cavitation and bubble dynamics", Oxford University Press, New York, ISBN: 0-19-509409-3

Bruus, H., Brask, A. and Kutter, J.P., 2004, "Nanofluidic components for electrokinetic micropumps", *Advances in Natural Sciences*, **5**(4), pp. 423-430.

Burns, M.A., Johnson, B.N., Brahmasandra, S.N., Handique, K., Webster, J.R., Krishnan, M., Sammarco, T.S., Man, P.M., Jones, D. and Heldsinger, D., 1998, "An Integrated Nanoliter DNA Analysis Device", *Science*, **282**(5388), pp. 484.

Burns, M.A., Johnson, B.N., Brahmasandra, S.N., Handique, K., Webster, J.R., Krishnan, M., Sammarco, T.S., Man, P.M., Jones, D. and Heldsinger, D., 1998, "An Integrated Nanoliter DNA Analysis Device", *Science*, **282**(5388), pp. 484.

Carlborg, C., Gylfason, K., Kaźmierczak, A., Dortu, F., Polo, M.J.B., Catala, A.M., Kresbach, G., Sohlström, H., Moh, T. and Vivien, L., 2010, "A packaged optical slot-waveguide ring resonator sensor array for multiplex label-free assays in labs-on-chips", *Lab on a Chip*, **10**(3), pp. 281-290.

Ceriotti, L., Weible, K., De Rooij, N. and Verpoorte, E., 2003, "Rectangular channels for lab-on-a-chip applications", *Microelectronic Engineering*, **67**, pp. 865-871.

Chabinye, M.L., Chiu, D.T., McDonald, J.C., Stroock, A.D., Christian, J.F., Karger, A.M. and Whitesides, G.M., 2001, "An integrated fluorescence detection system in poly(dimethylsiloxane) for microfluidic applications", *Analytical Chemistry*, **73**(18), pp. 4491-4498.

Chandrasekaran, A., and Packirisamy, M., 2005, "MOEMS based integrated microfluidic fiber-optic waveguides for Biophotonic applications" Proceedings of SPIE, **5969**, pp. 178 – 186.

Chandrasekaran, A., Packirisamy, M., Stiharu, I. and Delage, A., 2006, "Hybrid bulk micro-machining process suitable for roughness reduction in optical MEMS devices", *International Journal of Manufacturing Technology and Management*, **9**(1), pp. 144-159.

Chandrasekaran, A. and Packirisamy, M., 2006, "Absorption detection of enzymatic reaction using optical microfluidics based intermittent flow microreactor system", *IEE proceeding of Nanobiotechnology*, **153**(6), pp. 137-143.

Chandrasekaran, A. and Packirisamy, M., 2007, "Wafer dicing strategic planning technique for clustered BioMEMS devices", *International Journal of Product Development*, **4**(3), pp. 296-309.

- Chandrasekaran, A., Acharya, A., You, J.L., Soo, K.Y., Packirisamy, M., Stiharu, I. and Darveau, A., 2007, "Hybrid Integrated Silicon Microfluidic Platform for Fluorescence Based Biodetection", *Sensors*, **7**, pp. 1901-1915.
- Chandrasekaran, A. and Packirisamy, M., 2008, "Enhanced fluorescence-based bio-detection through selective integration of reflectors in microfluidic lab-on-a-chip", *Sensor Review*, **28**(1), pp. 33-38.
- Chandrasekaran, A., Pakkiriswami, S., You, J.L., Acharya, A., Maxwell D., and Packirisamy, M., 2008, "Bioresistive identification of Heat Shock Protein", *Biomicrofluidics*, **2**(3) pp 034102:1-10.
- Chandrasekaran, A. and Packirisamy, M., 2009a, "Experimental investigation of evanescence-based infrared biodetection technique for micro-total-analysis systems", *Journal of Biomedical Optics*, **14**(05), pp. 054050.
- Chandrasekaran, A., and Packirisamy, M., 2009b, "Integrated biophotonic Micro Total Analysis Systems for flow cytometry and particle detection" Photonics North, Quebec City, *Proceedings of SPIE*, **7386**, 738603.
- Chandrasekaran, A., and Packirisamy, M., 2010, "Integrated microfluidic biophotonic chip for laser induced fluorescence detection", *Journal of Biomedical Microdevices*, **12**(5), pp. 923-933.
- Chandrasekaran, A., and Packirisamy, M., 2011, "Geometrical tuning of microdiffuser/nozzle for valveless micropumps" *Journal of Micromechanics and Microengineering*, **21**(4), pp. 45035-45050(16)
- Chandrasekaran, A., Rinaldi, G., and Packirisamy, M., 2011, "Label-free Detection of Enzymatic Interaction through Dynamic Behavior of Microstructures", *Journal of Advances in Engineering Sciences and Applied Mathematics*, **2**(1-2), pp. 1-7
- Chang, W.J., Akin, D., Sedlak, M., Ladisch, M.R. and Bashir, R., 2003, "Poly (dimethylsiloxane)(PDMS) and Silicon Hybrid Biochip for Bacterial Culture", *Biomedical Microdevices*, **5**(4), pp. 281-290.
- Chen, C.H. and Santiago, J.G., 2002, "A planar electroosmotic micropump", *Journal of Microelectromechanical Systems*, **11**(6), pp. 672-683.
- Chen, C. H., Cho, S.H., Tsai, F., Erten, A., and Lo, Y., 2009, "Microfluidic cell sorter with integrated piezoelectric actuator" *Journal of Biomedical Microdevices*, **11**(6) pp. 1223-1231
- Chen, J., Lin, Y. and Chen, G., 2007, "Fabrication of poly (methyl methacrylate) microfluidic chips by redox-initiated polymerization", *Electrophoresis*, **28**(16), pp. 2897-2903.

Chen, P.J., Shih, C.Y. and Tai, Y.C., 2006, "Design, fabrication and characterization of monolithic embedded parylene microchannels in silicon substrate", *Lab on a Chip*, **6**(6), pp. 803-810.

Chen, Y.T., Kang, S.W., Wu, L.C. and Lee, S.H., 2008, "Fabrication and investigation of PDMS micro-diffuser/nozzle", *Journal of Materials Processing Technology*, **198**(1-3), pp. 478-484.

Chung, A.J., Kim, D. and Erickson, D., 2008, "Electrokinetic microfluidic devices for rapid, low power drug delivery in autonomous microsystems", *Lab on a Chip*, **8**(2), pp. 330-338.

Cohen, D.A., Nolde, J.A., Wang, C.S., Skogen, E.J., Rivlin, A. and Coldren, L.A., 2004, "Biophotonic integrated circuits", *Proceedings of SPIE*, **5594**, pp. 81-93.

COMSOL v3.5a, <http://www.comsol.com>.

Cui, L., Zhang, T. and Morgan, H., 2002, "Optical particle detection integrated in a dielectrophoretic lab-on-a-chip.", *Journal of Micromechanics and Microengineering*, **12**(1), pp. 7-12.

Darhuber, A.A., Valentino, J.P., Troian, S.M. and Wagner, S., 2003, "Thermocapillary actuation of droplets on chemically patterned surfaces by programmable microheater arrays", *Journal of Microelectromechanical Systems*, **12**(6), pp. 873-879.

de Boer, M.J., Tjerkstra, R.W., Berenschot, J., Jansen, H.V., Burger, G., Gardeniers, J., Elwenspoek, M. and van den Berg, A., 2000, "Micromachining of buried micro channels in silicon", *Journal of Microelectromechanical Systems*, **9**(1), pp. 94-103.

de Jong, J., Geerken, M., Lammertink, R. and Wessling, M., 2007, "Porous microfluidic devices-Fabrication and applications", *Chemical Engineering & Technology*, **30**(3), pp. 309-315.

de la Fuente, P., Etxeberria, J., Berganzo, J., Arroyo, M., Castano, E., Gracia, F. and Ruano-Lopez, J., 2005, "A SU-8 microfluidic total analysis system integrating silicon photodiodes and buried waveguides", *Electron Devices, 2005 Spanish Conference on*, , pp. 461-464.

de Mello, A., 2002, "Plastic fantastic?", *Lab on a chip*, **2**(2), pp. 31N-36N.

De Vos, K., Bertolozzi, I., Bienstman, P., Baets, R. and Schacht, E., 2006, "Optical Biosensor based on Silicon-on-Insulator Microring Resonators for Specific Protein Binding Detection", *Proc.of Symposium IEEE/LEOS Benelux Chapter*, pp. 213-216.

Psaltis, D., Quake, S.R., and Yang, C., 2006, "Developing optofluidic technology through the fusion of microfluidics and optics", *Nature*, **442**, pp. 381-386.



Demierre, N., Braschler, T., Muller, R. and Renaud, P., 2008, "Focusing and continuous separation of cells in a microfluidic device using lateral dielectrophoresis", *Sensors & Actuators: B.Chemical*, **132**(2), pp. 388-396.

Densmore, A., Xu, D., Waldron, P., Janz, S., Cheben, P., Lapointe, J., Delge, A., Lamontagne, B., Schmid, J., and Post, E., 2006a, "A Silicon-on-Insulator Photonic Wire Based Evanescent Field Sensor", *Photonics Technology Letters, IEEE*, **18**, pp. 2520-2522.

Densmore, A., Xu, D., Waldron, P., Janz, S., Delage, A. and Cheben, P., 2006b, "Silicon Microphotonic Waveguides for Biological Sensing", *International Symposium on Biophotonics, Nanophotonics and Metamaterials, 2006*, pp. 15-18.

Deshpande, M., Gilbert, J., Bardell, R. and Forster, F., 1998, "Design analysis of non-moving-parts valves for micropumps", *Micro-Electro-Mechanical Systems (MEMS) 1998 (ASME DSC)*, **66**, pp. 153-8.

DiNello, R. and Dolphin, D., 1981, "Substituted hemins as probes for structure-function relationships in horseradish peroxidase", *Journal of Biological Chemistry*, **256**(13), pp. 6903.

Dittrich, P.S. and Manz, A., 2006, "Lab-on-a-chip: microfluidics in drug discovery", *Nature Reviews Drug Discovery*, **5**(3), pp. 210-218.

Dittrich, P.S., Tachikawa, K. and Manz, A., 2006, "Micro total analysis systems. Latest advancements and trends", *Analytical Chemistry*, **78**(12), pp. 3887-3908.

Eames, I., Azarbadegan, A. and Zanganeh, M., 2009, "Analytical Model of Valveless Micropumps", *Journal of Microelectromechanical Systems*, **18**(4), pp. 878-883.

Edwards, T.L., Mohanty, S.K., Edwards, R.K., Thomas, C.L. and Frazier, A.B., 2002, "Rapid micromold tooling for injection molding microfluidic components", *Sensors and materials*, **14**(3), pp. 167-178.

Ehrfeld W., Hessel V., Löwe H., 2000, "Microreactors, New Technology for Modern Chemistry", *Wiley-VCH Verlag GmbH*, Print ISBN 3-527-29590-9.

El-Sayed, I. H., Huang, X., and El-Sayed, M. A., 2005, "Surface Plasmon Resonance Scattering and Absorption of anti-EGFR Antibody Conjugated Gold Nanoparticles in Cancer Diagnostics: Applications in Oral Cancer" *Nano Letters*, **5** (5), pp. 829-834.

Emerson, D.R., Cieřlicki, K., Gu, X. and Barber, R.W., 2006, "Biomimetic design of microfluidic manifolds based on a generalised Murray's law", *Lab on a Chip*, **6**(3), pp. 447-454.

*Epigem Inc.*, United Kingdom, <http://www.epigem.co.uk>

- Fadl, A., Zhang, Z., Geller, S., Tölke, J., Krafczyk, M. and Meyer, D., 2009, "The effect of the microfluidic diodicity on the efficiency of valve-less rectification micropumps using Lattice Boltzmann Method", *Microsystem Technologies*, **15**(9), pp. 1379-1387.
- Fan, B., Song, G. and Hussain, F., 2005, "Simulation of a piezoelectrically actuated valveless micropump", *Smart Materials and Structures*, **14**, pp. 400 - 405.
- Fester, V., Mbiya, B., and Slatter P., 2008, "Energy losses of non-Newtonian fluids in sudden pipe contractions" *Chemical Engineering Journal*, **145**(1), pp. 57-63
- Fiedler, S., Shirley, S. G., Schnelle, T. and Fuhr, G., 1998, "Dielectrophoretic sorting of particles and cells in a microsystem", *Analytical Chemistry*, **70**(9), pp. 1909-1915.
- Fiorini, G.S. and Chiu, D.T., 2005, "Disposable microfluidic devices: fabrication, function, and application", *BioTechniques*, **38**(3), pp. 429-446.
- Fiorini, G.S., Yim, M., Jeffries, G.D.M., Schiro, P.G., Mutch, S.A., Lorenz, R.M. and Chiu, D.T., 2007, "Fabrication improvements for thermoset polyester (TPE) microfluidic devices", *Lab on a Chip*, **7**(7), pp. 923-926.
- Fortina, P., Surrey, S. and Kricka, L.J., 2002, "Molecular diagnostics: hurdles for clinical implementation", *Trends in molecular medicine*, **8**(6), pp. 264-266.
- Friis, P., Hoppe, K., Leistiko, O., Mogensen, K.B., Hübner, J. and Kutter, J.P., 2001, "Monolithic integration of microfluidic channels and optical waveguides in silica on silicon", *Applied Optics*, **40**(34), pp. 6246-6251.
- Fu, J. L., Fang, Q., Zhang, T., Jin, X.H. and Fang, Z.L., 2006, "Laser-induced fluorescence detection system for microfluidic chips based on an orthogonal optical arrangement", *Analytical Chemistry*, **78**(11), pp. 3827-3834.
- Fu, Y., Du, H., Huang, W., Zhang, S. and Hu, M., 2004, "TiNi-based thin films in MEMS applications: a review", *Sensors & Actuators: A.Physical*, **112**(2-3), pp. 395-408.
- Gamboa, A. R., Morris, C. J. and Forster, F.K., 2005, "Improvements in fixed-valve micropump performance through shape optimization of valves", *Journal of Fluids Engineering*, **127**, pp. 339.
- Gaudioso, J. and Craighead, H., 2002, "Characterizing electroosmotic flow in microfluidic devices", *Journal of Chromatography A*, **971**(1-2), pp. 249-253.
- Gerlach, T. and Wurmus, H., 1995, "Working principle and performance of the dynamic micropump", *Sensors & Actuators: A.Physical*, **50**(1-2), pp. 135-140.
- Gerlach, T., 1998, "Microdiffusers as dynamic passive valves for micropump applications", *Sensors & Actuators: A.Physical*, **69**(2), pp. 181-191.

Groß, G., Thelemann, T., Schneider, S., Boskovic, D. and Köhler, J., 2008, "Fabrication and fluidic characterization of static micromixers made of low temperature cofired ceramic (LTCC)", *Chemical Engineering Science*, **63**(10), pp. 2773-2784.

Guenat, O., Ghiglione, D., Morf, W. and de Rooij, N., 2001, "Partial electroosmotic pumping in complex capillary systems Part 2: Fabrication and application of a micro total analysis system ( $\mu$ TAS) suited for continuous volumetric nanotitrations", *Sensors & Actuators: B.Chemical*, **72**(3), pp. 273-282.

Günther, A., Khan, S.A., Thalmann, M., Trachsel, F. and Jensen, K.F., 2004, "Transport and reaction in microscale segmented gas-liquid flow", *Lab on a Chip*, **4**(4), pp. 278-286.

Haeberle, S. and Zengerle, R., 2007, "Microfluidic platforms for lab-on-a-chip applications", *Lab on a Chip*, **7**(9), pp. 1094-1110.

Hartnett, J. and Kostic, M., 1989, "Hast transfer to newtonian and non-newtonian fluids in rectangular ducts", *Advances in heat transfer*, **19**, pp. 347-356.

Hellman, A. N., Rau, K.R., Yoon,H.H., Bae, S., Palmer, J.F., Phillips,K.S, Allbritton, N.L., and Venugopalan,V., 2007, "Laser-Induced Mixing in Microfluidic Channels" *Analytical Chemistry*, **79** (12), pp 4484-4492

Hernandez, C., Bernard, Y. and Razek, A., 2010, "A global assessment of piezoelectric actuated micro-pumps", *The European Physical Journal Applied Physics*, **51**(2), pp. 20101 – 1:8.

Hessel, V., Hardt, S., Löwe, H. and Schönfeld, F., 2003, "Laminar mixing in different interdigital micromixers: I. Experimental characterization", *AIChE Journal*, **49**(3), pp. 566-577.

Hetsroni, G., Mosyak, A., Pogrebnyak, E. and Yarin, L., 2005, "Fluid flow in micro-channels", *International Journal of Heat and Mass Transfer*, **48**(10), pp. 1982-1998.

Homola, J., Yee, S.S. and Gauglitz, G., 1999, "Surface plasmon resonance sensors: review", *Sensors and Actuators B: Chemical*, **54**(1-2), pp. 3-15.

Horváth, R., Lindvold, L. and Larsen, N., 2002, "Reverse-symmetry waveguides: theory and fabrication", *Applied Physics B: Lasers and Optics*, **74**(4), pp. 383-393.

Hossain, S., 2010, "Microfluidic-Microstructure Interaction Study under Oscillating Flows: Design, Modeling, Testing & Verifications", *Masters Thesis, Concordia University, Montreal, Canada*.

Hsu, Y.C., Hsu, J.L. and Le, N.B., 2009, "An experimental and numerical investigation into the effects of the PZT actuator shape in polymethylmethacrylate (PMMA) peristaltic micropumps", *Microsystem Technologies*, **15**(4), pp. 565-571.

Hu, X., Bessette, P.H., Qian, J., Meinhart, C.D., Daugherty, P.S. and Soh, H.T., 2005, "Marker-specific sorting of rare cells using dielectrophoresis", *Proceedings of the National Academy of Sciences*, **102**(44), pp. 15757.

Huang, L.R., Cox, E.C., Austin, R.H. and Sturm, J.C., 2004, "Continuous particle separation through deterministic lateral displacement", *Science*, **304**(5673), pp. 987.

Huh, D., Gu, W., Kamotani, Y., Grotberg, J.B. and Takayama, S., 2005, "Review: Microfluidics for flow cytometric analysis of cells and particles", *Physiological measurement*, **26**, pp. R73-R98.

Huh, Y.S., Chung, A.J., Cordovez, B. and Erickson, D., 2009, "Enhanced on-chip SERS based biomolecular detection using electrokinetically active microwells", *Lab on a Chip*, **9**(3), pp. 433.

Irawan, R., Tay, C.M., Tjin, S.C. and Fu, C.Y., 2006, "Compact fluorescence detection using in-fiber microchannels-its potential for lab-on-a-chip applications", *Lab on a chip*, **6**(8), pp. 1095-1098.

Izzo, I., Accoto, D., Menciassi, A., Schmitt, L. and Dario, P., 2007, "Modeling and experimental validation of a piezoelectric micropump with novel no-moving-part valves", *Sensors and Actuators A: Physical*, **133**(1), pp. 128-140.

Jackman, R.J., Floyd, T.M., Ghodssi, R., Schmidt, M.A. and Jensen, K.F., 2001, "Microfluidic systems with on-line UV detection", *Journal of Micromechanics and Microengineering*, **11**, pp. 263-269.

Jacobson, S.C. and Ramsey, J.M., 1996, "Integrated microdevice for DNA restriction fragment analysis", *Anal. Chem*, **68**(5), pp. 720-723.

Jacobson, S.C., Hergenroder, R., Koutny, L.B., Warmack, R. and Ramsey, J.M., 1994, "Effects of injection schemes and column geometry on the performance of microchip electrophoresis devices", *Analytical Chemistry*, **66**(7), pp. 1107-1113.

Jacobson, S.C., Hergenroder, R., Koutny, L.B., Warmack, R. and Ramsey, J.M., 1994, "Effects of injection schemes and column geometry on the performance of microchip electrophoresis devices", *Analytical Chemistry*, **66**(7), pp. 1107-1113.

Jakeway, S.C., de Mello, A.J. and Russell, E.L., 2000, "Miniaturized total analysis systems for biological analysis", *Fresenius' journal of analytical chemistry*, **366**(6-7), pp. 525-539.

Jang, L.S., Li, Y.J., Lin, S.J., Hsu, Y.C., Yao, W.S., Tsai, M.C. and Hou, C.C., 2007, "A stand-alone peristaltic micropump based on piezoelectric actuation", *Biomedical Microdevices*, **9**(2), pp. 185-194.

- Janz, S., Balakrishnan, A., Charbonneau, S., Cheben, P., Cloutier, M., Delage, A., Dossou, K., Erickson, L., Gao, M. and Krug, P., 2004, "Planar waveguide echelle gratings in silica-on-silicon", *Photonics Technology Letters, IEEE*, **16**(2), pp. 503-505.
- Jeetender, A., Stiharu, I. and Packirisamy, M., 2005. "Micro-opto mechanical biosensors for enzymatic detection", *Proceedings of SPIE*, **5969**, pp. 59690V.
- Jokerst, J., Jacobson, J.W., Bhagwandin, B., Floriano, P.N., Christodoulides, N., McDevitt, J. T., 2010, "Programmable Nano-Bio-Chip Sensors: Analytical Meets Clinical", *Analytical Chemistry*, **82**(5), pp. 1571–1579.
- Jiang, L., Gerhardt, K.P., Myer, B., Zohar, Y. and Pau, S., 2008, "An SU-8 based fluidic immuno-spectroscopic lab-on-a-chip for rapid quantitative detection of biomolecules", *Micro Electro Mechanical Systems, 2008.MEMS 2008.IEEE 21st International Conference on*, , pp. 204-207.
- Jiang, L., Gerhardt, K.P., Myer, B., Zohar, Y. and Pau, S., 2008, "Evanescent-wave spectroscopy using an SU-8 waveguide for rapid quantitative detection of biomolecules", *Journal of Microelectromechanical Systems*, **17**(6), pp. 1495-1500.
- Jiang, X., Zhou, Z., Huang, X., Li, Y., Yang, Y. and Liu, C., 1998, "Micronozzle/diffuser flow and its application in micro valveless pumps", *Sensors & Actuators: A.Physical*, **70**(1-2), pp. 81-87.
- Jones, T., Gunji, M., Washizu, M. and Feldman, M., 2001, "Dielectrophoretic liquid actuation and nanodroplet formation", *Journal of Applied Physics*, **89**, pp. 1441.
- Jugessur, A., Dou, J., Aitchison, J., De La Rue, R. and Gnan, M., 2009, "A photonic nano-Bragg grating device integrated with microfluidic channels for bio-sensing applications", *Microelectronic Engineering*, **86**(4-6), pp. 1488-1490.
- Katoh, T., Nishi, N., Fukagawa, M., Ueno, H. and Sugiyama, S., 2001, "Direct writing for three-dimensional microfabrication using synchrotron radiation etching", *Sensors & Actuators: A.Physical*, **89**(1-2), pp. 10-15.
- Ke, C., Kelleher, A.M., Berney, H., Sheehan, M. and Mathewson, A., 2007, "Single step cell lysis/PCR detection of Escherichia coli in an independently controllable silicon microreactor", *Sensors & Actuators: B.Chemical*, **120**(2), pp. 538-544.
- Kenis, P.J.A., Ismagilov, R.F., Takayama, S., Whitesides, G.M., Li, S. and White, H.S., 2000, "Fabrication inside microchannels using fluid flow", *Accounts of Chemical Research*, **33**(12), pp. 841-848.
- Kim, D. and Beebe, D.J., 2007, "A bi-polymer micro one-way valve", *Sensors & Actuators: A.Physical*, **136**(1), pp. 426-433.

- Kim, J. and Gale, B.K., 2008, "Quantitative and qualitative analysis of a microfluidic DNA extraction system using a nanoporous AlO<sub>x</sub> membrane", *Lab on a Chip*, **8**(9), pp. 1516-1523.
- Kim, P., Kwon, K.W., Park, M.C., Lee, S.H., Kim, S.M. and Suh, K.Y., 2008, "Soft lithography for microfluidics: a review", *Biochip Journal*, **2**, pp. 1-11.
- Koch, M., Evans, A. and Brunnschweiler, A., 1998a, "The dynamic micropump driven with a screen printed PZT actuator", *Journal of Micromechanics and Microengineering*, **8**, pp. 119-122.
- Koch, M., Harris, N., Evans, A.G.R., White, N.M. and Brunnschweiler, A., 1998b, "A novel micromachined pump based on thick-film piezoelectric actuation", *Sensors & Actuators: A.Physical*, **70**(1-2), pp. 98-103.
- Kohl, M., Abdel-Khalik, S., Jeter, S. and Sadowski, D., 2005, "An experimental investigation of microchannel flow with internal pressure measurements", *International Journal of Heat and Mass Transfer*, **48**(8), pp. 1518-1533.
- Krawczyk, S., 2003, "Discussion on optical integration in Lab-on-a-Chip microsystems for medical diagnostics", *Physica Status Solidi- Conference*, pp. 998-1012.
- Krishnamurthy, S. and Peles Y., 2010, "Flow boiling on micro pin fins entrenched inside a microchannel — flow patterns and bubble dynamics," *Journal of Heat Transfer*, **132**(4), 041007:1-10.
- Krüger, J., Singh, K., O'Neill, A., Jackson, C., Morrison, A. and O'Brien, P., 2002, "Development of a microfluidic device for fluorescence activated cell sorting", *Journal of Micromechanics and Microengineering*, **12**, pp. 486-494.
- Krulevitch, P., Benett, W., Hamilton, J., Maghribi, M. and Rose, K., 2002, "Polymer-Based Packaging Platform for Hybrid Microfluidic Systems", *Journal of Biomedical Microdevices*, **4**(4), pp. 301-308.
- Kuiper, G., 1981, "Cavitation inception on ship propeller models", *PhD Thesis*, Delft University of Technology, Netherlands.
- Kuswandi, B., Huskens, J. and Verboom, W., 2007, "Optical sensing systems for microfluidic devices: a review", *Analytica Chimica Acta*, **601**(2), pp. 141-155.
- Lagally, E.T., Medintz, I., and Mathies, R.A., 2001, "Single-Molecule DNA Amplification and Analysis in an Integrated Microfluidic Device", *Analytical Chemistry*, **73** (3), pp 565–570.
- Lai, S., Wang, S., Luo, J., Lee, L.J., Yang, S.T. and Madou, M.J., 2004, "Design of a compact disk-like microfluidic platform for enzyme-linked immunosorbent assay", *Anal.Chem*, **76**(7), pp. 1832-1837.

- Landsberger, L., Naseh, S., Kharizi M., and Pranjape M., "On hillocks generated during anisotropic etching of silicon in TMAH", *Journal of Microelectromechanical Systems*, **5**(2), pp 106-116, 1996.
- Laser, D. and Santiago, J., 2004, "A review of micropumps", *Journal of Micromechanics and Microengineering*, **14**(6), pp. 35–64.
- Lauks I. , and Maczuszenko A., 2010, "Diagnostic devices incorporating fluidics and method of manufacture", *United States Patent Application 20100321004*, .
- Lee, C.J., Sheen, H.J., Tu, Z.K., Lei, U. and Yang, C.Y., 2009, "A study of PZT valveless micropump with asymmetric obstacles", *Microsystem Technologies*, **15**(7), pp. 993-1000.
- Lee G.B., Lin C.H., and Chang G.L., 2003a, "Micro flow cytometers with buried SU-8/SOG optical waveguides", *Sensors and Actuators A* **103**, pp. 165–170.
- Lee, J.N., Park, C. and Whitesides, G.M., 2003, "Solvent compatibility of poly (dimethylsiloxane)-based microfluidic devices", *Analytical Chemistry*-, **75**(23), pp. 6544-6554.
- Lee, L., Berger, S., Liepmann, D. and Pruitt, L., 1998, "High aspect ratio polymer microstructures and cantilevers for bioMEMS using low energy ion beam and photolithography", *Sensors & Actuators: A.Physical*, **71**(1-2), pp. 144-149.
- Lee, S. H., Lee, C.S., Kim, B.G. and Kim, Y.K., 2008, "An integrated microfluidic chip for the analysis of biochemical reactions by MALDI mass spectrometry", *Biomedical Microdevices*, **10**(1), pp. 1-9.
- Lee, H. H, Smoot, J., McMurray, Z., Stahl, D. A, Yager P., 2006, "Recirculating flow accelerates DNA microarray hybridization in a microfluidic device", *Lab-on-a-Chip*, **6**(9), pp.1163-1170.
- Leeds, A., Van Keuren, E., Durst, M., Schneider, T., Currie, J. and Paranjape, M., 2004, "Integration of microfluidic and microoptical elements using a single-mask photolithographic step", *Sensors and Actuators A: Physical*, **115**(2-3), pp. 571-580.
- Leistiko, O. and Jensen, P.F., 1998, "Integrated bio/chemical microsystems employing optical detection: the clip-on", *Journal of Micromechanics and Microengineering*, **8**(2), pp. 148-150.
- Leung, C., Xirouchaki, C., Berovic, N. and Palmer, R.E., 2004, "Immobilization of protein molecules by size-selected metal clusters on surfaces", *Advanced Materials*, **16**(3), pp. 223-226.
- Li, P.C.H., 2006. "Microfluidic lab-on-a-chip for chemical and biological analysis and discovery", CRC, ISBN: 1574445723

- Li, S. and Chen, S., 2003, "Analytical analysis of a circular PZT actuator for valveless micropumps", *Sensors and Actuators A*, **104**(2), pp. 151-161.
- Li, X., Yu, X., Zhang, D., Li, Z. and Xu, W., 2007 "A Micro Diffuser/Nozzle Pump with Fins on the Sidewall", *Solid-State Sensors, Actuators and Microsystems Conference 2007*, pp. 2207-2210.
- Lien, V., Berdichevsky, Y., Lo, Y.H., Khandurina, J. and Guttman, A., 2003, "Monolithic photonics-microfluidics integration for micrototal analysis systems", *Conference on Lasers and Electro-Optics, CLEO'03.*, pp. 4.
- Lin, R. and Burns, M.A., 2005, "Surface modified polyolefin microfluidic devices for liquid handling", *Journal of Micromechanics and Microengineering*, **15**, pp. 2156-2162.
- Lin, C.M., Lai, Y.S., Liu, H.P., and Wo, A.M., 2008, "Microvortices and recirculating flow generated by an oscillatory microplate for microfluidic applications" *Applied Physics Letters*, **93** (13), pp. 133503 - 133506
- Lin, V.S.Y., Motesharei, K., Dancil, K.P.S., Sailor, M.J. and Ghadiri, M.R., 1997, "A porous silicon-based optical interferometric biosensor", *Science*, **278**(5339), pp. 840.
- Liou, A.C. and Chen, R.H., 2006, "Injection molding of polymer micro-and sub-micron structures with high-aspect ratios", *The International Journal of Advanced Manufacturing Technology*, **28**(11), pp. 1097-1103.
- Liu, J., Yap, Y.F. and Nguyen, N.T., 2009, "Behavior of microdroplets in diffuser/nozzle structures", *Microfluidics and Nanofluidics*, **6**(6), pp. 835-846.
- Lomel S., Falk L., Commenge J. M., Houzelot J. L., and Ramidani K., 2006, "THE MICROREACTOR: A Systematic and Efficient Tool for the Transition from Batch to Continuous Process?", *Chemical Engineering Research and Design*, **84**(A5); pp. 363–369.
- Lu, B., Iwuoha, E.I., Smyth, M.R. and O'Kennedy, R., 1997, "Effects of acetonitrile on horseradish peroxidase (HRP)-anti HRP antibody interaction", *Biosensors & bioelectronics*, **12**(7), pp. 619-625.
- Lu, H., Schmidt, M.A. and Jensen, K.F., 2001, "Photochemical reactions and on-line UV detection in microfabricated reactors", *Lab on a Chip*, **1**(1), pp. 22-28.
- Luff, B., Harris, R., Wilkinson, J., Wilson, R. and Schiffrin, D., 1996, "Integrated-optical directional coupler biosensor", *Optics Letters*, **21**(8), pp. 618-620.
- Luo, J., Fu, Y., Li, Y., Du, X., Flewitt, A., Walton, A. and Milne, W., 2009, "Moving-part-free microfluidic systems for lab-on-a-chip", *Journal of Micromechanics and Microengineering*, **19**(5), pp. 4001.



Mala, M., 1999, "Flow characteristics of water in microtubes", *International Journal of Heat and Fluid Flow*, **20**(2), pp. 142-148.

Manz, A., Graber, N. and Widmer, H., 1990, "Miniaturized total analysis systems: A novel concept for chemical sensors", *Sensors and Actuators B*, **1**(1), pp. 244-248.

Mazurczyk, R., Vieillard, J., Bouchard, A., Hannes, B. and Krawczyk, S., 2006, "A novel concept of the integrated fluorescence detection system and its application in a lab-on-a-chip microdevice", *Sensors and actuators.B, Chemical*, **118**(1-2), pp. 11-19.

McDonald, J.C., Duffy, D.C., Anderson, J.R., Chiu, D.T., Wu, H., Schueller, O.J.A. and Whitesides, G.M., 2000, "Fabrication of microfluidic systems in poly (dimethylsiloxane)", *Electrophoresis*, **21**(1), pp. 27-40.

Medoro, G., Manaresi, N., Leonardi, A., Altomare, L., Tartagni, M., Guerrieri, R., Biosystems, S. and Bologna, I., 2003, "A lab-on-a-chip for cell detection and manipulation", *Sensors Journal, IEEE*, **3**(3), pp. 317-325.

Melles Griot, 2051, Palomar Airport Road, 200, Carlsbad, California, <http://www.mellesgriot.com>

Metz, S., Bertsch, A., Bertrand, D. and Renaud, P., 2004, "Flexible polyimide probes with microelectrodes and embedded microfluidic channels for simultaneous drug delivery and multi-channel monitoring of bioelectric activity", *Biosensors and Bioelectronics*, **19**(10), pp. 1309-1318.

Micronics Inc., <http://www.micronics.net>

Minas, G., Wolffenbuttel, R.F. and Correia, J.H., 2005, "A lab-on-a-chip for spectrophotometric analysis of biological fluids", *Lab on a chip*, **5**(11), pp. 1303-1309.

Mishra C., and Peles, Y., 2005a, "Cavitation in MicroElectroMechanical Systems (MEMS): Importance, Deviations From Conventional Scale, and Preliminary Results", *ASME 2005 Fluids Engineering Division Summer Meeting, Houston, Proceedings of ASME*, **2**, pp. 581-586.

Mishra C., and Peles, Y., 2005b, "Cavitation in flow through a micro-orifice inside a silicon microchannel", *Physics of Fluids*, **17**(1), pp. 013601:1-15.

Mishra, C. and Peles, Y., 2006, "An experimental investigation of hydrodynamic cavitation in micro-venturis," *Physics of Fluids*, **18**(10), 103603:1-5.

Mitchell, M., Kim, D. P. and Kenis, P., 2006, "Ceramic microreactors for on-site hydrogen production", *Journal of Catalysis*, **241**(2), pp. 235-242.

Mogensen, K. B., El-Ali, J., Wolff, A. and Kutter, J.P., 2003, "Integration of polymer waveguides for optical detection in microfabricated chemical analysis systems", *Applied Optics*, **42**(19), pp. 4072-4079.

- Momeni, B., Huang, J., Soltani, M., Askari, M., Mohammadi, S., Rakhshandehroo, M. and Adibi, A., 2006, "Compact wavelength demultiplexing using focusing negative index photonic crystal superprisms", *Optics Express*, **14**(6), pp. 2413-2422.
- Monkkonen, K., Pakkanen, T.T., Hietala, J., Paakkonen, E.J., Paakkonen, P., Jaaskelainen, T. and Kaikuranta, T., 2002, "Replication of sub-micron features using amorphous thermoplastics", *Polymer Engineering & Science*, **42**(7), pp. 1600–1608.
- Morris, C.J. and Forster, F.K., 2000, "Optimization of a circular piezoelectric bimorph for a micropump driver", *Journal of Micromechanics and Microengineering*, **10**(3), pp. 459-465.
- Neale, S.L., MacDonald, M.P., Dholakia, K. and Krauss, T.F., 2005, "All-optical control of microfluidic components using form birefringence", *Nature Materials*, **4**(7), pp. 530-533.
- Nguyen, N.T. and Huang, X., 2001, "Miniature valveless pumps based on printed circuit board technique", *Sensors and Actuators A: Physical*, **88**(2), pp. 104-111.
- Nguyen, N.T., Lam, Y.C., Ho, S.S. and Low, C.L.N., 2008, "Improvement of rectification effects in diffuser/nozzle structures with viscoelastic fluids", *Biomicrofluidics*, **2**, pp. 034101.
- Ogawa, J., Kanno, I., Kotera, H., Wasa, K. and Suzuki, T., 2009, "Development of liquid pumping devices using vibrating microchannel walls", *Sensors & Actuators: A.Physical*, .
- Olsson, A. and Stemme, G., 1996, "Diffuser-element design investigation for valve-less pumps", *Sensors and Actuators A: Physical*, **57**(2), pp. 137-143.
- Olsson, A., 1998, "Valve-less diffuser micropumps", *PhD Thesis, Royal Institute of Technology, Stockholm, Sweden*.
- Olsson, A., Enoksson, P., Stemme, G. and Stemme, E., 1997, "Micromachined flat-walled valveless diffuser pumps", *Journal of Microelectromechanical Systems*, **6**(2), pp. 161-166.
- Olsson, A., Stemme, G. and Stemme, E., 1995, "A valve-less planar fluid pump with two pump chambers", *Sensors & Actuators: A.Physical*, **47**(1-3), pp. 549-556.
- Olsson, A., Stemme, G. and Stemme, E., 2000, "Numerical and experimental studies of flat-walled diffuser elements for valve-less micropumps", *Sensors & Actuators: A.Physical*, **84**(1-2), pp. 165-175.
- Olsson, A., Enoksson, P., Stemme, G. and Stemme, E., 1996. An improved valve-less pump fabricated using deep reactive ionetching, *The Ninth Annual International Workshop on Micro Electro Mechanical Systems, 1996, MEMS'96, Proceedings.'An Investigation of Micro Structures, Sensors, Actuators, Machines and Systems'. IEEE, 1996*, pp. 479-484.

Ong, B.H., Yuan, X., and Tjin, S.C., 2006, "Adjustable refractive index modulation for a waveguide with SU-8 photoresist by dual-UV exposure lithography", *Applied Optics*, **45**, pp. 8036-8039.

Ory, E., Yuan, H., Prosperetti, A., Popinet, S. and Zaleski, S., 2000, "Growth and collapse of a vapor bubble in a narrow tube", *Physics of Fluids*, **12**, pp. 1268.

Pabit, S. A., and Hagen, S., 2002, "Laminar-Flow Fluid Mixer for Fast Fluorescence Kinetics Studies", *Biophysical Journal*, **83**(2872), pp. 2872 - 2878.

Packirisamy, M., 1990, "Prediction of cavitation behavior of pumps", *Masters thesis*, Indian Institute of Technology, Madras, India.

Packirisamy, M., and Chandrasekaran, A., 2010, "Nano-Enhanced Evanescence integrated Technique (NEET) based microphotonic device and sample analysis system" Provisional patent Application number PCT/CA2010/001429.

Packirisamy, M., Balakrishnan, A., "Planar waveguide based grating device and spectrometer for species-specific wavelength detection" *U.S Patent No. 7324195*, January 2008

Pal, R., Yang, M., Lin, R., Johnson, B., Srivastava, N., Razzacki, S., Chomistek, K., Heldsinger, D., Haque, R. and Ugaz, V., 2005, "An integrated microfluidic device for influenza and other genetic analyses", *Lab on a Chip*, **5**(10), pp. 1024-1032.

Pan, L., Ng, T., Wu, X. and Lee, H., 2003, "Analysis of valveless micropumps with inertial effects", *Journal of Micromechanics and Microengineering*, **13**, pp. 390.

Park, J.Y. and Kricka, L.J., 2007, "Prospects for nano- and microtechnologies in clinical point-of-care testing", *Lab on a chip*, **7**(5), pp. 547-549.

Pattekar, A.V. and Kothare, M.V., 2004, "A microreactor for hydrogen production in micro fuel cell applications", *Journal of Microelectromechanical Systems*, **13**(1), pp. 7-18.

Pavri, S., 1992, "Essentials of Diabetes Mellitus and its treatment with Homeopathy" *Jain publishers Ltd., ISBN 81-7021-639-7*.

Peng, X., Peterson, G. and Wang, B., 1994, "Frictional flow characteristics of water flowing through rectangular microchannels", *Experimental Heat Transfer*, **7**(4), pp. 249-264.

Perozziello, G., Bundgaard, F. and Geschke, O., 2008, "Fluidic interconnections for microfluidic systems: a new integrated fluidic interconnection allowing plug 'n' play functionality", *Sensors & Actuators: B.Chemical*, **130**(2), pp. 947-953.

*Piezo Systems Inc.*, <http://www.piezo.com>

Pollack, M.G., Shenderov, A.D. and Fair, R.B., 2002, "Electrowetting-based actuation of droplets for integrated microfluidics", *Lab on a chip*, **2**(2), pp. 96-101.

Pranov, H., Rasmussen, H.K., Larsen, N.B. and Gadegaard, N., 2006, "On the injection molding of nanostructured polymer surfaces", *Polymer Engineering & Science*, **46**(2), pp.160-171.

Prieto, F., Sepulveda, B., Calle, A., Llobera, A., Domínguez, C. and Lechuga, L.M., 2003, "Integrated Mach-Zehnder interferometer based on ARROW structures for biosensor applications", *Sensors and Actuators B: Chemical*, **92**(1-2), pp. 151-158.

Prieto, F., Sepulveda, B., Calle, A., Llobera, A., Dominguez, C., Abad, A., Montoya, A. and Lechuga, L., 2003, "An integrated optical interferometric nanodevice based on silicon technology for biosensor applications", *Nanotechnology*, **14**(8), pp. 907-912.

*Protolyne microfluidic process technology*, Micralyne Inc., Edmonton, Alberta, Canada.

Quake, S. R., and Scherer A., 2000, "From Micro- to Nanofabrication with Soft Materials" *Science*, **290**, pp.1536-1540

Reyes, D.R., Iossifidis, D., Auroux, P.A. and Manz, A., 2002, "Micro total analysis systems. 1. Introduction, theory, and technology", *Analytical Chemistry*, **74**(12), pp. 2623-2636.

Rosa, S. and Pinho, F., 2006, "Pressure drop coefficient of laminar Newtonian flow in axisymmetric diffusers", *International Journal of Heat and Fluid Flow*, **27**(2), pp. 319-328.

Roulet, J. C., Volkel, R., Herzig, H.P., Verpoorte, E., de Rooij, N., and Dandliker, R., 2002, Performance of an Integrated Microoptical System for Fluorescence Detection in Microfluidic Systems, *Analytical Chemistry*, **74**, pp. 3400-3407

Ruano, J.M., Glidle, A., Cleary, A., Walmsley, A., Aitchison, J.S. and Cooper, J.M., 2003, "Design and fabrication of a silica on silicon integrated optical biochip as a fluorescence microarray platform", *Biosensors and Bioelectronics*, **18**(2-3), pp. 175-184.

Rusu, C., van't Oever, R., de Boer, M., Jansen, H., Berenschot, J., Bennink, M., Kanger, J., de Grooth, B., Elwenspoek, M. and Greve, J., 2001, "Direct integration of micromachined pipettes in a flow channel for single DNA molecule study by optical tweezers", *Journal of Microelectromechanical Systems*, **10**(2), pp. 238-246.

Scarmozzino, R., Gopinath, A., Pregla, R., and Helfert, S., 2000, "Numerical techniques for modeling guided-wave photonic devices" *IEEE Journal of Selected Topics in Quantum Electronics*, **6**(1), pp. 150-162.

- Schomburg, W., Vollmer, J., Bustgens, B., Fahrenberg, J., Hein, H. and Menz, W., 1994, "Microfluidic components in LIGA technique", *Journal of Micromechanics and Microengineering*, **4**, pp. 186-191.
- Schueller, O.J.A., Zhao, X.M., Whitesides, G.M., Smith, S.P. and Prentiss, M., 1999, "Fabrication of liquid-core waveguides by soft lithography", *Advanced Materials*, **11**(1), pp. 37-41.
- Schwarz, M.A. and Hauser, P.C., 2001, "Recent developments in detection methods for microfabricated analytical devices", *Lab on a chip*, **1**(1), pp. 1-6.
- Seo, J. and Lee, L.P., 2004, "Disposable integrated microfluidics with self-aligned planar microlenses", *Sensors & Actuators: B.Chemical*, **99**(2-3), pp. 615-622.
- Shelby J.P., Lim D.S.W., Kuo J.S., Chiu D.T.: 'High radial acceleration in microvortices', *Nature*, 2003, 425, p. 38
- Shen, C.Y. and Liu, H.K., 2008, "Fabrication and drive test of piezoelectric PDMS valveless micro pump", *Journal of the Chinese Institute of Engineers*, **31**(4), pp. 615-623.
- Sheridan, A., Stewart, G., Ur-Reyman, H., Suyal, N. and Uttamchandani, D., 2009, "In-Plane Integration of Polymer Microfluidic Channels With Optical Waveguides—A Preliminary Investigation", *IEEE Sensors Journal*, **9**(12), pp. 1627.
- Singh, R. and Peles, Y., 2009, "The effects of fluid properties on cavitation in a micro domain", *Journal of Micromechanics and Microengineering*, **19**(2), 025009:1-8.
- Singhal, V., Garimella, S.V. and Murthy, J.Y., 2004, "Low Reynolds number flow through nozzle-diffuser elements in valveless micropumps", *Sensors & Actuators: A.Physical*, **113**(2), pp. 226-235.
- Skivesen, N., Horvath, R., Thinggaard, S., Larsen, N.B. and Pedersen, H.C., 2007, "Deep-probe metal-clad waveguide biosensors", *Biosensors & bioelectronics*, **22**(7), pp. 1282-1288.
- Sousa, P., Pinho, F., Oliveira, M. and Alves, M., 2010, "Efficient microfluidic rectifiers for viscoelastic fluid flow", *Journal of Non-Newtonian Fluid Mechanics*, .
- Splawn, B.G. and Lytle, F.E., 2002, "On-chip absorption measurements using an integrated waveguide", *Analytical and bioanalytical chemistry*, **373**(7), pp. 519-525.
- Splawn, B.G. and Lytle, F.E., 2002, "On-chip absorption measurements using an integrated waveguide", *Analytical and bioanalytical chemistry*, **373**(7), pp. 519-525.
- Steinfeldt-Visscher J, Teerenstra S, Gunnewiek JM, and Weerwind PW., 2008, "Evaluation of the i-STAT point-of-care analyzer in critically ill adult patients.", *J Extra Corpor Technol.*, **40**(1), pp. 57-60.

- Stemme, E. and Stemme, G., 1993, "A valveless diffuser/nozzle-based fluid pump", *Sensors and Actuators A: Physical*, **39**(2), pp. 159-167.
- Stroock, A.D. and Whitesides, G.M., 2003, "Controlling flows in microchannels with patterned surface charge and topography", *Accounts of Chemical Research*, **36**(8), pp. 597-604.
- Strook, A., Dertinger, S., Ajdari, A., Mezic, I., Stone, H., and Whitesides, G., 2002, "Chaotic mixer for microchannels" *Science*, **295**, pp. 647–651.
- Su, X.T., Singh, K., Capjack, C., Petreck, J., Backhouse, C. and Rozmus, W., 2008, "Measurements of light scattering in an integrated microfluidic waveguide cytometer", *Journal of Biomedical Optics*, **13**, pp. 024024.
- Suárez, G., Jin, Y.H., Auerswald, J., Berchtold, S., Knapp, H.F., Diserens, J.M., Leterrier, Y., Månson, J.A.E. and Voirin, G., 2009, "Lab-on-a-chip for multiplexed biosensing of residual antibiotics in milk", *Lab on a Chip*, **9**(11), pp. 1625-1630.
- Sukas, S., Elif Erson, A., Sert, C. and Kulah, H., 2008, "A parylene-based dual channel micro-electrophoresis system for rapid mutation detection via heteroduplex analysis Abbreviations: HDA heteroduplex analysis  $\mu$ -CE microchip capillary electrophoresis PR photoresist", *Electrophoresis*, **29**(18), pp. 3752–3758.
- Sun, C. and Lin, G.C., 2010, "The Flow Rectification of a Vaned Microdiffuser: A Numerical Investigation", *Journal of the Chinese Institute of Engineers*, **33**(1), pp. 1-13.
- Sun, C. and Yang, Z.H., 2007, "Effects of the half angle on the flow rectification of a microdiffuser", *Journal of Micromechanics and Microengineering*, **17**, pp. 2031.
- Sundaram, N., and Tafti, D. K., 2004, "Evaluation of Microchamber Geometries and Surface Conditions for Electrokinetic Driven Mixing" *Analytical Chemistry*, **76** (13), pp. 3785 -3793.
- Szabo, Z., Kadar, G., Balazs, J., 2006, "Simulation of photonic crystal waveguides with dispersion", *Current Applied Physics*, **6**, pp. 149–153
- Tabeling, P., 2005, "Introduction to microfluidics" *Oxford University Press*
- Tadd, A.R., Gould, B.D. and Schwank, J.W., 2005, "Packed bed versus microreactor performance in autothermal reforming of isooctane", *Catalysis Today*, **110**(1-2), pp. 68-75.
- Tanaka, M., Matsuura, K., Yoshioka, S., Takahashi, S., Ishimori, K., Hori, H. and Morishima, I., 2003, "Activation of Hydrogen Peroxide in Horseradish Peroxidase Occurs within 200  $\mu$ s Observed by a New Freeze-Quench Device", *Biophysical journal*, **84**(3), pp. 1998-2004.

Tang, J., Cheng, S., F., Hsu, W., T., Chiang, T.Y., and Chau, L.K., 2006, "Fiber-optic biochemical sensing with a colloidal gold-modified long period fiber grating" *Sensors and Actuators B: Chemical*, **119**(1), 2006, pp. 105-109

Tarantino, A. and Mongiovi, L., 2001, "Experimental procedures and cavitation mechanisms in tensiometer measurements", *Geotechnical and Geological Engineering*, **19**(3), pp. 189-210.

Thrush, E., Levi, O., Ha, W., Wang, K., Smith, S.J. and Harris, J.S., 2003, "Integrated bio-fluorescence sensor", *Journal of Chromatography A*, **1013**(1-2), pp. 103-110.

Tien, J., Nelson, C.M. and Chen, C.S., 2002, "Fabrication of aligned microstructures with a single elastomeric stamp", *Proceedings of the National Academy of Sciences*, **99**(4), pp. 1758.

Tung C.-H., Wu L.-Z., Zhang L.-P., Li H.-R., Yi X.-Y., Kai Song, Xu M., Yuan Z.-Y., Guan J.-Q., Wang H.-W., Ying Y.-M., and Xu X.-H., 2000, "Microreactor-controlled selectivity in organic photochemical reactions", *Pure and Applied Chemistry*, **72**(12); pp. 2289–2298.

Ullmann, A., Fono, I., Taitel, Y., 2001, "A Piezoelectric Valve-Less Pump-Dynamic Model", *Journal of Fluids Engineering*, **123**(1), pp. 92-99.

Ullmann, A., Fono, I., 2002, "The piezoelectric valve-less pump - improved dynamic model", *Journal of Microelectromechanical Systems*, **11**(6), pp. 655-664.

Upchurch Scientific, <http://www.upchurch.com>

Van de Pol, F.C.M., 1989, "A pump based on micro- engineering techniques", *PhD Thesis; University Twente; Netherlands*.

Van der Wijngaart, W., Andersson, H., Enoksson, P., Noren, K. and Stemme, G., 2000, "The first self-priming and bi-directional valve-less diffuser micropump for both liquid and gas", *Technical Digest, The 13th IEEE International Conference on MEMS, Miyazaki, Japan, 2000*, pp. 27.

Van Kan, J., Bettiol, A., Wee, B., Sum, T., Tang, S. and Watt, F., 2001, "Proton beam micromachining: a new tool for precision three-dimensional microstructures", *Sensors & Actuators: A.Physical*, **92**(1-3), pp. 370-374.

Verpoorte, E., Manz, A., Ludi, H., Widmer, H., van der Schoot, B., de Rooij, N. and Ciba-Geigy, B., 1991, "A novel optical detector cell for use in miniaturized total chemical analysis systems", *Solid-State Sensors and Actuators, 1991.Digest of Technical Papers, TRANSDUCERS'91, 1991 International Conference on*, , pp. 796-799.

Verpoorte, E., Schoot, B., Jeanneret, S., Manz, A., Widmer, H. and Rooij, N., 1994, "Three-dimensional micro flow manifolds for miniaturized chemical analysis systems", *Journal of Micromechanics and Microengineering*, **4**(4), pp. 246-256.

Vestad, T., Marr, D. and Oakey, J., 2004, "Flow control for capillary-pumped microfluidic systems", *Journal of Micromechanics and Microengineering*, **14**, pp. 1503-1506.

Vieillard, J., Mazurczyk, R., Morin, C., Hannes, B., Chevolut, Y., Desbene, P.L. and Krawczyk, S., 2007, "Application of microfluidic chip with integrated optics for electrophoretic separations of proteins", *Journal of chromatography.B, Analytical technologies in the biomedical and life sciences*, **845**(2), pp. 218-225.

Vilkner, T., Janasek, D. and Manz, A., 2004, "Micro total analysis systems. Recent developments", *Analytical Chemistry*, **76**(12), pp. 3373-3385.

Vollmer, F. and Arnold, S., 2008, "Whispering-gallery-mode biosensing: label-free detection down to single molecules", *Nature Methods*, **5**(7), pp. 591-596.

Wagner, F. and Hoffmann, P., 1999, "Structure formation in excimer laser ablation of stretched poly (ethylene terephthalate) (PET): the influence of scanning ablation", *Applied Physics A: Materials Science & Processing*, **69**, pp. 841-844.

Walther G., Jones G., Jensen S., Quaade U.J., and Horch S., 2009, "Oxidation of methane on nanoparticulate Au/TiO<sub>2</sub> at low temperature: A combined microreactor and DFT study", *Catalysis Today*, **142**, pp. 24-29.

Wang, G., Santiago, J., Mungal, M., Young, B. and Papademetriou, S., 2004, "A laser induced cavitation pump", *Journal of Micromechanics and Microengineering*, **14**, pp. 1037.

Wang, Y.C., Hsu, J.C., Kuo, P.C. and Lee, Y.C., 2009, "Loss characteristics and flow rectification property of diffuser valves for micropump applications", *International Journal of Heat and Mass Transfer*, **52**(1-2), pp. 328-336.

Webster, J.R., Burns, M.A., and Burke, D., 1998. "An inexpensive plastic technology for microfabricated capillary electrophoresis chips", *Micro total analysis systems' 98: proceedings of the [Mu] TAS'98 Workshop, held in Banff, Canada, 13-16 October 1998, 1998a*, Kluwer Academic Publishers, pp. 249.

Webster, J.R., Burns, M.A., Burke, D. and Mastrangelo, C.H., 2001, "Monolithic capillary electrophoresis device with integrated fluorescence detector", *Analytical Chemistry*, **73**(7), pp. 1622-1626.

Wego, A. and Pagel, L., 2001, "A self-filling micropump based on PCB technology", *Sensors & Actuators: A.Physical*, **88**(3), pp. 220-226.

West, J., Karamata, B., Lillis, B., Gleeson, J.P., Alderman, J., Collins, J.K., Lane, W., Mathewson, A. and Berney, H., 2002, "Application of magnetohydrodynamic actuation to continuous flow chemistry", *Lab on a Chip*, **2**(4), pp. 224-230.



- Weston, D., Smekal, T., Rhine, D. and Blackwell, J., 2001, "Fabrication of microfluidic devices in silicon and plastic using plasma etching", *Journal of Vacuum Science & Technology B: Microelectronics and Nanometer Structures*, **19**, pp. 2846.
- White, I.M., Zhu, H., Suter, J., Hanumegowda, N.M., Oveys, H., Zourob, M. and Fan, X., 2007, "Refractometric sensors for lab-on-a-chip based on optical ring resonators", *IEEE Sensors Journal*, **7**, pp. 28-35.
- Wilson, N.G. and McCreedy, T., 2000, "On-chip catalysis using a lithographically fabricated glass microreactor—the dehydration of alcohols using sulfated zirconia", *Chemical Communications*, **2000**(9), pp. 733-734.
- Woiias, P., 2005, "Micropumps—past, progress and future prospects", *Sensors & Actuators: B.Chemical*, **105**(1), pp. 28-38.
- Wolfe, B., Ashcom, J., Hwang, J., Schaffer, C., Mazur, E. and Whitesides, G., 2003, "Customization of poly (dimethylsiloxane) stamps by micromaching using a femto-second pulsed laser", *Advanced Materials (FRG)(Germany)*, **15**(1), pp. 62-65.
- Wu, J., Day, D. and Gu, M., 2008, "A microfluidic refractive index sensor based on an integrated three-dimensional photonic crystal", *Applied Physics Letters*, **92**, pp. 071108.
- Wu, S., Lin, Q., Yuen, Y. and Tai, Y., 2000, "MEMS flow sensors for nano-fluidic applications", *The Thirteenth Annual International Conference on Micro Electro Mechanical Systems, Miyazaki, Japan*, pp. 745-750.
- Xia, F., Tadigadapa, S. and Zhang, Q., 2006, "Electroactive polymer based microfluidic pump", *Sensors & Actuators: A.Physical*, **125**(2), pp. 346-352.
- Yalcin, A., Popat, K.C., Aldridge, J.C., Desai, T.A., Hryniewicz, J., Chbouki, N., Little, B.E., King, O., Van, V. and Chu, S., 2006, "Optical sensing of biomolecules using microring resonators", *Selected Topics in Quantum Electronics, IEEE Journal of*, **12**(1), pp. 148-155.
- Yalin, A., Popat, K.C., Aldridge, J.C., Desai, T.A., Hryniewicz, J., Chbouki, N., Little, B.E., King, O., Van, V. and Chu, S., 2006, "Optical Sensing of Biomolecules Using Microring Resonators", *IEEE Journal of Selected Topics in Quantum Electronics*, **12**(1), pp. 148 – 155.
- Yamahata, C., Lacharme, F., Burri, Y. and Gijs, M.A.M., 2005, "A ball valve micropump in glass fabricated by powder blasting", *Sensors & Actuators: B.Chemical*, **110**(1), pp. 1-7.
- Yang, B., Yang, L., Hu, R., Sheng, Z., Dai, D., Liu, Q. and He, S., 2009, "Fabrication and characterization of small optical ridge waveguides based on SU-8 polymer", *Journal of Lightwave Technology*, **27**(18), pp. 4091-4096.

- Yang, H., Deschatelets, P., Brittain, S. and Whitesides, G., 2001a, "Fabrication of high performance ceramic microstructures from a polymeric precursor using soft lithography", *Advanced Materials*, **13**(1), pp. 54-58.
- Yang, K.S., Chen, Y., Shew, B.Y. and Wang, C.C., 2004, "Investigation of the flow characteristics within a micronozzle/diffuser", *Journal of Micromechanics and Microengineering*, **14**, pp. 26-31.
- Yang, Y., Zhou, Z., Ye, X. and Jiang, X., 1996, "Bimetallic thermally actuated micropump", *The 1996 ASME International Mechanical Engineering Congress and Exposition, Atlanta, GA, USA, 11/17-22/96*; pp. 351-354. 1996, ASME, New York, USA, pp. 351-354.
- Yegnanarayanan, S., Roman W., Soltani, M., Cremona, G., Lu, H., and Adibi, A., 2007. "On-chip Integration of Microfluidic Channels with Ultra-high Q Silicon Microdisk Resonators for Lab-on-a-Chip Sensing Applications", *The 20th Annual Meeting of the IEEE Lasers and Electro-Optics Society, 2007, LEOS. 2007*, , pp. 50-51.
- Yuan, H., Ouz, H. and Prosperetti, A., 1999, "Growth and collapse of a vapor bubble in a small tube", *International Journal of Heat and Mass Transfer*, **42**(19), pp. 3643-3657.
- Yuqing, M., Jianguo, G. and Jianrong, C., 2003, "Ion sensitive field effect transducer-based biosensors", *Biotechnology Advances*, **21**(6), pp. 527-534.
- Zellner, P., Renaghan, L., Hasnain, Z. and Agah, M., 2010, "A fabrication technology for three-dimensional micro total analysis systems", *Journal of Micromechanics and Microengineering*, **20**, pp. 045013.
- Zellner, P., Renaghan, L., Hasnain, Z. and Agah, M., 2010, "A fabrication technology for three-dimensional micro total analysis systems", *Journal of Micromechanics and Microengineering*, **20**, pp. 045013.
- Zeng, J. and Korsmeyer, T., 2004, "Principles of droplet electrohydrodynamics for lab-on-a-chip", *Lab on a Chip*, **4**(4), pp. 265-277.
- Zheng, Z.P., Cheng, W.H., Huang, F.Y. and Yan, B.H., 2007, "3D microstructuring of Pyrex glass using the electrochemical discharge machining process", *Journal of Micromechanics and Microengineering*, **17**, pp. 960-966.
- Zhong, J.F., Chen, Y., Marcus, J.S., Scherer, A., Quake, S.R., Taylor, C.R. and Weiner, L.P., 2008, "A microfluidic processor for gene expression profiling of single human embryonic stem cells", *Lab on a Chip*, **8**(1), pp. 68-74.
- Zourob, M., Mohr, S. and Goddard, N., 2007, "Integrated Deep-Probe Optical Waveguides for Label Free Bacterial Detection", *International Symposium on Signals, Systems and Electronics, ISSSE'07*, pp. 49-52.

Zourob, M., Mohr, S., Fielden, P. and Goddard, N., 2003, "Small-volume refractive index and fluorescence sensor for micro total analytical system ( $\mu$ TAS) applications", *Sensors and Actuators B: Chemical*, **94**(3), pp. 304-312.

Zourob, M., Mohr, S., Fielden, P.R. and Goddard, N.J., 2005, "An integrated disposable dye clad leaky waveguide sensor for micro-TAS applications", *Lab on a chip*, **5**(7), pp. 772-777.